DESIGN STUDY FOR LANDSAT-D ATTITUDE CONTROL SYSTEM

February 1977

Contract No. NAS5-21188

Prepared for

NASA GODDARD SPACE FLIGHT CENTER
Greenbelt, Maryland 20771

TRW
DEFENSE AND SPACE SYSTEMS GROUP

ONE SPACE PARK • REDONDO BEACH • CALIFORNIA 90278

FINAL TECHNICAL REPORT

DESIGN STUDY FOR LANDSAT-D ATTITUDE CONTROL SYSTEM

February 1977

Prepared by: R. P. Iwens
G. E. Bernier
R. F. Hofstadter
R. A. Mayo
H. Nakano

Approved by: _____
A. M. Frew, Manager
Control Systems Engineering Department

Approved by: _____
W. A. Finley, Manager
Control and Sensor Systems Lab

Contract NAS5-21188

Prepared for

National Aeronautics and Space Administration
Goddard Space Flight Center
Greenbelt, Maryland 20771

TRW
DEFENSE AND SPACE SYSTEMS GROUP

SUMMARY

This final technical report addresses design and performance evaluation of the LANDSAT-D attitude control system (ACS). The baseline system concept for LANDSAT-D is the NASA Multi-Mission Modular Spacecraft (MMS). Control and configuration of the gimballed Ku-band antenna system for communication with the Tracking and Data Relay Satellite (TDRS), and control of the solar array drive, are considered a part of the ACS and are also addressed here. An interim technical report for this study was published in December 1976. The present final technical report covers the entire study and the material presented earlier in the interim report is also included here.

Considerable effort has been expended in the study on the gimballed Ku-band antenna system for communication with TDRS. By means of an error analysis it is demonstrated that the antenna cannot be open loop pointed to TDRS by an on-board programmer but that an autotrack system is required. After some tradeoffs, a two-axis, azimuth-elevation type gimbal configuration is recommended for the antenna. It is shown that gimbal lock only occurs when LANDSAT-D is over water where a temporary loss of the communication link to TDRS is of no consequence. A preliminary gimbal control system design is also presented.

A digital computer program was written that computes antenna gimbal angle profiles, assesses percent antenna beam interference with the solar array (as a function of antenna mast length), and determines whether the spacecraft is over land or water, a lighted earth or a dark earth, and whether the spacecraft is in eclipse. Besides checking for optical blockage of the antenna beam by the solar array paddle, another important application of this program is to determine when the spacecraft is over lighted land, since this is directly proportional to the Thematic Mapper (TM) electric power duty cycle. For one typical 15 orbit (24 hours) case, the spacecraft spent only 16.5% of the time over lighted land.

A solar array control strategy was developed that eliminates interference with the Ku-band antenna beam. The array is driven at orbit rate as long as the spacecraft is within ±45 degrees of the ecliptic plane. When the spacecraft is outside this region the array is kept fixed at the orientation it had at ± 45 degrees away from the ecliptic and this orientation is maintained until the earth becomes dark. At that point the array is slewed again to its optimal position normal to the sun line and it continues to track the sun until the spacecraft goes into eclipse. This strategy requires the Ku-band antenna mast to be only 2.11 meters (6.9 feet) in length in order to eliminate all interference. The key is the 37.5 degree cant in the array which permits the antenna to look past the array when it is within ± 45 degrees of the ecliptic. Outside this region the array would rapidly obstruct the field-of-view of the antenna if it were not stopped as described above. The total power loss associated with this solar array control strategy is only 4% and it can be easily compensated for by increasing the array area by 4%. The 2.11 meter long antenna mast has been computed for a 4% increased array area.

External disturbance torques acting on LANDSAT-D were modelled and sized. Aerodynamic, gravity gradient, magnetic, and solar-pressure disturbance torques were considered. Ku-band antenna mast length and antenna orientation were observed to affect the magnitude of the disturbance torques only insignificantly.

The disturbance torque sizing results were then used to assess whether the four 20 Nms (15 foot-pound-seconds) reaction wheels and the three orthogonal 100,000 pole-cm magnetic torque bars provided in the MMS ACS module have sufficient capability for the LANDSAT application. The conclusions were that the spacecraft can operate effectively in its 705 km orbit environment even when using only the 50,000 pole-cm windings on the magnetic bars. Momentum excursions in the wheels were observed to be less than ± 2.0 Nms of nominal and since the reaction wheel momentum storage capacity is 20 Nms, it is recommended that all four wheels be run at a biased speed. This avoids wheel speed reversal and associated attitude transients due to nonlinear wheel friction. The four wheels are speed biased such that a net

zero momentum system results (not possible with only three wheels). Should one wheel fail, then the three remaining wheels must be operated about zero speed and the wheel speed reversal attitude transients of about 90 μrad (18.5 arc-seconds) must be accepted. This would occur about four times per orbit, mainly in roll, due to the interaction of the external disturbance torques with the magnetic unloading law.

Initialization of the fine control mode is addressed in this report. Two methods to perform fine stellar acquisition, i.e., to initialize the on-board stellar-inertial attitude reference system, are presented. Before entering the stellar acquisition mode the spacecraft is sun pointing (in the fine sun acquisition mode) and only a relatively coarse determination of the spacecraft orientation about the sun line is needed for correct star identification. One method uses magnetic field measurements and is capable of providing attitude knowledge about the sun line within about 2 degrees. The other method correlates observed stars in a swath about the sun line with star catalog entries and determines attitude about the sun line to within approximately 0.2 degree (uncalibrated gyros assumed). The magnetic field measurement method is simpler and the 2 degree attitude knowledge is sufficient for unambiguously identifying the first few stars when the stellar-inertial attitude reference system is initialized. Using the real star field it is demonstrated that the linearized (extended) Kalman filter algorithm assumed to be used by the on-board attitude reference system is capable of converging rapidly from large (2 degrees) initial attitude uncertainties. The converged attitude reference filter predicted accuracies in the 5 to 10 arc-second (1σ) range and the gyro biases were calibrated to within about 0.0013 degree/hour.

A normal on-orbit ACS design was conducted using all four reaction wheels in speed biased mode of operation to avoid wheel speed reversals. Performance was assessed by analysis and simulation and the specified 0.01 degree (1σ) pointing accuracy could be met, even when the ephemeris error (assumed as 300 meters, 3σ) was included. The specified 10.5 μrad (1σ) attitude stability (jitter) over 20 minutes could also be met, but with only a small design margin. The major contributors to the attitude jitter are

the single-sided, stepped, flexible solar array (FRUSA) with 2.8 μrad, the gyro random drift effects in the attitude reference system with about 8 μrad, and the gyro noise effect in the ACS rate loop with 1.8 μrad (all 1σ). Controller dynamics contributed 1.5 μrad due to the magnetic unloading laws. Effects of reaction wheel mass imbalance (0.5 $inch^2$-ounces assumed), fast Ku-band antenna motions near gimbal lock, and the rocking scan mirror motions of the Multi-Spectral Scanner (MSS) and the Hughes version of the Thematic Mapper (TM) contribute only very little to the vehicle jitter in the rigid body sense. The TRW version of the TM does not contribute at all to attitude jitter since its scan wheel rotates at a constant speed in steady-state operation. Effects of the flexible Ku-band antenna mast are quite small since in steady-state operation the flexible mast is not excited and since the flexible mode is well damped. A mast damping of about 0.27 could be obtained when the natural frequency of the mast was at about 70% of the bandwidth of the gimbal servo. A stiffer mast with higher natural frequency reduced the achievable dynamic damping of the mast, but the decay time constant of the oscillations remained constant (or even decreased), since the frequency had increased. Thus, a stiff, short mast is desirable, but a softer mast can be used provided its natural frequency is within the bandwidth of the gimbal controller. A 10 foot boom (mast) with stiffness of 350,000 $pound\text{-}feet^2$ corresponding to a boom-tip-mass natural frequency of 30 rad/second yielded good performance for gimballed antenna controllers having autotrack bandwidths of BW = 22 rad/second or 44 rad/second. For the BW = 44 rad/second gimbal servo a damping ratio of $\zeta = 0.27$ was achieved with a boom time constant of $\tau_{boom} = 0.124$ second. Thus, vehicle jitter due to boom vibration transients excited during abrupt and rapid antenna motions, are damped out fast.

A study of the periodic velocity correction for maintaining the orbit of LANDSAT-D showed that it was necessary to use all four 5 pound thrusters in an open loop, preprogrammed differentially modulated fashion. The latter was necessitated by a significant, known center of mass offset. Unless this offset is reduced substantially (by balancing), there is no thruster redundancy for this operation. The unknown components of the disturbance

torques due to thruster misalignments and thrust variations are smaller than the known components, so that pointing of the thrust vector, i.e., spacecraft attitude control, can be maintained by either the 0.2 pound or the closed loop modulated 5 pound thrusters. The rotational motion about the thrust vector must be controlled by the smaller thrusters. Although the relatively large disturbance torques preclude the use of the reaction wheel system, the thrust vector pointing can be maintained to within $\pm$ 0.2 degree with the peak limit cycle rate less than 0.25 degree/second. The required duration of thruster actuation is slightly over 8 seconds for an orbit adjust maneuver of ΔV = 0.35 meter/second which will be required every 16 days.

Attitude determination and attitude control software requirements were also established assuming that the NASA Standard Space Computer, NSSC-1, is used. Total memory requirement was established as about 4000 words of program memory and 2150 words of read/write memory. Computation time per minor cycle (400 mseconds) during normal on-orbit operations is 44.4 mseconds when no ephemeris benchmarks or star data are being processed; with star data processing and ephemeris and attitude update computations, the computation time is 316.8 mseconds. The latter includes also acquisition of the TDRS link by the gimballed Ku-band antenna which in this mode is under spacecraft computer control. In the normal mode of operation the Ku-band antenna functions autonomously maintaining lock on TDRS via an autotrack system.

An exploratory study of temporal autonomous registration of the TM boresight was also conducted. The desired registration accuracy is 3 meters (1σ) on the ground. This corresponds to 10% of the TM's resolution limit, i.e., 10% of the 30 x 30 meters instantaneous field-of-view (pixel). The recommended approach uses, in part, cooperative landmark registration deviations to estimate pseudo attitude and attitude rate commands for eliminating registration errors caused by changes in spacecraft position, velocity, attitude, gyro bias, and TM to attitude reference system (ARS) misalignments between successive 16 day passes. Stellar and gyro inertial references are used to determine the spacecraft attitude. The DOD Navigation Satellite Global Positioning System (GPS) is assumed to be used to determine spacecraft ephemeris.

In summary, a TM boresight registration accuracy of 3 meters (1σ) can be achieved if measurements/estimates of the LANDSAT-D inertial attitude, ephemeris, and cooperative landmark registration deviations (between successive 16 day passes) are known to within the following accuracies:

Inertial Attitude:	0.707 arc-sec (1σ)
Ephemeris:	2.12 meters (1σ) (every 200 sec)
Landmark Registration Deviation:	2.12 meters (1σ) (every 200 sec)

It is assumed that landmark and ephemeris updates are available every 200 seconds. The above requirements push the limit of the current state-of-the-art in satellite attitude and ephemeris determination. However, with the advent of GPS and through the use of high quality stellar-inertial sensors, the goal may be achievable in the future.

It became apparent during the study that additional, more detailed work should be performed in a number of areas. Flexible body dynamics and excitation of spacecraft structural modes are of foremost concern. The effects of a highly flexible, canted array on spacecraft attitude stability (jitter) should be investigated using more complex and more realistic two-axis models (required because of the 37.5 degree array cant angle) than the simple single-axis models that were used here. Analytic results should be verified by simulation. A good single-axis, planar model of the flexible antenna boom is presented in this study. This model should be used to construct a simulation that can be utilized to examine how the expected normal on-orbit antenna gimbal angle motions affect the excitation of the boom flexible mode. Even though it has been shown that the boom mode can be very well damped by appropriate gimbal servo design, continuous low level excitation of the mode could couple into the vehicle causing undesirable jitter effects during normal operations. This should be especially investigated when the antenna is tracking TDRS near gimbal lock and higher rates and accelerations are called for.

In a rigid body sense, reaction wheel mass imbalance and MSS and TM (Hughes version) scan mirror motions cause little concern. But these small, periodic disturbances could excite spacecraft structural bending modes at their respective frequencies. Work in this area requires a detailed structural model of the MMS to assess the situation. The periodic disturbances occur usually at frequencies considerably above the ACS bandpass. However, they still may be within the bandpass of the gyros. When the gyros are sampled at a rate compatible with the low frequency requirements of the ACS, these higher frequency body rate signals will be aliased and could produce erroneous gyro measurements. A brief preliminary investigation conducted by simulation in this study showed that no adverse effects are expected from aliasing of higher frequency gyro signals because of the low power/amplitude of these signals. However, a more detailed analytical study of the problem should be made. Finally, the random drift characteristics of the DRIRU-II gyro pack should be reexamined as more data on these gyros becomes available, since meeting the 10.5 μrad jitter spec is significantly influenced by gyro quality.

TABLE OF CONTENTS

TABLE OF CONTENTS
(continued)

TABLE OF CONTENTS
(continued)

TABLE OF CONTENTS
(continued)

TABLE OF CONTENTS
(continued)

1.0 INTRODUCTION

TRW Defense and Space Systems has performed a series of Application Studies for NASA Goddard Space Flight Center under contract NAS5-21188. These studies have focused upon three-axis attitude control system designs employing momentum/reaction wheels with magnetic or thruster momentum unloading. The studies encompass conceptual design, system tradeoff, control law development, performance analysis and simulation, and hardware implementation considerations. The current study is directed toward design and performance evaluation of the LANDSAT D attitude control system (ACS). Control and configuration of the gimballed Ku-band antenna system for communication with the Tracking and Data Relay Satellite (TDRS), and control of the solar array drive are considered a part of the ACS and are also addressed here.

The LANDSAT D mission, a follow-on to LANDSAT's A, B, and C, is currently in the planning stages and it will utilize the NASA Multi-Mission Modular Spacecraft. It will fly at an altitude of 705 km in a sun synchronous, 9:30 a.m. (descending node) orbit. Complete earth coverage is obtained in 16 days; exact revisit time is 233 orbits. Launch is tentatively planned for early in 1981. The payload consists of a Thematic Mapper (TM) and a Multi-Spectral Scanner (MSS). Both sensors collect spectral radiation data of (lighted) land masses. This data will be used to produce land use theme maps to better manage the earth resources. Potential users have a broad spectrum of interests including agriculture, mineralogy, and urban planning, to cite a few. The spatial resolution of the Thematic Mapper is 30 meters corresponding to the 30 meter square footprint on the ground of a square detector in the instrument. The resolution of the MSS is 80 meters. The spacecraft pointing accuracy is specified as 0.01 deg (1σ) with a jitter stability of $\pm 10.5\mu$Rad (1σ) over 20 minutes. The ultimately desired temporal registration (essentially repeatability of ground track after 16 days) of the Thematic Mapper images is to be within 3 meters (1σ).

The primary objective of this study is to assess the adequancy of the Multi-Mission Modular Spacecraft (the MMS attitude control system in particular) to perform the LANDSAT-D mission, and to identify and configure mission peculiar equipment that may be required. Examples are the gimballed Ku-band antenna and the single sided solar array and drive. To this end, preliminary design studies and performance assessments were conducted using the MMS as the baseline system concept. In particular, the following topics were addressed.

- Gimballed TDRS Ku-band antenna system: autotrack versus programmed pointing, gimbal lock problem and gimbal control.
- Gimballed TDRS antenna mast height and solar array interference with the antenna beam.
- Percent time when LANDSAT-D is over lighted land/Thematic Mapper duty cycle.
- External disturbance torques.
- Initialization of fine control.
- Normal on-orbit attitude control including the effects of internal spacecraft motions and the effects of flexible appendages (mast and solar array); on-board software sizing.
- LANDSAT-D stationkeeping.
- Feasibility of autonomous Thematic Mapper boresight registration.

These topics are studied using both analysis and simulation where required. Section 2.0 describes the LANDSAT-D mission in more detail. Important currently available mission data is summarized and a brief description of the MMS and the two payload sensors is provided. Section

3.0 addresses various problems associated with the gimballed Ku-band antenna system, Section 4.0 examines external disturbance torques and Section 5.0 the initialization of the fine pointing control mode. Section 6.0 treats normal on-orbit attitude control and performance evaluation addressing also internal motion and flexible appendages. Stationkeeping/ altitude control is discussed in Section 7.0. Section 8.0 addresses autonomous Thematic Mapper boresight registration and Section 9.0 provides on-board software sizing estimates.

2.0 LANDSAT-D MISSION

LANDSAT-D is the planned fourth mission in the LANDSAT program whose primary objective is to evaluate and monitor the earth's resources from satellite observations. Formerly, this program was known as the Earth Resources Technology Satellite (ERTS) program. The spacecraft to be flown on the LANDSAT-D mission, as well as the mission itself, have in the past also been referred to as LANDSAT Follow-On (LF/O). The primary mission payload sensor for LANDSAT-D (L-D) is the Thematic Mapper (TM), a large multi-spectral instrument which uses solid state detectors to produce earth imaging data which is digitized and transmitted to the ground in a 120 megabit per second serial data stream. Potential users of TM data have a broad spectrum of interests including agriculture, mineralogy, and urban planning, to cite a few.

Agriculture as it relates to the economy and to the world food supply is one of the driving forces behind the LANDSAT program. Data from the Thematic Mapper can be used to determine how much wheat, corn, barley, etc. have been planted, how well the crops are doing, and combined with watershed data also collected by the Thematic Mapper, predictions of yield can be made. The system can collect this data on a world-wide basis. The public benefit is expected to be enormous. Shortages can be predicted and additional acerage planted - perhaps in a different hemisphere. Surpluses in one crop may be avoided by planting different crops. Effects of disease or insects can be assessed and hopefully minimized by early detection.

Two LANDSAT spacecraft are currently in orbit, LANDSAT's A and B, with an instrument known as the Multi-Spectral Scanner (MSS) being their primary payload sensor; the MSS is basically a smaller and less advanced/less powerful version of a Thematic Mapper type instrument. LANDSAT's A and B are producing image data which is primarily being used for research in remote sensing technology, data interpretation techniques, etc. A third spacecraft, LANDSAT-C, is being prepared for launch with a modestly upgraded Multi-Spectral Scanner instrument which will include a long wave infra red (10.5 to 12 microns) sensing capability in addition to the four

spectral bands carried on LANDSAT's A and B. This upgraded version of the MSS will also be flown as a secondary payload on LANDSAT-D. It will provide continuing service to users who have not yet upgraded their ground stations and data processing capabilities to handle Thematic Mapper data. It will also provide an opportunity to directly compare spectral signature data from the two instruments, maximizing learning transfer and enhancing capability to compare Thematic Mapper data with historic MSS data.

2.1 LANDSAT-D Orbital Data

The LANDSAT-D (L-D) spacecraft will fly in a circular, 9:30 a.m., descending node, sun synchronous orbit. The terminology "sun-synchronous" refers to the property that the line of nodes of the orbit advances at the same rate as the earth's orbital rate about the sun. The orbit altitude is 705 km (380 nautical miles) and the orbit plane inclination is 98.2 degrees. The orbital period can be calculated as 1.648 hours (98.88 minutes), or stating it differently, there are exactly 14 9/16 orbits in a 24 hour period. Figure 2-1 shows the L-D orbit relative to the earth equatorial plane at vernal equinox, illustrating the 9:30 a.m. sun synchronous orbit feature. It simply means that throughout the year the spacecraft will cross the equator on its north-to-south descending pass at 9:30 a.m. local ground time. Since the orbit is almost polar, the ground time is close to 9:30 a.m. over the entire sun lit side of the earth, and close to 9:30 p.m. over the entire dark side of the earth.

Nominally the Thematic Mapper (TM) data is transmitted in real time from the L-D to a geostationary Tracking and Data Relay Satellite (TDRS) which retransmits the data to the ground. By 1981 when L-D is scheduled to be launched, there will at least be two operational TDRS's in geosynchronous equatorial orbit. They will be positioned above the equator at the following longitudes.

- TDRS East: 41° West Longitude
- TDRS West: 171° West Longitude

The TDRS equatorial orbit is also indicated in Figure 2-1.

LANDSAT-D Orbit Summary

- 9:30 a.m., descending node, sun synchronous orbit
- Inclination i = 98.2 deg
- Altitude h = 705 km
- Orbit Period T_o = 1.648 hrs
- Orbit Rate ω_o = 0.06068 deg/sec

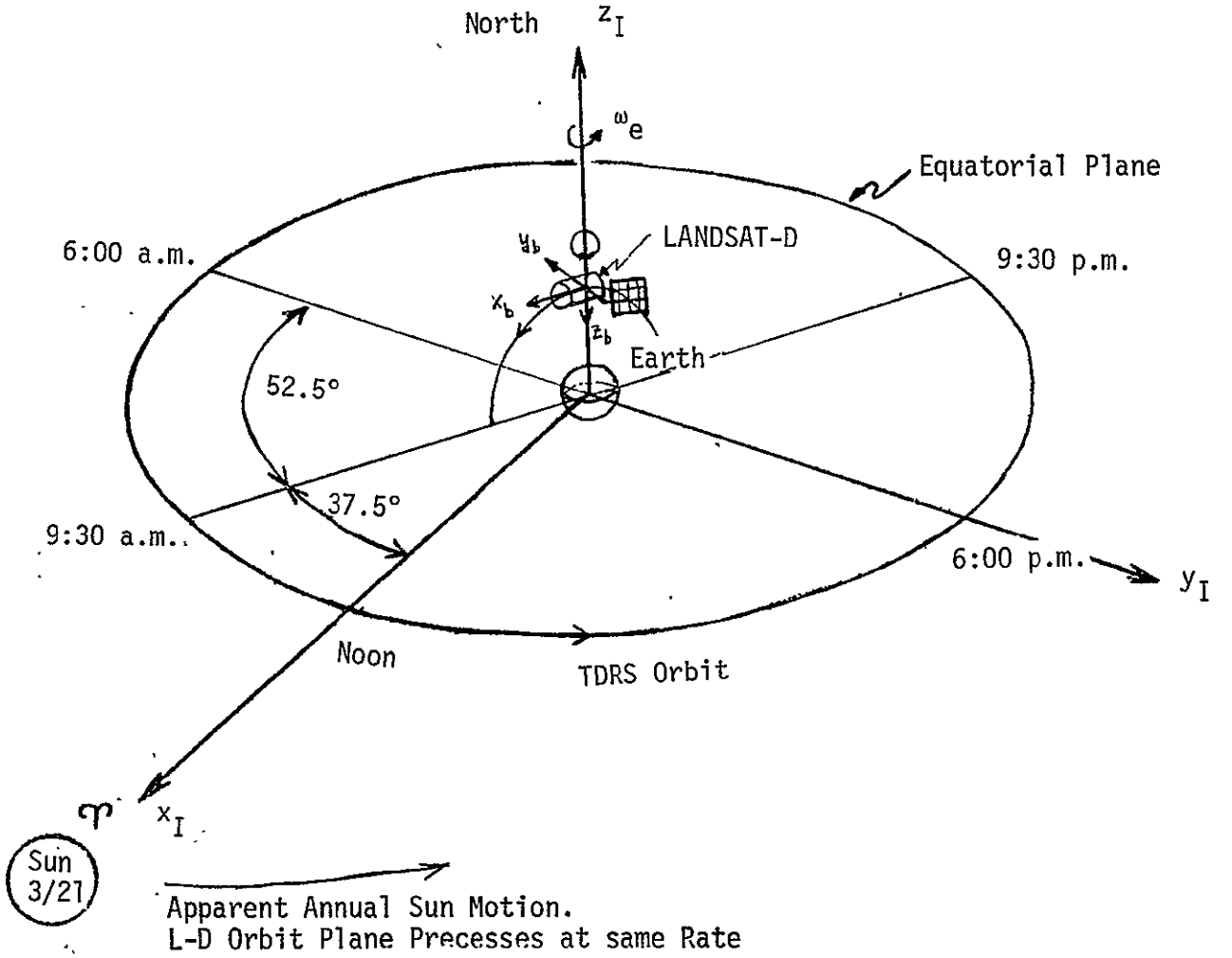

Figure 2-1. LANDSAT-D Orbit

Solar time on earth repeats at integer multiples of 24 hours. Let T_o be the L-D orbit period in hours. Then the smallest number of orbits n such that $n\ T_o$ is an integer multiple of 24 hours is the L-D revisit time, i.e., the satellite will be exactly above the same point on earth after exactly n orbits (ideal orbits assumed). If the north-south ground path illuminated by the payload sensor field of view is chosen to be of appropriate width, then the revisit time is also the time it takes to obtain total earth coverage, i.e., obtain data from the entire earth surface, with the exception of two small regions about each of the earth's poles which cannot be seen because the orbit inclination is 98.2 degrees, that is, more than 90 degrees. Since the orbit period of L-D is

$$T_o = \frac{24}{14\ 9/16} = \frac{(24)\ x\ (16)}{233}\ \text{hrs}$$

one must find the smallest integer n such that

$$\frac{(24)\ x\ (16)}{233}\ n = 24\ m$$

where m must be an integer. This leads to m = 16 and n = 233. Thus the revisit time is 16 days during which the spacecraft completes 233 orbits.

L-D is scheduled to be launched in 1981 on a Thor Delta 3910 booster, but the spacecraft and payload designs must also be compatible with future launch, resupply, and retrieval by the Space Shuttle. L-D mission life has been preliminarily specified as 3 years.

After orbit insertion of the spacecraft, initial orbit corrections are performed to assure orbit circularity and correct altitude and orbit inclination. Thereafter, ΔV stationkeeping maneuvers will only be performed to make up for orbit decay due to atmospheric drag. A $\pm$ 6.5 km E-W ground track drift due to spacecraft altitude and attendant orbit period change is the maximum permissible error. Using a conservative drag model, this implies that the orbital velocity must be corrected by applying a ΔV = 0.35 m/second at most every 16 days.

2.2 Spacecraft Configuration

Because the TM is a larger payload sensor than the MSS, the LANDSAT-D mission will require a new spacecraft design to support the TM's greater weight, provide more power, provide more accurate pointing control, and to relay higher data rates to the ground. It has been decided by NASA that the L-D mission will be performed using the Multi-Mission Modular Spacecraft (MMS). The MMS is a concept that has been developed by NASA Goddard Space Flight Center (GSFC) over the past 6 years. It was originally known as the Low Cost Modular Spacecraft and Reference 1 provides an excellent description of its projected characteristics and capabilities. The brief discussion that follows is entirely based on Reference 1, and the illustrations of the MMS in Figures 2-2 through 2-5 are those of Reference 1.

2.2.1 Multi-Mission Modular Spacecraft

The MMS is an independent three-axis stabilized vehicle using three or four reaction wheels in conjunction with a stellar-inertial attitude reference system to provide accurate and stable spacecraft attitude control. As the name implies, the MMS is composed of a set of standard modules: ACS module, Communications and Data Handling (CDH) module and Power module. The propulsion module is generally optional and comes in two standard versions known as SPS-I and SPS-II (L-D will require the SPS-I propulsion module). The baseline MMS configuration contains the above mentioned three subsystem modules supported by a module support structure, as shown in Figure 2-2. A transition adapter and a vehicle adapter complete the structural elements of the system. Mission unique and adapted items include the solar array, the solar array drive, the solar drive deployment mechanisms, a set of deployable TDRS antennas and booms, and a mission adapter and payload (see Figures 2-3 and 2-4). The three spacecraft modules are physically the same size. As shown in Figure 2-3, they measure 18 inches deep, 48 inches high, and 48 inches wide. The ACS module is of particular interest in this study and a preliminary equipment layout of the module is shown in Figure 2-5.

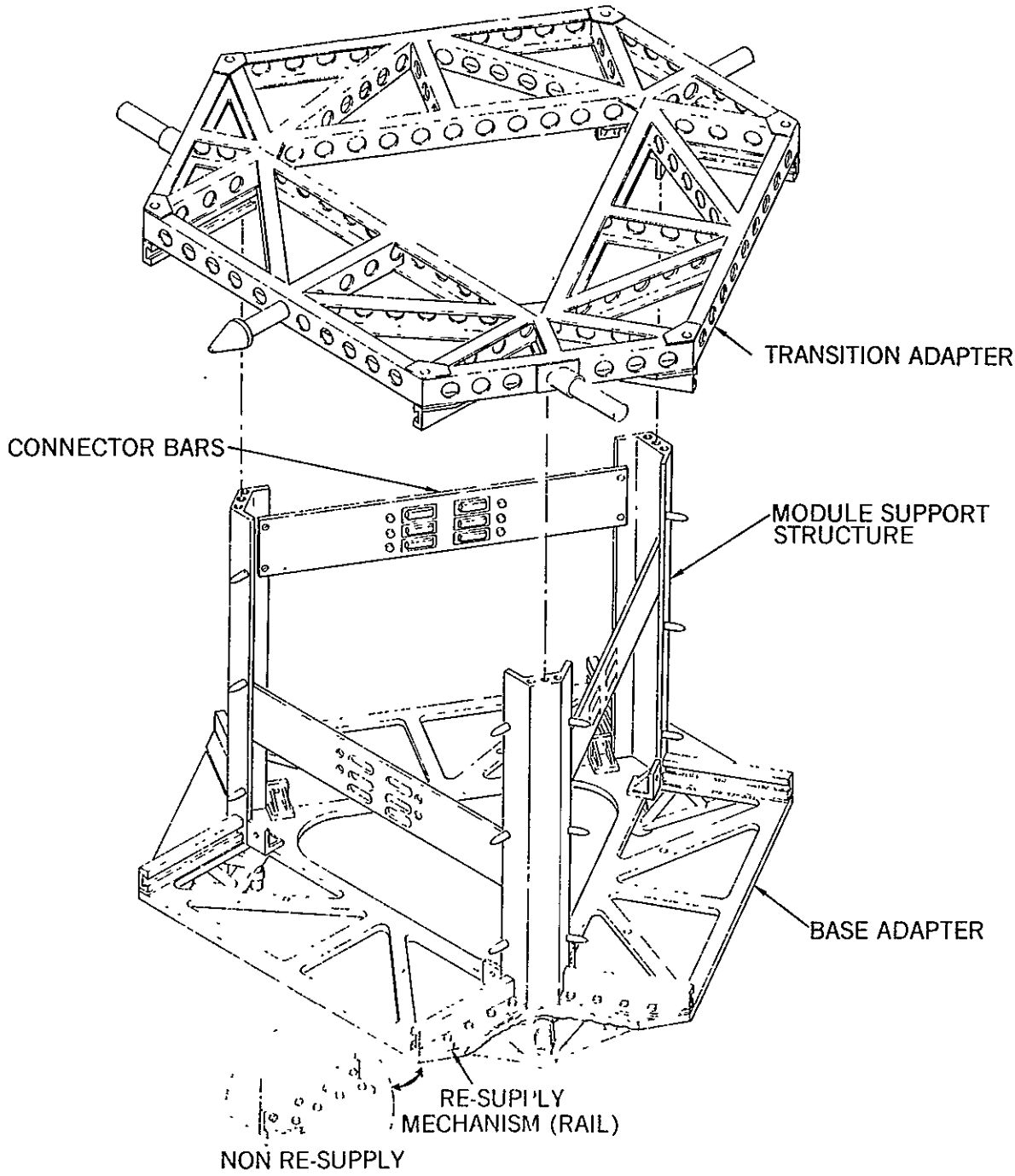

Figure 2-2. Module Support Structure
(Taken from Reference 1)

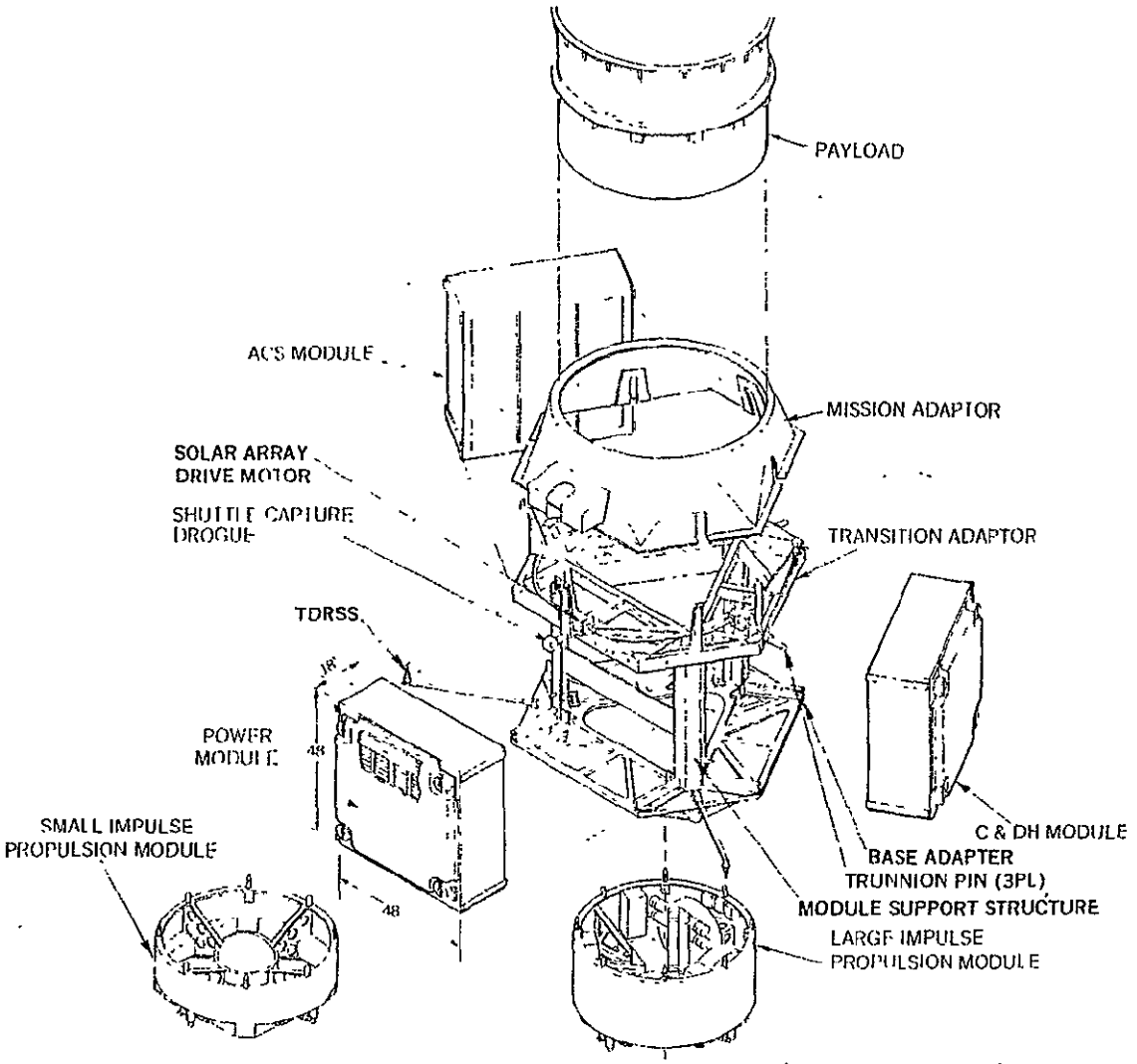

Figure 2-3. Multi-Mission Modular Spacecraft (Exploded View)
(Taken from Reference 1)

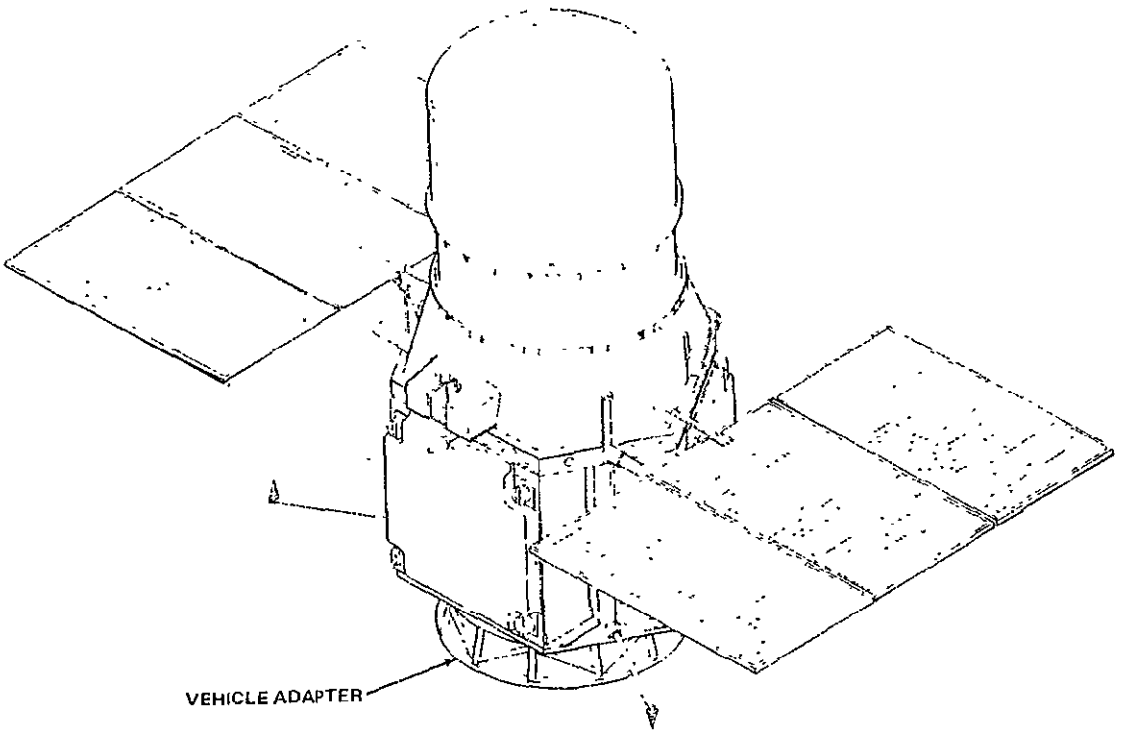

Figure 2-4. Multi-Mission Modular Spacecraft
(Taken from Reference 1)

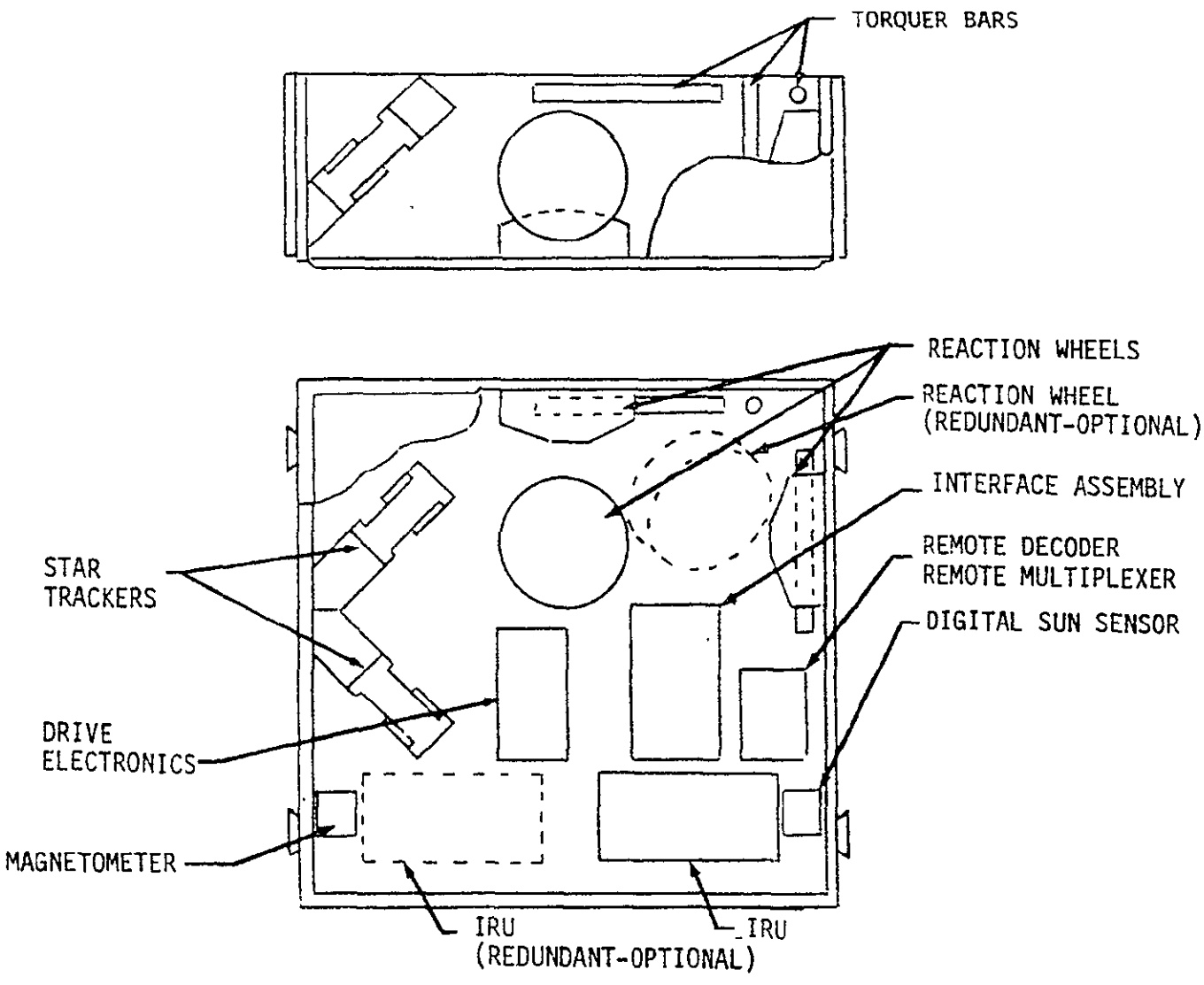

Figure 2-5. ACS Module

Alignment between the attitude control subsystem and the payload reference axis is maintained by the transition adapter during orbit operations. The transition adapter has other unique features which allow a shuttle orbiter capture, docking, retrieval and servicing by a manipulator system. The transition adapter also supports the solar array launch restraint and deployment mechanism and the solar array drive motors. The communication antennas are attached to the spacecraft to suit the mission. Optional attachment points include the area above the separation interface on the base adapter and also the transition adapter. The antennas and boom assembly can be folded into the recess formed by the adjacent edges of the modules. Total spacecraft weight without payload is 1235 pounds for the baseline configuration and 1590 pounds for the fully redundant configuration. This does not include the propulsion module.

2.2.2 LANDSAT-D Configuration and Mass Properties

Figure 2-6 shows a simplified block diagram of the L-D spacecraft system. On the left, the three standardized subsystem modules and their supporting structure is indicated. In the middle of Figure 2-6, the L-D payload is indicated. The payload instruments are supported by a mission unique forward structure and feed their output data to mission unique transmitters and antennas operating at K-band to handle the 120 megabit/second TM data rates. Capability is planned for real time relay via the Tracking and Data Relay Satellite System (TDRSS) to the continental U.S. and for direct downlink to K-band equipped ground stations in view of the spacecraft.

Figure 2-7 shows the overall L-D/MMS spacecraft in its on-orbit configuration with antennas and the solar array deployed. For this mission a one sided solar array is used to maintain clear fields of view for the passive radiation coolers used by both the TM and the MSS. For in flight replacement by the shuttle, the TM can be slid upward away from the nadir direction after disconnecting three attach fittings. The TDRSS compatible K-band antenna dish and transmitter are gimballed and deployed on a boom to allow the antenna more rotational freedom in tracking TDRS and to

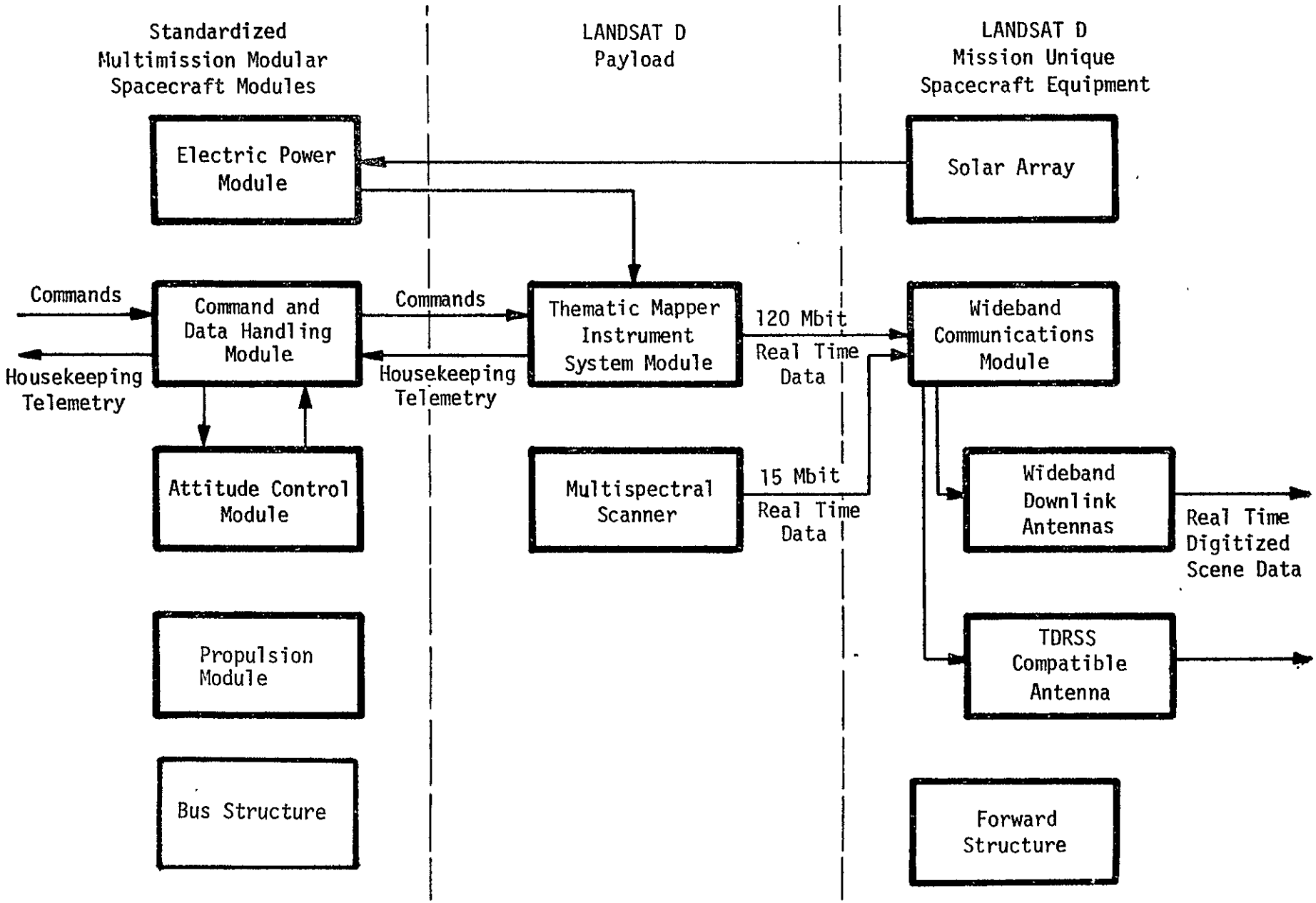

Figure 2-6. LANDSAT-D System Block Diagram

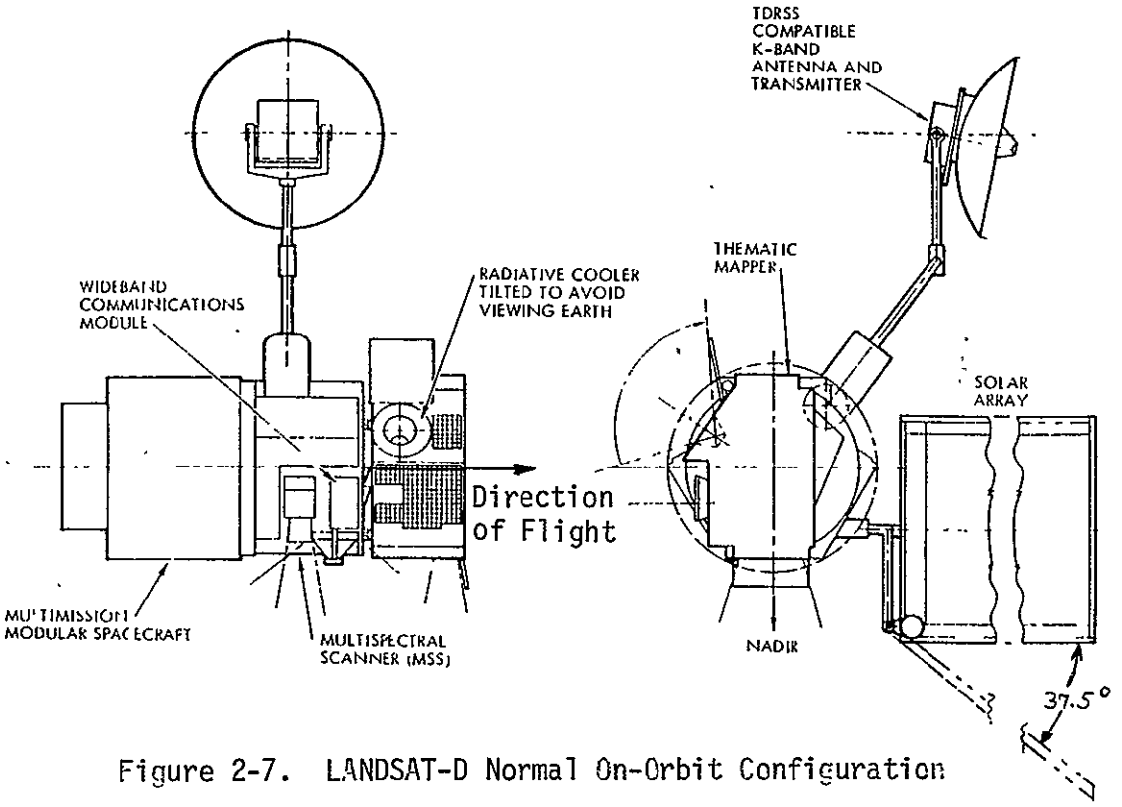

Figure 2-7. LANDSAT-D Normal On-Orbit Configuration

minimize antenna radiation pattern interference with the solar array and other parts of the spacecraft. The direct access antenna for downlink K-band communication is not shown in Figure 2-7.

The driven solar array is of the FRUSA type (Flexible Rolled-Up Solar Array developed by Hughes Aircraft Company) and it is canted 37.5 degrees relative to its axis of rotation (parallel to the spacecraft pitch axis) so that a coincal array envelope results. Because of the 9:30 a.m. orbit of L-D, the cant angle must be 37.5 degrees in order to maintain the plane of the solar array normal to the sun line when the array rotates about the spacecraft pitch axis at orbit rate (see also Figure 2-1). The array dimensions are 6.33 ft x 27 ft (1.93 m x 8.23 m) of which the solar cell area comprises 5 ft x 27 ft (1.525 m x 8.23 m). The array weight is approximately 50 pounds (22.7 kg) and the array efficiency after 3 years on-orbit is about 7.5 watts/square-foot (80.73 watts/m^2), resulting in a little over 1 Kw of generated electric power.

The total spacecraft on-orbit weight is estimated at

$$m = 3500 \text{ lb } (1587 \text{ kg})$$

and preliminary assessments of the principal moments of inertia are (Reference 2)

$$I_x = 1500 \text{ slug-ft}^2 \qquad (2034 \text{ kg m}^2)$$
$$I_y = 1970 \text{ slug-ft}^2 \qquad (2671 \text{ kg m}^2)$$
$$I_z = 1750 \text{ slug-ft}^2 \qquad (2373 \text{ kg m}^2)$$

2.3 Payload Description

2.3.1 Thematic Mapper

The Thematic Mapper is planned as the primary payload instrument for LANDSAT-D, to be launched early in 1981.

The name "Thematic Mapper" derives from the intended use of the instrument to produce land use theme maps which may be tailored to the data requirements of particular researchers, responsible government agencies, or private companies who can make use of remotely sensed data to better manage our earth resources. The Thematic Mapper will provide significant improvements in instrument performance compared to the current generation Multi-Spectral Scanner (MSS). The Thematic Mapper will provide coverage in at least seven spectral bands versus five in the MSS, 30 meter spatial resolution versus 80 for the MSS, better radiometric accuracy, and better geometric accuracy. Figure 2-8 shows a conceptual drawing of LANDSAT-D in operation. The spacecraft is in a circular, nearly polar orbit and provides complete global coverage every 16 days.

TRW Defense and Space Systems, teamed with Perkin-Elmer, and Hughes Aircraft Company (HAC) have submitted competing bids to NASA GSFC to develop and build a flight version of the TM. This competition has not yet been decided and for this reason the description of the TM provided here

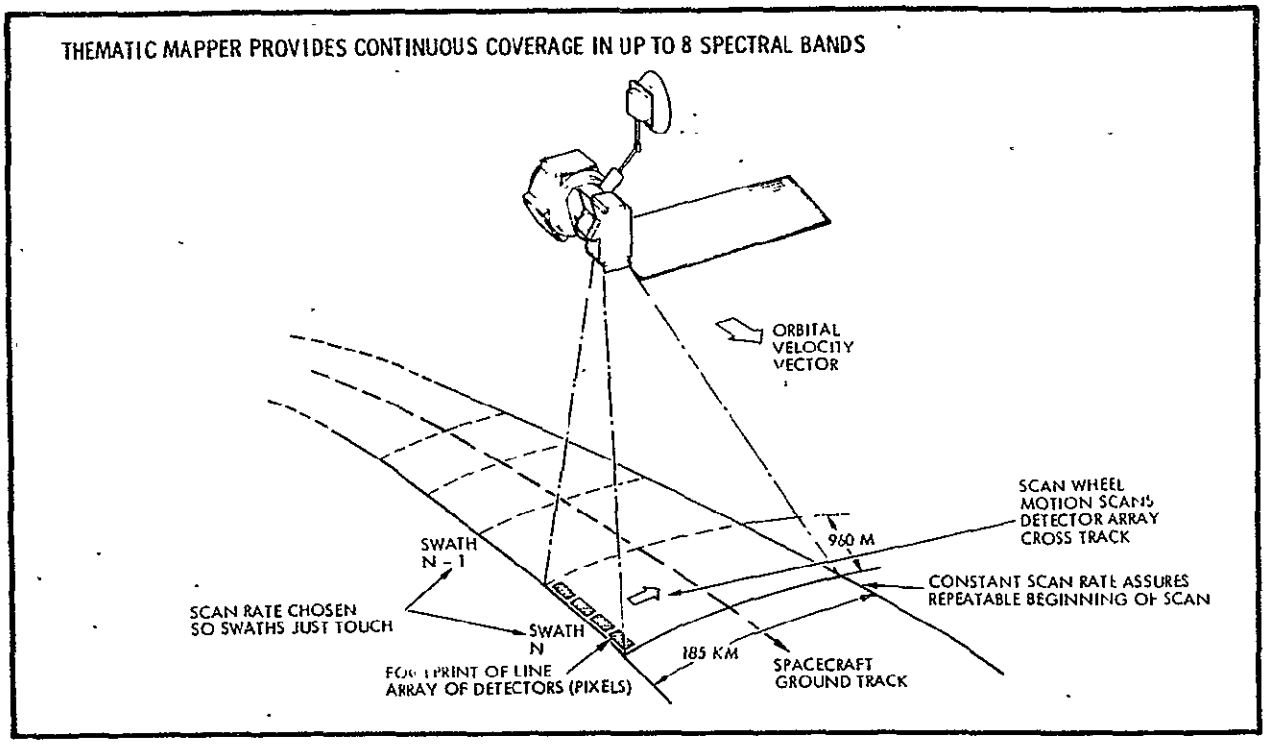

Figure 2-8. Crosstrack Optical Scanning Provides Continuous Coverage of 185 km (100 nmi) Swath

must be more of a general nature, omitting details. The Thematic Mapper optics include a scan mechanism which causes the line of sight of the instrument to scan across track; with the TRW/P-E design each scan is linear and from West to East. The scanned image is relayed to a focal plane assembly where the light is split into at least six spectral bands (options may add a seventh and eighth band). Each 0.004 inch square detector in a line array has a 30 meter square footprint on the ground when projected back through the optics. The six spectral bands are specified as follows where band edge is the wavelength that results in 50% of the maximum response.

Band Number	Lower Band Edge (μm)	Upper Band Edge (μm)	Maximum Edge Slope (μm)
1	0.45 ± 0.01	0.52 ± 0.01	0.02
2	0.52 ± 0.01	0.60 ± 0.01	0.02
3	0.63 ± 0.02	0.69 ± 0.01	0.02
4	0.76 ± 0.02	0.90 ± 0.01	0.03
5	1.55 ± 0.02	1.75 ± 0.02	0.05
6	10.4 ± 0.10	12.5 ± 0.10	0.30

In each spectral band, the moving image scene is swept past a line array of detectors (with the line array parallel to the direction of flight) by the scanning action crosstrack as outlined above. As the ground footprint of each detector moves 30 m across track, the detector output is sampled, converted to an 8 bit digital word, and ultimately multiplexed into a single 120 megabit/second data stream which is relayed to the wideband communications module.

As indicated in Figure 2-8, each scan sweeps out a swath 960 meters (along track) by 185 kilometers (cross track) and the scan rate is chosen so the swaths just touch, providing continuous coverage along the spacecraft ground track.

The major difference between the TRW and HAC TM designs is the scan mechanism. The HAC design uses a reciprocating scan mirror while the TRW design uses a uni-directional scan wheel, referred to as the roof mirror scanning wheel, since it has roof mirrors spaced around its circumference. The roof mirror scanning wheel converts the fixed image from the telescope into an image which moves across the detectors. The concept is illustrated in Figure 2-9.

The scan mechanism of the TM is of some importance for the ACS studies because of potential attitude disturbances resulting from the moving parts. During normal on-orbit operations the TRW scan wheel rotates at a constant

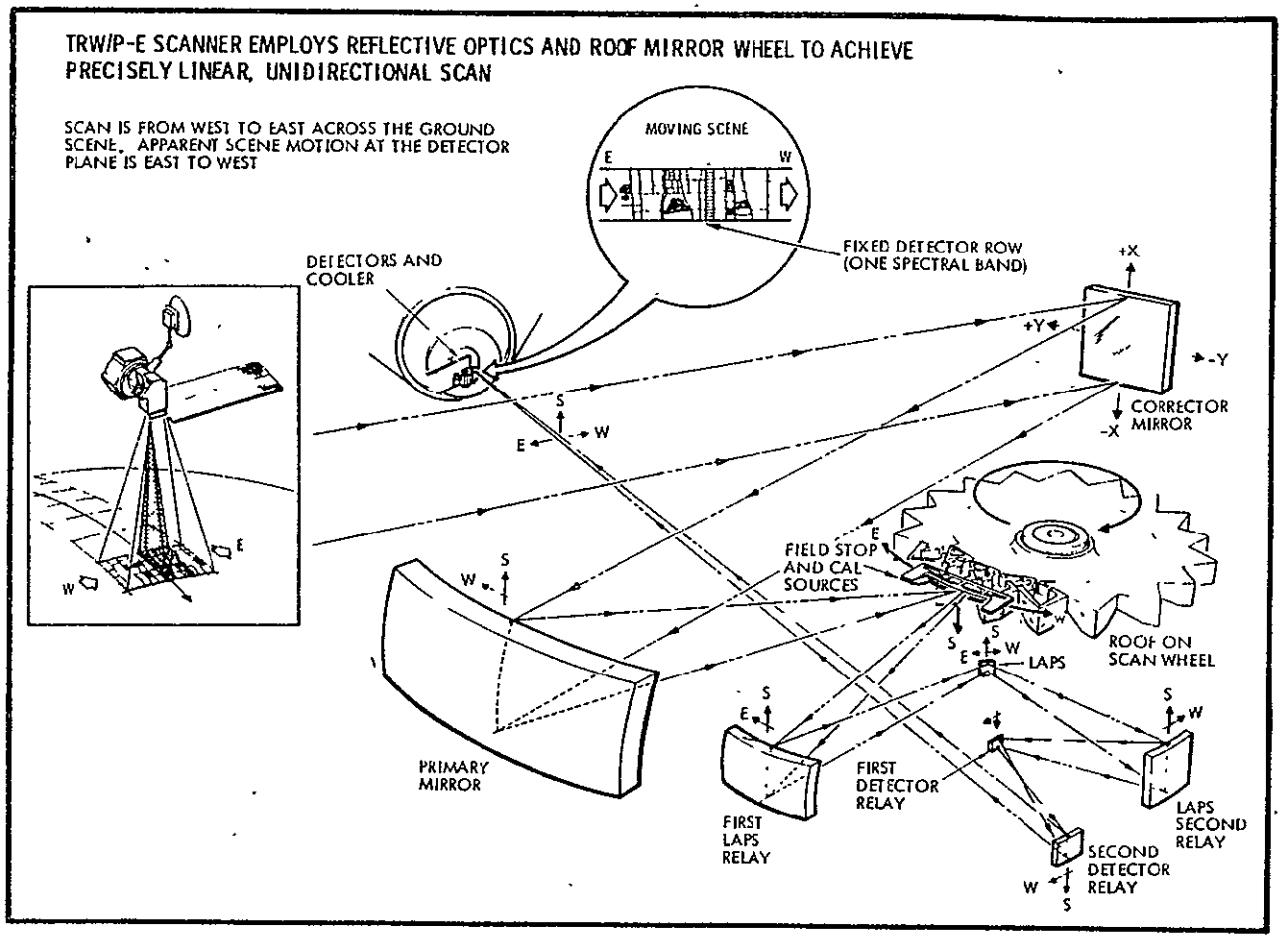

Figure 2-9. Schematic of the Scanning Telescope Optical Path

speed of 23.45 RPM and has a moment of inertia of 224 ounce-inch-seconds^2 (1.58 kg-m^2). No attitude disturbance occurs in steady state operation. The angular position of the HAC reciprocating mirror follows a triangular wave shape with rounded corners at a frequency of 7.14 Hz and $\pm$ 74 mradian (4.24 degrees) amplitude. The moment of inertia of the mirror about its pivot is 0.02614 kg-m^2.

The TM is nominally in a data taking mode only during those portions of the orbit when the L-D is flying over land masses which are in daylight. Data obtained over water (oceans) or a dark earth are of little practical value and consequently this type of data will be acquired only occasionally for experiment's sake. The fact that nominally no TM data need be transmitted to TDRS over water or over a dark earth is an important ground rule

in this study. It is key to the proposed solar array control strategy and the proposed TDRS antenna gimbal configuration and mast length. The proposed configuration does allow, however, for data being taken at night and over water, but not under any arbitrary circumstances. This will be discussed in more detail in Section 3.0.

To give a feel for the size of the TM instrument the following mass property and power data of the TRW design are provided.

Thematic Mapper Physical Parameters (TRW Design)

- Outline Dimensions: 1.12 x 1.94 x 0.96 meters (3.7 x 6.4 x 3.1 ft)
- Overall Weight: 223 kg (490 lb)
- Power Consumption: 228 watts (operating mode) 152 watts (night only)

2.3.2 Multi-Spectral Scanner

The secondary payload for L-D is the Multi-Spectral Scanner (MSS) as it will be flown on LANDSAT-C. The MSS is currently flying on LANDSAT's A and B, but the LANDSAT-C version will contain an additional (fifth) channel.

The MSS is an object plane scanner that was developed by Hughes Aircraft Company to provide radiometric measurements and imagery of the ground scene in the following spectral bands:

(1) 0.5 to 0.6 microns

(2) 0.6 to 0.7 microns

(3) 0.7 to 0.8 microns

(4) 0.8 to 1.1 microns

(5) 10.4 to 12.6 microns (LANDSAT's C and D only)

The uni-directional cross track scanning is provided by a high duty cycle (65%) rocking mirror at a frequency of 18.5 Hz over ± 74 mradians (4.24 degrees). The total weight of the MSS is 125 pounds (56.7 kg) and the power consumption is about 60 watts. The MSS data rate is 15 megabits/second.

2.4 LANDSAT-D Pointing Performance Requirements

Preliminary spacecraft pointing requirements are derived from the MMS ACS specifications of Reference 2. The yaw requirements are dervied by making the yaw error contribution at 92.5 km (= 0.5 frame width) from nadir correspond approximately to the roll and pitch error contribution.

- Pointing Accuracy

  Roll and Pitch: 0.01 deg (1σ)
  Yaw: 0.05 deg (1σ)

- Pointing Stability

  Average Rate/Axis: $< 10^{-6}$ deg/sec (1σ)
  Stability over 20 Minutes:
  Roll and Pitch: ± 10.5 μrad (1σ)
  Yaw: ± 80 μrad (1σ)

These requirements are referenced to the spacecraft coordinate reference axes which coincide with the optical cube on the star tracker. This means that the spacecraft to TM misalignments are not included in these performance specifications. Ephemeris errors are also excluded.

The ultimate temporal registration accuracy desired (essentially repeatability of the ground track after 16 days) for the TM is 3 meters (0.1 of a pixel) which corresponds to an attitude stability of about 4.2 μrad over 16 days if no ephemeris error were incurred. Exploratory studies on the autonomous on-board Thematic Mapper boresight registration are presented in Section 8.0. It is clear, however, that registration within 3 meters is a very stringent performance goal for LANDSAT-D.

3.0 PAYLOAD DATA RELAY SYSTEM

This section addresses various system aspects of the TM data relay system. In particular, system configuration, control, and operational aspects of the mast-deployed, gimballed Ku-band antenna, relaying TM data to TDRS, will be discussed. The antenna will often simply be referred to as the TDRS antenna (of L-D) to distinguish it from the undeployed and ungimballed direct access antenna which must also operate at Ku-band. This section will also discuss the interference of the solar array with the TDRS antenna beam and propose a solution to the problem. A digital computer program that computes on-orbit antenna motion profiles, determines percent solar array interference incurred, and determines whether the spacecraft is over land or sea, over a lighted earth or a dark earth, is also presented.

In order to decide whether the LANDSAT-D TDRS antenna can be pointed open loop by programmed command, or whether closed loop RF tracking, i.e., autotracking, is required, an antenna pointing error analysis was conducted first. This is the subject of the following section.

3.1 TDRS Antenna Pointing Error Analysis

Due to the constraint of limited TWT power, a large size L-D antenna dish (6 feet) is required in order to achieve sufficient EIRP for the return link to the TDRS. This results in a narrow beamwidth of about 0.7 degrees and necessitates very accurate antenna pointing in the order of 0.1 degree (3σ).

This section discusses the antenna pointing accuracies available from two basic antenna tracking techniques: program pointing by ground or onboard stored commands (open loop) and autotrack (closed loop). Detail sources of pointing error are identified for both systems and the associated errors are computed or estimated from accumulated data on current programs and tracking systems hardware.

The results show that the proposed open loop pointing error (Rayleigh circular error probability) is 0.61 (3σ), which corresponds to an antenna gain loss (from peak gain) of 8.2 dB for receive, and 9.9 dB for transmit, and that the proposed closed loop pointing error (Rayleigh CEP) is 0.052 degree (3σ), which corresponds to approximately 0.1 dB antenna gain loss for both receive and transmit.

The major error source for the open loop system comes from thermal distortion of the assumed 20 foot "Astro Mast" type of antenna boom. Since the closed loop system can track out the pointing error caused by antenna boom distortion, as well as many of the other open loop pointing errors identified in the open loop system budget, a considerable reduction in pointing error is realized with the recommended autotrack antenna system.

3.1.1 Program Pointing Performance

Six general sources of error were found to contribute to the inaccuracies involved in open loop pointing the L-D Ku-band antenna at the TDRS. These error sources, their breakdowns, and the error magnitudes are summarized in Table 3-1.

Spacecraft Position

The errors in the target direction arise from uncertainties in the position of the TDRS and the L-D. The maximum error in the TDRS position is 61 m, assuming there is no correction immediately following each TDRS momentum dump (Reference 3). The TDRS orbit radius is 4.224×10^4 km and the L-D orbit radius is 7.083×10^3 km, so the minimum distance between them is about 3.5×10^4 km. At this distance, a 61 m error is equivalent to a 10^{-4} degree line-of-sight error. An L-D position uncertainty of 100 m (Reference 1) contributes 1.64×10^{-4} degrees error. These two effects are negligible compared to the other errors shown in Table 3-1.

Spacecraft Attitude

The spacecraft alignment error is dominated by the 0.01 degree pointing accuracy of the spacecraft and the relative error at the canister mounting surface due to thermal and other distortions of the spacecraft itself.

Table 3-1. Antenna Open Loop Pointing Error Summary

Error Source				3σ Error (degree)	
1. Spacecraft position					1.92×10^{-4}
TDRSS ephemeris, 61 m				1.0×10^{-4}	
LF/O ephemeris, 100 m				1.64×10^{-4}	
2. Spacecraft attitude					0.014
Attitude control of ACS module (gyros, star tracker and RW control errors)				0.010	
Spacecraft structural/thermal alignment (ACS to canister mount)				0.010	
3. Pointing computation and command					0.023
Computer roundoff and quantization (16 bits)				0.005	
Gimbal angle encoder (14 bits)				0.022	
4. Servo and gimballed platform errors					0.023
Servo step size (0.03 degree)				0.015	
Gimbal axes alignment (orthogonality and bearing runout)				0.017	
5. Antenna mast errors (20' Astro-mast)					0.520
Canister mounting and alignment (thermal)				0.017	
Mast deployment/repeatability					
Bending	0.1°	(3σ)	CEP	0.129	
Torsional	0.12°	(3σ)			
Thermal distortion					
Bending	0.05°	(3σ)	CEP	0.503	
Torsional	0.5°	(3σ)			
6. Antenna errors (boresight relative to mounting platform)					0.093
Antenna attachment misalignment				0.057	
Mechanical (thermal) boresight alignment				0.028	
Electrical boresight alignment				0.057	
Precomparator amplitude imbalance				0.036	
Precomparator-postcomparator phase imbalance				0.016	
Total rss error (3σ)					0.529

Pointing Computation and Command

The computation and command error is dominated by the gimbal angle encoder error. The on-board data handling system uses 16 bits in double precision, but the payload drive encoder may well have fewer bits. The computational error, e_N, is found by letting the N bits cover a complete 360 degree range

$$e_N = \frac{360 \text{ deg}}{2^N}$$

The computer roundoff and quantization error is found by letting N = 16 or $e_{16} = 5.49 \times 10^{-3}$ degrees. The gimbal encoder error is $e_{14} = 0.022$ degree. The resultant error is 0.023 degree.

The gimbal, servo, and platform error capabilities were taken from Reference 4 where it was determined that the combined gimbal and steady-state servo error is 1 arc-minute (0.017 degree) and the error due to gimbal step size of 0.03 degree is 0.015 degree. The total error for this category is 0.023 degree.

Antenna Mast Errors

The main source of pointing errors is the Astro-mast. Basically, these errors relate the total error from the canister mounting surface to the gimbal mounts. The baseline mast is assumed to be 20 feet long* and 9 inches in diameter when deployed. The mounting and alignment error in the table (0.017 degree) is the mast mounting error. The other errors are based on information obtained from Mr. Peter Preiswerk of Astro Research.

*It will be shown in subsequent sections that this was a conservative assumption, i.e., the actual mast length is expected to be about 10 feet or less. The conclusions arrived at, namely that autotracking is required, is still believed to be valid, however.

The 3σ numbers provided by Mr. Preiswerk assumed a standard 9-inch diameter, 20-foot long Astro-mast that is canister deployed. These numbers are given in Table 3-1 under item 5. The bending and torsional errors are combined and represented by a Rayleigh circular error. The maximum antenna pointing error due to the Astro-mast is 0.520 degree.

Antenna Errors

The antenna errors category includes all alignment errors from the antenna platform to the beam center. The 0.093 degree error assumes a graphite reflector and the error is compatible with that of a similar 5-foot dish currently being used on another TRW project.

The resultant RSS errors for open loop pointing is 0.529 degrees/axis or a Rayleigh circular error of 0.61 degree (3σ). Since an open loop pointing accuracy of about 0.1 degree (3σ) is required for satisfactory communication with TDRS, it must be concluded that an autotrack system is required.

3.1.2 Autotrack Performance

A description of the recommended antenna autotrack system and acquisition procedure is presented in a companion report on the L-D mission unique communication system, Reference 5. Autotrack performance is given there in terms of the RSS of tracking errors due to thermal noise, precomparator amplitude imbalance, precomparator and post-comparator phase imbalances, and drive step size. The autotrack errors are summarized in Table 3-2.

The single-channel amplitude comparison autotrack system shown functionally in Figure 3-1 has been recommended over other tracking techniques such as interferometer, self (beam)-steering, mechanical scan, conical scan, etc., because of its low risk, low cost, minimum hardware complexity, and its good performance in tracking the Ku-band, spread spectrum RF signal.

In summary, the recommended autotrack design provides excellent tracking performance. Practical limits of precomparator amplitude imbalance and precomparator and post-comparator phase imbalances do not cause

Table 3-2. Autotrack Errors (3σ)

Error Source	Error (deg)	Notes
Precomparator amplitude imbalance	0.036	
Precomparator/post-comparator phase imbalances	0.018	
Drive step size	0.015	0.03° step size
Servo loop dynamics	0.015	Estimated
RSS	0.0455	
Thermal noise	0.0004	$(S/N)_{IF}$ = 11 dB
RSS total	0.0455	Per axis
Circular error	0.052	
Antenna pointing loss		
Receive	0.06 dB	3 dB beamwidth = 0.80°
Transmit	0.07 dB	3 dB beamwidth = 0.73°

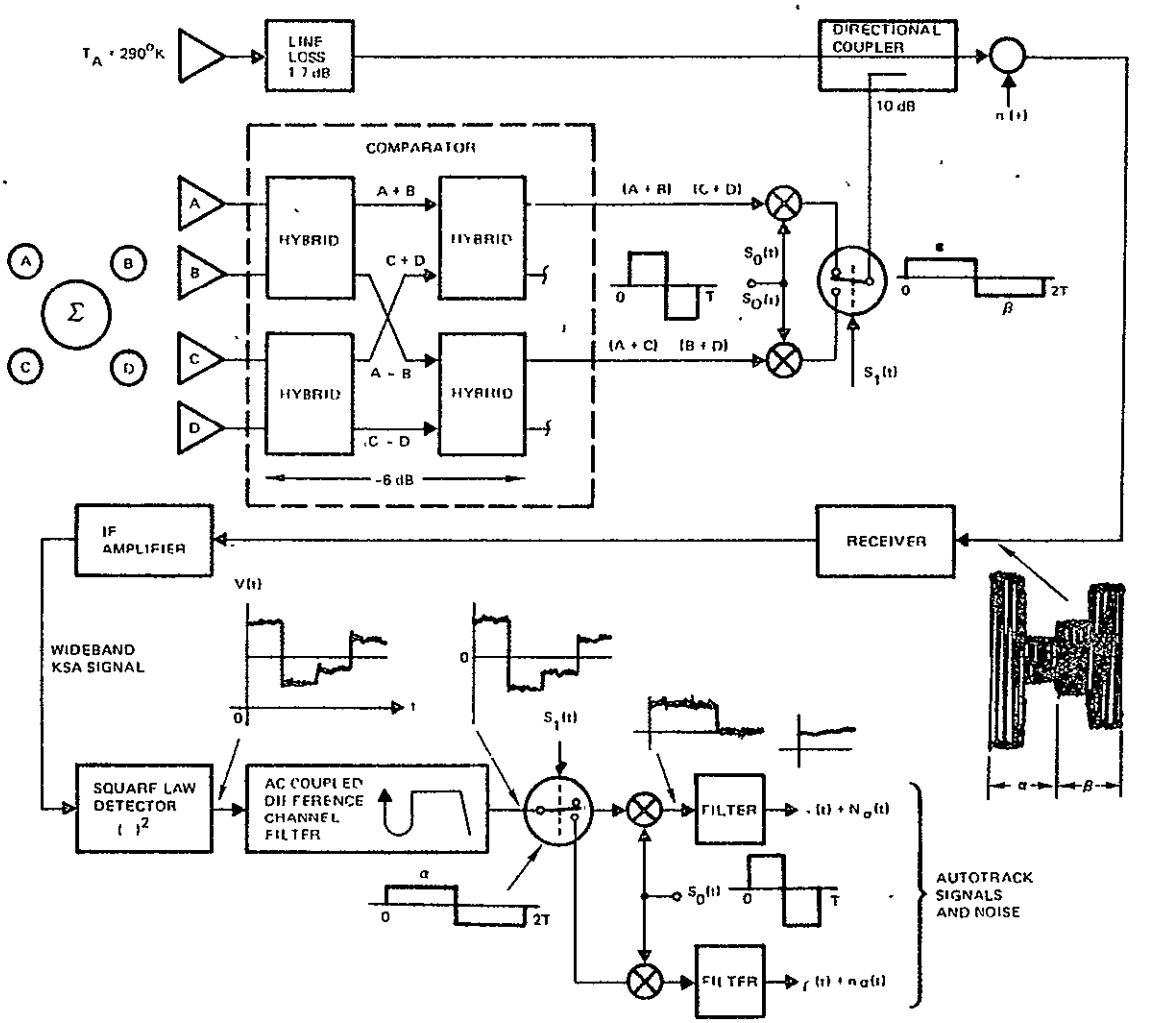

Figure 3-1. Antenna Autotrack Functional Block Diagram

appreciable contributions to the autotrack error. The errors associated with motor step size and servo loop dynamics are also minimal. The tracking error due to thermal noise is negligible at acquisition and autotrack receive signal levels.

3.2 Antenna Gimbal Configuration

Figure 3-2 shows a sketch of L-D in its normal on-orbit orientation. The figure mainly serves to define the body-fixed reference coordinate set, $\{\hat{x}_b, \hat{y}_b, \hat{z}_b\}$, and the earth half cone angle θ_E which equals 64.2 degrees at a spacecraft altitude of 705 km. It follows from the geometry indicated that the gimballed Ku-band antenna must be able to track TDRS in a cone of approximately $\pm$ 120 degrees (exactly: 90° + 25.8° = 115.8 degrees) centered about the $-\hat{z}_b$ axis, and that the maximum antenna dip angle below the spacecraft's local horizontal plane is 25.8 degrees.

The Ku-band antenna target, namely TDRS, follows a cone about the spacecraft's $\hat{y}_b$ axis which is constantly changing in size. This means that a two-gimbal arrangement should have the outer gimbal axis in or near the $\hat{x}_b$-$\hat{z}_b$ plane so that frequent gimbal resetting is not necessary. The problem with a two-axis (2-degree-of-freedom) gimbal lock problem exists and its effects must be carefully considered in the choice of the gimbal configuration and the degress of freedom. Four different gimbal configurations were considered. They are:

(1) x over y* two-axis gimbal.

(2) y over x two-axis gimbal.

(3) Azimuth-elevation two-axis gimbal.

(4) Three-axis gimbal using azimuth-elevation plus a third axis, cross elevation gimbal.

---

*The notation means x rotation <u>after</u> y, i.e., the outer gimbal axis is aligned with the S/C $\hat{y}_b$ axis and the inner gimbal axis (at outer gimbal null) with the S/C $\hat{x}_b$ axis.

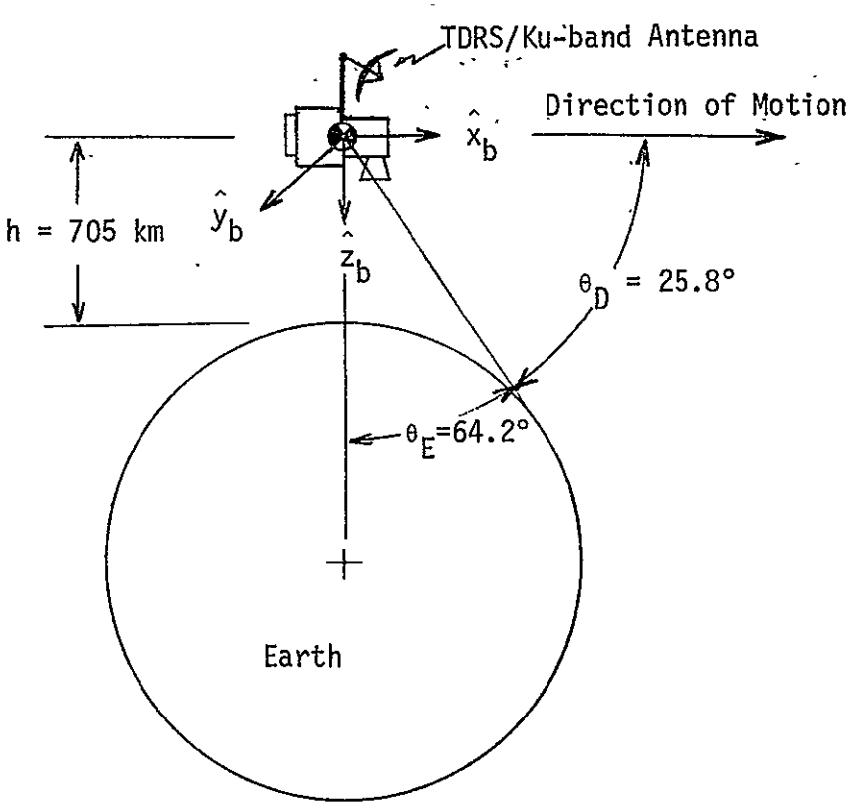

Figure 3-2. LANDSAT-D Normal On-Orbit Attitude and Geometry (not to scale)

The x and y two-axis gimbal would need ± 180 degrees freedom about the y-axis and 0 degrees to 120 degrees in x. Since the line-of-sight to TDRS tends to come around the spacecraft's $\hat{y}_b$ axis, this gimbal configuration would operate often close to gimbal lock and high rates about the y gimbal axis would be required. For the same reason, it would also require frequent resetting of the outer gimbal because of the effective ± 180 degree stops necessitated by the coax cables which are run across the gimbals and do not permit a wind-up motion about $\hat{y}_b$. Since the gimbal lock tends to interfere with the L-D operational scenario, the x over y gimbal arrangement is discarded as a configuration candidate.

The y over x gimbal would need 0 - 120 degree freedom in both gimbal axes. Gimbal lock can occur twice per orbit. Gimbal lock would occur when the TDRS is either straight ahead along the spacecraft velocity vector ($+\hat{x}_b$) or when the TDRS is exactly behind the spacecraft ($-\hat{x}_b$ direction).

These situations would occur when TDRS is crossing the L-D orbit plane at the time L-D descends from the North Pole toward the equator, and again a little later when L-D is half way on its way to the South Pole. The y over x gimbal is a feasible configuration but not particularly attractive since the gimbal lock conditions interfere with normal L-D operations.

The azimuth-elevation gimbal (with azimuth being rotation about the $\hat{z}_b$ axis = mast axis) has one well defined gimbal lock condition per TDRS: whenever TDRS is in the spacecraft zenith, i.e., whenever TDRS is in the L-D orbit plane directly above the spacecraft ($-\hat{z}_b$ direction). Fast antenna rotation near gimbal-lock occurs then mainly about yaw ($\hat{z}_b$ axis) and is expected to cause minimal interaction with the spacecraft which could adversely affect payload pointing. The mechanical design of an azimuth-elevation gimbal is relatively uncomplicated and, moreover, a third gimbal, should it ever be required, can be added quite easily by putting a cross elevation hinge into the antenna mast. The azimuth gimbal about $\hat{z}_b$ should ideally have a freedom of 360 degrees without mechanical stops, but because of a cable transfer across the gimbal hinge, a cable wrap providing $\pm$ 200 degrees of freedom with attendant overlapping $\pm$ 200 degrees mechanical stops, will be required. The elevation gimbal freedom must be at least from -26 degrees to +90 degrees. The azimuth-elevation gimbal configuration looks attractive and will be further considered.

A three-axis gimbal avoids gimbal-lock conditions but the gimbal configuration is mechanically more complex, bulkier, heavier, and costlier. At certain times two gimbal axes may be parallel and control laws and gimbal servo cross-talk problems become more complex. It has been decided to avoid a three-axis gimbal system if satisfactory operation can be achieved with a two-axis gimbal.

3.2.1 Gimbal Lock Problem

The potential gimbal-lock problem for the two-axis gimbal configurations in general, and for the azimuth-elevation configuration in particular, can be solved in one of two ways. Referring to the gimbal-lock point as the keyhole, one can

(1) Show that the target (TDRS) is never in the keyhold.

(2) Place the keyhole so that the data which is lost, by the antenna not tracking TDRS, is not required.

Option 1 can be viewed as: show that whenever one TDRS is in the keyhole, it is acceptable to use the other one as the target. This is best considered in terms of the target location. For an azimuth-elevation arrangement, gimbal-lock occurs when the target is in the L-D orbit plane. At that time the other TDRS is 130 degrees out of the orbit plane where it is hidden by the earth; thus there is no increase in coverage available by switching targets -- in fact, since the other target would have to be tracked for the whole L-D orbit, there would be a larger reduction in coverage by switching targets. This exercise can be repeated for other two-axis gimbal configurations, but the result is the same. Since the outer gimbal axis must be near the $\hat{x}_b$-$\hat{z}_b$ plane, gimbal-lock will occur when a TDRS is near the L-D orbit plane. At that time, the other TDRS is 50 degrees out of the L-D orbit plane and cannot be tracked throughout the L-D orbit.

Option 2 is a feasible solution. Using the azimuth-elevation arrangement, gimbal-lock will occur when the L-D is directly beneath the TDRS, and so loss of the TDRS link will occur at 41 degrees and 171 degrees west longitude, i.e., beneath the station locations of the two TDRS's. These points are over the ocean where coverage is not essential. The loss of the TDRS link at 41 degrees west occurs close to the coast of Brazil, and at 171 degrees west there may be some Pacific islands of interest. Thus it is of some importance to precisely establish the size of the loss of coverage zone on the ground and to investigate if this zone could be shifted if required.

The loss of coverage zone can be shifted by tilting the outer gimbal axis, which for the azimuth-elevation gimbal would mean to tilt the mast. This is demonstrated in Figure 3-3, where tilting the gimbal axis by the angle α, moves the loss of coverage zone by an amount γ. The relationship between these angles is found from:

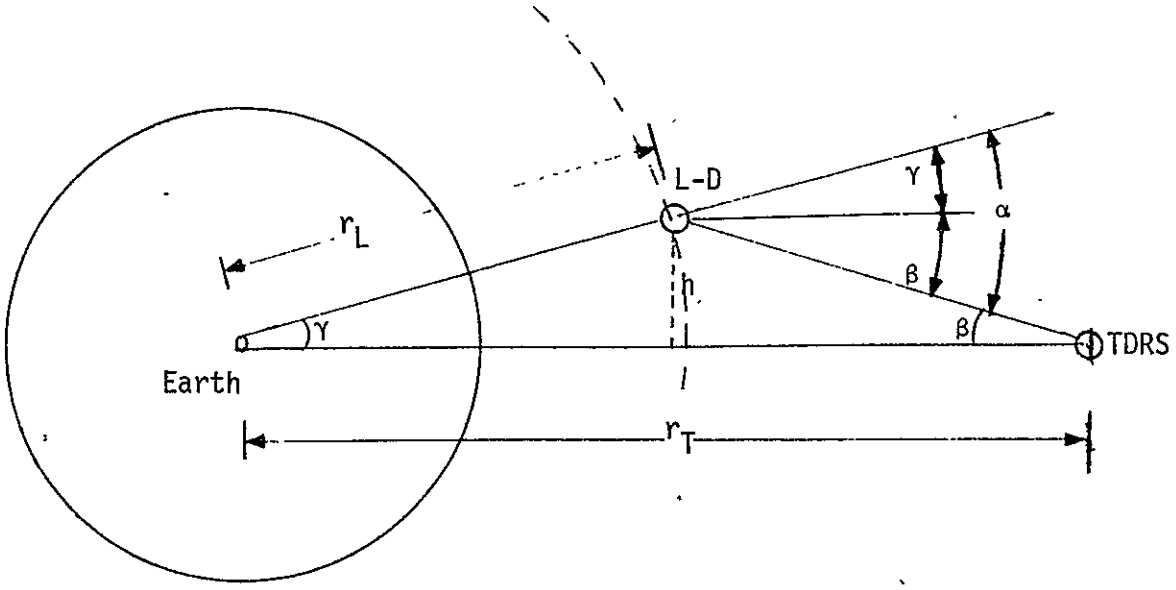

Figure 3-3. Moving the Loss of Coverage Zone by Tilting the Outer Gimbal Axis

$$\alpha = \beta + \gamma \tag{3.2-1}$$

and

$$h = r_L \sin \gamma = (r_T - r_L \cos \gamma) \tan \beta \tag{3.2-2}$$

thus

$$\alpha = \gamma + \tan^{-1} \left\{ \frac{r_L \sin \gamma}{r_T - r_L \cos \gamma} \right\} \approx \frac{r_T}{r_T - r_L} \gamma \tag{3.2-3}$$

where the approximation is for small angles. Using the values r_L = 7074 km and $r_T = 4.224 \times 10^4$ km, a $\approx 1.2\ \gamma$. For example, if the gimbal axis is tilted 6 degrees, the coverage hole moves about 5 degrees.

The size of the loss of coverage zone can be estimated by assuming that normal operation of the antenna gimbal can be maintained until one

gets within $\pm$ 2 degrees of gimbal-lock. Using Equation (3.2-3) with $\alpha = \pm$ 2 degrees, this becomes $\gamma = \pm$ 1.664 degrees of the earth's sphere on the ground which equals $\pm$ 185 km. Since a swath of the TM happens to be exactly 185 km wide in the east-west direction, the loss of coverage zone in the worst situation is at most three swaths wide (555 km $\approx$ 5 degrees on earth sphere), and for the best situation at least two swaths wide (370 km $\approx$ 3.3 degrees). In the north-south direction, the loss of coverage zone extends always $\pm$ 185 km ($\pm$ 1.664 degrees) if gimbal-lock can be approached to within 2 degrees. This is illustrated in Figure 3-4. Referring to appropriate maps showing the north-east coast of Brazil and the Pacific Ocean, respectively, it can be seen that the loss of coverage zone contains only water (the coast of Brazil is barely missed for the worst situation), with the exception of perhaps some of the Gilbert Islands in the Pacific. Thus, the antenna mast need not necessarily be tilted. If a tilt is considered, because normal tracking operation can only be maintained to within, say, 5 degrees of gimbal-lock, then the mast could be tilted by 6 degrees to 12 degrees toward $+\hat{x}_b$ so that the now larger loss of coverage zone would move 6 degrees to 12 degrees north at the descending node (daylight), where no nearby land masses exist. But this is acceptable only if the loss of coverage due to gimbal-lock is acceptable at night: if the zone is shifted one way at the descending node, it is shifted in the opposite direction at the ascending node. It would be possible to place the zone over the ocean all the time by tilting the gimbal axis 36 degrees from the $\hat{z}_b$ axis in the $\hat{x}_b$-$\hat{z}_b$ plane. This moves the zone 30 degrees north or south depending on the L-D direction at the time.

3.2.2 Baseline Gimbal Configuration

The azimuth-elevation gimbal configuration has been selected as the baseline gimbal for the L-D Ku-band (TDRS) antenna. The occurrence of gimbal-lock is well defined for this gimbal configuration and it was shown that the resultant loss of coverage zone is always situated over water.

The gimbal configuration is shown in its null position in Figure 3-5. Gimbal-lock occurs when the elevation angle g_2 = 90 degrees and the antenna views zenith. The coordinates $\{\hat{x}, \hat{y}, \hat{z}\}$ are identical to the body

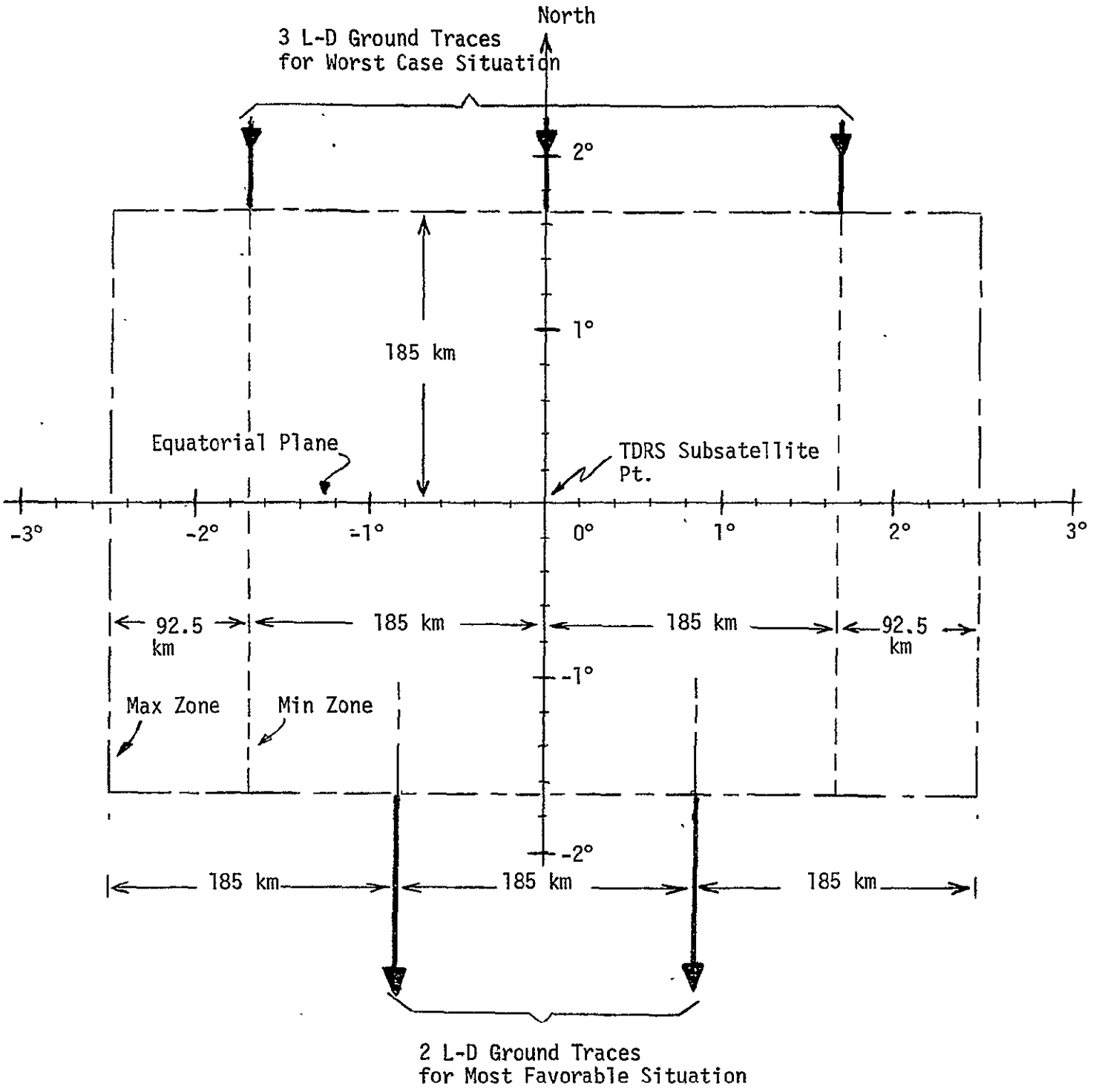

Figure 3-4. Zone of Loss of TDRS Link Due to Gimbal-Lock (Normal Operation Assumed to Within ± 2 degrees of Gimbal-Lock)

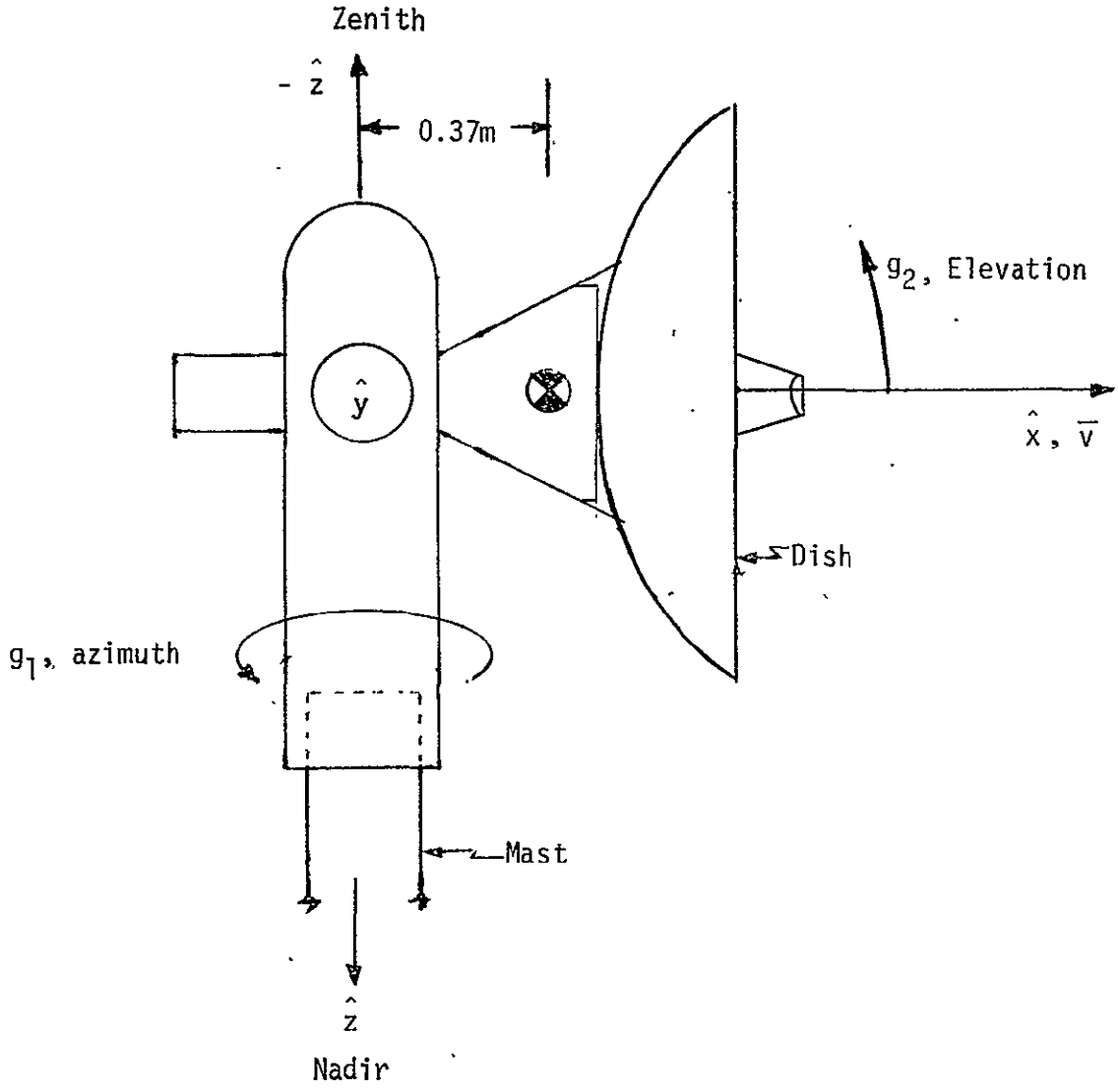

Figure 3-5. Ku-Band Antenna in the Null Position

fixed set defined in Figure 3-2, i.e., in its null position the antenna faces in the direction of travel of the satellite. This is important in view of the cable wrap limits specified as ± 200 degrees from the origin, since near gimbal-lock, the antenna must be able to rotate nearly 180 degrees in azimuth from $+\hat{x}$ to $-\hat{x}$ without crossing a cable wrap limit. A single mechanical stop in azimuth is unacceptable since the antenna must be able to fine-track a TDRS at any arbitrary azimuth angle. Thus, an overlapping cable wrap and attendant overlapping mechanical stops (to

prevent cable damage) are required. The peak gimbal rate occurs in azimuth near gimbal-lock. It can be shown that if gimbal-lock is approached to within ε degrees, then, for small ε, the peak azimuth rate is given by

$$\dot{g}_{1_{max}} = \frac{\omega_o}{\varepsilon} \qquad (3.2\text{-}4)$$

where ω_o is the orbit rate of L-D. For $\varepsilon = 2$ degrees, this yields

$$\dot{g}_{1_{max}} = 1.74 \text{ deg/sec}$$

The peak azimuth rate could be decreased if the elevation angle were allowed to "follow through" beyond 90 degrees, i.e., the elevation gimbal freedom were $-30° \leq g_2 \leq 210$ degrees. The software of the gimbal controller would also become more complicated, however, since gimbal steering is not unique anymore.

Table 3-3 summarizes the baseline gimbal design requirements. A servo loop controlled stepper motor has been assumed for the gimbal drive. Step size and other requirements are compatible with the antenna pointing requirements and the autotracking baseline system established in Section 3.1. The slew rate and acceleration requirements assure that:

- The azimuth can be reoriented by 180 degrees sufficiently fast (1 minute) to resume tracking TDRS when it emerges again from the gimbal-lock zone, assumed at $\pm$ 2 degrees about the keyhole. (That is, the time to reorient the azimuth gimbal is limited by the time it takes L-D to cross the gimbal-lock zone.)

- The antenna can be slewed from one TDRS to the other in less than 2 minutes.

- The system has sufficient acceleration capability for a spiral search pattern to find and lockup on TDRS, in case the open loop pointing command did not bring the target within the acquisition field of view of the autotrack system.

Table 3-3. Baseline Gimbal Configuration Design Requirements

Angular Freedom:	
Azimuth	± 200° (overlapping stops)
Elevation	-26° to +90° (minimum) -30° to +210° (desirable)
Maximum Tracking Rate:	2.0 deg/sec
Maximum Slew Rate:	4.0 deg/sec
Maximum Acceleration:	1.5 deg/sec^2
Output Step Size:	< 0.03 deg
Readout Accuracy:	Better than 0.2 deg
Open Loop Pointing:	Better than 0.25 deg

3.3 Antenna Control System Functional Design

This section presents a preliminary design for a control system to point the L-D Ku-Band antenna at a TDRS. There are two major control modes. Mode 1 is an open loop pointing mode in which the on-board computer generates gimbal angle commands based on the computed location of the target. In this mode the gimbal angle readouts provide the feedback. Mode 1 is used to:

(a) Slew from one TDRS to the other.

(b) Reset the azimuth gimbal angle when one of the ± 200 degrees cable wrap stops are close to interferring with nominal operation.

(c) Move the antenna through the zone of TDRS link loss due to gimbal-lock.

(d) Follow TDRS through the zone of exclusion over the Indian Ocean where both TDRS's are hidden by the earth so that autotrack may resume as soon as a TDRS comes again into the field of view.

Operations (a) through (c) will nominally all be accomplished when the spacecraft is near the polar regions so that no data loss (i.e., no effective communication loss) is incurred. The loss of coverage over the Indian Ocean, item (d) above, is not under the control of the L-D mission; it is a characteristic of the TDRSS as currently configured.

If the open loop antenna pointing accuracy is worse than 0.657 degrees, it may not be possible to establish the RF link for locking on to the TDRS. In this case the computer generates a spiral search pattern to bring the TDRS within the field of view of the autotrack system. The search pattern is generated in Mode 1a.

Mode 2 is a closed loop tracking mode which does not use the on-board computer. The pointing error is sensed by the autotrack system, and the controller removes the measured error directly.

3.3.1 Acquisition Procedure

Acquisition procedures between the L-D and the TDRS are outlined in Table 3-4. The data was taken from the TDRSS "User Spacecraft Acquisition Procedures," P-805-1, June 1976, GSFC. For L-D acquisition independent of the S-band TT&C link (except for initial antenna pointing programming and

Table 3-4. TDRSS User Spacecraft Acquisition Procedures

3.1 KSA ACQUSITION SEQUENCE NO. 1

3.1.1 An SSA return link is established with the user spacecraft using the normal SSA acquisition procedure.

3.1.2 The user spacecraft radiates a minimum S-band EIRP of +13 dBw.

3.1.3 TDRSS uses the S-band return link signal to aid antenna pointing. TDRSS radiates, within 5 seconds of user S-band turn-on and in the direction of the user spacecraft, a Ku-band +40 dBw (minimum) signal EIRP compatible with the forward link signal parameters defined in either Table 2-1 or Section 8.2.1.1 of S-805-1. The Ku-band carrier and PN clock shall include doppler compensation as scheduled.

3.1.4 The user spacecraft acquires the TDRSS Ku-band signal, begins autotracking, and begins radiating a +30 dBw (minimum) signal EIRP at Ku-band in the direction of TDRSS.

3.1.5 TDRSS then:

a. Autotracks the user Ku-band signal within 5 seconds of user turn-on (P_{acq} = 0.99 for user EIRP = +30 dBw).

b. Begins radiating normal power mode signal EIRP or high power mode signal EIRP as scheduled.

c. Either establishes return link DG 1 service and/or DG 2 service, or Shuttle Ku-band service within 5 seconds.

3.2 KSA ACQUISITION SEQUENCE NO. 2

3.2.1 An SSA forward link is established with the user spacecraft using the normal SSA acquisition procedure.

3.2.2 The user spacecraft is commanded to point its Ku-band antenna at TDRSS and to transmit in the direction of TDRSS a minimum of +30 dBw EIRP at Ku-band compatible with the return link signal parameters defined in either Table 2-2 or Section 8.2.1.2 of S-805-1.

3.2.3 TDRSS searches for the Ku-band signal and begins autotracking within 10 seconds of user turn-on (P_{acq} = 0.99 for user EIRP = +30 dBw).

3.2.4 TDRSS radiates normal power or high power EIRP at Ku-band in the direction of the user spacecraft compatible with the forward link signal parameters defined in Table 2-1 or Section 9.2.1.1 of S-805-1. The Ku-band carrier and PN clock shall include doppler compensation as scheduled.

3.2.5 The user spacecraft acquires the TDRSS Ku-band signal and begins autotracking.

3.2.6 TDRSS either establishes return link DG 1 service and/or DG 2 service within 5 seconds.

other tracking considerations given below), KSA acquisition sequence 2 is recommended for the L-D mission. The acquisition procedure has also been discussed in Reference 5.

L-D antenna tracking is accomplished as follows. Prior to coming over the horizon, the L-D Ku-band steerable antenna is program-pointed at the TDRS within a factor of 1.8 (open loop pointing error) of the one-sided, half-power beamwidth (0.365 degree). This open loop uncertainty does not reduce the L-D EIRP below the minimum 30 dBW EIRP required for TDRS Ku-band antenna acquisition and autotrack. A margin of greater than 18 dB exists.

Upon acquiring and autotracking the L-D signal beacon, which consists of the normal composite 120 Mbps and 15 Mbps instrument signal, the TDRS begins transmitting a spread spectrum beacon signal to the L-D. The TDRS beacon signal will be within 10 dB of the L-D Ku-band high gain antenna peak. This signal level is above the threshold level which initializes autotrack.

The autotrack design provides for the inclusion of a small acquisition horn (BW $\approx$ 12 degrees) to provide a broadbeam Ku-band beacon for initial TDRS acquisition of the L-D. The acquisition horn is considered as a back-up acquisition aid in the event of temporary pointing anomolies (attitude control, boom distortion, etc.). Furthermore, a preprogram search routine in the communication and data handling module on-board computer provides a search pattern for L-D antenna acquisition and autotrack. This is also considered a backup mode.

3.3.2 System Functional Description

A functional block diagram of the controller is shown in Figure 3-6. The required electronics are shown functionally by the block diagram in Figure 3-6a; a separate compensator may be needed for Modes 1 and 2 due to the different requirements. The autotrack measures the antenna pointing errors - ε_1 and ε_2 - in antenna-fixed axes and they need be resolved

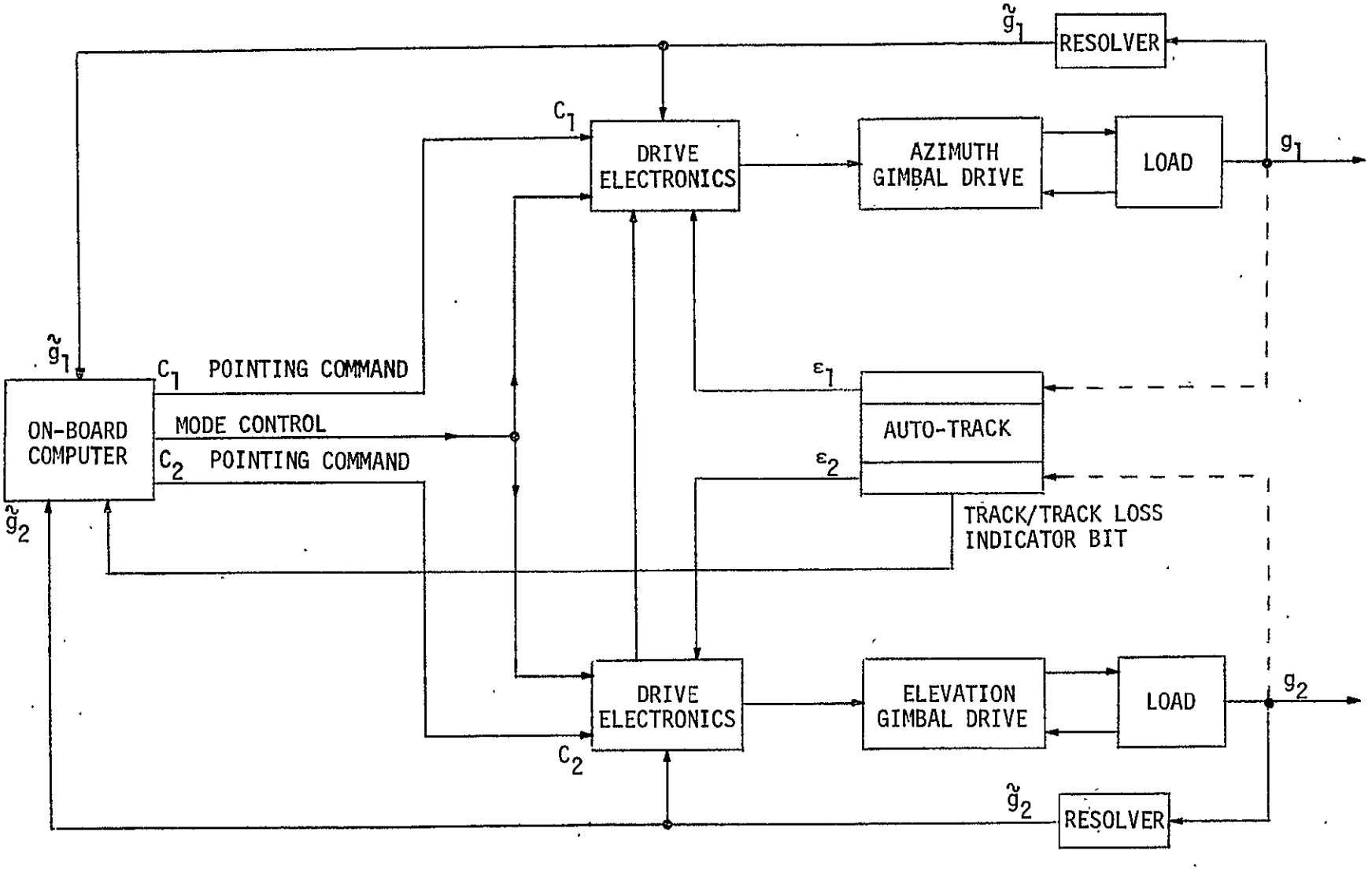

Figure 3-6. Functional Block Diagram of Antenna Control System

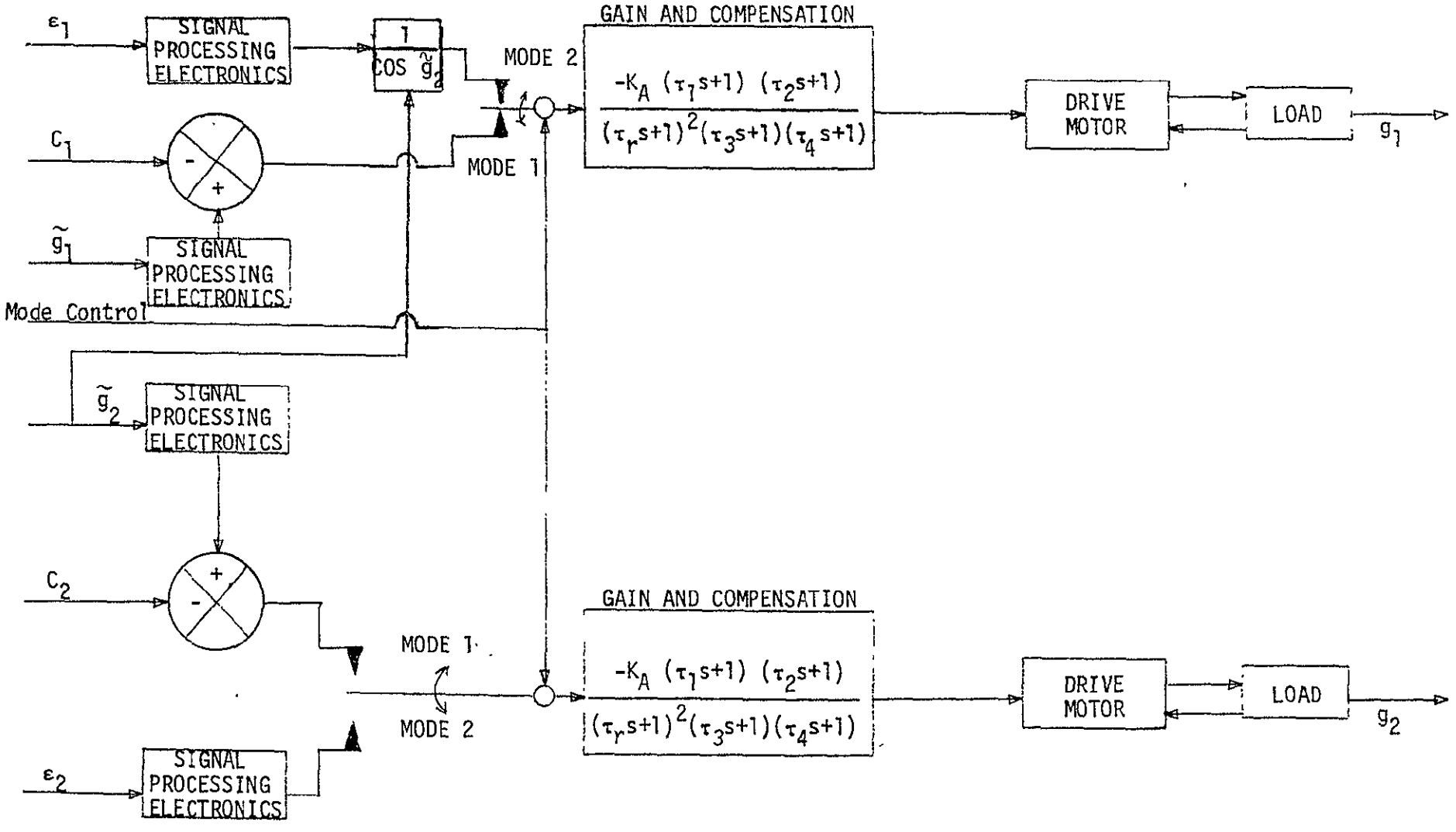

Figure 3-6a. Functional Block Diagram of Drive Electronics

into gimbal coordinates. One of these axes is aligned with the inner gimbal axis, so the measured pointing error is also the gimbal angle error, i.e., for the elevation gimbal,

$$\varepsilon_2 = C_2 - g_2 \tag{3.3-1}$$

where C_2 is the commanded gimbal angle and g_2 the actual (measured) gimbal angle. But, the pointing error about the outer axis (azimuth) differs from the gimbal angle error according to the target location:

$$\varepsilon_1 = \cos g_2 \, (C_1 - g_1) \tag{3.3-2}$$

This factor is removed as shown in Figure 3-6.

In Mode 1, the computer must calculate the required gimbal angles to point the antenna at the target given the TDRS location and the L-D location and attitude. The necessary equations will now be derived.

Assuming that the L-D and TDRS positions are known in the standard earth centered inertial (ECI) coordinate frame {I} ($\hat{z}_I$ axis through North Pole, $\hat{x}_I$ axis toward vernal equinox), denote the L-D and TDRS position vectors by $\{\bar{r}_L\}_I$ and $\{\bar{r}_T\}_I$, respectively. Then the vector pointing from L-D to TDRS is given in ECI coordinates by

$$\{\bar{p}\}_I = \{\bar{r}_T\}_I - \{\bar{r}_L\}_I \tag{3.3-3}$$

and in L-D body coordinates by

$$\{\bar{p}\}_b = A_{bI} \{\bar{p}\}_I \tag{3.3-4}$$

where A_{bI} is the direction cosine matrix of L-D specifying its attitude relative to ECI. Denote the normalized pointing vector to TDRS in L-D body coordinates by

$$\hat{T}_b = \{\bar{p}\}_b / ||\bar{p}|| \tag{3.3-5}$$

Denote A_{ab} the direction cosine matrix that transforms from body fixed coordinates to antenna fixed coordinates. Then, performing two ordered rotations g_1 and g_2,

$$A_{ab} = [g_2]_y [g_1]_z$$

$$A_{ab} = \begin{bmatrix} \cos g_2 \cos g_1 & \cos g_2 \sin g_1 & -\sin g_2 \\ -\sin g_1 & \cos g_1 & 0 \\ \sin g_2 \cos g_1 & \sin g_2 \cos g_1 & \cos g_2 \end{bmatrix} \tag{3.3-6}$$

Note that when $g_1 = g_2 = 0$, the antenna fixed axes coincide with the body fixed axes and the antenna boresight is aligned with the spacecraft $\hat{x}_b$ axis. The gimbal angles g_1 and g_2 that align the antenna boresight with the normalized pointing vector $\hat{T}_b$, must then satisfy

$$\begin{bmatrix} 1 \\ 0 \\ 0 \end{bmatrix} = A_{ab} \hat{T}_b = A_{ab} \begin{bmatrix} T_{bx} \\ T_{by} \\ T_{bz} \end{bmatrix} \tag{3.3-7}$$

which leads to

$$\text{azimuth:} \quad g_1 = \tan^{-1} (T_{by}/T_{bx}) \tag{3.3-8}$$

and

$$\text{elevation:} \quad g_2 = -\sin^{-1} (T_{bz}) \qquad -30° \leq g_2 \leq 90° \tag{3.3-9}$$

When the antenna is pointed at the computed target location, Mode 2 is initiated if the autotrack "sees" the TDRS beacon, and Mode 1a

otherwise. In Mode 1a, the computer generates the search pattern and switches to Mode 2 when the autotrack "sees" the beacon. The search pattern assumed here is a spiral:

$$a_1 = g_1 \sin g_2 = K\, t \sin \omega t \tag{3.3-10}$$

$$a_2 = g_2 = K\, t \cos \omega t \tag{3.3-11}$$

At the end of n full periods

$$a_1(n) = \frac{2\pi nK}{\omega} \sin 2\pi n = 0$$

$$a_2(n) = \frac{2\pi nK}{\omega} \cos 2\pi n = \frac{2\pi nK}{\omega}$$

Thus the distance between successive scan centers is $d = \frac{2\pi K}{\omega}$. With the 0.8 degree FOV width, sufficient overlap could be achieved with d = 0.6 degree, or $K/\omega = 0.0955$ degree. This scan will cover a circle of radius $r_c = 3$ degrees in n = 5 cycles.

The peak gimbal rate within that circle would occur at the end of the fifth cycle, where

$$\dot{a}_1(n) = [K \sin \omega t + K\, \omega t \cos \omega t]_{t = \frac{2\pi n}{\omega}} = 2\pi nK \tag{3.3-12}$$

$$\dot{a}_2(n) = [K \cos \omega t - K\, \omega t \sin \omega t]_{t = \frac{2\pi n}{\omega}} = K \tag{3.3-13}$$

are the rates at the end of the n^{th} cycle. Further, from (3.3-10)

$$\dot{g}_1 \simeq \frac{\dot{a}_1}{\sin g_2} \tag{3.3-14}$$

For acquisition with $g_2 \leq 60$ degrees, this becomes

$$\dot{a}_1 \leq 0.5\ \dot{g}_1 \leq 1 \text{ deg/sec} \qquad (3.3\text{-}15)$$

where $\dot{g}_1$ and $\dot{g}_2$ are each limited to 2 degrees/second by the design requirements. Combining (3.3-12) and (3.3-15)

$$Kn \leq 0.1592 \text{ deg}$$

Since this rate requirement is only necessary thru the fifth cycle, one chooses K = 0.03 degree/second. Since $K/\omega = 0.0955$ degree, this results in $\omega = 0.314$ rad/second, and the period is 20 seconds/cycle. The peak gimbal acceleration can be shown to be 0.6 degree/second^2 where the gimbal design requirement is 1.5 degrees/second^2. In summary, in Mode 1a the computer must compute gimbal angles according to Equations (3.3-10) and (3.3-11) with K = 0.03 degree/second, and $\omega = 0.314$ rad/second. A computer cycle time of 256 msecond would allow the gimbal commands to be updated 80 times per search cycle.

3.4 Digital Program for Antenna Motion Profile and Solar Array Interference

One of the requirements of the LANDSAT-D study was to develop a digital computer program for studying solar array interference with the Ku-band antenna. Program LFO (Landsat Follow-On) satisfies this requirement and is additionally a more general program that can be used to study various other spacecraft/orbital phenomena. In particular, the main outputs of the program are:

- Antenna gimbal angle motion profiles
- Percent transmission to TDRS (interference problem)
- Spacecraft eclipsed or not eclipsed
- Longitude and latitude of the subsatellite point
- Subsatellite point over land or water
- Subsatellite point over lighted earth or dark earth

The objective of this section is to discuss the underlying theory on which the program is based, provide a brief description of the program organization and its use, and to present and discuss some of the results obtained. Program flow diagrams are given in Appendix A and a program listing (FORTRAN IV) is given in Appendix B.

3.4.1 Program Description

This program is primarily used for computations involving a spacecraft in an arbitrary circular orbit -- specifically the LANDSAT-D (L-D) -- and another spacecraft which is in an earth-synchronous orbit -- specifically the TDRS. The geometrical relationships are shown in Figure 3-7; this figure also defines several of the variables and parameters used in the program. The earth centered, sun referenced, coordinate system, s, has the z_s axis pointing north along the polar axis and the sun lying in the $y_s = 0$ plane generally in the $+x_s$ direction; the x_s axis and y_s axis lie in the equatorial plane. The TDRS's are located by the angles γ_1 and γ_2 measured relative to the x_s axis -- nominally TDRS1 is at 41°W longitude and TDRS2 is at 171°W longitude. The L-D orbit is defined by its inclination angle γ_I and the location of its descending node γ_D. In this orbit plane, the spacecraft is located by orbit angle γ_L measured from the point 90 degrees ahead of the equatorial plane. The orbit coordinate system is located at the spacecraft c.m. with the z_o axis pointing at the earth center and the x_o axis in the direction of spacecraft orbital motion. In the program the body coordinate system is assumed to be identical with the orbital frame 0 -- no pointing errors. The angle between the sun vector and the equatorial plane is γ_s; this varies over the range [-23.5 degrees, 23.5 degrees] depending on the time of year.

The mainline program contains minimal computation. Instead, it primarily ties together the various subroutines; this allows the user to easily supply special purpose subroutines to meet the needs of a particular situation. The flow charts of the total program are given in Appendix A. The subroutines DOT, CROSS, BASIS, CITOO, COTOA, UNIT and ROT are minor computational subroutines used for various vector manipulations and coordinate system transformations; their specific functions are shown in Table 3-5.

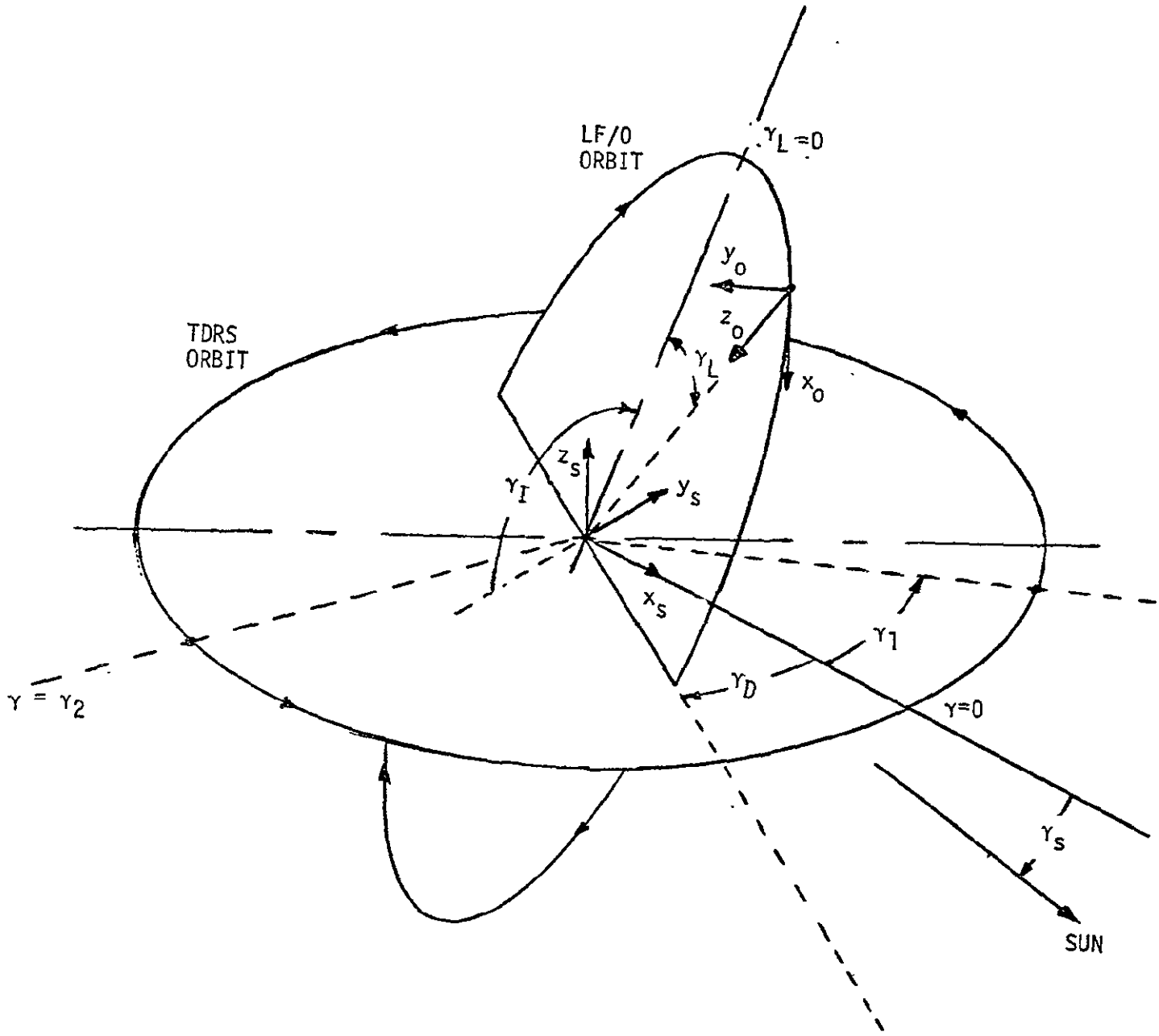

Figure 3-7. Geometrical Relationships

Table 3-5. Minor Subroutines in LFO

Subroutine Name	Inputs	Outputs	Description
DOT	$\overline{X}$, $\overline{Y}$	A	$A = \overline{X} \cdot \overline{Y}$
CROSS	$\overline{A}$, $\overline{B}$	$\overline{C}$	$\overline{C} = \overline{A} \times \overline{B}$
BASIS	$\overline{A}$	$\hat{B}$, $\hat{C}$	The unit vectors $\hat{B}$ and $\hat{C}$ form an orthonormal basis with $\hat{A}$
UNIT	$\overline{X}$	$\hat{Y}$	$\hat{Y} = \overline{X}/\lvert\overline{X}\rvert$
ROT	$\overline{XI}$, A, N	$\overline{XO}$	$\overline{XO} = [A]_N \overline{XI}$, N is nth axis
CITOO	$\overline{X}$, γ_L	$\hat{Y}$	Transforms vector $\overline{X}$ in s coord. system to unit vector $\hat{Y}$ in O coord. system.
COTOA	$\overline{A}$, ρ	$\overline{B}$	Transforms vector $\overline{A}$ in O coord. system to $\overline{B}$ in array centered coord. system (see Section 5).

The subroutines INPUT and OUTPUT do just what their names imply; they are separate subroutines in order to keep the mainline program simple and straightforward. The remaining subroutines are the main computational elements of the program; their functions are described briefly in Table 3-6. More complete descriptions of ARRAY and GIMBAL are given in Section 3.4.3.

Table 3-6. The Main Computational Subroutines in LFO

Subroutine Name	Inputs	Outputs	Description
UPDATE	t, γ_1, γ_2, γ_L	t, γ_1, γ_2, γ_L	Increments variables between computation times
ARRAY	$\hat{T}$, $\hat{S}$	R	With antenna target at $\hat{T}$ and sun at $\hat{S}$, R = Per cent of antenna pattern not blocked by array
ECLIPSE	$\hat{S}$, R_E	ISUN, IDAY	ISUN = { 1, L-D in sun; 0, L-D eclipsed } IDAY = { 1, subsatellite point lighted; 0, subsatellite point dark }
LAT	γ_1, γ_L, γ_I, γ_D, ALAT 1	ALAT, ALONG	Computes geographical latitude and longitude of subsatellite point.
GIMBAL	$\hat{T}$	G_1, G_2	Given antenna target at $\hat{T}$, computes the antenna gimbal angles
LANDSEA	ALAT, ALONG	LAND	LAND = { 0, L-D over water; 1, L-D over land }

The current version of the program assumes uniform step sizes between computation times, a simple rectangular array driven to follow the sun, circular orbits, and the target (TDRS) in a geosynchronous orbit. These assumptions are not necessary, and they could be changed by revising the various subroutines. For example, subroutine UPDATE could be changed to include the effects of an elliptical orbit or to make the intervals between computation times vary -- possibly dependent upon the program outputs.

Subroutine LAT contains an equation for converting true latitude to geographic latitude. The difference is shown in Figure 3-8 where ϕ_T is the true latitude calculated from the L-D position and ϕ_g is the geographic latitude which depends on the "local vertical".

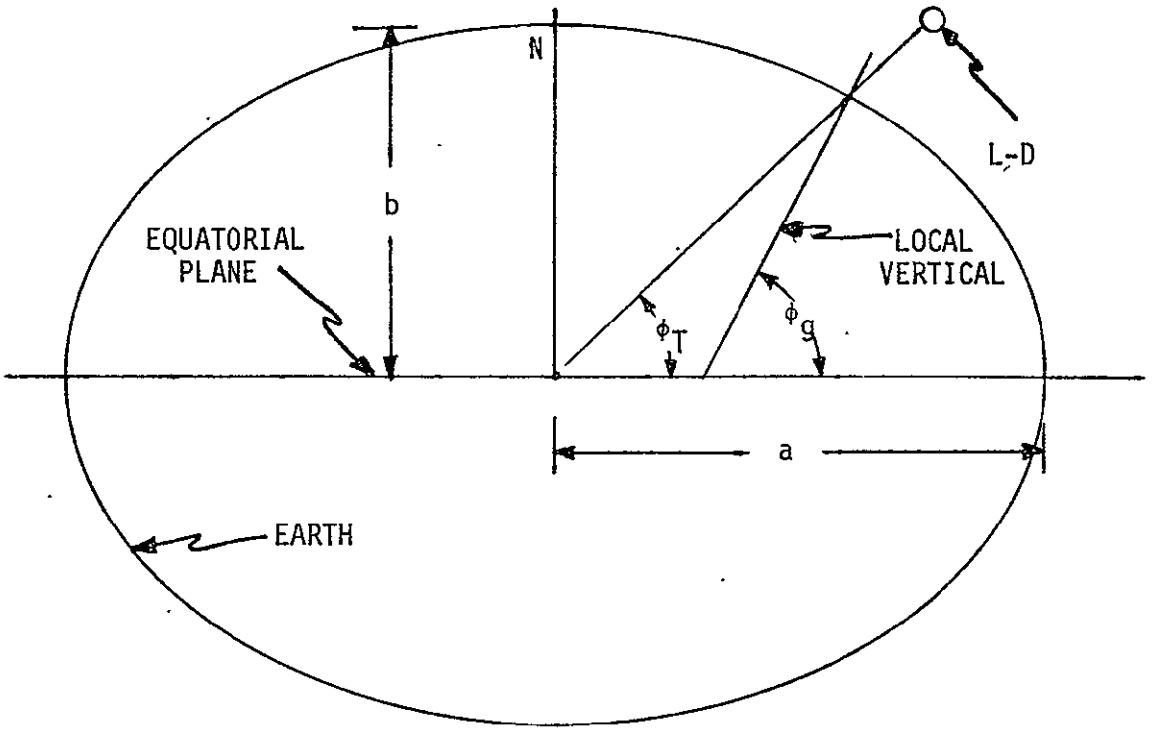

Figure 3-8. Illustration of the Difference Between True and Geographic Latitude

In Reference 6, the two angles are related by the equation

$$\sin \phi_T = \frac{\sin \phi_g}{\left[\sin^2 \phi_g + \left(\frac{a}{b}\right)^4 \cos^2 \phi_g\right]^{1/2}} \qquad (3.4\text{-}1)$$

where

$$\frac{a}{b} = 1.00336417$$

But this easily reduces to the more convenient form

$$\tan \phi_g = \left(\frac{a}{b}\right)^2 \tan \phi_T \qquad (3.4\text{-}2)$$

which is used in the subroutine. This latitude correction changes the latitude by a maximum of 0.2 degree. The longitude computed in LAT is positive for western longitudes and negative for eastern longitudes. The subroutine LANDSEA uses the latitude and longitude to determine whether the point is over land or water. This subroutine was originally written for another program and has been incorporated into this program. The information is stored in 42,261 bits, each representing a 111.2 x 111.2 km piece of the earth's surface -- 1° x 1° at the equator.

3.4.2 Program LFO Abbreviated Users' Guide

The L-D user supplies the program input variables using a namelist file on TAPE3 called "IN". The variables supplied are listed in Table 3-7. The program supplies default values for most of the variables, as shown; the remaining variables must be supplied by the user. Some example runs are given later, but a sample input file is shown in Table 3-8. For the sample input shown, the output file -- from TAPE4 -- is shown in Table 3-9. In practice, the information on the output file would be plotted as in the examples given in Section 3.4.4.

The input variables have the units shown in Table 3-7. The various angles are supplied in degrees for convenience; the program converts the angles to radians for internal use, and then the output angles are reconverted to degrees.

Table 3-7. Program LFO Input Variables

Variable Name	Symbol	Description	Default Value
ALAT1		Longitude of TDRS #1 (Deg)	+41.0
ALPHAS	α_s	Antenna FOV Skirt (Deg)	2.
ARRL	ℓ	Length of Solar Array (Ft)	--
ARRW	ω	Width of Solar Array (Ft)	--
ATMAST	$\bar{a}$	Vector from Edge of Array to Base of MAST (Ft)	$\bar{0}$
CANT	α_c	Solar Array Cant Angle (Deg)	37.5
DELTA1	Δ_1	Rate of Change of γ_1 (Deg/Hr)	15.
DELTAL	Δ_L	Rate of Change of γ_L (Deg/Hr)	220.31
DELTAT	Δ_T	Time Increment (Hr)	--
DIRMAST	$\bar{m}$	Vector Along MAST Toward Antenna	(0,0,-1)
FINALT	T_F	Final Time (Hr)	--
GAMMA1	γ_1	(Initial) Position of TDRS #1 (Deg)	0.
GAMMAD	γ_D	- Angle of Descending Node (Deg)	37.5
GAMMAI	γ_I	L-D Orbit Inclination Angle (Deg)	98.2
GAMMAL	γ_L	(Initial) Position of L-D (Deg)	0.
GAMMAS	γ_S	Angle of Sun Below Equatorial Plane (Deg)	0.
HMAST	h	Antenna Mast Length (Ft)	--
RDISH	R_D	Radius of Ku-Band Antenna Dish (ft)	3.
REARTH	R_E	Earth Half-Angle from L-D (Deg)	64.2
RL	R_L	L-D Orbit Radius (Km)	7074.
RT	R_T	TDRS Orbit Radius (Km)	4.22×10^4

Table 3-8. A Sample LFO Input

```
P$IN
  DELTAT=0.05
  FINALT=1.6
  HMAST=6.34
  ARRW=5.
  ARRL=25.6
  $END
```

Table 3-9. Output with Input Shown in Table 3-8

T	Y_L	Y_1		g_1,Az	g_2,EL	Y_2		g_1,Az	g_2,EL					
TIME	LF/D	TDRS1	TRANS	GIMBAL	ANGLES	TDRS2	TRANS	GIMBAL	ANGLES	DAY	SUN	LAT	LONG	LAND
0.000	0.0	0.0	100.0	-37.2	-4.6	-130.0	100.0	92.5	-17.4	1	1	81.9	-11.5	0
.050	11.0	.7	100.0	-39.1	4.1	-129.2	100.0	90.2	-17.6	1	1	76.4	43.0	1
.100	22.0	1.5	100.0	-42.2	12.6	-128.5	100.0	87.8	-17.2	1	1	66.7	60.6	1
.150	33.0	2.2	100.0	-46.8	20.7	-127.7	100.0	85.7	-16.3	1	1	56.2	68.4	1
.200	44.1	3.0	100.0	-53.1	28.0	-127.0	100.0	83.9	-14.8	1	1	45.5	73.1	1
.250	55.1	3.7	100.0	-61.6	34.1	-126.2	100.0	82.5	-13.0	1	1	34.7	76.6	0
.300	66.1	4.5	100.0	-72.1	38.3	-125.5	100.0	81.7	-10.9	1	1	23.8	79.4	0
.350	77.1	5.2	100.0	-84.1	40.2	-124.7	100.0	81.4	-8.7	1	1	12.8	81.9	0
.400	88.1	6.0	100.0	-96.2	39.3	-124.0	100.0	81.7	-6.4	1	1	1.9	84.2	0
.450	99.1	6.7	100.0	-107.1	35.9	-123.2	100.0	82.6	-4.1	1	1	-9.1	86.6	0
.500	110.2	7.5	100.0	-115.8	30.7	-122.5	100.0	84.0	-2.1	1	1	-20.1	89.0	0
.550	121.2	8.2	100.0	-122.3	24.2	-121.7	100.0	86.0	-.5	1	1	-31.0	91.7	0
.600	132.2	9.0	100.0	-126.9	16.9	-121.0	100.0	88.3	.7	1	1	-41.8	94.9	0
.650	143.2	9.7	100.0	-129.8	9.3	-120.2	100.0	91.0	1.2	1	1	-52.6	99.0	0
.700	154.2	10.5	100.0	-131.4	1.6	-119.5	100.0	93.7	1.2	1	1	-63.2	105.5	0
.750	165.2	11.2	100.0	-131.8	-5.9	-118.7	100.0	96.5	.4	1	1	-73.3	118.2	0
.800	176.2	12.0	100.0	-131.0	-13.2	-118.0	100.0	99.0	-.9	0	1	-81.0	155.8	0
.850	187.3	12.7	91.4	-129.2	-20.0	-117.2	100.0	101.3	-2.9	0	1	-79.1	-137.0	1
.900	198.3	13.5	-20.0	-126.2	-25.8	-116.5	100.0	103.0	-5.4	0	1	-70.1	-111.4	1
.950	209.3	14.2	-20.0	-122.0	-25.8	-115.7	100.0	104.2	-8.3	0	0	-59.8	-101.5	0
1.000	220.3	15.0	-20.0	-116.5	-25.8	-115.0	100.0	104.8	-11.4	0	0	-49.2	-96.0	0
1.050	231.3	15.7	-20.0	-109.7	-25.8	-114.2	100.0	104.6	-14.6	0	0	-38.4	-92.3	0
1.100	242.3	16.5	-20.0	-102.0	-25.8	-113.5	100.0	103.7	-17.8	0	0	-27.5	-89.3	0
1.150	253.4	17.2	-20.0	-93.8	-25.8	-112.7	100.0	102.1	-20.8	0	0	-16.6	-86.7	0
1.200	264.4	18.0	-20.0	-85.7	-25.8	-112.0	100.0	99.7	-23.5	0	0	-5.6	-84.3	0
1.250	275.4	18.7	-20.0	-78.3	-25.8	-111.2	100.0	96.6	-25.6	0	0	5.4	-82.0	0
1.300	286.4	19.5	-20.0	-72.1	-25.8	-110.5	-20.0	92.9	-25.8	0	0	16.3	-79.6	1
1.350	297.4	20.2	-20.0	-67.1	-25.8	-109.7	-20.0	88.8	-25.6	0	0	27.3	-77.0	1
1.400	308.4	21.0	-20.0	-63.5	-25.8	-109.0	-20.0	84.4	-25.8	0	0	38.2	-74.0	1
1.450	319.4	21.7	48.3	-61.2	-22.7	-108.2	-20.0	80.1	-25.8	0	0	49.0	-70.3	1
1.500	330.5	22.5	56.9	-59.9	-17.2	-107.5	100.0	76.0	-25.3	0	1	59.6	-64.9	1
1.550	341.5	23.2	66.9	-59.8	-11.6	-106.7	100.0	72.4	-22.7	0	1	69.9	-55.2	0
1.600	352.5	24.0	100.0	-60.6	-6.0	-106.0	100.0	69.4	-19.4	0	1	79.0	-30.2	0
1.650	363.5	24.7	100.0	-62.4	-.8	-105.2	100.0	67.2	-15.5	1	1	81.1	36.5	1

3.4.3 Two Key Subroutines

The purpose of the subroutine ARRAY is to compute the fraction of the Ku-band antenna field-of-view pattern that is blocked by the solar array. The solar array is assumed to be a rectangular array of length ℓ and width w. It is also assumed that the array is mounted in such a way that it is canted to the spacecraft $-\hat{y}_o$ axis and is driven to rotate about the $\hat{y}_o$ axis to track the sun. This is illustrated in Figure 3-9, where $\hat{s}$ is the sun vector, $\hat{T}$ is the target vector and θ_c is the array cant angle. The distance indicated as L in Figure 3-9 is the distance from the x-y plane to the top of the mast; this has been referred to as the "mast length" in previous work. In the program, the variable HMAST is used instead to represent the true mast length as measured from the spacecraft mounting point to the hinge.

The field-of-view of the antenna is a cylindrical beam of radius R_D extending out from the antenna dish plus a 1 to 2 degree skirt all around the cylinder. The solar array interference is found by:

(1) The solar array orientation is determined from the sun vector $\hat{s}$.

(2) A ray of the antenna beam at the center of the dish is found and used to determine the average distance from the dish to the plane of the array.

(3) That distance is used to determine the FOV diameter at the plane of the array -- this includes the skirt.

(4) A pair of unit vectors that form an orthonormal basis with $\hat{T}$ are used to construct a uniform distribution of points in the FOV.

(5) A ray of the antenna beam through each of those points is extended to the plane of the array.

(6) The portion of those rays that intersect the array is the interference.

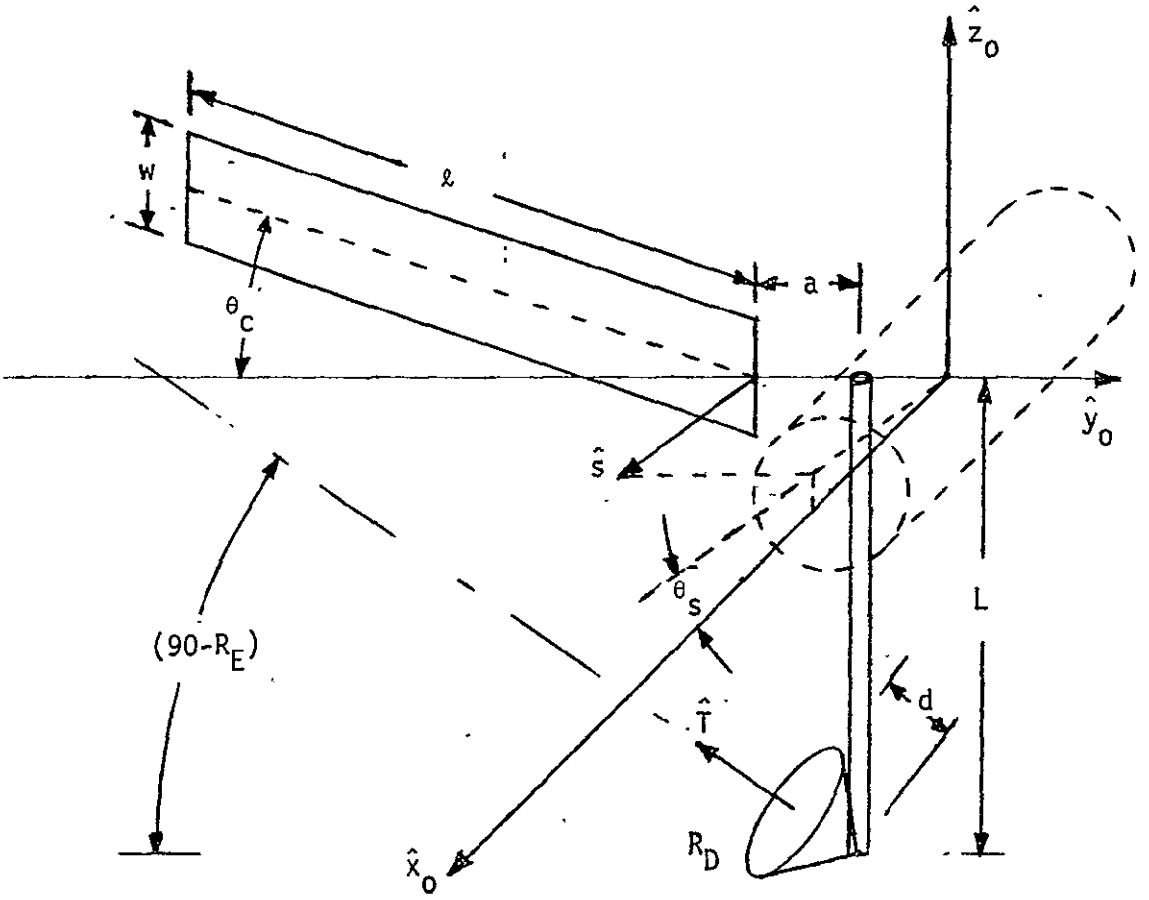

Figure 3-9. The Antenna and Solar Array in Orbit Coordinates

Given the sun unit vector, $\hat{s} = [s_x, s_y, s_z]^T$, the array rotation angle θ_s in Figure 3-9 is given by

$$\theta_s = \tan^{-1}\left(\frac{s_x}{s_z}\right) \tag{3.4-3}$$

where θ_s is the angle between the x axis and the projection of the sun vector onto the $\hat{x}$-$\hat{z}$ plane. This means θ_s is zero when the spacecraft is over the North Pole -- 8.2 degrees away, actually -- at a solstice. If the array cant angle is θ_c, then a vector in body coordinates O can be written in array coordinates A as

$$\bar{r}_A = [\theta_c]_x [-\theta_s]_y \bar{r}_o = T_{AO} \bar{r}_o \tag{3.4-4}$$

This assumes that the two coordinate systems have the same origin, which is an acceptable assumption in the case of the sun and TDRS vectors. The coordinate system A is the one in which the solar array lies in the x_A-y_A plane with its inner edgelying on the x_A axis.

In the program, the mast length h is called HMAST, the mast direction $\hat{m}$ is given by the vector DIRMAST and the antenna mast base is located by the vector ATMAST ($\bar{a}$) relative to the origin of the coordinate system A -- the above vectors are given in the O coordinate system. Thus, in array coordinates, the antenna hinge is at the point

$$\bar{v} = T_{AO} \{\bar{a} + h \hat{m}\} \tag{3.4-5}$$

Since the antenna is pointed at the target, the center ray of the beam -- which is aligned with the hinge -- intersects the points

$$\bar{r}_o = \bar{v} + \alpha \hat{T} \tag{3.4-6}$$

where α is a parameter. Thus the distance from the hinge to the plane of the array is given by

$$\alpha_o = - \frac{(\bar{v})_z}{(\hat{T})_z} \tag{3.4-7}$$

because that is the value which makes $(\bar{r}_o)_z \equiv 0$. This can be used to compute the FOV radius at the plane of the array:

$$R_c = R_D + (\alpha_o - d) \tan (\alpha_s) \tag{3.4-8}$$

where R_D is the radius of the dish, α_s is the angle of the skirt and

$$d = \frac{R_D}{\tan (R_E)} \tag{3.4-9}$$

where R_E is the earth half-angle.

Given $\hat{T}_A$ -- the target unit vector in array coordinates -- and a suitable unit vector $\hat{e}_o$, a pair of orthogonal unit vectors in the plane P perpendicular to $\hat{T}_A$ are formed as

$$\hat{e}_1 = (\hat{T}_A \times \hat{e}_o)/(|\hat{T}_A \times \hat{e}_o|) \tag{3.4-10}$$

and

$$\hat{e}_2 = \hat{T}_A \times \hat{e}_1 \tag{3.4-11}$$

These basis vectors are then used to form a set of 625 points uniformly distributed over the square in P that circumscribes the FOV circle of radius R_c. A particular point is given by

$$\bar{c} = a_1 \hat{e}_1 + a_2 \hat{e}_2 \tag{3.4-12}$$

where

$$a_1 = \frac{2i - n - 1}{n} R_c \quad , \quad i=1,\ldots,n \tag{3.4-13}$$

and

$$a_2 = \frac{2j - n - 1}{n} R_c \quad , \quad j=1,\ldots,n \tag{3.4-14}$$

where n = 25.

The ray parallel to $\hat{T}_A$ through one of the points is given by

$$\bar{r} = \bar{r}_o + \bar{c} = \bar{v} + \bar{c} + \alpha \hat{T}_A \tag{3.4-15}$$

If α is chosen so that $(\bar{r})_z = 0$, then $\bar{r}$ is the intersection of the ray with the plane of the solar array. This point of intersection is compared with the array boundaries to determine whether or not it intersects the array. The subroutine output is the percent transmission of the antenna which is

$$R = 100 \left[1 - \left(\frac{M_2}{M_1}\right)\right] \tag{3.4-16}$$

where M_1 is the number of points lying in the circle and M_2 is the number of those points that emanate rays which intersect the solar array.

Subroutine Gimbal

The purpose of this subroutine is to compute the gimbal angles required to point the Ku-band antenna at the target. In the subroutine, it is assumed that there are two gimbals with the inner gimbal angle being the elevation angle and the outer gimbal angle being the azimuth angle. In the normal or null position, the antenna is pointed along the roll axis and the elevation axis is the spacecraft pitch axis -- see Figure 3-10. Thus for a normalized target vector $\hat{T}$, the required gimbal angles g_1 and g_2 are found from

$$\begin{bmatrix} 1 \\ 0 \\ 0 \end{bmatrix} = [g_2]_y [g_1]_z \hat{T} \tag{3.4-17}$$

which is rearranged to obtain

$$T = \begin{bmatrix} T_x \\ T_y \\ T_z \end{bmatrix} = \begin{bmatrix} \cos g_1 \cos g_2 \\ \sin g_1 \cos g_2 \\ -\sin g_2 \end{bmatrix} \tag{3.4-18}$$

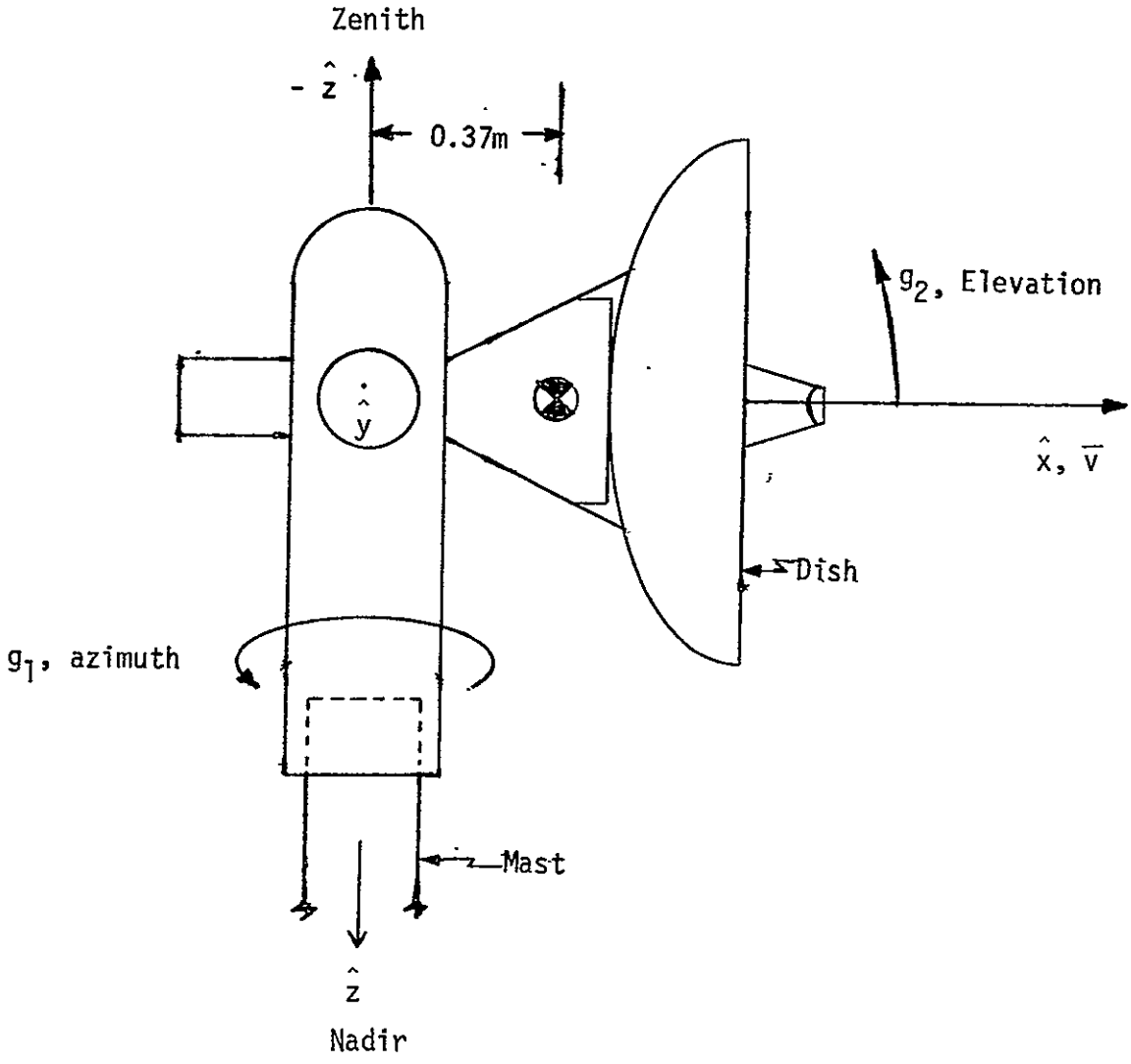

Figure 3-10. Ku-Band Antenna in the Null Position

Solving this for the gimbal angles:

$$g_1 = \tan^{-1}\left[\frac{T_y}{T_x}\right] \tag{3.4-19}$$

$$g_2 = \sin^{-1}\left[-T_z\right] \tag{3.4-20}$$

The gimbal equations for several two-gimbal configurations are given in Table 3-10. As discussed earlier, a third gimbal would be used only to overcome a severe gimbal-lock problem. Because there are several ways to utilize the third gimbal, it is not convenient to include the three-gimbal configuration in Table 3-10.

Table 3-10. Antenna Gimbal Equations

Outer Gimbal Axis	Inner Gimbal Axis	Nominal Antenna Direction	Outer Gimbal Angle, g_1	Inner Gimbal Angle, g_2
$\hat{z}$	$\hat{y}$	$[1 \quad 0 \quad 0]^T$	$\tan^{-1}[T_y/T_x]$	$\sin^{-1}[-T_z]$
$\hat{z}$	$\hat{y}$	$[0 \quad 0 \quad -1]^T$	$\tan^{-1}[T_y/T_x]$	$\cos^{-1}[-T_z]$
$\hat{z}$	$\hat{x}$	$[0 \quad 0 \quad -1]^T$	$\tan^{-1}[(-T_x)/T_y]$	$\cos^{-1}[-T_z]$
$\hat{y}$	$\hat{x}$	$[0 \quad 0 \quad -1]^T$	$\tan^{-1}[(-T_x)/(-T_z)]$	$\sin^{-1}[T_y]$
$\hat{x}$	$\hat{y}$	$[0 \quad 0 \quad -1]^T$	$\tan^{-1}[T_y/(-T_z)]$	$\sin^{-1}[-T_x]$

3.4.4 Examples

Although the cases in this section are examples of the use of Program LFO, they are also meaningful cases to the L-D study. In all cases the antenna mast length above the attachment point has been chosen as 6.34 feet. In the first example, the L-D passes through the "zone of exclusion" -- an area over the Indian Ocean where the earth blocks transmission to both TDRS's simultaneously. The input file is shown in Table 3-11, and the results of the run are shown in Figures 3-11 through 3-15. Figure 3-11 shows the percent transmission for the two potential targets. Note that toward the end of the first orbit shown, the earth blocks both targets -- this is the "zone of exclusion" (ZOE). Figure 3-12 indicates when the L-D is over a lighted earth, when it is eclipsed, and when it is over land. Note that the earth blockage of both TDRS's occurs over a dark earth in this case, but it could just as easily occur over a lighted earth. The solar array interference is much worse over this dark earth than over a lighted earth because the array follows the hidden sun. For the few orbits shown, TDRS2 would be chosen as the target because of the 100 percent transmission over the lighted earth.

Table 3-11. Input for First Example Showing the Zone of Exclusion

```
PSIN
 DELTAT=0.02
 FINALT=7.
 HMAST=6.34
 ARRW=5.
 ARRL=25.6
 GAMMA1=8.9
 $END
```

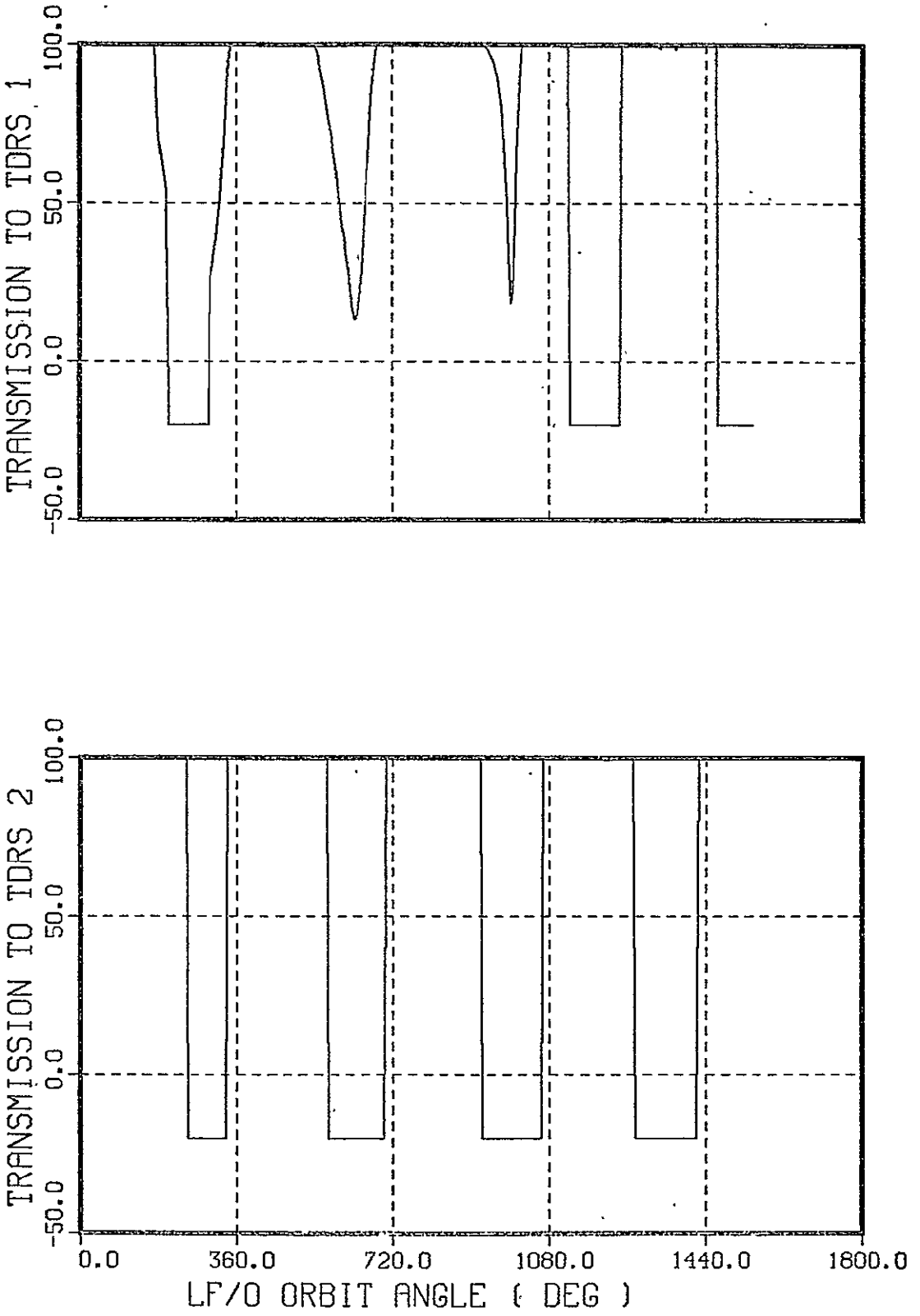

Figure 3-11. Zone of Exclusion at Night

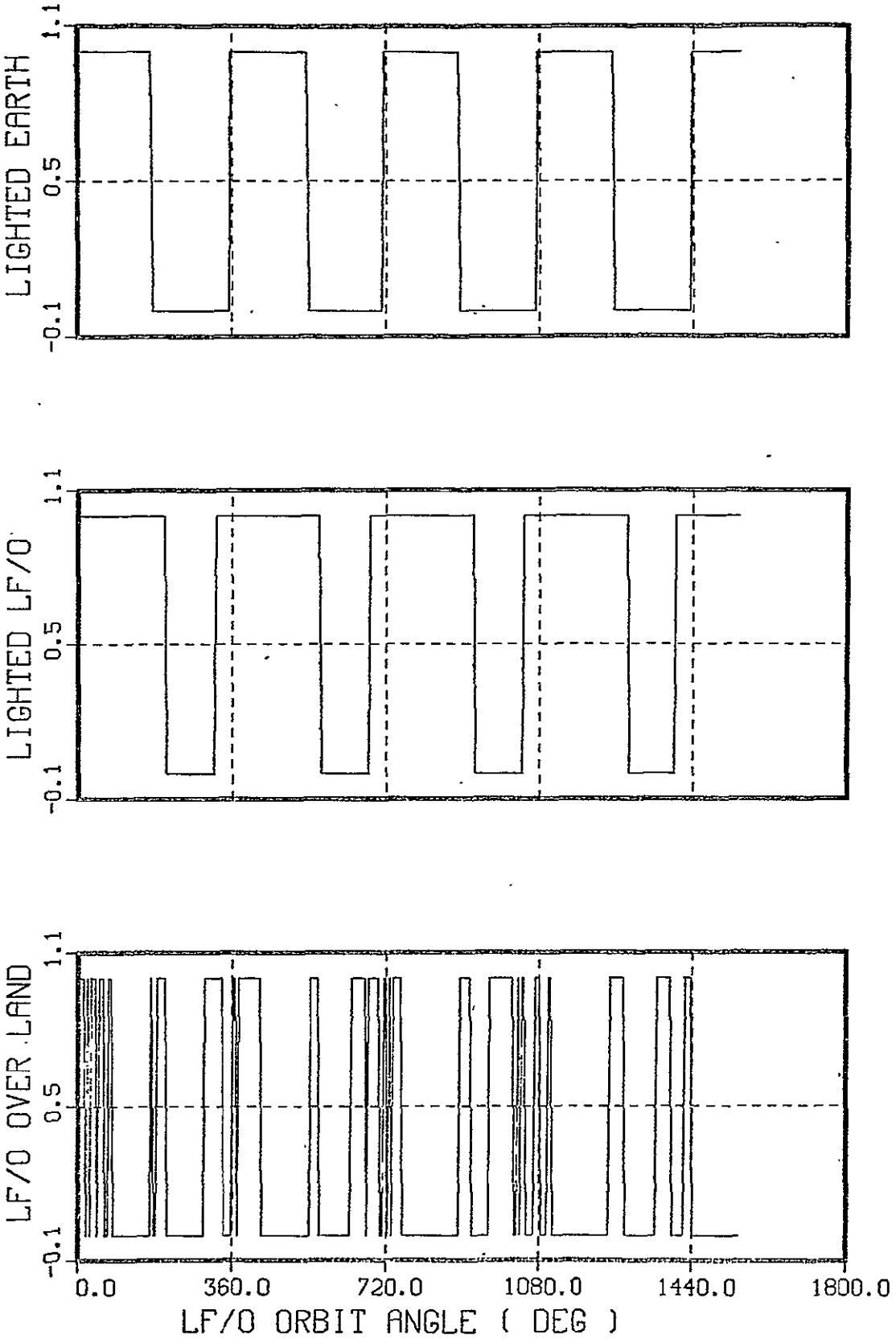

Figure 3-12. Zone of Exclusion at Night

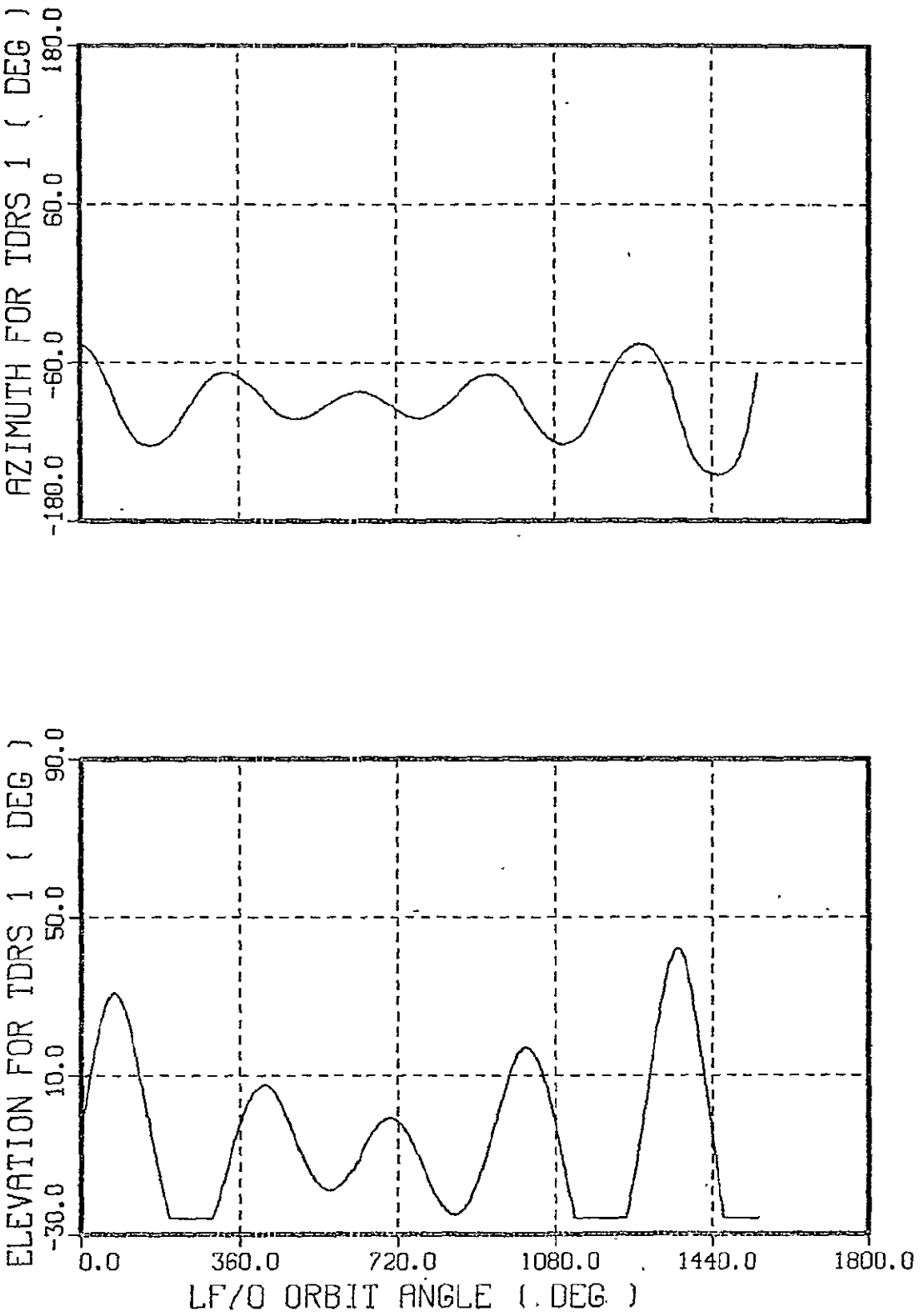

Figure 3-13. Zone of Exclusion at Night

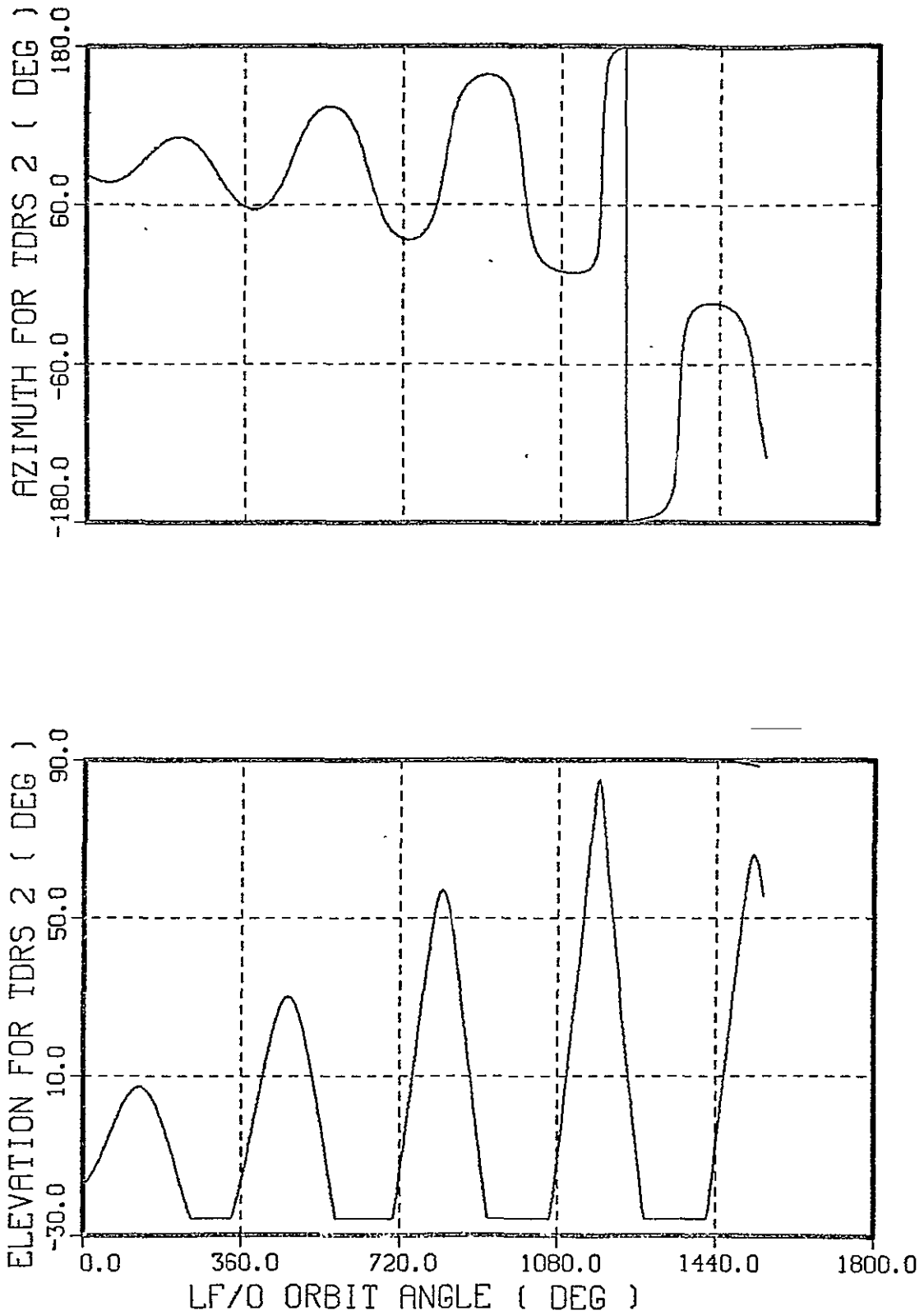

Figure 3-14. Zone of Exclusion at Night

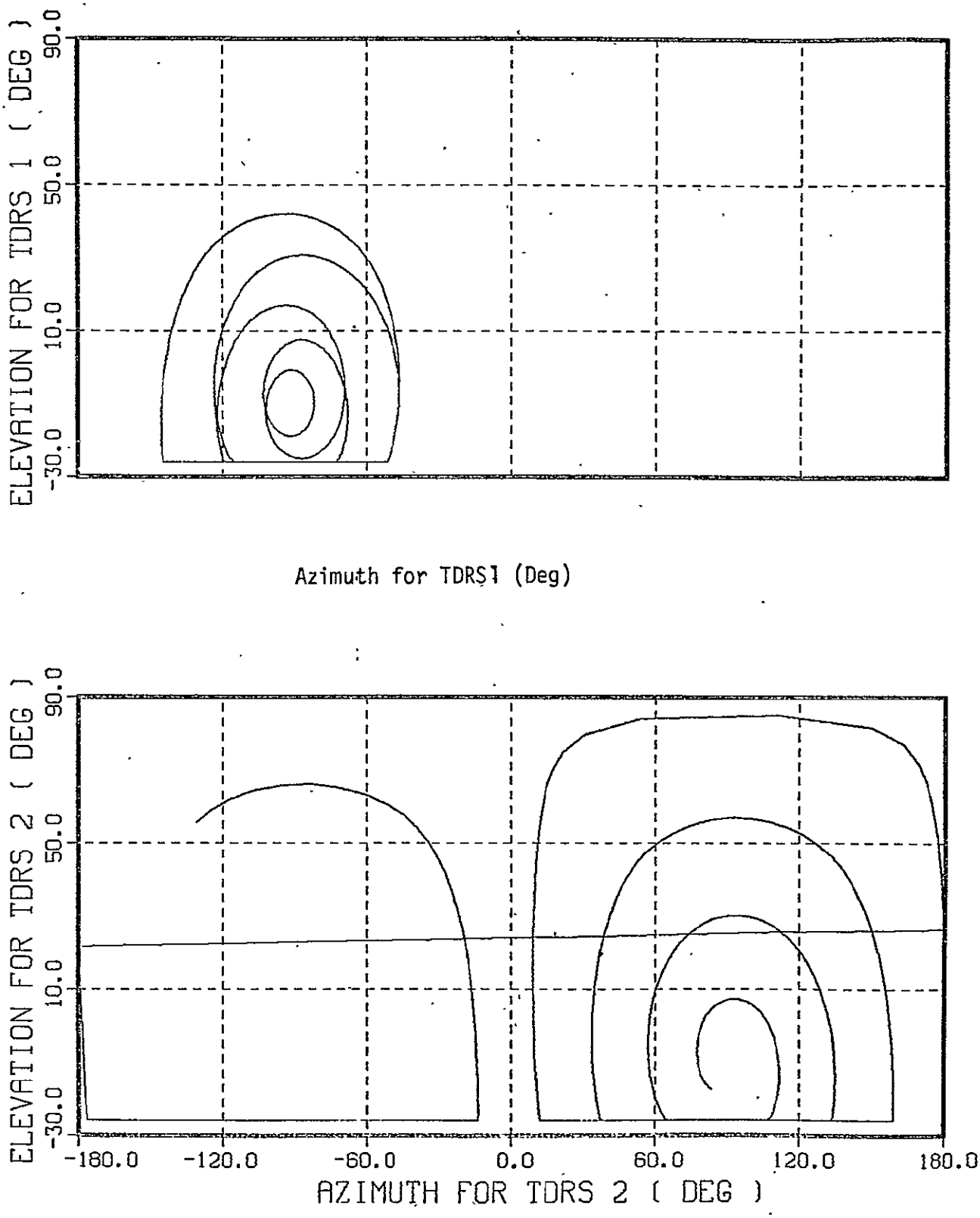

Figure 3-15. Zone of Exclusion at Night

Figures 3-13 and 3-14 show the required antenna gimbal angles. The elevation angle stops at -25.8 degrees because that is the edge of the earth: when the TDRS position is at an elevation beyond -25.8 degrees, it is hidden behind the earth. Note in Figure 3-14 that TDRS2 passes through the L-D orbit plane, requiring that the azimuth gimbal be reset. Also, the elevation angle is very nearly 90 degrees -- gimbal-lock occurs when the elevation angle is 90 degrees. Finally, Figure 3-15 shows the elevation angle plotted versus the azimuth angle.

The results of the second example are shown in Figures 3-16 through 3-20; the input file is in Table 3-12. This run shows the gimbal-lock case as indicated in Figure 3-20. According to Figure 3-16, the target should be TDRS2 during these four orbits. When the gimbal-lock occurs -- for a L-D orbit angle of about 800 degrees as seen in Figure 3-19 -- the earth blocks TDRS1, so TDRS2 is still the proper target.

The third example shows the L-D passing through the ZOE over a lighted earth. The input file is in Table 3-13, and the results are shown in Figures 3-21 through 3-25. Note that the solar array interference is much less than it was in the first example, this is because the solar array is rotated away from the antenna when the sun is overhead.

A fourth example consists of a 24 hour run (15 orbits) at vernal equinox conditions. Of main interest here is a summary of the percent of lighted land encountered. The program was initialized so that the first orbit contained the longest continuous land swath extending from the northern rim of Russia, across the middle east, to the southern tip of Africa. The lighted land data is important for the spacecraft power budget since nominally the TM needs be in the active data taking mode only when the spacecraft is over lighted land. The results are summarized in Figure 3-26 which gives percent lighted land per half and full orbit and percent land per orbit. For this particular 24 hour run (repetition occurs only after 16 days!) the L-D was over lighted land only 16.56% of the 24 hour period. The spacecraft was over land, lighted or dark, 34.23% of the 24 hour period.

Table 3-12. Input for Second Example Showing Gimbal Lock

```
P$IN
 DELTAT=0.02
 FINALT=7.
 HMAST=6.34
 ARRW=5.
 ARRL=25.6
 GAMMA1=38.
 $END
```

Table 3-13. Input for Third Example Showing the ZOE Over a Lighted Earth

```
P$IN
 DELTAT=0.02
 FINALT=7.
 HMAST=6.34
 ARRW=5.
 ARRL=25.6
 GAMMA1=-159.
 $END
```

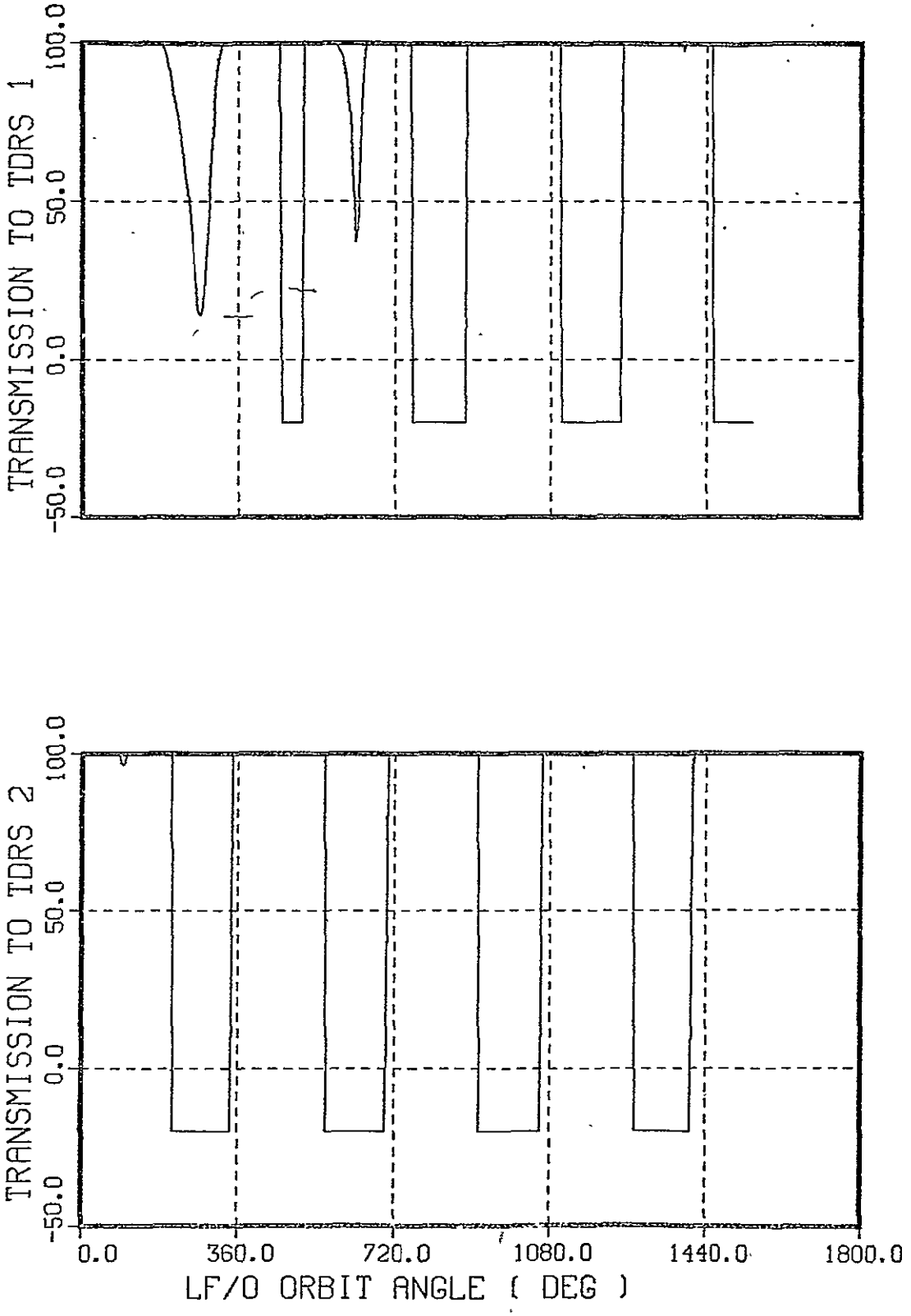

Figure 3-16. Gimbal Lock

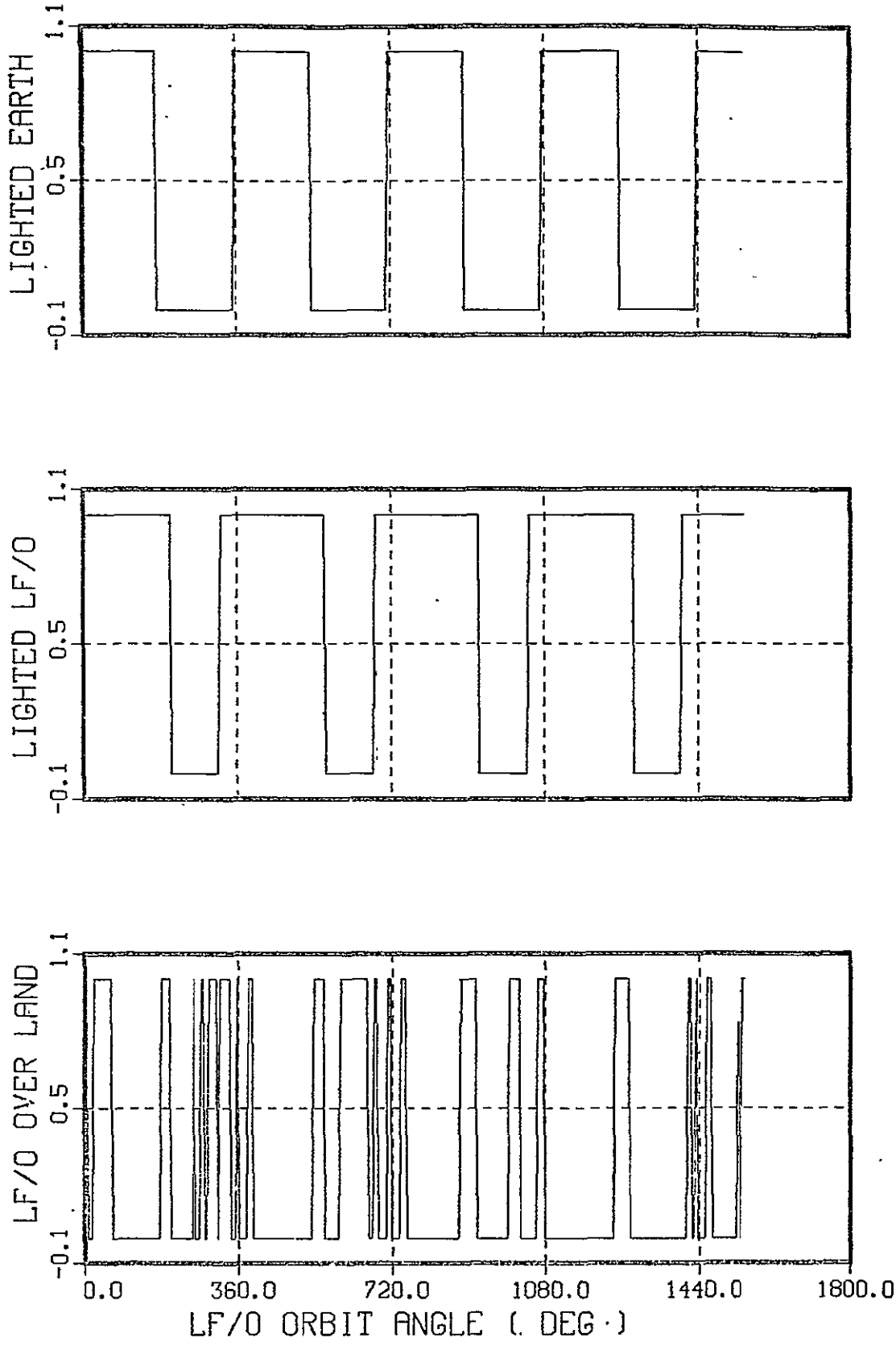

Figure 3-17. Gimbal Lock

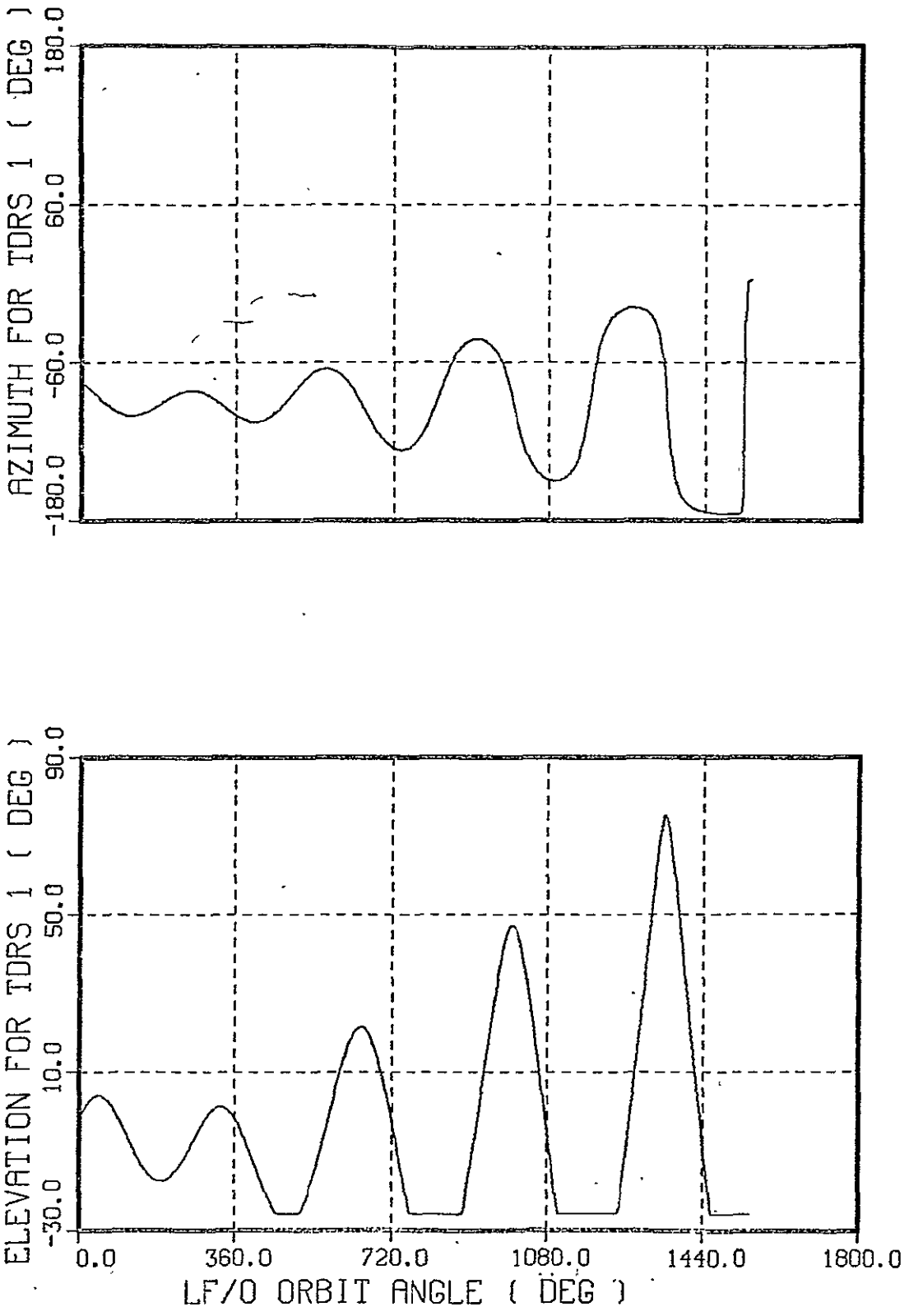

Figure 3-18. Gimbal Lock

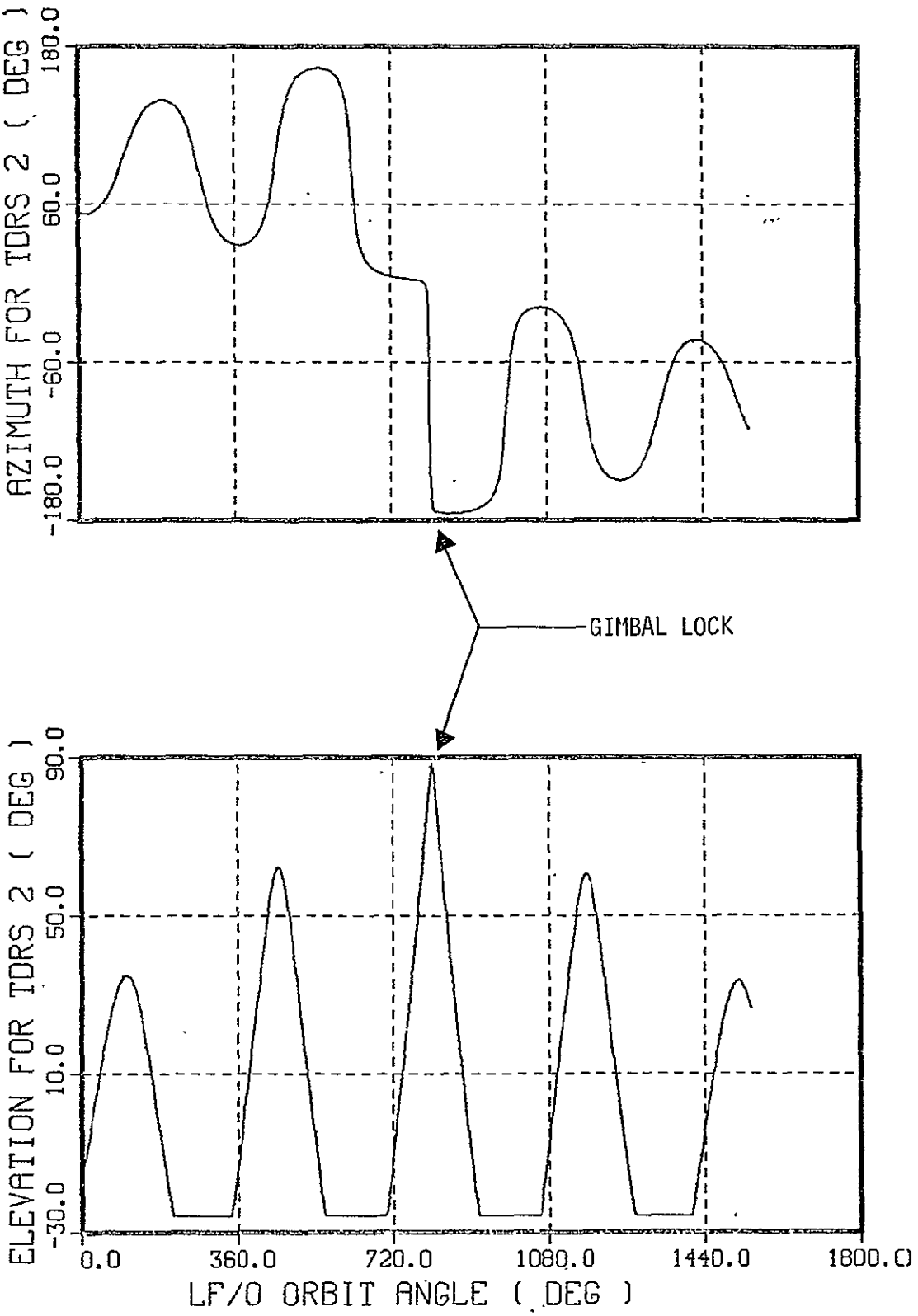

Figure 3-19. Gimbal Lock

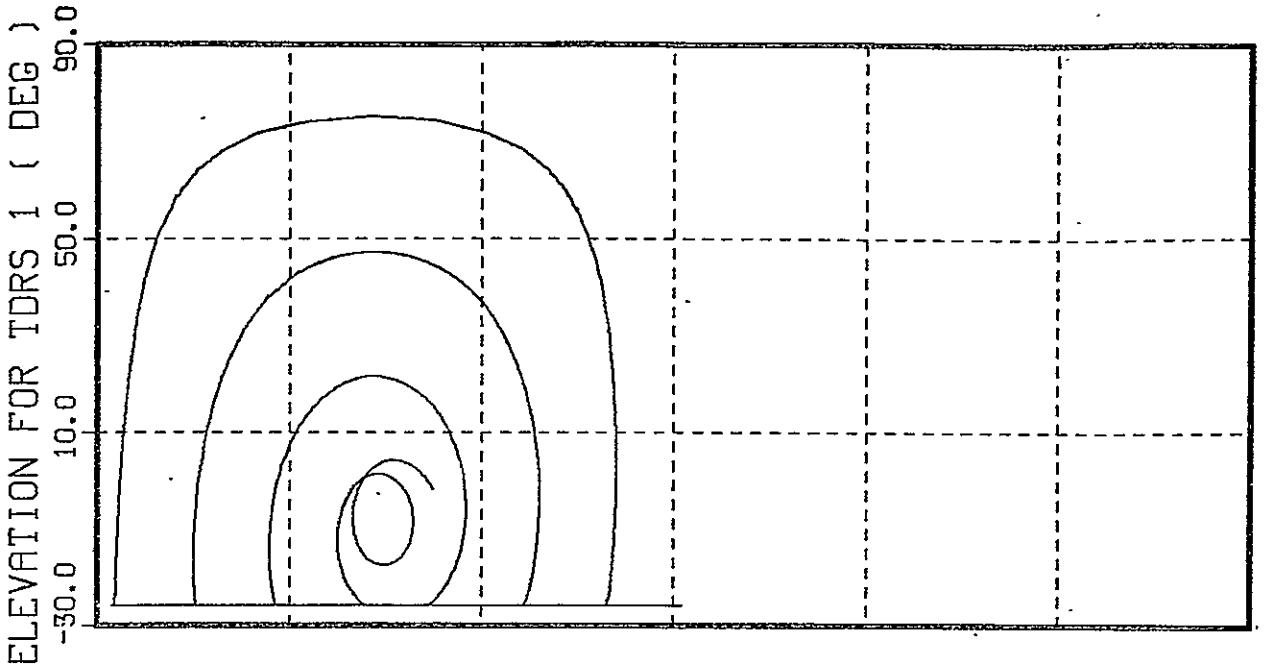

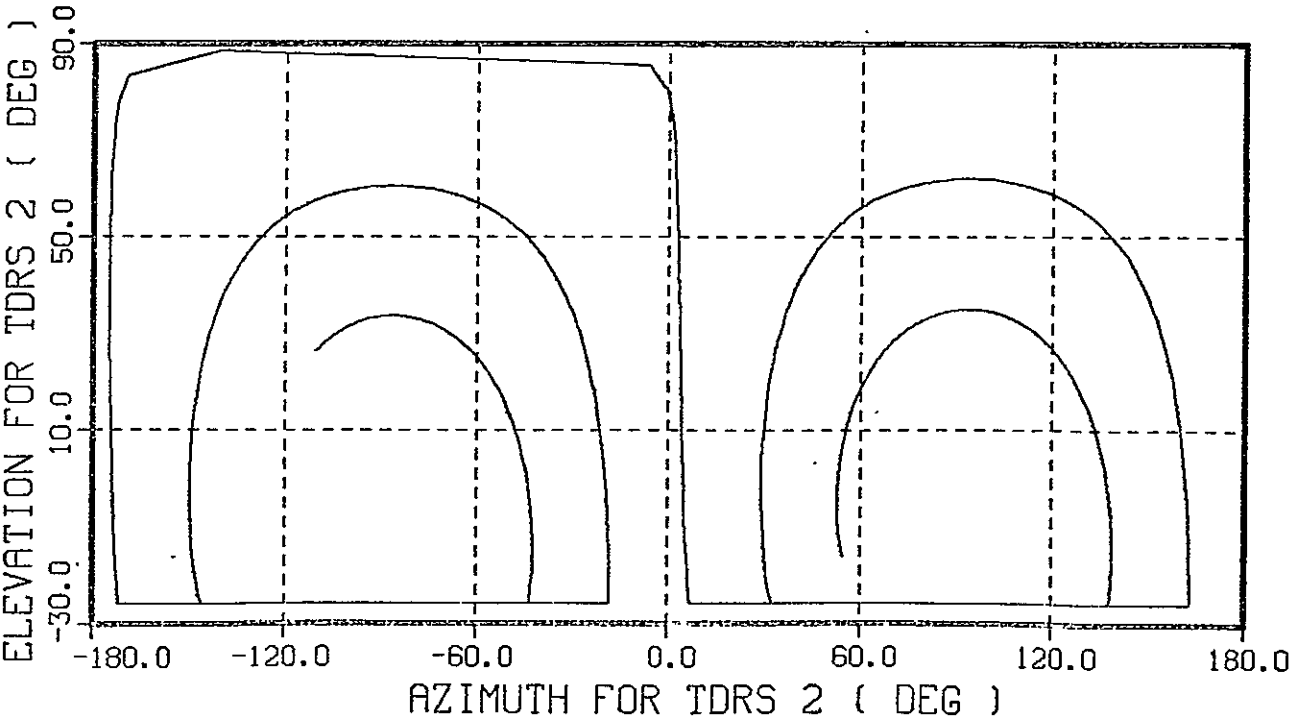

Figure 3-20. Gimbal Lock

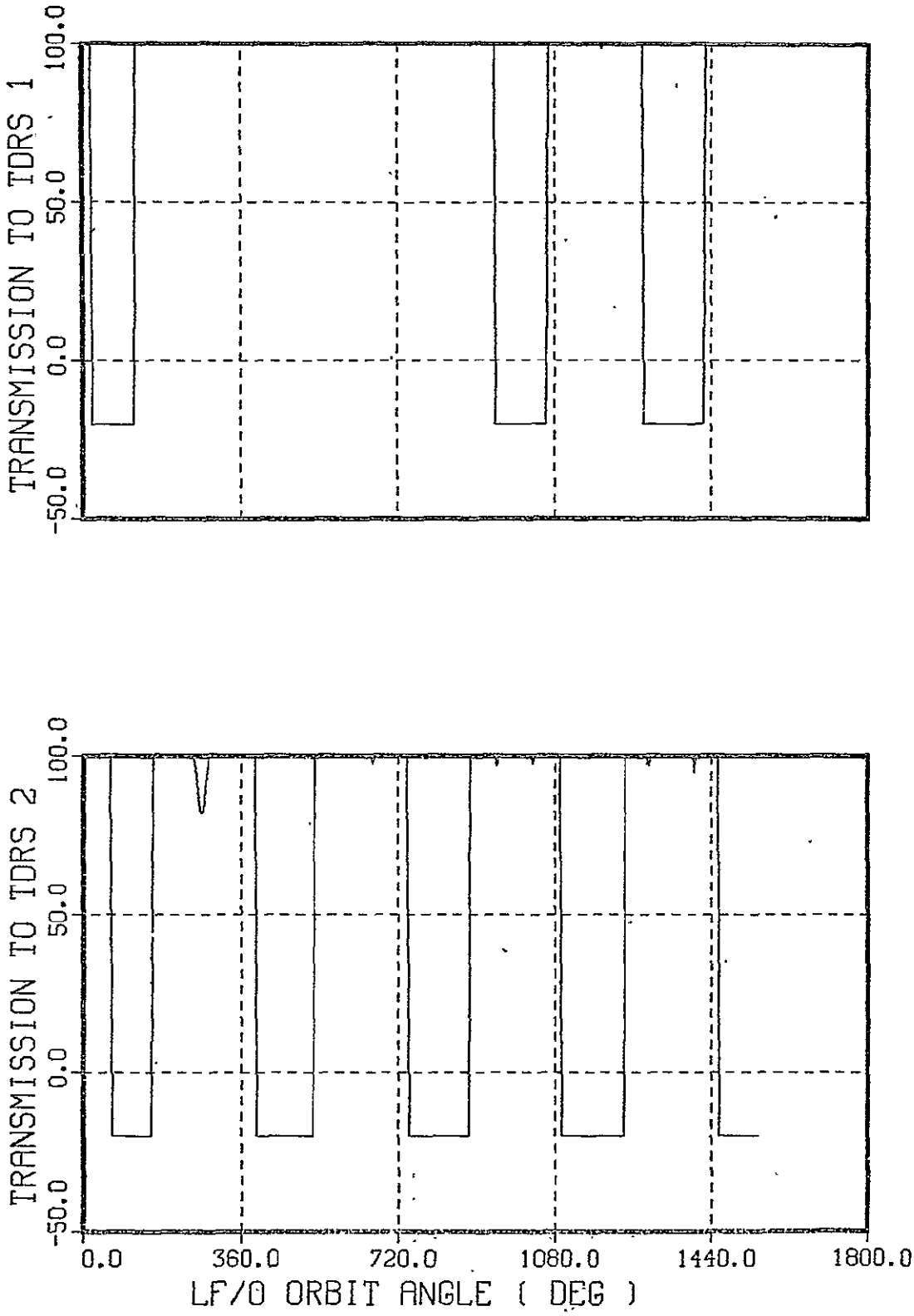

Figure 3-21. Zone of Exclusion Over Daylight

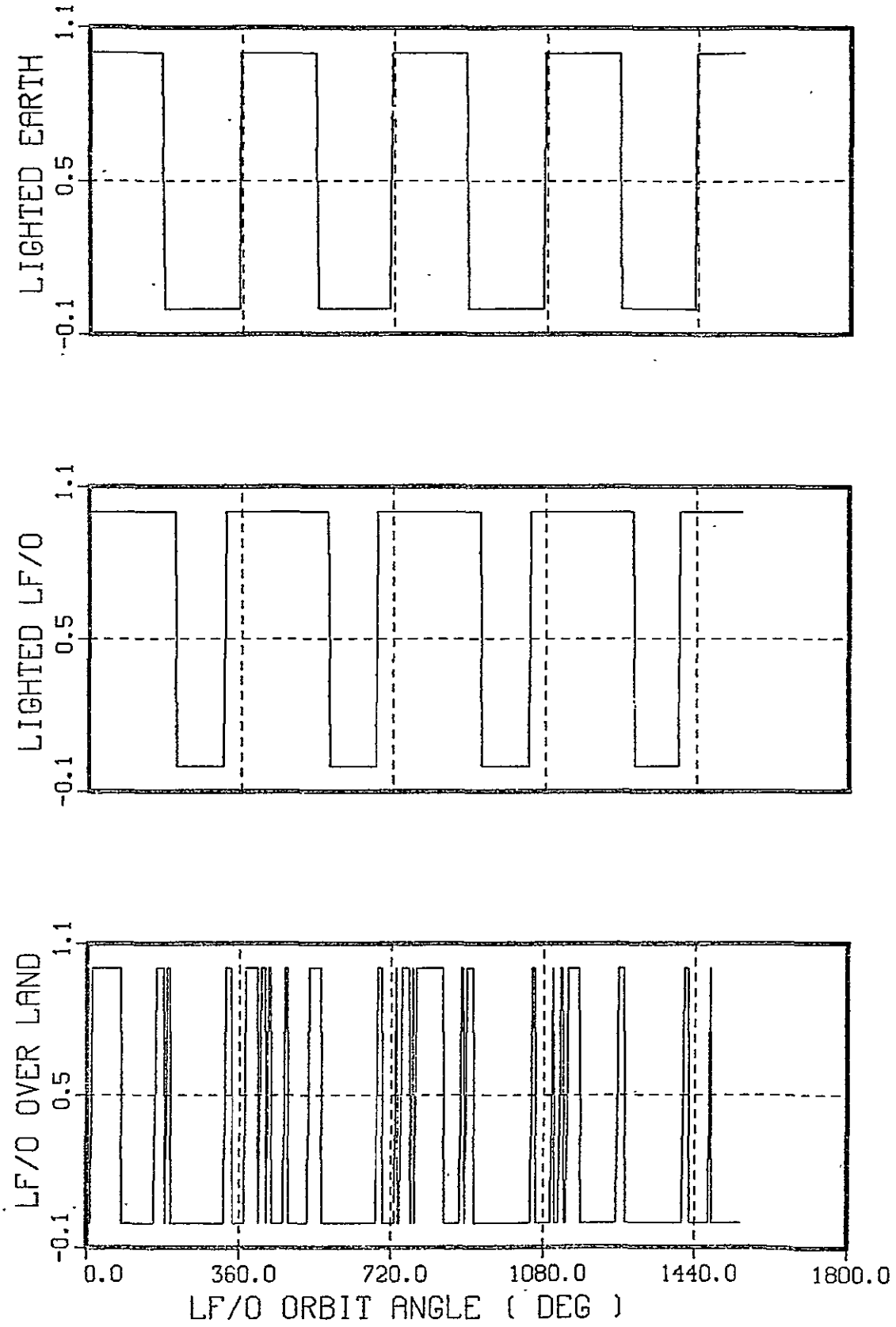

Figure 3-22. Zone of Exclusion Over Daylight

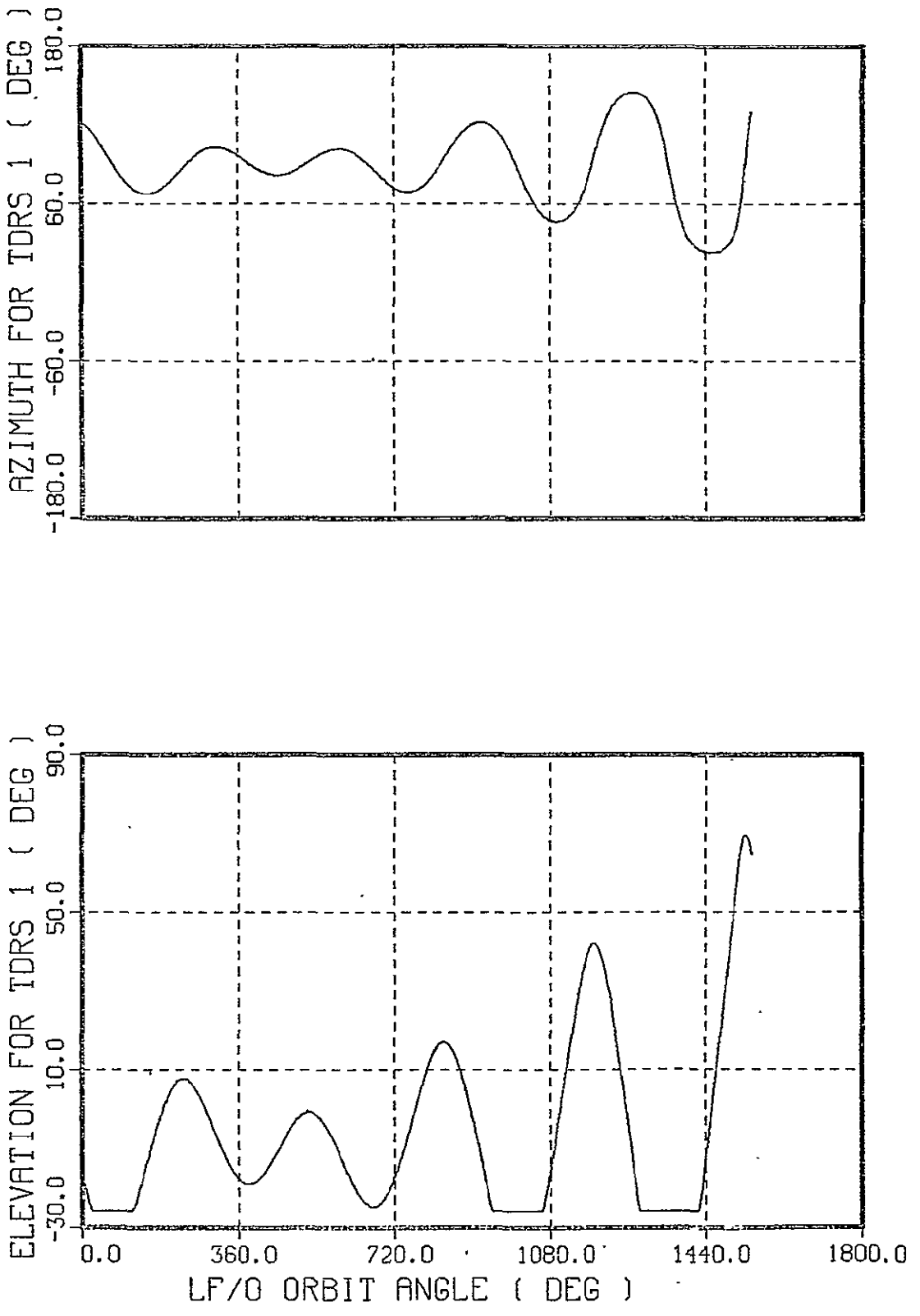

Figure 3-23. Zone of Exclusion Over Daylight

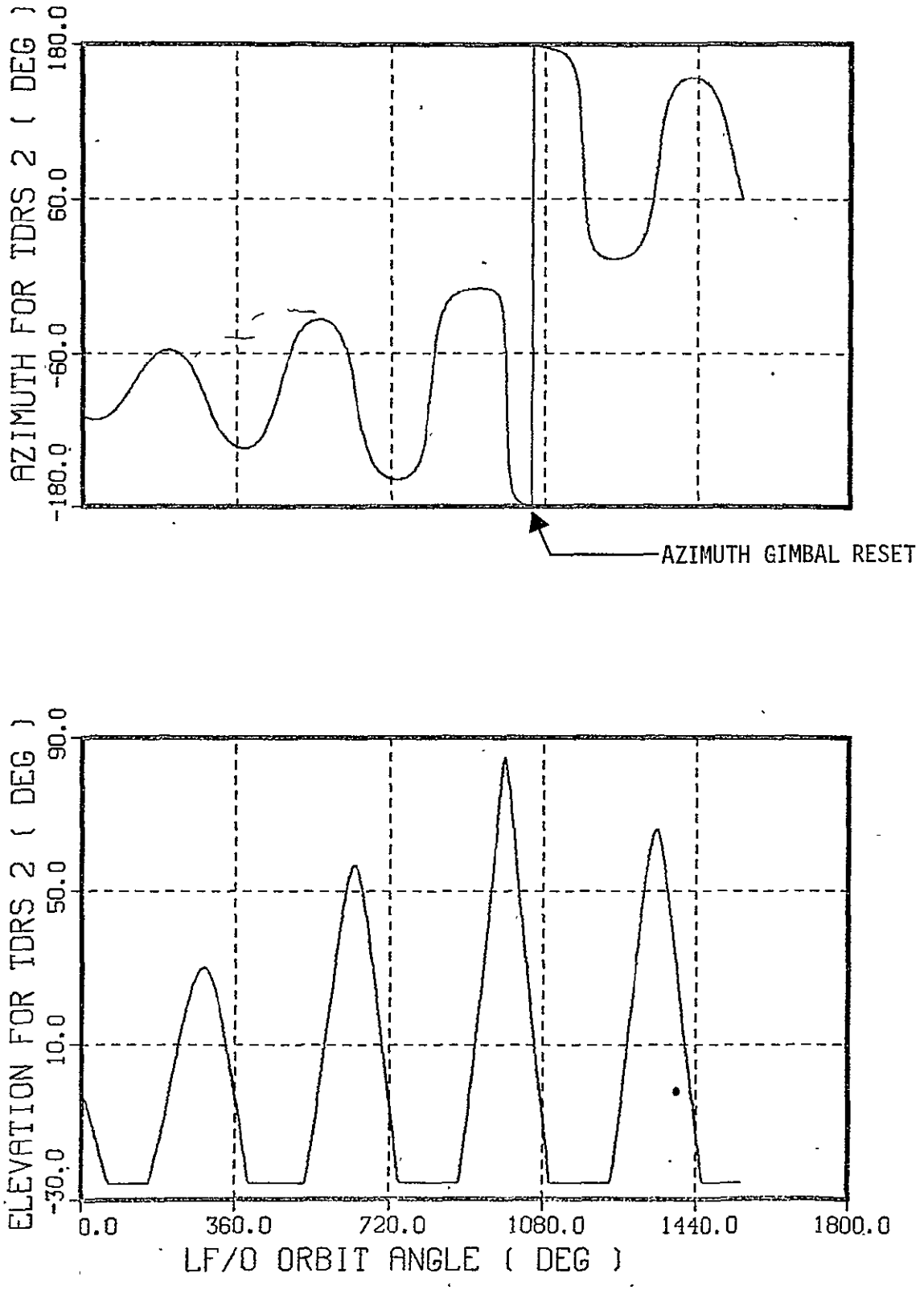

Figure 3-24. Zone of Exclusion Over Daylight

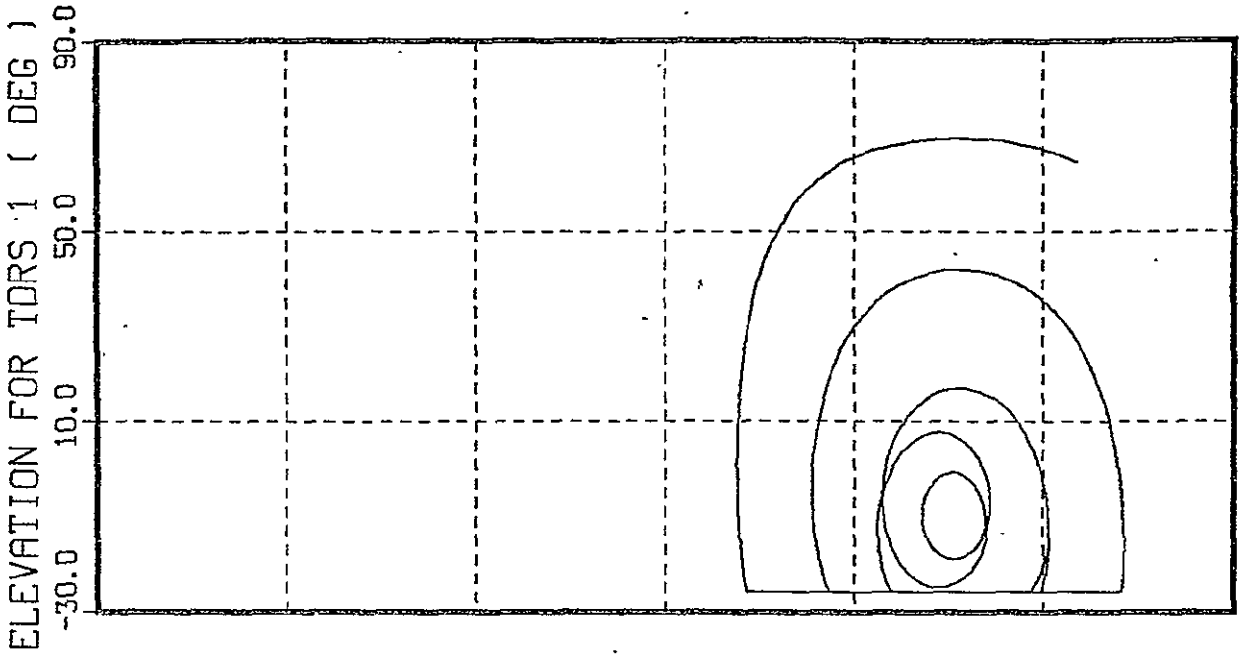

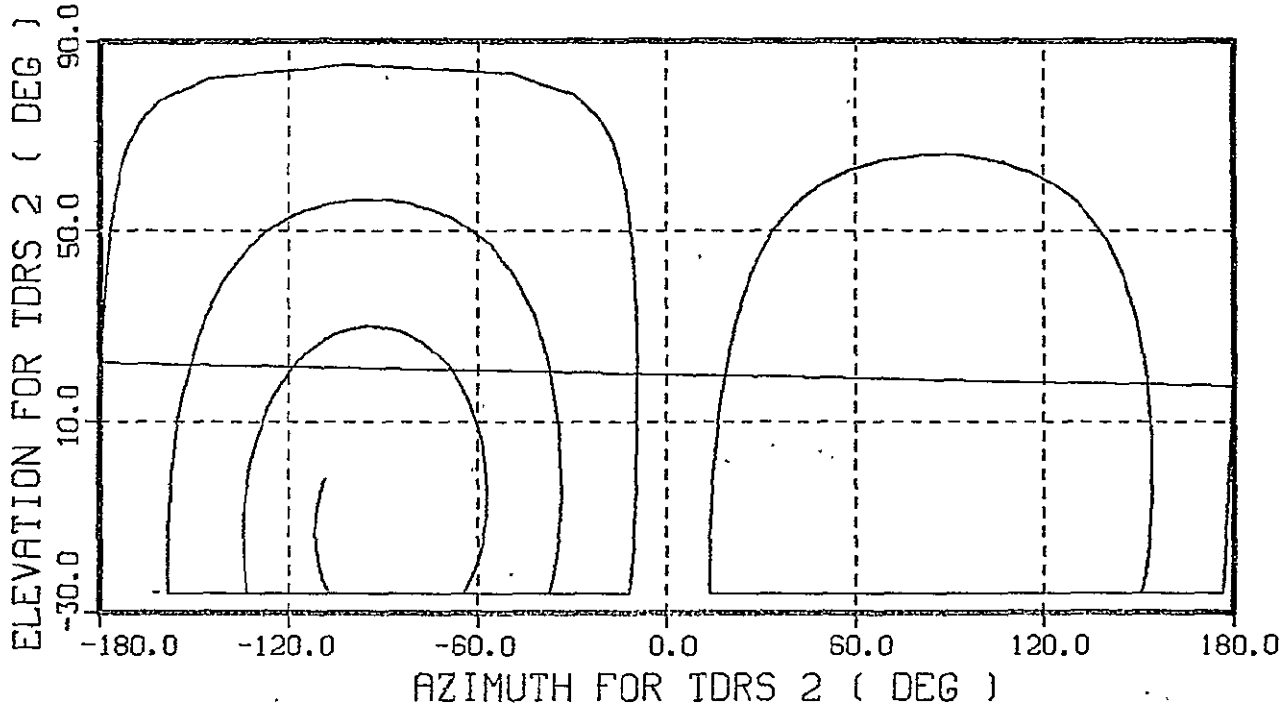

Figure 3-25. Zone of Exclusion Over Daylight

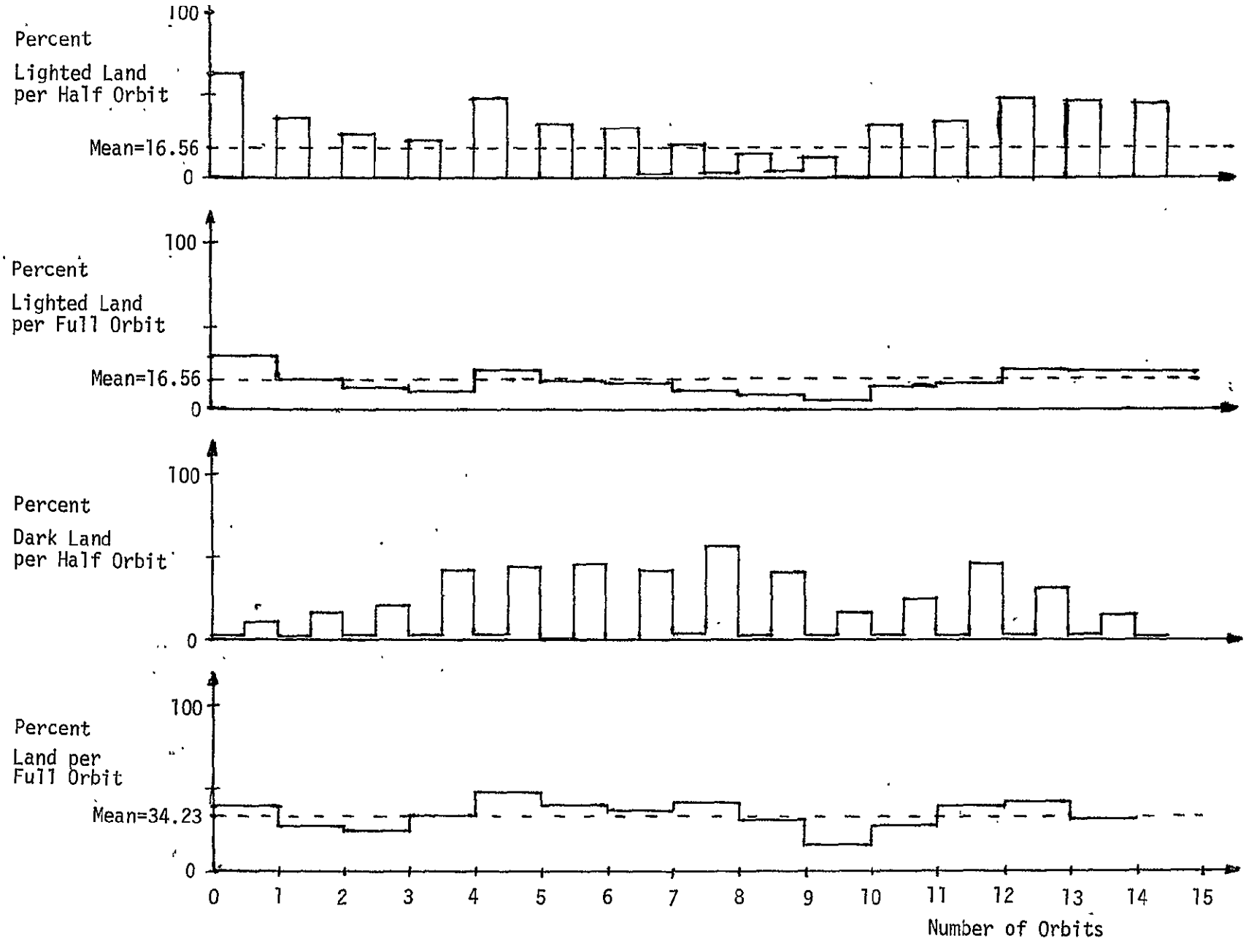

Figure 3-26. 24-Hour Run: Percent Lighted Land

Note that in the percent per half orbit plots in Figure 3-26, the lighted or dark land does not always split exactly along the half orbit time line. The reason for this is the 98.2 degree orbit inclination and the half orbit definition as $\pm$ 90 orbital degrees from crossing the equator. On the light side of the orbit (descending path), for example, the spacecraft will reach dark land (the Antarctic) near its "southern" most point (90 orbital degrees after crossing the equator). This can be seen best on the "Percent Dark Land per Half Orbit" graph in Figure 3-26.

3.5 Solar Array Control to Minimize Interference with Antennta Beam

The purpose of this section is to support the recommendation of a solar array configuration and array control strategy such that optical interference with the Ku-band antenna beam is eliminated. This is to be accomplished under the constraint of keeping the antenna mast as short as possible (mainly for spacecraft for structural reasons), since a sufficiently long mast permitting the antenna a field of view above all obstacles presents itself as an obvious solution to the problem.

The L-D solar array can be stationary relative to the spacecraft, or it can be driven to rotate about the $\hat{y}_b$ axis and follow the sun. The former design has the advantage of not requiring a drive mechanism, but it also has the potential disadvantage of necessitating a longer Ku-band antenna mast. There are many options available in designing the solar array. Two assumptions were made to eliminate some of the unnecessary options:

(1) It is assumed that interference with TDRS transmission over earth night is acceptable.

(2) It is assumed that the array shape will be rectangular.

The spacecraft with the Ku-band antenna is shown in Figure 3-27. The antenna is a circular dish with a 0.91 meter (3 foot) radius mounted on and rotating about the end of the mast. The mast is mounted parallel to the $\hat{z}_b$ axis; as shown, but generally lies near the edge of the spacecraft

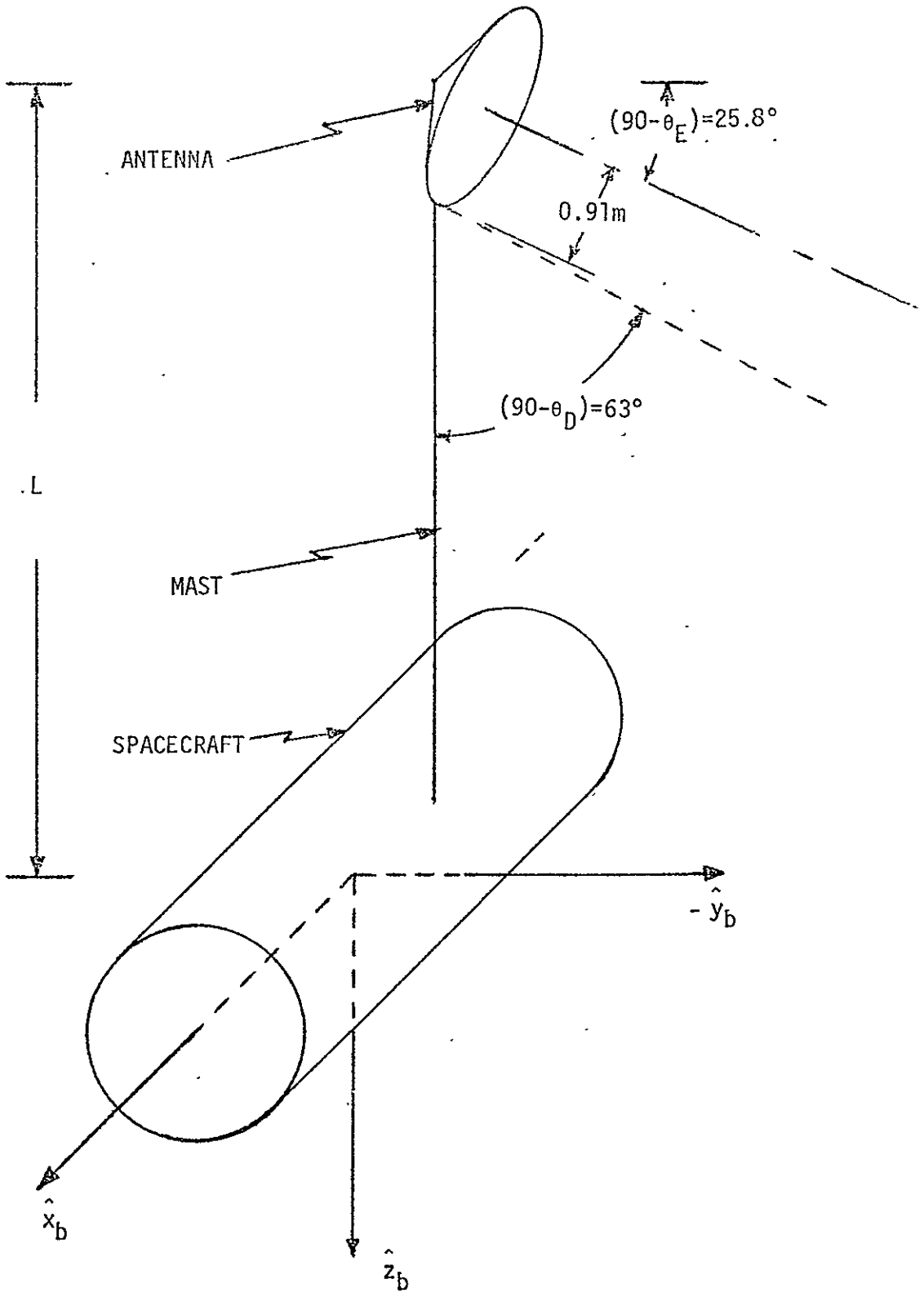

Figure 3-27. Ku-Band Antenna Mounted on Spacecraft

body rather than at the c.m. The mast length, L, is measured from the $\hat{x}_b$-$\hat{y}_b$ plane to the hinge point of the antenna; but note that the actual mast could be made shorter than this by mounting it on the top of the spacecraft instead of in the $\hat{x}_b$-$\hat{y}_b$ plane. The antenna field-of-view pattern is the 6 foot diameter cylinder extending out from the dish plus a 1 to 2 degree skirt -- the skirt is assumed to be 1.2 degrees in Figure 3-27. The antenna is only allowed to dip 25.8 degrees below the spacecraft horizontal, because that is where its line-of-sight grazes the earth -- 64.2 degree half angle.

The region which does not interfere with the antenna FOV is the 63 degree half angle cone centered on the mast with its apex at the point where the edge of the dish touches the mast. This apex of the cone is then given by A = (0.91 m)/(sin 64.2°) = 1.01 meter (3.33 feet) below the hinge point. Define a new coordinate system by shifting the body coordinate system so that the origin coincides with the base of the mast. Now, if the 3-tuple (x, y, z) is used to specify a point in this coordinate system, the set of points lying within the cone satisfies the inequality

$$x^2 + y^2 \leq L - \left(\frac{0.91}{\sin \theta_E}\right) + z^2 \cot^2 \theta_D \qquad (3.5\text{-}1)$$

where θ_E is the earth half angle and θ_D is the maximum angle by which the antenna beam dips below the horizontal.

3.5.1 The Driven Array

The driven array will be a rectangular array canted 37.5 degrees to the $-\hat{y}_b$ axis and rotating about the $\hat{y}_b$ axis so that its face remains normal to the sun line. When the spacecraft is in the ecliptic plane over earth day, this array is in the position shown in Figure 3-28, which is the position of least interference with the Ku-band antenna. As the L-D rotates out of the ecliptic, the array rotates about the $\hat{y}_b$ axis and moves toward the cone where it may interfere with the antenna. That interference is avoided by mounting the antenna at the end of a mast, but that mast should be as short as possible.

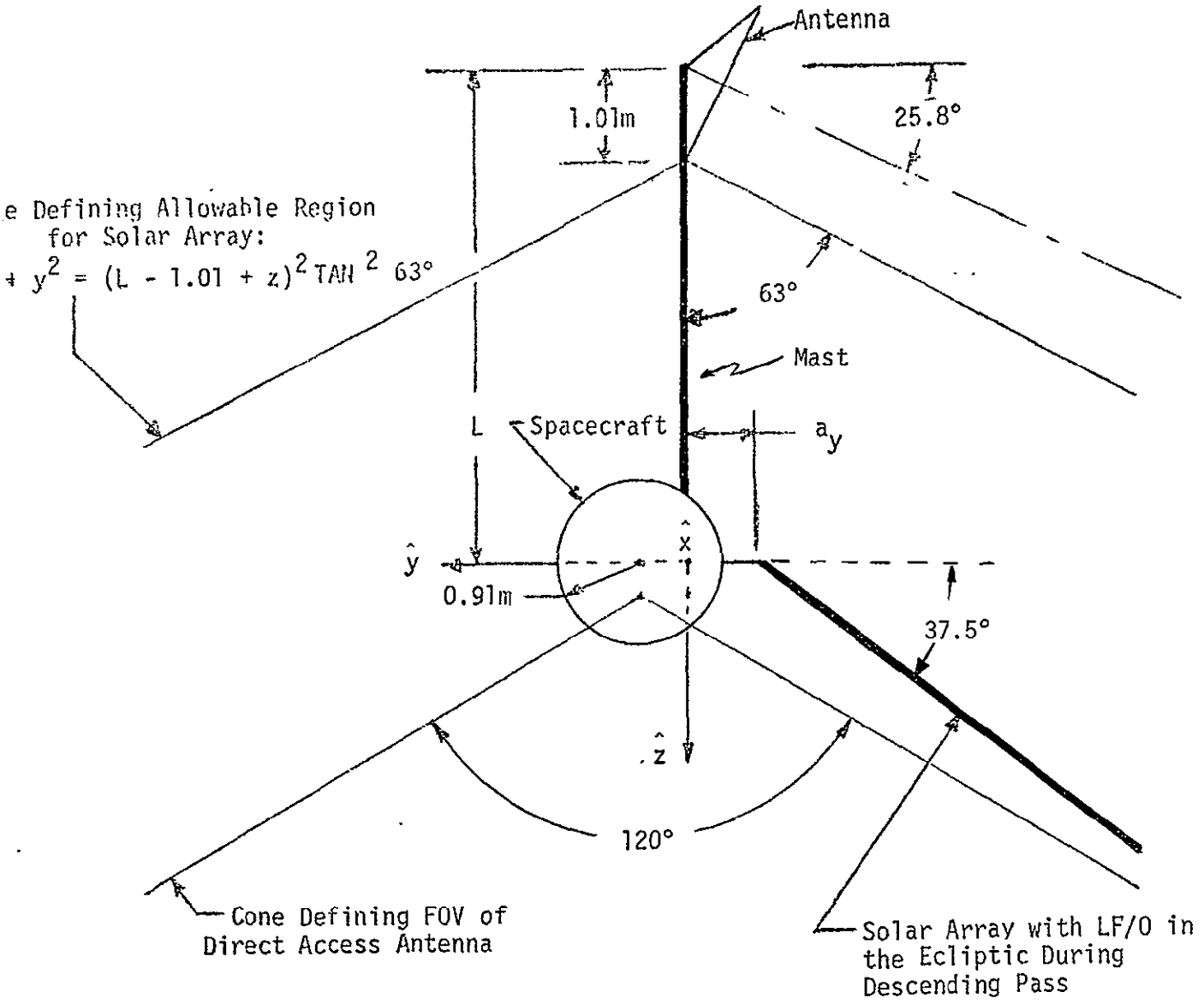

Figure 3-28. The Spacecraft with the Driven Array

The mast length can be minimized by proper choice of the shape of the rectangular array. The mast can also be kept short by keeping the array close to the position shown in Figure 3-28 while the antenna is transmitting. This can be accomplished by letting the array follow the sun whenever the spacecraft is over earth night but not eclipsed -- interference is acceptable -- and whenever the spacecraft is within some predetermined angle, θ_L, of the ecliptic. When the spacecraft is in the

remaining region, the array will be stationary at the position which would have it aligned with the sun at θ_L from the ecliptic (see Figure 3-29).

This approach reduces the average solar array power over an orbit. That average power is computed using

$$P_{avg} = \frac{1}{360} \int_0^{360} P(\theta)\, d\theta \qquad (3.5\text{-}2)$$

where θ is the orbit position of the L-D and $P(\theta)$ is the normalized instantaneous power measured as the projected array area normal to the sun line divided by the nominal area 11.89 m^2 (128 $foot^2$). The L-D is eclipsed by the earth when within $\pm$ 56.73 degrees of the ecliptic over the earth night, so if the array follows the sun throughout the orbit,

$$P(\theta) = \begin{cases} 0, & \text{in eclipse region} \\ 1, & \text{outside eclipse region} \end{cases} \qquad (3.5\text{-}3)$$

Thus,

$$P_0 = \frac{1}{360} \left\{ \int_{-33.27}^{213.27} \right\} d\theta = 0.6848 \qquad (3.5\text{-}4)$$

for this ideal case, where the zero angle is taken to be the point of the orbit where the L-D is 90 degrees of revolution ahead of the daylight crossing of the ecliptic. This number, P_0, represents the required average normalized power per orbit.

Now, if the array is stopped when the L-D is more than θ_L from the ecliptic, the average power per orbit with a 11.89 m^2 (128 $foot^2$) array would be given by:

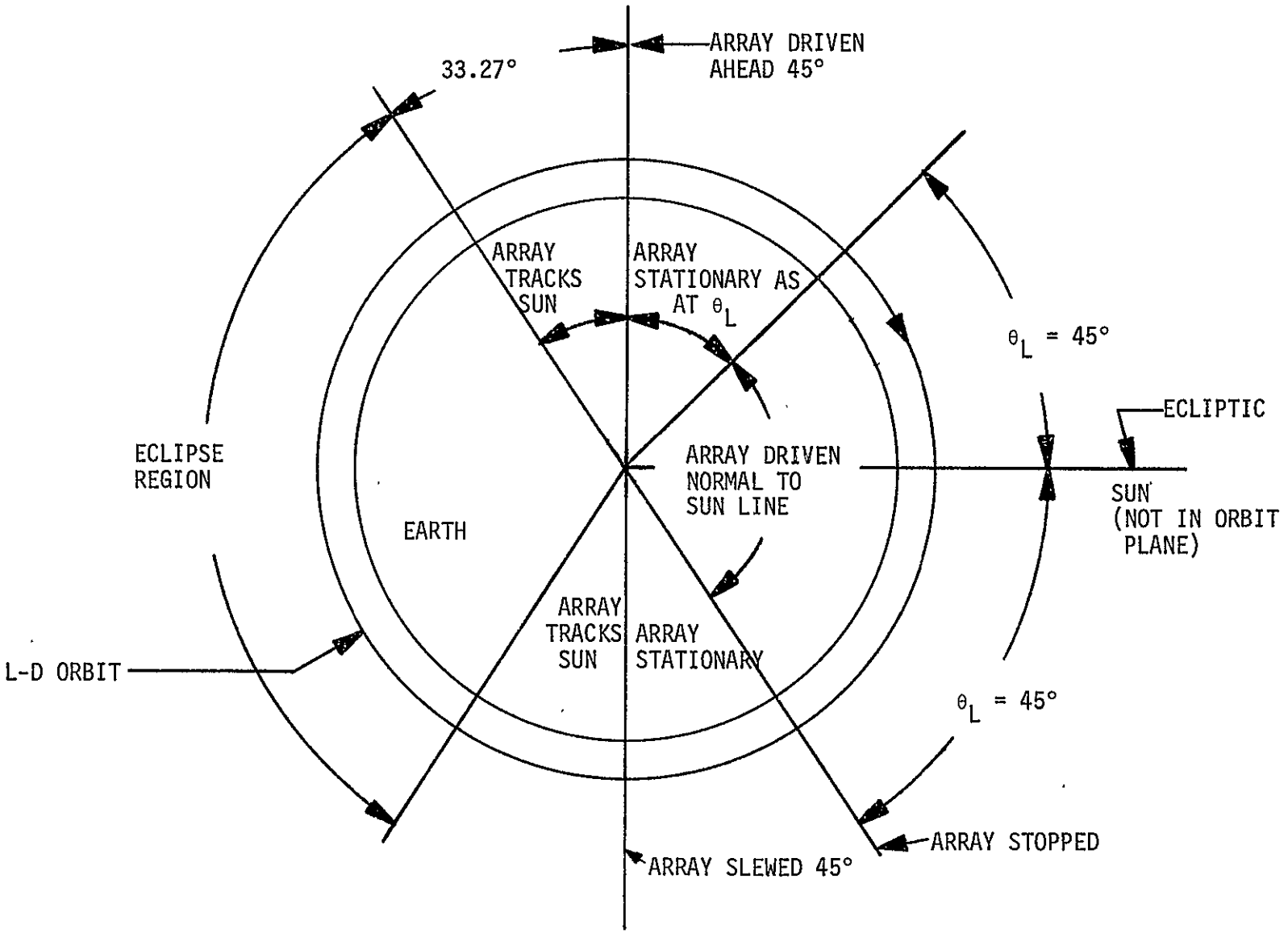

Figure 3-29. The LF/O Orbit

$$P_{avg} = \frac{2}{360} \left\{ \int_{-33.27}^{0} d\theta + \frac{180}{\pi} \int_{0}^{90-\theta_L} \cos\,(90 - \theta_L - \theta)\, d\theta + \int_{90-\theta_L}^{90} d\theta \right\} = \left[\frac{\theta_L + 33.27}{180} + \frac{\sin\,(90 - \theta_L)}{\pi} \right] \qquad (3.5\text{-}5)$$

The efficiency is given by

$$\eta = \frac{P_{avg}}{P_0} \times 100\% = \frac{100\%}{P_0} \left\{ \frac{\theta_L + 33.27}{180} + \frac{\sin\,(90 - \theta_L)}{\pi} \right\} \qquad (3.5\text{-}6)$$

The efficiency is plotted versus θ_L in Figure 3-30.

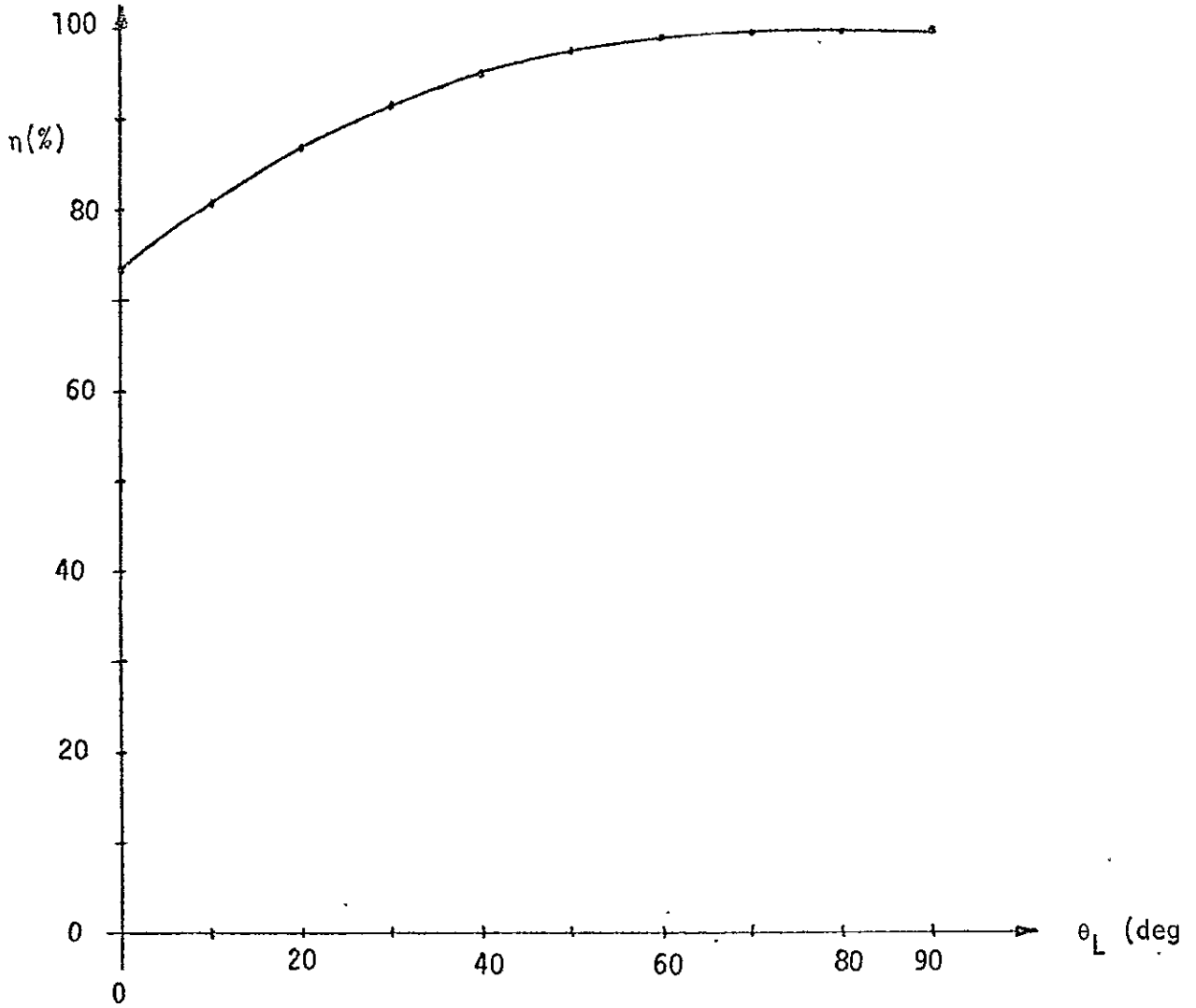

Figure 3-30. Solar Array Efficiency versus Stop Angle θ_L from the Ecliptic

In summary, the approach, wherein the array does not follow the sun throughout the orbit, reduces the average solar array power over an orbit. The overall reduction is on the order of 4% and relatively insignificant. It can also easily be compensated by a correspondingly small increase in array area.

The minimum mast length can be determined by comparing the location of the worst-case point of the array with the cone represented by Equation (3.5-1). The worst case point on the array is some point on the "top" edge when the array is rotated the maximum amount toward the antenna -- θ_L degrees from the lowest point as shown in Figure 3-28. It is obvious that because the cone is convex the worst case point is at one end or the other of the top edge. Let the vector representing one of these points be $\bar{c}$. Then, from Equation (3.5-1), the minimum mast length so that the point $\bar{c}$ does not lie in the FOV of the antenna is given by

$$L_{MIN} = \sqrt{c_x^2 + c_y^2} \tan \theta_D + \frac{3}{\sin \theta_E} - c_z \qquad (3.5\text{-}7)$$

Let the array have length ℓ, measured along the shaft, and width ω. Now, the unit vector along the array shaft is

$$\hat{\ell} = [\theta_L - 90]_y \, [\theta_c]_z \begin{bmatrix} 0 \\ -1 \\ 0 \end{bmatrix} = \begin{bmatrix} -\sin \theta_c \sin \theta_L \\ -\cos \theta_c \\ \sin \theta_c \cos \theta_L \end{bmatrix} \qquad (3.5\text{-}8)$$

where θ_c is the array cant angle -- nominally 37.5 degrees -- and the notation $[\theta]_z$ means a rotation of the coordinate system through the angle θ about the z axis. The unit vector along the end of the array is

$$\hat{\omega} = \begin{bmatrix} -\cos \theta_L \\ 0 \\ -\sin \theta_L \end{bmatrix} . \qquad (3.5\text{-}9)$$

Using these unit vectors, the vector representing an arbitrary point of the top edge of the array is

$$\bar{c}_\alpha = \alpha \ell \hat{\ell} + \frac{\omega}{2} \hat{\omega} + \bar{a} \qquad (3.5\text{-}10)$$

where $\bar{a}$ is the vector representing the close end of the array shaft and $\alpha \in [0,1]$ determines the particular point of the top edge -- the two points of interest are $\bar{c}_0$ and $\bar{c}_1$. The vector elements a_x and a_z are assumed to be 0, and a_y is nominally 0 but may be as much as -0.91 (3 feet). Equations (3.5-6), (3.5-7) and (3.5-10) were used to create Table 3-14 showing the baseline design and several variations.

It is evident by comparing the first and last entries of Table 3-14 that the baseline design is much better than having the array follow the sun throughout the orbit. Note also that for a shallow array rotation angle such as θ_L = 45 degrees the FRUSA* array is nearly as good as the best rectangular array. Further, the table shows that only a slight increase in array area is needed to bring the efficiency up to 100%. Recalling that the actual mast length could be smaller than that shown by mounting it higher up on the spacecraft, it is concluded that a normal boom rather than an Astro-mast type boom is sufficient for mounting the antenna.

This baseline design is recommended as the rotating array design. The array rotation scenario for an orbit is as follows: as the L-D comes out of eclipse, the array tracks the sun until the northern terminator is reached -- this is within 23.5 degrees of the North Pole depending on the season; during this period the array could be in the antenna FOV, but there is no Thematic Mapper data to transmit. At the northern terminator, the array "jumps" ahead approximately** 45 degrees and stops until the L-D travels a compensating 45 degrees. At this time, the array is again driven to follow the sun through 90 degrees of L-D travel where it again stops

*6.33 foot wide Flexible, Roll Up Solar Array with 5 foot wide cell region.
**Inclination i = 98.2°.

Table 3-14. Various Driven Array Configurations

Mast-Array Separation a_y (m) (Fig. 2-2)	Array Cant Angle, θ_C (deg)	Angle from Ecliptic within which the Array tracks the Sun θ_L (deg)	Maximum Antenna Dip Angle, θ_D (deg)	Solar Array Actual Surface Area, (m^2)	Efficiency (%)	Minimum Mast Length for FRUSA (m) (1.52 m = 5 ft wide cell reg.)	Optimal Array Width (m)	Minimum Mast Length (m)
0	37.5	45	27	12.32	100	2.11	0.90	1.82
0	37.5	45	27	11.89	96.37	2.11	0.89	1.80
0	37.5	40	27	12.49	100	2.01	----	----
0	37.5	50	27	12.20	100	2.55	1.41	2.35
0	30	45	27	12.32	99.14	2.84	1.85	2.63
0	30	45	27	12.43	100	2.85	1.85	2.64
0	37.5	45	28	12.32	100	2.28	1.16	2.06
-0.61	37.5	45	27	12.32	100	2.38	0.91	2.09
0	37.5	60	27	11.89	98.91	3.41	2.04	3.11
0	37.5	70	27	11.89	99.68	4.29	2.56	3.70
0	37.5	90	27	11.89	100	5.96	2.75	4.50

until the L-D reaches the southern terminator at which point the array catches up. Finally, the array tracks the sun into eclipse and the process is repeated for the next orbit. This design insures that the array will not interfere with the antenna during transmission periods, but on many orbits the array can follow the sun throughout without interference due to the favorable TDRS locations. This subject can be studied more thoroughly using the computer program presented in Section 3.4. Note also that while the L-D is eclipsed by the earth, the array position is immaterial; thus it could be moved out of the way of the antenna to allow data transmission at night.

3.5.2 The Fixed Array

If the solar array is to be fixed relative to the spacecraft so that it can not follow the sun, it should always have the same area normal to the sun line. Since the sun cones about the vehicle pitch axis, the array should be mounted normal to this axis as shown in Figure 3-31. In this configuration, the solar array position can be moved along the $\hat{z}_b$ axis. Thus, the only fixed distance to be considered is the distance from the lower edge of the array to the antenna pivot point; this is the dimension h in Figure 3-31. The antenna position is assumed to be directly over the array in the baseline design.

The largest rectangular array that can be enclosed by the triangle as shown has height a and base b where

$$a = \frac{1}{2}\left(h - \frac{0.91}{\sin \theta_E}\right) \tag{3.5-11}$$

and

$$b = \frac{1}{\tan \theta_D}\left(h - \frac{0.91}{\sin \theta_E}\right) \tag{3.5-12}$$

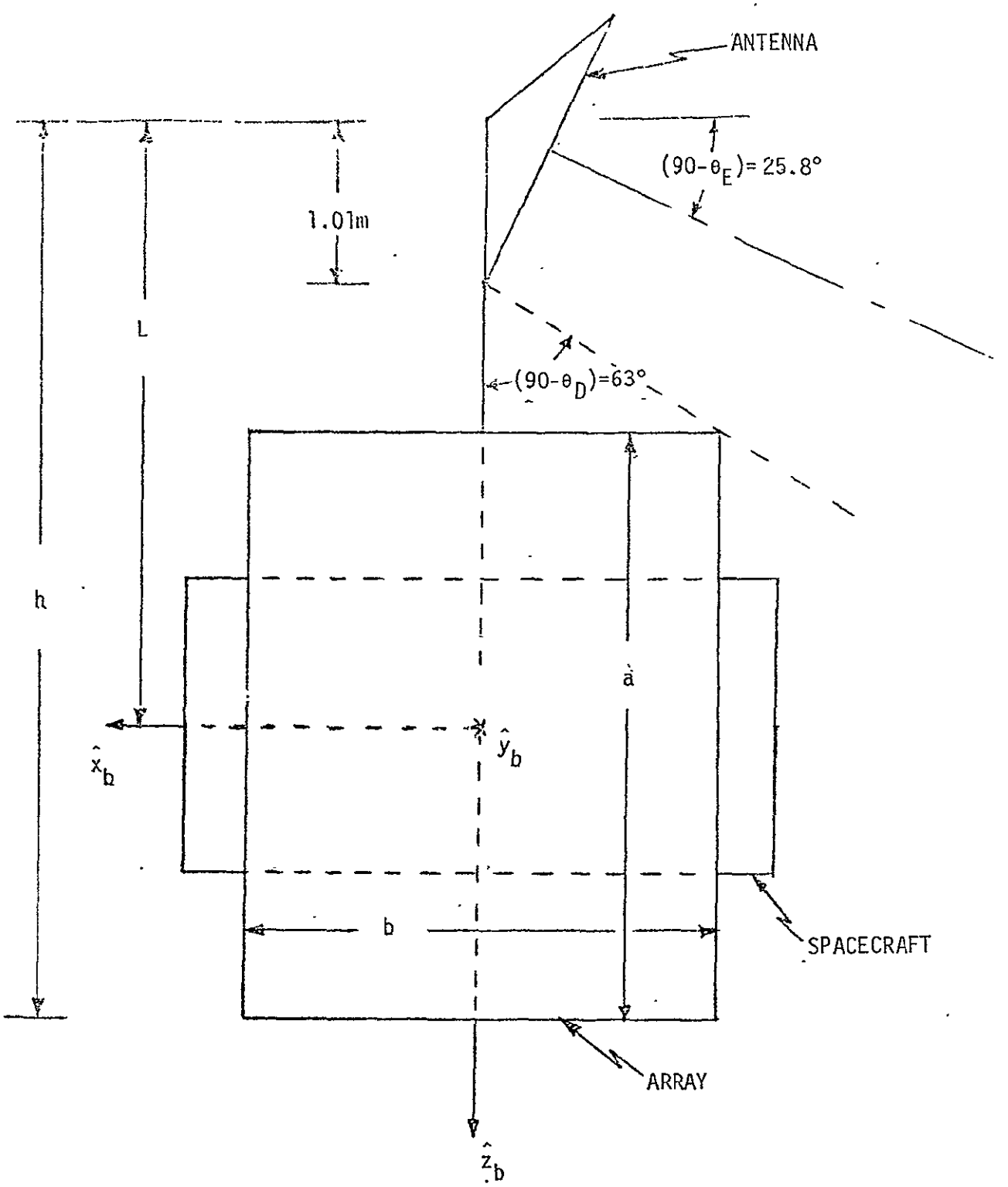

Figure 3-31. Location of Fixed Array on Spacecraft

Then the area is given by

$$A = ab = \frac{1}{2 \tan \theta_D} \left(h - \frac{0.91}{\sin \theta_E} \right)^2 \qquad (3.5\text{-}13)$$

For this design, the sun strikes the array at an angle of 52.5 degrees, so the area must be

$$A = (11.89\ m^2)/(\cos 52.5°) = 19.53\ m^2\ (210.26\ ft^2) \qquad (3.5\text{-}14)$$

and Equation (3.5-13) results in h_{min} = 5.47 m (17.95 feet). The lower edge of the array can not be much more than 0.61 m (2 feet) below the $\hat{x}_b$-$\hat{y}_b$ plane without interfering with the direct access antenna. Thus the mast length, L, as defined earlier would have to have a length at least L = 4.88 m (16 feet).

This required mast length would be increased still further if the antenna were laterally offset from the array. Also, any change in the sun incidence angle would cause a change in the array size and thus the mast length. For example, if the descending node occurred at 10:00 a.m. instead of 9:30 a.m., the array area would become A = 23.78 m^2 (256 $foot^2$) and the required mast length would be increased to 5.33 m (17.5 feet).

3.5.3 Recommended Solar Array Configuration

Each of the two solar array configurations -- the fixed array and the driven array -- described above are satisfactory. The fixed array has the advantage of not requiring a drive mechanism, but it has the disadvantages of increased size, weight and cost. Also, the fixed array requires a much longer antenna mast; this extra mast length is undesirable because it affects the spacecraft and antenna flexible dynamics. The driven array would exhibit dynamic interaction with the spacecraft, but this would probably be a smaller effect than that due to the structural flexibility of the large fixed array. Based on the above tradeoffs, the driven FRUSA array as shown in line 1 of Table 3-14 is recommended.

4.0 DISTURBANCE TORQUES AND MOMENTUM MANAGEMENT FOR LANDSAT-D

This section summarizes the results of a disturbance torque-momentum management investigation for the present concept of the LANDSAT spacecraft configuration. The purpose is to determine magnetic unloading torque levels and associated peak stored momentum values which will indicate if standard reaction wheels and torquer magnets are sufficient for the design of the system. Detailed disturbance torque models and an ideal spacecraft with zero attitude errors are used to establish torque and momentum patterns and magnitudes. Based on the disturbance torque signals for one orbit, a Fourier coefficient set is compiled which approximates the spectral content of the disturbances. These may be used in later simulations as simplified disturbance models. Eclipse conditions occurring for the 9:30 a.m. sun-synchronous orbit are included in the disturbance model.

Based on the results of this study, it appears that the single 50,000 pole-cm magnet windings are sufficient for momentum unloading. Thus the two windings per magnet may be used in a redundant mode. Only a short interval of magnet command limiting at 50,000 pole-cm is observed per orbit.

Momentum excursions of less than 2.0 N-m-s occur at all axes. This is considerably less than the allowable excursion of 7.32 N-m-s for speed-biased operation of the wheels with equal allowed excursions for all wheels. Thus it is concluded that the 20 N-m-s NASA Standard Reaction Wheels are sufficient for the design.

Sensitivity to antenna mast heights is not dramatic for the heights presently under consideration. These effects, and the effects of antenna orientation, are thus not a major concern with regard to momentum storage and disturbance torques.

4.1 Spacecraft Model

The diagrams in Figure 4-1 display the pertinent measurements for the LANDSAT. Since antenna height has not been definitely decided upon, it is treated as a parameter to obtain an estimate of its effects on the

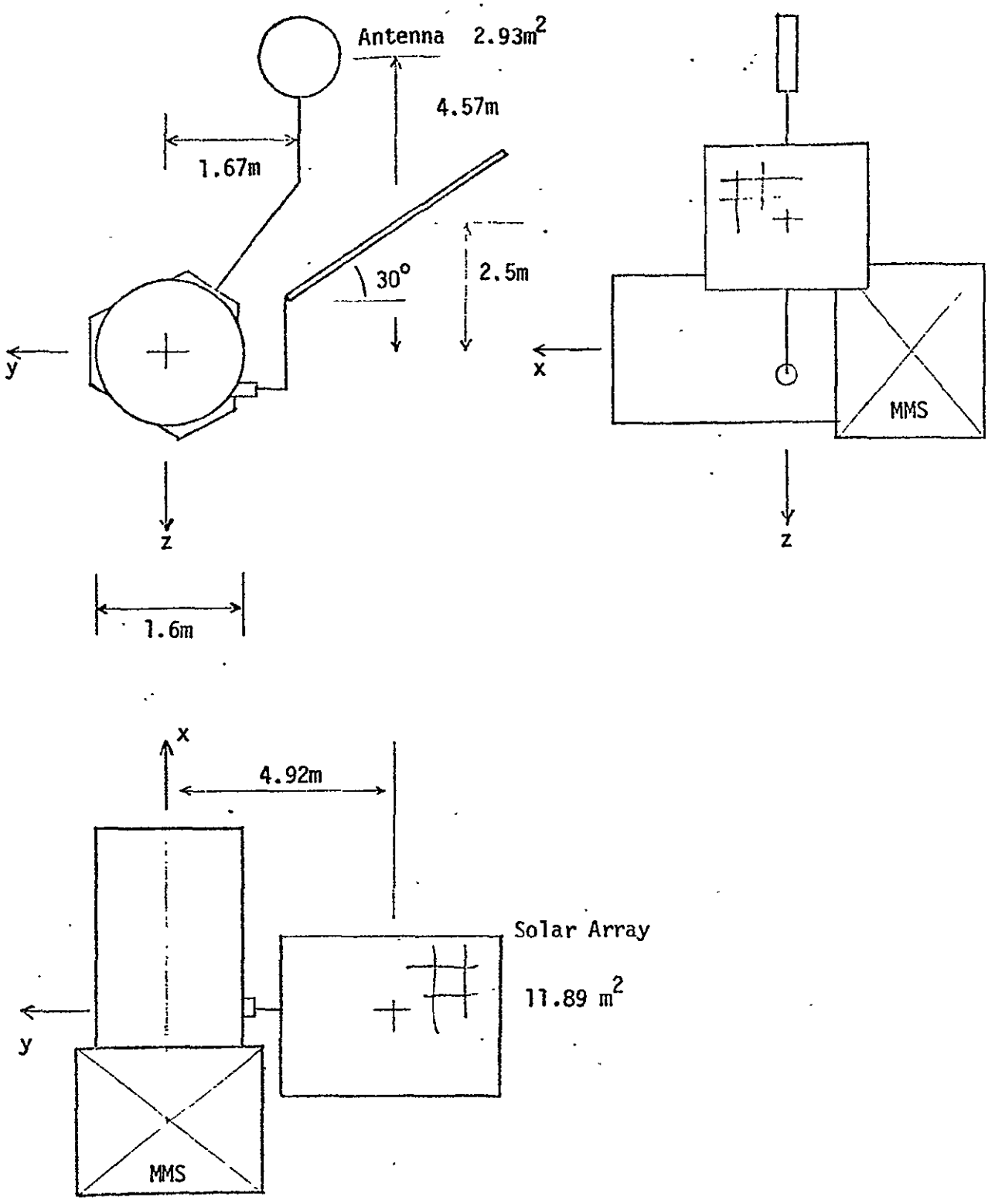

Figure 4-1. Simplified LANDSAT Configuration Schematic for Solar and Aero Disturbances

disturbance torques. Various antenna orientations, primarily looking forward or zenith, are considered to also determine their effect on disturbance levels. These orientations are chosen because the antenna coverage pattern is approximately a hemisphere over the minus $\hat{Z}$ body axis. The spacecraft model consists of a standard configuration for the MMS ACS, CDH, power modules, and adapter plate. For simplicity, the payload is modelled as a cylinder with an end plate since more refined surface models are not available. The sun pointing array is modelled as a flat plate that rotates at a cone angle of *30 degrees in body coordinates, and the antenna is modelled as a thin wide cylinder at mast heights of 3.05 m (10 feet), 4.57 m (15 feet) and 6.10 m (20 feet).

Since the array rotates in body coordinates, its center of pressure varies for aerodynamic torque calculations. This time varying function is modelled in the simulation. The time varying surface normal to the solar panel from the sun is also computed.

Moments of inertia for the present configurations are I_{xx} = 2033.7 kg-m^2, I_{yy} = 2670 kg-m^2, and I_{zz} = 2372.7 kg-m^2. Weights are 1496.6 kg for the spacecraft and 22.7 kg for the solar array and for the antenna. The relatively small effects of a time varying inertia matrix are not modelled. Cross products of inertia are also time-varying, depending primarily on array position. These affect primarily the gravity gradient torques, and are modelled as an average of 271.2 kg-m^2 in all axes.

For a specified antenna mast size, the center of mass (c.m.) of the spacecraft moves slightly as the antenna is rotated. The maximum distance is on the order of 1 inch (2.54 cm), and thus a fixed average c.m. is chosen for the model. Changes are included for various antenna heights.

Table 4-1 summarizes the solar-aero surface model data for the present study. An antenna height of 4.57 m (180 inches) is shown in the table.

---

*Based on Grumman layout drawing; a 9:30 a.m. orbit would correspond to an array cant angle of 37.5 degrees. The difference in the resultant disturbance torque is insignificant.

Table 4-1. LANDSAT Solar-Aero Model

Surface Description	Surface Number	Area (in^2)	Center of Pressure (in)			Inward Normal Vector			Reflect. ν	Acc. Coef. f_n, f_T
			r_x	r_y	r_z	n_x	n_y	n_z		
Solar Array Front	1	18432.	Time Varying, Inernal			Time Varying, Internal			0.2	0.85
Solar Array Back	2	18432.							0.56	0.85
Interface Back	3	828.	48	0	0	1	0	0	0.56	0.85
(Spare)	4	0	0	0	0	0	0	1	0.56	0.85
ACS Module	5	2304	24	31.9	0	0	-1	0	0.56	0.85
	6	864	24	22.9	-24	0	0	1	0.56	0.85
	7	864	24	22.9	24	0	0	-1	0.56	0.85
CDH Module	8	2304	24	-15.95	-27.6	0	0.5	0.866	0.56	0.85
	9	864	24	19.5	-31.8	0	-0.866	0.5	0.56	0.85
	10	864	24	-32.2	-7.79	0	0.866	-0.5	0.56	0.85
Power Module	11	2304	24	-15.9	27.6	0	0.5	-0.866	0.56	0.85
	12	864	24	19.5	31.8	0	-0.866	-0.5	0.56	0.85
	13	864	24	-32.2	7.79	0	0.866	0.5	0.56	0.85
Spacecraft Bottom	14	4010	0	0	0	1	0	0	0.56	0.85
Interface Front	15	1979	48	0	0	-1	0	0	0.56	0.85
Payload Front	16	3040	145	0	0	1	0	0	0.56	0.85
Antenna Front	17	4536	72.58	-66	-180	0	0	1	0.56	0.85
Antenna Back	18	4536	72.58	-66	-180	0	0	-1	0.56	0.85
Payload Body Cyl.	19	*	100	0	0	1	0	0	0.56	0.85
Antenna Edge	20	**	72.58	-66	-180	0	0	1	0.56	0.85

*Dia = 62.2, Length = 89.9
**Dia = 76.0, Length = 10.0

4.2 Disturbance Models

A standard detailed earth magnetic dipole field model is used as the source of the magnetic disturbance torques and for the generation of the unloading torques. It is described, for example, in [1] and is not repeated here. A spacecraft residual magnetic moment of 10,000 pole-cm at a fixed random orientation is used. Based on a commonly used estimate of 1 pole-cm per pound of weight, the 10,000 pole-cm value is conservative. Provision is made for rotation of the dipole field as a result of earth rotation, but over the short time of one or three orbits considered here, this effect is very small and is set to zero.

Solar torques are computed as a function of position in orbit and relative sun location using the detailed surface model. An eclipse condition is included to zero the solar torques within an angle of $\pm$ 56.7 degrees of the ascending node*. Shading effects which may be present during portions of the orbit are not included.

Aerodynamic torques are computed with the detailed surface model used for the solar torques. Gravity gradient torques are computed using the complete theoretical expressions, but the use of an idealized spacecraft with zero attitude errors results in constant gravity gradient torques resulting from the assumed cross products of inertia. Otherwise the periodic orbital variations in other disturbance torques would result in small attitude errors and resulting periodic content in the gravity gradient torques.

The theoretical expression for the gravity gradient torque is given by

$$\overline{T}_g = 3 w_o^2 \overline{R} \times (\overline{\overline{I}} \cdot \overline{R})$$

*Assuming an equinox.

where

w_o - is the orbit rate

$\overline{R}$ - is the distance to the center of the earth

$\overline{\overline{I}}$ - is the inertia dyadic

From the preceding equation, the gravity gradient torque expressions are

$$T_{gx} = 3 w_o^2 [(I_{zz}-I_{yy}) \phi - I_{xy} \theta + I_{yz}]$$

$$T_{gy} = 3 w_o^2 [-(I_{xx}-I_{zz}) \theta - I_{xy} \phi - I_{xz}]$$

$$T_{gz} = 3 w_o^2 [I_{xz} \phi + I_{yz} \theta]$$

and by setting the pitch angle error θ to zero, the following expressions are obtained for small ϕ angles.

$$\frac{T_{gx}}{\phi} = 3 w_o^2 (I_{zz}-I_{yy}) \quad \frac{N\text{-}m}{rad}$$

$$\frac{T_{gy}}{\phi} = -3 w_o^2 I_{xy} \quad \frac{N\text{-}m}{rad}$$

$$\frac{T_{gz}}{\phi} = 3 w_o^2 I_{xz} \quad \frac{N\text{-}m}{rad}$$

These may be used to estimate gravity gradient torques for small ϕ angles. Similarly, the relations

$$\frac{T_{gx}}{\theta} = -3\,w_o^2\,I_{xy} \quad \frac{N\text{-}m}{rad}$$

$$\frac{T_{gy}}{\theta} = -3\,w_o^2\,(I_{xx}-I_{zz}) \quad \frac{N\text{-}m}{rad}$$

$$\frac{T_{gz}}{\theta} = 3\,w_o^2\,I_{yz} \quad \frac{N\text{-}m}{rad}$$

yield torques for small θ attitude errors.

4.3 Momentum Unloading System

Magnetometers are used to sense the earth's $\overline{B}$ field, and a magnetic moment $\overline{M}$ is generated by the three-axis arrangement of the bars. The command $\overline{M}$ is generated according to the linear law

$$\overline{M} = -K\,\overline{B} \times \overline{H}_e$$

where K is a suitable constant and $\overline{H}_e$ is the momentum error vector. The preceding unloading law may be arrived at either by minimization of an error $\overline{e}$ between $\overline{M} \times \overline{B}$ and $-K\,\overline{H}_e$ or by geometric considerations. This control law is simulated to obtain continuous momentum unloading of the reaction wheels.

The dipole magnets for the generation of $\overline{M}$ are available in standard sizes of two 50,000 pole-cm windings on a single core. Those windings may be used singly in which case one winding is redundant for backup purposes, or they may be used together to obtain 1×10^5 pole-cm with no redundancy. The choice is determined by the on-orbit torque levels that are required.

4.4 Stored Momentum Determination

It is desired to use the NASA Standard Reaction Wheel (SRW) for reaction torque and angular momentum storage. This is a 20 N-m-s wheel and in the present application four of them will be used in a speed-biased

arrangement. It is thus necessary to determine if the orbital momentum variations remain below the maximum allowable as measured from the nominal speed-biased momentum value. In fact, it is desired to operate the wheels as closely as possible to the speed bias.

To do that, disturbance and magnetic unloading torques are computed for an idealized spacecraft in a simulation. The net external torque on the spacecraft is transformed to inertial space, integrated to provide inertial momentum, and transformed back to body coordinates. Since perfect attitude control is assumed, the momentum in body coordinates represents stored wheel momentum as a function of orbital position. The roll, pitch and yaw momenta may be resolved into wheel axes to obtain the excursions from nominal speed-biased momenta.

4.5 Results

Initial results indicated that magnet signals slightly in excess of 50,000 pole-cm would be required for momentum unloading. Thus magnet command limits of 50,000 pole-cm were applied to determine if unloading could be accomplished using just one winding. The results are summarized in Table 4-2 for 4.57 and 6.10 meter antenna heights.

Table 4-2. Maximum Magnet Commands and Reaction Wheel Momenta

Antenna, Position	$\lvert\bar{M}\rvert_{max}$ pole-cm	$\lvert\bar{h}\rvert_{max}$ N-m-s
4.57 m, looking $-\hat{Z}$	61,864	1.78
4.57 m, looking $+\hat{X}$	60,073	1.86
6.10 m, looking $+\hat{X}$	58,947	1.85

The magnet commands and limiting are more apparent in the plots of Figure 4-2a. There it is seen that only the pitch magnet is saturated at 50,000 pole-cm, and only for a brief portion of the orbit near the descending node. Although the desired unloading level is not achieved during this time, the system carries the momentum error until it can be unloaded thus keeping the resultant momentum less than 2.0 N-m-s. Later paragraphs examine allowable momenta levels, but accepting the 1.86 N-m-s as permissible it can be concluded that the single winding 50,000 pole-cm is sufficient. Thus the magnets may be used in redundant mode.

The total external disturbance torques are shown in Figure 4-2b. Since eclipse occurs at $\pm$ 56.7 degrees from the ascending node, a check is easily made on the magnitude of the jump in the solar torques. Without allowing for antenna effects, the values should be

$4.07 \times 10^{-4} \cos 56.7° = 2.23 \times 10^{-4}$ N-m roll

$4.07 \times 10^{-4} \sin 56.7° = 3.40 \times 10^{-4}$ N-m yaw

These agree closely with the plot values.

From Table 4-2 and from the series of plots in Figure 4-2, it is also seen that the sensitivity to antenna mast height and antenna orientation is fairly small. This is of interest in estimating effects of possible configuration changes. Studies made with a 3 m antenna height show disturbance torques and stored momenta slightly less than for the 4.57 m antenna mast. Since the latter are acceptable, the 3 m results are also acceptable and are not tabulated here.

For four reaction wheels in speed-biased operation, with one wheel on each of three major body axes and the fourth wheel equiangularly placed from the other three, a vector diagram shows that the fourth wheel should have $-\sqrt{3}$ time the (equal) momentum in the other three wheels for a net zero momentum. And to give all wheels equal momentum ranges, a simple calculation shows that the bias momentum should be 7.32 N-m-s for wheels

Figure 4-2a. 4.57 m Antenna, Zenith Pointing: Magnetic Moments

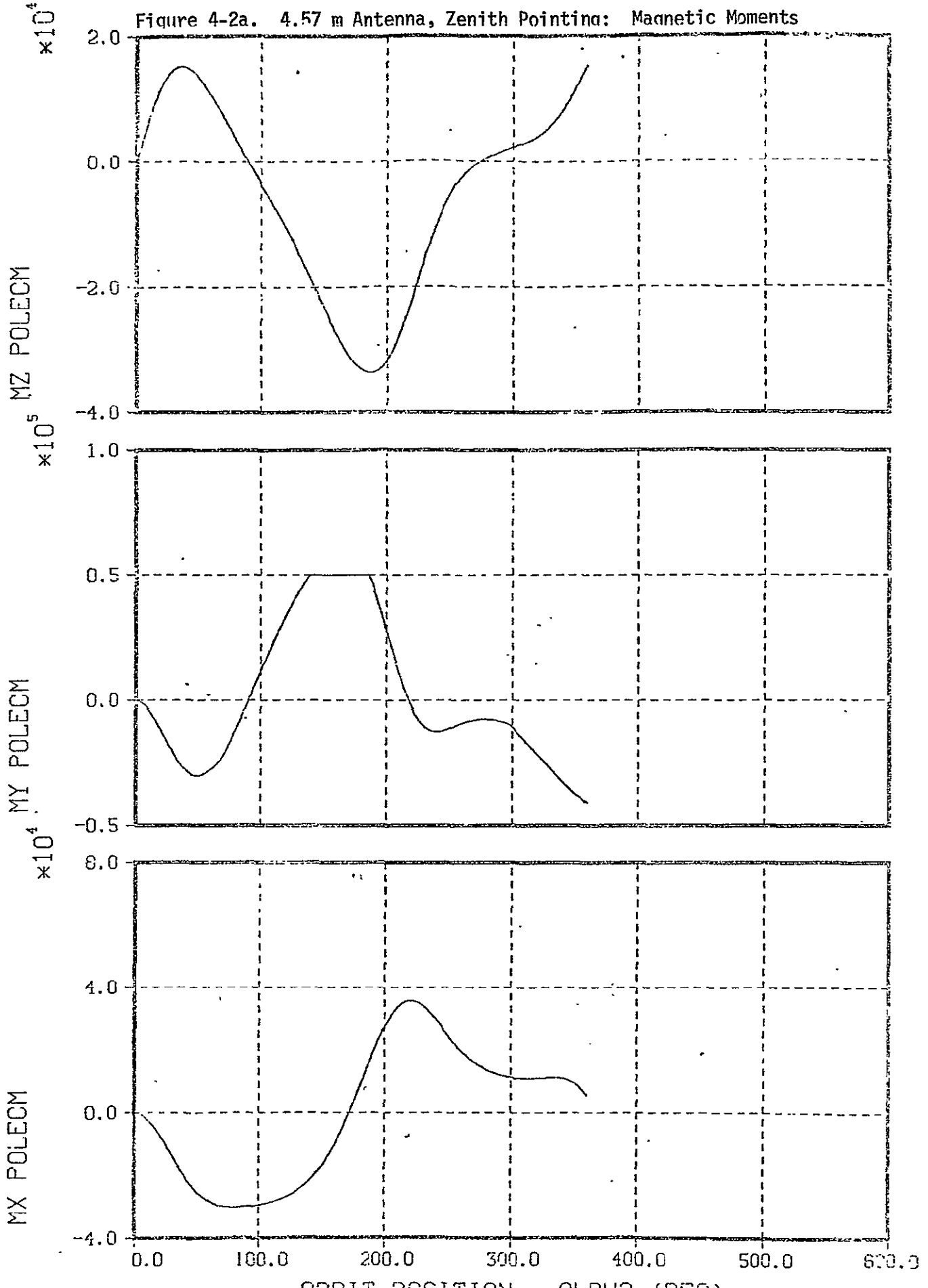

Figure 4-2b. 4.57 m Antenna, Zenith Pointing: Disturbance Torques

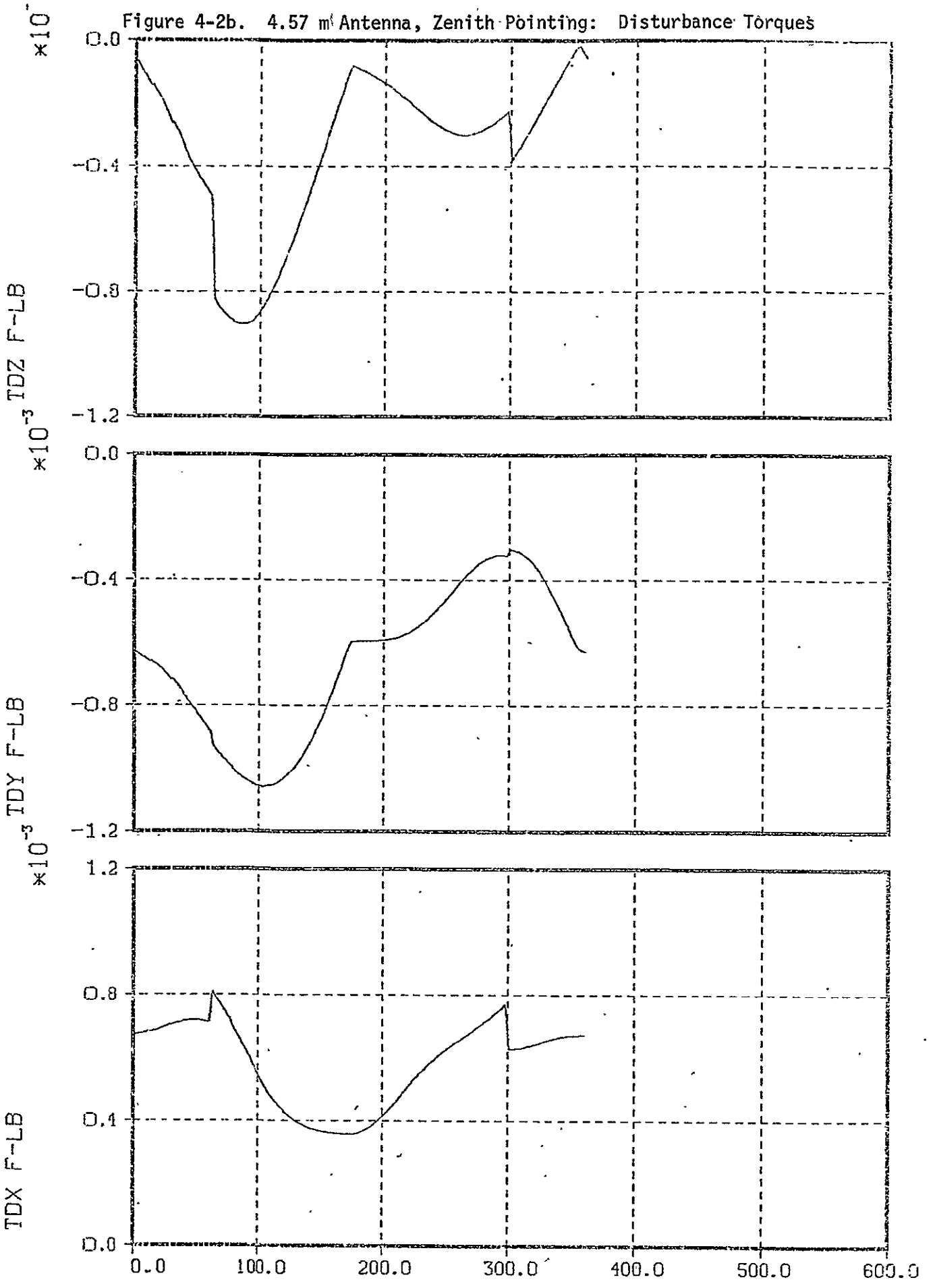

Figure 4-2c. 4.57 m Antenna, Zenith Pointing: Wheel Momenta

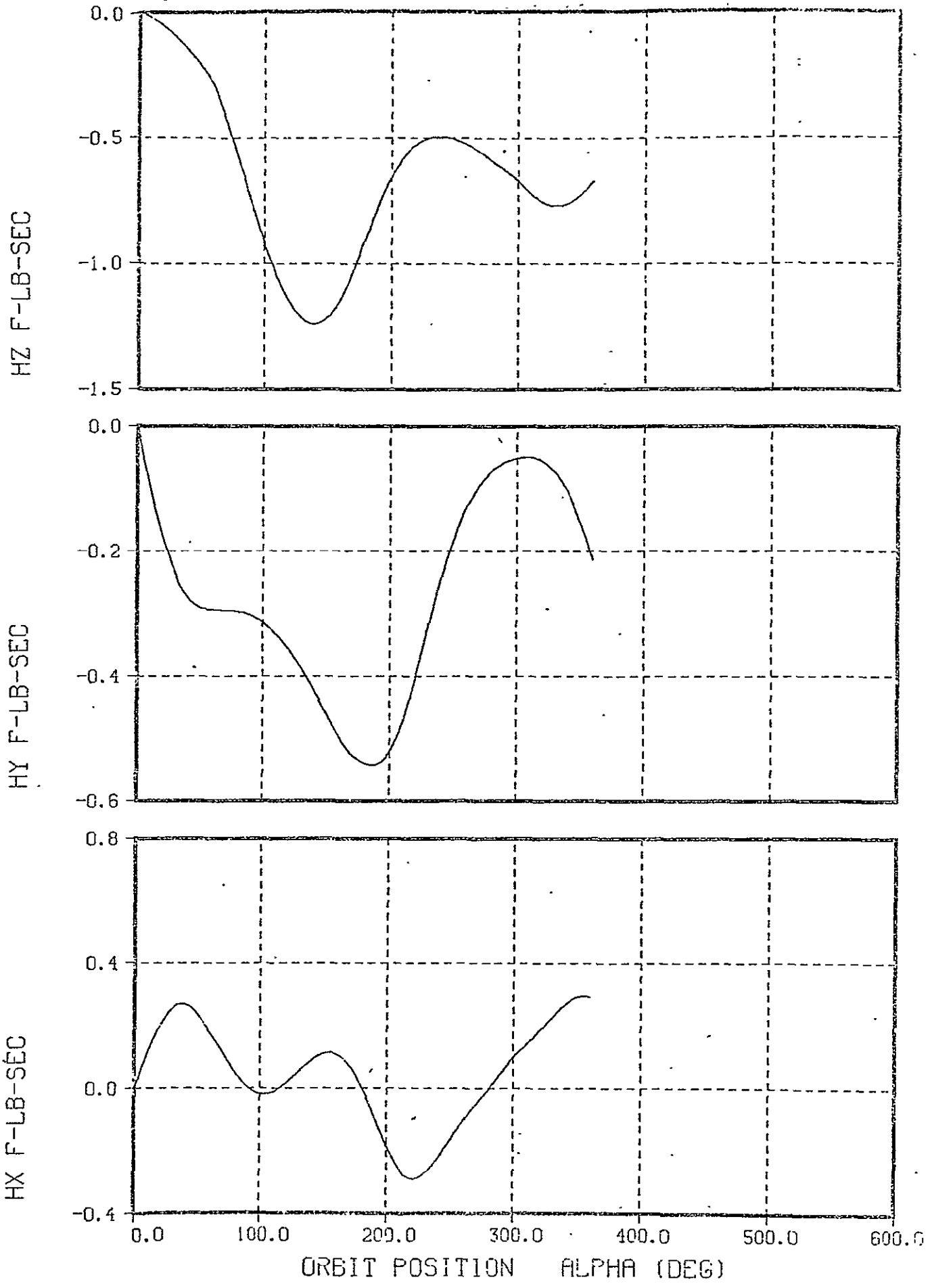

Figure 4-2d. 4.57 m Antenna, Pointing Ahead: Magnetic Moments.

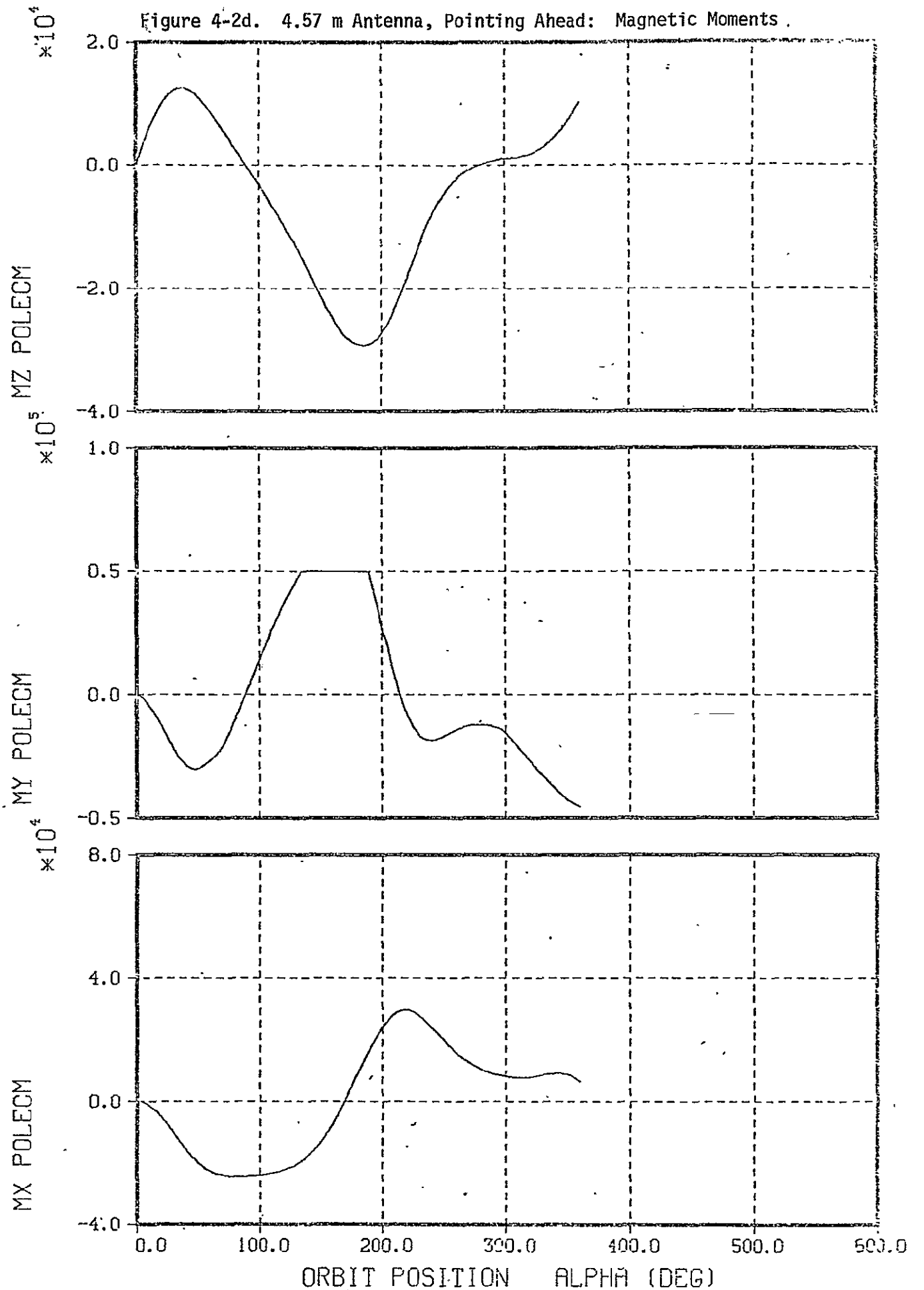

Figure 4-2e. 4.57 m Antenna, Pointing Ahead: Disturbance Torques

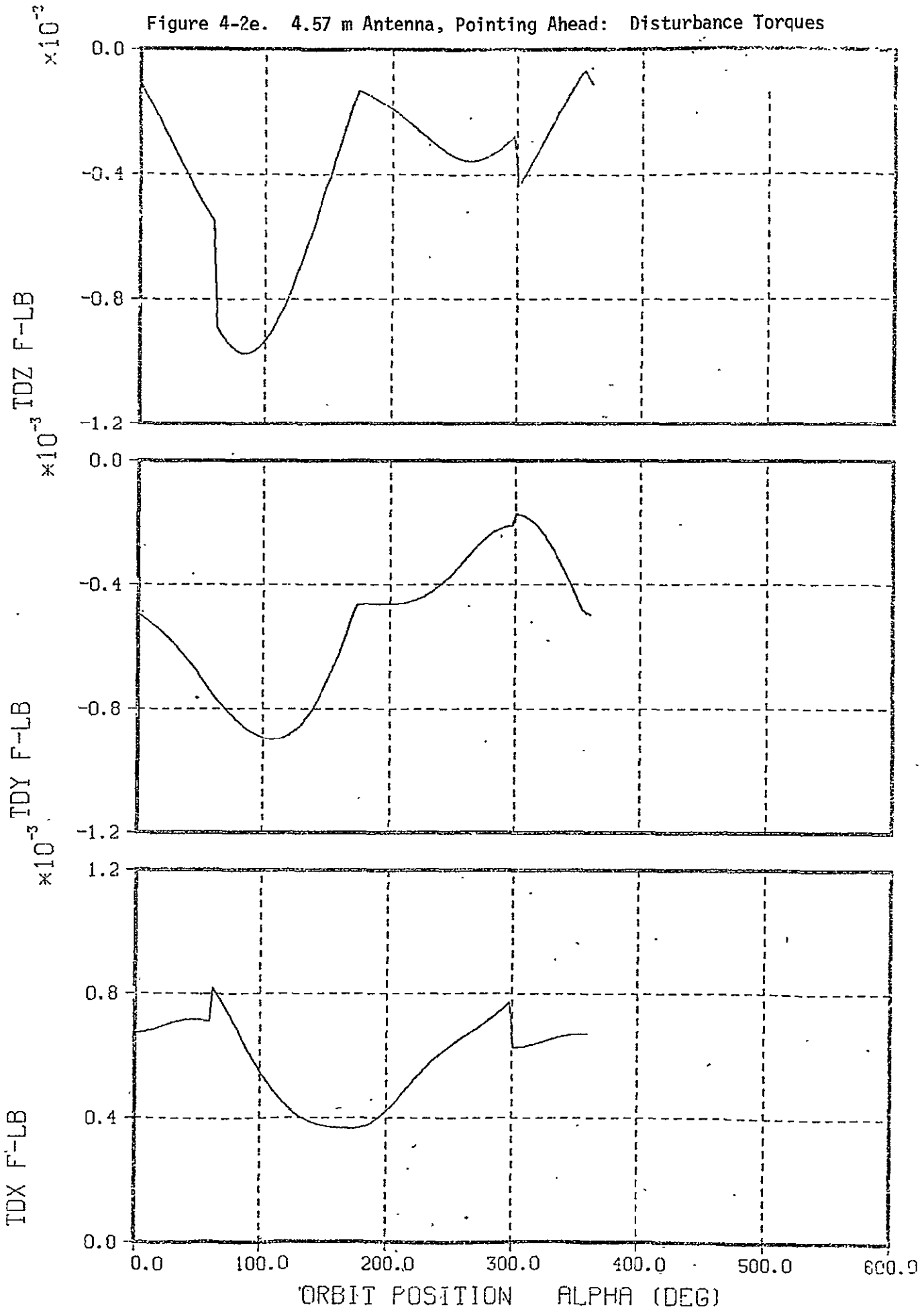

Figure 4-2f. 4.57 m Antenna, Pointing Ahead: Wheel Momenta

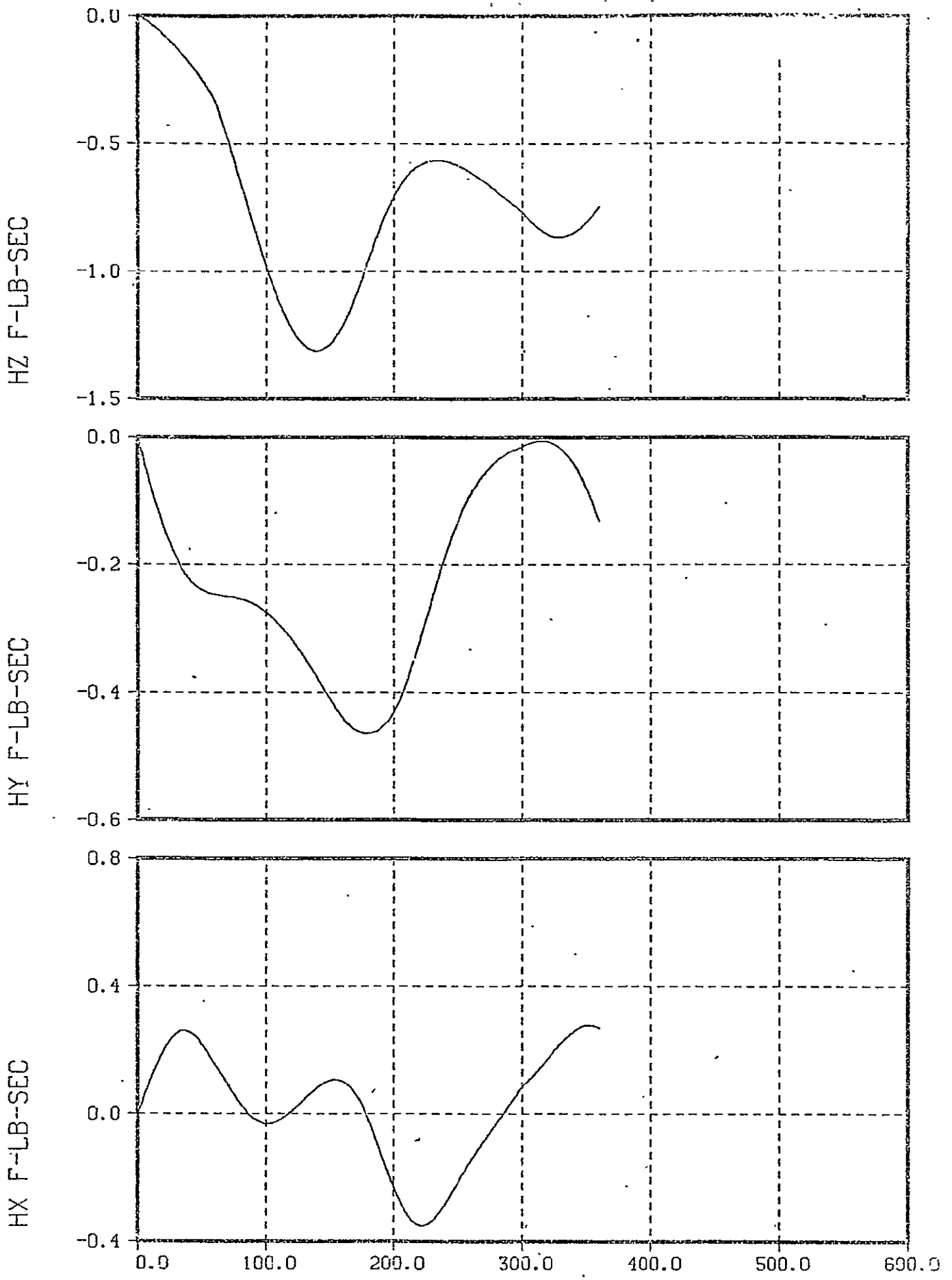

Figure 4-2g. 6.1 m Antenna, Pointing Ahead: Magnetic Moments

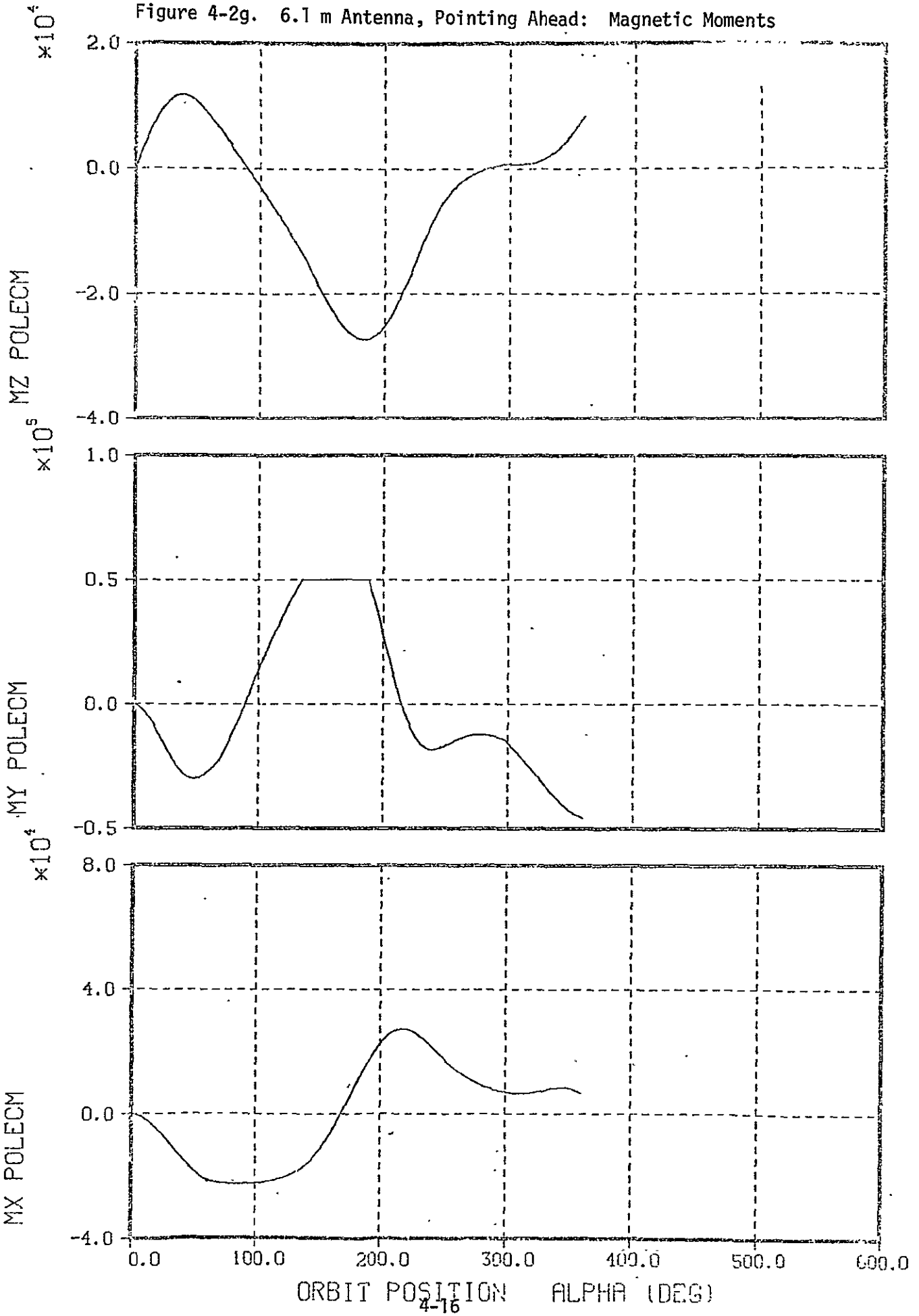

Figure 4-2h. 6.1 m Antenna, Pointing Ahead: Disturbance Torques

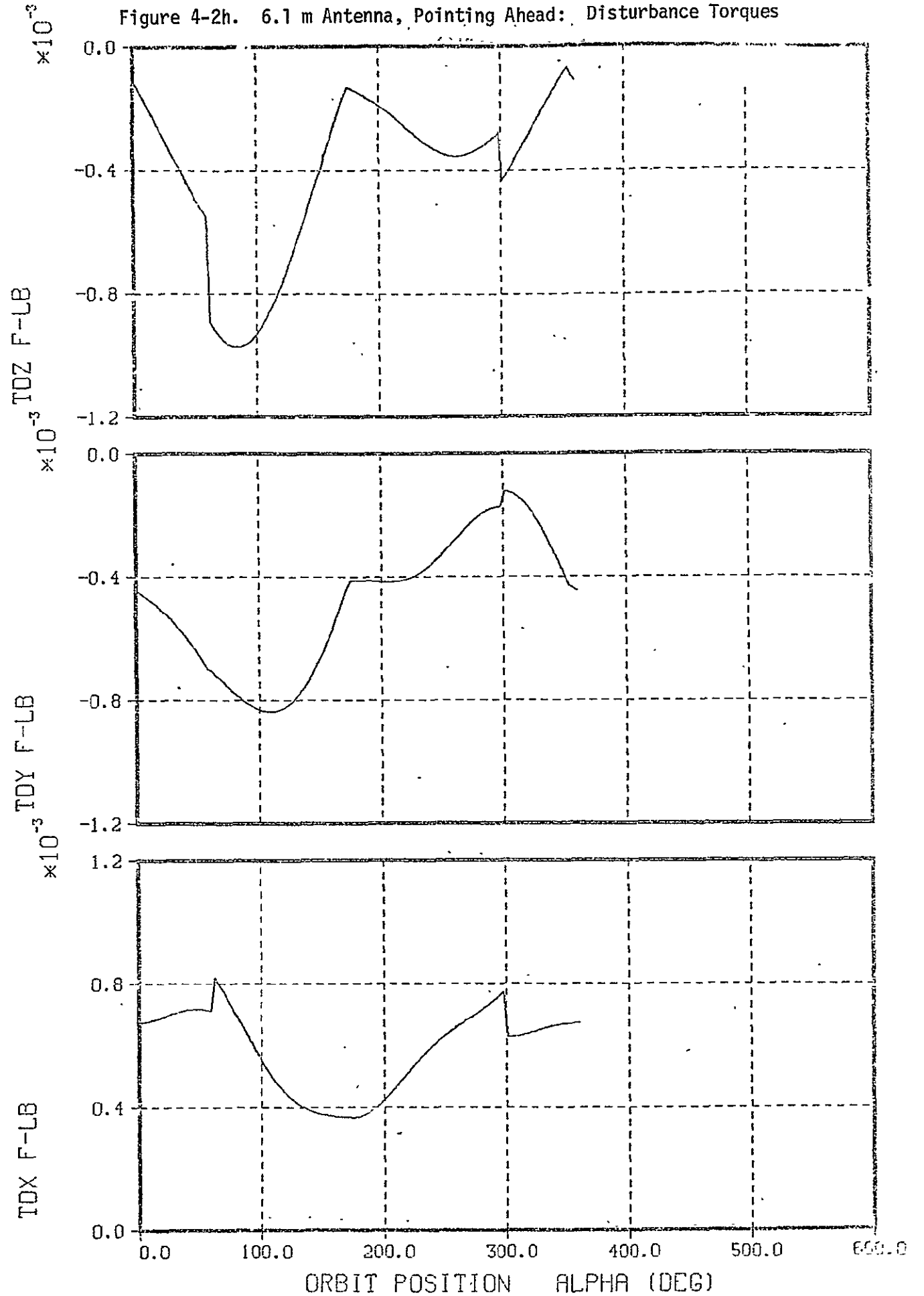

Figure 4-2i. 6.1 m Antenna, Pointing Ahead: Wheel Momenta

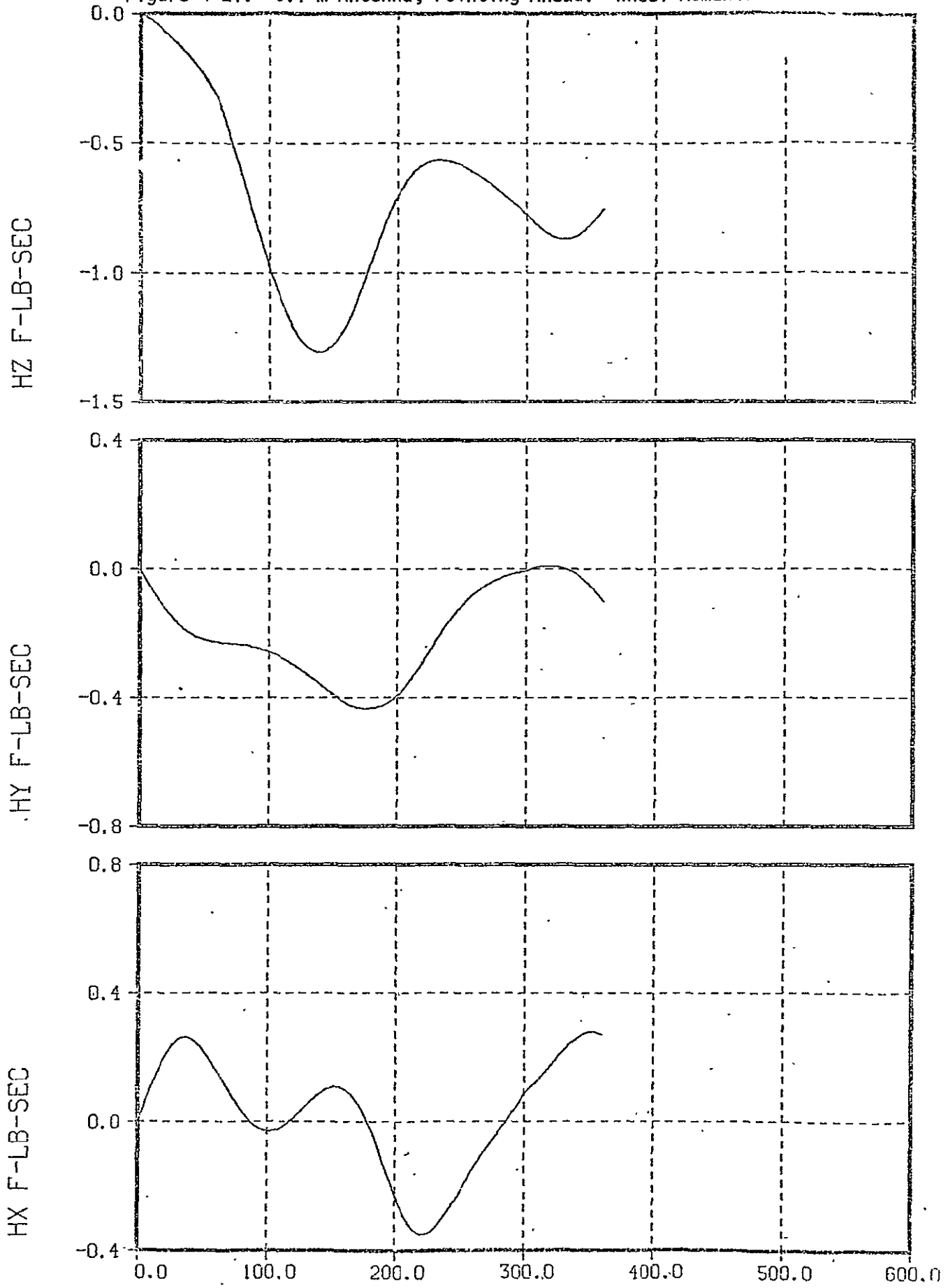

on the axes and -12.68 N-m-s for the fourth wheel. This will allow the fourth wheel to accumulate -7.32 N-m-s before momentum saturation, and will allow each of the other three wheels to lose 7.32 N-m-s before dropping to zero speed.

The preceding bias set point may be tailored slightly to specific orbits if it is known that the stored momentum will show a bias. However, the range of $\pm$ 7.32 N-m-s is used here. Based on it, the 1.86 N-m-s maximum excursion shown in Table 4-2 can be easily handled by the proposed 20 N-m-s SRW's.

Figure 4-2c contains plots of the roll, pitch, and yaw wheel momenta which show that the roll momentum is approximately zero biased. Although the initial momentum was zero at the ascending node, a complete orbit shows that there is a net accumulated momentum. To insure that the momentum does not continue to accumulate on succeeding orbits, three-orbit simulation plots are shown in Figure 4-3. These show more clearly that the roll momentum is zero biased and periodic. However, although the pitch and yaw momenta are periodic after an initial transient, there is a net bias momentum.

This bias is caused by the magnetic unloading law which requires that a certain momentum error $\bar{H}_e$ exists before any unloading torques are generated. The observed bias values thus reflect the equilibrium condition of the magnetic unloading law. These biases may be reduced by increasing the unloading gain K or by changing the magnetic control law to include a lead term representing an estimate of the disturbance torque in body coordinates. In inertial coordinates, the momentum biases are about equal in all axes, but in body coordinates they mainly appear in pitch and yaw. The results of the present investigation into the adequacy of the wheels and the magnetic torque bars are not affected by the biases since they are relatively small compared to the reaction wheel momentum capacity. Thus reduction of the biases will not be further pursued at this time.

Figure 4-3a. 4.57 m Antenna, Pointing Ahead: Magnetic Moments

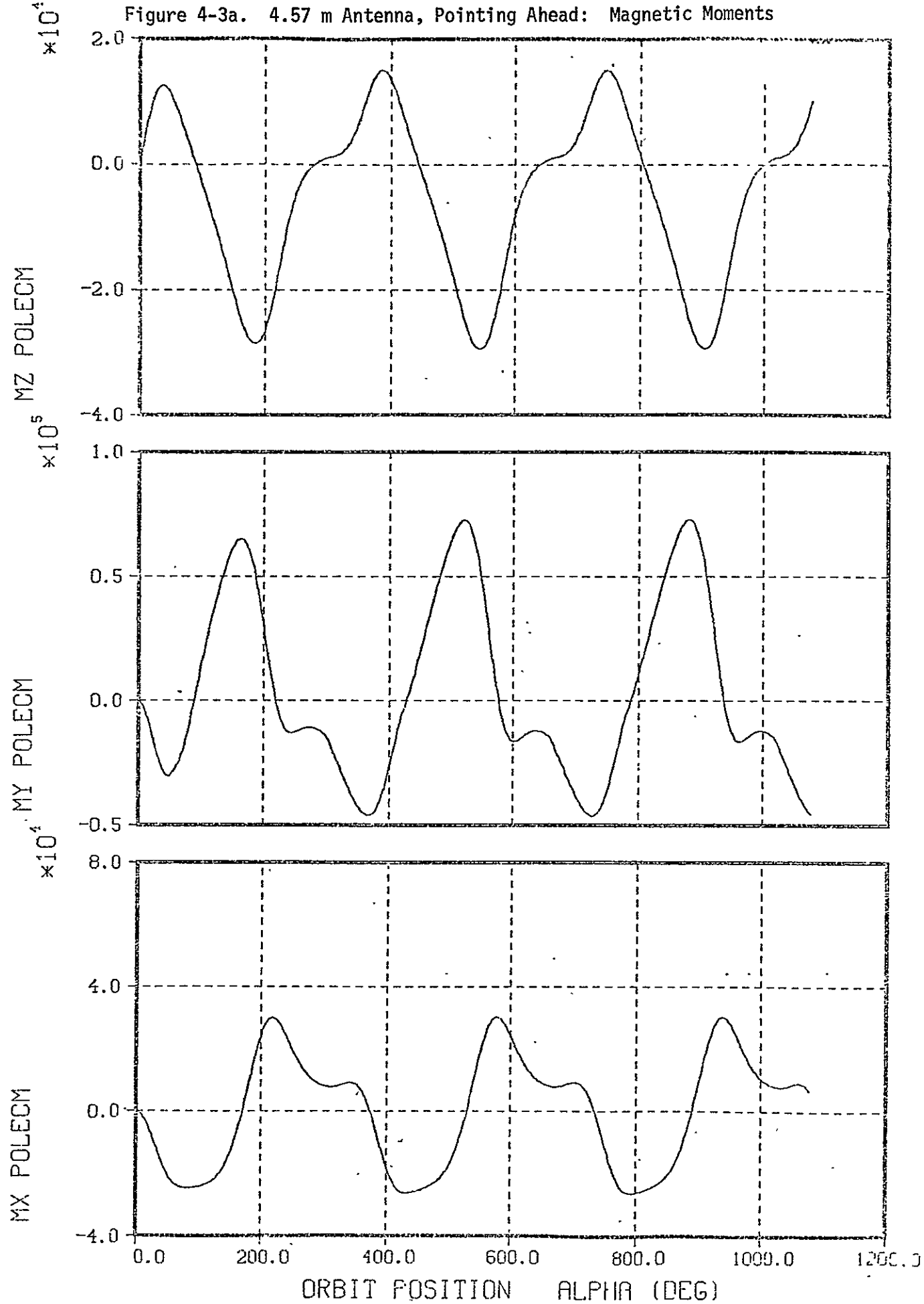

on the axes and -12.68 N-m-s for the fourth wheel. This will allow the fourth wheel to accumulate -7.32 N-m-s before momentum saturation, and will allow each of the other three wheels to lose 7.32 N-m-s before dropping to zero speed.

The preceding bias set point may be tailored slightly to specific orbits if it is known that the stored momentum will show a bias. However, the range of $\pm$ 7.32 N-m-s is used here. Based on it, the 1.86 N-m-s maximum excursion shown in Table 4-2 can be easily handled by the proposed 20 N-m-s SRW's.

Figure 4-2c contains plots of the roll, pitch, and yaw wheel momenta which show that the roll momentum is approximately zero biased. Although the initial momentum was zero at the ascending node, a complete orbit shows that there is a net accumulated momentum. To insure that the momentum does not continue to accumulate on succeeding orbits, three-orbit simulation plots are shown in Figure 4-3. These show more clearly that the roll momentum is zero biased and periodic. However, although the pitch and yaw momenta are periodic after an initial transient, there is a net bias momentum.

This bias is caused by the magnetic unloading law which requires that a certain momentum error $\bar{H}_e$ exists before any unloading torques are generated. The observed bias values thus reflect the equilibrium condition of the magnetic unloading law. These biases may be reduced by increasing the unloading gain K or by changing the magnetic control law to include a lead term representing an estimate of the disturbance torque in body coordinates. In inertial coordinates, the momentum biases are about equal in all axes, but in body coordinates they mainly appear in pitch and yaw. The results of the present investigation into the adequacy of the wheels and the magnetic torque bars are not affected by the biases since they are relatively small compared to the reaction wheel momentum capacity. Thus reduction of the biases will not be further pursued at this time.

Figure 4-3a. 4.57 m Antenna, Pointing Ahead: Magnetic Moments

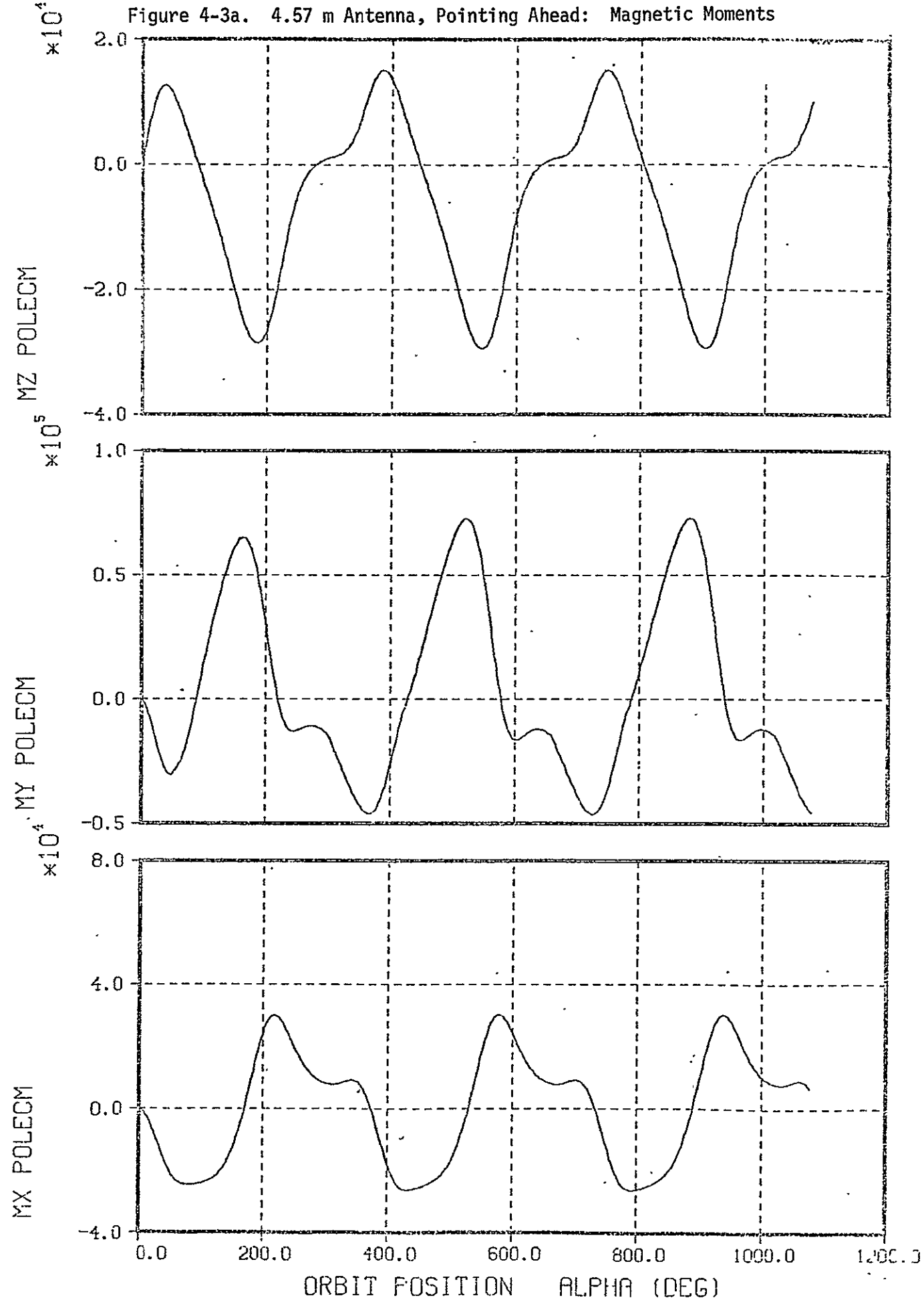

Figure 4-3b. 4.57 m Antenna, Pointing Ahead: Disturbance Torques

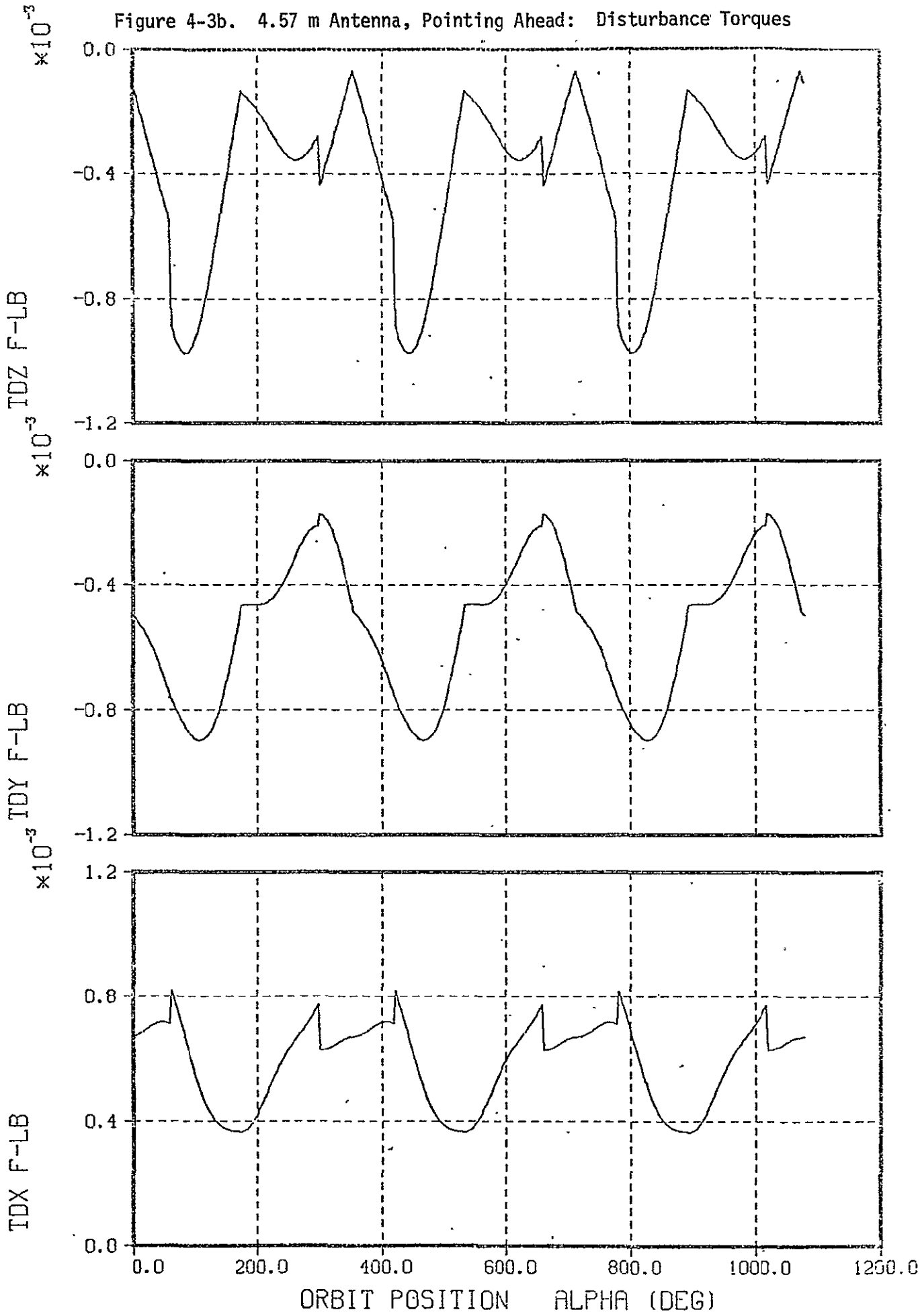

Figure 4-3c. 4.57 m Antenna, Pointing Ahead: Wheel Momenta

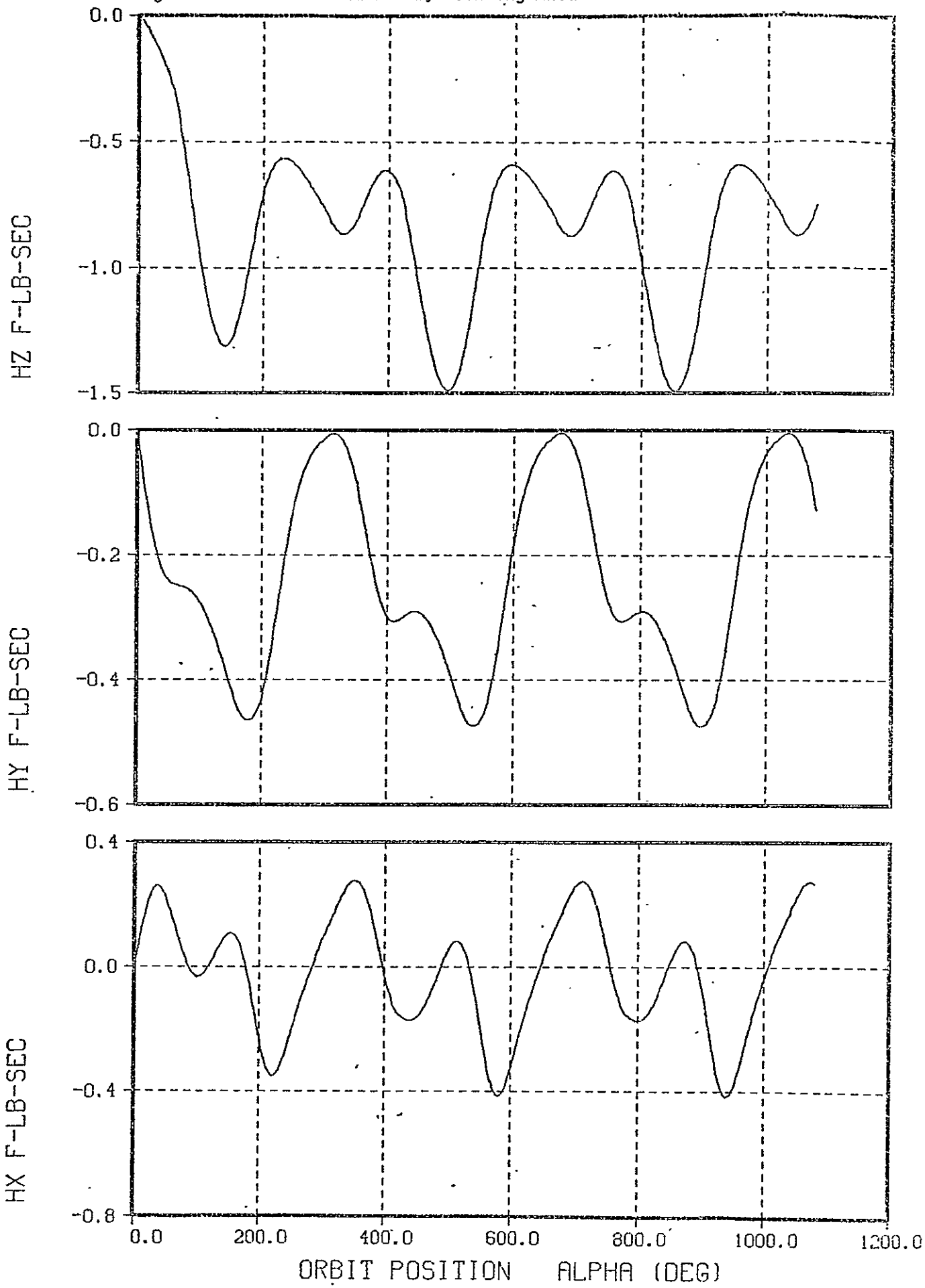

For the plots shown in Figures 4-2 and 4-3, the spacecraft was started in orbit at the ascending node with zero wheel momenta. Other plots not included here show that the wheel momenta appearance varies when the spacecraft is started at orbit positions of 90 and 180 degrees with zero initial momenta. The reason is that an unloading error exists depending on the relative orientations of the $\overline{H}_e$ and $\overline{B}$ vectors, which in fact depends on the initial conditions. Additional studies should examine the possibility of reducing the bias momentum on succeeding orbits. This may require a more detailed study of unloading gains.

Figure 4-4 shows the momentum for the three axes as it accumulates when no unloading torques are commanded. The RSS value for one orbit is approximately 4.6 N-m-s. In the pitch axis, the aerodynamic torque on the antenna (looking ahead) is primarily causing the constant buildup, while the small superimposed oscillation is from solar effects.

To show the sensitivity of the disturbance torques to the mast height and antenna orientation, the Fourier coefficients for the fundamental and first harmonic are tabulated in Table 4-3. These may also be used later for simulation models. In the Table, T_{sx}, T_{sy}, T_{sz} denote the solar roll, pitch, and yaw torques, T_{ax}, T_{ay}, T_{az}, the aerodynamic roll, pitch, and yaw torques, T_{gx}, T_{gy}, T_{gz}, the gravity gradient roll, pitch, and yaw torques, T_{mx}, T_{my}, T_{mz}, the residual magnetic torques, and T_{dx}, T_{dy}, T_{dz} denote the total disturbance torques. The Fourier model is

$$T_{ij} = a_o + \sum_{n=1}^{2} a_n \cos n w_o t + b_n \sin n w_o t$$

where

$i = s, a, g, m, d$

$j = x, y, z$

Figure 4-4. No Unloading, 4.57 m Antenna Looking Ahead: Wheel Momenta

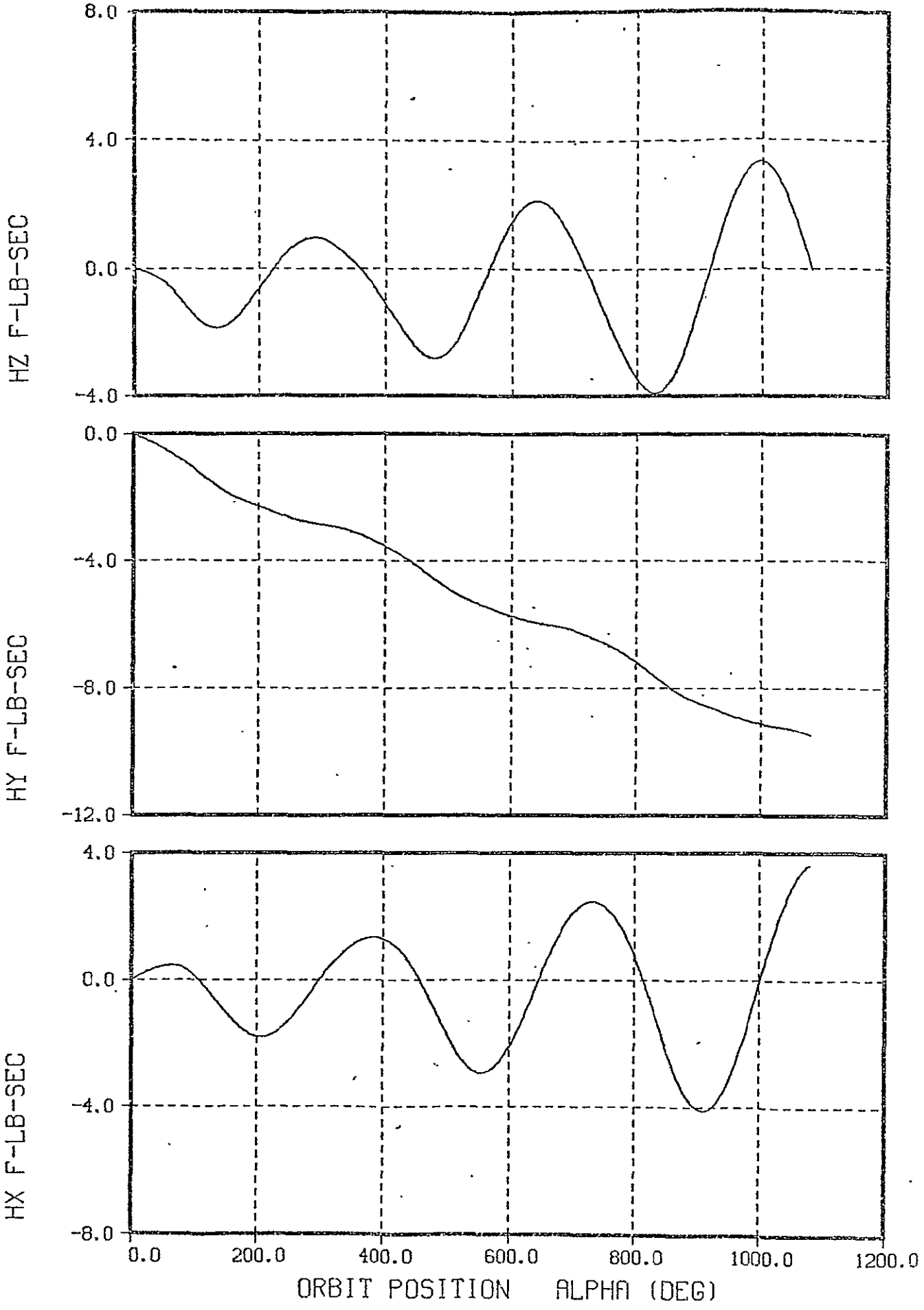

Table 4-3. Fourier Coefficients for Disturbance Torques

4.57 m Antenna, Pointing Zenith

Torques N-m	Fourier Coefficients				
	a_o	a_1	b_1	a_2	b_2
T_{sx}	-12.5×10^{-5}	2.19×10^{-4}	-2.17×10^{-5}	-1.03×10^{-4}	1.20×10^{-5}
T_{sy}	4.07×10^{-5}	-6.49×10^{-5}	-1.05×10^{-5}	2.39×10^{-5}	3.09×10^{-6}
T_{sz}	-4.66×10^{-5}	2.63×10^{-5}	-2.97×10^{-4}	3.32×10^{-5}	1.09×10^{-4}
T_{ax}	2.77×10^{-6}	-1.26×10^{-6}	-1.15×10^{-5}	1.00×10^{-5}	6.07×10^{-5}
T_{ay}	-2.96×10^{-5}	1.53×10^{-4}	2.36×10^{-5}	3.88×10^{-5}	-2.49×10^{-5}
T_{az}	-4.68×10^{-4}	-3.29×10^{-6}	-3.00×10^{-5}	3.15×10^{-4}	-6.72×10^{-5}
T_{gx}	9.10×10^{-4}	0.	0.	0.	0.
T_{gy}	-9.10×10^{-4}	0.	0.	0.	0.
T_{gz}	-1.53×10^{-13}	0.	0.	0.	0.
T_{mx}	0.	0.	0.	0.	0.
T_{my}	-2.10×10^{-10}	2.64×10^{-8}	-4.47×10^{-10}	-4.19×10^{-10}	-1.14×10^{-8}
T_{mz}	1.87×10^{-4}	0.	0.	0.	0.
T_{dx}	7.95×10^{-4}	2.18×10^{-4}	-3.32×10^{-5}	-9.34×10^{-5}	7.27×10^{-5}
T_{dy}	-8.98×10^{-4}	8.79×10^{-5}	-4.34×10^{-4}	6.26×10^{-5}	-2.18×10^{-5}
T_{dz}	-4.81×10^{-4}	2.30×10^{-5}	-3.27×10^{-4}	3.47×10^{-4}	4.15×10^{-5}

Table 4-3. Fourier Coefficients for Disturbance Torques (continued)

4.57 m Antenna, Pointing Ahead

Torques N-m	Fourier Coefficients				
	a_0	a_1	b_1	a_2	b_2
T_{sx}	-1.19×10^{-4}	2.10×10^{-4}	-2.17×10^{-5}	-1.04×10^{-4}	1.28×10^{-5}
T_{sy}	3.97×10^{-5}	-6.22×10^{-5}	2.09×10^{-5}	2.35×10^{-5}	-3.24×10^{-6}
T_{sz}	-5.07×10^{-5}	2.75×10^{-5}	-3.02×10^{-4}	3.84×10^{-5}	1.08×10^{-4}
T_{ax}	2.77×10^{-6}	-1.26×10^{-4}	-1.15×10^{-5}	1.00×10^{-5}	6.07×10^{-5}
T_{ay}	1.49×10^{-4}	1.53×10^{-4}	2.36×10^{-5}	3.88×10^{-5}	-2.49×10^{-5}
T_{az}	-5.42×10^{-4}	-3.29×10^{-6}	-3.00×10^{-5}	3.15×10^{-4}	-6.72×10^{-5}
T_{gx}	9.10×10^{-4}	0.	0.	0.	0.
T_{gy}	-9.10×10^{-4}	0.	0.	0.	0.
T_{gz}	-1.53×10^{-13}	0.	0.	0.	0.
T_{mx}	0.	0.	0.	0.	0.
T_{my}	2.10×10^{-10}	2.64×10^{-8}	-4.47×10^{-10}	-4.19×10^{-10}	-1.14×10^{-8}
T_{mz}	3.23×10^{-5}	0.	0.	0.	0.
T_{dx}	7.93×10^{-4}	2.13×10^{-4}	-3.32×10^{-5}	-9.40×10^{-5}	7.35×10^{-5}
T_{dy}	-7.20×10^{-4}	9.06×10^{-5}	-4.03×10^{-4}	6.22×10^{-5}	-2.82×10^{-5}
T_{dz}	-5.60×10^{-4}	2.43×10^{-5}	-3.32×10^{-4}	3.53×10^{-4}	4.11×10^{-5}

Table 4-3. Fourier Coefficients for Disturbance Torques (continued)

6.10 m Antenna, Pointing Ahead

Torques N-m	Fourier Coefficients				
	a_o	a_1	b_1	a_2	b_2
T_{sx}	-1.17×10^{-4}	2.12×10^{-5}	-2.17×10^{-5}	-1.06×10^{-4}	1.30×10^{-5}
T_{sy}	3.95×10^{-5}	-6.13×10^{-5}	3.40×10^{-5}	2.30×10^{-5}	-6.87×10^{-6}
T_{sz}	-5.14×10^{-5}	2.75×10^{-5}	-3.02×10^{-4}	3.84×10^{-5}	1.08×10^{-4}
T_{ax}	2.77×10^{-6}	-1.30×10^{-6}	-1.18×10^{-5}	1.00×10^{-5}	6.07×10^{-5}
T_{ay}	2.17×10^{-4}	1.53×10^{-4}	2.36×10^{-5}	4.01×10^{-5}	-2.52×10^{-5}
T_{az}	-5.42×10^{-4}	-3.29×10^{-6}	-3.00×10^{-5}	3.15×10^{-4}	-6.72×10^{-5}
T_{gx}	9.10×10^{-4}	0.	0.	0.	0.
T_{gy}	-9.10×10^{-4}	0.	0.	0.	0.
T_{gz}	-1.53×10^{-13}	0.	0.	0.	0.
T_{mx}	0.	0.	0.	0.	0.
T_{my}	-2.10×10^{-16}	2.64×10^{-8}	-4.47×10^{-4}	-4.19×10^{-10}	-1.14×10^{-9}
T_{mz}	3.23×10^{-5}	0.	0.	0.	0.
T_{dx}	7.96×10^{-4}	2.12×10^{-4}	-3.36×10^{-5}	-9.59×10^{-5}	7.38×10^{-5}
T_{dy}	-6.54×10^{-4}	9.17×10^{-5}	-3.90×10^{-4}	6.32×10^{-5}	-3.20×10^{-5}
T_{dz}	-5.60×10^{-4}	2.43×10^{-5}	-3.32×10^{-4}	3.53×10^{-4}	4.11×10^{-5}

Note that the cross products of inertia contribute small constant gravity gradient torques. These may be computed to be 9.1×10^{-4} and -9.1×10^{-4} N-m in roll and pitch, respectively. These compare very well with the table values for roll and pitch.

5.0 INITIALIZATION OF FINE CONTROL

After completion of the initial orbit acquisition, and later on if necessary after stationkeeping or any other maneuvers, the fine control mode must be initiated. The TDRS antenna must be deployed and the solar array drive placed into normal operation.

Normal on-orbit attitude control of the L-D is accomplished using reaction wheels (RW's) and only two areas important to fine control mode initialization must be examined.

(1) When entering the RW attitude control mode, the spacecraft body rates must be compatible with the RW capabilities and the minimum impulse bit of the reaction control system (RCS) used for momentum unloading.

(2) An accurate and stable attitude reference for earth pointing must be available.

Since the L-D mission will be flown on an MMS bus, point 1 above hardly needs any further examination. The mass expulsion RCS and the torque and momentum capabilities of the RW's specified for the MMS [1,2], are compatible. When under mass expulsion attitude control, the MMS is capable of reducing spacecraft rates to less than 0.1 deg/sec per axis. The RW attitude control system (ACS) is capable of stabilizing the spacecraft within 30 minutes from initial rates of up to 0.25 deg/sec about any axis [2]. The minimum torque impulse bit available from the 0.2 lbf thruster is conservatively estimated for L-D as 0.06 ft-lb-sec which is more than two orders of magnitude smaller than the wheel capacity of 15 ft-lb-sec (20 Nms) and the ability to unload the wheel is assured. In conclusion, there exists no problem in transferring from RCS to RW attitude control.

Establishing an accurate and stable attitude reference for earth pointing is thus the main problem encountered when initializing the fine control mode and this section is therefore mainly concerned with the

initialization of the MMS stellar-inertial attitude reference system. The latter task separates into two sub-tasks. Following the normal MMS acquisition procedure (described below) it must first be shown that stars sighted by the on-board star trackers can be identified, and secondly, that the on-board attitude reference algorithm (filter) will converge from the attendant, relatively large, initial attitude uncertainty. Sections 5.2 and 5.3, respectively, will address two different methods of star identification for initializing the on-board stellar-inertial attitude reference system (ARS). The method presented in Section 5.2 utilizes earth magnetic field measurements to aid in the initial star identification, while the method in Section 5.3 correlates observed star sightings with entries in a reduced star catalog. The convergence of the on-board filtering algorithm is demonstrated in Section 5.4. Initialization of the fine control mode appears to pose no problems for L-D.

Once a precise inertial attitude reference of the spacecraft has been established, L-D ephemeris data is used to convert the inertial reference to an earth pointing reference. Then ACS commands are issued that cause the spacecraft to maneuver from an inertial hold mode to its normal on-orbit attitude: yaw ($\hat{z}_b$) to nadir, pitch ($\hat{y}_b$) normal to the orbit plane, and roll ($\hat{x}_b$) in direction of orbital motion. The RW's will be used to perform this maneuver. Any further maneuvers performed during the life of the spacecraft, such as stationkeeping, for example, will not require a reinitialization of the ARS. At the end of even the longest of any such maneuvers, the inertial reference unit (gyros) provides an attitude reference that will certainly be accurate enough to identify the stars sighted by the trackers. Attitude and gyro bias updates can then be computed.

The TDRS antenna should be deployed once coarse sun acquisition has been completed. Since MMS/L-D will probably acquire the sun with the negative yaw ($-\hat{z}_b$) axis, the antenna dish could find itself looking directly into the sun, a situation rarely encountered during normal on-orbit operations. To assure thermal loads compatible with normal on-orbit conditions the antenna elevation angle should be commanded to its

maximum dip angle of -26° and the azimuth to +90° so that the antenna looks away from the sun and in the positive pitch direction.

The solar array will be placed into normal operation (see Section 3.5) once the spacecraft has maneuvered to its nominal earth pointing orientation. Correct initial positioning of the array will be accomplished by ground command. Spacecraft ephemeris in ECI coordinates and time of year are sufficient information to compute the correct array angle relative to the solar array/spacecraft scribe-mark. The correct array orientation can be verified from telemetry data of the coarse sun sensor which is mounted on the solar array.

5.1 Normal MMS/L-D Acquisition Sequence

During launch the ACS is in a standby condition and the actuators are disabled. After separation from the launch vehicle (shuttle or Delta 3910 booster) the ACS is enabled and the solar array is deployed and subsequently rotated to a predetermined position relative to its scribe-mark. For L-D the solar cells will look toward $-\hat{z}_b$. The normal MMS acquisition sequence is to be autonomous by utilizing the on-board computer.

Coarse Sun Acquisition

After array deployment the spacecraft acquires the sun with its negative yaw axis ($-\hat{z}_b$ axis) and the spacecraft rates are reduced to an appropriate level. This maneuver is accomplished by the on-board computer using coarse sun sensors located on the solar array, the Inertial Reference Unit (gyros) for rate information, and the reaction control jets, magnetic torquers and/or reaction wheels to provide control torques. Normally coarse sun acquisition seeks an orientation with the solar array normal to the sun line. Because of the array cant angle of 37.5° (9:30 am orbit) the sun line would then not be aligned with one of the principal control axes of the spacecraft. Since it may be required to perform a rotation about the sun line to acquire appropriate stars into the fields of view of the star trackers, it is preferred to align the $-\hat{z}_b$ axis with the sun which keeps the solar array at 52.5°(90°-37.5°) to the sun line. The 20 percent

loss in generated electrical power is not critical since the payload sensors, which consume more than 50 percent of the power, are not yet activated. For one axis, the output signals of the array-mounted coarse sun sensors must then either be biased by 37.5° to account for the array cant angle, or the coarse sun sensors must be mounted to the uncanted portion of the solar array shaft.

Utilizing the mass expulsion system, the ACS is capable of completing a coarse sun acquisition sequence within 15 minutes in a sunlit segment of the orbit for initial rates of up to 2 deg/sec about each control axis. This would apply to acquisition after separation from a Delta 3910 launch vehicle. Utilizing reaction wheels, which would apply to acquisition after a shuttle launch, the ACS can complete coarse sun acquisition within 30 minutes in a sunlit segment of the orbit for initial rates of up to 0.25 deg/sec about each control axis. Coarse sun acquisition is considered complete when the attitude error between the sun line and the coarse sun sensor reference axis (biased) is less than ten (10) degrees (including albedo effects), the maximum rate about each of the control axes is less than 0.05 degree per second and control is maintained by the reaction wheels. Following coarse sun acquisition, the magnetic torquers and/or the mass expulsion system are used to reduce the reaction wheel speeds to less than 25 percent of no load speed.

Fine Sun Acquisition Mode

In the fine sun acquisition mode the coarse sun sensor is replaced by the fine digital sun sensor located in the ACS module with reference axis aligned with the $-\hat{z}_b$ axis. The initial conditions for the fine sun acquisition mode are defined by the final conditions of the coarse sun acquisition mode. Fine sun acquisition shall be considered complete when the attitude error between the sun line and the fine sun sensor reference is less then 0.1 degree, the maximum rate about each of the control axes is less than 0.05 degree per second, and the reaction wheel speeds are less than 25 percent of no load speed. Fine sun acquisition can be completed within ten (10) minutes of entering the mode.

After completion of the fine sun acquisition mode the spacecraft enters the stellar acquisition mode, which, as was mentioned above, is part of the main topic of this section.

Stellar Acquisition Mode

The initial conditions for the stellar acquisition mode are defined by the fine sun acquisition mode. Stellar acquisition shall be considered complete when the attitude of the ACS reference (optical cube) in the ACS module is aligned within 0.1 degree (each of three axes) of a specified inertial attitude (including verification of required guide stars), the maximum rate about each of the control axes is less than 0.01 degree per second, and the reaction wheel speeds are less than 25 percent of no load speed. Stellar acquisition must be completed within four hours after entering the mode. At the end of stellar acquisition for spacecraft is considered to be in an inertial hold mode from which its normal on-orbit orientation is acquired by performing the appropriate maneuver.

5.2 Star Identification/Attitude Determination From Magnetic Field Measurements

Conditions at the completion of fine sun acquisition establish the initial conditions for the start of attitude determination from magnetometer measurements. The conditions are that the negative yaw axis is within 0.1 degree of the sun line and that the maximum rates are 0.05 deg/sec about any of the control axes. The attitude about the sun line is unknown and is to be estimated. The preferred way to do this for low orbit missions is to wait for a point in the sunlit portion of the orbit at which the earth's magnetic field is oriented more or less orthogonal to the sunline (60° or more). For high inclination missions, such as L-D, the portion of the orbit around the poles is generally not satisfactory. One purpose here is to point out angular error sources in the overall magnetic attitude determination scheme.

5.2.1 Magnetic $\vec{B}$ Field Modeling

Autonomous attitude determination is desired and to do this a sufficiently accurate magnetic $\vec{B}$ field model must be available on-board at the

time of attitude determination. Comparisons of a simple tilted dipole field model and the standard spherical harmonic model reveal that the $\vec{B}$ field vectors computed by the models may differ in direction by as much as 10-15° or more. This rules out the possibility of using the tilted dipole model on-board for autonomous attitude determination since the star tracker field-of-view is only 8° x 8° and a 10° - 15° uncertainty would also be unsatisfactory for star identification. Since launch date and therefore approximate vehicle location in the $\vec{B}$ field is known before launch, a local portion of the spherical harmonic model may be stored into the on-board processor. This would still permit autonomous attitude determination. However, storage of a complete harmonic model may be prohibitive, and if it should be required, the model would have to be computed on the ground and sent up for use at the proper time.

Finally, the agreement between the harmonic model and nature has to be determined since it is a direct error source in the attitude determination. Estimates of the divergence between the harmonic model and nature are not well known because of a lack of data, but published results [7] show that solar-magnetic field attitude determination produces accuracies of 1 to 3.5 degrees from field measurements that are in error by up to 9.2 degrees. Repeated measurements at successive points in orbit do, however, help to reduce the field uncertainty effects.

To be of use in the attitude estimation process, the magnetic field must be available in a proper coordinate frame for on-board use. This coordinate frame is referred to as the sun frame and is defined in detail in the next section. Typically, the tenth order harmonic model $\vec{B}$ field is computed in spherical coordinates as

$$\vec{B} = \begin{bmatrix} B_r \\ B_\lambda \\ B_\theta \end{bmatrix}$$

where r is the radius from the geocenter to the field point, λ is the East longitude, and θ is the colatitude. This field vector is then transformed

by suitable routine orthogonal transformations to obtain it finally in sun coordinates. Possible errors in the final field vector as a result of unknown angular errors in the transformations are discussed after the coordinate systems are defined. In any event, the magnetic field is assumed to be transformed error-free into a standard set of Earth-Centered-Inertial coordinates which will be related to the sun coordinates by standard orbit transformations. The error-free assumption is justified because up to that point the transformation does not involve orbital geometry.

5.2.2 Coordinate Transformations and Frames

It is convenient to have a set of Earth-Centered-Inertial coordinates $\hat{x}_I\ \hat{y}_I\ \hat{z}_I$ with $\hat{x}_I$ toward the vernal equinox point, $\hat{z}_I$ normal to the equatorial plane, and $\hat{y}_I$ completing the set. It is in this set that the magnetic field is assumed available by error-free transformation from magnetic coordinates.

To perform the attitude determination, it is convenient to establish a set of sun coordinates $\hat{x}_S, \hat{y}_S, \hat{z}_S$ centered in the spacecraft with $-\hat{z}_S$ toward the sun, $\hat{x}_S$ in the orbital plane, and $\hat{y}_S$ completing the set. Then the vehicle body coordinate set $\hat{x}_B, \hat{y}_B, \hat{z}_B$ is defined by the respective rotations α, β, γ where α is about the $\hat{x}_S$ axis, β is about the intermediate $\hat{y}$ axis, and γ is about the final $\hat{z}_B$ axis. Angles α and β are less than or equal to 0.1 degree as noted earlier, and γ is arbitrary about the $\hat{z}_B$ axis which is nominally the anti-sun line. Figure 5-1 shows the frames and angles involved.

The transformation from sun to body coordinates is $[A]_{BS}$ given by

$$[A]_{BS}=\begin{bmatrix} \cos\gamma\cos\beta & \cos\gamma\sin\beta\sin\alpha+\sin\gamma\cos\alpha & -\cos\gamma\sin\beta\cos\alpha+\sin\gamma\sin\alpha \\ -\sin\gamma\cos\beta & -\sin\gamma\sin\beta\sin\alpha+\cos\gamma\cos\alpha & \sin\gamma\sin\beta\cos\alpha+\cos\gamma\sin\alpha \\ \sin\beta & -\cos\beta\sin\alpha & \cos\beta\cos\alpha \end{bmatrix}$$

and is explicitly required for the least-squares attitude determination in Section 5.2.3.

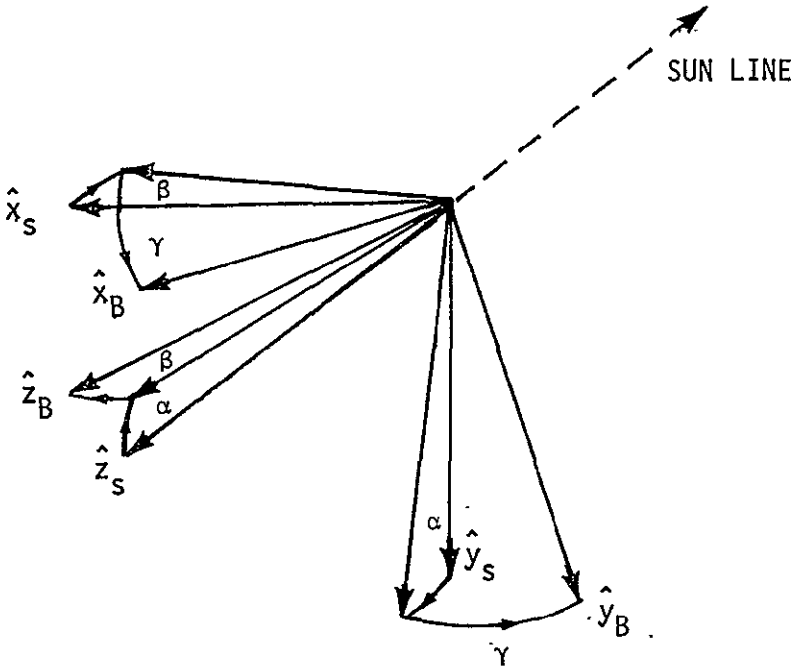

Figure 5-1. Sun-Body Coordinate Conventions

Additional transformations are required also, but those involve angular quantities such as orbit inclination, orbit position angle, and angle of the ascending node which are all known quite accurately. For instance, spacecraft position is assumed known to within 100 meters which, at an altitude of 705 km (388 nautical miles) creates an angular error of approximately 3 arc-sec. Errors such as this in the computation of transformations are entirely negligible compared to the potential disagreement between the magnetic model and nature so they may be ignored. The errors are also negigibly small compared to the 8° x 8° field-of-view for the star tracker. Thus the overall transformation from ECI coordinates to sun coordinates is designated as $[A]_{SI}$ and with it the magnetic field available in ECI coordinates may be transformed to the sun coordinates by

$$\bar{B}_s = [A]_{SI}\, \bar{B}_I$$

for use in the attitude determination.

5.2.3 Attitude Determination

Magnetic field measurements are obtained from the magnetometers in body axes, and since the field model is known in sun coordinates as $\vec{B}_s$, the measurement equation may be written as

$$\bar{z} = [A]_{BS}\, \vec{B}_s + \bar{V}$$

where $\bar{z}$ is the vector of three measurements are

$$\bar{B}_s = \begin{bmatrix} B_{xs} \\ B_{ys} \\ B_{zs} \end{bmatrix}$$

The additive noise is represented by the vector $\bar{V}$, and since the measurements are processed at discrete times in orbit, the covariance matrix of $\bar{V}$ may be written as

$$E[\bar{V}(t_i)\ \bar{V}^T(t_j)] = [R]\ \delta_{ij}$$

where [R] is a constant matrix. Modeling the noise as uncorrelated between the axes and with equal variance in all axes permits writing [R] as

$$[R] = \begin{bmatrix} \sigma_v^2 & 0 & 0 \\ 0 & \sigma_v^2 & 0 \\ 0 & 0 & \sigma_v^2 \end{bmatrix}$$

For the magnetometers considered here, the resolution is 0.004 gauss which yields a $\sigma_v = 0.001$ gauss if a rounding-error model with a uniform distribution is used. The noise is considered zero mean although bias may result since the accuracy of the magnetometers is $\pm 1\%$ of the full scale value of ± 0.5 gauss.

The emphasis here is on a computationally simple algorithm that will produce estimates for the angle about the sun line accurately enough so that unambigous star identifications can be made and the stellar-inertial attitude reference system can be initialized. Thus the extended Kalman filter is not considered for magnetic attitude determination. Also of importance is the fact that rates about the sun line can be appreciable at this time and thus the yaw attitude may change between successive magnetometer attitude determinations. Thus the yaw gyro rate has to be integrated so that the yaw angle change can be propagated between successive attitude determinations. Since the yaw axis is within 0.1 degree of the sunline, α and β are always small and accurate enough for stellar convergence; however they may also readily be estimated by the least squares procedure if desired. The procedure is as follows.

Let $\bar{x}^o$ represent the initial best estimate of the vector $\bar{x} \triangleq (\alpha,\beta,\gamma)^T$. Since the measurement equation is nonlinear and implicitly involves $\bar{x}$, it may be written as

$$\bar{z} = h(\bar{x}) + \bar{V}$$

$$h(\bar{x}) = \begin{bmatrix} c\eta c\beta B_{xs} & + (c\gamma s\beta s\alpha + s\gamma c\alpha)\, B_{ys} & + (-c\gamma s\beta c\alpha + s\gamma s\alpha)\, B_{zs} \\ -s\gamma c\beta B_{xs} & + (-s\gamma s\beta s\alpha + c\gamma c\alpha)\, B_{ys} & + (s\gamma s\beta c\alpha + c\gamma s\alpha)\, B_{zs} \\ s\beta B_{xs} & - c\beta s\alpha\, B_{ys} & + \quad c\beta c\alpha\, B_{zs} \end{bmatrix}$$

and linearized about $\bar{x} = (0\ ,\ 0\ ,\ \gamma^{o})$ to obtain the matrix H defined as

$$H = \left.\frac{\partial h(\bar{x})}{\partial \bar{x}}\right|_{\bar{x} = \bar{x}^{o}}$$

$$H = \begin{bmatrix} \sin\gamma^{o}\, B_{zs} & -\cos\gamma^{o}\, B_{zs} & -\sin\gamma\, B_{xs} + B_{ys} \\ \cos\gamma^{o}\, B_{zs} & \sin\gamma^{o}\, B_{zs} & -\cos\gamma\, B_{xs} - \sin\gamma\, B_{ys} \\ -B_{ys} & B_{xs} & 0 \end{bmatrix}$$

The complete linearization may now be written as

$$\Delta\bar{z} = H\,\Delta\bar{x} + \bar{V}$$

where the $\bar{x}$ and $\bar{z}$ are defined as

$$\Delta\bar{x} = \bar{x} - \bar{x}^{o}$$

$$\Delta\bar{z} = \bar{z} - [A(\bar{x}^{o})]_{BS}\,\bar{B}_{s}$$

These equations would be suitable for estimating the attitude $\bar{x}$ based on $\Delta\bar{x}$ computed from the relation

$$\Delta\bar{x} = H^{-1}\,\Delta\bar{z}$$

However, in the present case α and β are known within 0.1° if the fine sun sensor is operative. This accuracy is probably greater than can be obtained from the magnetic field, and thus α and β do not normally have to be estimated. The preceding formulation is still applicable with some notational changes as follows.

Using only the last column of matrix H, define

$$M = \begin{bmatrix} -\sin\gamma^{o} B_{xs} + B_{ys} \\ -\cos\gamma^{o} B_{xs} - \sin\gamma^{o} B_{ys} \end{bmatrix}$$

Then the measurement equation may be condensed to

$$\begin{bmatrix} \Delta z_1 \\ \Delta z_2 \end{bmatrix} = M \Delta\gamma + \begin{bmatrix} V_1 \\ V_2 \end{bmatrix}$$

from which a least squares estimate for $\Delta\gamma$ may be obtained as

$$\Delta\gamma = (M^T M)^{-1} M^T \begin{bmatrix} \Delta z_1 \\ \Delta z_2 \end{bmatrix}$$

The attitude γ is then obtained from

$$\gamma = \gamma^{o} + (M^T M)^{-1} M^T (\Delta\bar{z} - [A'(\bar{x}^{o})_{BS}] \bar{B}_s) \qquad \text{(5.2-1)}$$

where $\Delta\bar{z}$ is understood to be

$$\Delta\bar{z} = \begin{bmatrix} \Delta z_1 \\ \Delta z_2 \end{bmatrix}$$

and the primed transformation $A'(\bar{x}^{o})_{BS}$ is obtained from $A(\bar{x}^{o})_{BS}$ by deleting the last row, as

$$[A']_{BS} = \begin{bmatrix} \cos\gamma\cos\beta & \cos\gamma\sin\beta\sin\alpha + \sin\gamma\cos\alpha & -\cos\gamma\sin\beta\cos\alpha + \sin\gamma\sin\alpha \\ -\sin\gamma\cos\beta & -\sin\gamma\sin\beta\sin\alpha + \cos\gamma\cos\alpha & \sin\gamma\sin\beta\cos\alpha + \cos\gamma\sin\alpha \end{bmatrix}$$

The first estimate of γ^0 will be determined shortly, and then $\bar{B}_s$, $[A'(\bar{x}^0)]_{BS}$, and the measurement $\bar{z}(t_i)$ are all known so that γ may be computed. Let the first estimate be $\gamma(t_1)$, and determine the incremental attitude change γ_g up to time b_2 by integration of the gyro outputs. Then the new initial estimate for the second least-squares determination is given by

$$\gamma^0(t_2) = \gamma(t_1) + \gamma_g(t_2)$$

Using this $\gamma^0(t_2)$, the computation in (5.2-1) may be repeated to determine the second attitude estimate $\gamma(t_2)$. The process is repeated until $\gamma(t_i)$ has converged, i.e., successive computed updates $\Delta\gamma$ are small and have zero mean.

The first estimate $\bar{x}^0(t_1)$, i.e., $\gamma^0(t_1)$, may be determined as follows. Since α and ρ are within 0.1 degree, they may be set to zero in the measurement equation

$$\bar{z} = [A]_{BS}\,\bar{B}_s$$

Writing the equation out and solving for the remaining unknown γ^0 yields the expression

$$\gamma^0 = \cos^{-1}\left[\frac{z_1 B_{sx} + z_2 B_{sy}}{B_{sx}^2 + B_{sy}^2}\right]$$

which provides the starting estimate.

The flow diagram which follows contains the main steps for the magnetometer attitude estimation.

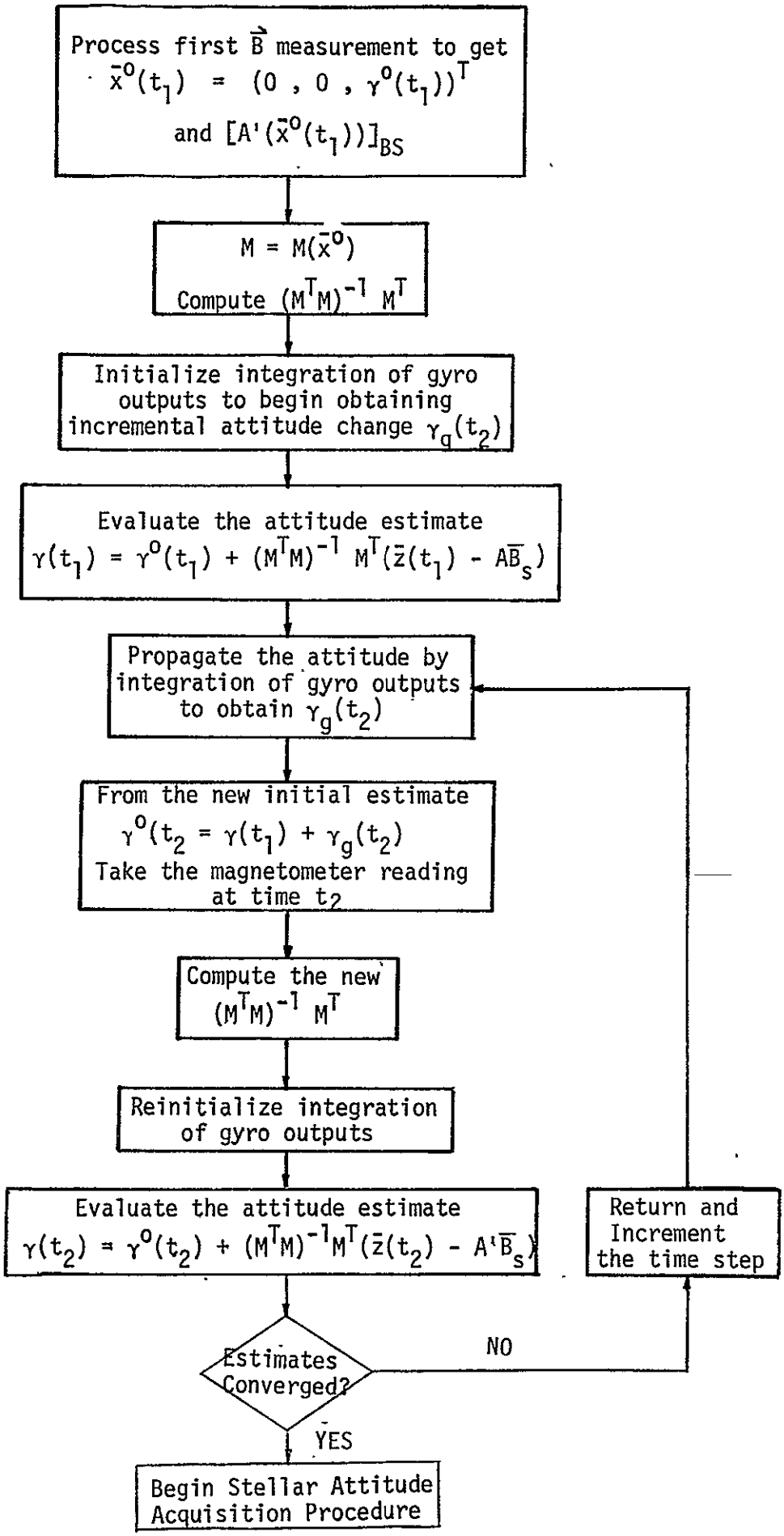

Figure 5-1a. Attitude Processing Flow Chart

The arrangement of the preceding flow chart is arbitrary in several places, and it is implicitly assumed that the computational time per estimate is negligible compared to the time difference $t_i - t_j$ between estimates.

5.2.4 Error Sources and Effects

This section summarizes the potential error sources and indicates the accuracy expected for the magnetic attitude determination. The error sources and their effects are:

(1) Divergence between the magnetic model and nature. A mean angular error is 4.3° extracted from Reference 1, with a maximum error of 9.2°. Effects of this divergence are reduced by repeated measurements at several points along the orbit.

(2) Magnetometer measurement noise of 0.004 gauss. These effects are also reduced by repeated measurements along the orbit.

(3) Errors in coordinate transformations. Since the transformations involve angular quantities that are accurately known, the error in attitude determination that results from an inaccurately transformed $\overline{B}$ field is negligible.

Results in Reference 7 show that attitude errors on the order of 1.56° (average) with a maximum of 3.5° are achievable. Such errors are well within the 8° x 8° field-of-view of the star tracker, and thus the solar-magnetic determination should be accurate enough to permit initiation of stellar acquisition.

5.3 Star Identification By Correlation

Another method of determining the orientation of the spacecraft about the sun line is by correlating star tracker observations with a star catalog. The star catalog contains only those stars above a certain brightness M_V which should be encountered by the spacecraft's star tracker as it sweeps out at a swath about the sun line. The correlation method will now be briefly described.

5.3.1 Description of Method

The spacecraft is commanded to rotate about the sun line at a fixed rate, say 0.1 deg/sec, and the star tracker sensitivity threshold is set such that it will detect only stars above a specified brightness which matches the brightness of the stars included in the catalog. At the beginning of the spacecraft rotation, or scan, the inertial reference system is initialized with a guess of zero rotation angle about the sun line, the rotation angle being referenced to a suitably defined sun pointing reference frame. The stars in the star catalog are sequentially ordered according to this reference point and each star is specified by an azimuth or scan angle ϕ_c measured from the reference (in the direction of spacecraft rotation) and a declination relative to the swath plane, δ_c (the subscript c stands for catalog). Then, as the star tracker sweeps out the swath, the time and the scan angle for each star encountered by the tracker will be recorded. The scan angle is obtained from the inertial reference unit, i.e., integrated gyro rate, and is denoted by ϕ_T (subscript T for tracker). If the spacecraft is controlled so that it remains well aligned with the sunline, one can start to correlate the sequence of star observations to the catalog entries after one revolution. If the spacecraft rotation axis does not remain well aligned with the sunline, some stars may be missed due to the resulting wobble, and 2-3 revolutions of data taking may be required. LANDSAT D will be maintained sun pointing to within 0.1 degree when using the fine digital sun sensor or an attitude reference and one revolution should suffice.

The correlation proceeds then as follows. The first star encountered by the tracker is assumed to be the first star in the catalog and the difference ϕ_0 of the scan angles is computed,

$$\phi_0(1) = \phi_c(1) - \phi_T(1)$$

The angle $\phi_0(1)$ may be considered the first update on the initial zero estimate for the orientation angle of the spacecraft about the sun line and it is added to all the observed scan angles $\phi_T(n)$. All the observed stars are now correlated with the entries in the star catalog, considering

all possible combinations, and the number of successful correlations or matches are recorded. A successful match is considered to occur between two stars when the observed star scan angle $\phi_T(n)$ falls within a specified ε of the catalog scan angle $\phi_c(m)$, i.e.,

$$|\phi_c(m) - \phi_T(n)| < \varepsilon$$

The process is then repeated for the next pair of stars, for example the first star encountered by the tracker is assumed to be star No. 2 in the catalog and the number of successful correlations are determined under this assumption. This process is repeated until all possible star pairs have been exhausted, and the pairing that produced the most matches is declared the winner and the corresponding scan phasing angle ϕ_o is the final estimate of the orientation angle of the spacecraft about the sun line. ϕ_o is not selected as the angle computed for the first forced pair in the sequence, but once good correlation for a particular sequence has been established, all star measurements are considered and a least squares fit to ϕ_o can be obtained. Initial calibration of the scan axis gyro bias can also be obtained. In principle, the elapsed time between two star observations, the $\Delta\phi_T$ scan angle as obtained from the gyros, and the $\Delta\phi_c$ for the two stars as obtained from the catalog, contain all the information to compute gyro bias. Namely

$$b_{g_{scan}} = \frac{\Delta\phi_c - \Delta\phi_T}{\Delta t}$$

In practice one uses all the data and computes a least squares fit estimate for the gyro bias.

Using this method the spacecraft orientation about the sun line can usually be determined within about 0.2 degree and the gyro bias estimate within 0.2 deg/hr. The errors are mainly due to bias and noise imperfections in the tracker and gyros. Residual gyro bias appears to be the main error source in the estimate of the scan phasing angle ϕ_o. The number of stars also influences the accuracy; the more data, the better the

estimate. The latter is, however, of little concern to LANDSAT D since one is not so much interested in the accuracy during initialization, as one is interested in a fast correlation process using only a few good stars.

A potential disadvantage of the correlation method is the length of time that may be required to obtain enough stars since trackers will not read accurately above a certain angular rate which limits the speed of commanded rotation about the sun line. Depending on the number of stars in the swath/catalog, a more serious requirement is the rather large amount of computation required to perform the correlation tests. Since the correlation is nominally only performed at the beginning of the mission, the software, which includes the swath catalog, should not be left in the computer. But erasing it and reading a new software from a special memory would require a ground command which does not fit the desired autonamous operation plan. Also, the ground command may have to be delayed until a certain favorable orbit position is reached. Since autonomous operation seems hard to attain with this method, it is recommended to perform the correlation task on the ground. In this case the star tracker data is telemetered to the ground and after convergence of the correlation procedure, the correct scan phasing angle about the sun line and the initial gyro bias calibration results are sent back to the spacecraft.

5.3.2 Simulated Star Identification by Correlation

Star identification by correlation has been simulated for L-D by a digital program using real star locations as obtained from the Yale star catalog. The time of year was assumed to be around July 20th such that the earth had moved 120° in the ecliptic away from the vernal equinox. The negative yaw axis of L-D was pointed to the sun with an accuracy of 0.1 degree and the spacecraft rotated about the sun line at 0.1 deg/sec. The cross axis rates were assumed in a sinusoidal limit cycle with peak rates of 0.05 deg/sec and position amplitude limited to 0.1 degree. Initial uncalibrated gyro biases were set at values averaging to 1.5 deg/hr and the sensitivity threshold of the 8° x 8° FOV star tracker (BBRC CT-401) was set

to $M_V = +4$. The latter will result in a small star catalog for the swath and provide for faster and less ambiguous star identification/correlation thereby taking full advantage of the relatively large field-of-view (FOV) of the tracker.

The tracker slant angle ϕ_S relative to the ACS module, see Figure 2-5, has been assumed as $\phi_S = 30°$, and the angle between the lines of sight of the two trackers as 70°, i.e., $\pm$ 35° from the projection of the pitch axis onto the plane defined by the lines of sight of the trackers. Since both trackers make the same angle of 65.8° with the negative yaw axis, only one tracker is used.

Figure 5-2 shows a plot of all stars of 4th order magnitude and brighter and also shows the line traced out by the tracker boresight on the celestial sphere. Figure 5-3 removes all stars which do not fall into the swath traced out by the field-of-view of the tracker and marks those which are eclipsed by the earth. As can be seen, only four stars are left making correlation of tracker observations with the catalog very simple. Figure 5-3 also shows the assumed starting point of the scan according to which the sequence of stars in the star catalog is organized, and also shows the actual starting point. Thus, the first star encountered by the tracker is actually the star with Yale number 3487 but the tracker assumed at first that it was star number 1038. During the correlation process all stars are eventually correctly identified and a scan phasing angle of $\hat{\phi}_0 = 224.9$ degrees is determined. This is within 0.1 degree of the actual scan phasing angle of $\phi_0 = 225$ degrees between the initially assumed scan starting point and the actual starting point. The yaw gyro bias was estimated as 1.2 deg/hr and its actual value was 1.4 deg/hr.

It is seen that the accuracy of the correlation method is much better than determination if the orientation about the sun line using magnetic field measurements. However, as shall be shown in the following section, this improved accuracy is not required to initialize the stellar-inertial attitude reference system and the magnetic method will work just fine.

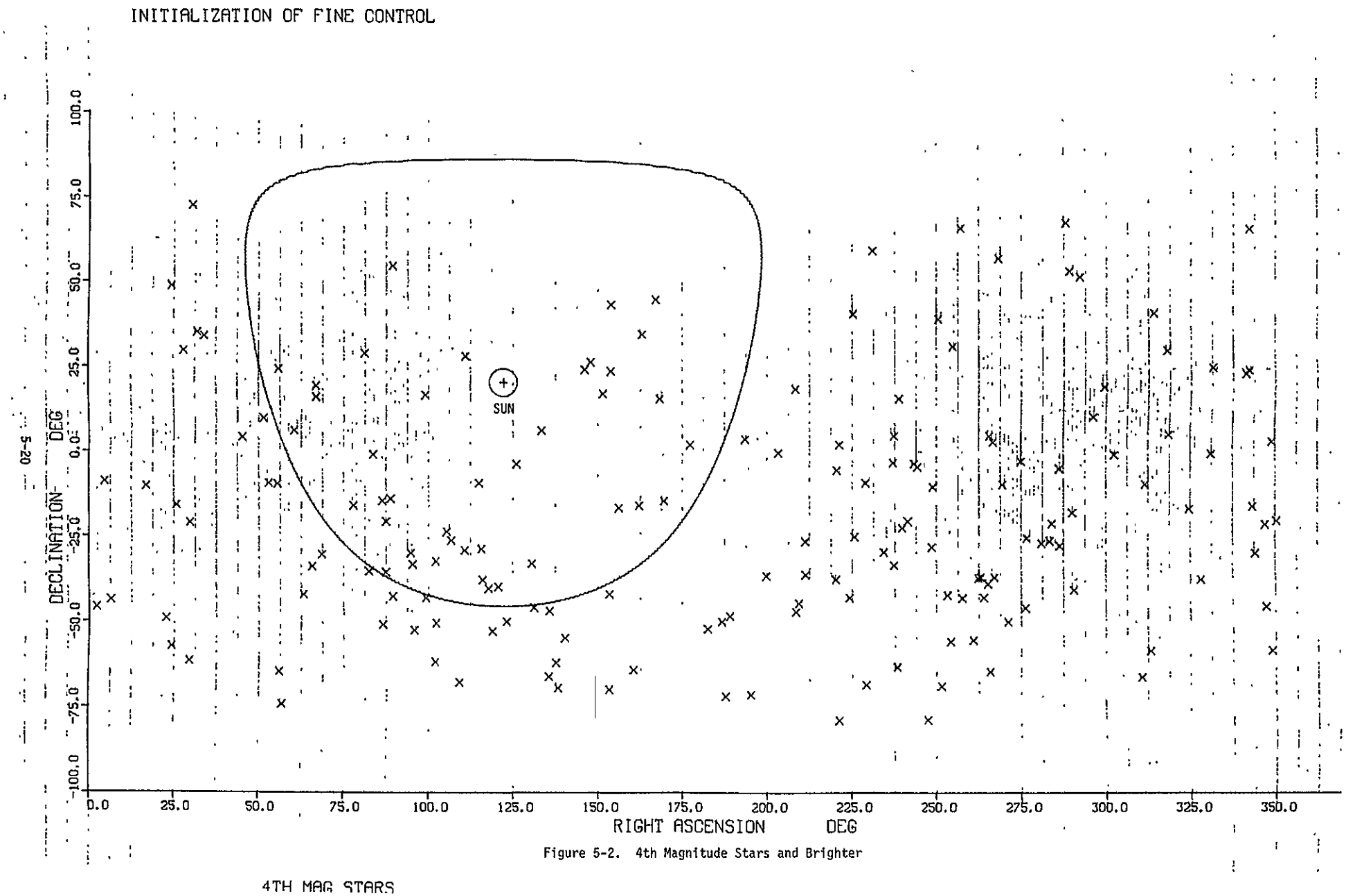

Figure 5-2. 4th Magnitude Stars and Brighter

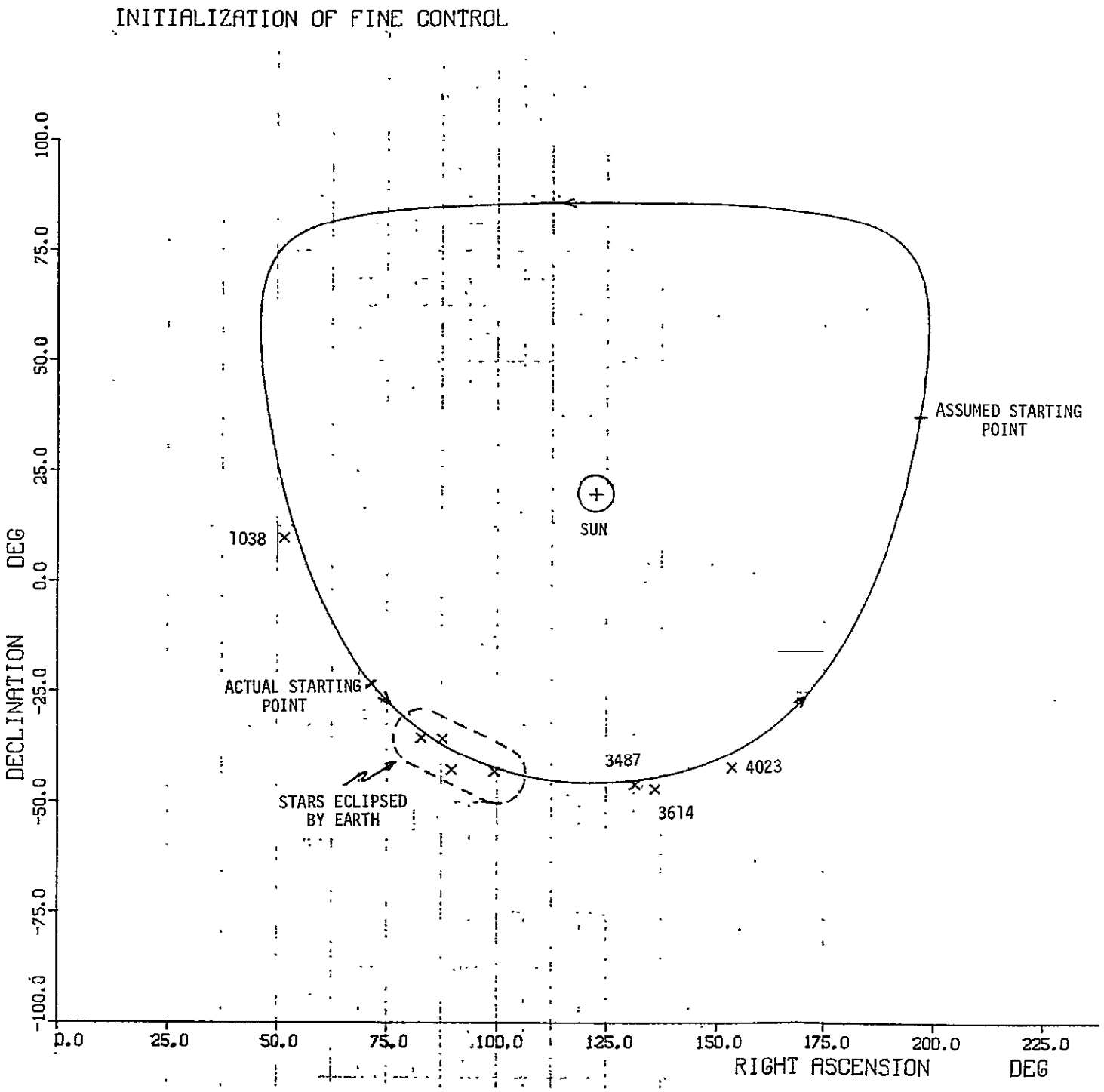

Figure 5-3. 4th Order Magnitude and Brighter Stars Seen by Tracker (8° x 8° FOV)

5.4 Convergence of On-Board Attitude Reference Filter

Attitude of the spacecraft about the sun line was estimated to within about 2° when magnetic field measurements were used, and to within about 0.1° when the star catalog correlation method was used. The magnetic method is simpler and faster and is preferred.

To demonstrate convergence of the on-board attitude reference filter with initial conditions corresponding to the nominal conditions at the end of magnetic-solar acquisition, an attitude estimation simulation was performed using an extended Kalman filter. For the spacecraft this is a part of the stellar acquisition mode. Since the negative yaw axis is sun pointing to within 0.1 degree, roll and pitch attitude uncertainties are a maximum of 0.1 degree at the initiation of fine stellar acquisition. These errors along with a nominal 2.0 degree estimation error about yaw resulting from the magnetic-solar attitude determination are used as initial conditions for the filter.

Actual stars that the star tracker would see are determined by selecting a time of year for the sun position. As in Section 5.3, the time around the 20th of July is again selected with the sun angle at 120° measured in the ecliptic plane. As described earlier, when the spacecraft is sun pointing the star trackers are inclined at an angle of 65.82° to the sun line. The star tracker sensitivity threshold has been set to $M_V = 5$ so that the tracker will sweep out a swath of fifth magnitude or brighter stars as shown in Figure 5.4 when the spacecraft is commanded to rotate about the sun line. The field-of-view is 8° x 8°, and stars eclipsed by the earth are not shown. Also several other stars satisfying the $M_V = 5$ or brighter criterion, are not shown and the stars indicated in Figure 5-4 represent the reference star catalog to be used in stellar convergence. The stars are listed in Table 5-1.

With a 2° attitude uncertainty about yaw at the end of solar-magnetic acquisition, it is doubtful whether the stars that happen to appear in the field-of-view of the trackers at that time are sufficiently separated from neighboring stars to yield an unambiguous star identification. To avoid

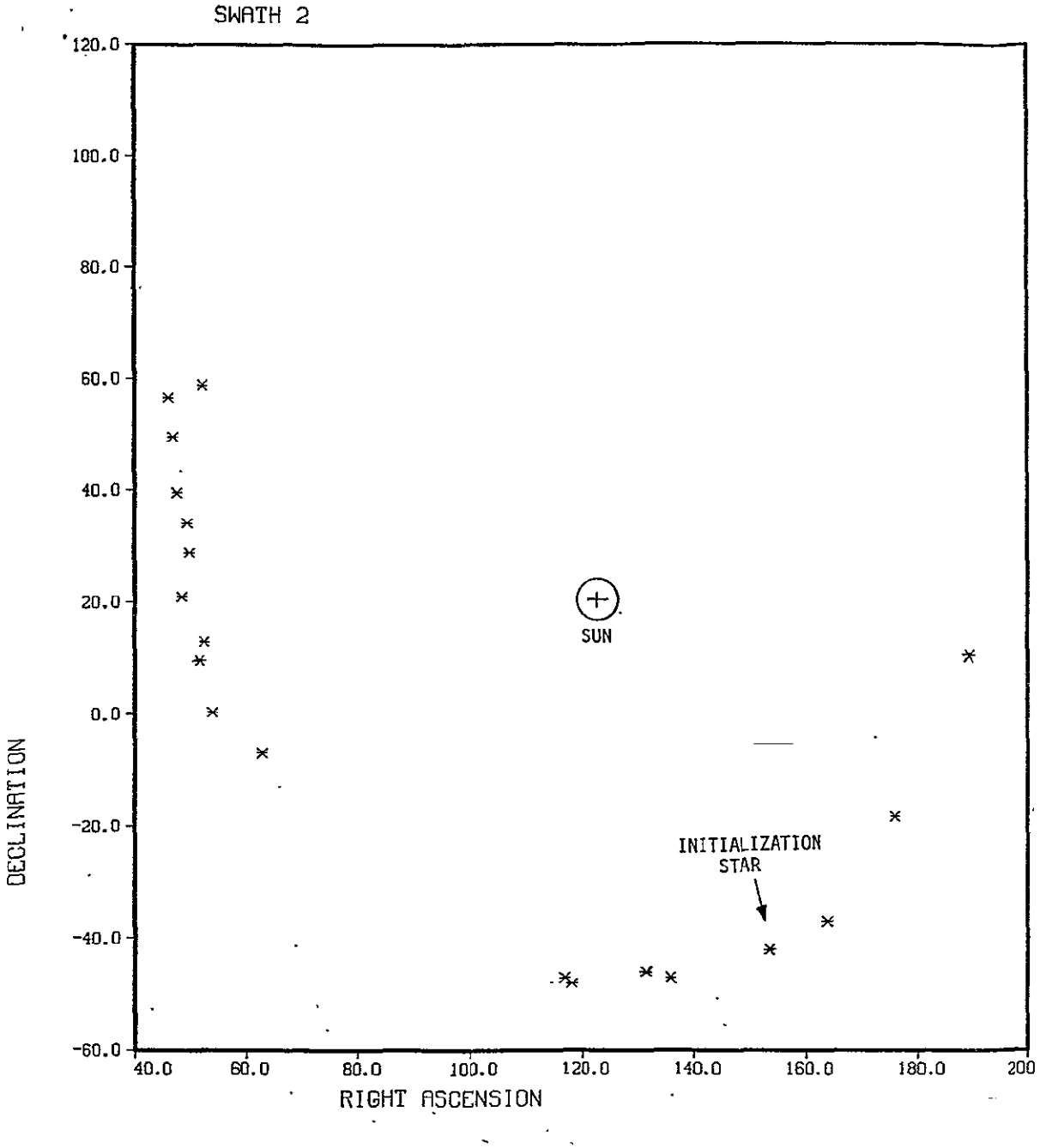

Figure 5-4. Reference Stars, M_v = +5 and Brighter

Table 5-1. Reference Star Catalog, Sun Pointing Mode

	Scan Angle in Swath Plane	Declin. Rel. Swath Plane	Yale Catalog Number	No Multiple No Variable	Right Ascension	Declination	Spectral Class	Galactic Longitude	Galactic Latitude	Visual Brightness, M_V		
1	-2.6077	24.043	4828	00	190.2175	10.343	A0	294.8	73.0	4.88		
2	23.0780	21.641	4983	00	197.7333	27.983	G0	43.2	85.4	4.26		
3	36.2469	23.332	4997	00	198.2025	40.257	K0	104.9	76.2	4.92		
4	69.5707	26.922	4795	00	188.4717	70.127	K2	125.0	47.0	4.94		ECLIPSED
5	86.4601	28.145	3751	00	143.5592	81.407	K3	130.7	32.7	4.28		
6	93.3292	27.435	2350	00	100.0692	82.133	A2	131.8	26.6	4.09	R	
7	109.0924	26.971	1148	00	57.0633	71.257	A3	136.3	13.3	4.65		
8	123.2687	27.416	1040	00	52.0758	58.813	A0	142.2	2.1	4.56		
9	125.8670	24.293	918	00	46.0075	56.637	K0	140.6	-1.5	4.75		
10	133.6278	24.658	937	00	46.9058	49.540	G0	144.6	-7.4	4.05		
11	144.6668	24.250	947	00	47.4983	39.540	K0	150.2	-15.7	4.61		
12	150.7687	25.026	991	00	49.3667	34.143	K2	154.6	-19.5	4.82		
13	156.4468	24.537	999	00	49.7808	28.977	K4	158.1	-23.5	4.47		
14	164.6785	21.632	972	00	48.4375	20.960	A0	162.4	-30.6	4.90		
15	174.2046	23.179	1066	00	52.4408	12.880	K0	172.1	-34.3	4.11		
16	177.2319	21.358	1038	00	51.5208	9.663	B8	174.0	-37.3	3.72		
17	187.5103	20.497	1101	00	53.9617	.337	F8	185.1	-41.7	4.28		
18	198.5253	25.597	1298	00	62.7225	-6.887	F2	199.3	-38.4	4.05		
19	235.7477	22.880	1862	00	82.6267	-35.497	K1	239.9	-30.9	3.86		
20	239.3636	25.150	2040	00	87.5650	-35.773	K2	241.4	-27.1	3.11		
21	241.0633	24.581	2067	00	88.6992	-37.120	G8	243.1	-26.5	4.96		ECLIPSED
22	245.1220	20.234	2120	00	89.6342	-42.817	K0	249.5	-27.2	3.95		
23	252.0069	23.242	2451	00	99.2883	-43.167	B8	251.9	-20.5	3.17		
24	259.5687	21.870	2740	00	107.9592	-46.733	F0	257.7	-16.0	4.48		
25	266.1247	22.620	3046	00	116.9383	-47.033	K0	260.7	-10.7	4.70		
26	267.1163	21.662	3090	00	118.1783	-48.063	B1	262.1	-10.4	4.23		
27	276.9083	23.325	3487	00	131.3350	-45.977	A0	265.4	-1.9	3.90		
28	279.9879	21.677	3614	00	135.8650	-47.020	K2	268.2	-.1	3.74		
29	294.4717	21.397	4023	00	153.4733	-42.033	A2	274.3	11.9	3.84	←	INITIALIZATION STAR
30	304.6007	20.565	4273	00	163.9458	-37.027	G5	278.9	20.3	4.59		
31	327.5218	24.782	4514	00	175.9383	-18.240	G8	281.5	41.7	4.72		

false identification, a bright star is selected that is sufficiently separated from neighboring stars, even if dimmer. The spacecraft is commanded to rotate about the sun line, look for this star, and use it to initialize the attitude filter. This assures correct identification of the star used in the first attitude update. This first update significantly improves attitude knowledge and identifications of subsequent stars of 5th order magnitude and brighter will pose no problems.

The required rotation about the sun line is the main reason why it was recommended that L-D should align the yaw axis with the sun line and not the (canted) solar array normal. Rotation about a non-principal axis that is not a spacecraft control axis and to which the star tracker lines of sight are not symmetric, appears undesirable.

The bright and isolated star selected here for initializing the filter is indicated by an arrow in Figure 5-4. It is star number 29 in Table 5-1 and it has the Yale Number 4023. In the filter simulation, the forward looking star tracker encounters this star almost immediately and convergence is rapid as shown in Figure 5-5. An enlarged plot of the same data is shown in Figure 5-6 where it is seen that the errors in all axes have converged to approximately 5 arc-sec (1σ) at the end of half a revolution (0.5 hr) about the sun line. Gyro biases were calibrated to within 0.0013 deg/hr (1σ). Both trackers were read in this simulation every 30 seconds. If both trackers are read only every 300 seconds, the results of Figures 5-7 and 5-8 are obtained where convergence to about 10 arc-sec (1σ) is achieved with gyro bias calibration being about the same, i.e., 0.0013 deg/hr (1σ). Both performances satisfy the requirements for successful stellar acquisition and the spacecraft can be considered in inertial hold mode.

With a precision stellar inertial attitude reference successfully established, spacecraft ephemeris data is used to obtain an earth pointing attitude reference. This may be done as follows. Let A_{br} denote the direction cosine matrix describing the spacecraft's attitude relative to the

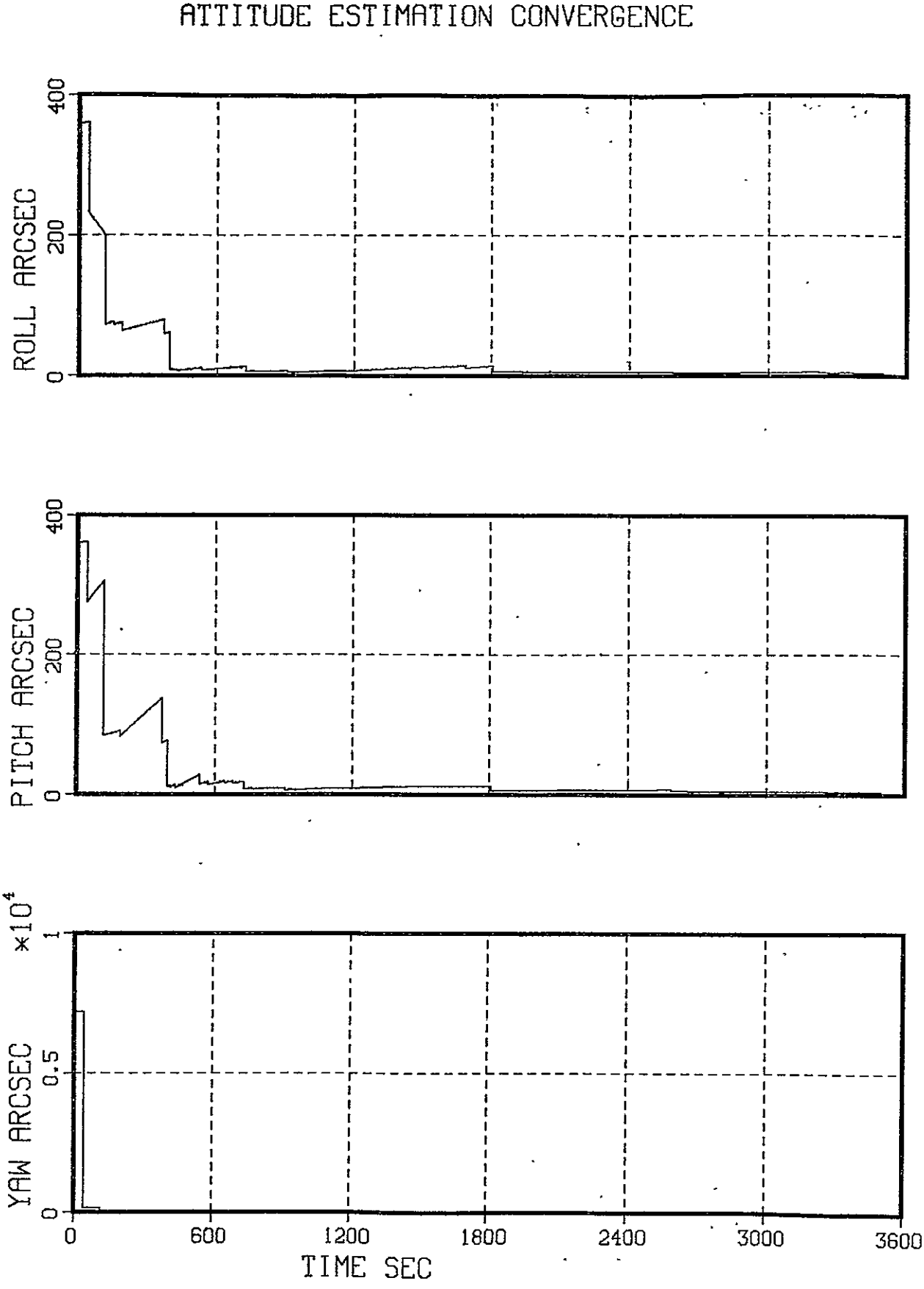

Figure 5-5. Attitude Reference Filter Convergence After Initialization from Large Attitude Uncertainties (30 Second Update Interval)

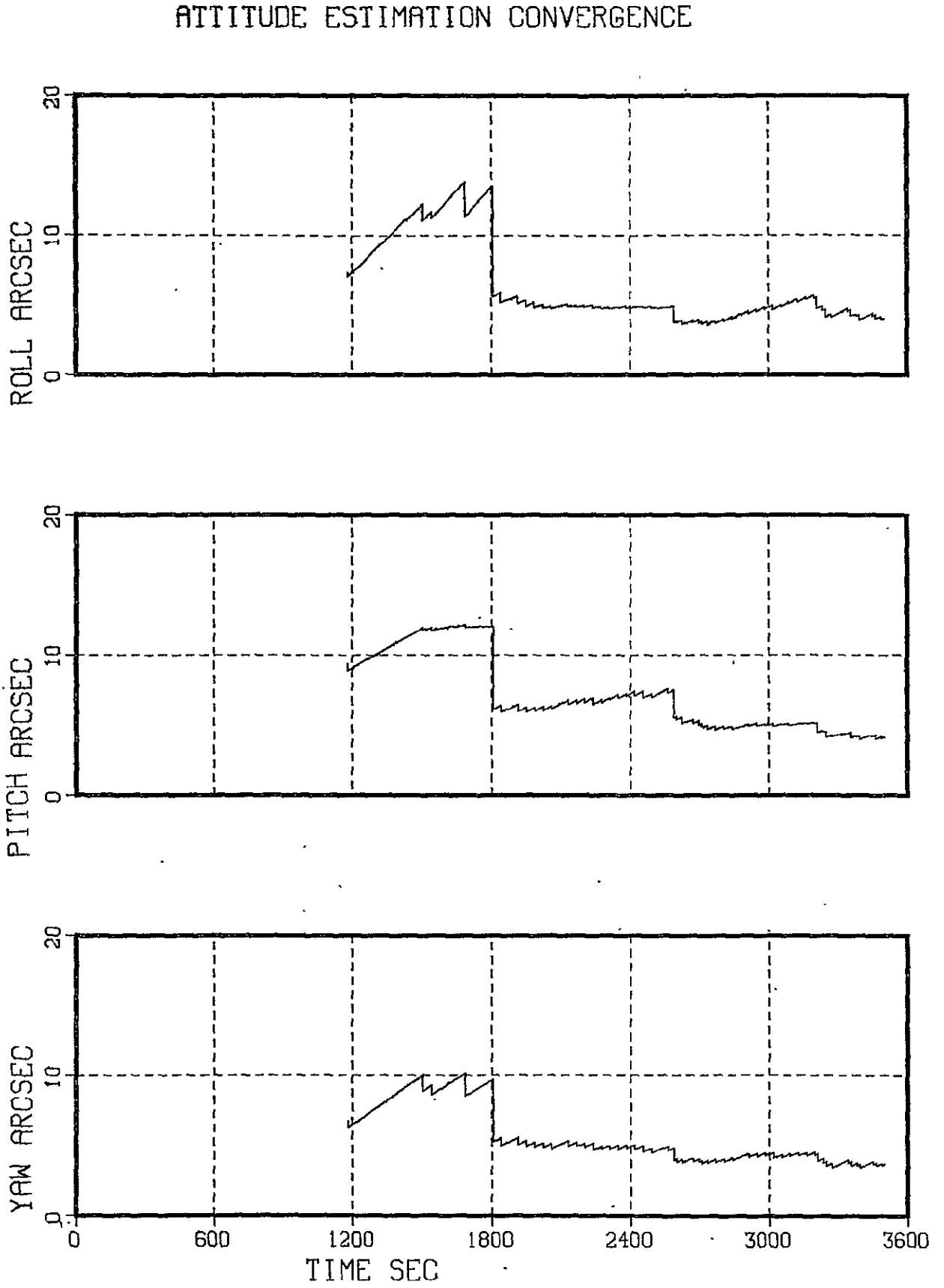

Figure 5-6. Attitude Reference Filter Convergence After Initialization (Expanded Scale Figure 5-5)

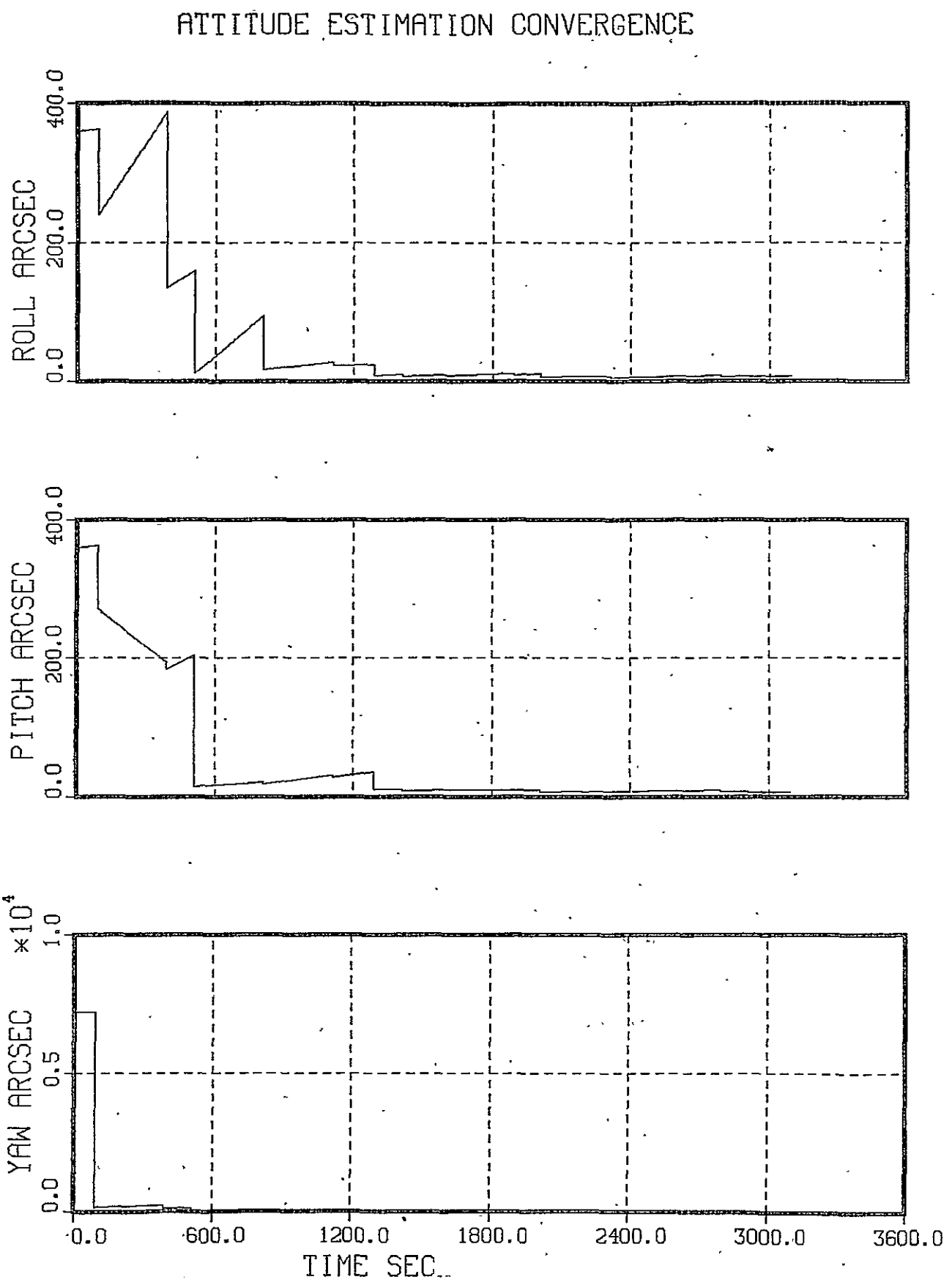

Figure 5-7. Attitude Reference Filter Convergence After Initialization from Large Attitude Uncertainties (300 Second Update Interval)

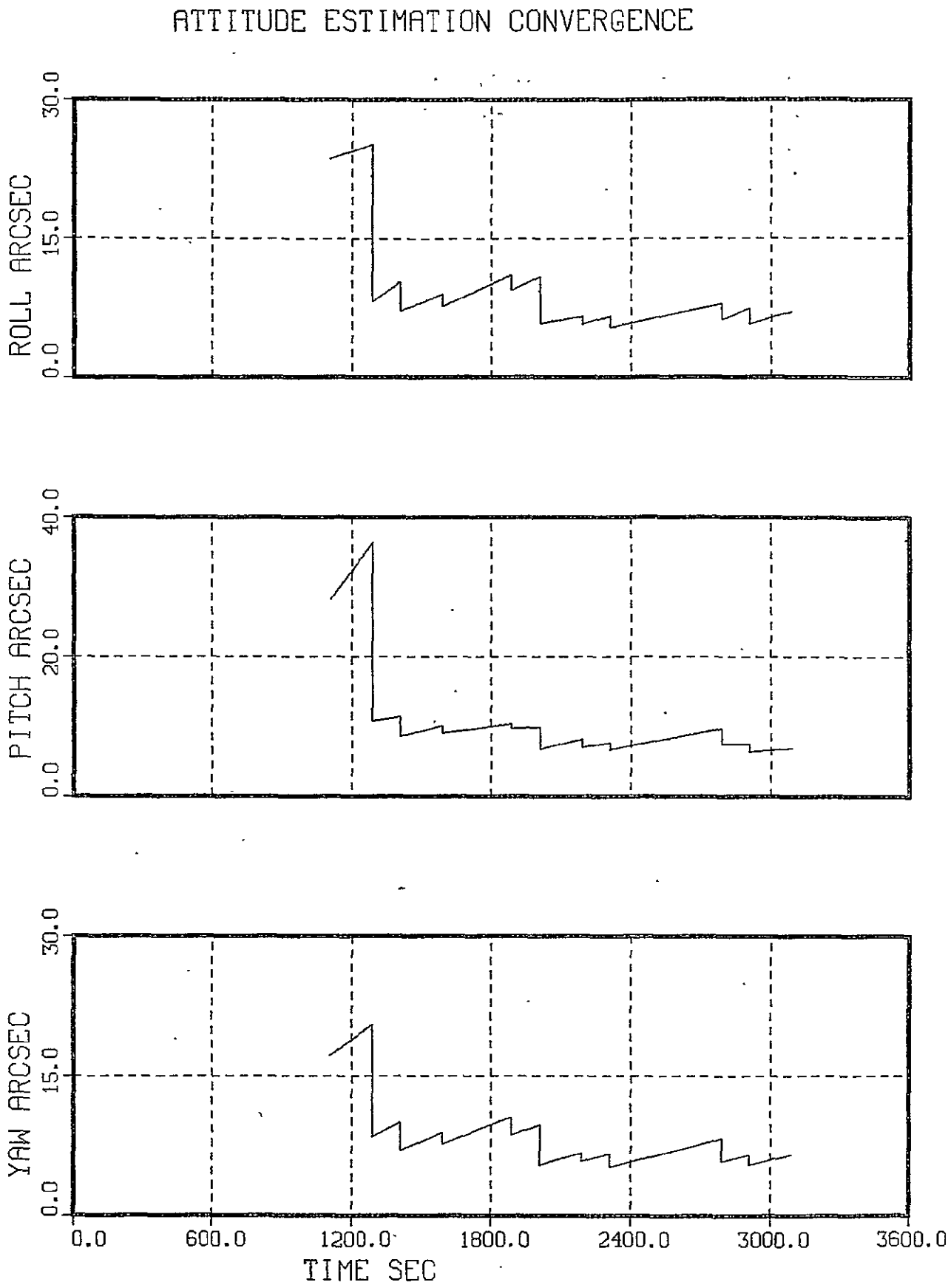

Figure 5-8. Attitude Reference Filter Convergence After Initialization (Expanded Scale Figure 5-7)

the earth pointing orbital reference frame $\{\hat{x}_r, \hat{y}_r, \hat{z}_r\}$. Then A_{br} is the desired earth pointing attitude reference. The stellar inertial attitude reference system provides the spacecraft's attitude relative to ECI given by the direction cosine matrix A_{bI}; the ephemeris provides the attitude of the earth pointing , orbital reference frame relative to ECI by the direction cosine matrix A_{rI}. Hence, the desired earth oriented attitude reference A_{br} is given by

$$A_{br} = A_{bI} A_{rI}^{T}$$

The above could have also been done in terms of quaternions and quaternion algebra, but frequently direction cosine matrices are required in any event and it is advantageous to perform the computations as indicated. Figure 5-9 shows a functional block diagram of the on-board attitude reference system.

With A_{br} established, the spacecraft is commanded to slew away from the sun and assume its earth pointing orientation. After attitude settling, the spacecraft is in the normal on-orbit fine pointing mode and ready to turn on the payload sensors and take data. A_{br} represents then a very-small-angle rotation matrix, and single axis, i.e., roll, pitch and yaw, control errors can be extracted from the appropriate off-diagonal terms of A_{br}.

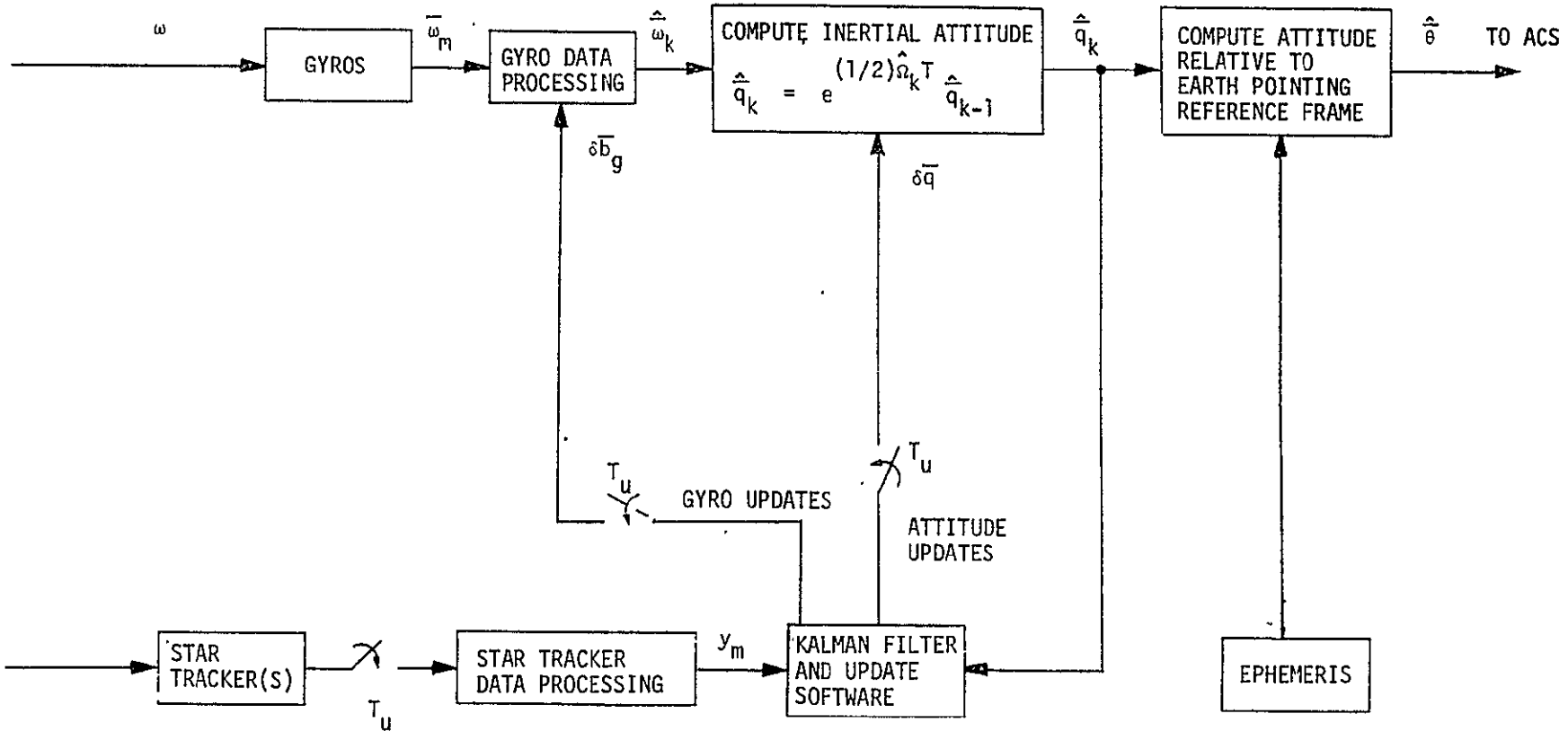

Figure 5-9. Functional Block Diagram Stellar Inertial ARS

6.0 NORMAL ON-ORBIT ATTITUDE CONTROL

The objective of this section is to present a preliminary design of the normal on-orbit attitude control system for L-D and to assess achievable performance. Since pointing stability is important to the LANDSAT-D mission and has been specified to a stringent $\pm$ 10.5 μrad (1σ) over 20 minutes, the effects of (internally) moving parts and appendages, as well as the effects of structural flexibility in the TDRS antenna mast and the solar array, must be included in the performance assessment. Section 6.1 will assess the effects of internally moving parts and appendages in a rigid body sense and determine whether any motion compensation is required, either by modification in the on-orbit control law, or by adding momentum compensation devices. In Section 6.2 the effects of a flexible Ku-band antenna mast are studied and criteria for selecting the stiffness of the mast are presented. In Section 6.3 the effects of a flexible solar array are studied. Section 6.4 addresses the normal on-orbit ACS design configuration, and Section 6.5 assess predicted system performance based on analysis and simulation.

6.1 Effects of Internal Motion

Reaction to the inertial motions of internal parts or components appended to the spacecraft causes rotation of the spacecraft. This section investigates the extent of the L-D spacecraft reaction to the motions of the Ku-band antenna, the solar array, the Thematic Mapper and Multi-Spectral Scanner scanning devices, and reaction wheel dynamic mass imbalance. Each of these devices will be considered in a separate subsection. The results are summarized in subsection 6.1.6. It will also be ascertained whether or not a standard stepper drive is acceptable for driving the solar array and whether or not any torque preemphasis or momentum compensation is needed for the disturbances studied. The L-D spacecraft performance specifications requires that the ACS control spacecraft pointing with a jitter stability of $\pm$ 10.5 μrad ($\pm$ 2.16 arc-seconds) 1σ, or better over a 20 minute period. The spacecraft reaction to the motions of the components listed above must, therefore, be significantly less than $\pm$ 2.16 arc-seconds, 1σ, since part of the error budget must be reserved for the attitude reference system.

6.1.1 General Two-Body Problem

The study of the spacecraft reaction to the motion of an appended component involves an analysis of the two-body problem in a plane as sketched in Figure 6-1. The dynamic equations can be shown to be

$$T_c = I_{11}\,\ddot{\theta} + I_{12}\,\ddot{\alpha} - \frac{m_1\,m_2}{m_1 + m_2}\,\ell_1\,\ell_2\,(2\dot{\theta} + \dot{\alpha})\,\dot{\alpha}\,\sin\alpha \qquad (6.1\text{-}1)$$

and

$$T_m = I_{21}\,\ddot{\theta} + I_{22}\,\ddot{\alpha} + \frac{m_1\,m_2}{m_1 + m_2}\,\ell_1\,\ell_2\,\sin\alpha\,\dot{\theta}^2, \qquad (6.1\text{-}2)$$

where T_c is the ACS control torque applied to the spacecraft, T_m is the hinge torque applied against the spacecraft and the appended component, θ is the spacecraft attitude error about the axis perpendicular to the paper, and the inertia parameters are given by

$$I_{11} = I_1 + I_2 + \frac{m_1\,m_2}{m_1 + m_2}\,(\ell_1^2 + \ell_2^2 + 2\ell_1\,\ell_2\,\cos\alpha) \qquad (6.1\text{-}3)$$

$$I_{12} = I_{21} = I_2 + \frac{m_1\,m_2}{m_1 + m_2}\,(\ell_2^2 + \ell_1\,\ell_2\,\cos\alpha) \qquad (6.1\text{-}4)$$

and

$$I_{22} = I_2 + \frac{m_1\,m_2}{m_1 + m_2}\,\ell_2^2 \qquad (6.1\text{-}5)$$

The nonlinear terms will be neglected to simplify the analysis -- this is acceptable because either α or the product $\ell_1\,\ell_2$ is small in the cases considered.

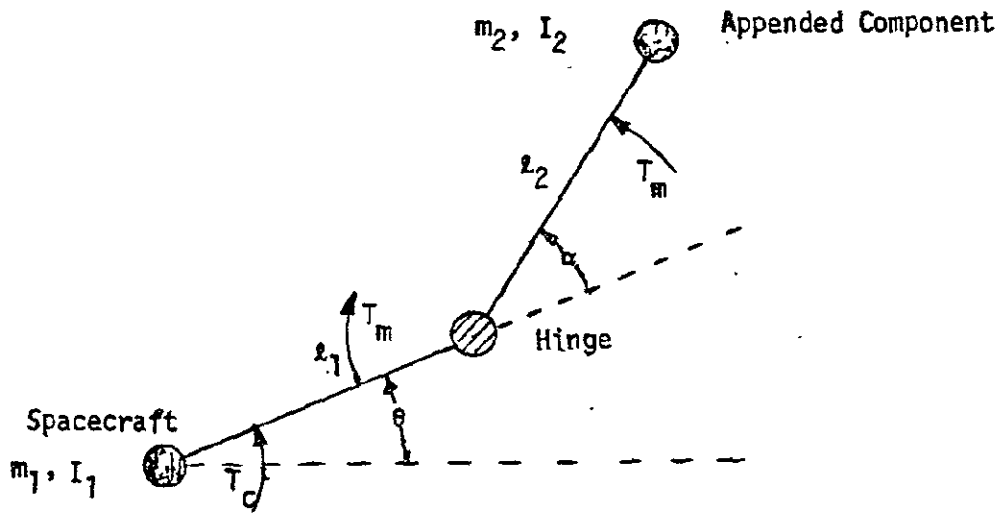

Figure 6-1. Schematic of the Two-Body Problem

The effect of the ACS can be ignored by letting $T_c = 0$; this results in

$$\ddot{\theta} = - \frac{I_{12}}{I_{11}} \ddot{\alpha} \tag{6.1-6}$$

which can be integrated twice -- if $\frac{I_{12}}{I_{11}}$ is constant -- to obtain

$$\theta = - \frac{I_{12}}{I_{11}} \alpha \tag{6.1-7}$$

Note that this approximation is valid only when the motion is fast relative to the ACS bandwidth. In general, it is desirable to include the effects of the ACS: from Equations (6.1-1) and (6.1-2) $\ddot{\theta}$ is found to be given by

$$\ddot{\theta} = \frac{I_{22}\, T_c - I_{12}\, T_m}{A_o} \tag{6.1-8}$$

where

$$A_o = I_{11}\, I_{22} - I_{12}^2 \tag{6.1-9}$$

This leads to the simplified block diagram in Figure 6-2 where the ACS controller is assumed to be a second-order system with $\xi = 0.5$ and $\omega_n = 0.5$ rad/second.

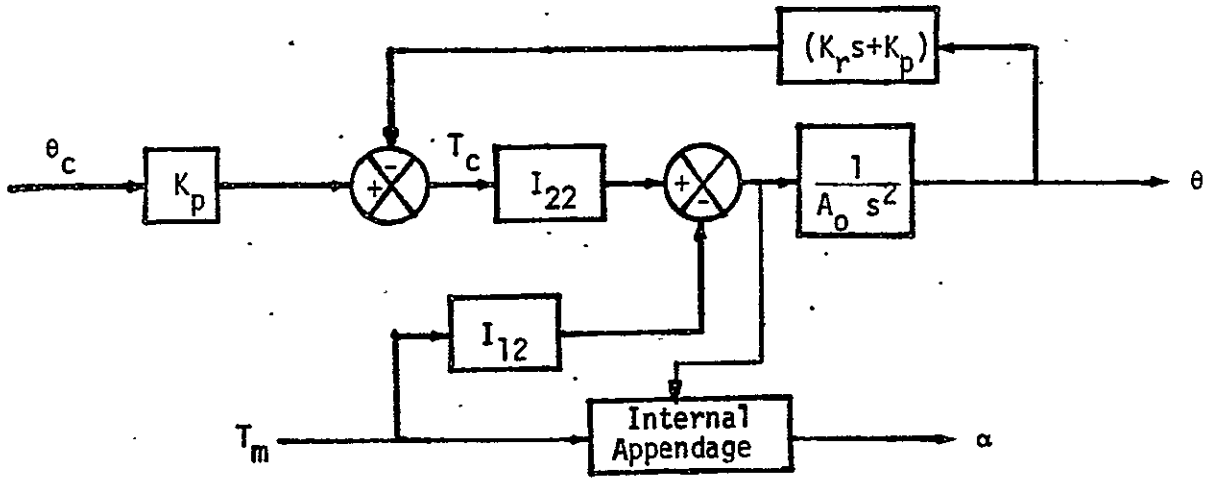

Figure 6-2. Simplified Controller Block Diagram

The spacecraft response to the torque T_m is given by

$$\frac{\theta}{T_m}(s) = \frac{I_{12}/A_o}{s^2 + \frac{I_{22}\,k_r}{A_o}s + \frac{I_{22}\,k_p}{A_o}} = \frac{I_{12}/A_o}{s^2 + 0.5s + 0.25} \cdot \qquad (6.1\text{-}10)$$

This equation along with Equations (6.1-3) - (6.1-5) and (6.1-9) is used to determine the spacecraft reaction $\theta(t)$, to the internal disturbance torques for each case considered in this memo. The spacecraft parameters are given in Table 6-1.

Table 6-1. Spacecraft Parameters

Parameter	Symbol	Value	
Mass	m_1	1498.26 kg	102.48 slugs
Roll Inertia	I_{xx}	2037 kg-m^2	1500 slug ft^2
Pitch Inertia	I_{yy}	2676 kg-m^2	1970 slug ft^2
Yaw Inertia	I_{zz}	2377 kg-m^2	1750 slug ft^2

6.1.2 Solar Array Motion

As recommended in Section 3.5, the solar array is a FRUSA array 8.08 m (26.52 feet) long and 1.93 m (6.33 feet) wide canted 37.5 degrees to the spacecraft $\hat{y}_b$-axis and rotating about that spacecraft axis. The inertia matrix is calculated assuming the array has negligible thickness and its mass is uniformly distributed. For the principal axes -- the primed axes in Figure 6-3 -- the inertia matrix is

$$I' = \begin{bmatrix} 7.04 & 0 & 0 \\ 0 & 123.37 & 0 \\ 0 & 0 & 130.41 \end{bmatrix} \text{ kg-m}^2 \qquad (6.1\text{-}11)$$

and for the unprimed axes -- where axis 1 is aligned with the spacecraft pitch axis, the axis of rotation --

$$I = \begin{bmatrix} 52.75 & 0 & -59.58 \\ 0 & 123.37 & 0 \\ -59.58 & 0 & 84.69 \end{bmatrix} \qquad (6.1\text{-}12)$$

The parameters pertaining to solar array motion about the spacecraft pitch axis are summarized in Table 6-2.

A standard stepper motor which is available for this application steps at the rate of 1.8 degrees per step, and a 100:1 harmonic drive gear train reduces this to 0.018 degree per step at the array. Since the array must rotate at the orbit rate of 220.31 degrees/hour, it must step once every 294.1 msecond, where each step can be accomplished by a torque doublet as shown in Figure 6-4. Since the sun is nearly stationary, the solar array

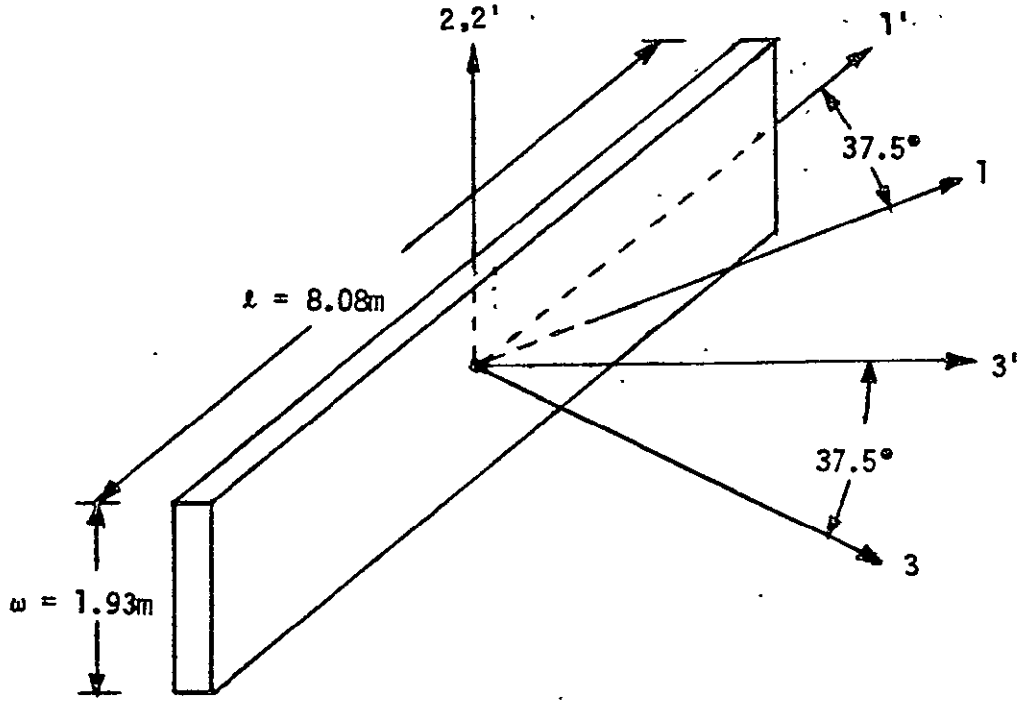

Figure 6-3. Sketch of the Solar Array

Table 6-2. Parameters for the Solar Array Analysis

Parameter	Value	
ℓ_1	0	0
ℓ_2	2.46 m	8.07 ft
m_1	1498 kg	102.48 slugs
m_2	22.66 kg	1.55 slugs
I_1	2676 kg-m^2	1970 slug ft^2
I_2	52.75 kg-m^2	38.84 slug ft^2
I_{11}	2863.32 kg-m^2	2108 slug ft^2
$I_{12} = I_{21}$	187.80 kg-m^2	138.28 slug ft^2
I_{22}	187.80 kg-m^2	138.28 slug ft^2

would be inertially fixed if it were driven to follow the sun continuously. But, each step is completed in such a short period of time that the spacecraft is essentially stationary and the effect is the same as moving the array inertially. Thus, using the assumed 30 mseconds torque double shown in Figure 6-4, the required array torque is T_o = 73.65 N-m (54.23 foot-pounds) -- 0.5423 foot-pounds of motor torque -- and Equation (6.1-10) reduces to

$$\theta(s) = \frac{2.737 \times 10^{-4} T_m(s)}{s^2 + 0.5S + 0.25} \qquad (6.1\text{-}13)$$

with $T_m(t)$ as shown in Figure 6-4, the steady-state spacecraft response is shown in Figure 6-5. The response of $\pm$ 0.60 arc-second is acceptable.

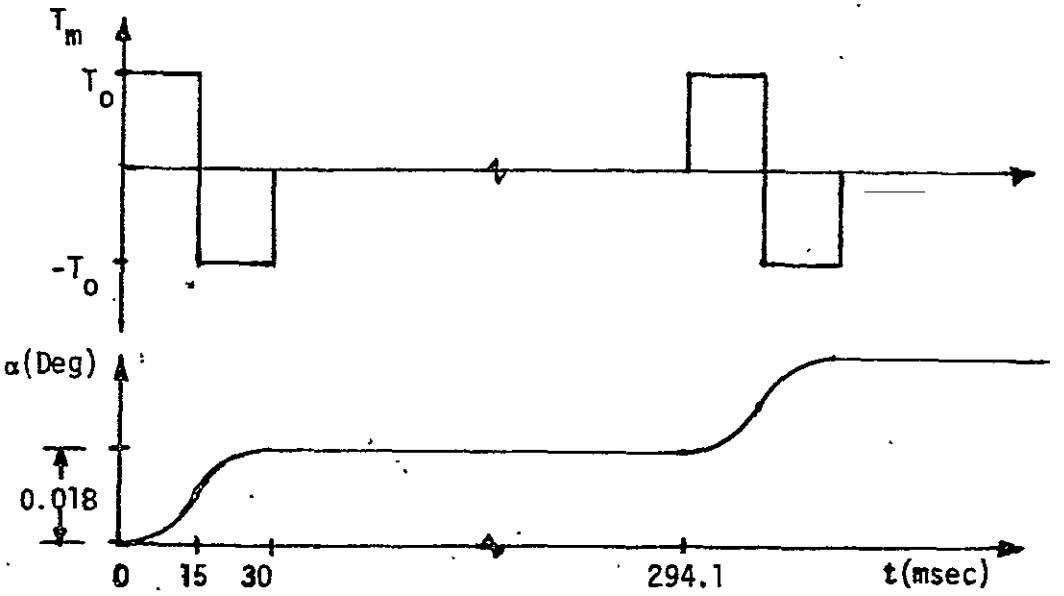

Figure 6-4. Solar Array Stepping

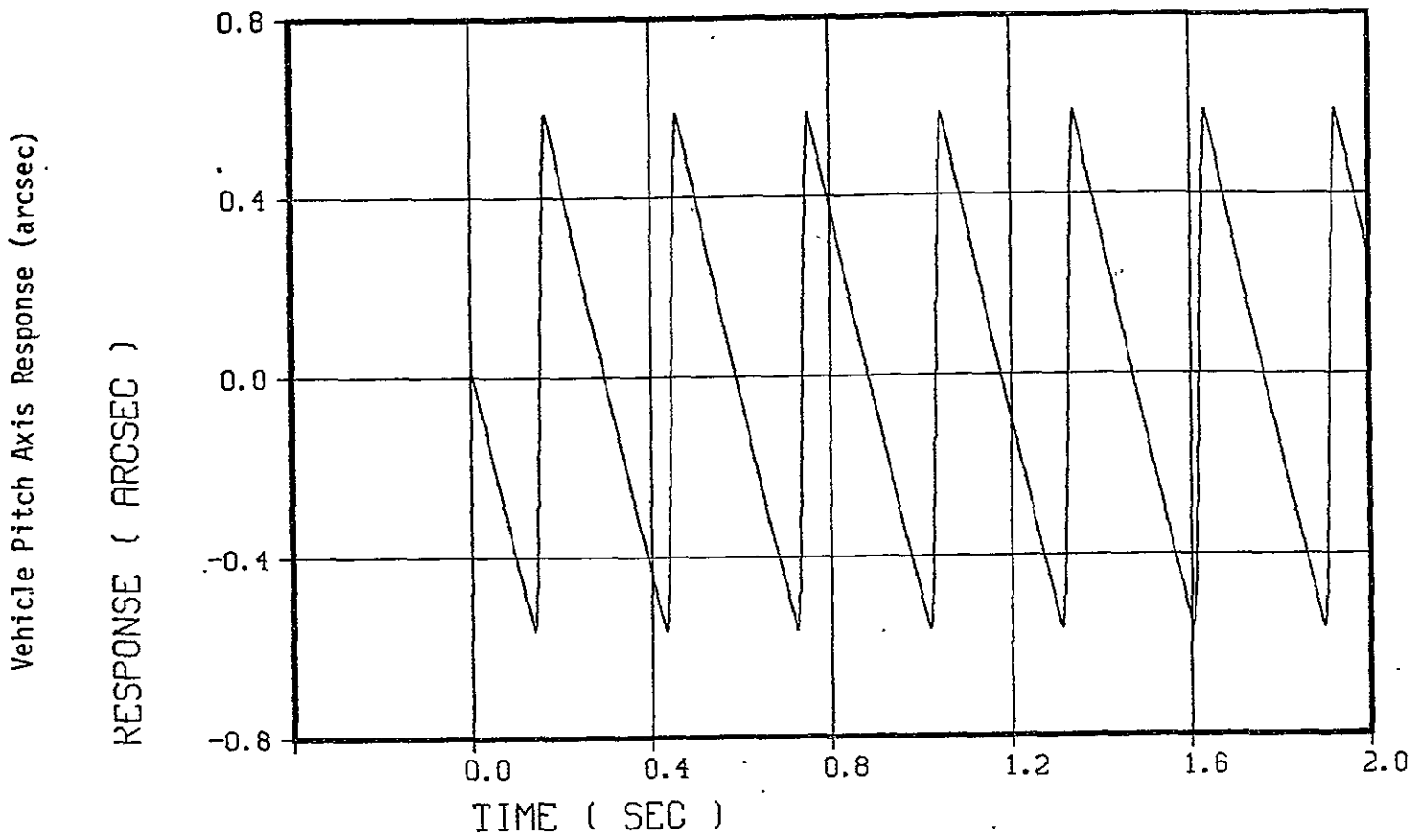

Figure 6-5. Steady-State Spacecraft Response to Solar Array Stepping

Because the solar array is canted from its axis of rotation, the torque applied to it is coupled into the other axes. The worst case occurs when the array is as shown in Figure 6-6 and the spacecraft is caused to rotate about its roll axis. The 73.65 N-m torque applied to the array produces the approximate force F_a = 16.17 N (3.65 pounds) at the array; and the reaction force $F_b = F_a$ applied a torque to the spacecraft which is given by T_{sc} = 14.87 N-m (10.95 foot-pounds). Thus the spacecraft roll reaction will have the same time history as shown in Figure 6-5 but with a time-varying amplitude that reaches a maximum of $\pm$ 0.13 arc-second. As the array rotates to other positions, the cross coupled torque is split between the yaw axis and the roll axis. When the coupling is all into the yaw axis, the maximum spacecraft reaction is $\pm$ 0.11 arc-second. This reaction is also acceptable.

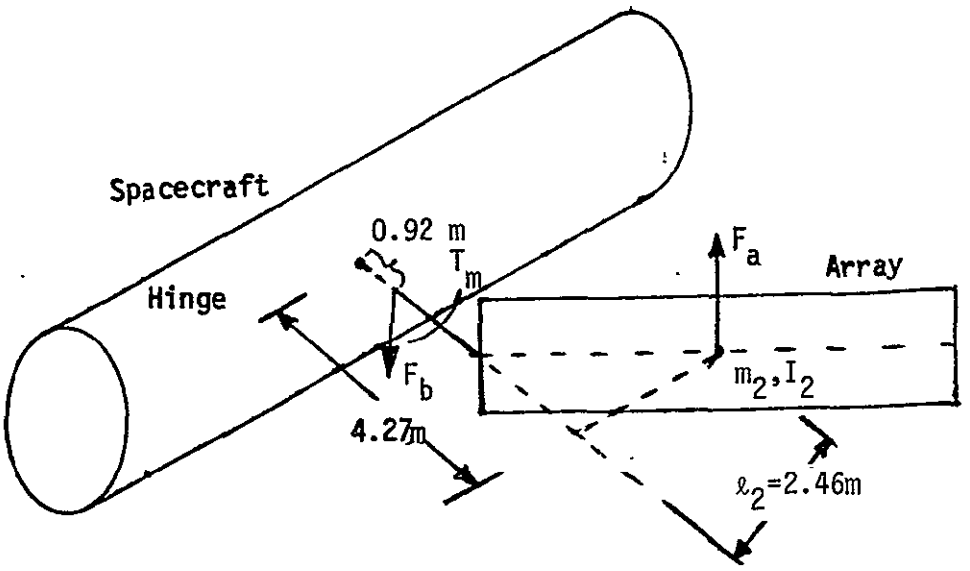

$$F_b = \frac{m_2 \ell_2 T_m}{I_2 + m_2 \ell_2^2}$$

Figure 6-6. Solar Array Torque Coupling into Spacecraft Roll Axis

One further requirement is that the solar array must occasionally be slewed through 45 degrees to avoid interference with the Ku-band antenna. Using the stepping motor arrangement described above, this would probably be accomplished by stepping more frequently: the slew rate is achieved by stepping every 30 mseconds -- provided 30 mseconds is required to complete the step -- so the 45 degree slew can be accomplished in as little as 75 seconds. The lower limit on the achievable slew time is found -- using the 250 step/second maximum response speed of the motor -- to be 10 seconds. In practice, this time is increased by the harmonic drive, etc. The 75 seconds for slewing the array corresponds to 0.34 degree of orbit angle. Because this slewing will be done over a dark earth, the spacecraft reaction is not important.

6.1.3 Ku-Band Antenna Motions

Antenna motions which cause spacecraft reactions are basically from two sources: the antenna slewing from one TDRS target to the other, and the antenna tracking a particular TDRS target. The mass properties of the antenna are as follows: the mass is 31.14 kg (2.13 slugs); the moments of inertia are 2.63 kg-m^2 (1.94 slug $feet^2$) about the boresight, 4.98 kg-m^2 (3.67 slug $feet^2$) about the mast axis, and 4.39 kg-m^2 (3.23 slug $feet^2$) about the remaining orthogonal ax is, and the c.m. is 0.37 m (1.21 feet) from the gimbal center along the boresight. Cross products of inertia are ignored. The antenna is shown in Figure 6-7.

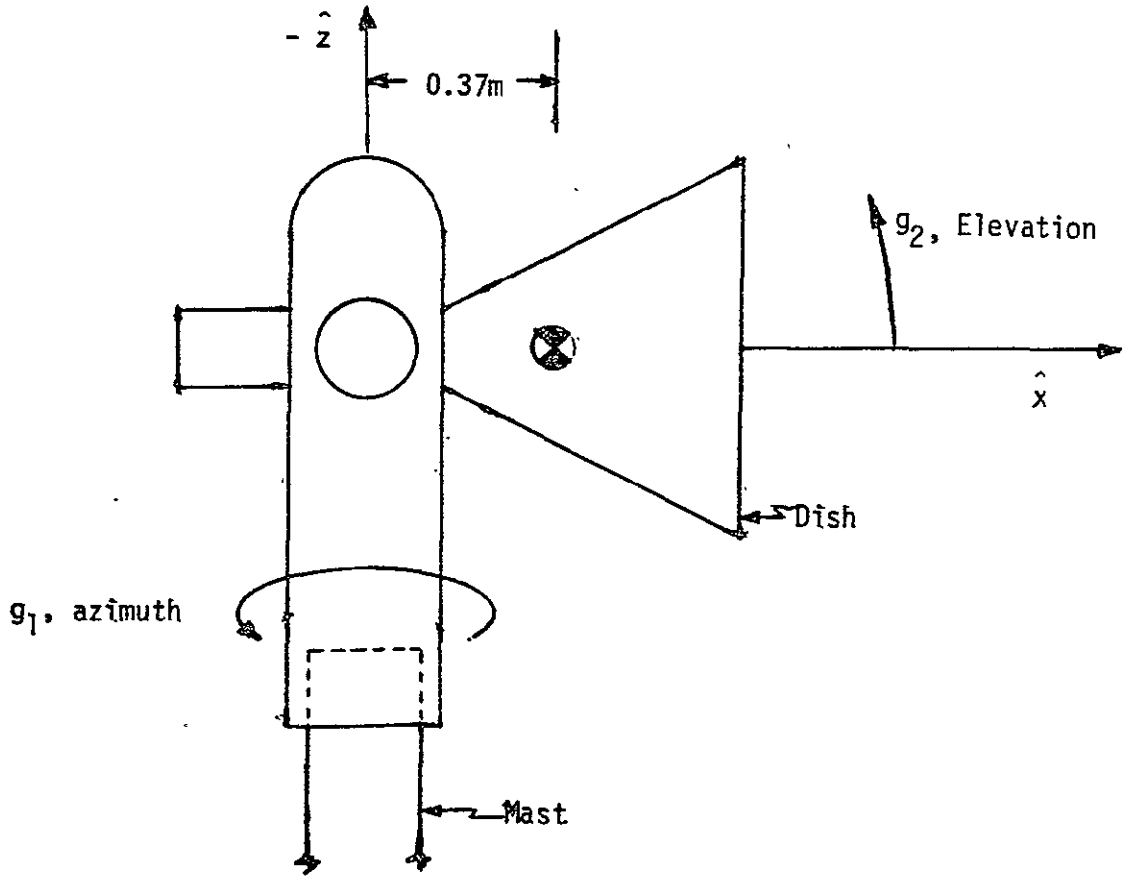

Figure 6-7. Ku-Band Antenna in the Null Position

If the antenna is assumed to slew 130 degrees about the azimuth axis while maintaining a 0 degree elevation, the parameters are as given in Table 6-3. Since the antenna is slewed over earth night, it is first assumed that 30 minutes is available. Thus the movement can be accomplished by applying a 2.56×10^{-5} N-m (1.885×10^{-5} foot-pounds) torque for 15 minutes followed by a -2.56×10^{-5} N-m (1.885×10^{-5} foot-pounds) torque for 15 minutes. This results in a peak spacecraft response of 0.025 arc-second; the first part of the response is shown in Figure 6-8. If instead, 2.5 minute torque pulses are applied, the torque level must be 9.22×10^{-4} N-m (6.79×10^{-4} foot-pounds) and the peak spacecraft reaction would be 0.90 arc-second, which is an acceptable solution. In fact, the time could be shortened even further, because the 2.16 arc-second pointing accuracy is not really necessary over the dark earth. Note in Figure 6-8 that the spacecraft has a steady-state "hang-off" error when the antenna is receiving the constant torque. This error could be reduced or removed by proper controller design, but the error is so small that such measures were not considered necessary.

Table 6-3. Antenna Slewing Parameters

Parameter	Value	
ℓ_1	0.91 m	3 ft
ℓ_2	0.37 m	1.21 ft
m_1	1498 kg	102.48 slugs
m_2	31.14 kg	2.13 slugs
I_1	2377 kg-m^2	1750 slug ft^2
I_2	4.98 kg-m^2	3.67 slug ft^2
I_{11}	2432 kg-m^2	1790 slug ft^2
$I_{12} = I_{21}$	19.42 kg-m^2	14.30 slug ft^2
I_{22}	9.14 kg-m^2	6.73 slug ft^2

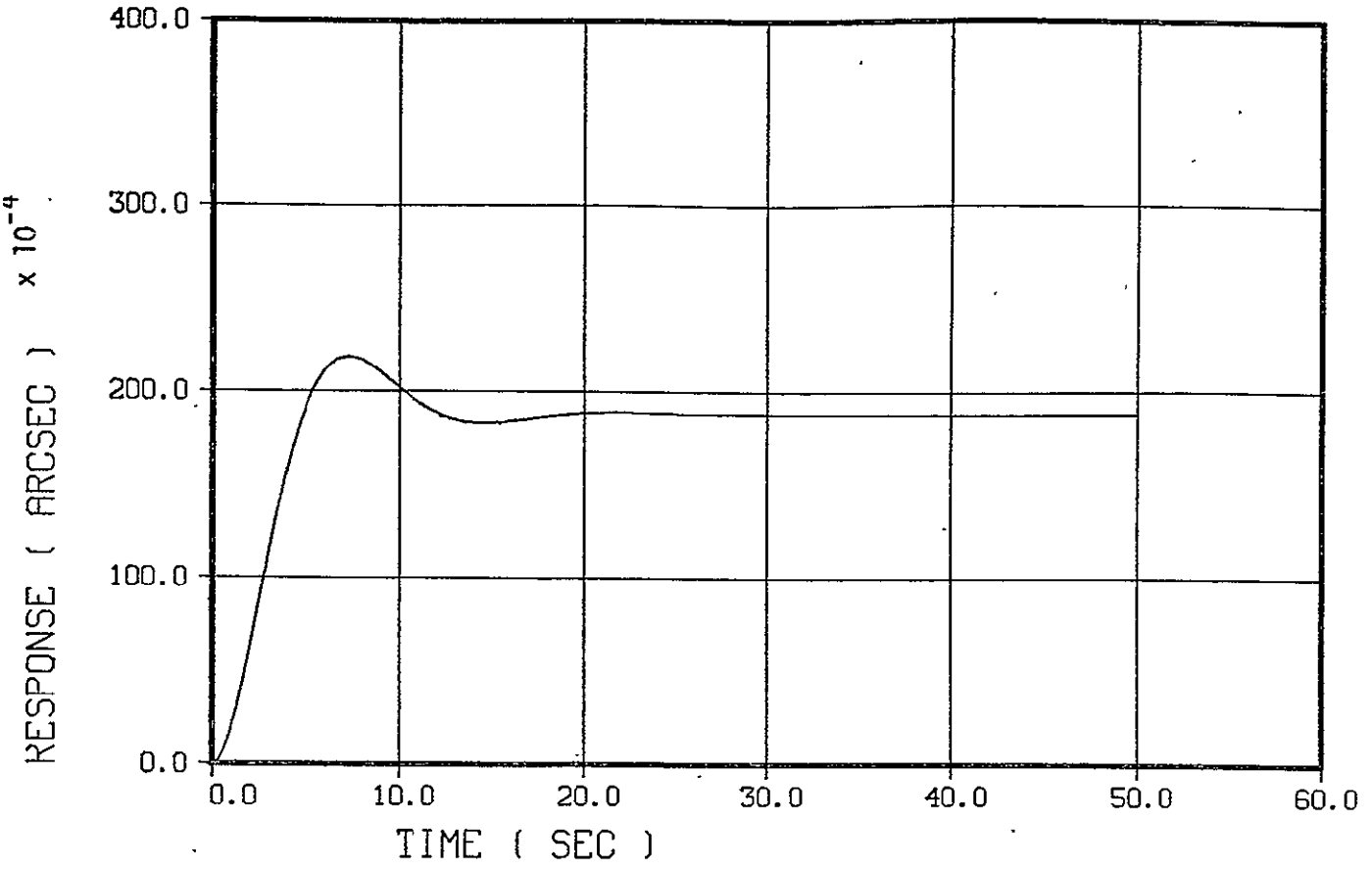

Figure 6-8. Spacecraft Response to Antenna Slewing

The largest rates and accelerations experienced by the antenna in tracking the TDRS target occur near gimbal-lock. This must not necessarily result in the largest spacecraft reaction because antenna inertia is at its minimum near gimbal-lock. Near gimbal-lock, the target is nearly aligned with the mast and the antenna inertia is 2.63 kg-m^2 (1.94 slug $feet^2$). But when the target is at 0 degrees elevation, the antenna inertia is 9.14 kg-m^2 (6.73 slug $feet^2$) -- I_{22} in Table 6-3. Since the ratio of these numbers is only 3.5, the worst spacecraft reaction could, however, be at or near gimbal-lock and the situation must be examined. The gimbal-lock case is analyzed in the following paragraphs.

The spacecraft reaction is due to the gimbal accelerations involved in following the target. The first step is to find these gimbal accelerations, $\ddot{g}_1$ and $\ddot{g}_2$. The geometry for the situation near gimbal-lock is

shown in Figure 6-9. The TDRS is ϵ degrees out of the L-D orbit plane, and -- as long as ϵ is small -- α is the orbit angle between the L-D and the target line. The coordinate system shown is centered at the L-D c.m. but is fixed inertially. Let the unit vector

$$\hat{T} = \begin{bmatrix} T_x \\ T_y \\ T_z \end{bmatrix}$$

represent the target direction from the L-D. The angle γ is the target elevation angle in the L-D orbit plane, so

$$T_y = \sin \epsilon \tag{6.1-14}$$

$$T_x = \cos \gamma \cos \epsilon \tag{6.1-15}$$

$$T_z = -\sin \gamma \cos \epsilon$$

The true gimbal angles are defined relative to a body-fixed coordinate system, but the gimbal motion is not a true indication of the inertial motion of the antenna. The angles g_1 and g_2 are defined relative to the inertial coordinates in Figure 6-9 so that

$$\tan g_1 = T_y/T_x \tag{6.1-17}$$

and

$$\sin g_2 = -T_z \tag{6.1-18}$$

If the coordinate system were body-fixed, these would be the true gimbal angles; in this case, they are a good approximation to the gimbal movements measured relative to inertial coordinates. Now, combining Equations (6.1-14) - (6.1-18), the pseudo-elevation angle is given by

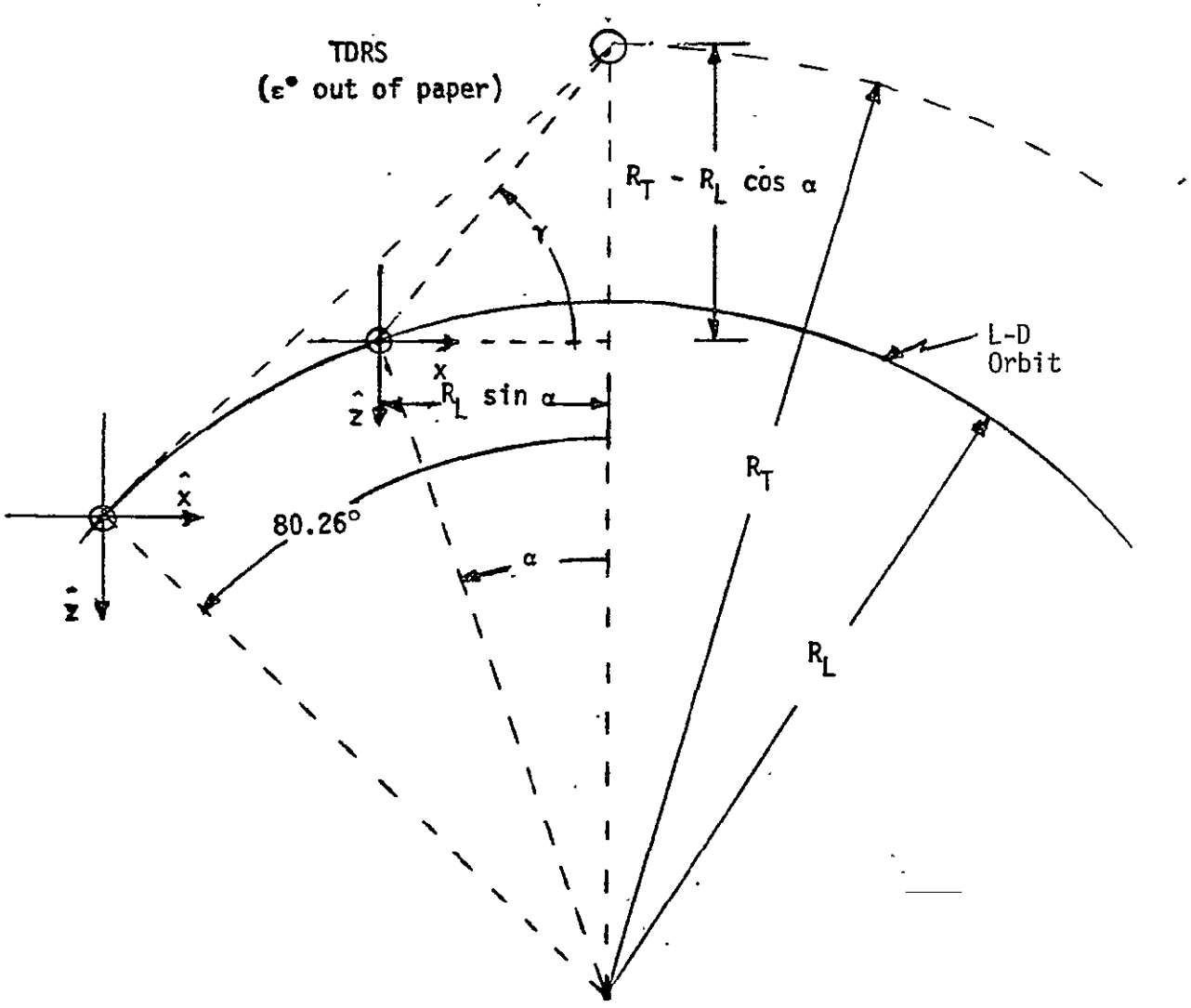

Figure 6-9. Geometry Near Gimbal-Lock

$$\sin g_2 = \sin \gamma \cos \varepsilon \tag{6.1-19}$$

and the pseudo-azimuth angle by

$$\tan g_1 = \frac{\tan \varepsilon}{\cos \gamma} \tag{6.1-20}$$

From Figure 6-9

$$\tan \gamma = \frac{\frac{R_T}{R_L} - \cos \alpha}{\sin \alpha}, \tag{6.1-21}$$

so as α varies from -80 degrees to +80 degrees, γ varies from 80 degrees to 100 degrees. This leads to the approximation

$$\sin \gamma \approx 1 \tag{6.1-22}$$

Thus

$$\tan g_1 = \frac{\tan \varepsilon}{\cos \gamma} \approx \tan \varepsilon \tan \gamma = \frac{\frac{R_T}{R_L} - \cos \alpha}{\sin \alpha} \tan \varepsilon \tag{6.1-23}$$

where ε is small, so $\tan \varepsilon \approx \varepsilon$. Differentiating (6.1-23) results in

$$\dot{g}_1 \sec^2 g_1 = \dot{\varepsilon} \tan \gamma + \dot{\alpha} \tan \varepsilon \frac{(1 - \frac{R_T}{R_L} \cos \alpha)}{\sin^2 \alpha}, \tag{6.1-24}$$

and substituting for $\sec^2 g_1$

$$\dot{g}_1 \approx \frac{\dot{\varepsilon} (\frac{R_T}{R_L} - \cos \alpha) \sin \alpha + \dot{\alpha} (1 - \frac{R_T}{R_L} \cos \alpha) \tan \varepsilon}{\sin^2 \alpha \sec^2 \varepsilon + (\frac{R_T}{R_L} - \cos \alpha)^2 \tan^2 \varepsilon}. \tag{6.1-25}$$

This approximation is valid for small ε and $\alpha < 30$ degrees.

Using the parameter values

(1) ε = 2 deg,

(2) $\dot{\varepsilon}$ = -15 deg/hr, and

(3) $\dot{\alpha}$ = 220.31 deg hr

and determining $\ddot{g}_1$ numerically from $\dot{g}_1$ in (6.1-25), results in $\ddot{g}_1$ as shown in Figure 6-10. The acceleration history can be replaced by the straight line box cart approximation as shown and a closed form spacecraft response can be computed. Using the parameters of Table 6-4, the calculated spacecraft response is plotted in Figure 6-11, where the peak response is seen to be slightly more then 0.02 arc-second. It is obvious that the straight line approximation to the acceleration does not result in an accurate response shape, but the fact that the peak response is 0.1 percent of the allowable indicates that the error is negligible. Also the reaction to the slight change in g_2 is negligible. If the true $\ddot{g}_1$ profile had been used instead of the approximation, the resulting spacecraft reaction would be smooth.

6.1.4 Payload Scanning Devices

The two scanning devices are the Multi-Spectral Scanner (MSS) and the Thematic Mapper (TM), and there are two versions of the TM: the TRW version and the Hughes version. The TRW Thematic Mapper has a continuously rotating scan wheel; so, after start-up, there are no disturbance torques, and the main consideration here is to determine how the TM wheel momentum can best be accommodated by the skewed wheel system. The TM wheel has inertia I_{TM} = 1.59 kg-m^2 (1.17 slug feet^2) and spins at the rate of ω_{TM} = 2.461 rad/second; thus its steady-state momentum is

$$M_{TM} = \omega_{TM} I_{TM} = 3.89 \text{ N-m-sec}$$

The axis of this wheel lies in the spacecraft $\hat{x}$-$\hat{z}$ plane and is canted 10 degrees to the roll axis.

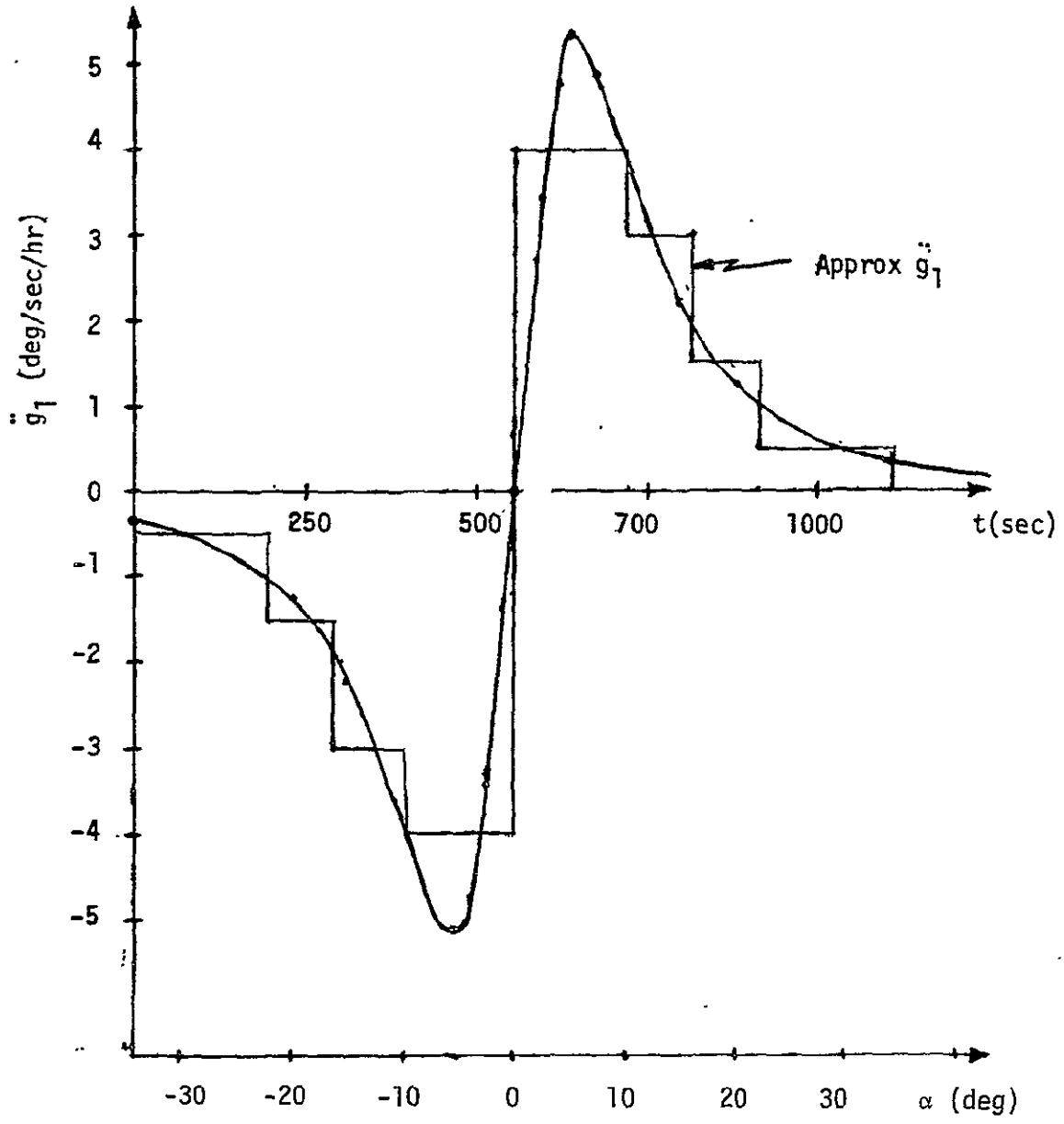

Figure 6-10. Pseudo-Azimuth versus Orbit Angle

Table 6-4. Parameters for Tracking Near Gimbal-Lock

Parameter	Value	
ℓ_1	0.91 m	3 ft
ℓ_2	0	0
m_1	1498 kg	102.48 slugs
m_2	31.14 kg	2.13 slugs
I_1	2377 kg-m^2	1750 slug ft^2
I_2	2.63 kg-m^2	1.94 slug ft^2
I_{11}	2405 kg-m^2	1771 slug ft^2
$I_{12} = I_{21}$	2.63 kg-m^2	1.94 slug ft^2
I_{22}	2.63 kg-m^2	1.94 slug ft^2

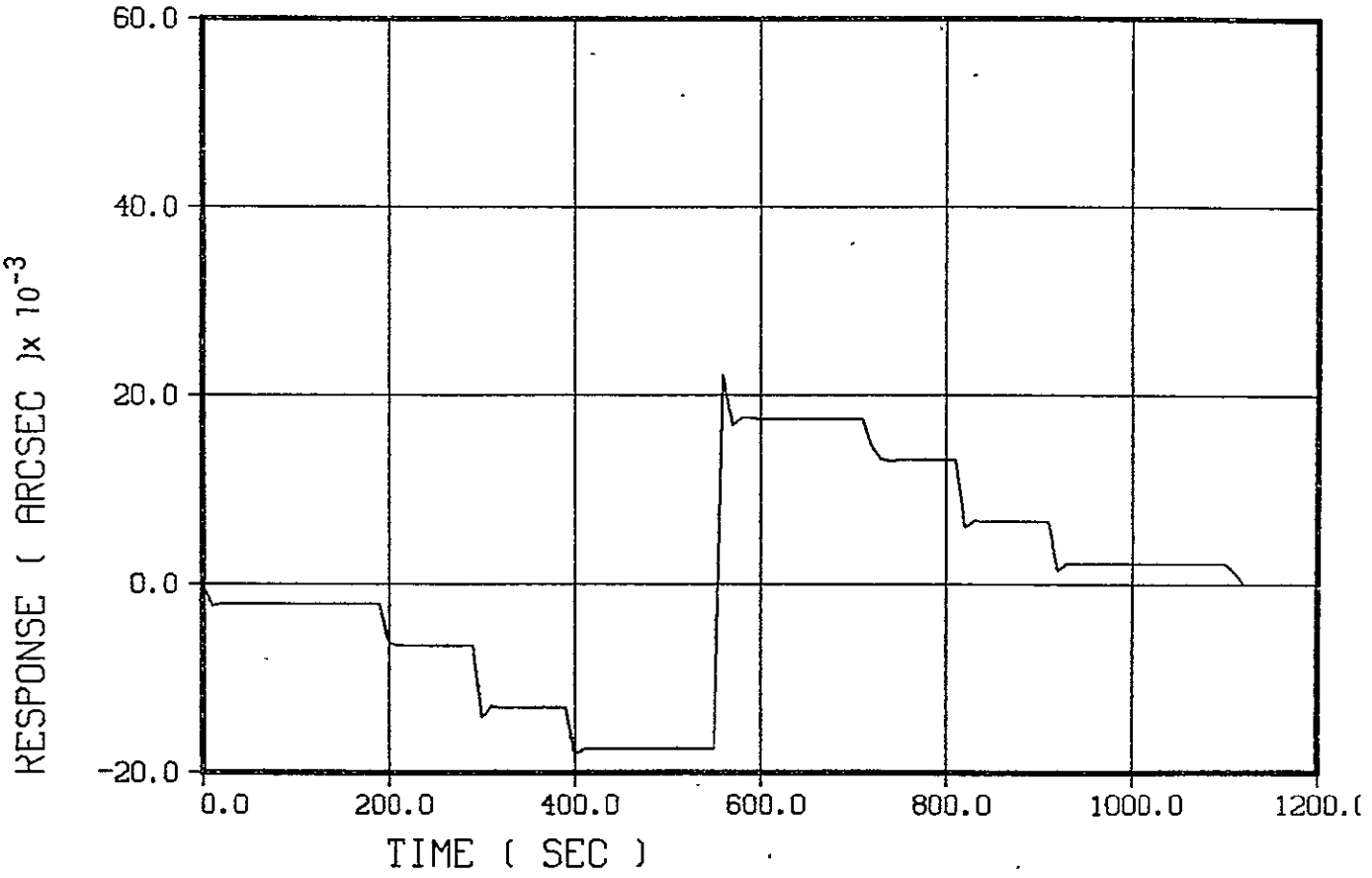

Figure 6-11. Approximated Spacecraft Response to Antenna Tracking Near Gimbal-Lock

Each of the four spacecraft reaction wheels is a NASA Standard Reaction Wheel (SRW) with a maximum stored momentum of $\pm$ 20 N-m-sec. Three of these are aligned with the orthogonal spacecraft body axes and the fourth one is skewed and positioned in such a way that its nominal momentum cancels the resultant moments of the other three wheels when the wheels are operated at a speed bias. In this way the spacecraft nominally has zero momentum bias. If only the four SRW's were considered, the nominal momentums would have to satisfy the question

$$M_{xo}\,\hat{x} + M_{yo}\,\hat{y} + M_{zo}\,\hat{z} + \bar{M}_{so} = \bar{0} \qquad (6.1\text{-}26)$$

where M_s is the momentum of the fourth or skewed wheel. But the TM wheel momentum must be added to the left side of the equation.

The nominal wheel momentums are chosen so that: 1) the fourth wheel does not have to run too much faster than half speed, and 2) the three orthogonal wheels have sufficient range to perform the necessary tasks without being required to go through zero speed. If there were no TM this could be accomplished with $M_{xo} = M_{yo} = M_{zo} = 7$ N-m-sec -- wheel speed of 840 RPM assuming a synchronous speed of 2400 RPM -- and $M_{so} = 12.12$ N-m-sec -- wheel speed of 1455 RPM. Assuming the TM wheel is aligned with the roll axis, it can be assumed to rotate in the opposite direction of the roll wheel so that M_{yo}, M_{zo}, and M_{so} remain unchanged but M_{xo} becomes 10.89 N-m-sec -- wheel speed of 1307 RPM. This actually increases the available range of the roll wheel and is the recommended solution.

The MSS and the HAC TM version have scanning devices which are very similar in operation. Each one scans back-and-forth at constant rate with a turn-around at each end as shown in Figure 6-12. These scan motions are accomplished with the torque pulses shown in Figure 6-12. The scanning parameters are summarized in Table 6-5, and the steady-state spacecraft responses to the two scanners are shown in Figures 6-13 and 6-14 -- the parameters for the Hughes TM are taken from Reference 8. It was assumed in the analysis that the scanning motion is about the spacecraft roll axis and that both mass centers lie on that axis; thus, $A_o/I_{12} = I_1 = 2037$ kg-m^2

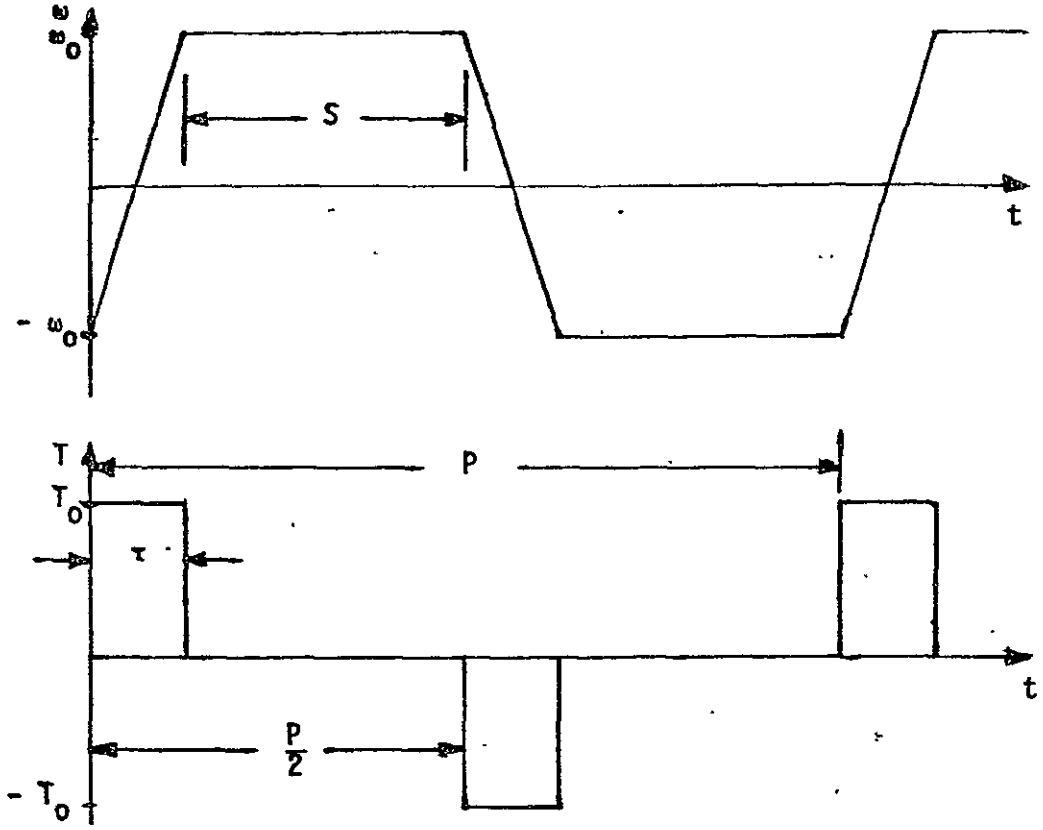

Figure 6-12. Rate and Torque Profiles for the Scanning Devices

Table 6-5. Results of Scanner Analyses

Parameter	MSS	Hughes TM
Frequency, f (Hz)	18.5	7.14
Scan Efficiency (%)	92	80
Active Scan Time, S (MSEC)	24.865	56
Period, P (MSEC)	54.054	140
Scan Rate, ω_o (RAD/SEC)	5.26	2.32
Inertia, I ($kg\text{-}m^2$)	0.0113	0.02614
Torque, T_o (N-m)	54.84	8.65
Peak Spacecraft Resp, (Sec)	0.08	0.2

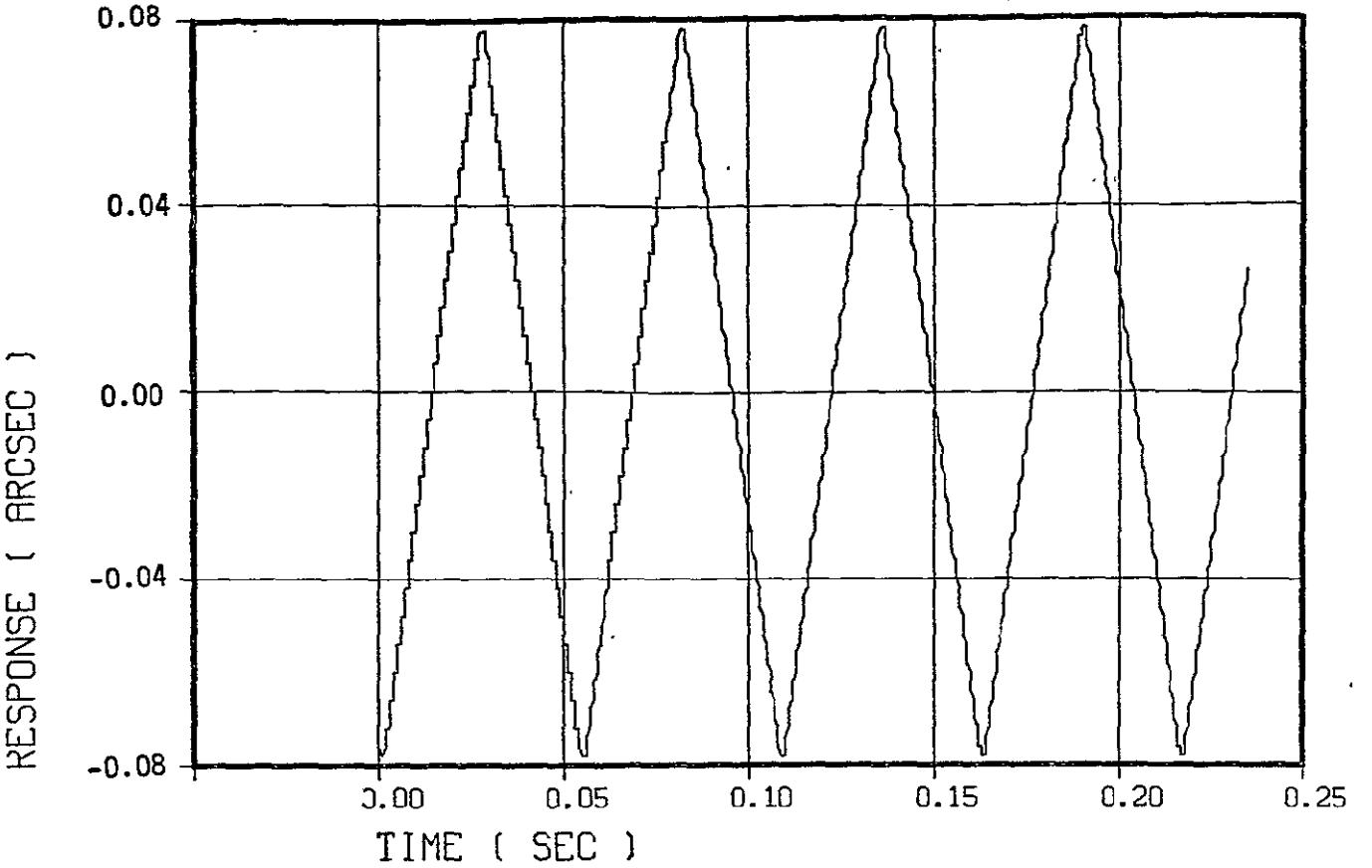

Figure 6-13. Steady-State Spacecraft Response to MSS Scanning

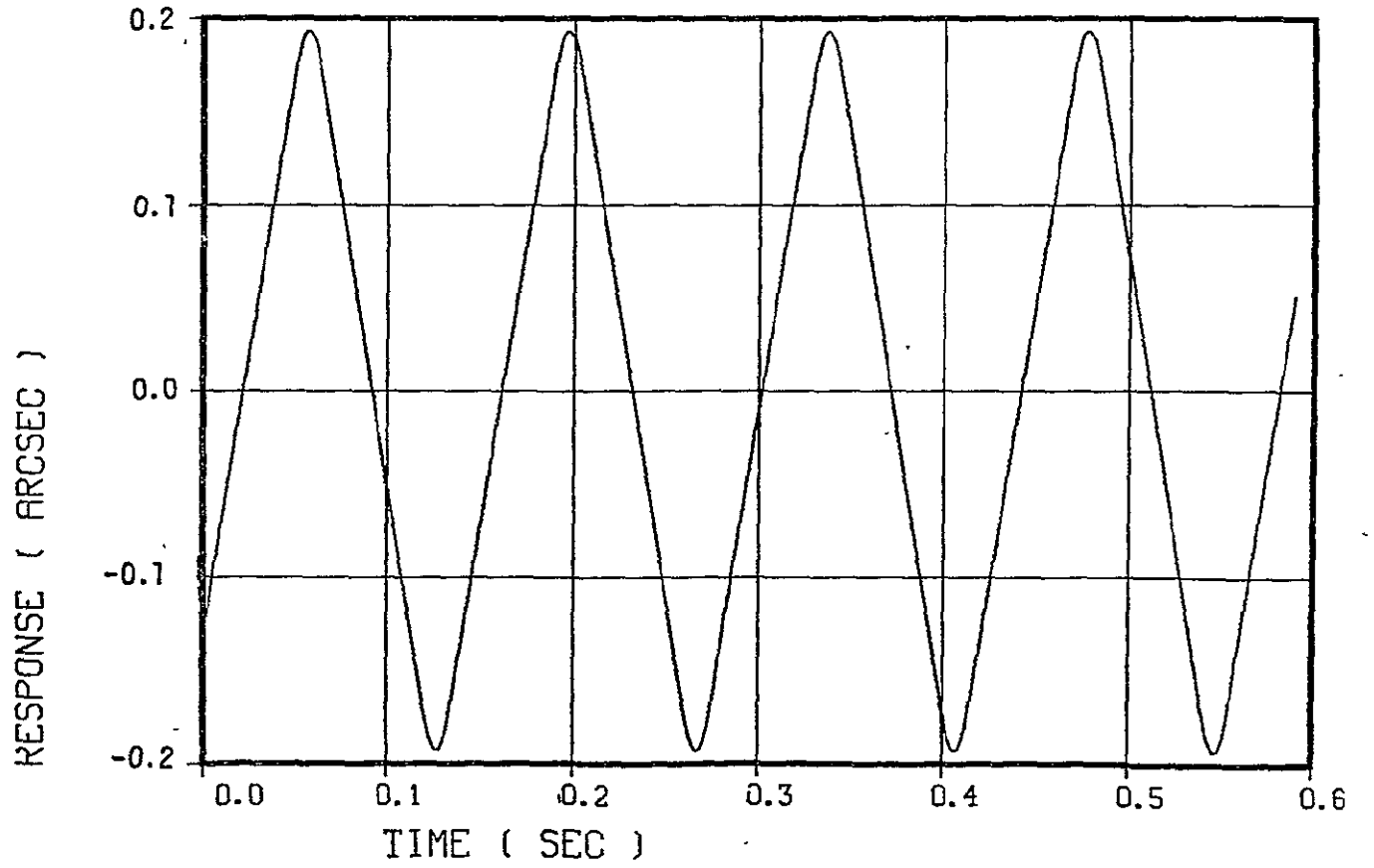

Figure 6-14. Steady-State Spacecraft Response to Hughes TM Scanning

(1500 slug feet^2). Both devices scan at frequencies considerably higher than the 0.5 rad/second bandwidth of the ACS, so the ACS has no noticeable effect on these results and the responses are related to the wheel motions by the inertia ratios as indicated by Equation (6.1-7). The responses shown are acceptable and no compensation is needed.

6.1.5 Reaction Wheel Dynamic Imbalance

Limitations in manufacturing accuracy result in small mass imbalances in the reaction wheel rotors. The effect of these imbalances creates small non-zero cross products of inertia which cause small sinusoidal disturbance torques at the wheel frequencies. To determine the effects of these imbalances on the rigid-body pointing jitter, the disturbance torques from the four wheels are combined to obtain the total disturbance in roll, pitch, and yaw. Since wheel speeds are continually changing in response to unloading torques, the relative phasing of the individual imbalance torques is also changing. To obtain the worst case, the individual wheel imbalance torques should have their magnitudes added directly, while an RSS value would give an average disturbance torque. The approach here is to examine the worst case for all wheel speeds near the nominal bias speed. The total roll axis disturbance torque is computed and applied to a single axis analytic model to estimate the amplitude of the resulting rigid-body motion which turns out to be very small.

The torque on the body is the negative of the torque on the rotor, so Euler's equation may be written

$$\bar{T} = -\frac{d\bar{H}}{dt}$$

$$H = \bar{\bar{I}}\,\bar{\omega}$$

where

$\bar{T}$ = the reaction torque applied to the vehicle in rotor coordinates

$\bar{T}_d$ = the reaction disturbance torque due to wheel dynamic mass imbalance

$\bar{H}$ = the total angular momentum of the rotor

$\bar{\bar{I}}$ = the rotor inertia matrix

$\bar{\omega}$ = rotor angular velocity

For the roll reaction wheel with its spin axis fixed along the spacecraft roll axis, the velocity of the rotor may be written

$$\bar{\omega} = [\omega_w, 0, 0]$$

Performing the differentiation in the torque balance equation yields

$$-\bar{T} = \bar{\bar{I}}\,\dot{\bar{\omega}} + \bar{\omega} \times \bar{\bar{I}}\,\bar{\omega}$$

and since the angular acceleration in response to external disturbance torques is small compared to the wheel speed, the previous equation may be written

$$\bar{T} = \begin{bmatrix} -I_{xx} & \dot{\omega}_w \\ \omega_w^2 & I_{xz} \\ -\omega_w^2 & I_{xy} \end{bmatrix}$$

as the total torque in wheel coordinates. The x-component is, of course, the desired control torque of the roll wheel. Since only the disturbance torque due to wheel imbalance is of interest here, one has

$$\bar{T}_d = \begin{bmatrix} 0 \\ \omega_w^2 & I_{xz} \\ -\omega_w^2 & I_{xy} \end{bmatrix}$$

This is transformed into body fixed coordinates by the time-varying transformation

$$A_{bw} = \begin{bmatrix} 1 & 0 & 0 \\ 0 & \cos \omega_w t & -\sin \omega_w t \\ 0 & \sin \omega_w t & \cos \omega_w t \end{bmatrix}$$

from wheel to body coordinates. Applying it to the rotor torques yields

$$\bar{T}_{body,roll} = \begin{bmatrix} T_{dx} \\ T_{dy} \\ T_{dz} \end{bmatrix} = \begin{bmatrix} 0 \\ \omega_w^2 I_{xz} \cos \omega_w t + \omega_w^2 I_{xy} \sin \omega_w t \\ \omega_w^2 I_{xz} \sin \omega_w t - \omega_w^2 I_{xy} \cos \omega_w t \end{bmatrix}$$

which shows the sinusoidal disturbance torque in the pitch and yaw axes perpendicular to the spin axis as expected.

Considering T_{dy} as an example, the sine and cosine terms could be combined into a single sinusoid of the form

$$\omega_w^2 \sqrt{I_{xz}^2 + I_{xy}^2} \cos (\omega_w t + \phi)$$

where ϕ is an appropriate phase angle. However, since torques from all wheels are to be combined "in-phase" so that their magnitudes add, the phase is irrelevant and may be set to zero. This yields

$$T_{dy} = \omega_w^2 \sqrt{I_{xz}^2 + I_{xy}^2} \cos \omega_w t$$

where $\sqrt{I_{xz}^2 + I_{xy}^2}$ is the dynamic imbalance.

Computations similar to the above may be performed for the pitch and yaw wheels to yield

$$\bar{T}_{body,pitch} \approx \begin{bmatrix} \omega_w^2 \sqrt{I_{yz}^2 + I_{xy}^2} \cos \omega_w t \\ 0 \\ \omega_w^2 \sqrt{I_{yz}^2 + I_{xy}^2} \cos \omega_w t \end{bmatrix}$$

$$\bar{T}_{body,yaw} = \begin{bmatrix} \omega_w^2 \sqrt{I_{yz}^2 + I_{xz}^2} \cos \omega_w t \\ \omega_w^2 \sqrt{I_{yz}^2 + I_{xz}^2} \cos \omega_w t \\ 0 \end{bmatrix}$$

the quoted imbalance value is 0.5 inch^2-ounces which converts to 9.15×10^{-6} kg-m^2, and the nominal wheel frequency is 91.5 rad/second which results in the required 7.32 N-m-s bias momentum value. Inserting these values in the disturbance torques and summing the results yields the disturbance torques for three wheel as

$$\bar{T}_d = \begin{bmatrix} .153 \cos 91.5t \\ .153 \cos 91.5t \\ .153 \cos 91.5t \end{bmatrix} \text{ Nm}$$

the fourth wheel is skewed symmetrically to the above three wheels and thus contributes disturbance torques into all three axes. In addition, the fourth wheel runs at a higher bias speed. Performing the computations for the fourth wheel yields

$$\bar{T}_{body,w4} = \begin{bmatrix} \frac{2}{\sqrt{3}} \omega_{w'}^2 \cos \omega_{w'} t \\ \frac{2}{\sqrt{3}} \omega_{w'}^2 \cos \omega_{w'} t \\ \frac{2}{\sqrt{3}} \omega_{w'}^2 \cos \omega_{w'} t \end{bmatrix} \cdot \quad 9.15 \times 10^{-6}$$

$$= \begin{bmatrix} .265 \cos 158.5t \\ .265 \cos 158.5t \\ .265 \cos 158.5t \end{bmatrix}$$

To evaluate the jitter level, the single axis roll diagram in Figure 6-15 may be used. The transfer function from the disturbance torque to the attitude may be computed as

$$\frac{\phi(s)}{T(s)} = \frac{I_{xx}^{-1}}{S^2 + \frac{K_{xR}}{I_{xx}} S + \frac{K_{xp}}{I_{xx}}}$$

and the coefficients evaluated as

$$\frac{K_{xR}}{I_{xx}} = 2\zeta\omega_n$$

$$\frac{K_{xp}}{I_{xx}} = \omega_n^2$$

for $\zeta = 0.5$ and $\omega_n = 0.7$ in the vehicle attitude controller. Considering first the total disturbance torque 0.153 from the three on-axis wheels, the response is

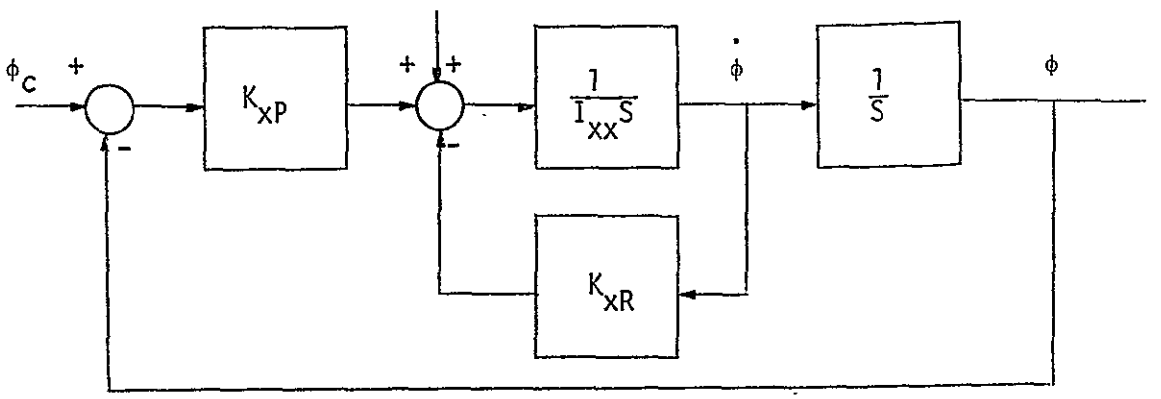

Figure 6-15. Roll Single-Axis Control Loop

$$\phi(s) = \left(\frac{I_{xx}^{-1}}{S^2 + 0.7S + 0.49}\right) \left(\frac{0.153S}{S^2 + \omega_w^2}\right)$$

The steady-state amplitude of this jitter may be computed to be

$$|\phi(t)| = 0.00898 \text{ μrad}$$
$$= 0.00185 \text{ arc-sec}$$

which is quite small compared to the total budget.

Similarly, the jitter from the fourth wheel may be computed to be

$$|\phi(t)| = 0.00518 \text{ μrad}$$
$$= 0.00106 \text{ arc-sec}$$

Directly adding these two values yields a worst case value of 0.0142 μrad jitter, although this could not persist for long because of the differences in wheel speeds. If the two values are root-sum-squared, the value becomes 0.0104 μrad RSS jitter.

Since wheel speeds will vary with magnetic unloading torques, the jitter values computed here will vary somewhat throughout orbit, but the overall effect of the dynamic mass imbalance still remains an insignificant portion of the error budget.

6.1.6 Summary of Internal Motion Effects

The peak spacecraft responses to each of the internal motions studied are summarized in Table 6-6. These results were obtained without the necessity of using torque preemphasis in the ACS or momentum compensation, and all of the results are well within the $\pm$ 2.16 arc-second requirement. The largest reaction is due to the motion of the solar array; this result is based on the use of a standard stepper motor and harmonic drive to move the array at 0.018 degree per step and one step every 294.1 msecond during normal operation. The TRW TM causes no spacecraft pointing error during normal operation because its only moving element is a continuously rotating wheel. It was shown that the momentum of this wheel can be accommodated with no reduction in the available SRW wheel momentums. Disturbances due to reaction wheel mass imbalance are completely negligible assuming that the space-raft body is rigid and no structural modes are excited.

Two other points shown in this memo are:

(1) The 45 degree solar array slewing to avoid interference with the Ku-band antenna can be accomplished in 75 seconds, which is 0.34 degree of orbit angle.

(2) The 3.89 N-m-sec momentum of the TRW TM can be absorbed by increasing the $\hat{x}$ SRW speed bias from a 7 N-m-sec equivalent to a 10.89 N-m-sec equivalent.

Table 6-6. Summary of Spacecraft Reaction to Internal Motions. Assumed ACS with $\xi = 0.5$ and $\omega_n = 0.5$ rad/sec

Internal Component	Peak Spacecraft Response (sec)		
	Roll	Pitch	Yaw
Solar Array (rigid body)	0.13	0.60	0.11
Ku-band Antenna (Tracking near Gimbal-Lock)	0	0	0.02
TRW TM	0	0	0
Hughes TM	0.20	0	0
MSS	0.08	0	0
RW Dynamic Mass Imbalance	0.003	0.0023	0.0026

6.2 Flexible Ku-Band Antenna Mast

This section contains the results of a study which examines the dynamic damping obtainable for the antenna boom by suitably designing the vehicle and antenna controllers. Since the design is in a preliminary stage, physical parameters are perturbed over expected ranges and appropriate corresponding controllers are designed to study boom damping.

Conclusions of this study show that:

(1) A stable coupled control system consisting of the vehicle and antenna controllers can be obtained for parameter ranges of interest.

(2) As long as the vehicle controller natural frequency is near the range 0.5 to 1.0 rad/second, changes in its bandwidth do not appreciably affect the attainable boom damping.

(3) For parameter ranges of interest, an optimum value of attainable dynamic boom damping exists as a function of boom stiffness and antenna controller bandwidth.

(4) If maximum dynamic boom damping is the criterion, it is necessary to design so that the antenna controller bandwidth is near the boom natural frequency. In this way, the controller "sees" the boom vibrating and acts to dynamically dampen the vibrations. Preferences for physical parameters to achieve maximum damping are short boom length, short masss-center offset of the antenna and boom stiffness matched to antenna controller bandwidth.

(5) If minimizing the decay time of boom oscillations is the design criterion, no single optimum boom stiffness matched to the antenna controller exists; the boom must merely be stiffer than a specified minimum which is a function of the antenna controller bandwidth. The rule of thumb here is simply that the undamped boom natural frequency should at least be 1.4 times the natural frequency of the antenna controller, or larger. In essence, a short and stiff boom is desirable, which is no surprise.

(6) A 10 foot boom having stiffness EI = 350,000 pound-feet^2, which corresponds to a boom/tip mass natural frequency of 30 rad/second, would yield good performance achieving a damping ratio of $\zeta = 0.27$ and an oscillation decay time constant of $\tau_{boom} = 0.124$ second when an antenna controller with natural frequency $\omega_c = .22$ rad/second is used.

The TDRS antenna is mounted on a boom and has a double gimballed dish with relatively high bandwidth controllers to meet pointing and slewing requirements. Presently, the boom length is expected to be between 1.83 m and 6.1 m and in any event is determined by line-of-sight clearance to Tracking Data Relay Satellites (TDRS). For the vehicle, the controller has a relatively low natural frequency of 0.5 to 1.0 rad/second. The purpose of the present study is to parametrically study the antenna controller designs to determine if sufficient dynamic damping is obtainable for the boom bending mode.

To obtain the controller designs and assess the boom damping, a linearized set of equations is obtained for a single axis dynamic model with a single-mode flexible massless boom. This model includes the cable-wrap spring torque occurring at the payload hinge point. Parameters treated parametrically are the boom length, boom stiffness, antenna mass center offset, and antenna controller bandwidth.

6.2.1 Antenna Mast and Vehicle System Model

A single axis dynamic model of the spacecraft, boom and antenna is shown in Figure 6-16. The spacecraft mass and inertia are shown by m_1 and I_1, respectively, while the antenna is represented by m_2 and I_2. L_1 represents the boom length to the antenna gimbal point and L_2 is the length of the antenna center-of-mass offset from the hinge. Torsional restraint by cable wrap at the hinge point is shown by $K_{\theta 2}$. Angles θ_1 and α represent inertial attitudes of the spacecraft and antenna, respectively, while x_1, x_2, y_1, y_2 represent lateral displacements of the mass centers as shown.

Angle θ_1 is controlled by the vehicle controller while the antenna controller controls α to follow α_c which may be a tracking angle or a slewing command to another target. Angle θ_b is statically determined by θ_1 and α since the boom is assumed to be massless.

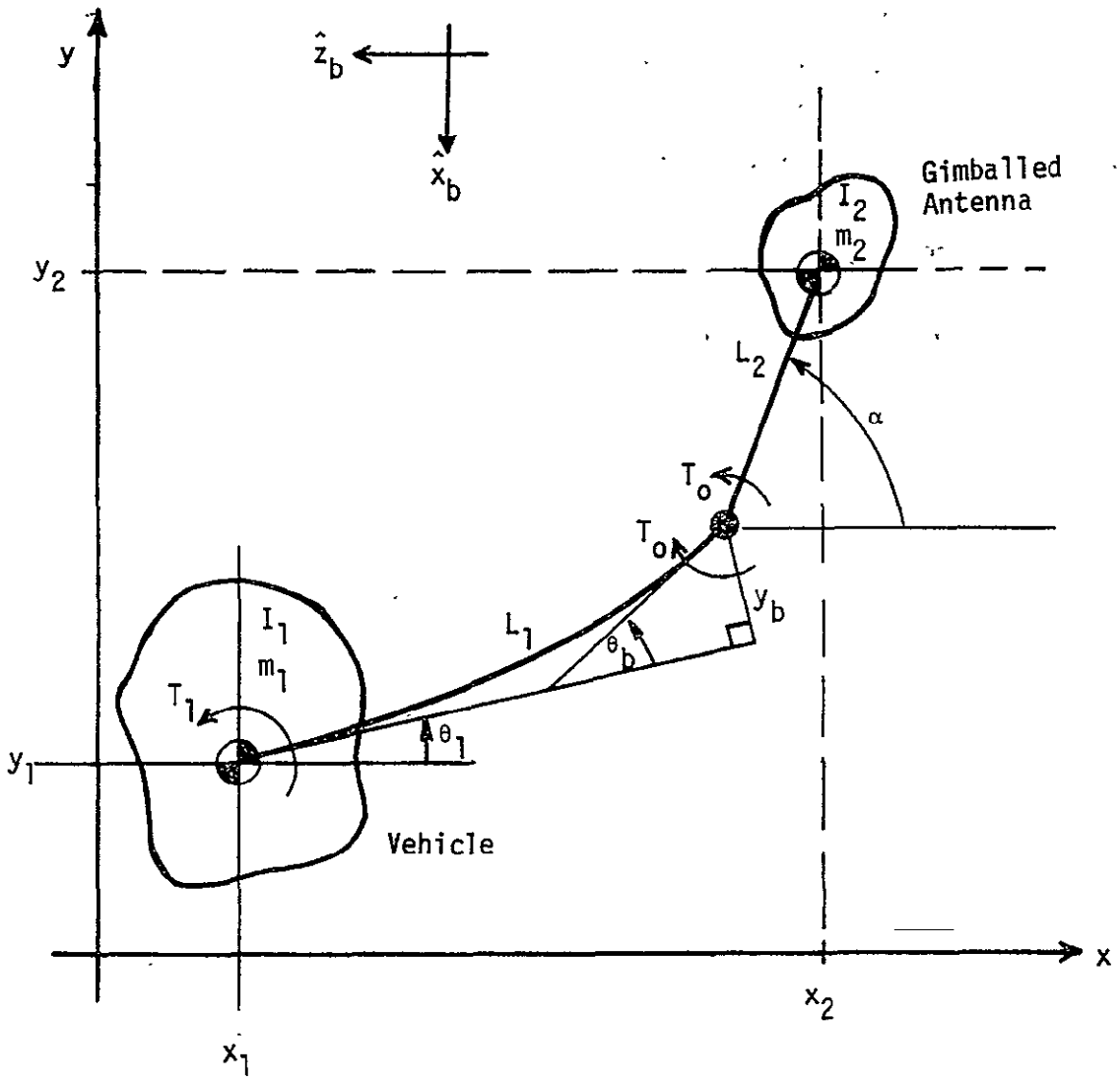

Figure 6-16. Single Axis Dynamic Model for Spacecraft, Flexible Boom, and Antenna with Mass Center Offset

Dynamic Equations

Equations to describe the dynamic model are derived in Appendix C. The problem here is similar to one that has been studied earlier in Reference 4 and thus only a brief outline of the derivation is included. Typically, the spacecraft inertial attitude θ_1 and boom angle θ_b are small, and thus the equations are derived for small θ_1 and θ_b but for large α. Inertial translation of the spacecraft is unimportant here, and thus it is convenient to work with new variables defined by

$$x = x_2 - x_1$$

$$y = y_2 - y_1$$

in order to reduce the number of independent system equations.

From Appendix C, the equations are:

$$I_1 \ddot{\theta}_1 + I_2 \ddot{\alpha} + a_o (L_1 \ddot{y} + L_2 \ddot{y} \cos \alpha - L_2 \ddot{x} \sin \alpha) = T_1 \tag{6.2-1}$$

$$L_1 I_2 \ddot{\alpha} k_{\theta 2} (L_1 \alpha + 2 L_2 \sin \alpha) + k_{\theta 2} L_1 \theta_1 - a_1 a_o \ddot{y}$$

$$+ L_1 L_2 a_o \ddot{y} \cos \alpha - 2 k_{\theta 2} y - a_o L_1 L_2 \ddot{x} \sin \alpha = L_1 T_o \tag{6.2-2}$$

$$C_1 I_1 \ddot{\theta}_1 + L_1 \theta_1 + L_2 \sin \alpha + a_o a_2 \ddot{y} - y = C_1 T_1 \tag{6.2-3}$$

$$x - L_1 - L_2 \cos \alpha = 0 \tag{6.2-4}$$

where

$$a_o = \frac{m_1 m_2}{m_1 + m_2} \qquad a_1 = k_{\theta 2} \frac{L_1 C_1}{3}$$

$$a_2 = \frac{L_1 C_1}{3} \qquad C_1 = \frac{L_1^2}{2 EI}$$

Since spacecraft inertial attitude θ_1 is small, linearized equations for $\theta_1 \simeq 0$ may be used for analysis. The antenna angle α is not necessarily small, and thus the equations may be linearized about a nominal α_o to yield:

$$I_1 \ddot{\theta}_1 + I_2 \ddot{\alpha} + a_o(L_1 + L_2 \cos \alpha_o) \ddot{y} - (a_o L_2 \sin \alpha_o) \ddot{x} = T_1 \qquad (6.2\text{-}5)$$

$$L_1 I_2 \ddot{\alpha} + k_{\theta 2}(L_1 + 2L_2 \cos \alpha_o) \alpha + k_{\theta 2} L_1 \theta_1 + a_o (L_1 L_2 \cos \alpha_o - a_1) \ddot{y}$$

$$-2 k_{\theta 2} y - a_o L_1 L_2 \ddot{x} \sin \alpha_o$$

$$= L_1 T_o - 2 k_{\theta 2} L_2 (\sin \alpha_o - \alpha_o \cos \alpha_o) \qquad (6.2\text{-}6)$$

$$C_1 I_1 \ddot{\theta}_1 + L_1 \theta_1 + L_2 \alpha \cos \alpha_o + a_o a_2 \ddot{y} - y$$

$$= C_1 T_1 - L_2 (\sin \alpha_o - \alpha_o \cos \alpha_o) \qquad (6.2\text{-}7)$$

$$x + (L_2 \sin \alpha_o) \alpha = L_1 + L_2 (\alpha_o \sin \alpha_o + \cos \alpha_o) \qquad (6.2\text{-}8)$$

A realistic and typical antenna pointing position is overhead, i.e., looking in the $-\hat{z}$ direction in body reference axes. For this case $\alpha_o = o$ and the Equations (6.2-5) to (6.2-8) decouple in x and y. The results are

$$I_1 \ddot{\theta}_1 + I_2 \ddot{\alpha} + (L_1 + L_2) a_o \ddot{y} = T_1 \qquad (6.2\text{-}9)$$

$$L_1 I_2 \ddot{\alpha} + k_{\theta 2} (L_1 + 2L_2) \alpha + k_{\theta 2} L_1 \theta_1 - a_o (a_1 - L_1 L_2) \ddot{y}$$

$$- 2 k_{\theta 2} y = L_1 T_o \qquad (6.2\text{-}10)$$

$$C_1 I_1 \ddot{\theta}_1 + L_1 \theta_1 + L_2 \alpha + a_o a_2 \ddot{y} - y = C_1 T_1 \qquad (6.2\text{-}11)$$

where the y motion is coupled with all the rotational motion. Taking Laplace transforms of (6.2-9), (6.2-10), (6.2-11) yields the following set of equations.

$$I_1 S^2 \theta_1(s) + I_2 S^2 \alpha(s) + a_o (L_1 + L_2) S^2 y(s) = T_1(s) \qquad (6.2\text{-}12)$$

$$k_{\theta 2} L_1 \theta_1(s) + \left[L_1 I_2 S^2 + k_{\theta 2}(L_1 + 2L_2)\right] \alpha(s)$$

$$- \left[a_o (a_1 - L_1 L_2) S^2 - 2k_{\theta 2}\right] y(s) = L_1 T_o(s) \qquad (6.2\text{-}13)$$

$$\left[C_1 I_1 S^2 + L_1\right] \theta_1(s) + L_2 \alpha(s) + \left[a_o a_2 S^2 - 1\right] y(s) = C_1 T_1(s) \qquad (6.2\text{-}14)$$

6.2.2 Control Law Development

Separate controllers are to be used for the vehicle and antenna which implies rate and position as the most straightforward control law since the possibility of designing a decoupled multivariable control system is ruled out by the separate controllers. With rate and position controllers, the overall system may be represented as shown in Figure 6-17. To achieve performance requirements on the antenna controller, an integral-of-position may have to be added. However, this will not significantly change the obtainable dynamic boom damping, and, since the analysis is considerably simplified without it, the integral term is not shown. Also, a rate command $\dot{\alpha}_c$ may be necessary for slewing but for the small-signal linearized analysis it is not used.

From the set of transformed Equations (6.2-12) to (6.2-14), all the various transfer functions relating input and output variables may be obtained by zeroing the undesired inputs and solving the resulting equations. They are listed here in factored form, but the coefficients for the polynomial form are shown in Appendix D.

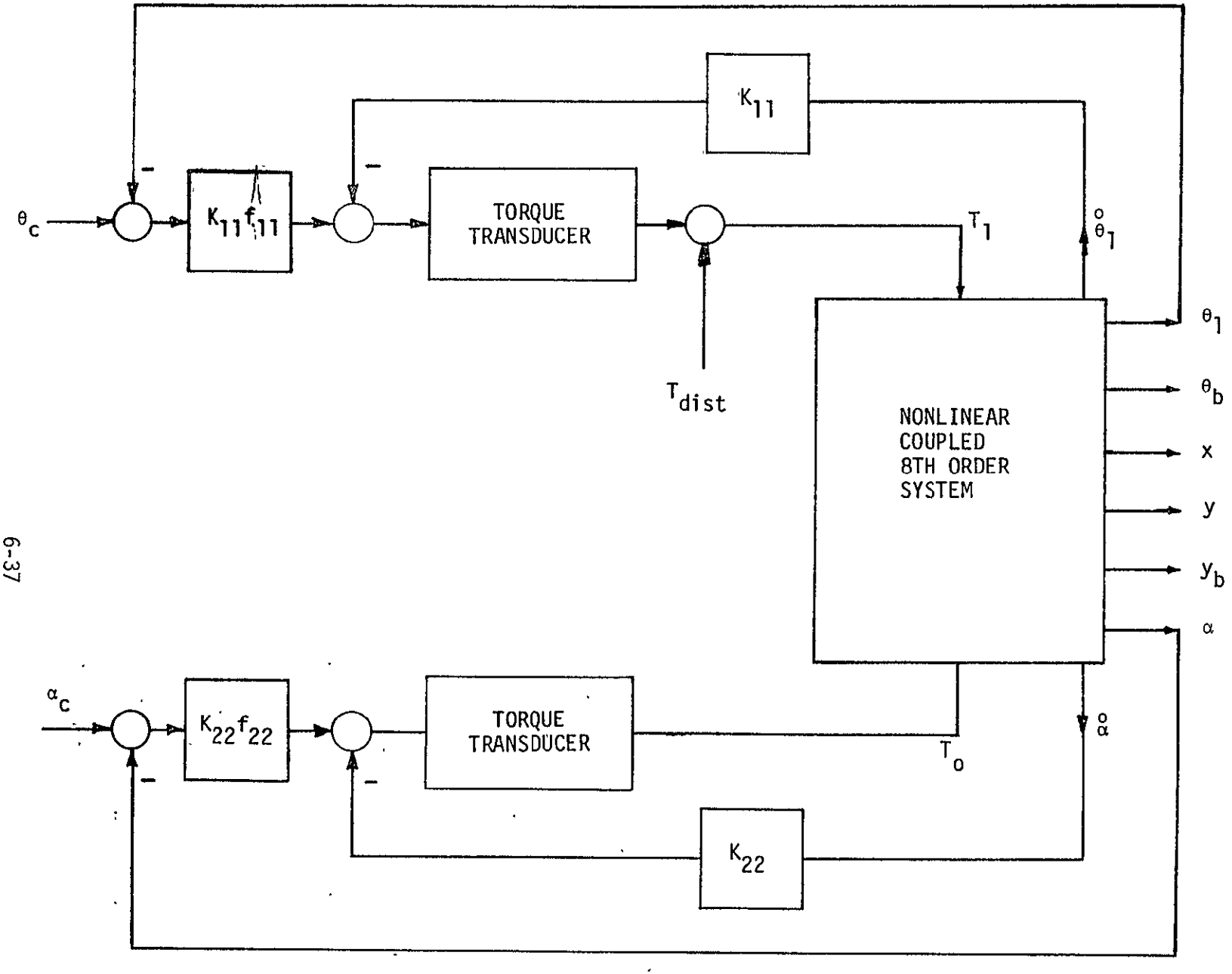

Figure 6-17. Representation of Coupled Dynamic System with Position and Rate Controllers

$$G_{11}(s) = \frac{\theta_1}{T_1} = \frac{1}{I_1} \frac{(s^2 - z_{11}^2)(s^2 - z_{12}^2)}{s^2 (s^2 - p_1^2)(s^2 - p_2^2)} \tag{6.2-15}$$

$$G_{21}(s) = \frac{\alpha}{T_1} = K_{12} \frac{(s-z)(s+z)}{s^2 (s^2 - p_1^2)(s^2 - p_2^2)} \tag{6.2-16}$$

$$G_{10}(s) = \frac{\theta_1}{T_o} = K_{10} \frac{(s-z_{10})(s + z_{10})}{(s^2 - p_1^2)(s^2 - p_2^2)} \tag{6.2-17}$$

$$G_{20}(s) = \frac{\alpha}{T_o} = K_{20} \frac{(s^2 - z^2_{20})}{(s^2 - p_1^2)(s^2 - p_2^2)} \tag{6.2-18}$$

Since repeated studies with various system parameters are planned, a computer program which computes the appropriate polynomial coefficients is shown in Appendix D. It also computes the complex roots and thus provides the factored forms required for analysis and design.

With the preceding transfer functions defined, the multivariable system may be drawn as shown in Figure 6-18. The torque transducers are assumed ideal with unity gain for the analysis since saturation, friction and possible hystersis nonlinearities should not affect the linearized analysis for damping.

6.2.3 Closed-Loop Dynamic Studies

The purpose of this section is to develop the methods for controller design and examine the resultant dynamic boom damping. Physical parameters are perturbed over expected ranges although not all combinations are tried because of the number of possibilities. In general, it is desired to draw conclusions that are indicative of general behavior without being heavily dependent on specific parameter values. Many of these can be arrived at heuristically, such as using the shortest possible boom length, but it is still necessary to quantify the results.

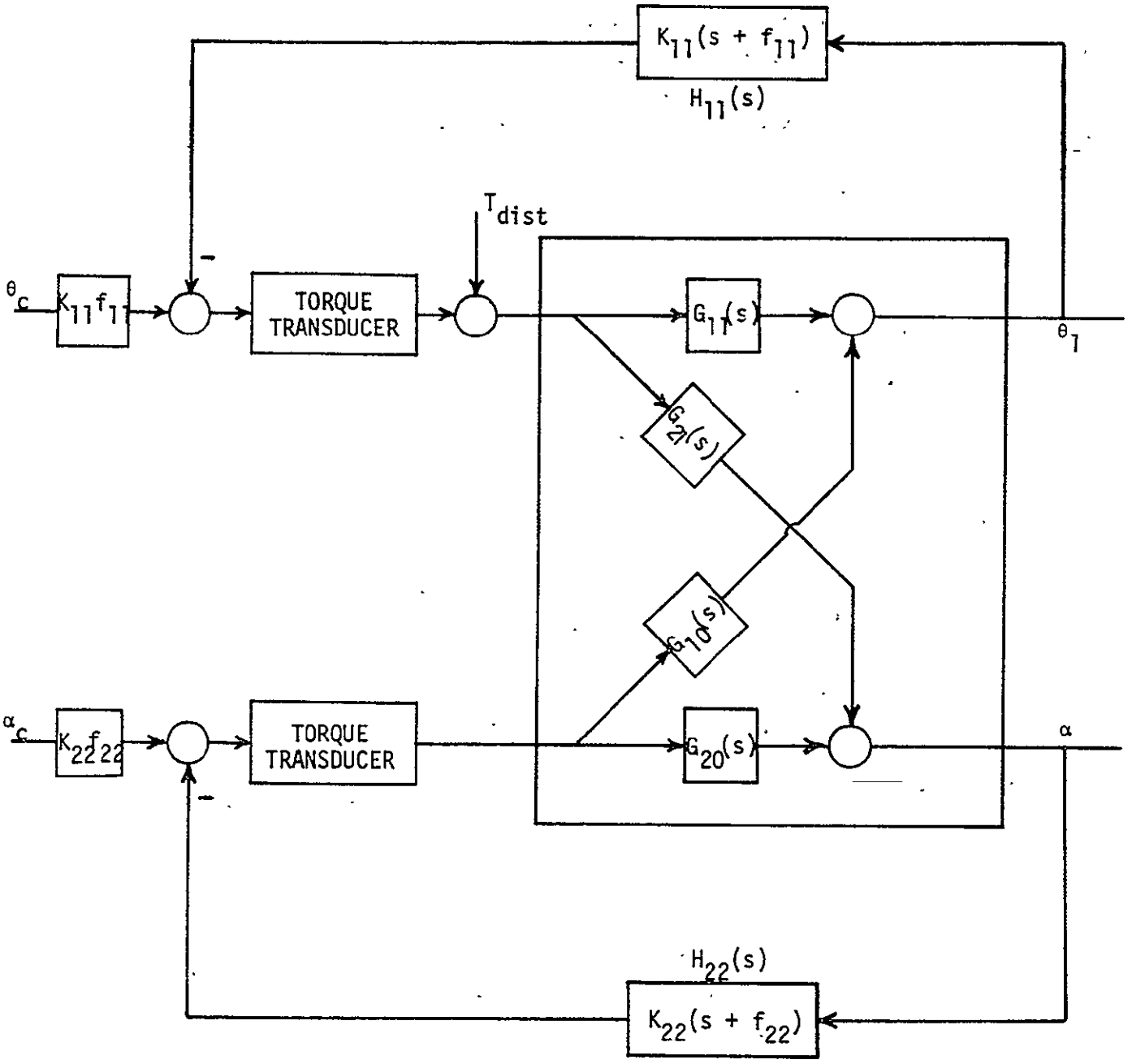

Figure 6-18. Transfer Function Description of the Coupled Dynamic System

Pertinent system design parameters and physical values are listed next for reference. Accuracy, angular ranges, and slewing requirements are not listed here since they do not bear directly on the linearized damping analysis. The following values are for the pitch axis with the antenna pointing to zenith.

SYSTEM PARAMETER VALUES

Spacecraft:	I_1 = 2671 kg-m^2	M_1 = 1496.6 kg
Antenna:	I_2 = 4.39 kg-m^2	M_2 = 29.8 kg
Boom:	L_1 = 1.83 to 6.10 m	EI = 33,060 to 206,625. N-m^2 (80,000 to 500,000 lb-ft^2)
Hinge:	$K_{\theta 2}$ = 0.013558 N-m/rad	
Antenna Offset:	L_2 = 0.3 to 0.45 m	

CONTROLLER SPECIFICATIONS

Spacecraft:	ζ_s = 0.5	ω_{ns} = 0.5 to 1.0 rad/sec
Antenna:	ζ_c = 0.5 to 0.7	ω_{nc} = 5. to 20. rad/sec

With the form of the control laws determined, it is necessary to design values for K_{11}, f_{11}, K_{22}, and f_{22} such that the damping ratio and bandwidth specifications are met.

Spacecraft Controller

Assuming that the coupling of the antenna and spacecraft is not very strong, the coupling transfer functions $G_{10}(s)$ and $G_{21}(s)$ may be neglected for now. Then the system takes the form shown in Figure 6-19. For this loop, the root locus takes the general form shown in Figure 6-20.

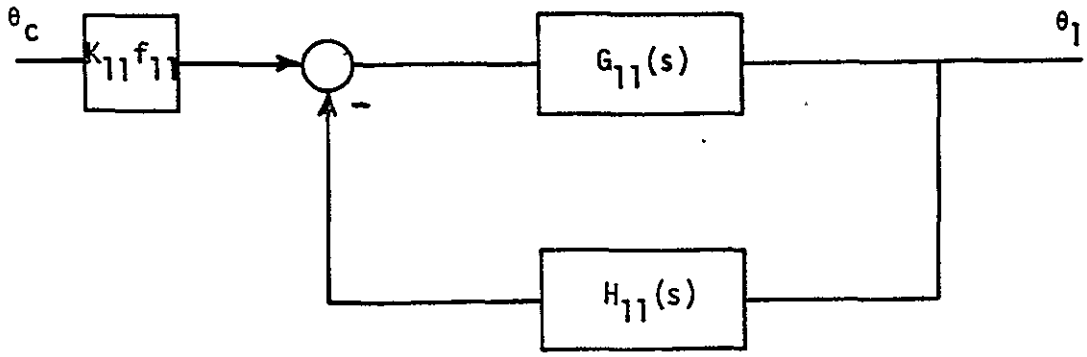

$$G_{11}(s) = \frac{\theta_1}{T_1} = \frac{1}{I_1} \frac{(s^2 - z_{11}^2)(s^2 - z_{12}^2)}{s^2 (s^2 - p_1^2)(s^2 - p_2^2)}$$

$$H_{11}(s) = K_{11}(s + f_{11})$$

Figure 6-19. Loop for Spacecraft Controller Design

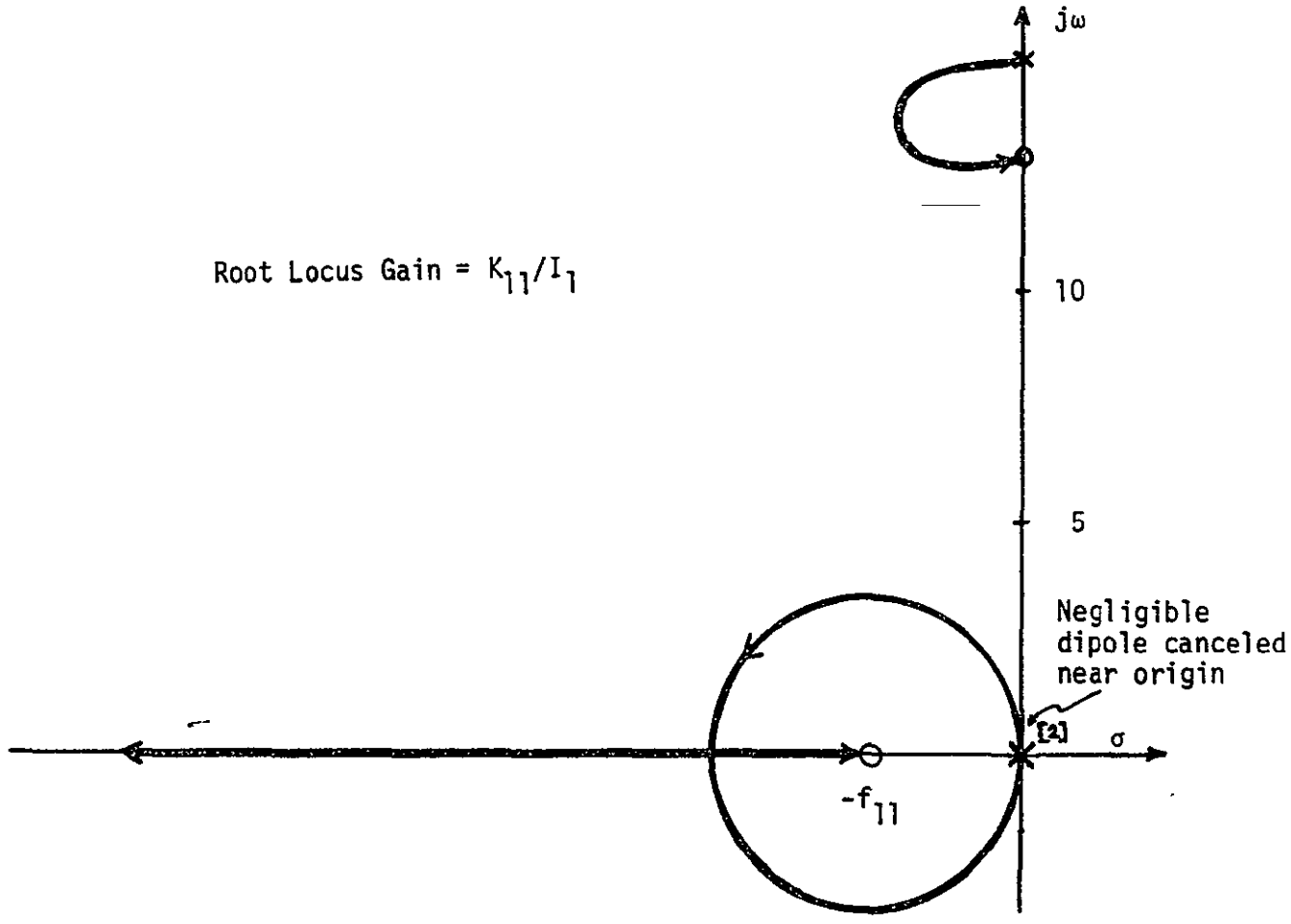

Figure 6-20. General Form of Root Locus for $G_{11}H_{11}$.

The zero at $-f_{11}$ mainly determines the bandwidth and must be determined. The upper pole-zero pair on the $j\omega$ axis is associated with the first bending mode of the boom while the low-frequency dipole is related to the torsional restraint $K_{\theta 2}$. The pair of poles at the origin is related to the combined vehicle-antenna body in free space.

For design purposes, the dipole at very low frequencies is entirely negligible. Usually the remaining boom mode pole-zero pair has only a very small effect on the root locus also, and thus it can be ignored in the first setting of f_{11}. The remaining dominant closed-loop pole pair is the basis for design and f_{11} is set to give the bandwidth approximately equal to w_n of the pair. Evaluation of the root locus gain then readily yields K_{11}.

In the final design, possible movement of the dominant pair of vehicle roots should be checked once K_{22} and f_{22} are determined since the $G_{10}(s)$ and $G_{21}(s)$ have been neglected.

Antenna Controller

With K_{11} and f_{11} determined, the vehicle loop may be closed, and the overall open-loop transfer function from $T_o(s)$ to $\alpha(s)$ may be computed. Coupling is no longer ignored. This may be done by solving the appropriate equations or by block-diagram manipulation. The steps are quite tedious and are not included here. Denote this transfer function by

$$\frac{\alpha(s)}{T_o(s)} = G_{20}'(s).$$

Then the closed loop may be drawn as in Figure 6-21. This is an exact representation for the antenna control dynamics when f_{11} and K_{11} are specified. The functional form for $G_{20}'(s)$ is given by

$$G_{20}'(s) = \frac{G_{20}(s) + [G_{20}(s)\, G_{11}(s) - G_{10}(s)\, G_{21}(s)]\, K_{11}\, (S + f_{11})}{1 + G_{11}(s)\, K_{11}\, (S + f_{11})}$$

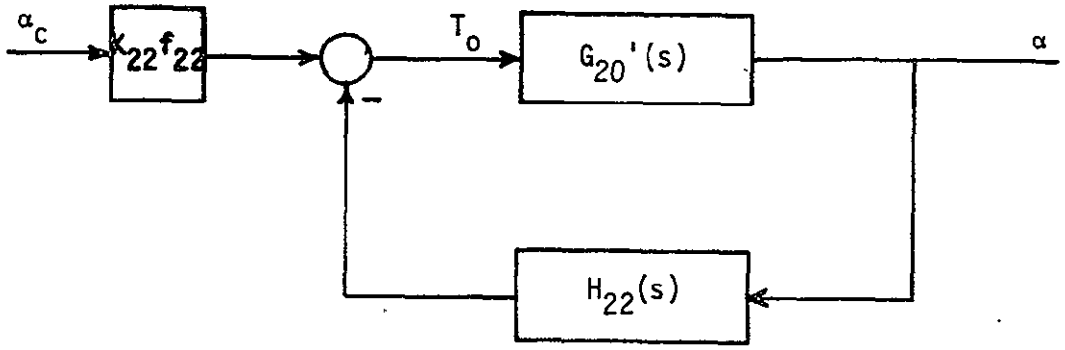

Figure 6-21. Loop for Antenna Controller Design.

Note that the closed loop poles of the vehicle loop become the open loop poles of $G_{20}'(s)$ because of the loop arrangements. When expanded into polynomial form, the poles and zeros of $G_{20}'(s)$ may be computed. The computer program of Appendix D evaluates the necessary coefficients and computes the polynomial roots in the same way as for $G_{11}(s)$.

Because of the loop arrangements, the zeros of $G_{20}'(s)$ are very nearly equal to the closed loop poles of the vehicle. An example is

$$S = -0.337 \pm j\ 0.626$$

$$S = -0.352 \pm j\ 0.636$$

and thus this dipole pair does not have any effect on the design of f_{22} and K_{22}. The resulting root locus has the general form shown in Figure 6-22. The pair of poles is shown slightly off the origin because of the torsional restraint $K_{\theta 2}$ at the hinge point. Depending on physical parameters and controller design, the boom mode pair may be close enough to the $1/S^2$ part of the locus to radically change the form of the root locus.

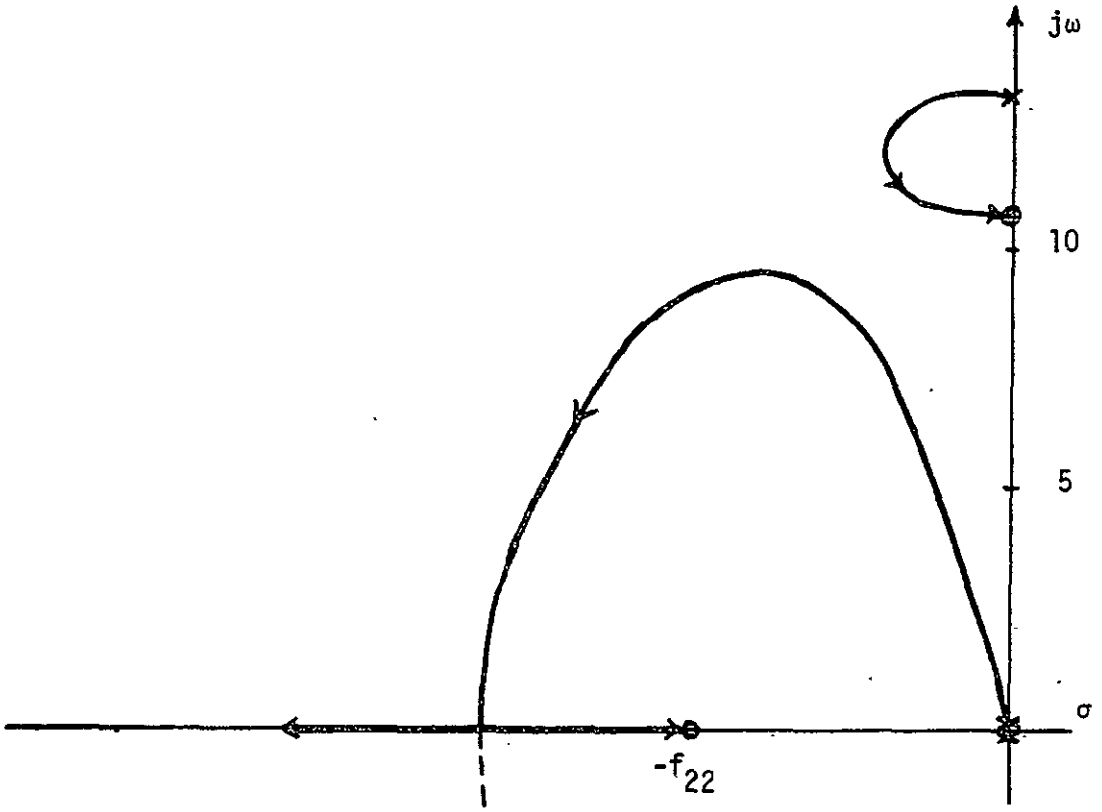

Figure 6-22. General Form of Root Locus for $G_{20}'H_{22}$.

With the root locus available, the position of f_{22} may be set to give approximately the desired bandwidth. K_{22} may be computed from the root locus gain and a check made on the final closed loop bandwidth. A typical case is shown in Figure 6-23 for L_1 = 3.05 m, L_2 = 0.3 m, EI = 33060 Nm^2 and f_{22} = 7.0. Depending on the value of controller damping selected, the natural frequency ranges from 9.5 to 12.5 rad/sec. For a value of ζ = 0.5 on the controller, a natural frequency of 9.5 rad/sec results and corresponding to the root locus gain of 75 a maximum boom damping of 0.27 is obtained.

Disregarding the negligible effects of the dipoles, the closed loop bandwidth of the controller may be quickly estimated from a Bode plot of the system function. Because of the zero at $-f_{22}$, the bandwidth is twice the natural frequency for a damping ratio of 0.7, while for a damping of 0.5

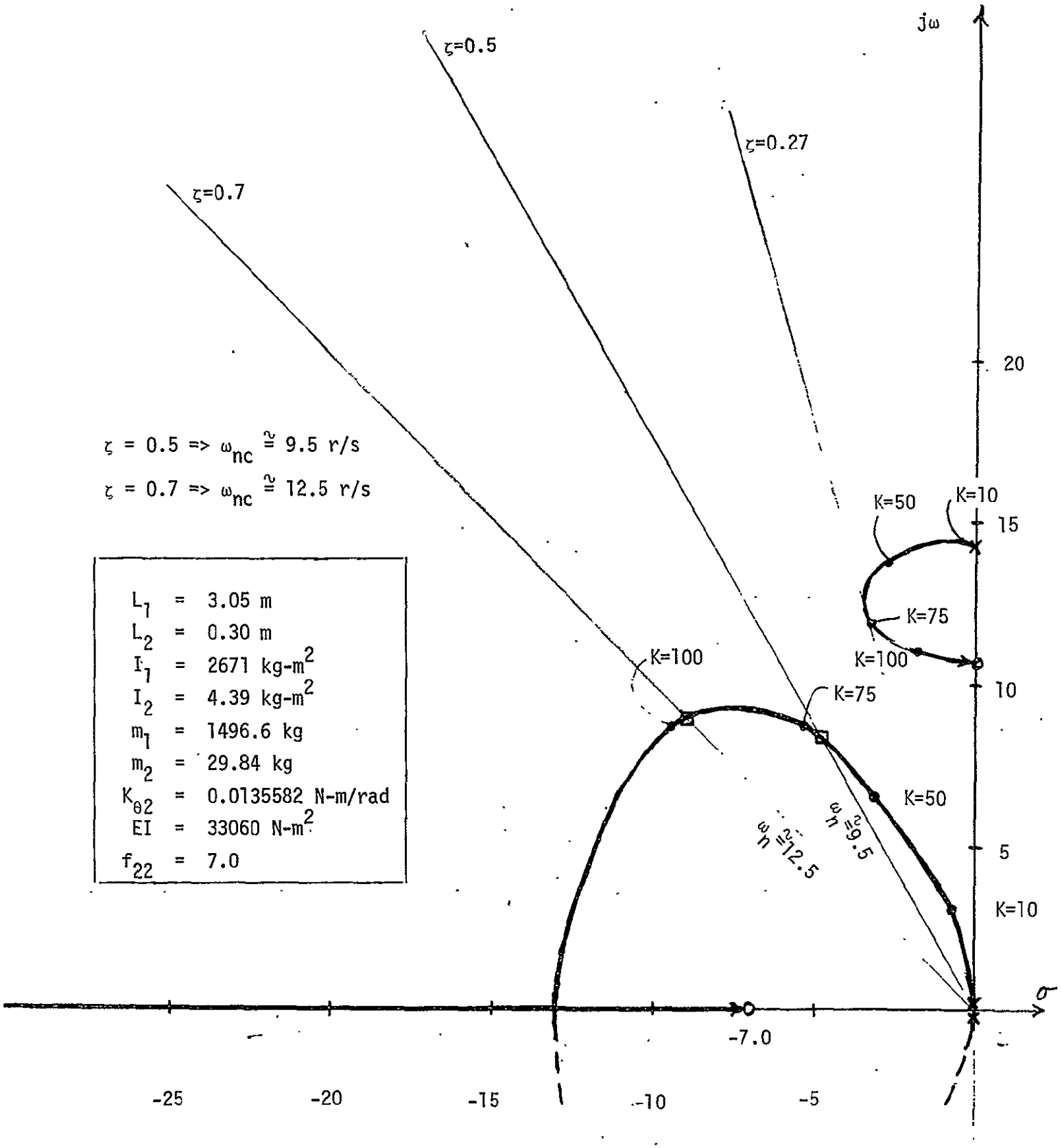

Figure 6-23. **Example Root Locus Showing Typical Bandwidths and Damping Ratios Obtainable for the Antenna Controller.**

the bandwidth is somewhat more than twice the natural frequency ω_{nc}. For brevity in following discussions, bandwidth and natural frequency are used almost synomously but the distinction should be kept in mind.

As a comparison with the boom natural frequencies indicated by the system functions, it is possible to treat the boom as a spring with a spring constant.

$$k_b = \frac{3EI}{L_1^3}$$

with a tip mass to obtain the approximate boom frequency. This is given by

$$\omega_{boom} = \sqrt{\frac{k_b}{m_2}}$$

Frequencies computed in this way are 20-25% lower than those from the root-locus plots, but calibrated curves may be plotted to yield the actual ω_{boom} from the approximation if desired.

6.2.4 Dynamic Boom Damping Studies

With the design procedures of the preceding sections, various values and parameters may be perturbed to study their effects. As already noted, the closed-loop poles of the vehicle controller form a close dipole with the zeros of $G_{20}'(s)$. Thus the effect of the vehicle controller bandwidth is negligible at least as long as it remains near 0.5 to 1.0 rad/sec. For this reason, the vehicle controller bandwidth is not varied in the following studies.

To fully characterize the dependence of achievable boom damping on boom stiffness EI and antenna controller natural frequency, a series of designs was examined. Root locus plots were generated for many different cases and achievable boom damping was studied parametrically. The baseline system used the parameters

$$L_1 = 3.05 \text{ m (10 ft)} \qquad L_2 = 0.3 \text{ m (1 ft)}$$

$$K_{11} = 2003 \frac{\text{Nm}}{\text{rad/sec}} \qquad f_{11} = 0.75 \text{ sec}^{-1}$$

Boom stiffness EI was varied between 60,000 pound-feet^2 and 500,000 pound-feet^2, i.e.,

$$24{,}795 \text{ Nm}^2 \leq EI \leq 206{,}625 \text{ Nm}^2$$

and the antenna controller natural frequency was varied between 7 and 25 rad/second with the damping ratio ζ_c constrained to remain between 0.5 and 0.7. The results are summarized in Figures 6-24 and 6-25 where achievable boom damping is plotted versus boom natural frequency. The boom frequency is that shown on the root locus plots, i.e., vehicle and antenna hinge dynamics are included, and it is about 20% higher than the frequency obtained from the simple boom formula given earlier. As will be shown, the most meaningful design criterion is ω_{boom} relative to ω_{nc}. It may be recalled that ω_{boom} is a function of L_1, M_2, and EI, and if L_1 and M_2 are fixed, ω_{boom} is directly proportional to EI. In Figures 6-24 and 6-25, the boxed legends contain the values of EI in pound-feet^2 that correspond to plotted points on the curves directly below. Also entered are the corresponding values of antenna controller natural frequency and damping.

Figure 6-24 displays the dynamic boom damping versus boom natural frequency when the antenna controller natural frequency is held constant at 11.0 and at 22.0 rad/second. The peaks are not too sharp thus showing moderate sensitivity to boom frequency, and the peak attinable values are almost equal. The slight improvement at increased bandwidth is negligible.

Figure 6-25 shows the boom damping when the largest attainable value is chosen with the antenna controller damping constrained to be in the design interval of $0.5 \leq \zeta_c \leq 0.7$ and the natural frequency is allowed to vary about some nominal value. In the present case, this implies choosing the lowest permissible ζ_c value as shown in the legend of Figure 6-25. Now the peak attainable boom damping is equal for the low and high bandwidth

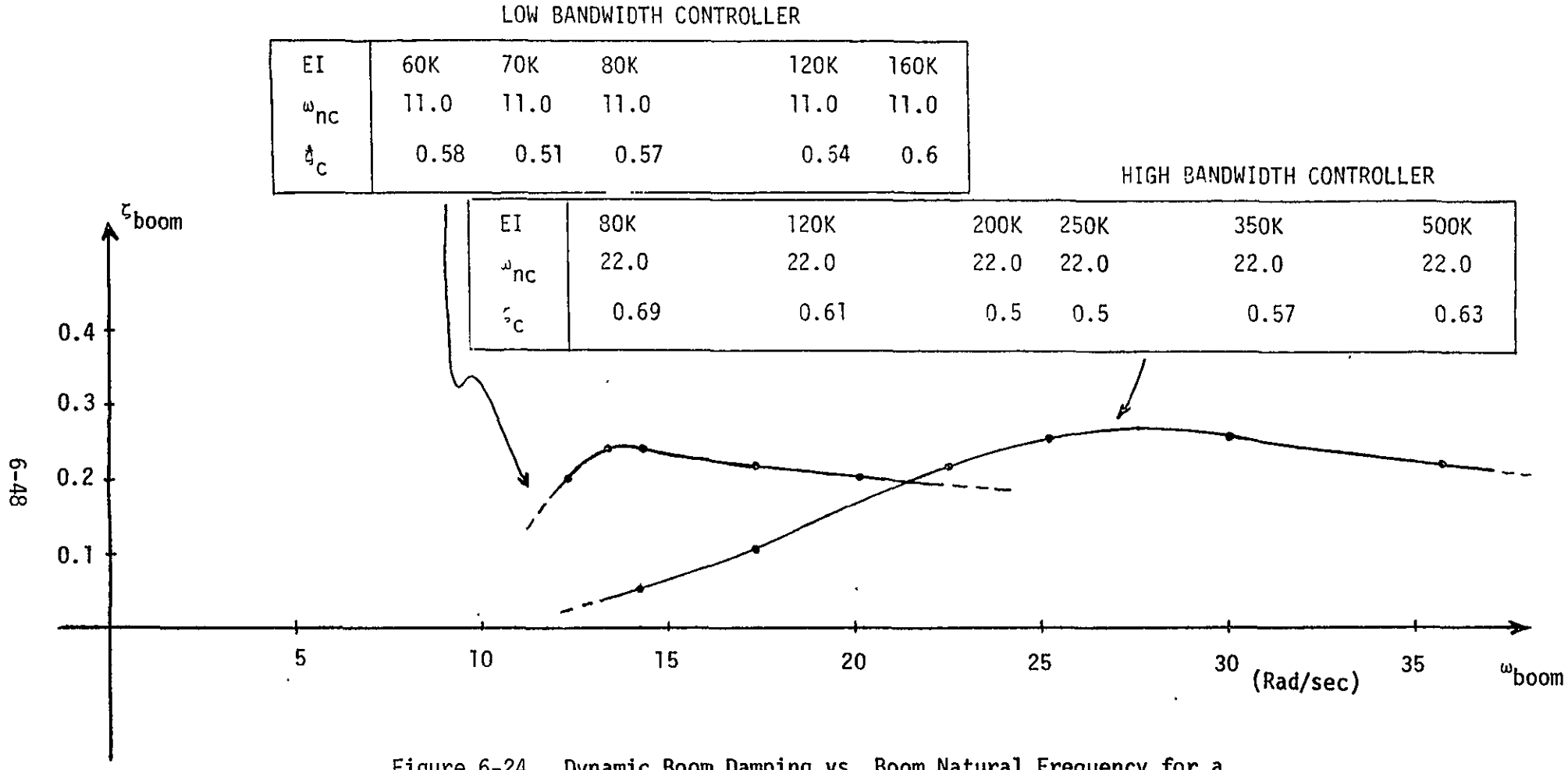

Figure 6-24. Dynamic Boom Damping vs. Boom Natural Frequency for a Fixed Value of Antenna Controller Natural Frequency ω_{nc}.

The boxes contain values for EI in lb-ft^2, the closed loop antenna controller natural frequency, ω_{nc}, and controller damping ζ_c which correspond to the plotted points directly beneath on the respective curves.

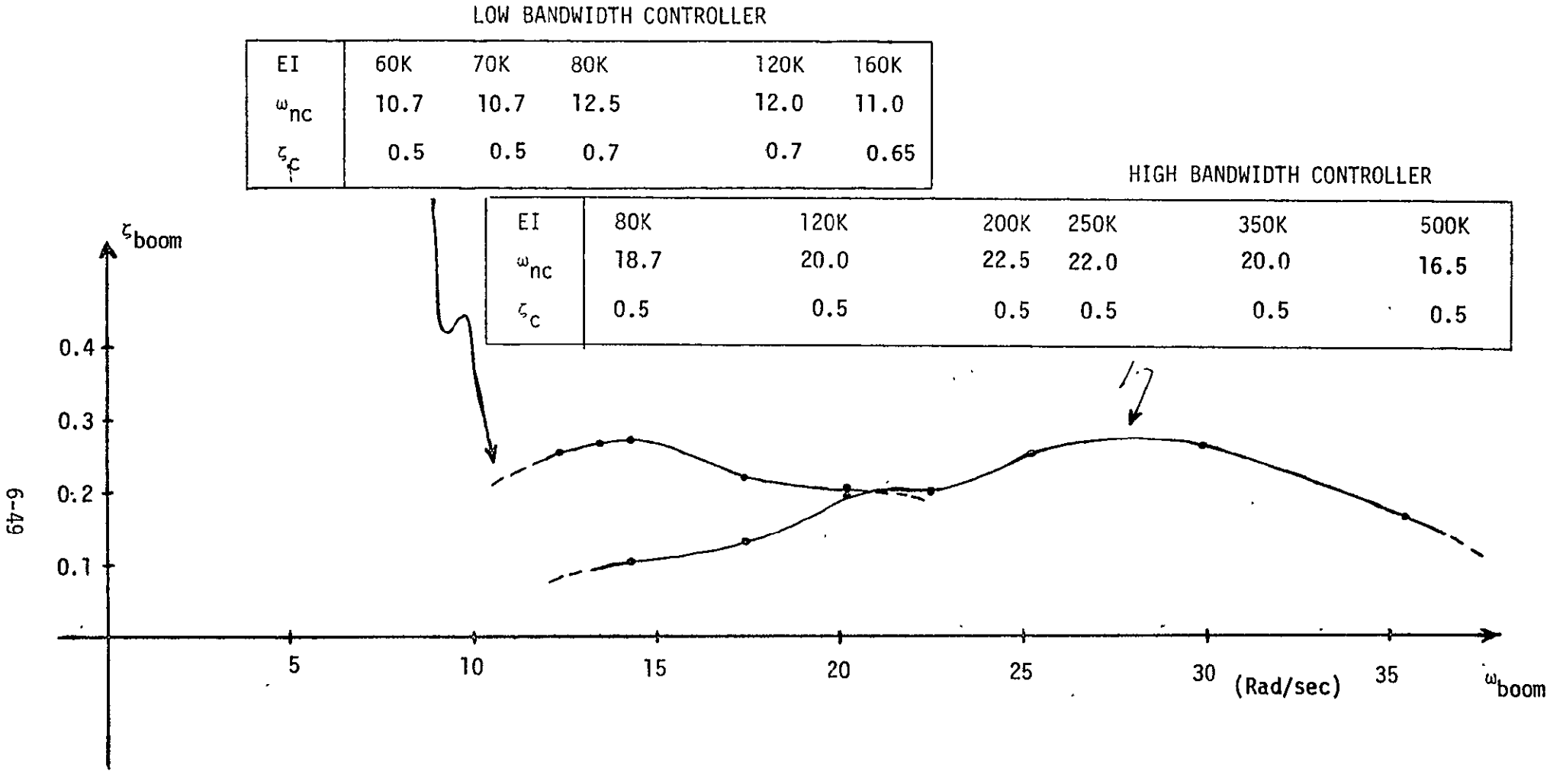

Figure 6-25. Dynamic Boom Damping vs. Boom Natural Frequency with Antenna Controller Damping Ratio Constrained to the Design Interval of 0.5 to 0.7.

The boxes contain values for EI in lb-ft^2, the closed loop antenna controller natural frequency, ω_{nc}, and controller damping ζ_c which correspond to the plotted points directly beneath on the respective curves.

cases. It is, however, important to note the need for increased boom stiffness as controller bandwidth is increased if boom damping is to be maintained. This translates physically into the fact that a very soft boom is difficult to damp while on the other hand the frequency of a stiffer boom must still be sufficiently near the controller frequency so that the controller "sees" the boom vibrating and can act to dampen the vibration. An interesting ratio may be computed as $\omega_{boom}/\omega_{nc}$ and in both cases the ratio is about 1.4. If this ratio is written in terms of the bandwidth of the controller, the result is ω_{boom} = 0.7 x bandwidth (assuming 0.7 damping for the antenna servo). This clearly shows that ω_{boom} must be within the bandwidth of the controller for maximum achievable boom damping.

The overall importance of the preceding four curves in Figures 6-24 and 6-25 is that an optimum boom stiffness exists when dynamic boom damping is to be maximized. Or conversely, if the boom stiffness is design-fixed, an optimum controller bandwidth (natural frequency) exists and should be determined. The latter may be constrained by servo performance requirements. The preceding study was discussed for a nominal 3.05 inch (10 feet) boom, but additional studies with various boom lengths indicated similar trends. This is clear, since ω_{boom} in effect is a normalized variable containing boom length, boom stiffness and tip mass.

Another, perhaps more meaningful criterion for selecting (optimum) boom stiffness and antenna controller parameters is the following. The response of the antenna boom may be considered to be damped, oscillatory, and second-order. Then, if rapid decay to small amplitude oscillation is considered the primary design criterion, the envelope time constant should be minimized as a function of boom stiffness. Using Figures 6-24 and 6-25, the attainable boom damping ζ_{boom} has been multiplied by the corresponding ω_{boom} and replotted here in Figures 6-26 and 6-27. The product of $\zeta_{boom}\ \omega_{boom}$ is the reciprocal envelope time constant of the damped second-order pole pair corresponding to the boom response and thus it is the quantity to be maximized.

LOW BANDWIDTH CONTROLLER

EI	60K	70K	80K	120K	160K
ω_{nc}	11.0	11.0	11.0	11.0	11.0
ζ_c	0.58	0.51	0.57	0.54	0.6

HIGH BANDWIDTH CONTROLLER

EI	80K	120K	200K	250K	350K	500K
ω_{nc}	22.0	22.0	22.0	22.0	22.0	22.0
ζ_c	0.69	0.61	0.5	0.5	0.57	0.63

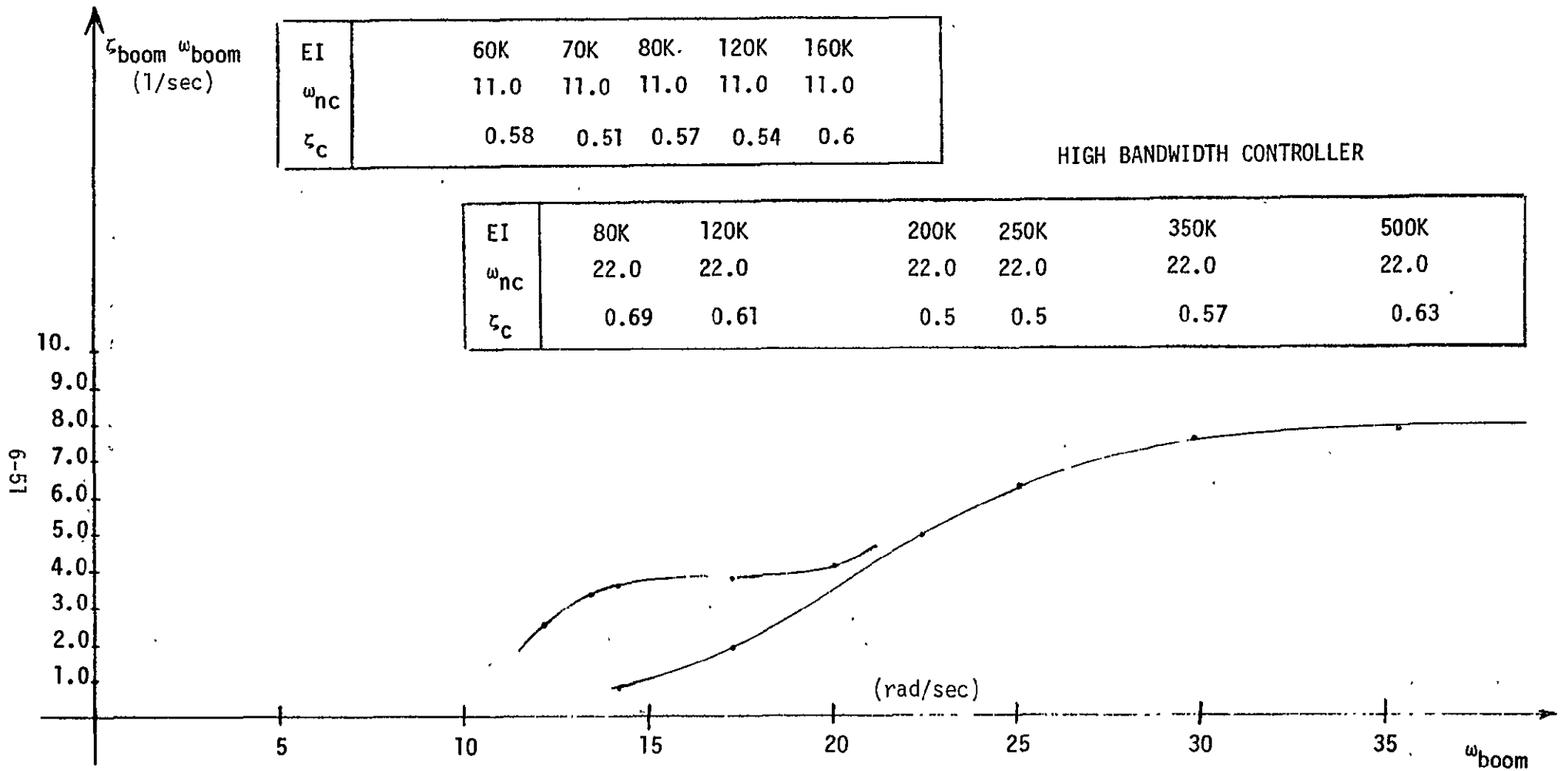

Figure 6-26. Reciprocal Time Constant ζ_{boom} vs. Boom Natural Frequency for a Fixed Value of Antenna Controller Natural Frequency ω_{nc}.

The boxes contain values for EI in lb-ft^2, the closed loop antenna controller natural frequency, ω_{nc}, and controller ζ_c which correspond to the plotted points directly beneath on the respective curves.

LOW BANDWIDTH CONTROLLER

EI	60K	70K	80K	120K	160K
ω_{nc}	10.7	10.7	12.5	12.0	11.0
ζ_c	0.5	0.5	0.7	0.7	0.65

HIGH BANDWIDTH CONTROLLER

EI	80K	120K	200K	250K	350K	500K
ω_{nc}	18.7	20.0	22.5	22.0	20.0	16.5
ζ_c	0.5	0.5	0.5	0.5	0.5	0.5

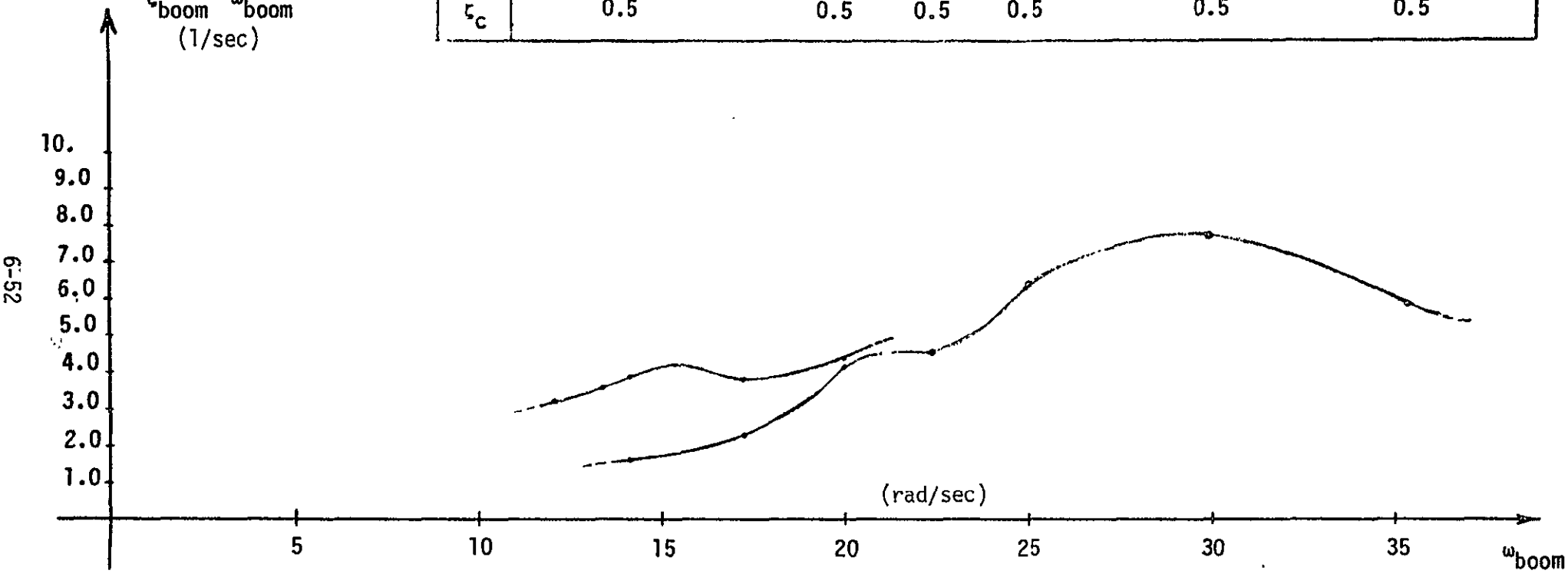

Figure 6-27. Reciprocal Time Constant ζ_{boom} vs. Boom Natural Frequency with Antenna Controller Damping Ratio Constrained to the Design Interval of 0.5 to 0.7.

The boxes contain values for EI in lb-ft^2, the closed loop antenna controller natural frequency, ω_{nc}, and controller damping ζ_c which correspond to the plotted points directly beneath on the respective curves.

Figure 6-26 shows the attainable reciprocal time-constant when the antenna controller natural frequency is held constant over the range of boom stiffness 24795 to 206625 N-m^2 (60,000 to 500,000 lb-ft^2). The shorter curve corresponds to an 11 rad/sec controller natural frequency while the other is for 22 rad/sec. Both curves show a region of saturation where further increase of boom stiffness does not yield faster envelope decay. The 11 rad/sec case indicates that the ω_{boom} factor begins to predominate at around 160,000 lb-ft^2 boom stiffness (ω_{boom} = 20 rad/sec), and the same behavior is expected for the 22 rad/sec curve at some value of stiffness above 500,000 lb-ft^2 (ω_{boom} = 35 rad/sec). Since the ζ_{boom} is decreasing beyond a certain point on both curves, an increased number of boom oscillations are being traded for faster decay time.

It is important to finally note in Figure 6-26 that the minimum attainable time constant is smaller for the case of a higher bandwidth antenna controller. This is in contraxt to Figures 6-24 and 6-25 where the peak damping ζ_{boom} is nearly the same for both low and high antenna controller bandwidth.

Figure 6-27 shows the attainable reciprocal time-constant when the optimum antenna controller damping ratio is selected within the design interval of 0.5 to 0.7. Except for small local variations, the behaviors and magnitude of the two cases are now quite similar to that in Figure 6-26 The exception is that there is a maximum around ω_{boom} = 30 rad/sec. Beyond this the time constant begins to increase again indicating longer decay times. Again, a faster decay time is obtainable for case of the high bandwidth antenna controller.

6.2.5 Antenna Boom Deflection Responses

Using the previous design results, a simulation was generated to obtain the form and amplitude of the boom deflection angle θ_b and the vehicle response. The coupled vehicle-antenna control system were shown in Figure 6-18.

Responses for a step $\alpha_c(t)$ command and a ramp $\alpha_c(t)$ command are considered here for the 11 rad/second and 22 rad/second natural frequency antenna controllers. For the 11 rad/second controller, the above studies indicated a boom stiffness of approximately 49,590 N-m^2 (120,000 pound-feet^2) while the 22 rad/second controller requires a stiffness of at least 144,637 N-m^2 (350,000 pound-feet^2) to obtain the fastest transient decay time. Boom motion in response to a unit step antenna angle command for these two cases are shown, respectively, in Figures 6-28 and 6-29. The upper plot of each Figure shows the vehicle attitude θ_1 while the middle plot shows the antenna angle α. The lower plot shows the boom deflection angle. Since the step input is unity and the system model is linear, the outputs may be scaled by inspection for various input units of interest. Degrees are indicated in the Figures.

At times the antenna will be steered with a slewing command which is taken here to be a representative 2 degrees/second. For other ramp inputs, the outputs may be scaled accordingly. Figure 6-30 shows the low (11 rad/second) natural frequency controller case while Figure 6-31 shows the high (22 rad/second) controller case. For both step and ramp inputs, the higher frequency response associated with the higher boom stiffness EI is evident in the plots. Also evident is the period of the vehicle controller. With the design value of ω_{ns} = 0.7 rad/second natural frequency for the vehilce controller, the period of $T = 2\pi/0.7 = 8.98$ is that shown in the plots. Note that the initial vehicle attitude transient in response to the antenna ramp command dies out quickly as the antenna continu-s to track/slew.

At the time the system designs were performed, the representative value of hinge restraint $K_{\theta 2}$ was 0.0135 N-m/rad which turns out to be slightly greater than the present estimate of 0.0093 N-m/rad. It was ascertained in design studies that the small hinge restraint $K_{\theta 2}$ has an almost negligible effect on responses α and vehicle attitude θ_1. However, a part of the boom deflection θ_b may be shown to be nearly proportional to $K_{\theta 2}$ as follows. From Equation (C-18) in Appendix C, the following equation may be obtained.

Figure 6-28. System step responses, 11 rad/sec controller

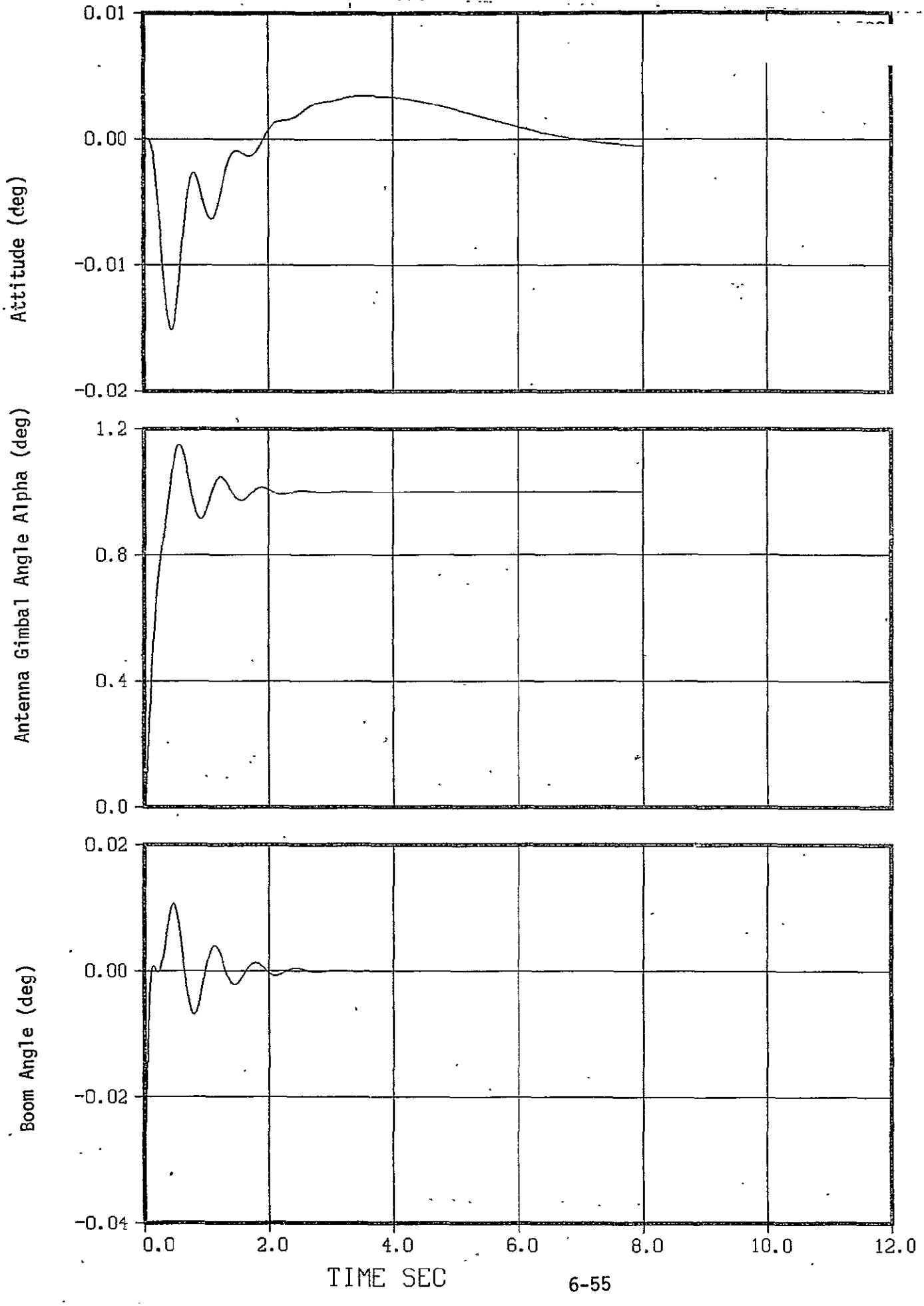

Figure 6-29. System step responses, 22 rad/sec controller

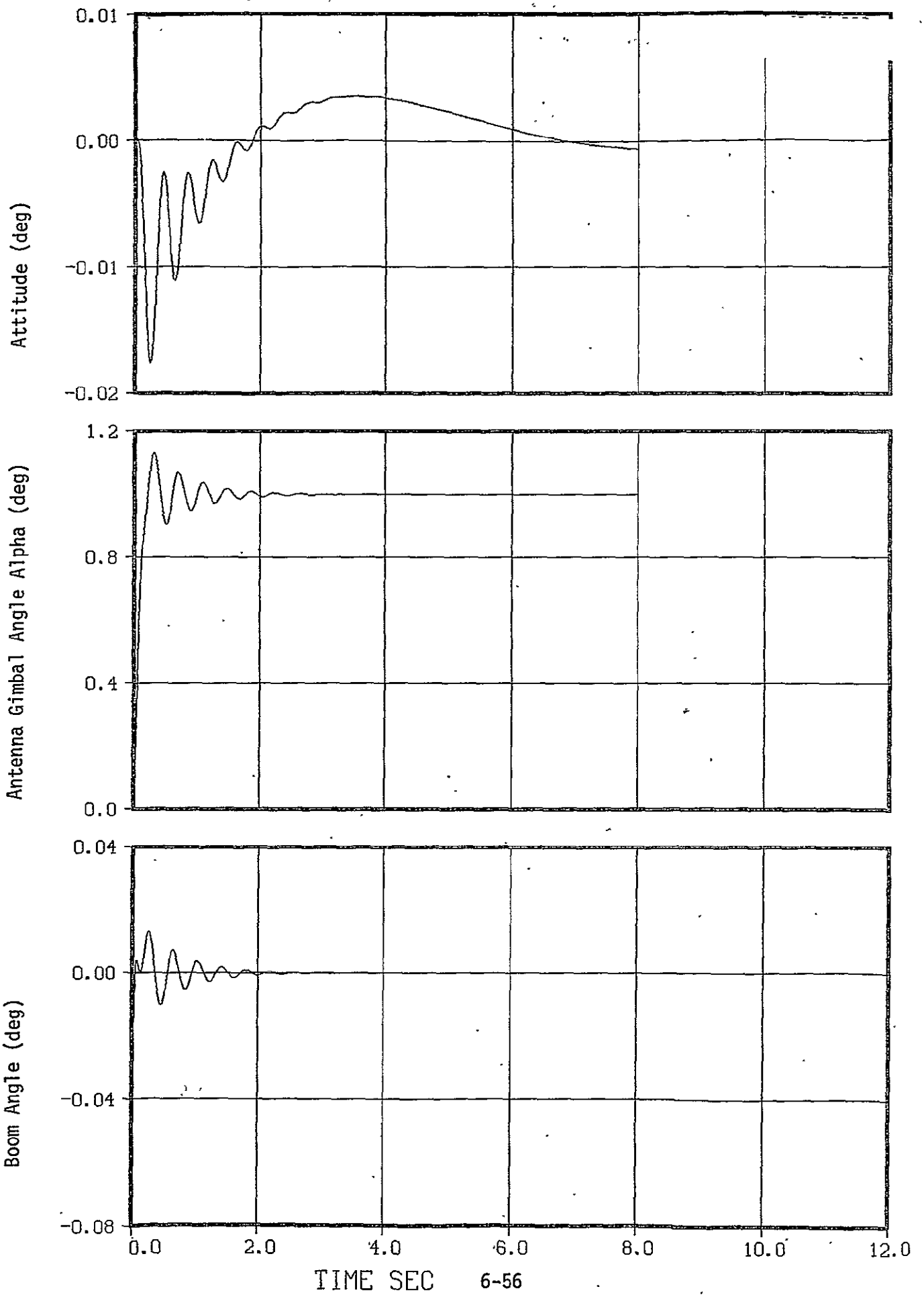

Figure 6-30. System ramp responses, 11 rad/sec controller

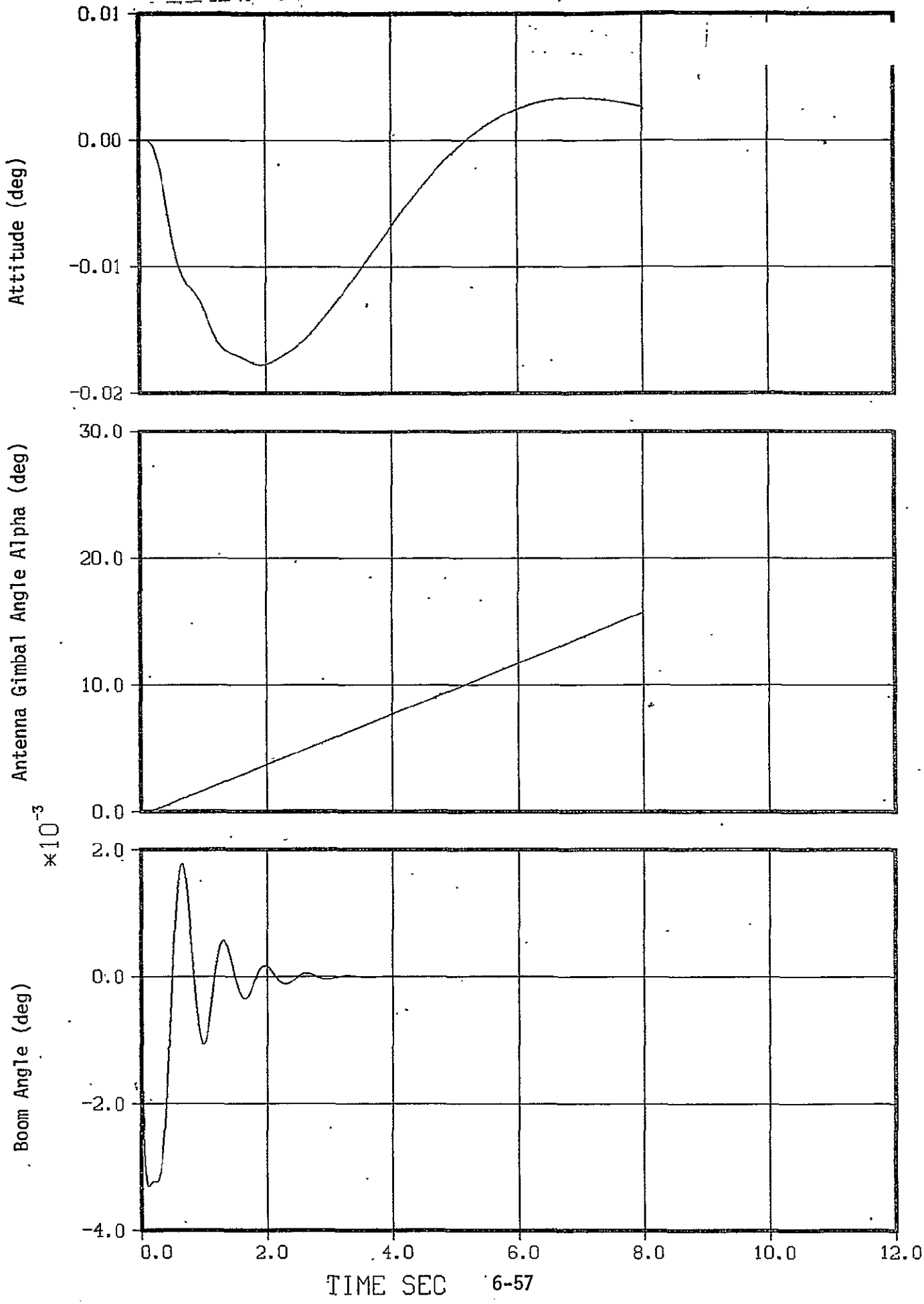

Figure 6-31. System ramp responses, 22 rad/sec controller

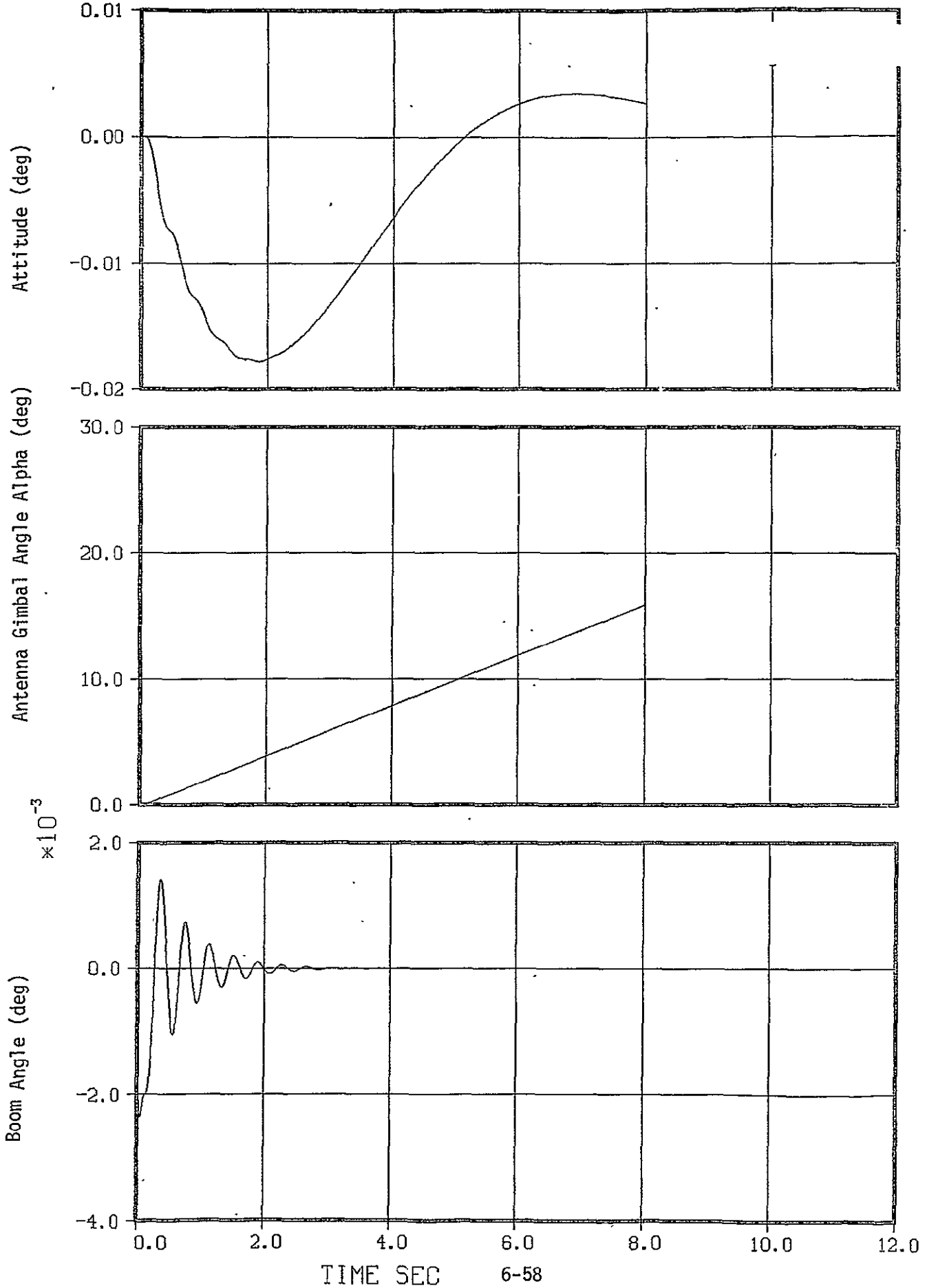

$$\theta_b \left(K_{\theta 2} + \frac{4EI}{L_1} - \frac{6EI}{L_1^2} y_b \right) = -T_o$$

where y_b is the lateral hinge point displacement, and T_o is the controller torque on the antenna. For the present flexible boom that is uniformly curved, the bending displacement y_b can be approximated by $L_1 \theta_b/2$. Inserting the latter expression in the preceding equation yields

$$\theta_b = K_{\theta 2} \frac{L_1}{EI} (\alpha - \theta_1) - \frac{L_1}{EI} T_o$$

For the present situation, with $K_{\theta 2}$ 0.01, the coefficient of the first term is two orders of magnitude smaller than the L_1/EI value and so the effect of $K_{\theta 2}$ on the boom is also nearly negligible. The preceding equation also shows that the boom deflection is inversely proportional to the stiffness EI as expected.

6.3 Flexible Solar Array Effects

Approximate single-axis models are used to study the effects of the solar array stepping motion on the vehicle attitude jitter for the LANDSAT-D spacecraft. Bending and torsional modes of array vibration are considered for the fundamental mode frequencies, and higher mode frequencies are computed. The higher modes are compared to the present cogging (stepping) frequency and it is found that torsional modes 4 and 5 are close to integer multiples of the cogging frequency.

The analyses here indicate that the bending disturbance from the array is small and that the total vehicle pitch disturbance from cogging is $\pm$ 5.5 μrad which is approximately one-half the budget of $\pm$ 10.6 μrad. Both the torsional and bending responses are stable for the lowest mode frequencies.

The analyses conducted here must be viewed as preliminary, since only simplified single-axis dynamic models were used. The actual problem is

much more complex, mainly due to the 37.5 degree cant angle of the array and the existence of higher order flexible modes.

Further investigation is, therefore, strongly recommended using more complete multi-axis dynamic models together with flexible array models to definitize vehicle jitter levels. Also, the responses of higher modes, particularly torsional modes 4 and 5, should be examined for jitter response levels if the present cogging frequency of 3.41 Hz (0.018 degree/step) is retained. Possible torsional modes arising from the flexible array shaft and spring constant of the harmonic-drive gear reduction may also require modelling and analysis.

6.3.1 Spacecraft and Array Bending Model

This brief study examines the effects that a flexible driven solar array has on the spacecraft attitude control system with respect to stability and pointing jitter. A preliminary spacecraft attitude control system design has been performed in Section 6.2 with necessary consideration given to the effects of a flexible antenna boom and an antenna controller. Using those design values, the purpose here is to determine how the motion of the flexible solar array affects the pointing stability of the spacecraft.

The problem is considerably complicated by the fact that the solar array is canted at an angle of 37.5 degrees to the main spacecraft body as shown in Figure 6-32. This immediately calls for a three-axis flexible-body modelling and analysis which is beyond the scope (available time/funding level) of the present study. Thus, some simplified analyses based on approximate models are performed and points of further study are outlined.

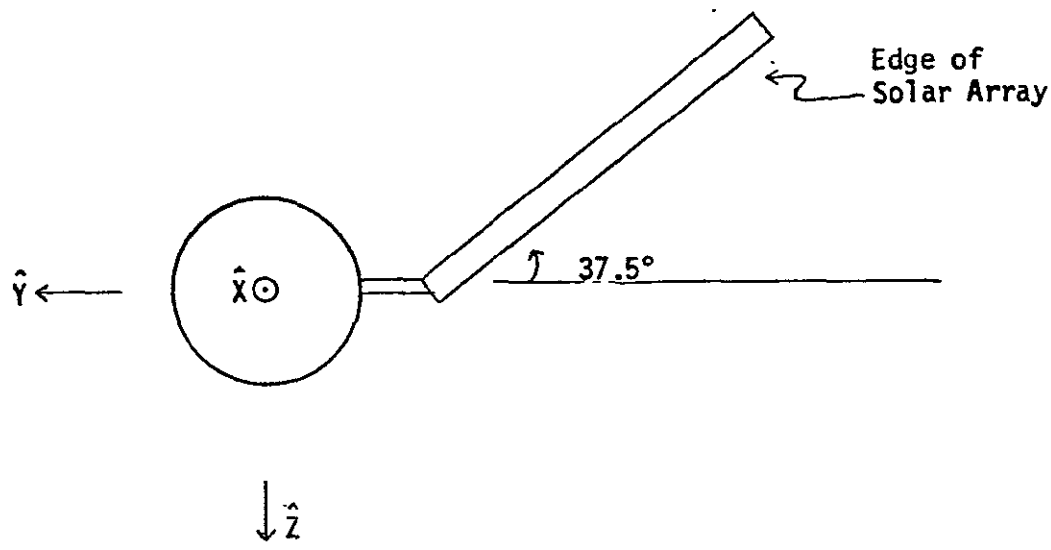

Figure 6-32. Array Orientation for Maximum Disturbance Torque

The array is known as a FRUSA (Flexible Rolled-Up Solar Array) and its structural complexity does not lend itself to simple modelling. However, structural information indicates that the array consideration as a flat plate has first bending frequency modes of 0.3 Hz (torsional mode) about the axis of rotation, and 0.08 Hz (bending mode) about an axis perpendicular to the axis of rotation and in the array plane. The possible interaction of these mode frequencies and their higher mode counterparts with the array cogging frequency is an integral aspect of the overall problem.

Since the roll moment of inertia I_{xx} is the smallest, the flapping motion of the array will produce the greatest effect on the main body when the array is oriented as shown in Figure 6-32 or when it is rotated 180 degrees. Analytically these positions are equivalent. The supporting shaft from the solar array drive unit is considered perfectly rigid for analysis at this time. In orbit, the array is being driven by a positive pitch axis cogging torque which advances the array 0.018 degree per step. This cogging motion induces a bending of the array about its root, and the bending then exerts a roll torque on the main body.

Since the distance from the main body center-of-mass to the root of the array is small compared to the array length, it is reasonable to model the bending as shown in Figure 6-33.

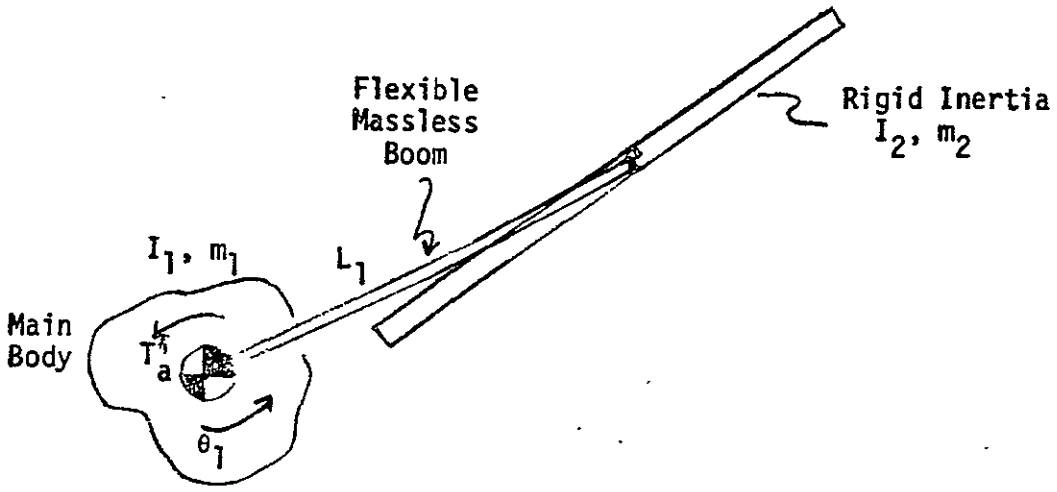

Figure 6-33. Analytic Dynamical Model of Array

T'_a represents the disturbance torque acting in roll which results from the array being stepped in the pitch axis. This interaxis coupling occurs because the array is canted. Magnitude and shape of this torque are established in the next section.

Since the lowest mode frequency is known, an equivalent boom stiffness EI may be computed from basic beam relations as follows:

$$w_1 = \sqrt{\frac{k}{M + .23m}}$$

where $$k = \frac{2\,EI}{\ell^2}$$

and M is the cantilevered mass, m is the boom mass and ℓ is the length. Inserting known values and solving for EI yields

$$EI = 178.8 \text{ N-m}^2$$

which is a low number as expected for a flexible array.

The equations of motion are derived in Appendix E and yield the following open-loop transfer function between $\theta_1(s)$ and $T_a'(s)$.

$$\frac{\theta_1(s)}{T_a'(s)} = G(s) = \frac{\alpha_4 s^4 + \alpha_2 s^2 + \alpha_o}{s^2 (\beta_4 s^4 + \beta_2 s^2 + \beta_o)} \qquad (6.3\text{-}1)$$

where the α_2 and β_2 are as defined in Appendix E.

The roll axis controller is treated here as rate plus position as discussed previously. Gain parameters consistent with the design procedure must be used here and these result in a roll system with 0.5 damping and natural frequency ω_n = 0.75 rad/second. With the roll axis controller prescribed, the closed-loop system may be drawn as in Figure 6-34.

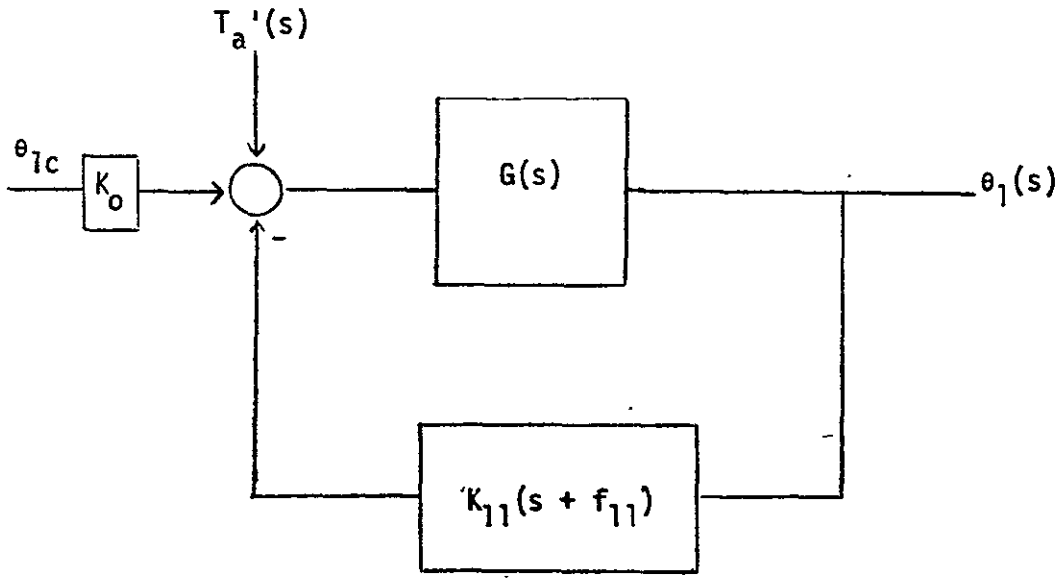

Figure 6-34. Closed-Loop Control System

Writing the overall closed-loop transfer function yields

$$\frac{\theta_1(s)}{T_a'(s)} = \frac{a_4 S^4 + a_2 S^2 + a_o}{b_6 S^6 + b_5 S^5 + b_4 S^4 + b_3 S^3 + b_2 S^2 + b_1 S + b_o} \qquad (6.3\text{-}2)$$

where

$$a_4 = \alpha_4 \qquad a_2 = \alpha_2 \qquad a_o = \alpha_o$$
$$b_6 = \beta_4 \qquad b_5 = K_{11}\,\alpha_4 \qquad b_4 = \beta_2 + K_{11}\,f_{11}\,\alpha_4$$
$$b_3 = K_{11}\,\alpha_2 \qquad b_2 = \beta_o + K_{11}\,f_{11}\,\alpha_2$$
$$b_1 = K_{11}\,\alpha_o \qquad b_o = K_{11}\,f_{11}\,\alpha_o.$$

Using the roll axis values for f_{11} and K_{11}, the closed-loop roots may be computed. When this is done, a dipole-pair cancellation may be made for the following pole-zero pair.

Numerator: $0.0 \pm j\ 3.0720$

Denominator: $.00058 \pm j\ 3.0742$

and the resulting transfer function becomes

$$\frac{\theta_1(s)}{T_a'(s)} = \frac{3.74 \times 10^{-4}\,(S^2 + 0.21)}{(S^2 + 0.96S + 0.79)\,(S^2 + 0.017\,S + 0.14)} \qquad (6.3\text{-}3)$$

It can be seen that the response will contain two second-order component responses one of which is very lightly damped. This is the array response with an $\omega_n = 0.37$ (0.06 Hz) and damping ratio of 0.023. The remaining complex pair of poles represents the attitude controller response with $\omega_n = 0.89$ and damping ratio 0.54. The periodic solar array disturbance torque T_a' is modelled in the next section, but first the unit-step response is shown to display the basic behavior.

Figure 6-35 shows the unit-step response of the system to a vehicle torque command which represents the array roll torque on the vehicle. The upper trace represents the attitude-controller contribution while the middle trace is the array response contribution. The sum of these two, plus the constant step-term not plotted, yield the bottom trace which is the net vehicle bending step response. As expected, the lightly damped array mode response persists for a considerable time, but the responses are stable. The purpose of the plot is to show the form of the response, and thus the input is a 1 N-m step torque which is orders of magnitude greater than the expected torque input. Also the 3.7×10^{-4} factor of Equation (6.3-3) was not included in the plots for simplicity. The actual offset shown may easily be computed to be 1.9 from the function in (3-3) and this agrees with the value in the total response.

6.3.2 Approximation of Array Torques on Vehicle

Although the step-response is informative, the periodic response of the vehicle to the periodic bending array mode is of more significance, and although the exact form of the array torque T_a' cannot be found without extensive additional multi-axis modelling and simulation, an approximation to it can be found as follows. The applied torque about the array shaft may be approximated as shown in Figure 3-36 and from it the angular pitch velocity of the array may be determined by considering the vehicle to be fixed.

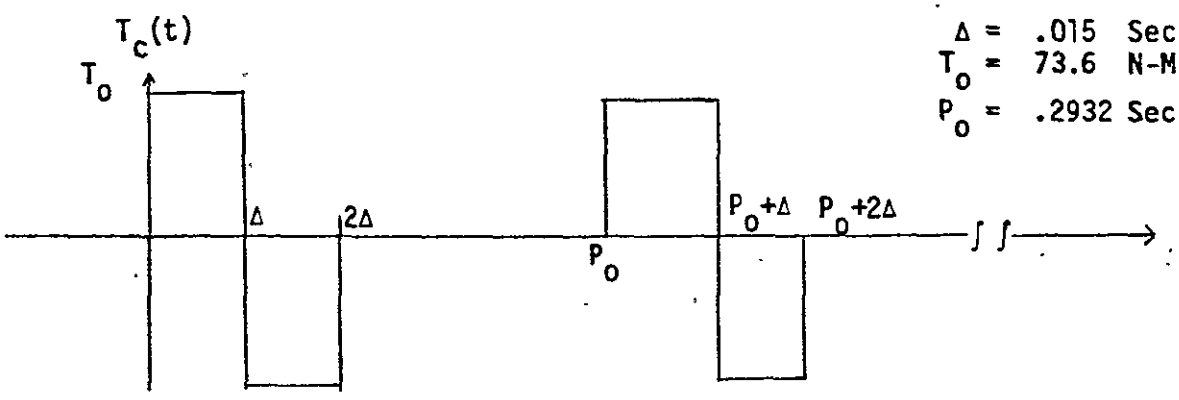

Figure 6-36. Cogging Torque Pulse Train

Figure 6-35. VEHICLE RESPONSE WITH ARRAY MODE 1

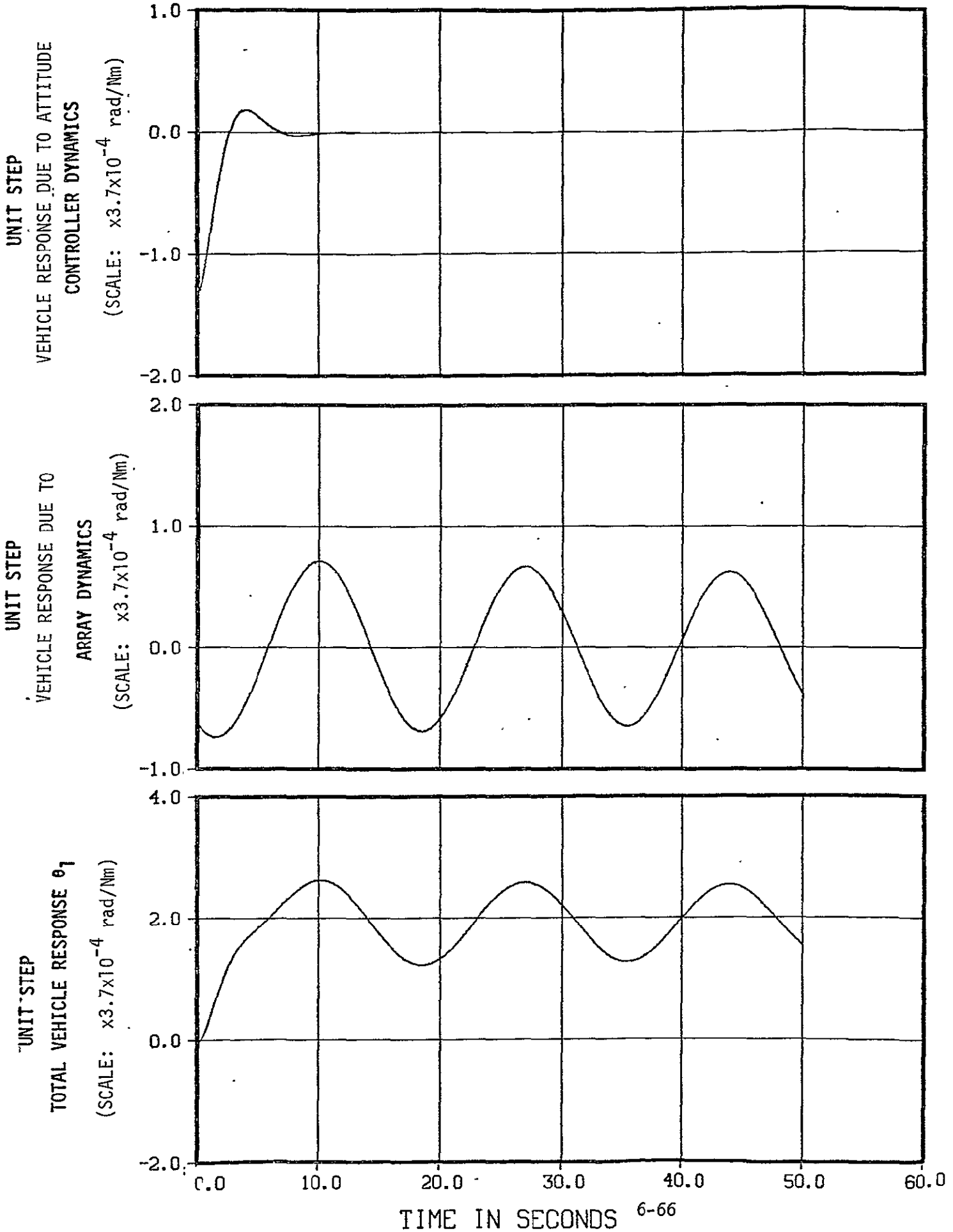

The angular velocity $\Omega(t)$ may be found by simply integrating $T_c(t)/I$ where I is the inertia of the array. Doing this yields the triangular wave train shown in Figure 3-37.

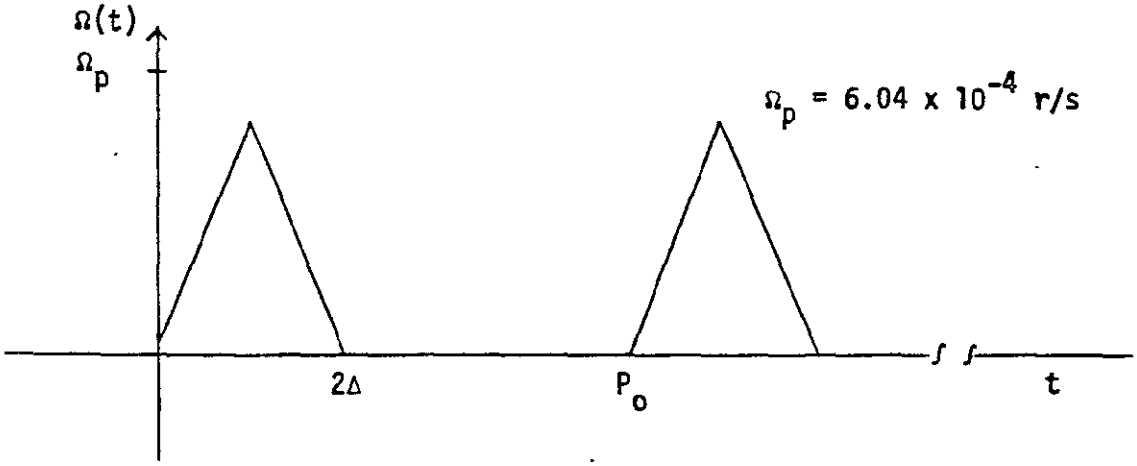

Figure 6-37. Array Angular Velocity Profile

Approximating the centrifugal force by $f_c(t) = mr\Omega^2(t)$ where r is the radius from the pitch axis to the array center of mass, the force acting on the center of the array takes the form of parabolic segments as shown in Figure 6-38.

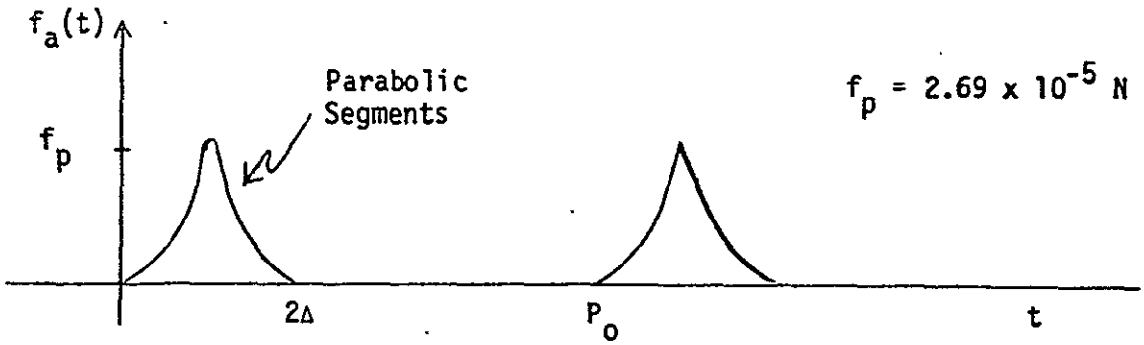

Figure 6-38. Array Centrifugal Force Profile

The geometry of the problem shows that there is a moment arm of 8.3 m from the array center-of-mass to the vehicle center-of-mass, and this used with the normal component of $f_a(t)$ permits evaluation of the array torque profile. It has the same form as shown in Figure 6-38, but a different amplitude. The peak amplitude of the pulse train is easily shown to be 1.77×10^{-4} N-m which may be applied as input to the transfer function in (6.3-3).

6.3.3 Vehicle Response to First Bending Mode

A simulation was developed to model the system of Figure 6-34 and the array torque of the preceding section was applied as input. Since the time interval Δ is small relative to the change in torque, a linear triangular approximation to the parabolic wave form was used. Figure 6-39 shows a short sequence of input pulses and the resulting output response. The response corresponds in a way to the rising early portion of the step response in Figure 6-35, since the train of torque pulses has a constant average value. The roll attitude will, therefore, converge to a small roll offset, since the simplified ACS model used here did not contain integral compensation. The jitter response of interest is barely discernable. To measure the jitter, a portion of the plot was expanded and replotted as shown in Figure 6-40. Based on it, the peak-peak jitter value is 2.26×10^{-9} rad which is very small compared to the specification allowance of $\pm$ 10.6 μrad jitter over a 20-minute interval (1σ). The step response hang-off portion of the response can be ignored because in the steady-state condition it will decay to zero when integral compensation is present, leaving only the forced jitter response. If the estimated amplitude of the triangular array torque is estimated in a very conservative manner, then a simple ratio of amplitudes shows that 0.83 N-m peak array torque T_a' may be tolerated before the $\pm$ 10.6 μrad specification is reached. While the 2.26×10^{-9} rad jitter is very small, it does agree with published remarks concerning the FRUSA array interaction with the attitude control system in physical experiments Reference 9.

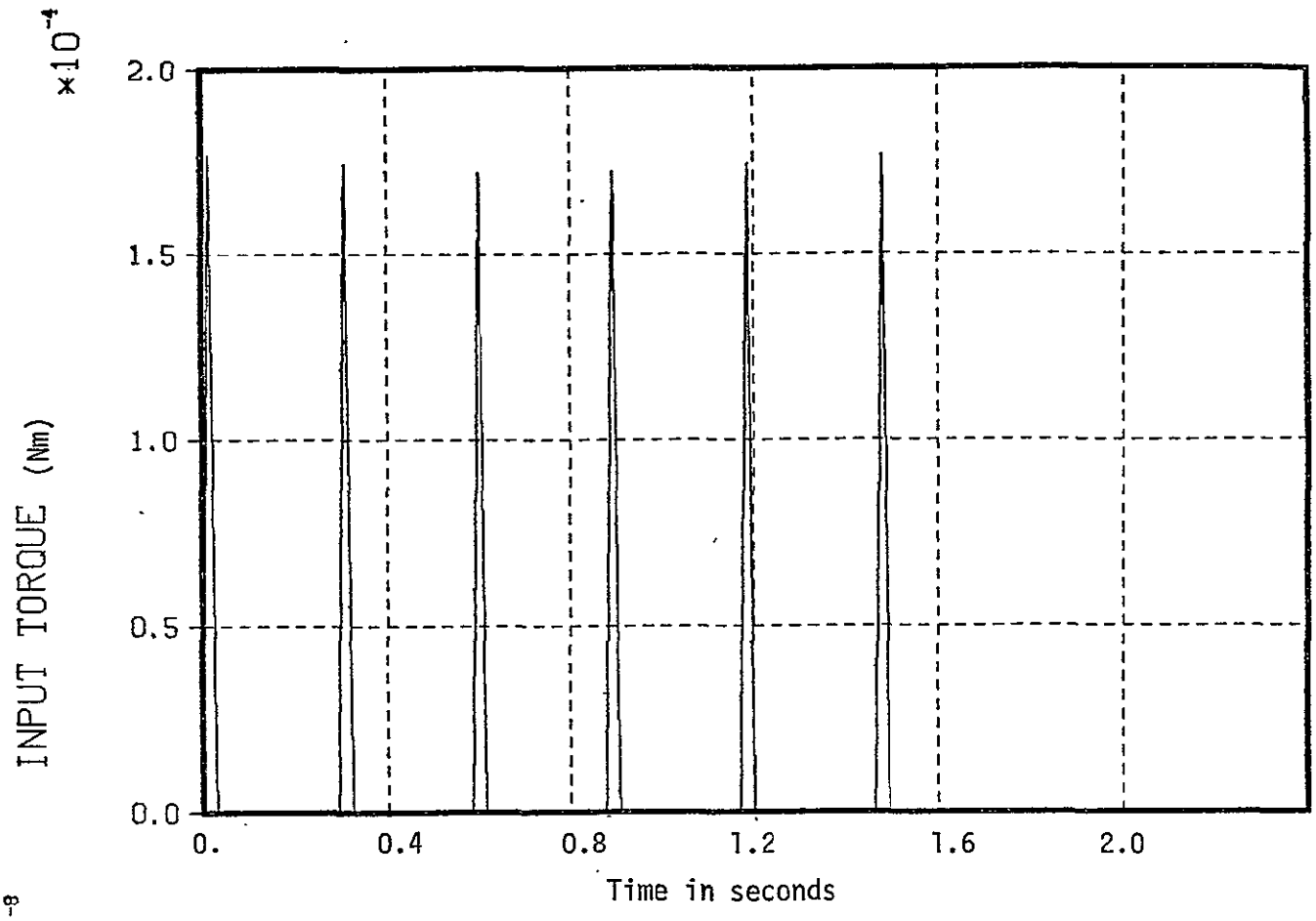

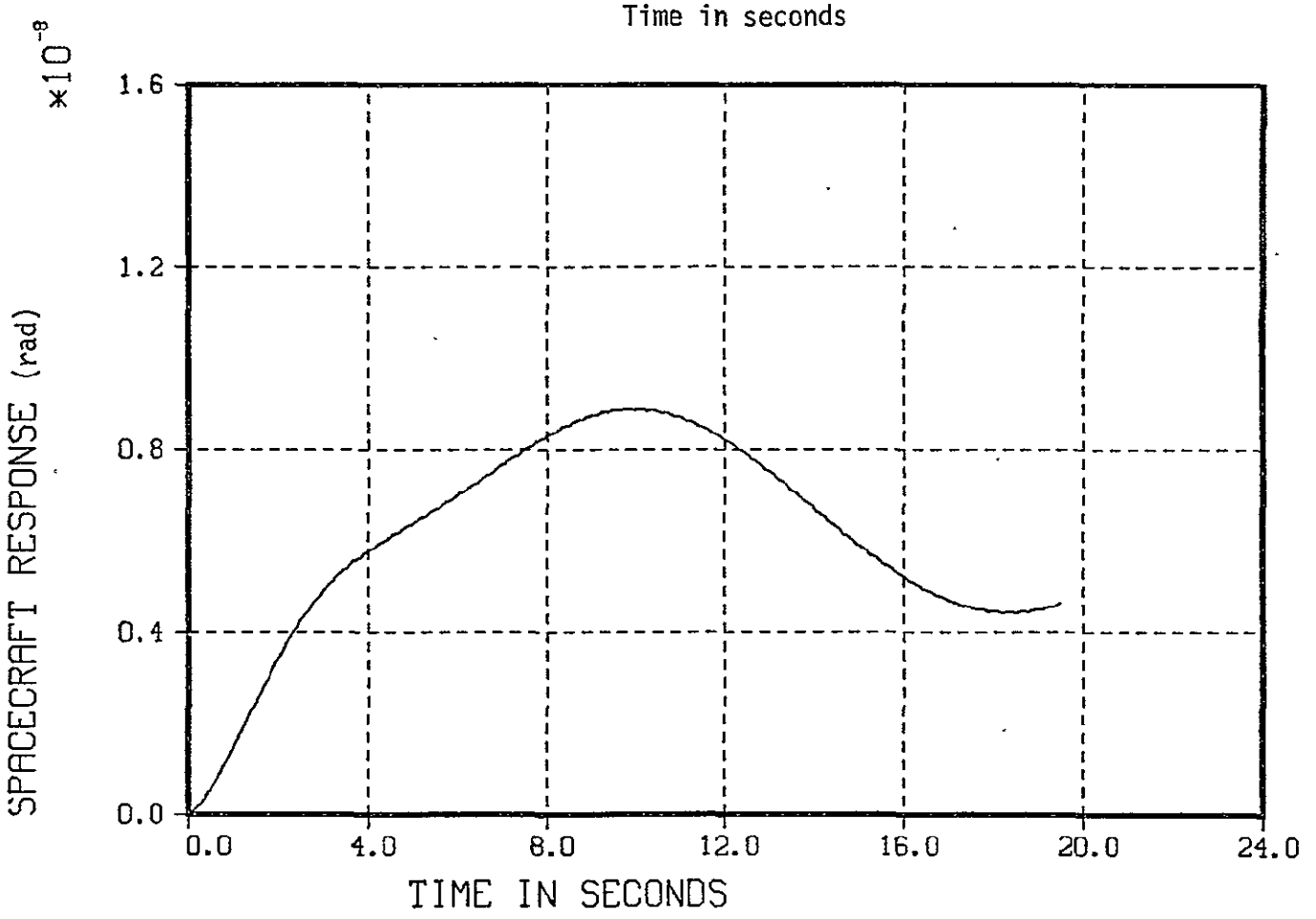

Figure 6-39. Spacecraft Attitude from Array First Mode Bending Torque

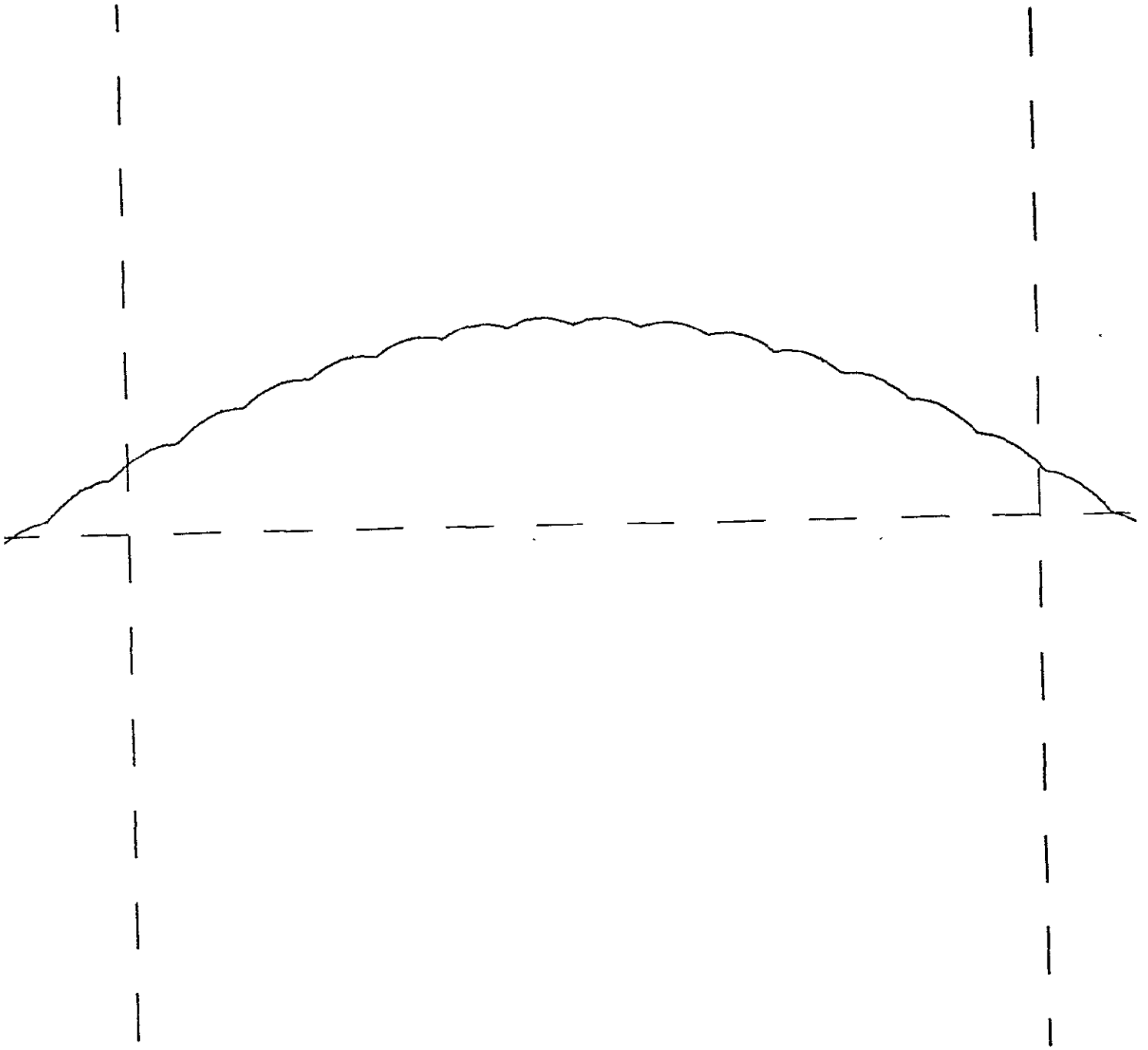

Figure 6-40. Enlarged Portion of Figure 6-39 to Display Bending Response

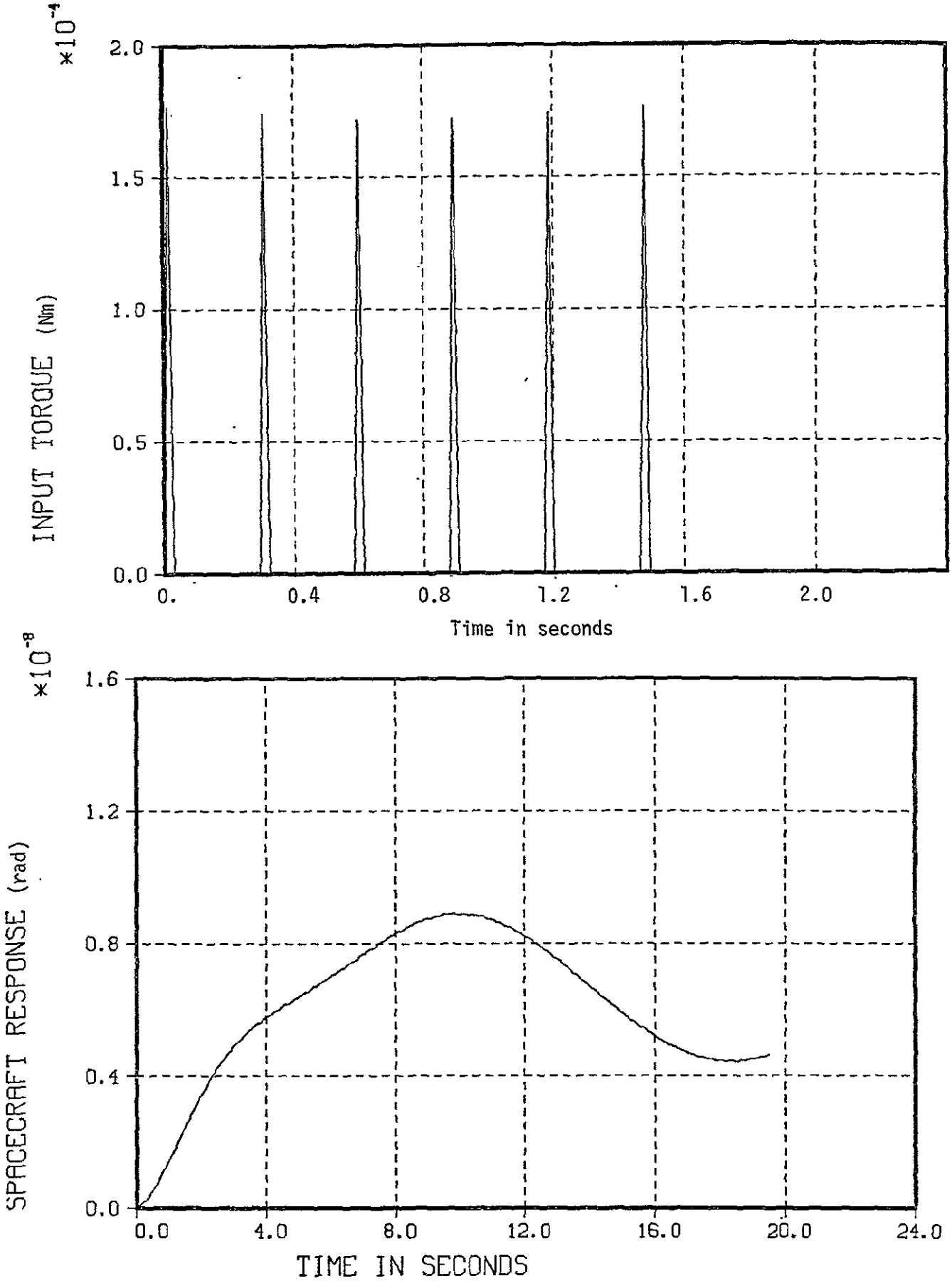

Figure 6-39. Spacecraft Attitude from Array First Mode Bending Torque

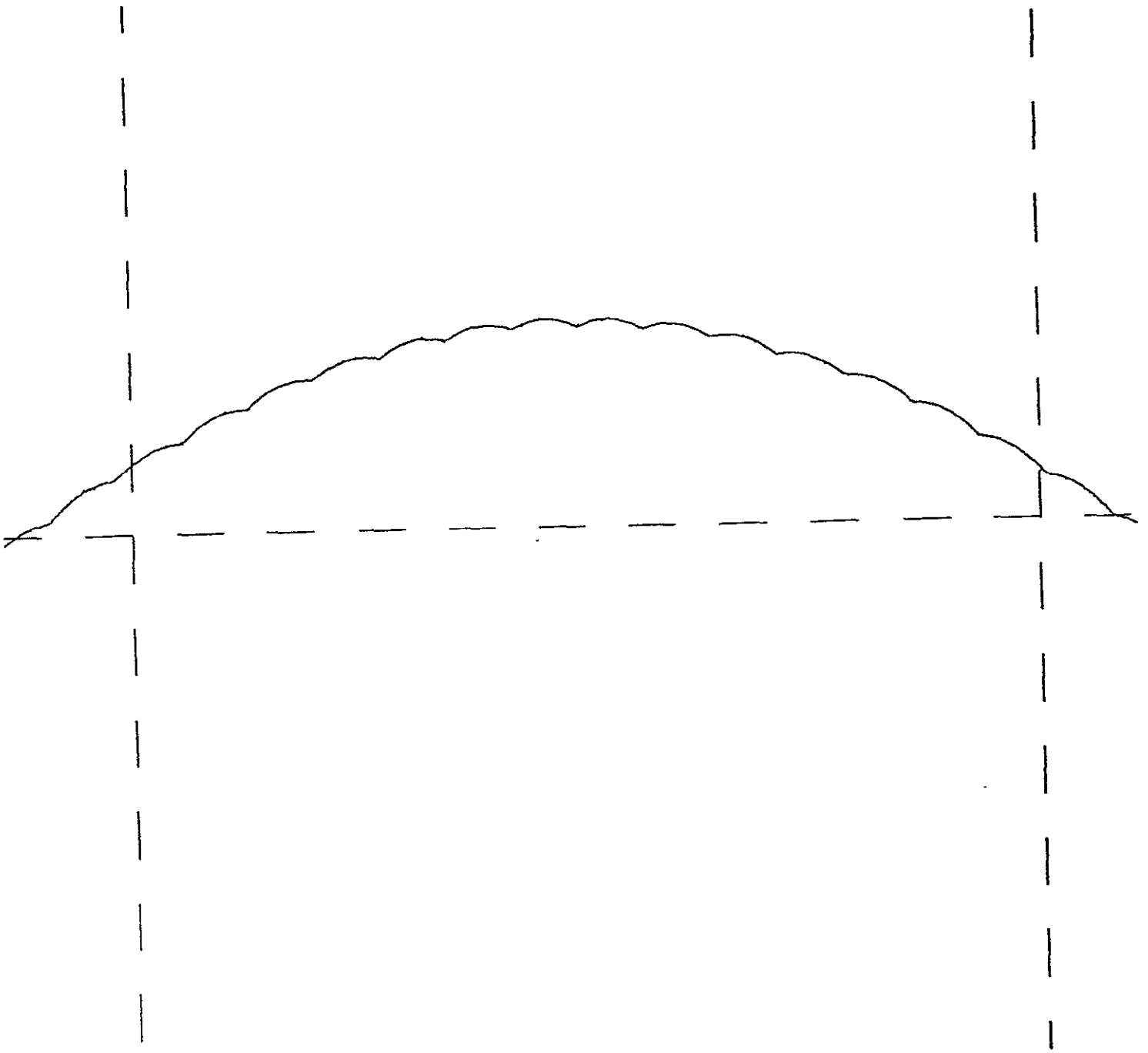

Figure 6-40. Enlarged Portion of Figure 6-39 to Display Bending Response

6.3.4 Spacecraft Model for Torsional Mode

Similar to the bending mode the torsional mode also requires a considerably more complicated analysis than called for in this study. Instead, a single axis model with torsional bending is used here to estimate the vehicle response to array cogging. Only the first torsional mode is considered. Figure 6-41 shows the single-axis model used for analysis.

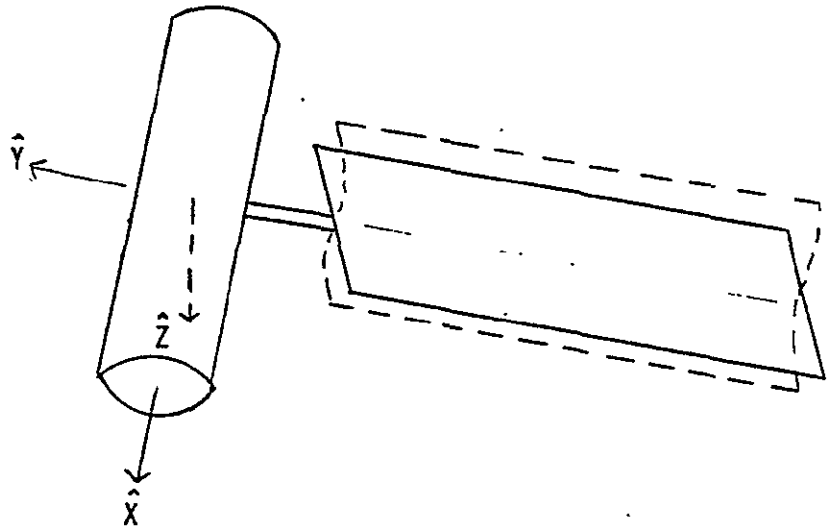

Figure 6-41. Torsional Mode Model

For a rigid main body with a rate plus position controller, perfect torque transducer, and a first bending mode, the block diagram of the system is customarily drawn as shown in Figure 6-42.

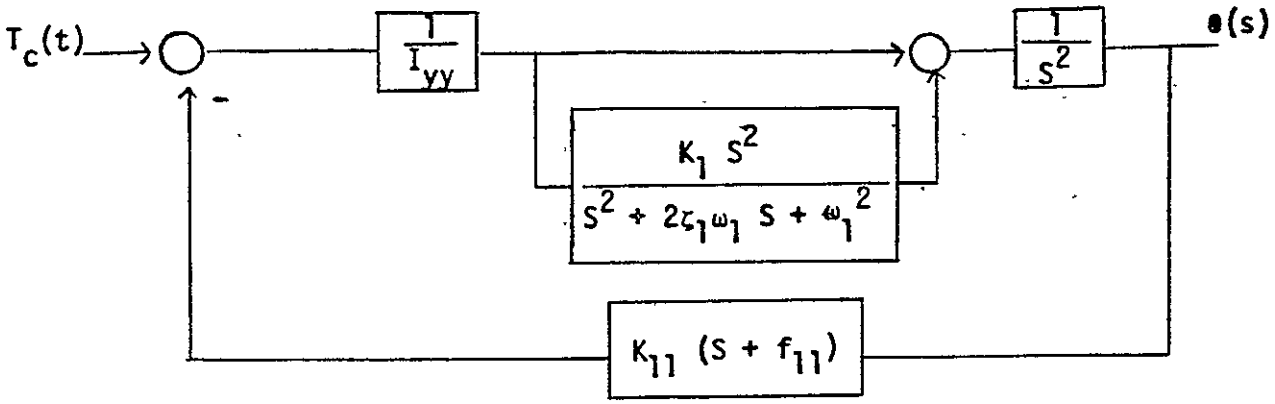

Figure 6-42. Torsional Mode System Diagram

The parameters I_{yy}, K_{11}, f_{11}, $T_c(t)$ retain the same meaning as before while $1/K_1$, ζ_1, and ω_1 represent the generalized mass, damping, and first mode frequency of the array. Details of calculating K_1 are given in Appendix F, while ω_1 is the specified mode frequency of 0.3 Hz. The damping ζ_1 should be obtained from physical data, but is customarily assigned a very low number on the order of 0.001 to indicate almost negligible structural array damping. A linear stability analysis of the system of Figure 6-42 showed that it is stable; the torsional mode merely adds a lightly damped dipole pair in the s-plane at the torsional mode frequency.

Treating the cogging torque as an equal and opposite torque on the main body, the $\theta(s)$ response may be obtained by simulation and examined for peak-peak jitter level. For an applied cogging torque, with profile as shown in Figure 6-36, the response is shown in Figure 6-43. The estimated peak-peak jitter value is 5.5×10^{-6} rad which is approximately one-half the specification budget of $\pm$ 10.6 μrad. The small staircase effect in the plot is a function of plotting quantization and does not represent system response.

6.3.5 Analysis of Mode Frequencies

Considering the array as a cantilevered beam permits the higher mode frequencies to be determined from the fundamental modes and array physical parameters. The relationship is

Figure 6-43. SPACECRAFT ATTITUDE FROM ARRAY TORQUE

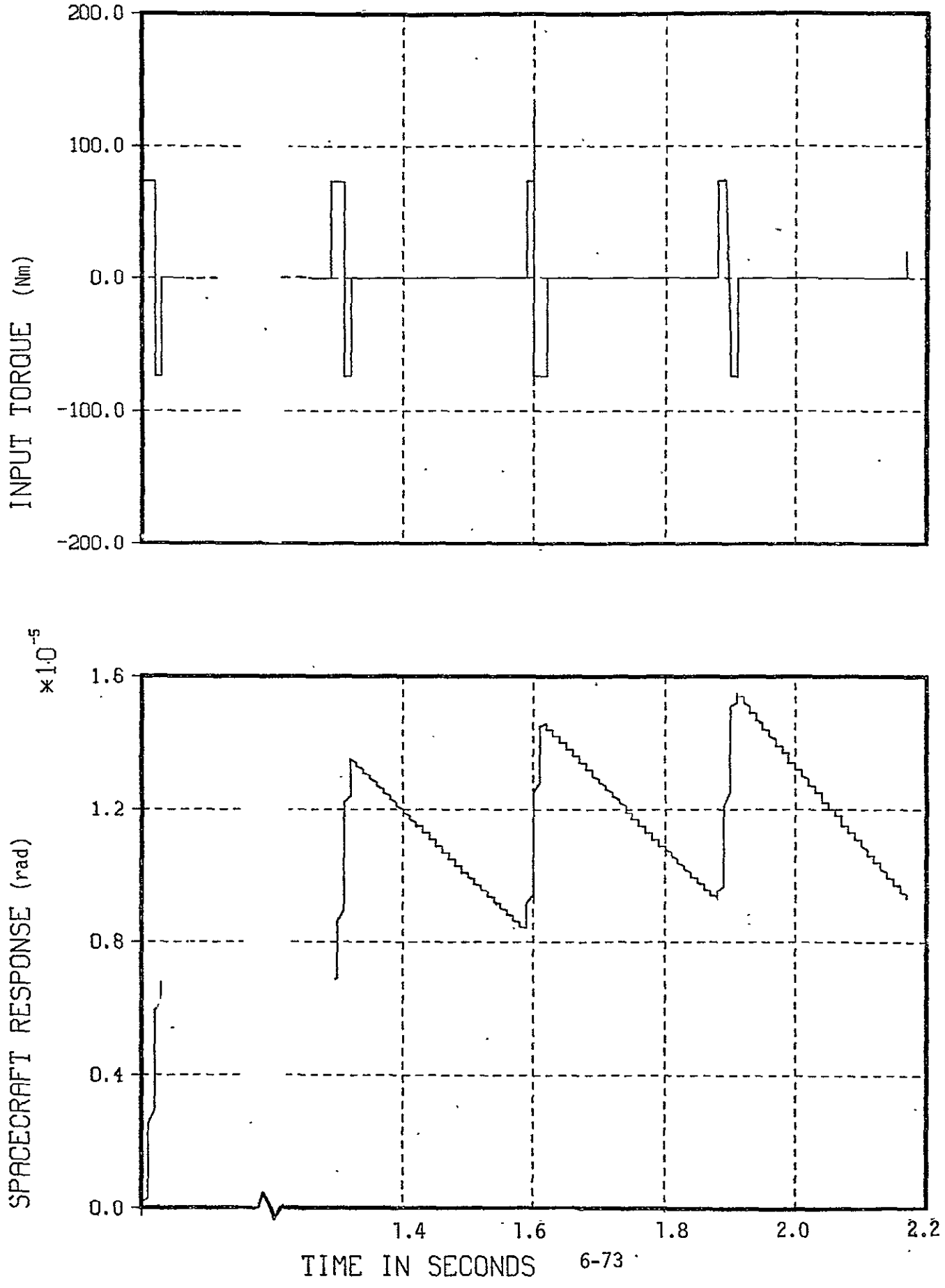

$$\omega_n = a_n \sqrt{\frac{EI}{\mu_1 \ell^4}}$$

where

μ_1 = Mass/Unit Length

ℓ = Length

EI = Stiffness

and a_n is an appropriate mode constant. The mode frequencies up to the fifth are shown in Table 6-7 for both the bending and torsional modes.

Table 6-7. Array Mode Frequencies

MODE	a_n	BENDING ω_n		TORSIONAL ω_n	
		Rad/Sec	hz	Rad/Sec	hz
First	3.52	0.50	0.08	1.88	0.30
Second	22.0	3.14	0.50	11.8	1.87
Third	61.7	8.81	1.40	33.0	5.25
Fourth	121.0	17.3	2.75	64.8	10.3
Fifth	200.0	28.6	4.54	107.1	17.0

The proposed cogging frequency of 3.41 hz (0.2932 sec period) may now be compared to all the mode frequencies to see if any integer ratios exist. It turns out that the torsional mode frequencies of ω_4 and ω_5 are integer multiples of the cogging frequency and the possibility exists of synchronously cogging the array in phase with its natural response. The remaining frequencies in the table are all non-integer ratios and are acceptable. It should be remembered at this point that although exact

numbers are obtained for higher mode frequencies, higher order modes must be considered to be in practice increasingly more indeterminate.

6.3.6 Conclusions

Based on the approximate analysis techniques of this study, the following conclusions can be drawn:

(1) For both the bending and torsional modes of array vibration, the response of the vehicle control system is stable with a cogged array drive.

(2) The vehicle jitter arising from the array cogging is very small for the 0.08 Hz bending mode; the present analysis showed a peak-peak jitter level of only 2.3×10^{-9} rad.

(3) The vehicle total jitter arising from the torsional mode and the array cogging torque is $\pm$ 5.5 μrad which is very near one-half the $\pm$ 10.6 μrad budget. This indicates the specification can be met.

(4) Torsional mode frequencies four and five are almost exact integer multiples of the proposed cogging frequency. If the latter is not changed, the response to these modes should be studied to determine if they are appreciable. Sensitivity analyses should also be conducted for ω_4 and ω_5 because of the indeterminacy of higher modes. Asynchronous array stepping may be considered as an alternative.

(5) If definitive answers regarding vehicle jitter are desired, considerably more complex two or three axis dynamic models should be derived which include the flexible array dynamics. Except for linearized stability and damping studies, these will probably require simulation because of their complexity.

6.4 Normal On-Orbit Control Law

This section formulates the LANDSAT on-orbit control laws. The speed-biased mode of reaction wheel operation is presented and normal on-orbit performance is examined for the magnetic momentum unloading control system and compared to earlier magnet sizing studies in Section 4.0 where a simpler simulation was used for sizing. Present results with a detailed 3 degree-of-freedom dynamic simulation confirm that the NASA Standard Reaction Wheels can be operated on L-D at a bias speed. They also show that the 50,000 pole-cm windings of the magnets are sufficient to achieve momentum unloading and thus they may be operated in the redundant mode using only one winding.

Normal on-orbit performance is studied for various gyro noise levels and scale factors. Results show that the jitter levels on an RSS basis are less than one-half the total attitude stability error budget of $\pm$ 10.5 μrad (1σ). The problem of gyro signal aliasing due to high frequency jitter sources such as wheel unbalance, etc., is briefly examined for a typical sampling frequency and appears not to be a problem.

6.4.1 Speed-Biased Control Law

The MMS ACS module, see Figure 2-5, contains nominally four NASA Standard Reaction Wheels having the characteristics shown in Table 6-8 below. The wheels are configured such that three are orthogonal, one along each of the three (x, y, z) control axes, and the fourth wheel is skewed equiangularly from the others so that its momentum vector contributes equally in all three control axes. The intended function of the fourth skewed wheel in the MMS ACS module is to provide standby redundancy in case one of the orthogonal wheels fails. With three-wheel operation on L-D, external disturbance torques together with non-uniform magnetic unloading (due to changes in the field) tend to produce wheel speed reversals on the order of 4-6 times per orbit. Because of the nonlinear static and coulomb friction characteristics of the wheels (0.005-0.01 Nm = 0.75-1.5 inch-ounces assumed) each wheel speed reversal produces attitude disturbances between 50 and 90 μrad (Reference 10) which violates the L-D attitude stability specification of 10.5 μrad.

Table 6-8. NASA Standard Reaction Wheel Characteristics

Momentum	20 Nms
Torque Capability Normal Mode (stall-0.5 sync) Super Torque (less than 5 min/ 100 min)	 0.15 Nm 0.3 Nm
Breakaway Torque	0.003 Nm
Synchronous Speed	2100-2700 RPM
Tachometer (optical)	240 pulses/rev
Power Running 0.5 sync speed Peak Torque at 20 Nms	 5 watts 75 watts
Weight	10 kg
Diameter	0.35 m
Height	0.15 m
Operating Life	5 years
Input Voltage Normal Mode Super Torque Mode	 28 volt zero-peak 400 Hz square wave (2 phase, 90 deg shift) 40 volt zero-peak 400 Hz square wave

To avoid wheel speed reversals, it is recommended to operate all four wheels at a speed bias while still maintaining a nominally zero momentum bias system. This can be accomplished by operating the skewed wheel at $-\sqrt{3}$ times the momentum of the orthogonal wheels. To give all wheels equal momentum ranges, a simple calculation shows that the bias should be 7.32 Nms for the orthogonal wheels and -12.68 Nms for the skewed wheel. Assuming that 2400 RPM corresponds to the nominal 20 Nms reaction wheel momentum capability, the nominal wheel speed biases become:

- Skewed Wheel Speed Bias ω_{WS} = -1521 RPM (-12.68 Nms)
- Orthogonal Wheel Speed Bias $\omega_{W\perp}$ = 878 RPM (7.32 Nms)

The roof mirror scanning wheel of the TRW Thematic Mapper adds a momentum source of 3.89 Nms to the spacecraft, almost exclusively in the x-axis (H_{TMX} = 3.89 cos (10 degrees); H_{TMZ} = 3.89 sin (10 degrees)), and the reaction wheels must be used to absorb this momentum. Thus the sign of the nominal x-wheel momentum bias should be selected to oppose the TM scan wheel momentum so that the 3.83 Nms can be added to the above computed nominal x-wheel bias. Thus, with the TRW TM the wheel speed biases become then:

RW Speed Biases with TRW Thematic Mapper

- Skewed Wheel Speed Bias ω_{WS} = -1521 RPM (-12.68 Nms)
- X-Wheel Speed Bias ω_{WX} = 1338 RPM (11.15 Nms)
- Y-Wheel Speed Bias ω_{WY} = 878 RPM (7.32 Nms)
- Z-Wheel Speed Bias ω_{WZ} = 960 RPM (8.0 Nms)

Note that each wheel can still swing $\pm$ 7.32 Nms.

In case one reaction wheel fails, the speed biased mode of operation must be abandoned and normal three-wheel operation initiated; the momentum bias of the TM must, however, be accounted for, i.e., if the skewed wheel has failed, the x-wheel would have to operate about a bias of 3.83 Nms and

the z-wheel about a bias of 0.675 Nms. An appropriate geometric distribution matrix must be applied if an orthogonal wheel has failed. The wheel speed reversal attitude transients must then be tolerated when only three wheels are operating. However, experience has shown (see Section 4.0) that due to the magnetic unloading law employed, both the y- and z-wheels tend to operate about a small bias and that speed reversals mainly occur in the x-wheel. Thus, the internal momentum bias introduced by the TM will be advantageous in reducing wheel speed crossovers, since it biases the x-wheel just sufficiently off null. The situation is somewhat different with an orthogonal wheel failed, but the scan wheel momentum bias introduced by the TRW Thematic Mapper still aids in avoiding wheel speed crossovers.

Speed-biased operation of all four reaction wheels is the recommended baseline normal on-orbit attitude control strategy for LANDSAT-D. There are essentially two basic ways to obtain the speed-biased wheel operation. The first is to control the fourth wheel at all times through the wheel geometry command distribution matrix T_{WB}. A second and more favored approach is to run the fourth wheel at a constant speed, here 1521 RPM, by supplying it with a small torque command to offset wheel friction. A relatively crude tachometer can monitor the wheel since a constant speed is commanded. One only should make sure that the speed command coincides with a tachometer quantization level to avoid speed dither of the wheel, which depending on the quantization and sampling time used, could otherwise contribute to pointing instability. With this approach, a means of restoring active control commands to the fourth wheel will be needed in the event that one of the other three wheels fail.

The three orthogonal wheels are used in conventional torque control mode, as opposed to momentum control mode, and will automatically maintain operation about their biased speeds as long as the fourth wheel is controlled as described. A previous study on STORMSAT (Reference 10) has shown that the torque mode is preferable, since the adverse effects of tachometer deadzone* and tachometer ripple* introduced in the momentum control

*Not applicable to speed biased operation when four wheels are active, but applies to three wheel operation; the entire discussion applies only to the three wheel fall-back operating condition.

mode outweigh the advantages of a feedback loop around the wheel friction nonlinearity (in speed-biased operation nonlinear friction plays no part). The momentum control mode advantage of not requiring gyro derived body rates for system damping is not applicable here, since an IRU (Inertial Reference Unit) is required in any event for attitude determination and is a standard component of the MMS ACS module. The STORMSAT study assumed a 100 pulse per revolution magnetic pick-off tachometer to be used in conjunction with momentum control; the now available 240 pulses per revolution optical encoder tachometer should yield slightly better momentum control performance. However, extrapolating from the previous results, no significant performance improvement can be hoped for and the adverse effects of tachometer ripple on attitude stability is expected to still exceed the effects of gyro noise whenever the wheel operates at low speeds. Moreover, the required control software/hardware is more complex for the momentum control mode due to the required wheel speed servo loops.

So torque control of the three orthogonal reaction wheels is baselined for L-D. For clarity a single axis control law block diagram is shown in Figure 6-44. Figure 6-45 shows all four reaction wheels. Note the constant speed control loop for the fourth skewed wheel and that its torque is only shown as a dashed line since it is nominally zero, except of course, when it is brought up to bias speed. Note also that for all wheels the integrators with their limiters are shown after the geometry distribution matrix T_{WB}, i.e., one integrator is associated with each wheel. The main function of the integrators is to offset wheel friction and aid in reducing wheel speed reversal transients during three wheel operation (constant, offset-producing disturbance torques are very small, but their effects are also negated by the integrators). The integrators are limited slightly above the wheel friction levels so that their effects of reducing system damping is not present during large signal attitude convergence transients. The limiters are thus associated with the friction level of each individual wheel and are easier to determine this way than if there were only three integrators outside (before) the geometry distribution matrix. Also, since the integrators are implemented digitally, their sign could, by special logic, be instantaneously reversed at

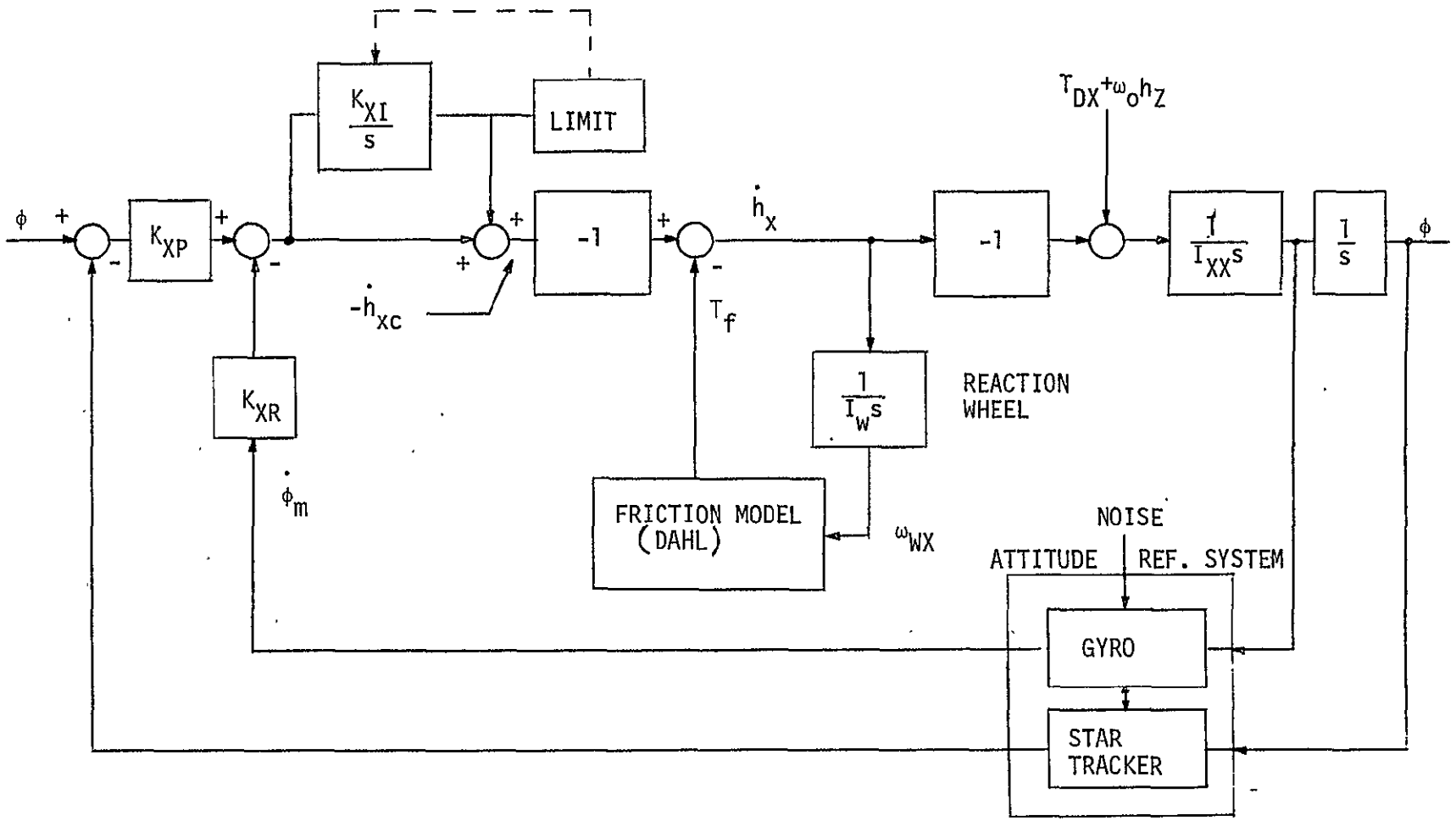

Figure 6-44. Single Axis Model of Torque Control Mode (Roll Channel)

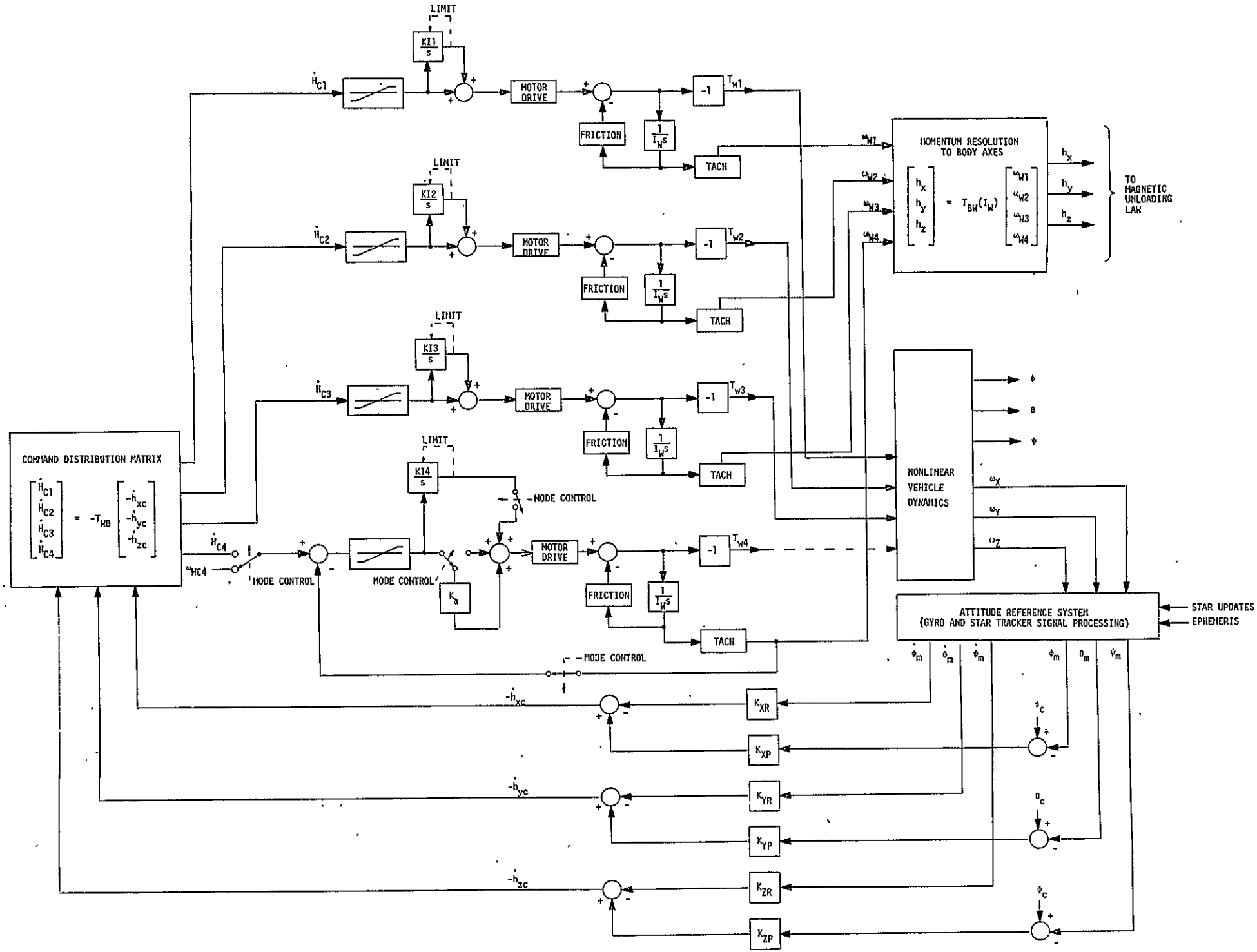

FIGURE 6-45. LANDSAT-D NORMAL ON-ORBIT ATTITUDE CONTROL SYSTEM BLOCK DIAGRAM

wheel speed reversal to suppress the attitude transient, and, therefore, one integrator should be directly associated with each wheel. One should note, however, that this entire discussion applies only to three wheel operation under the assumption that one of the orthogonal wheels has failed. Otherwise the command distribution matrix is

$$T_{WB} = \begin{bmatrix} 1 & 0 & 0 \\ 0 & 1 & 0 \\ 0 & 0 & 1 \\ 0 & 0 & 0 \end{bmatrix}$$

and it really does not matter where the integrators are situated.

Table 6-9 below summarizes nominal on-orbit attitude control system parameters. The Dahl friction model used for the reaction wheels is shown in Figure 6-46.

6.4.2 Normal Operation

A functional block diagram of the attitude control system is shown in Figure 6-47, including solar array and Ku-band (TDRS) antenna control. Factors affecting the solar array and antenna steering control laws are the array clearance with the antenna line-of-sight to the TDRS, Thematic Mapper activity, day and night conditions, and TDRS location. For the solar array control law, Figure 6-48 displays the main factors to be considered. As shown there, the solar array is rotated to remain perpendicular to the sun's rays while the vehicle is within $\pm$ 45 degrees of the ecliptic plane (descending node at equinox). In the angular regions beyond $\pm$ 45 degrees and extending to the terminator line, the solar array is stationary to avoid blockage of the TDRS antenna. This requires that the array be other than perpendicular to the sun's rays at various times and a small loss in power is incurred (see Section 3.5 for more details). In the third region, when the vehicle is still in sunlight but the earth below is in darkness, the array is again driven to be perpendicular to the sun rays because the

Table 6-9. Nominal Attitude Control System Parameters

		Axis		
		Roll (x_b)	Pitch (y_b)	Yaw (z_b)
	Moment of Inertia, I_{ii} ($kg\text{-}m^2$)	2034	2671	2373
For Small Signals Only*	Natural Frequency, ω_n (rad/sec)	0.7	0.7	0.7
	Damping Ratio, ζ	0.4	0.4	0.4
	Position Gain, K_p (N-m/rad)	509	668	593
	Rate Gain, K_R (N-m-sec/rad)	1017	1335	1186
	Integral Gain, K_I (N-m/rad-sec)	1.0	1.0	1.0
	Integrator Limit, L_I (N-m)	0.02	0.02	0.02
Dahl Friction Parameters	Slope Parameter, γ $(N\text{-}m\text{-}rad)^{-1}$	10^6	10^6	10^6
	Running Friction, T_{fo} (N-m)	0.01	0.01	0.01

*For large signals with saturated integrator, ω_n = 0.5 rad/sec, ζ = 0.5.

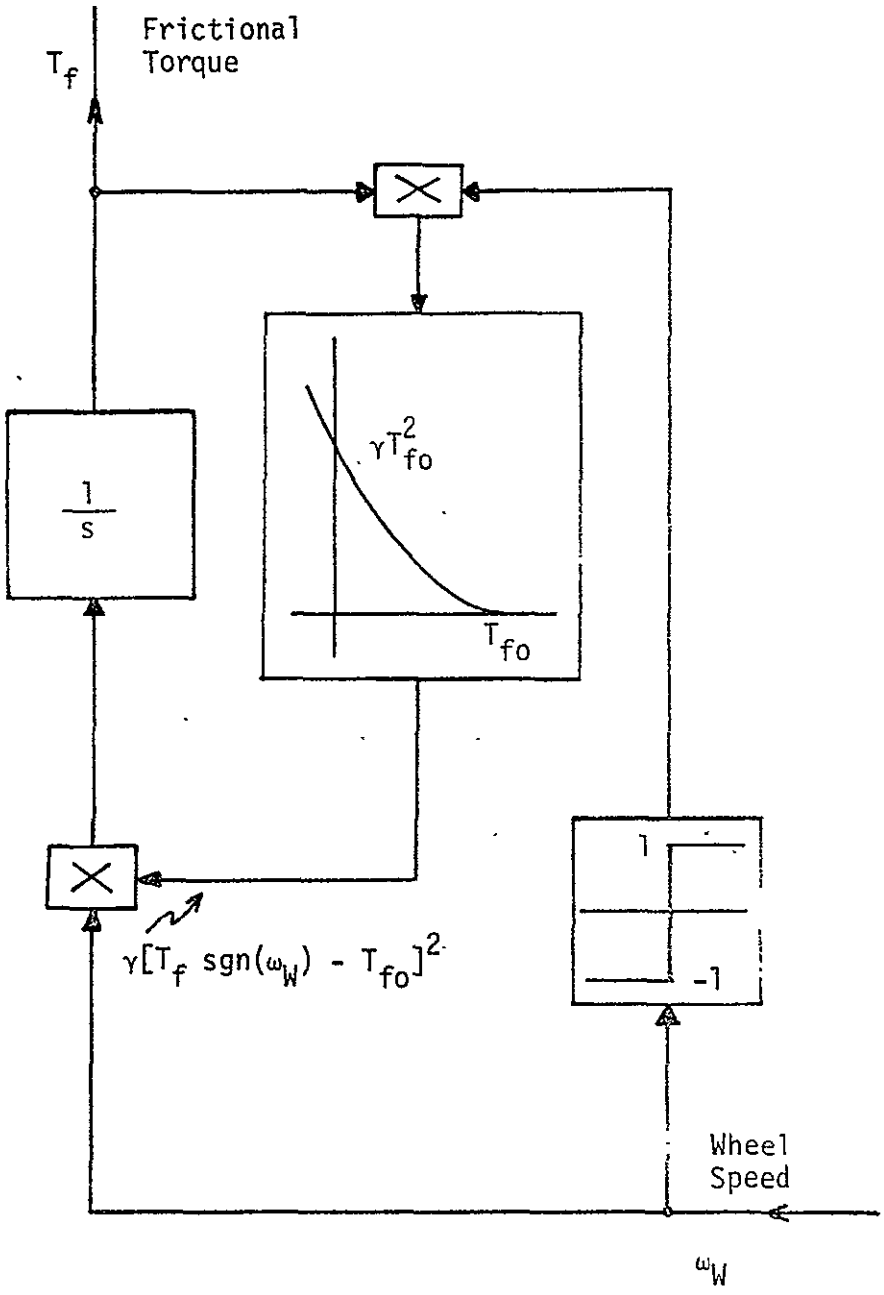

Figure 6-46. Dahl Active Friction Model

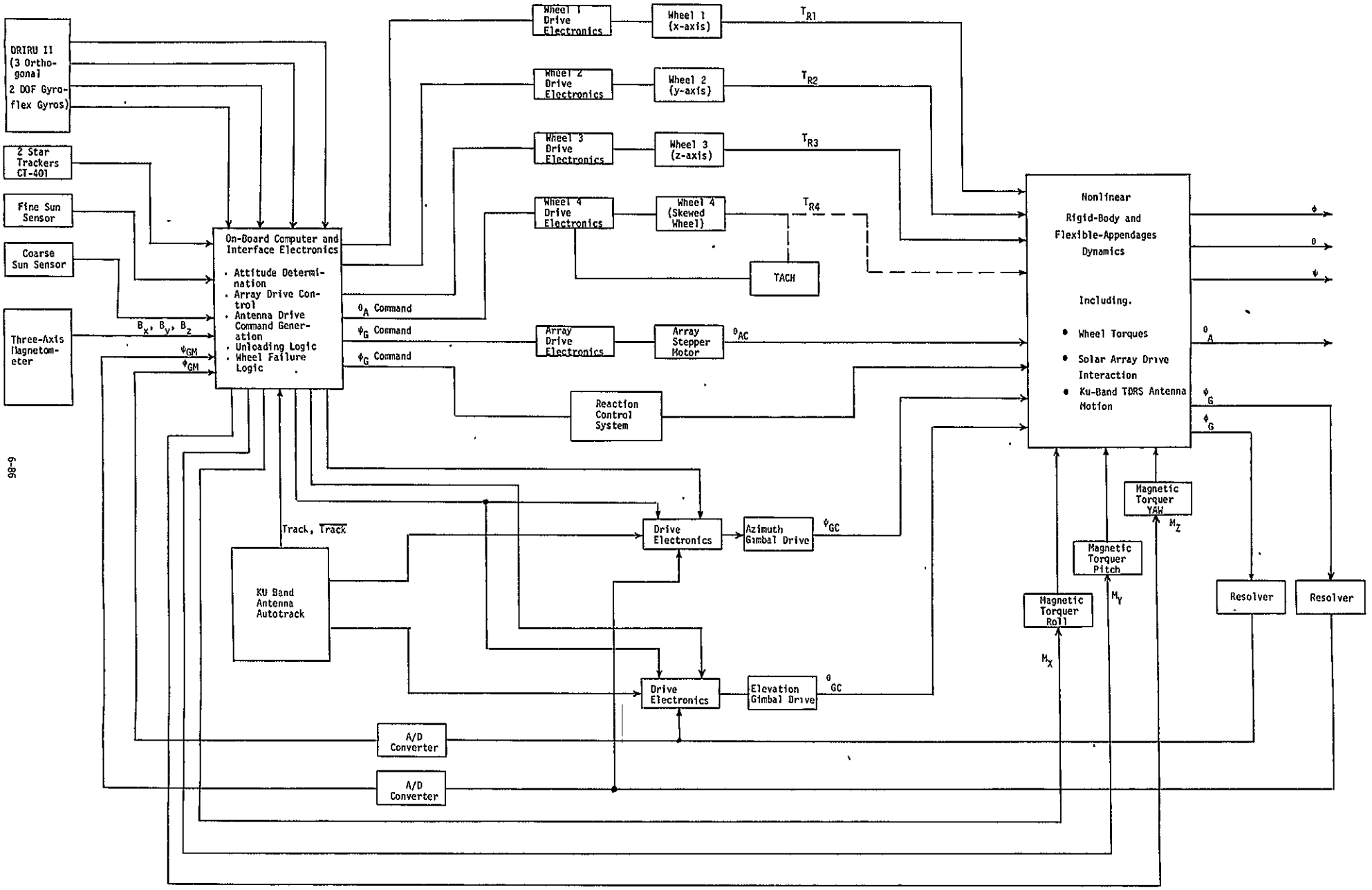

Figure 6-47. ACS Functional Block Diagram

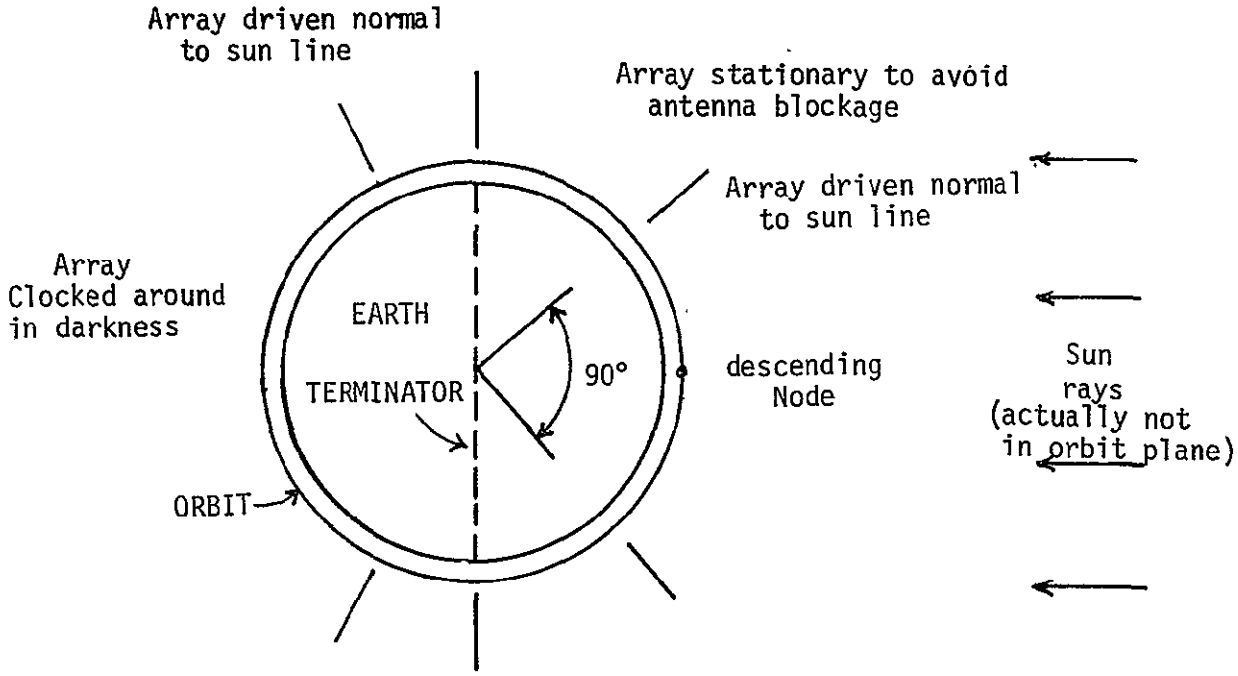

Figure 6-48. Solar Array Drive Conditions

Thematic Mapper is no longer taking data to be relayed to the TDRS. Finally, as the vehicle enters darkness, the array is clocked around open-loop to be perpendicular to the sun rays as the vehicle again enters sunlight.

For the antenna, the control scheme is as follows. The antenna gimbals are commanded by the on-board processor as shown in Figure 6-47 to point the antenna at an expected TDRS location. If the TDRS is acquired, the autotrack assumes command of the antenna to keep it trained on the TDRS. If the TDRS is not acquired at the expected location, the 12 degree beamwidth acquisition horn is used or a spiral search pattern is initiated until the TDRS is located and then the autotrack assumes command.

The reaction control system (RCS) is only used during the acquisition sequence and during stationkeeping maneuvers (ΔV). The coarse and fine sun sensors are nominally also used only during the acquisition sequence. Momentum unloading takes place continuously using torque derived from the

interaction of the magnetic bars with the earth's magnetic field. The commanded magnetic moment $\overline{M}$ is generated according to the linear law

$$\overline{M} = -K\,\overline{B} \times \overline{H}_e$$

where

- K - is a suitable constant
- $\overline{H}_e$ - is the momentum error vector
- $\overline{B}$ - is the measured earth field

Other magnetic unloading laws should also be examined. A potential disadvantage of the above law is that a certain average equilibrium momentum error $\overline{H}_e$ must first be accumulated before the law becomes effective. This creates a small momentum bias. By adding a term containing estimated disturbance torque, the momentum offset error can be reduced.

Three-axis attitude reference is derived from integrated gyro data processed by the on-board computer and combined with ephemeris information for earth oriented reference. Attitude and gyro biases are updated periodically from strapdown star tracker measurements which are processed by an on-board algorithm, typically an extended six-state Kalman filter. A functional block diagram of the on-board stellar-inertial attitude reference system is shown in Section 5.0 in Figure 5-9. Body rate information for ACS damping is also obtained from processed gyro data. In its normal on-orbit mode of operation the L-D yaw axis (z) is commanded to point to nadir with the pitch axis (y) normal to the orbit plane and the roll axis (x) along the orbital velocity vector, with an accuracy as specified in Section 2.4. Normal on-orbit operation of L-D does not call for offset pointing or maneuvers.

6.4.3 Performance Evaluation by Simulation

A detailed digital simulation modelling nonlinear three-axis spacecraft dynamics and sampled, pulse rebalanced gyro operation plus associated noise (only for short-term runs), was used for performance verification/

evaluation of the normal on-orbit L-D attitude control system; the disturbance torque model derived in Section 4.5, Table 4-3 (antenna pointing ahead), was also employed. The simulation was first used to examine orbital attitude performance and the operation of the magnetic unloading laws. The three orthogonal wheels were initialized at a speed bias corresponding to 7.32 Nms and the skewed wheel at -12.68 Nms. Internal motion and jitter effects due to reaction wheel unbalance, solar array stepping and the flexible antenna mast have been studied and simulated separately in previous sections and were not included in the orbital simulation. Accounting for these effects would overcomplicate a three-axis simulation and the CPU time for even short-term runs would become excessive because of the higher frequencies involved in these jitter sources.

The results of the orbital run are shown in Figure 6-49. The magnet commands, the wheel momenta and the resulting vehicle attitude are shown. The agreement with previously presented (Section 4.0) magnet sizing results (using a much simpler, idealized digital program) are very good. Only the 50,000 pole-cm magnet windings are utilized. The momenta of the reaction wheels stay well within their limits and the maximum observed steady-state peak-peak momentum change is 1.3 Nms for the x-wheel. The maximum attitude error (without jitter sources) can be observed in roll as 2.5×10^{-4} degree (0.9 arc-second = 4.4 μrad). The small roll offset of 1.8×10^{-4} degree (0.65 arc-second = 3.2 μrad) is caused by the average momentum bias representing the equilibrium momentum error $\overline{H}_e$ of the magnetic unloading law; the orbit rate momentum $-\omega_o I_{yy} \hat{y}_b$ also enters into the momentum equilibrium kinematics.

A detailed dynamic simulation with gyro and noise models was run for various values of sampled gyro noise standard deviation $\sigma_{\Delta\theta}$ and scale factor K_g. Details of the gyro and noise model are described in Reference 10, and the results of the present study are summarized in Figures 6-50 and 6-51. In Figure 6-50 for a processor sampling period of 200 ms, the plots coincide for both gyro scale factors of 0.01 and 0.1 arc-second per pulse which means that the noise effects outweigh the quantization effects. Thus both cases in Figure 6-50 satisfy the RSS allotment of one-half the error budget.

Figure 6-49a. Magnet Commands

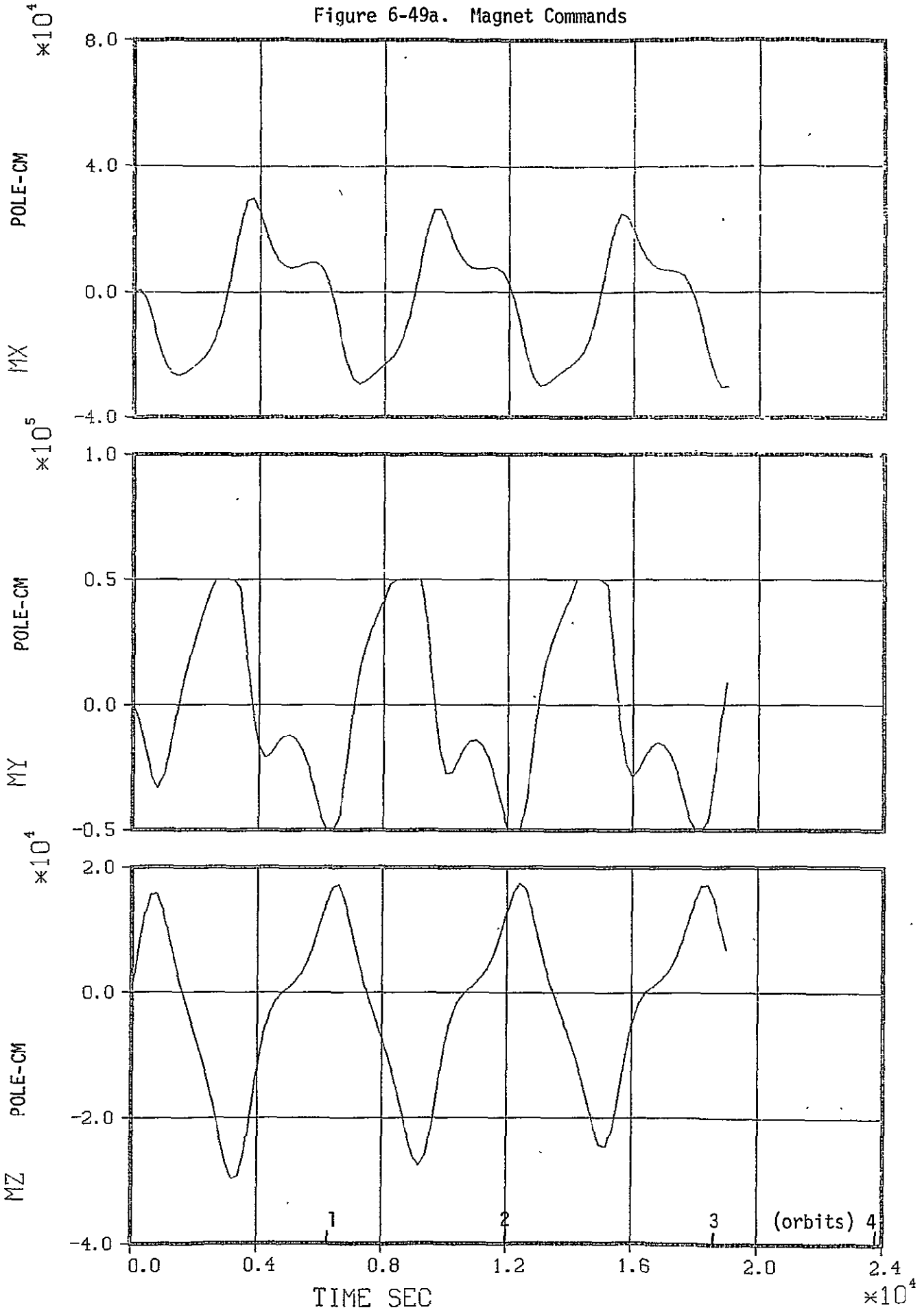

Figure 6-49b. Wheel Momenta

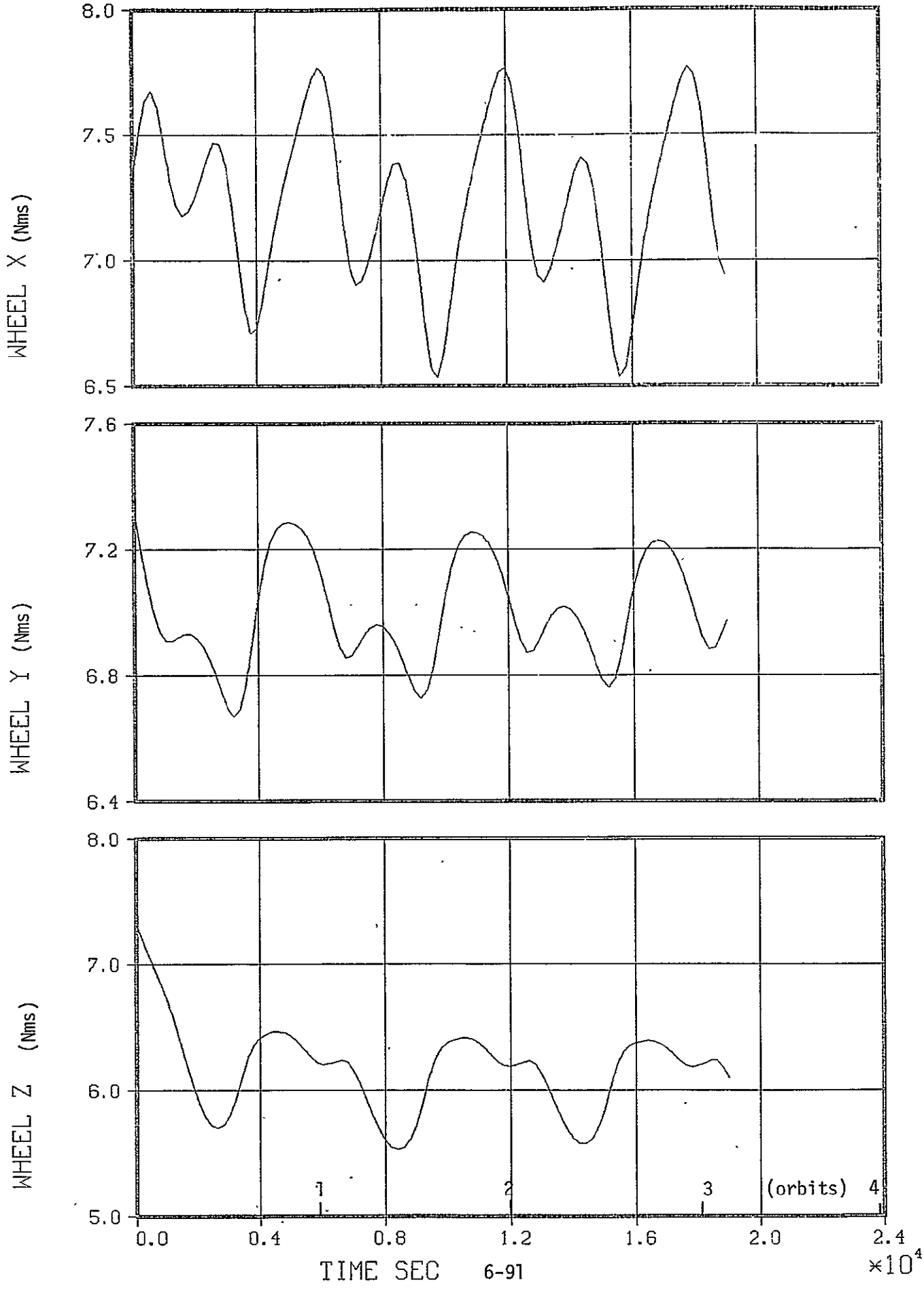

Figure 6-49c. Vehicle Attitude

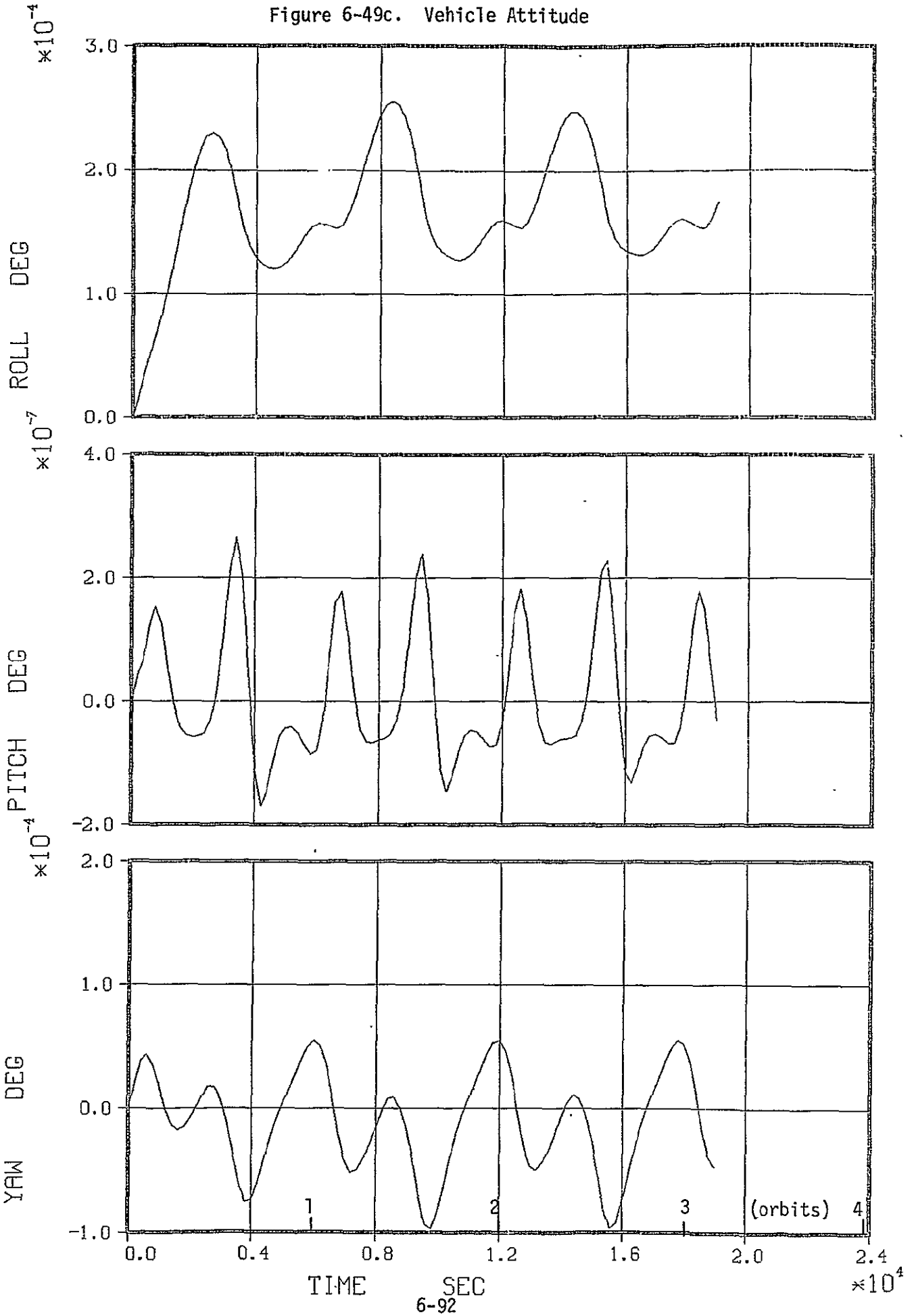

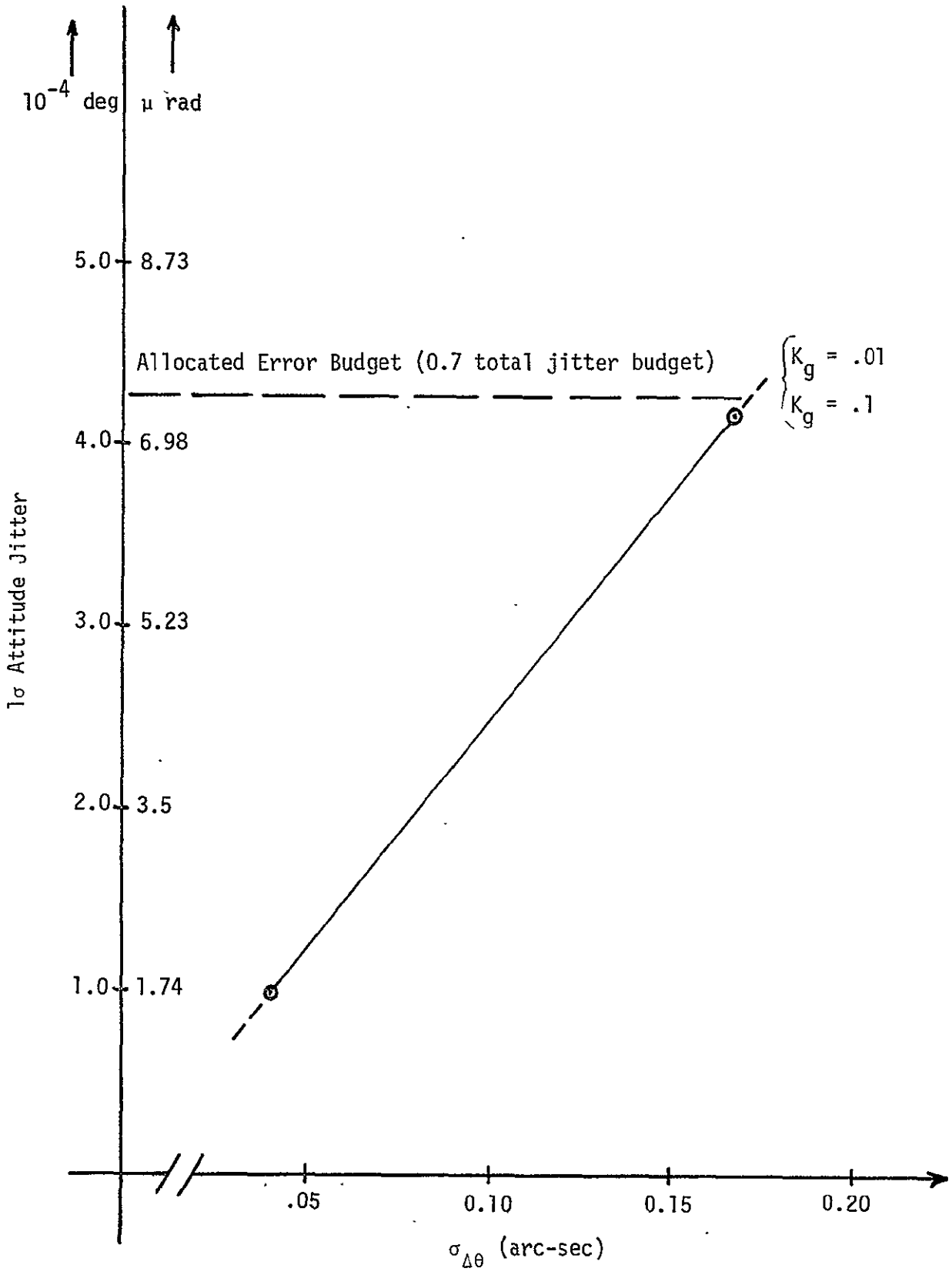

Figure 6-50. Attitude Jitter for the 200 ms Processor Interval

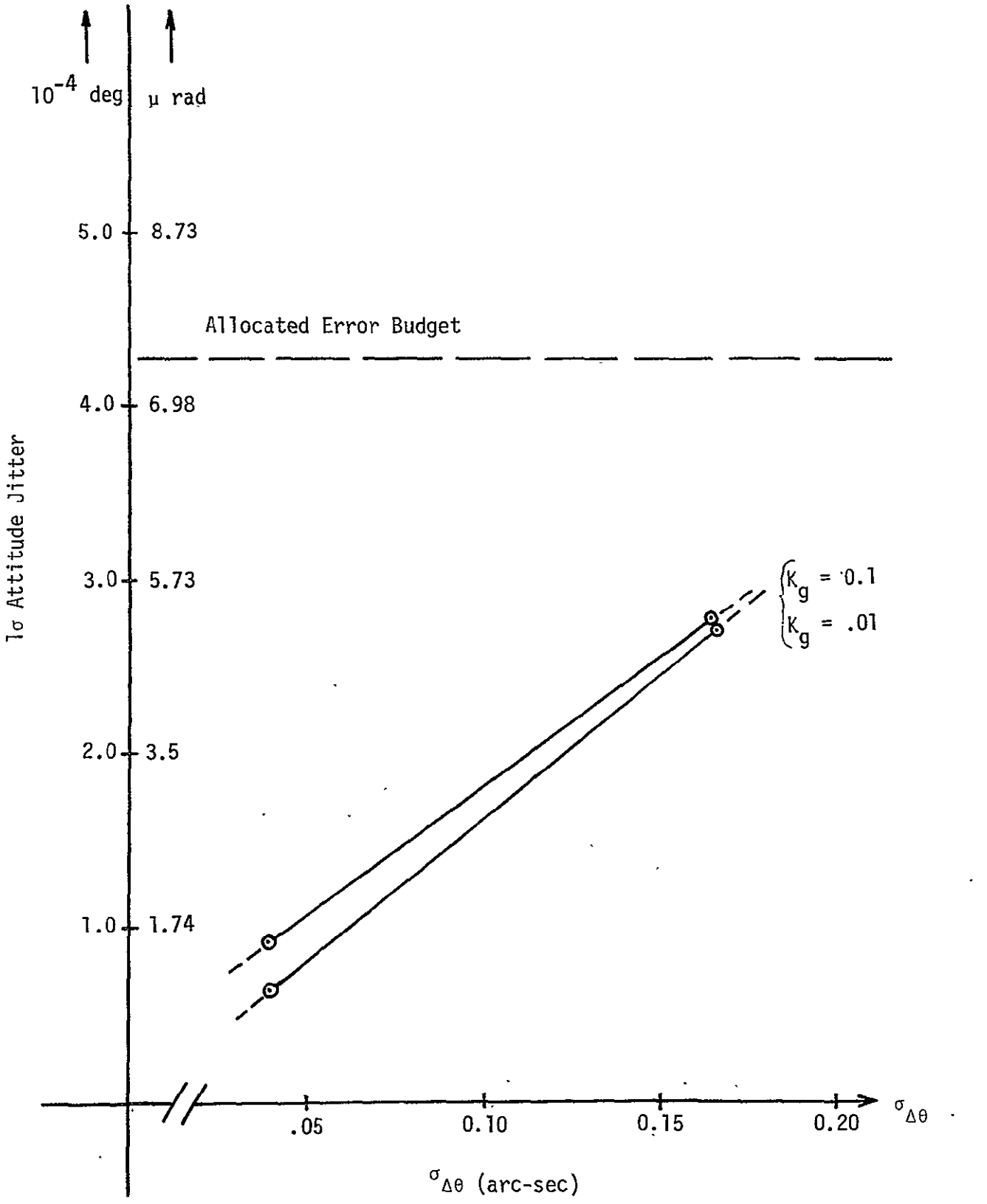

Figure 6-51. Attitude Jitter for the 400 ms Processor Interval

In Figure 6-51, for the case of a 400 ms processor sampling time, the scale factor K_g does have a small effect. However, in both cases the jitter levels are lower than for the 200 ms case and easily satisfy the ACS error budget allotment. For both Figures 6-50 and 6-51, extrapolation is not recommended beyond the circled data points. To indicate the form of the jitter, Figure 6-52 shows representative roll, pitch and yaw attitude signals from which the 1σ jitter values were determined. This particular plot corresponds to a 400 ms sampling time, a scale factor K_g = 0.01 arc-second per pulse, and a noise of standard deviation $\sigma_{\Delta\theta}$ = 0.04 arc-second per $\Delta\theta$ sample.

As documented previously in Table 6-6, oscillatory motion of spacecraft internal parts at frequencies beyond the ACS bandpass results in small attitude rate and position errors. The errors may, however, be within the bandpass of the gyros and since the gyros and on-board processor operate in a discrete time sampled mode, there is a possibility of a signal aliasing problem. This was briefly studied by injecting applicable attitude and rate error signals into the 3 degree-of-freedom simulation operated in a sampled mode with detailed gyro models. The amplitude and frequency for the signals used correspond to the rigid body disturbance caused by the scan mirror motion of the Multi-Spectral Scanner (MSS), where the frequency is 18.5 Hz and the amplitude is 0.08 arc-second. The signals were injected as shown in Figure 6-53 to avoid high frequency integration; the disturbance actually acts at the T_{dis} junction.

For a processor sampling time of 200 ms, the sampling frequency is 5 Hz which is clearly far below the Nyquist frequency for the 18.5 Hz MSS disturbance signals. Thus "aliasing" or overlap of the spectral density of the rate signal does occur. However, for the values cited above, simulation results show that there is no problem as indicated by Figure 6-54. It shows the roll attitude to be stable with approximately a 1.75 μrad jitter level. This includes both the gyro noise and MSS scan mirror effects and is about the same jitter as observed previously in Figure 6-52 without the MSS as a jitter source. The absence of any signal divergence or build-up shows that the aliasing is not a problem for the parameters used. However,

Figure 6-52. Representative Attitude Jitter Signals

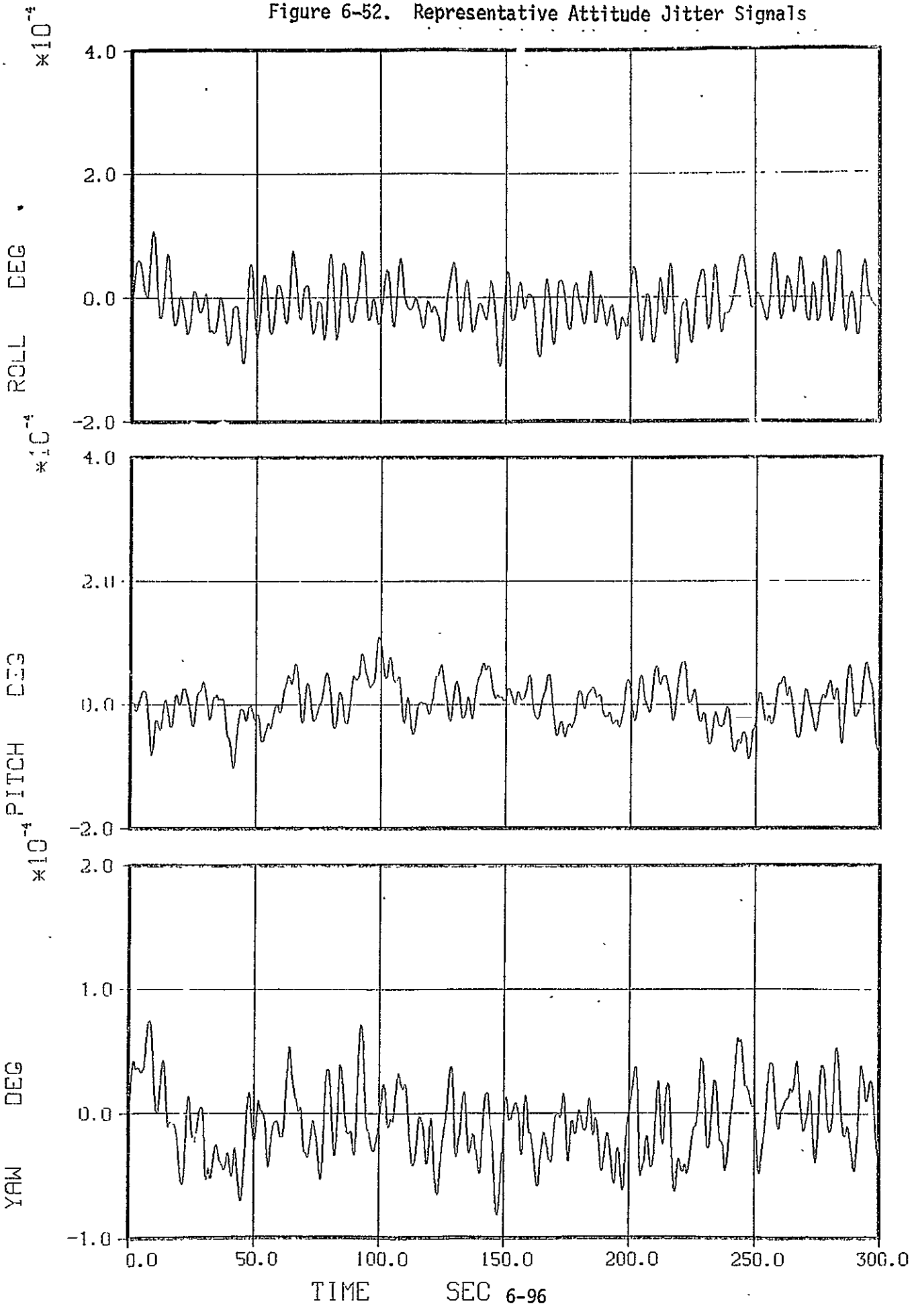

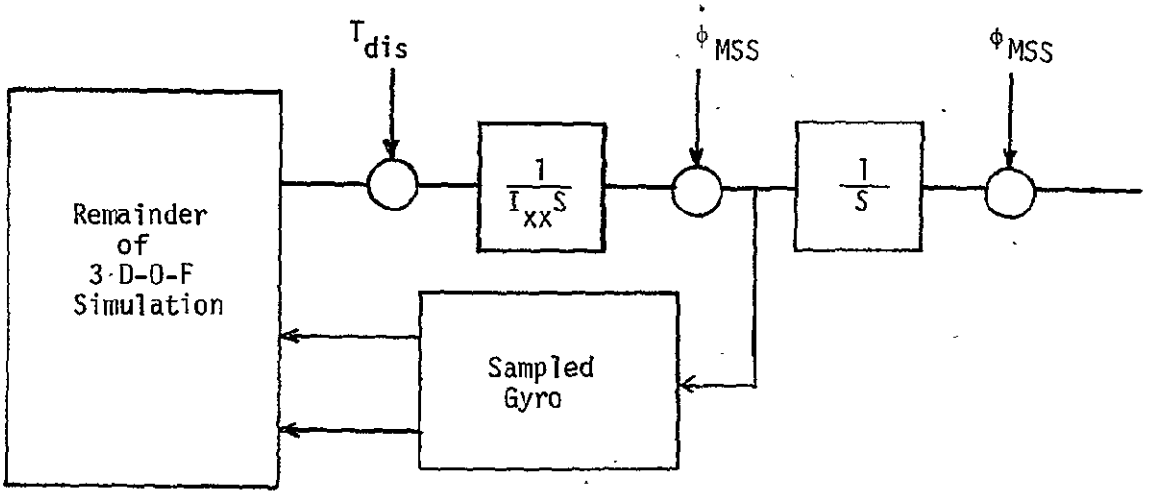

Figure 6-53. Jitter Disturbance Injection ϕ_{MSS}, $\dot{\phi}_{MSS}$ to Study Aliasing Problem

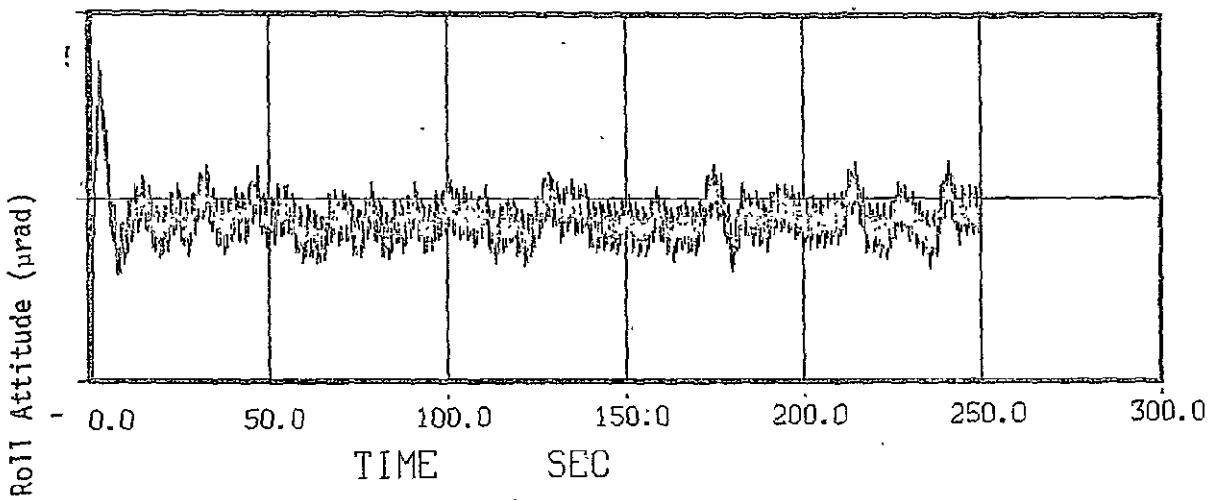

Figure 6-54. Roll Attitude Error with Gyro Signal Aliasing

more extensive studies should be performed at a later time. Jitter frequencies should then be carefully selected; the 18.5 Hz employed here are realistic for the MSS and realistic with respect to the aliasing effect when sampled at 5 Hz, but probably exceed the gyro bandpass which typically is between 10 and 15 Hz. Because of the low power (low amplitude) contained in most of the jitter signals produced by internally moving parts, their effects are expected to be negligible even if they enter the ACS as aliased signals. In general, a sure method for guarding against adverse effects caused by aliasing of high frequency gyro signals, is to low-pass filter the gyro output before it is sampled. For instance, if the gyro sampling period is 200 msecond (5 Hz sampling frequency) a filter with a 2.5 Hz cutoff frequency should be inserted before the 5 Hz sampler which is the on-board processor input . For an analog rebalanced gyro this would be an analog filter before the ADC; for a pulse rebalanced gyro with an output register which is normally being strobed for a READ by the on-board processor, a digital filter (built of special purpose digital hardware, perhaps programmable digital electronics) must be used between the gyro output register and a new register to be strobed by the on-board processor. This could be a costly modification of the gyro output electronics/processor interface and should be omitted if one can establish with high confidence that aliasing of high frequency gyro signals has negligible effects on the system.

6.5 Estimated Performance Summary

The L-D attitude reference system has not been investigated in detail in this study. The MMS proposed stellar-inertial attitude reference system was, however, studied previously by TRW for NASA/GSFC for a synchronous orbit application (Reference 10). Extrapolating from the results obtained there, no problems are expected for the lower L-D orbit where due to the increased orbit rate, star availability over a given time interval will actually be improved. Sun interference with the star tracker will also be no problem for L-D, since the trackers always look toward the shaded side of the 9:30 a.m., sun synchronous orbit. Calibrated accuracy of the NASA standard tracker (BBRC CT-401) is about 11 arc-seconds (1σ), of which 4 arc-seconds are fixed residual biases and 7 arc-seconds appear to the

user as randomly varying errors. A supporting error analysis of the tracker is presented in Table 6-10. It should be noted that the magnets must be turned off when reading the trackers.

The exact performance characteristics of the NASA Standard DRIRU II gyro pack are currently not well defined, but a calibrated gyro drift rate bias of less than 0.0013 degree/hour (1σ) and a calibrated gyro sacle factor uncertainty between 50 and 100 ppm (parts per million) can be expected. Gyro scale factor error and residual uncalibrated gyro alignment errors play, however, no significant part in an earth pointing application where no spacecraft maneuvers are required. Scale factor and alignment errors lump with gyro bias errors due to the constant orbit rate and are estimated and corrected for as such. As stated previously, gyro signal generator noise per incremental attitude sample $\Delta\theta$ has been assumed between 0.04 and 0.1 arc-second (1σ) for sampling intervals ranging from 200 to 400 milli-seconds. Accounting also for gyro random drift noise, for commutation error, quantization and computer roundoff errors, the total gyro contributed attitude reference error over a conservative 15 minute period, should be no more than 8 μrad (1σ) ($\approx$ 1.65 arc-second). Attitude and gyro bias updates from processed star tracker measurements can, and probably will, be obtained much more frequently than 15 minutes and the attitude reference error contributed by the gyros is likely to be smaller. Conversely, should the DRIRU II characteristics turn out to be worse than currently expected, more frequent star updates in the order of every 3-5 minutes can be utilized to curb the gyro error build-up.

Total estimated performance of the L-D ACS may now be assessed by combining the various error sources from the attitude reference system, the attitude control system and the effects of the moving and flexible appendages. This has been done in Table 6-11. The error analysis is per axis, using the worst errors encountered per axis from each error source and is, therefore, conservative. All attitude errors refer to the MACS reference cube, and not the TM boresight. Absolute open-loop pointing accuracy of the TM is not critical, but attitude stability is of importance. TM boresight misalignments can be calibrated in flight by known landmark

Table 6-10. BBRC CT-401, 8° x 8° FOV Star Tracker Characteristics

Error Source	Error Without Compensation	1σ Error With External Compensation (arc-sec)	Comments
Slowly Varying Biases			
Null Offset & Nominal Dynamic Lag	18 arc-sec (1σ)	---	Calibrated out by bench test
Aging (Nullshifts, Dynamic Lag Shifts, etc.)	4 arc-sec (1σ)	4.0	No further compensation
Total Biases (RSS)	18.4	4.0	
Errors Appearing Random for Discrete Star Observ.			
Nonlinearity & Nonorthogonality	10 arc-min (peak)	3.0	Bench calibration by polynominal fit: 60 coeffi.
Temperature & Power Sensitivity (±30°C)	2 arc-sec/°C		
External Magnetic Field (0.4 gauss)	10 arc-sec (peak)	2.5	Correction factors/terms obtained from bench test
Star Intensity (ΔM_V = 3)	30 arc-sec (1σ)	2.5	
Scale Factor Changes (Aging)	10 arc-sec (1σ)	1.5	Occasional updates from ground-based Kalman filter
Subtotal (RSS)	203.5	4.9	
Noise			
NEA (Noise Equivalent Angle)	5 arc-sec (1σ) (τ = 0.5 sec, M_V = 6)	5.0	No compensation
Total Random Errors for Discrete Star Observ. (RSS)	203.6	7.0	
Total 1σ Accuracy ($\sum$ Random + Bias)	222 arc-sec	11 arc-sec	

Table 6-11. Estimated Normal On-Orbit Performance Summary (Per Axis)

Error Source	Short-Term (60 seconds) Attitude Stability (1σ) μrad	Long-Term (20 minutes) Attitude Stability (1σ) μrad	Earth Pointing Attitude Determination Accuracy (1σ) μrad		ACS Pointing Accuracy (1σ)*** μrad	
			Random Varying	Biases	Earth Pointing	Relat. Commanded Iner. Reference
ATTITUDE REFERENCE SYSTEM						
• Gyros	1.0	8.0	8.0			
• Star Tracker (Filtered)	---	---	25.0	19.4		
• Ephemeris (100 m, 1σ)	---	---		142.0		
SUBTOTAL ARS			Σ(RSS) 169.6		169.6	45.6
ATTITUDE CONTROL SYSTEM						
• Gyro Noise & Quantization	1.8	1.8	---		1.8	1.8
• Controller Dynamics	1.5	1.5	---		4.4	4.4
• RW Mass Imbalance	0.015	0.015	---*		0.015	0.015
APPENDAGE MOTION						
• Solar Array	2.8	2.8	---*		2.8	2.8
• Ku-Band Antenna & Mast	0.1	0.1	---*		0.1	0.1
• TM (HAC Design)**	1.0	1.0	---*		1.0	1.0
• MSS	0.4	0.4	---*		0.4	0.4
STRUCTURE						
• Misalignments (STA LOS/Cube)	---	---	5.0		5.0	5.0
• Thermal Shifts	---	1.0	1.0		1.0	1.0
Total (RSS)	4.0	8.9	169.7		169.8 (0.0097°)	46.3 (0.0027°)

*Preliminary investigations showed that there is no problem with gyro signal aliasing due to sampling of higher frequencies
**The TRW TM design creates no disturbance in the steady-state since the roof mirror scan wheel turns at a constant rate
***Referenced to MMS MACS optical reference cube

observations, and if the misalignments should turn out to be large, the ACS commands can be biased accordingly. Four-wheel speed biased ACS operation is assumed and the given dynamic error reflects only magnetic unloading attitude perturbations. With only three wheels operating the attitude stability requirements will be violated at wheel speed reversals which with the present magnetic unloading law mainly occur in the x-axis about four times per orbit.

As can be seen all performance requirements could be met. The ephemeris error, assumed as 300 meters (3σ), is by far the largest contributor to spacecraft pointing error. With improved geopotential models as they become available now, ephemeris accuracy (using the NASA tracking network) is expected to be improved to about 100 meters (3σ). However, even with the present ephemeris capability, it appears that 0.01 degree (1σ) pointing is achievable. The L-D/MMS specifications given in Section 2.4 required pointing to only 0.01 degree (1σ) without accounting for the ephemeris error.

The "first look" results of the effects of moving flexible appendages showed that they pose no problem. However, as mentioned earlier, additional studies are recommended. The long-term attitude stability of 10.5 μrad (1σ) can be met, but with no big margin, and achieving this performance specification should be closely watched as L-D progresses in its development. The main error contributors are the gyro drift between updates and the stepping of the flexible FRUSA array. More detailed flexible array analysis is recommended together with a reevaluation of the stability of the gyro derived attitude reference when more data on the DRIRU II becomes available. It is expected, however, that in both cases the presently given error budgets will not change significantly.

7.0 STATIONKEEPING

This section presents a brief study of the periodic orbit velocity correction required to maintain the altitude of the LANDSAT-D (L-D) satellite. It shows that it is required to use all four 5 pound thrusters for the required thrust in a differentially modulated fashion. The latter is necessitated by a significant known center of mass offset. Unless this offset is reduced significantly, therefore, there is no redundancy for this operation. The unknown components of the disturbance torques are smaller than the known components. Thus, the pointing of the thrust vector can be controlled by either the 0.2 or 5 pound thrusters. The rotational motion about the thrust vector must be controlled by the smaller thrusters. Although the relatively large disturbance torques preclude the use of the reaction wheel system, the thrust vector pointing can be maintained to within $\pm$ 0.2 degree with the peak limit cycle rate less than 0.25 degree/second. The required duration of thruster actuation is slightly over 8 seconds for an orbit adjust maneuver of ΔV = 0.35 m/second.

7.1 Problem Definition

Altitude sustenance of the L-D satellite is required to prevent gradual orbit decay which will cause a period decrease, hence a drift in the east-west ground track. As noted elsewhere in the study, this orbit sustenance is accomplished by means of the orbital velocity increase (ΔV) of 0.35 m/second every 16 days. The intent of this section is to determine how the reaction wheel system and the MMS propulsion module are best utilized for this stationkeeping ΔV operation and to assess the potential attitude control capabilities during ΔV. The discussion is, therefore, divided into two parts along these subjects. Various parameters either given or assumed for the analysis are listed in Table 7-1. The coordinate definition and thruster arrangement are illustrated in Figure 7-1.

7.2 Selection of Thrust and Torque Actuation During ΔV

The linear force required in a ΔV operation can be supplied by either the 0.2 or 5 pound thrusters. The torque required for attitude control

Table 7-1. Parameters Used in Analysis

Parameters		Symbols	Values
ΔV frequency			Once every 16 days
Required velocity increase		ΔV	0.35 m/sec
Orbit rate		ω_o	1.059×10^{-3} rad/sec = 14 9/16 orbits/day
Orbit radius		R	7083.47 km
Mass		M	1590 kg
Moments of inertia	x	I_{xx}	2030 kg-m^2
	y	I_{yy}	2670 kg-m^2
	z	I_{zz}	2370 kg-m^2
CM location	x*		0
	y		-17.8 cm
	z		-21.3 cm
Thrust force	0.2 lb thruster	F_1	0.89 N
	5 lb thruster	F_2	22.24 N
Torque arm	about x		0.6 m
	about y or z	L	1.6 m
Reaction wheel torque			0.15 N-m
Momentum storage capability			20 N-m-sec

*By definition

a) Coordinate Definition

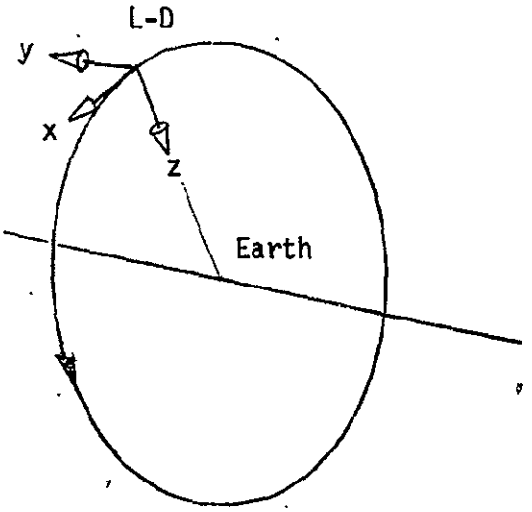

b) Thruster Arrangement

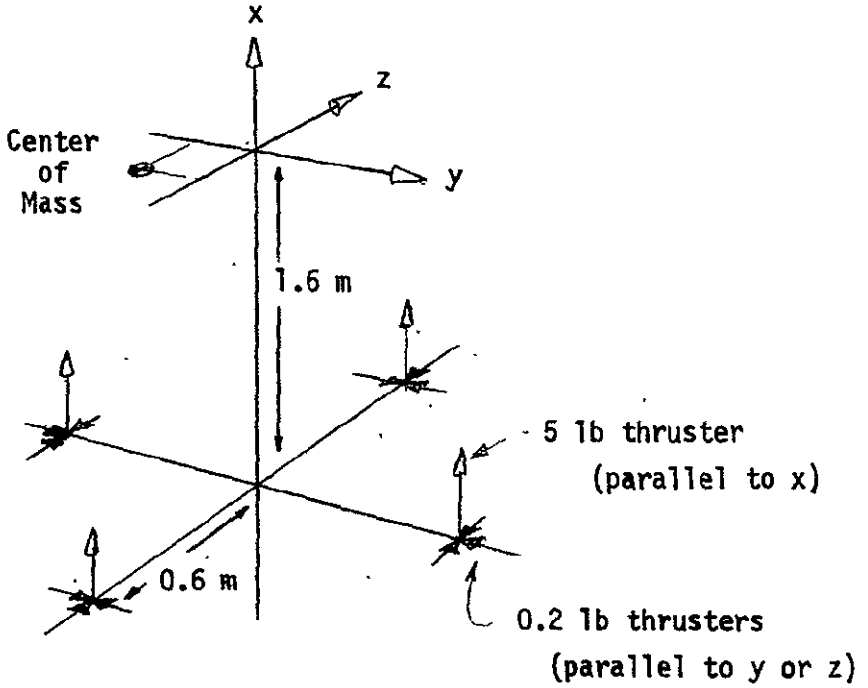

Figure 7-1. Basic Geometry

during the ΔV operation can be supplied by either of these thrusters or the reaction wheel motors. Combinational feasibility of these force and torque actuations is first investigated on the basis of the ΔV requirements, spacecraft geometry and torquing capabilities.

7.2.1 Feasibility of 0.2 Pound Thrusters for ΔV

Nominally the spacecraft z-axis is pointed toward the earth and the x-axis is along the direction of the orbital motion. Since the 0.2 pound thruster axes are parallel to either the y- or z-axis, a 90 degree maneuver will be required before and after each ΔV operation (along the orbital path). In addition, actuation of each thruster will be accompanied by a torque of 1.42 newton-m due to the torque arm. The duration ΔT is given by

$$\Delta T = \frac{M \cdot \Delta V}{F_1} \tag{7-1}$$

The torque exerted over ΔT will be manifested in the stored wheel momentum, ΔH.

$$\Delta H = F_1 \cdot L \cdot \Delta T = M \cdot \Delta V \cdot L = 890 \text{ N-m-sec} \tag{7-2}$$

Compared to the torque and momentum storage capabilities (0.15 N-m and 20 N-m-sec, respectively) of each reaction wheel, it is clear that the 0.2 pound thrusters are totally unsuitable for the ΔV operation.

7.2.2 Number of 5 Pound Thrusters Required

Whether two or four 5 pound thrusters are to be used is determined next by examining the disturbance torque components about y and z generated by a significant center of mass offset. Since the offset is nominally -21.3 cm (-8.4 inches) in the z direction, the torque about y due to two thrusters is 2 x 22.24 N x 0.213 m = 9.49 N-m. Similarly a torque of 7.91 N-m about z is generated by the c.m. offset of -17.8 cm (-7 inches) in the y direction. With a torque arm length of 1.6 meter each 0.2 pound thruster

can provide a control torque of 1.42 N-m. It can be seen that these disturbance torque components cannot be countered even with three 0.2 pound thrusters (4.27 newton-m). On the other hand, each 5 pound thruster can produce a torque of 22.24 N x 0.6 m = 13.34 N-m. Thus, the larger thrusters have to be operated in pairs, differentially modulated, to generate both the linear force required for the ΔV and the torque required to counter the known disturbance during the ΔV. Furthermore, since the disturbance due to the c.m. offset causes torques about both y and z, all four 5 pound thrusters must be utilized. This means that there will be no redundancy unless the c.m. offset is reduced significantly.

7.2.3 Attitude Control Consideration

Finally the attitude control torque requirement is assessed by examining the disturbance torques due to other sources. These are the unpredictable torque components which cannot be countered by the pre-programmed thruster modulation. Of these the major sources are the uncertainties in the c.m. location, thrust vector orientation (alignment) and thrust force mismatch. The variational ranges of these anomalies are determined on the basis of the design tolerances used in other current spacecraft programs such as HEAO and FLTSATCOM.

The 3σ c.m. uncertainty is first assumed to be $\pm$ 2 cm ($\approx$ 0.8 inch) in the y or z direction. The disturbance torque τ_{dl} about each of these axes is

$$\tau_{dl} = 2 \times 22.24 \times 0.02 = 0.89 \text{ N-m}$$

From Equation (7-1) the average activation time ΔT for each thruster is found to be

$$\Delta T = \frac{1590 \text{ kg} \times 0.35 \text{ m/sec}}{4 \times 22.25 \text{ N}} = 6.26 \text{ sec} \qquad (7\text{-}3)$$

Therefore, the total angular momentum to be removed by the attitude control action is

$$\Delta H_1 = 0.89 \times 6.26 = 5.57 \text{ N-m-sec}$$

The 3σ thrust vector alignment uncertainty is assumed to be $\pm$ 1 degree. When the opposing thrusters are misaligned to the same side of the xy or xz plane, a y or z torque will be generated. Since the misalignments are statistically independent, the disturbance torque τ_{d2} due to each thruster pair is given by

$$\tau_{d2} = 22.24 \times 1.6 \times \sin \sqrt{1^2 + 1^2} = 0.88 \text{ N-m}$$

If the misalignment is opposite of these planes, the resulting torque will be about x. If all four thrusters are contributing to the x torque in the same sense, its magnitude τ_{d2x} is given by

$$\tau_{d2x} = 22.24 \times 0.6 \times \sin \sqrt{1^2 + 1^2 + 1^2 + 1^2} = 0.47 \text{ N-m}$$

The corresponding momentum to be removed is ΔH_2 = 5.5 N-m-sec for y or z and ΔH_{2x} = 2.92 N-m-sec for x.

The 3σ thrust force mismatch between the opposing thrusters is assumed to be $\pm$ 10% in L-D. Thus the disturbance torque τ_{d3} about y or z is given by

$$\tau_{d3} = 22.24 \times 0.1 \times 0.6 = 1.33 \text{ N-m-sec}$$

The corresponding ΔH_3 = 8.35 N-m-sec.

The total effect can be represented by the root-sum-square of these torques.

$$\left.\begin{aligned} \tau_{dx} &= 0.47 \text{ N-m} \\ \tau_{dy} \text{ or } \tau_{dz} &= \sqrt{0.89^2 + 0.88^2 + 1.33^2} = 1.83 \text{ N-m} \end{aligned}\right\} \quad (7\text{-}4)$$

The momentum components to be removed are

$$\left.\begin{aligned} \Delta H_x &= 2.92 \text{ N-m-sec} \\ \Delta H_y \text{ or } \Delta H_z &= \sqrt{5.57^2 + 5.5^2 + 8.35^2} = 11.45 \text{ N-m-sec} \end{aligned}\right\} \quad (7\text{-}5)$$

It is clear that these disturbance torque components cannot be countered by the reaction wheels. If a pair of 0.2 pound thrusters are used the control torque available for x is 2 x 0.89 x 0.6 = 1.07 N-m, which is twice as large as τ_{dx}. The control torque about y or z is 2.82 N-m, about 50% greater than τ_{dy} or τ_{dz}. If three 0.2 pound thrusters are used for y or z, the available control torque is 4.27 N-m, more than twice as large as τ_{dy} or τ_{dz}. Thus the attitude control during ΔV can be accomplished by either 0.2 or 5 pound thrusters. Using the smaller thrusters will be convenient since an attitude control system utilizing these will be already available on MMS. On the other hand, the larger thrusters can be used for the attitude control by modifying the differential modulation program required to overcome the known components of the disturbance torque. Since the choice between these thruster sets is not obvious at this point, a further comparison is made in the following section.

7.3 Attitude Control Characteristics

The suitability of different size thrusters for the attitude control during the stationkeeping ΔV operation is compared by investigating the difference in the performance characteristics. The latter are discussed in terms of pointing accuracy, thruster pulsewidth, duty cycle and propellant consumption.

7.3.1 Thrust Vector Pointing Accuracy

When thrusters of fixed force and orientation are used in attitude control, the torque actuation is necessarily of a pulsing type. The

attitude hold accuracy is then determined primarily by the deadzone magnitude designed into the controller. Since a high degree of pointing accuracy cannot be achieved without a reaction wheel system, it seems reasonable to assume that the pointing accuracy required during ΔV is predicated on the allowable orbit perturbation. Therefore, the magnitude of the orbit perturbation is first calculated by using a simple orbit momentum model.

As shown in the figure below, the angular rate of the satellite around the earth can be represented by the angular momentum H, the magnitude of which is given by

$$H = M R^2 \omega_o = 8.4487 \times 10^{13} \text{ N-m-sec} \tag{7-6}$$

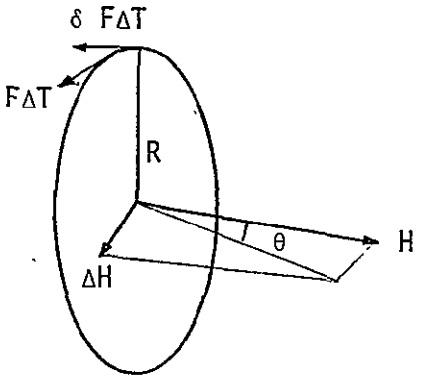

If the deadband for the thrust vector pointing control is ψ_{db} and the control is achieved in a one-sided limit cycle, the maximum possible momentum change ΔH of the satellite body due to the thrust force component normal to the main thrust vector is given by

$$\Delta H = 4 F_2 \cdot \Delta T \cdot \sin \psi_{db} \cdot R \tag{7-7}$$

where ΔT = duration of ΔV operation = 6.26 seconds. Since ΔT is relatively short compared to the orbit period (= 5933 seconds), ΔH is practically an impulse. Thus the orbit precession θ is given by

$$\theta = \frac{\Delta H}{H} = \frac{F \cdot \Delta T \cdot \sin \psi_{db} \cdot R}{M R^2 \omega_o} = \frac{M \cdot \Delta V \cdot \sin \psi_{db}}{M R \omega_o} = \frac{\Delta V \cdot \sin \psi_{db}}{R \omega_o} \qquad (7\text{-}8)$$

For ψ_{db} = 1 degree, θ is calculated to be 4.67×10^{-5} degrees. At the equator this corresponds to about 5 m of east-west shift. Although the orbital requirements are not known at this point, the effect of a deadband on the order of 2 or 3 degrees seem negligibly small. This is also compatible with the MMS pointing and rate requirements of 3 degrees and 0.5 degree/second during orbit adjustment (Reference 2). The effect of thrust misalignment in the orbit plane causing orbit eccentricity was not investigated. It is assumed that a pitch deadband of the similar magnitude is acceptable.

7.3.2 Differential Modulation of Thrusters

A transverse torque can be generated by differentially modulating a pair of thrusters which nominally produce, when activated together, only a linear force with zero torque. When there is a fixed known disturbance torque, the simplest way to modulate the thrusters is to activate one continuously while pulsing the other at a prescribed duty cycle. The resulting limit cycle characteristics are first analyzed.

In an ideal limit cycle, the body rate varies linearly between plus and minus ω as shown below.

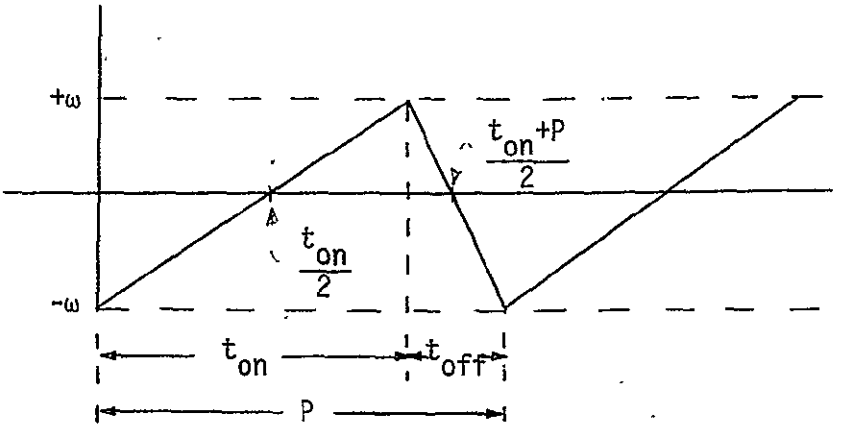

While both thrusters are on (t_{on}), the net torque about the control axis is $\tau_c - \tau_c + \tau_{on} = \tau_{on}$ where τ_c = control torque due to each thruster and τ_{on} = disturbance torque, positive in this example. While one thruster is off (t_{off}), the net torque is $\tau_{off} - \tau_c$ and the polarity is reversed, where τ_{off} is disturbance during this period. Thus the peak rate ω is related to the torques and the modulation period $P = t_{on} + t_{off}$ by

$$2\omega = \frac{\tau_{on} \cdot t_{on}}{I} = \frac{(\tau_c - \tau_{off})\ t_{off}}{I} \qquad (7\text{-}9)$$

If the duty cycle is defined by

$$\lambda = \frac{t_{on}}{P} \qquad (7\text{-}10)$$

$$\tau_{on}\ \lambda P - (\tau_c - \tau_{off})(1-\lambda)\ P = [\tau_{off} - \tau_c + (\tau_{on} - \tau_{off} + \tau_c)\ \lambda]\ P = 0$$

$$\lambda = \frac{\tau_c - \tau_{off}}{\tau_{on} - \tau_{off} + \tau_c} \qquad (7\text{-}11)$$

$$\omega = \frac{\tau_{on}\ \lambda P}{2I} \qquad (7\text{-}12)$$

The peak-to-peak angular excursion is the measure of the velocity vector pointing error. This is represented by the triangular area when the rate is positive or negative.

$$\Delta\psi_{P-P} = \frac{t_{on} + t_{off}}{2} \frac{\omega}{2} = \frac{\tau_{on} \lambda P^2}{8I} \tag{7-13}$$

If the disturbance torque is due to c.m. offset, $\tau_{on} = 2\tau_{off}$. Therefore, Equations (7-11) through (7-13) can be written as

$$\left.\begin{aligned} \lambda &= \frac{\tau_c - \tau_{off}}{\tau_{off} + \tau_c} \\ \omega &= \frac{\tau_{off} \lambda P}{I} \\ \Delta\psi_{P-P} &= \frac{\tau_{off} \lambda P^2}{4I} \end{aligned}\right\} \tag{7-14}$$

For the pitch axis Equation (7-14) can be calculated by using various parameters shown in the last section

$$\tau_c = 13.34 \text{ N-m}$$

$$\tau_{on} = 9.49 \text{ N-m} = 2\tau_{off}$$

$$\left.\begin{aligned} \lambda &= 0.475 \\ \omega &= 0.0484 \text{ deg/sec}^2 \cdot P \\ \Delta\theta_{P-P} &= 0.0121 \text{ deg/sec}^2 \cdot P^2 \end{aligned}\right\} \tag{7-15}$$

For yaw

$$\left.\begin{aligned} \tau_{on} &= 7.91 \text{ N-m} \\ \lambda &= 0.543 \\ \omega &= 0.0519 \text{ deg/sec}^2 \cdot P \\ \Delta\psi_{p-p} &= 0.0130 \text{ deg/sec}^2 \cdot P^2 \end{aligned}\right\} \quad (7\text{-}16)$$

The peak limit cycle rates and angles are plotted in Figure 7-2b as functions of P. It can be seen that the limit cycle rate and angular excursion do not reach the level of 0.5 degree/second and 3 degrees during the ΔV period of 6 seconds or so.

The total thruster actuation period T required for each ΔV operation can be calculated from

$$M\,\Delta V = F\,(2T + \lambda_y\,T + \lambda_z\,T)$$

$$T = \frac{M\,\Delta V}{F\,(2 + \lambda_y + \lambda_z)} \quad (7\text{-}17)$$

where

F = force of each thruster

M = mass of the satellite

The number of modulation cycles N required for pitch and yaw are then determined by

$$N = \frac{T}{P} \quad (7\text{-}18)$$

a) Thruster Actuation

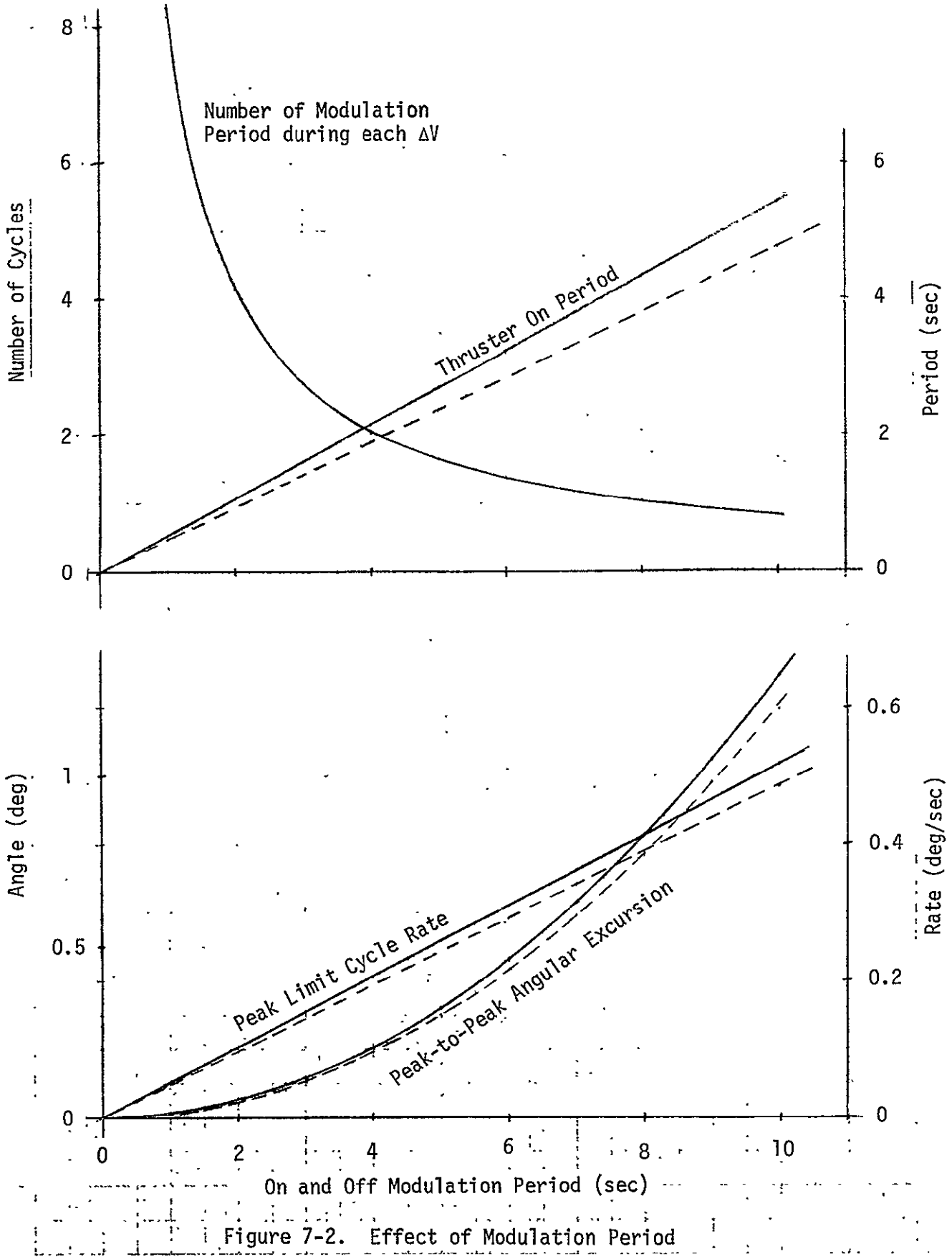

Figure 7-2. Effect of Modulation Period

The duty cycle and number of modulation cycles are plotted in Figure 7-2a. Thus the selection of the modulation period is a tradeoff problem between the thruster actuation and the limit cycle characteristics. The peak rate and pointing error decreases with the modulation period. However, this will cause the number of the thruster actuation to increase and the thruster efficiency to decrease due to shorter "on" time, particularly below modulation period of 3 seconds.

7.3.3 Attitude Control with 5 Pound Thrusters

The thruster modulation described above is an open loop technique to counter known torque components during ΔV. As described earlier, there will be also some unknown torques due to various anomalies in thrusters and mass properties. The y and z components of these torques can be countered by superposing an attitude control logic on the open loop modulation. Since the worst case unknown disturbance torque of 1.83 N-m about y or z (Equation (7-4)) is considerably smaller than the known torque components, the attitude control will be accomplished by varying the "on" period of the one-sided modulation. Assuming that an ideal control laws exists, the effects of the unknown components are briefly analyzed.

With the addition of the unknown torque component τ_d, the quantities shown by Equation (7-14) can be written as

$$\lambda = \frac{\tau_c - \tau_{off} + \tau_d}{\tau_{off} + \tau_c}$$

$$\omega = \frac{(\tau_{on} + \tau_d)\,\lambda P}{2I} \qquad (7\text{-}19)$$

$$\Delta\psi_{p\text{-}p} = \frac{\omega P}{4} = \frac{(\tau_{on} + \tau_d)\,\lambda P^2}{8I}$$

For $-1.83 \leq \tau_d \leq 1.83$ N-m, the variational ranges of these quantities for the pitch axis are

$$\left.\begin{aligned} \lambda_y &= 0.371 \sim 0.576 \\ \omega_y &= 0.0307 \sim 0.07 \text{ deg/sec}^2 \cdot P \\ \Delta\theta_{p-p} &= 0.00769 \sim 0.0175 \text{ deg/sec}^2 \cdot P^2 \end{aligned}\right\} \quad (7\text{-}20)$$

For yaw

$$\left.\begin{aligned} \lambda_z &= 0.437 \sim 0.648 \\ \omega_z &= 0.0321 \sim 0.0763 \text{ deg/sec}^2 \cdot P \\ \Delta\psi_{p-p} &= 0.0080 \sim 0.0191 \text{ deg/sec}^2 \cdot P^2 \end{aligned}\right\} \quad (7\text{-}21)$$

Using Equation (7-17), the variational range of the ΔV period is found to be 7.76 to 8.9 seconds. As an example, these various quantities are summarized in Table 7-2 for the yaw axis when P = 3 seconds. The velocity vector pointing error, of course, needs not increase with the unknown torque component. The error can be bounded by means of the attitude control deadband. In this case the number of thruster modulation cycle will increase slightly.

7.3.4 Attitude Control with 0.2 Pound Thrusters

Since the x-axis control cannot be achieved by the larger thrusters, it must be done with the smaller ones. The control about other axes can be also done with the smaller thrusters. Since the attitude controller using these thrusters is a typical on-off reaction controller, the attitude errors and rates are functions of the deadband, rate feedback gain, etc. Therefore, the discussion here is limited to the estimation of the required propellant.

Assuming that the attitude control is accomplished mostly in a one-sided limit cycle, the required impulse is calculated by mutiplying the torque with the duration of the ΔV operation. For the x-axis, the

Table 7-2. Sample Yaw Axis Performance Using 5 Pound Thrusters for Attitude Control (Modulation Period = 3 sec)

Quantities	Units	Variational Range		
Unknown Disturbance	N-m	- 1.83	0	+ 1.83
Total ΔV Period	sec	8.9	8.29	7.76
Number of Modulated Thruster Firing	/ΔV /year	3 69	3 69	3 69
Modulated Thruster "On" Period	sec	1.96	2.44	2.92
Peak Limit Cycle Rate	deg/sec	0.10	0.16	0.23
Velocity Vector Pointing Accuracy	deg	± 0.07	± 0.12	± 0.17

maximum disturbance torque is 0.47 N-m (Equation (7-4)). Multiplying this with the longest possible ΔV period of 8.9 seconds, the total torque impulse is 4.18 N-m-sec. Since the torque arm for the x-axis control is about 0.6 m, the thrust impulse is 6.97 N-sec. Since one ΔV is to be performed every 16 days, the annual impulse requirement for x is 159 N-sec (= 35.8 pound-seconds). Even with a low specific impulse of 150 seconds, this corresponds to 0.11 kg (weight) of propellant.

When the smaller thrusters are used for the attitude control for the y and z axes, the nominal ΔT will be 8.29 seconds. Again assuming the one-sided limit cycle, the impulse requirement for both axes will be

$$\frac{2 \times 1.83 \times 8.29}{1.6} \frac{365}{16} = 432.6 \text{ N-sec } (= 97.25 \text{ lb-sec})$$

For the specific impulse of 150 seconds, the above requirement in terms of the propellant weight is 0.29 kg (weight) per year. This is certainly a very small amount of the propellant. Considering that the reaction control with the 0.2 pound thrusters will be available as a part of the standard MMS attitude control system, the use of the smaller thrusters for the attitude control during each ΔV appears more attractive. Though already small, the propellant requirement can be reduced further if the uncertainty in the disturbance torques is reduced by means of in-orbit calibrations of various anomalies. In the event of critical propellant requirement the 5 pound thrusters can be considered for the attitude control. However, an appropriate control law must be developed.

7.4 Summary of Stationkeeping Policy and Performance

Summarizing the foregoing discussions, the following is the recommended stationkeeping policy and its attendant risk. The potential attitude control capability is also described and the pertinent numerical data are presented in Table 7-3.

Table 7-3. Summary of Stationkeeping Policy

a) Use of 5 Pound Thrusters for ΔV and Control of Known Disturbance Torque

Axis	Known Disturbance		Control Torque Capability (N-m)		Thruster "On" Time (sec)
	Torque (N-m)	Momentum (N-m-sec)			
x	0	0	0		0
y	+9.49	59.4	+y	13.34	3.94
			-y	-13.34	8.29
z	+7.91	49.5	+z	13.34	4.50
			-z	-13.34	8.29

b) Use of 0.2 Pound Thrusters for Attitude Control

Axis	Unknown Disturbance (3σ)		Min. Control Torque Capability (N-m)	Thruster "On" Time (sec)
	Torque (N-m)	Momentum (N-m-sec)		
x	$\pm$ 0.47	3.9	1.07	3.64
y	$\pm$ 1.83	15.17	$\pm$ 2.82	5.38
z	$\pm$ 1.83	15.17	$\pm$ 2.82	5.38

Linear Impulse:

The orbit velocity increase ΔV of 0.35 m/second every 16 days required for the altitude sustainance, hence the stationkeeping, can be accomplished only by actuating all four 5 pound thrusters. Due to a significant center of mass offset large +y and +z torque components are generated during the ΔV operation. This can be countered only by off-modulation of the 5 pound thrusters, i.e., by operating one pair of thrusters (causing +y and +z torques) at about 50% duty cycle while the other thrusters are actuated continuously for about 8.3 seconds.

Risk:

This implies that there is no thruster redundancy in the stationkeeping capability unless the center of mass offset is drastically reduced.

Method of Attitude Control:

The unknown portion of the disturbance torque components due to the uncertainties in the center of mass location, thrust vector alignment, thrust force mismatch, etc. can be countered most simply by the MMS reaction control system using the 0.2 pound thrusters. The additional propellant required for this is quite modest. Assuming a low specific impulse of 150 seconds, the annual requirement is 0.11 kg (= 0.24 pound) for x and 0.29 kg (= 0.65 pound) for y and z. The attitude control about y and z can be accomplished also by modifying the thruster duty cycle described above. This will require no additional propellant, since the total ΔV period is predicated upon the total impulse delivered. The control laws required for this, however, must be developed in addition to the existing MMS control laws.

Attitude Control Capability:

During the ΔV fine pointing cannot be maintained since the use of the MMS reaction wheel system is precluded due to its insufficient torque capability. Thus the attitude control capability is

dependent on the deadband of the MMS reaction control system and the modulation period of the programmed 5 pound thruster actuation. The relationship between the pointing accuracy and the modulation period is shown in Figure 7-2. It does not appear difficult at all to maintain the velocity vector pointing to within $\pm$ 0.2 degree with the peak limit cycle rate of 0.25 degree/second. This is much more stringent than the MMS pointing requirements of $\pm$ 3 degrees and 0.5 degree/second during orbit adjustment.

8.0 AUTONOMOUS REGISTRATION

The feasibility of autonomous elimination of scene-to-scene temporal registration errors for the L-D Thematic Mapper (TM) is addressed. Temporal registration error is defined as the apparent shift in landmark location with respect to two successive frames separated by the L-D revisit time of exactly 16 days. A performance goal of 0.1 pixel (1σ) registration repeatability has been set. From an altitude of 705 km, this is equivalent to a 3 meter (1σ) pointing uncertainty on the ground.

8.1 Introduction

Autonomous registration is accomplished by on-board estimation of pseudo attitude and attitude rate commands for eliminating registration errors caused by changes in spacecraft position, velocity, attitude, gyro bias uncertainty, and TM to attitude reference system (ARS) reference cube misalignment between successive 16 day passes. The MMS stellar and gyro inertial references are used to determine the spacecraft inertial attitude. The DOD Navigation Satellite Global Positioning System (GPS) is assumed to be used to determine spacecraft ephemeris.

The complete Kalman filter state consists of six ephemeris states, six ARS attitude and gyro bias uncertainty states, and nine misalignment states. The state transition matrices representing spacecraft position and velocity evolution, ARS attitude and gyro bias uncertainty evolution, and the misalignment evolution are all distinctly different. The use of landmark measurements for enhancing the estimation of the full 21 states suffers from state separability problems (see References 11 and 12). The Kalman filter without the misalignment states becomes indecisive in separating range from pitch and track from roll when landmark data is used. For short time intervals, however, the filter attitude and ephemeris states can be combined to yield a simplified model with a filter state of lower dimension consisting of separable states for which landmark measurements can be used to good advantage. Adequate covariance performance of this simplified Kalman filter, however, does not imply feasibility of autonomous registration error

elimination because of modelling errors in the system description on which the covariance analysis is based. In view of the desired 3 meter (1σ) registration, these errors can be significant.

The modelling errors impact the selection of the state noise covariance matrix in the simplified Kalman filter formulation. These errors are used to configure a recommended autonomous registration scheme, specify the necessary quality of stellar references, gyro performance, and GPS position and velocity uncertainty requirements. Registration accuracy, the frequency of landmark updates, allowable thermal misalignments, and the 1σ performance goal of the simplified Kalman filter are established.

8.2 Problem Formulation

The spacecraft attitude control and determination system (ACDS) contains a stellar-inertial attitude reference system. This system employs precision gyros for obtaining high-bandwidth, short-term attitude information, and strapdown star trackers which provide measurements for periodic on-board estimation of the attitude and gyro bias updates. This study is restricted to the earth pointing mode for which the spacecraft yaw axis nominally points along nadir, the roll axis points in the direction of the orbital velocity, and the pitch axis is nominally perpendicular to the orbit plane. Ephemeris data is required for on-board estimation of the local vertical reference. Attitude control relative to the local vertical is maintained through the action of four reaction wheels mounted as three orthogonal wheels plus one skewed wheel.

Additional assumptions are a circular orbit inclined 98.2 degrees relative to the equatorial plane and an orbiting altitude of 705 km.

8.2.1 Registration Error

Registration in this document refers specifically to temporal registration which is the apparent shift in landmark location with respect to two successive frames separated by the revisit time of approximately 16 days. In Figure 8.2-1, the original frame sequence on the first pass is

Registration Error

The registration error is the apparent shift in landmark location with respect to two successive frames (separated by 16 days)

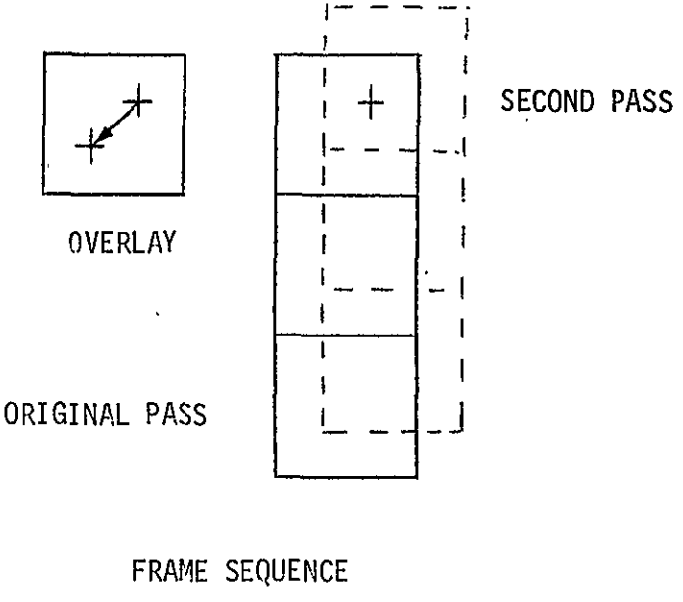

Problem Definition

Elimination of scene-to-scene registration errors

Performance Goal

Eliminate registration deviations to within 0.1 pixel (1σ) which is 3 meters at an altitude of 705 km.

Figure 8.2-1. Registration Error, Problem Definition, and Performance Goals

indicated by the solid lines. Without autonomous registration and 16 days later the frame sequence for the second pass may appear relative to the earth's surface as shown by the dashed lines. The landmark, shown as a highway intersection, appears in the upper right-hand corner of the third frame on the original pass and in the lower left-hand corner of the third frame on the second pass. Relative to the frame the landmark appears to have shifted as the overlay shows. Temporal registration error is the apparent shift of the landmark relative to two successive frames as indicated by the overlay.

8.2.2 General Approaches to Registration Error Elimination

There are three basic approaches to registration error elimination

(1) Reorient the mapper boresight such that subsequent trackes fall within a 3 meter (1σ) band of the initial track.

(2) Eliminate registration errors before transmission using on-board software modification of the TM data.

(3) Transmit the registration error with each frame to the ground such that a "canned" ground software program can correct the TM data.

The first approach can be accomplished by using (1) accurate ephemeris, attitude and cooperative landmark data; (2) only landmark deviations; or (3) a combination of both (1) and (2) to derive pseudo attitude and attitude rate commands to compensate for registration errors caused by changes in spacecraft position, velocity, attitude, gyro bias uncertainty, and TM to ARS reference frame misalignment.

The second approach requires excessive data storage and on-board data handling and will not be considered as a viable alternative. In terms of the definition of registration error, its elimination on-board prior to transmission to the ground by satellite link would require storage of the

previous cooperative landmark data in addition to a) the estimation of the registration error and error rate from distinct landmarks and b) accurate modelling of the registration error evolution between landmarks.

The third alternative is a simplified version of the second approach. It involves the on-board estimation of the registration error and error rate, in addition to accurate modelling of the registration error evolution between landmarks. The actual shifting of the data and redefinition of the frames along with image enhancement is performed on ground.

For this study, emphasis is placed on establishing the feasibility of the first approach. The modelling errors incurred by accepting the inseparability of pitch from ephemeris downrange and roll from ephemeris cross-track and combining these states using a simplified on-board Kalman filter implementation of the first approach will also shed light on the feasibility of the third alternative.

8.2.3 Registration Error Sources

Figure 8.2-2 shows an example TM pointing ground track relative to the reference ground track with both relative to landmark characteristics. The reference ground track is a hypothetical track in the sense that if the TM attitude and position matched the local vertical reference frame for the ideal orbit, then the TM pointing would coincide with the reference track. Suppose that the geometry of Figure 8.2-2 represents the outcome of the first pass. Note that there is an initial offset of the first pass from the reference track which pictorially represents the initial state. Sixteen days later the spacecraft goes into the second pass. What are the major sources of registration error during the second pass?

Figure 8.2-3 shows a block diagram of a typical attitude control system for the earth pointing mode and without autonomous registration software. The second pass sources of registration error are

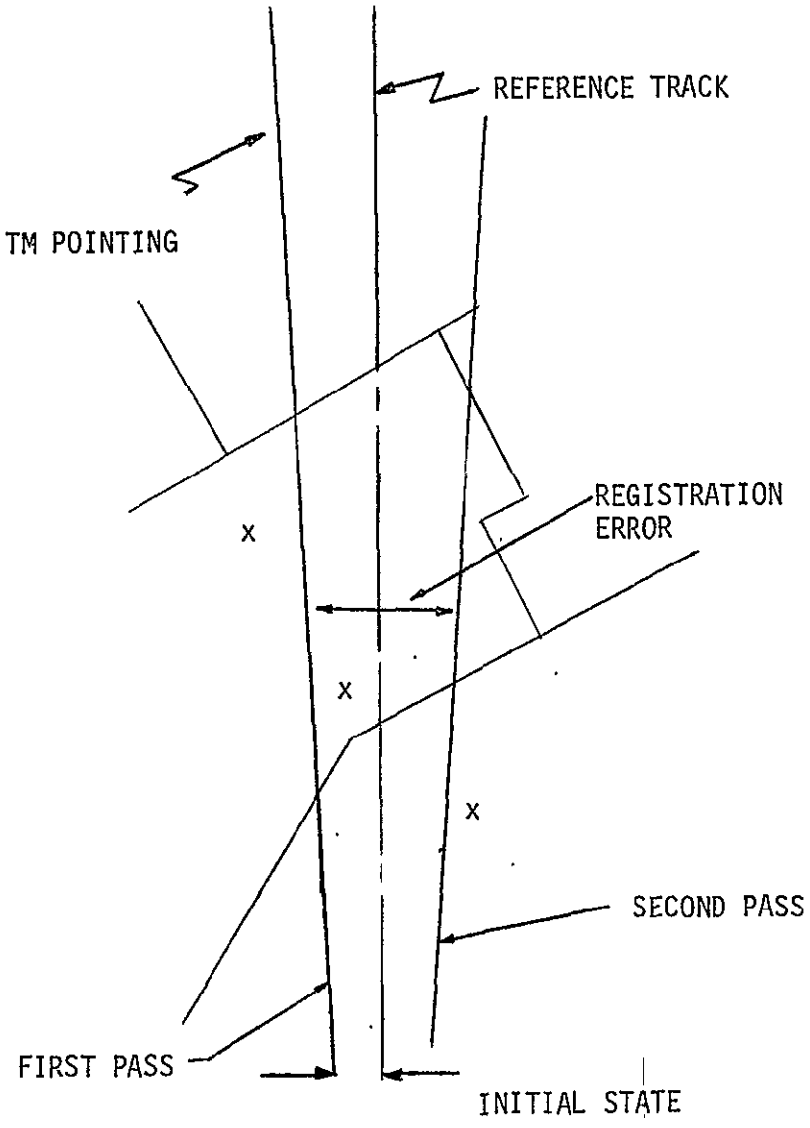

Second Pass Sources of Error

- Difference in desired attitude
- Same desired attitude, different initial state
- Same desired attitude, same initial state but different actuator and sensor noise

Figure 8.2-2. Autonomous Registration Error Sources

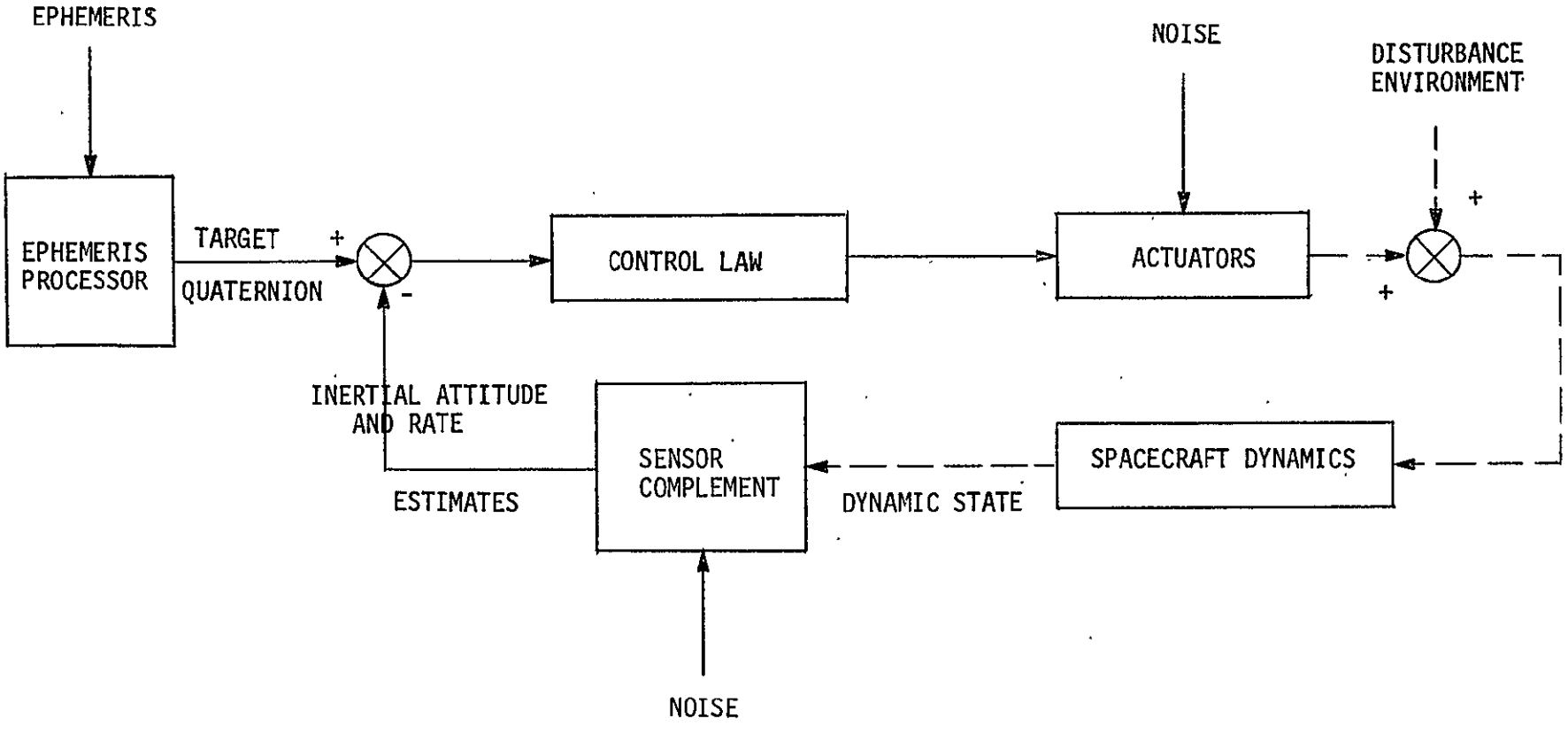

Figure 8.2-3. Attitude Control System Without Autonomous Registration Software

- Difference in the target quaternion*, i.e., the desired attitude due to different ephemeris.

- Same desired attitude but different initial state.

- Same desired attitude, same initial state but different actuator and sensor noise.

This list is expanded in Table 8.2-1. The performance goal is repeatability in the TM boresight ground track to within a 1σ uncertainty of 3 meters.

8.2.4 Approach to Autonomous Registration

The recommended approach to autonomous registration is to

- Attribute TM pointing error to an error in spacecraft attitude and attitude bias commands.

- Lump ephemeris position and attitude error into a pointing error that will be called pseudo attitude error

- Lump ephemeris velocity error, gyro bias, and thermal misalignment rate into pointing error rate.

- Estimate pseudo attitude error caused by change in spacecraft orbital position, and TM attitude; use landmark measurement data, i.e., landmark registration deviations.

- Estimate pseudo rate bias due to velocity error, misalignment rate error, and change in gyro bias; use cooperative landmark registration deviations.

*The target quanternion is the commanded spacecraft attitude relative to ECI.

Table 8.2-1. Registration Error Sources

The second ground track may differ from the first because:

- Ephemeris is different
- Spacecraft attitude state is different
- Misalignment between primary sensor, actuators, and sensor complement changes
- High frequency actuator and sensor noise is present
- Change in sensor and actuators has occurred
- Change in spacecraft mass properties has taken place
- Disturbance environment changes

Problem: Must have repeatability in TM boresight ground track to within a 1σ uncertainty of 3 meters

The required processing elements are shown in Figure 8.2-4. There are four basic processing elements

- Reference Command Processor
- Spacecraft Relative State Error Estimator
- Instrumentation Error Estimator
- Ground Control Point Processor

The Reference Command Processor uses the ephemeris information to synthesize the commanded earth pointing attitude (LV reference) in terms of a target quaternion referenced to ECI, and LV reference rate profile. On subsequent passes the spacecraft attitude command is biased by the error in the two successive ground track estimates. Changes in the spacecraft attitude and rate relative to the LV reference frame will cause a registration

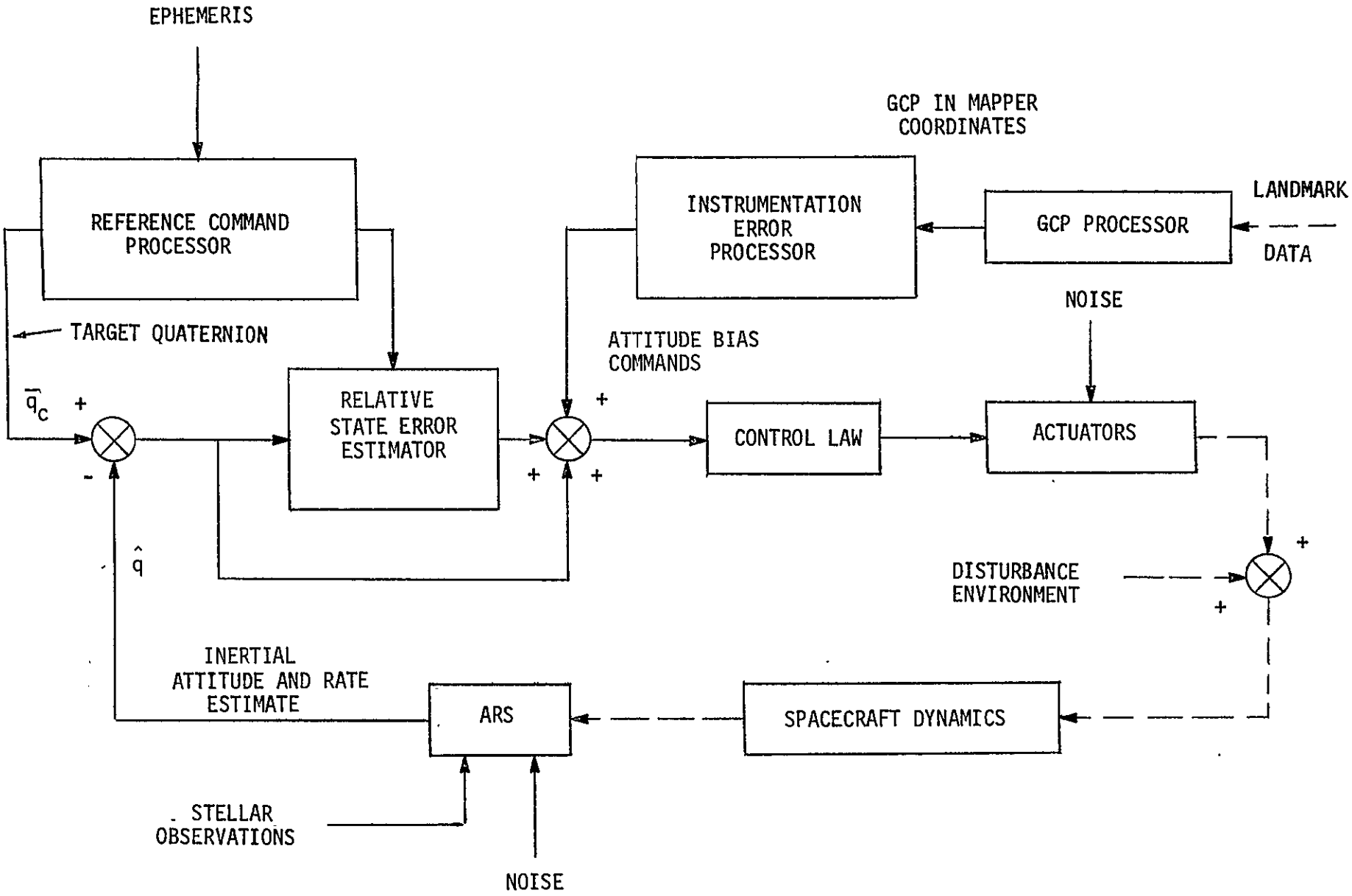

Figure 8.2-4. Autonomous Registration

error going into the second pass. The Spacecraft Relative State Error Estimator attempts to estimate the change in the attitude and gyro bias using information from the reference command processor and the ARS. Attitude and attitude rate commands are derived so that changes in the system state can be compensated for prior to the first landmark. The Instrumentation Error Estimator operates during all subsequent passes. This estimator derives pseudo attitude and attitude rate signals for compensation of registration deviations caused by changes in the TM to ARS misalignment history, the gyro bias history, and the ephemeris history. This estimator uses landmark registration deviations. The Ground Control Point (GCP) Processor obtains GCP location to within a 1σ of 0.0707 pixel which yields a one-tenth pixel (1σ) registration deviation.

In summary, the recommended approach to autonomous registration based on the trades in Section 8.2.3 has been further clarified in terms of the functional requirements of the basic processing elements. The concrete analytic details of three processing techniques will be outlined and traded in Section 8.3. The first technique uses accurate ephemeris, attitude, and cooperative landmark data for estimating the changes in satellite orbital position, velocity, attitude, gyro bias, and ARS to TM misalignment states. These state estimates are in turn used to synthesize pseudo attitude and attitude rate commands for eliminating the registration error between successive 16 day passes. This technique relies on very accurate geodetic coordinates of the cooperative landmarks. The second technique uses cooperative landmark deviations to estimate on ground TM boresight pointing errors and rates between two successive passes. This technique does not require extremely accurate geodetic coordinates for the cooperative landmarks.

The third technique is a combination of the first two software techniques and uses cooperative landmark deviations and accurate ephemeris data.

8.3 Filtering Models, Modelling Errors, and Performance Requirements

The key to eliminating registration deviations is repeatability. Since repeatability in geodetic ground track, spacecraft attitude, attitude control instrumentation, and disturbance environment is just not possible, an active on-board technique of spacecraft maneuvering for ground track repeatability must be used. There are three basic processing techniques for autonomous registration. The first technique relies on accurate ephemeris (GPS), attitude, and cooperative landmark data for estimating the full 21 states in the complete syste model. The second technique uses only landmark deviations on subsequent passes to estimate the range and crosstrack errors and rates. The third technique employs a combination of the first two in an attempt to attenuate the modelling errors due to nonrepeatability of the states.

Using the resultant modelling errors as a source of state noise which diverges between landmark updates, GPS, ARS, and TM to ARS misalignment requirements are established.

The perturbation equations for a spacecraft moving in the neighborhood of a circular orbit through an inverse square law gravitation field are used in the analysis. The nominal spacecraft attitude is shown in Figure 8.3-1 coincident with the local vertical. Because of the uncertainty in estimating the gyro bias, the spacecraft attitude reference drifts from the nominal attitude. The attitude error relative to the local vertical reference frame is denoted $(\psi_x, \psi_y, \psi_z)^*$ and $(n_x, n_y, n_z)^*$ denotes the gyro bias uncertainty. The ephemeris error is $(r_x, r_y, r_z; v_x, v_y, v_z)^*$.

8.3.1 Kalman Filter States

The first 12 Kalman filter states are

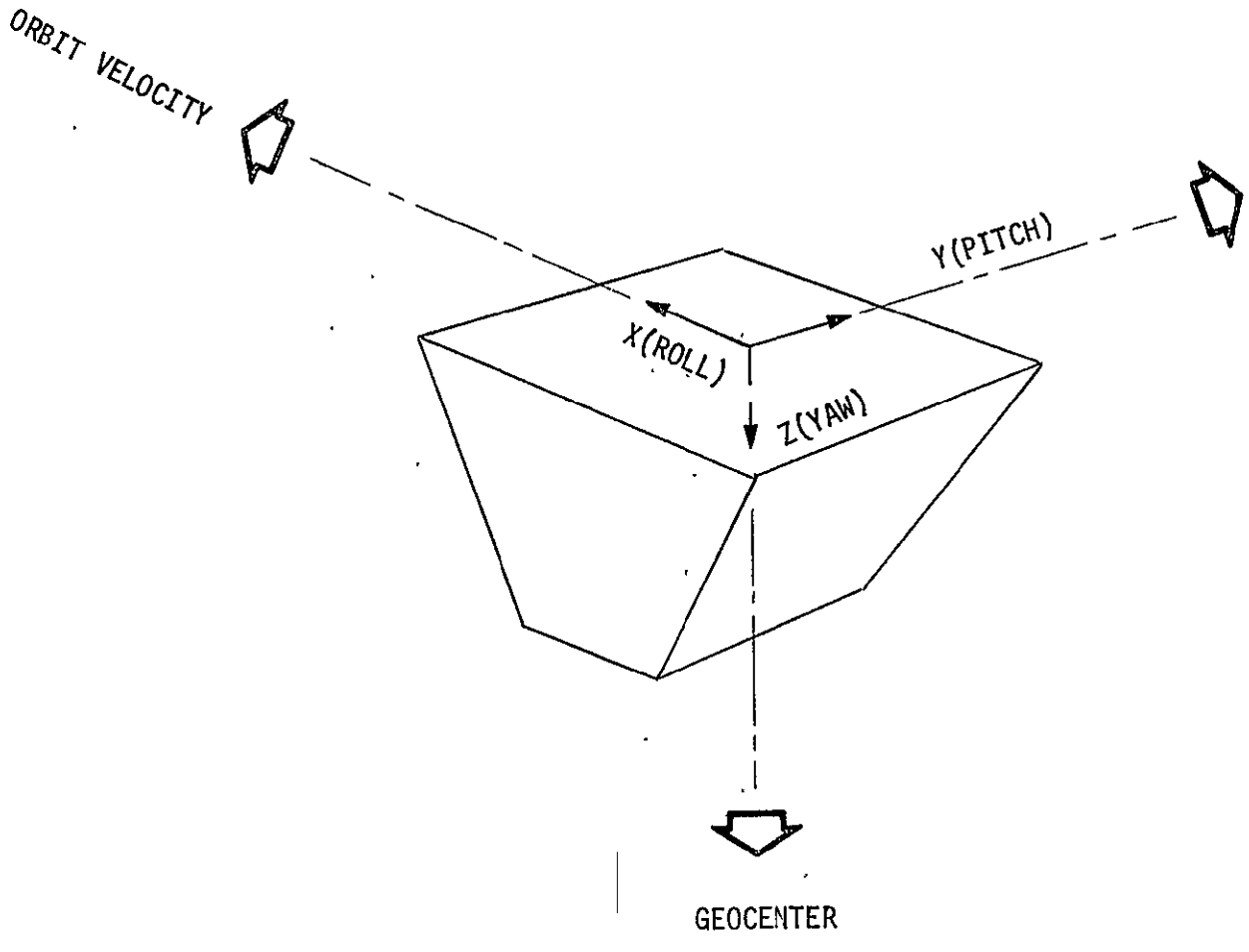

Figure 8.3-1. Spacecraft in Nominal Attitude

$x_1 = r_x$ downrange

$x_2 = r_y$ crosstrack

$x_3 = r_z$ altitude

$x_4 = v_x$ downrange velocity

$x_5 = v_y$ crosstrack velocity

$x_6 = v_z$ altitude velocity

$x_7 = \psi_x$ roll

$x_8 = \psi_y$ pitch

$x_9 = \psi_z$ yaw

$x_{10} = \eta_x$ roll gyro bias

$x_{11} = \eta_y$ pitch gyro bias

$x_{12} = \eta_z$ altitude gyro bias

Sources of registration error are not only ephemeris position and velocity, but also spacecraft ARS error† and the misalignment between the TM reference and the ARS reference. The misalignment angles $(\alpha_x, \alpha_y, \alpha_z)$* are parameterized as

$$\alpha_x = C_x + A_x \sin(\omega_p t + \Delta\theta_x)$$
$$\alpha_y = C_y + A_y \sin(\omega_p t + \Delta\theta_y) \qquad (8.3\text{-}1)$$
$$\alpha_z = C_z + A_z \sin(\omega_p t + \Delta\theta_z)$$

†Perfect attitude control up to the accuracy of the ARS if assumed.

Each α_k requires three states Z_k^j; j = 1, 2, 3. Where

$$
\begin{aligned}
Z_k^1(t) &\triangleq C_x \\
Z_k^2(t) &\triangleq A_k \sin(\omega_p t + \Delta\theta_k) \\
Z_k^3(t) &\triangleq \omega_p A_k \cos(\omega_p t + \Delta\theta)
\end{aligned}
\tag{8.3-2}
$$

The state transition matrix for a typical set of three misalignment states $(Z_k^1, Z_k^2, Z_k^3)^*$ is

$$
\begin{bmatrix} Z_k^1(t) \\ Z_k^2(t) \\ Z_k^3(t) \end{bmatrix} = \begin{bmatrix} 1 & 0 & 0 \\ 0 & c & s/\omega_p \\ 0 & -\omega_p s & c \end{bmatrix} \begin{bmatrix} Z_k^1(t_o) \\ Z_k^2(t_o) \\ Z_k^3(t_o) \end{bmatrix} \tag{8.3-3}
$$

The state transition for the states $(\psi_x, \psi_y, \psi_z; \eta_x, \eta_y, \eta_z)^*$ is

$$
\begin{bmatrix} \psi_x(t) \\ \psi_y(t) \\ \psi_z(t) \\ \eta_x(t) \\ \eta_y(t) \\ \eta_z(t) \end{bmatrix} = \begin{bmatrix} c & 0 & s & s/\omega_p & 0 & (1-c)/\omega_p \\ 0 & 1 & 0 & 0 & \Delta t & 0 \\ -s & 0 & c & -(1-c)/\omega_p & 0 & s/\omega_p \\ 0 & 0 & 0 & 1 & 0 & 0 \\ 0 & 0 & 0 & 0 & 1 & 0 \\ 0 & 0 & 0 & 0 & 0 & 1 \end{bmatrix} \begin{bmatrix} \psi_x(t_o \\ \psi_y(t_o) \\ \psi_z(t_o) \\ \eta_x(t_o) \\ \eta_y(t_o) \\ \eta_z(t_o) \end{bmatrix} \tag{8.3-4}
$$

The ephemeris position and velocity state transition matrix is given in Table 8.3-1. Note that the definitions

$$\Delta t = (t - t_0)$$

$$\gamma = \omega_p \Delta t$$

$$s = \sin \gamma$$

$$c = \cos \gamma$$

in Table 8.3-1, also hold in the misalignment and attitude transition relations.

8.3.2 Simplified Kalman Filter Model

A simplified Kalman filter is recommended for estimating the downrange registration error and rate, and the crosstrack registration error and rate (measured on the ground). The downrange and crosstrack registration errors provide pseudo pitch and roll attitude commands, respectively. The downrange and crosstrack registration error rates are used to derive pseudo pitch and roll attitude rate commands. The goal is the elimination of the registration error throughout the FOV by driving the TM pointing deviation between successive passes to zero. The yaw requirement for a 15 degree FOV and an altitude of 705 km is 3.61 arc-second (1σ)*. From single widely separated landmarks or landmark clusters the yaw error between successive 16 day passes is not accurately obtained. If we relie on the ARS then the error induced by the gyros between landmark updates must certainly be bounded by 3.61 arc-seconds (1σ) and the attitude update uncertainty must also be well within 3.61 arc-seconds (1σ). Another alternative would be to use a natural distributed landmark such as a highway that appears throughout the FOV prior to going into the pass so that an accurate yaw attitude can be determined and a maneuver initiated.

---

*The requirement derives from roll/yaw coupling through the orbit rate. This computation assumes a landmark update of 200 seconds.

Table 8.3-1. Ephemeris State Transition Relation

$$\begin{bmatrix} r_x(t) \\ r_y(t) \\ r_z(t) \\ v_x(t) \\ v_y(t) \\ v_z(t) \end{bmatrix} = \begin{bmatrix} (2c-1) & 0 & -(2s-3\gamma) & (4s-3\gamma)/\omega_p & 0 & -2(c-1)/\omega_p \\ 0 & c & 0 & 0 & s/\omega_p & 0 \\ -s & 0 & (2-c) & -2(1-c)/\omega_p & 0 & s/\omega_p \\ -\omega_p s & 0 & -\omega_p(c-1) & (2c-1) & 0 & s \\ 0 & -\omega_p s & 0 & 0 & c & 0 \\ -\omega_p(c-1) & 0 & \omega_p(3\gamma-s) & -(3\gamma-2s) & 0 & (2-c) \end{bmatrix} \begin{bmatrix} r_x(t_o) \\ r_y(t_o) \\ r_z(t_o) \\ v_x(t_o) \\ v_y(t_o) \\ v_z(t_o) \end{bmatrix}$$

$\Delta t = (t-t_o)$

$\gamma = \omega_p \Delta t$

$s = \sin \gamma$

$c = \cos \gamma$

It is assumed that yaw can be accurately determined so that repeatability in yaw can be achieved. Registration deviation of the TM boresight will, therefore, be studied.

8.3.3 TM Pointing Deviations

Suppose that during the initial pass that the system state $\bar{x}$ has some initial value $\bar{x}_i$. Assume that there is no variation in the geopotential and that the attitude control loop is designed so that oscillations in the spacecraft attitude relative to the reference can be neglected. The TM pointing error† relative to the geodetic ground track can be written as a linear combination of the state $\bar{x}(t)$. The downrange component $R_x(t)$ is

$$R_x(t) = -r_x(t) - h\left\{\psi_y(t) + Z_y^1(t) + Z_y^2(t)\right\} \tag{8.3-5}$$

where h is orbit altitude, here h = 705 km.

The crosstrack component of the pointing error is

$$R_y(t) = -r_y(t) + h\left\{\psi_x(t) + Z_x^1(t) + Z_x^2(t)\right\} \tag{8.3-6}$$

The on ground pointing error vector $(R_x, R_y)^*$ can be written as

$$\bar{R}(t) = A\,\bar{x}(t) = A\,\Phi\,(t,t_o)\,\bar{x}_i(t_o) \tag{8.3-7}$$

The initial time t_o is arbitrary and can be set equal to zero. Letting $\Delta\,\bar{x}_i$ denote the error in the state going into the second pass, or any subsequent pass, the pointing deviation becomes

$$\Delta\,\bar{R}(t) = A\,\Phi\,(t,o)\,\Delta\,\bar{x}_i(o) \tag{8.3-8}$$

---

†The TM pointing error for the perturbation analysis is the error measured on the earth surface tangent plane constructed at the zero state nadir. The earth is assumed to be spherical.

where t is the time into the pass. The downrange deviation 1σ in meters is shown in Figures 8.3-1 and 8.3-2 for the various pertinent states. The crosstrack deviation 1σ in meters is shown in Figures 8.3-3 and 8.3-4. The misalignment states impact each axis the same. The results are shown in Figure 8.3-5 for repeatability uncertainties of 0.1 arc-second (1σ) in Z_j^1 and Z_j^2. The repeatability uncertainty in Z_j^3 is taken as 0.1 ω_p arc-second (1σ) where ω_p is the orbit rate (1.058×10^{-3} rad/second at 705 km).

The window for state repeatability* is much too small. The gyro bias uncertainty 1σ of 0.0013 degree/hour, which is not unreasonable for a 20 minute ARS stellar update causes a 1 meter (1σ) pointing deviation in just over 200 seconds. The state repeatability requirements on ephemeris (position and velocity) are not feasible considering the stationkeeping requirements at 705 km which require a ΔV_x increment of at most 0.35 meter/second every 16 days. Active compensation techniques are required.

8.3.4 Estimation of Registration Deviations Using Full 21 Kalman Filter States

Since the window for state repeatability is much too small an active technique for eliminating registration deviations must be used. One such technique requires estimation of the full 21 states using GPS, stellar data, and cooperative landmarks. Cooperative landmarks are those landmarks such as beacons or reflecting parabolic mirrors for which accurate geodetic coordinates are available. Using accurate state estimation for update purposes along with accurate on-board modelling of the state evolution between updates would allow prediction of the registration deviations and the synthesis of pseudo attitude and attitude rate commands for actively eliminating these deviations by maneuvering the spacecraft. Because we are dealing with the elimination of registration deviations to within 3 meters (1σ) on the ground, the ephemeris position 1σ must be better than $(3/\sqrt{2})$ meters. An expected limit for GPS is a position uncertainty in the GPS satellite

*The window for state repeatability is that volume in state space centered on the initial state and within which we must target our state in order to meet the TM pointing requirements.

Figure 8.3-1. TM Boresight Downrange Pointing Error as a Function of State Error Between Two Successive Passes

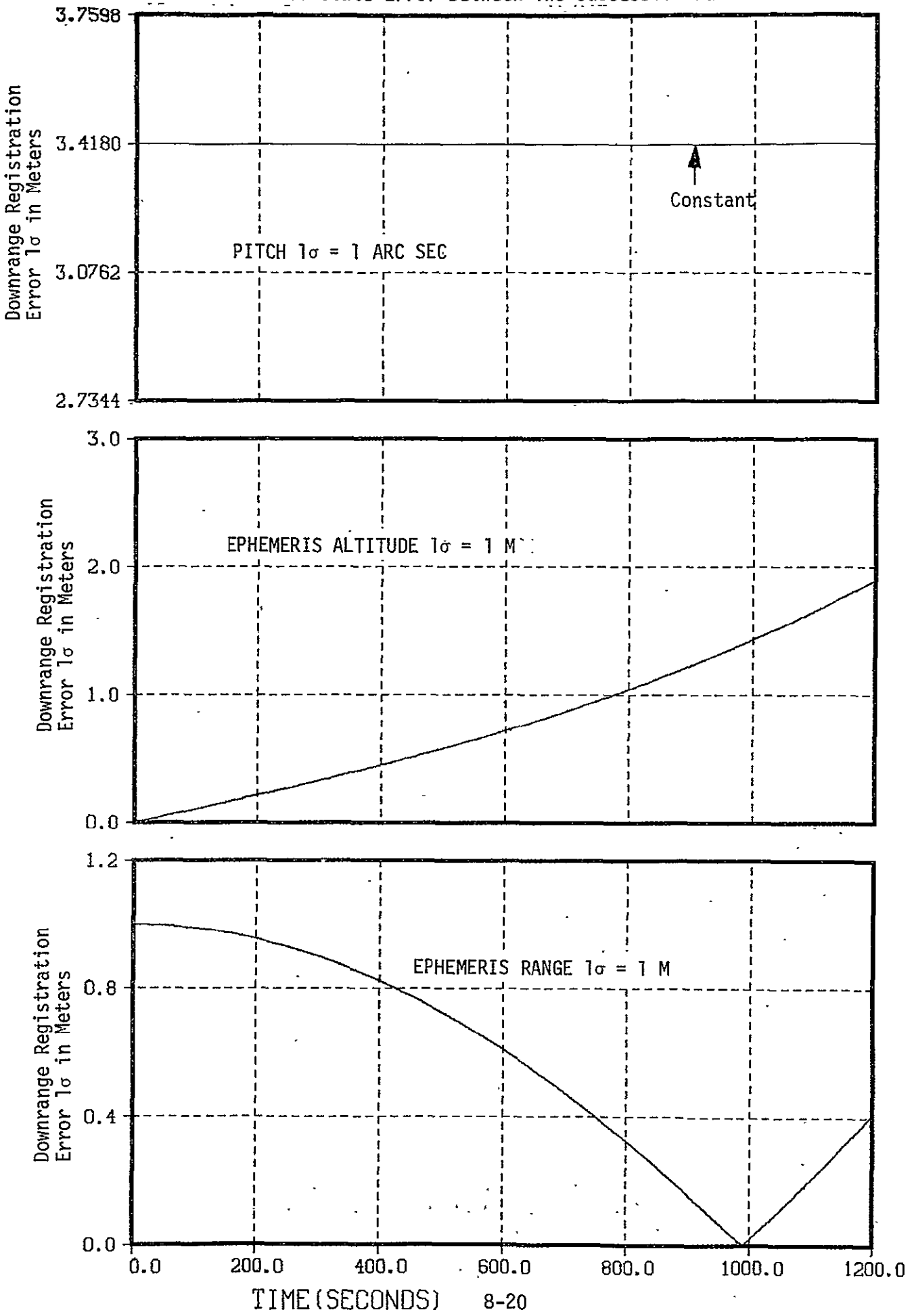

Figure 8.3-2. TM Boresight Downrange Pointing Error as a Function of State Error Between Two Successive Passes

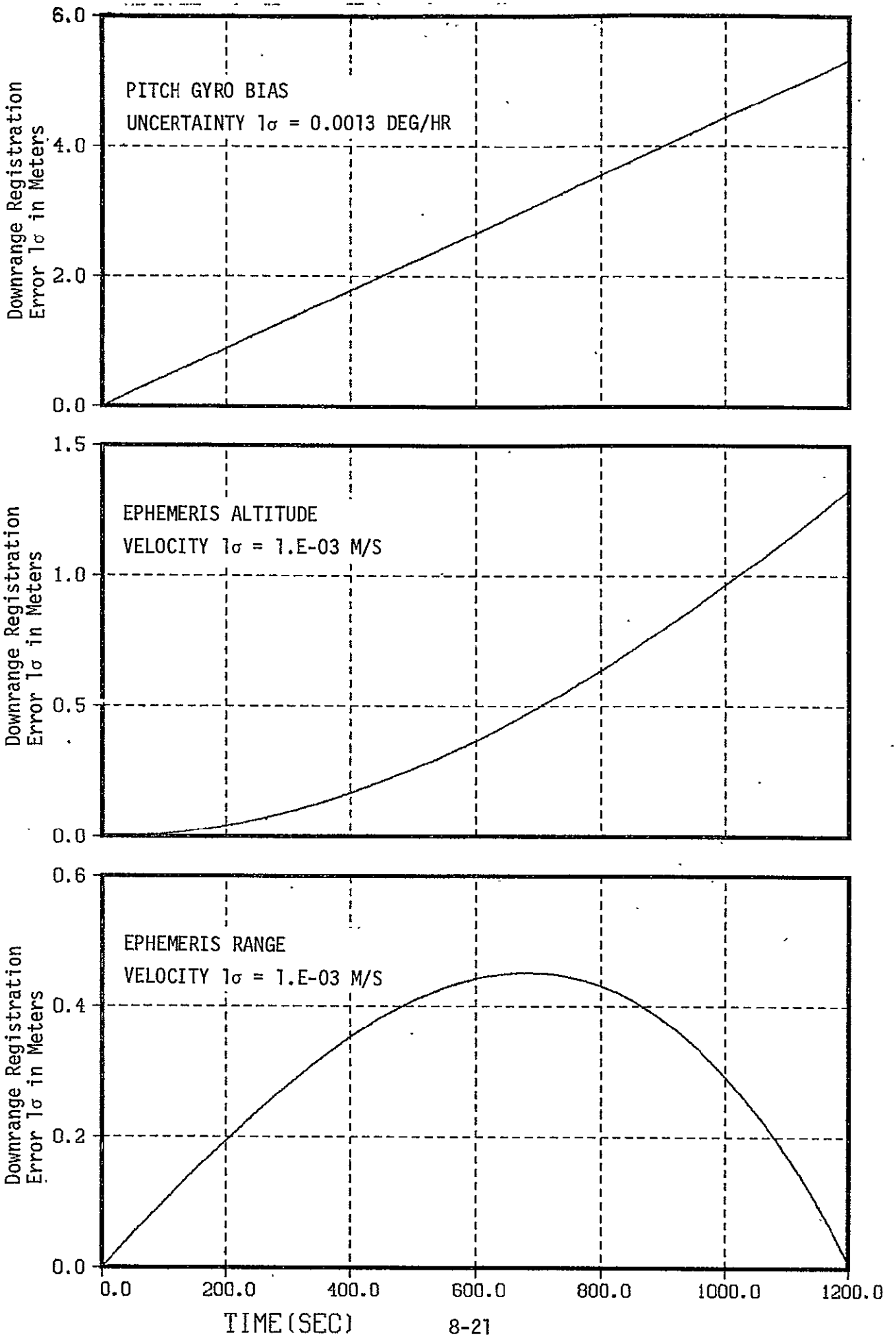

Figure 8.3-3. TM Boresight Crosstrack Pointing Error as a Function of State Error Between Two Successive Passes

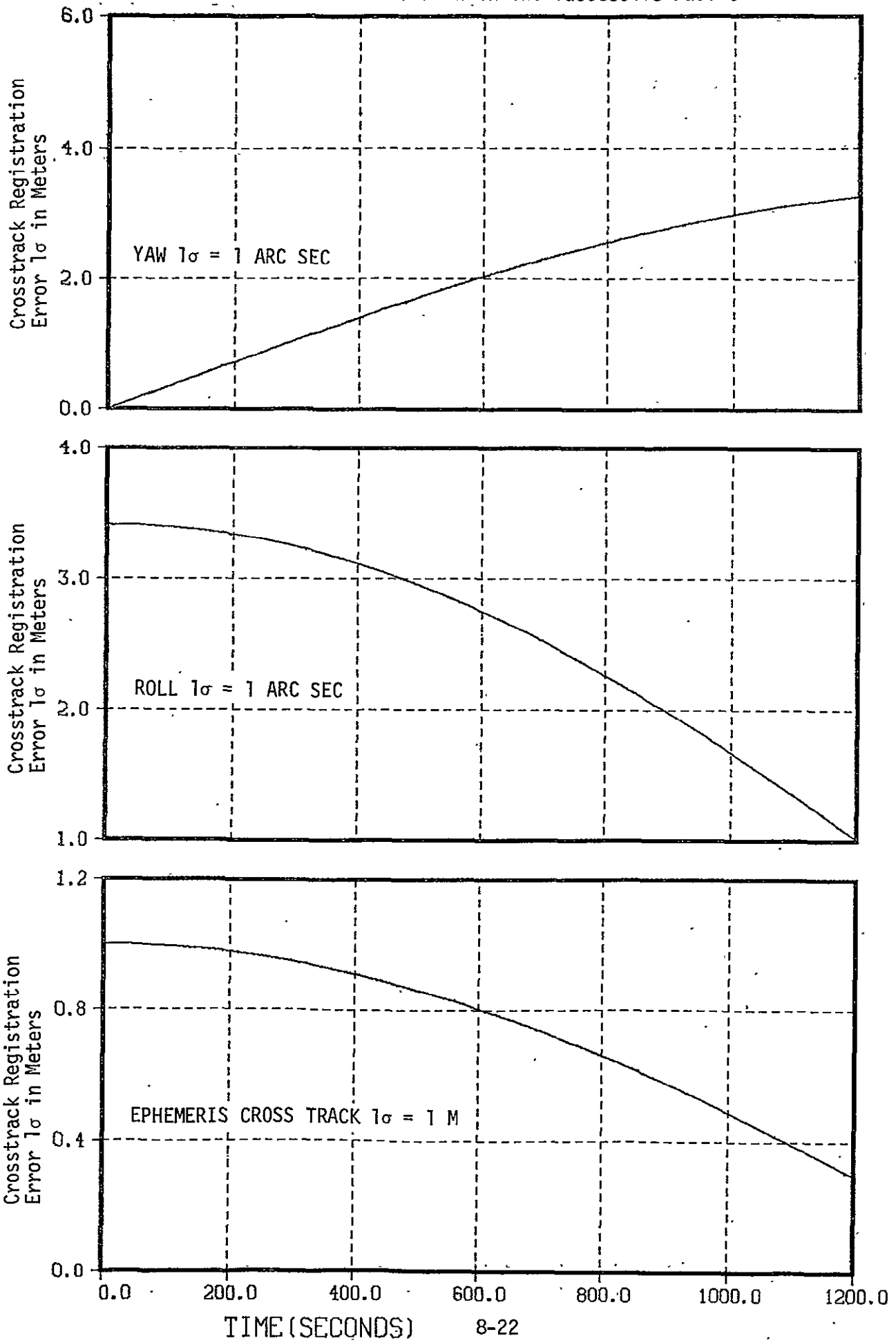

Figure 8.3-4. TM Boresight Crosstrack Pointing Error as a Function of State Error Between Two Successive Passes

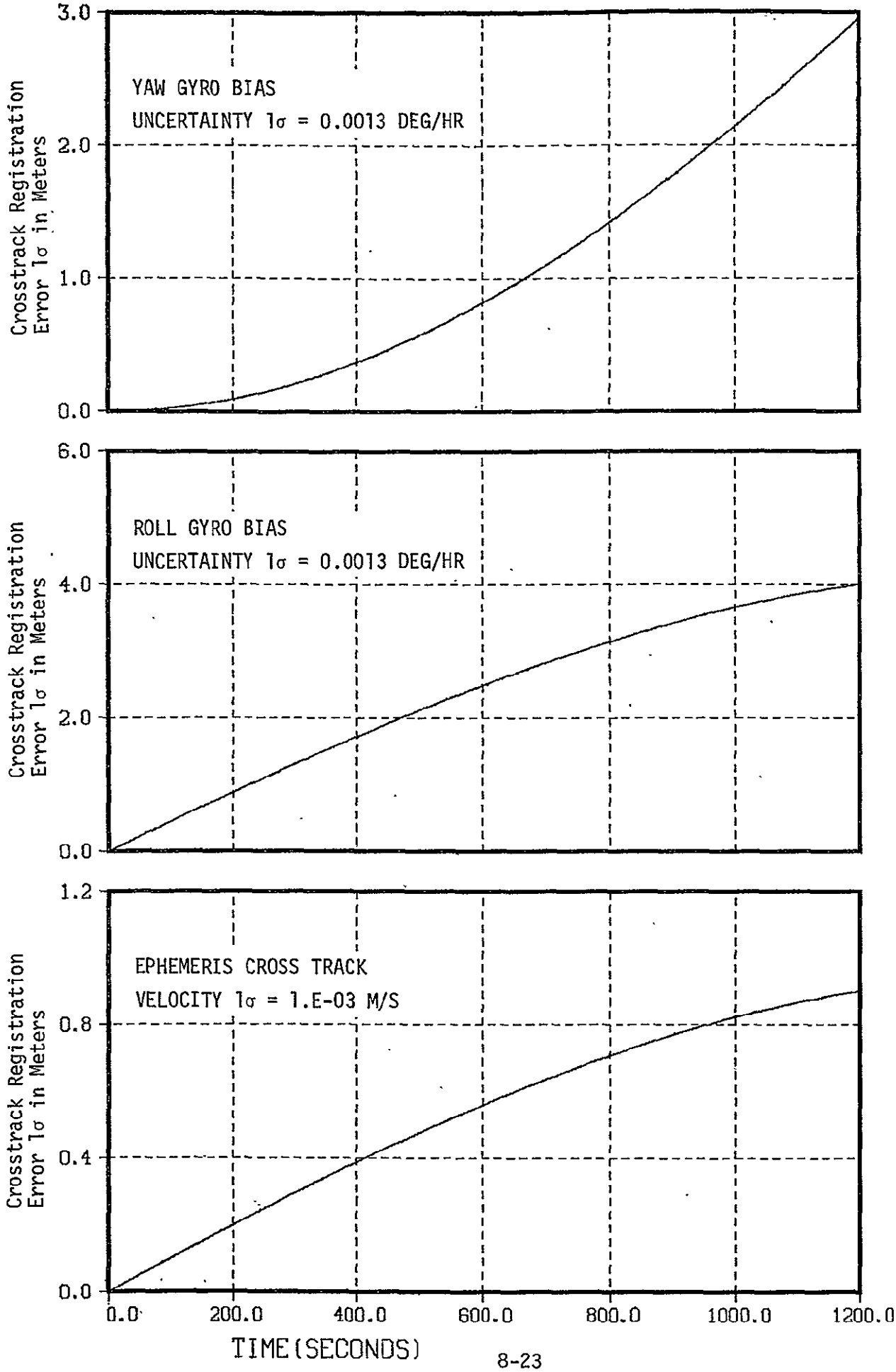

Figure 8.3-5. TM Boresight Downrange (or Crosstrack) Pointing Error as a Function of the TM to ARS Misalignment

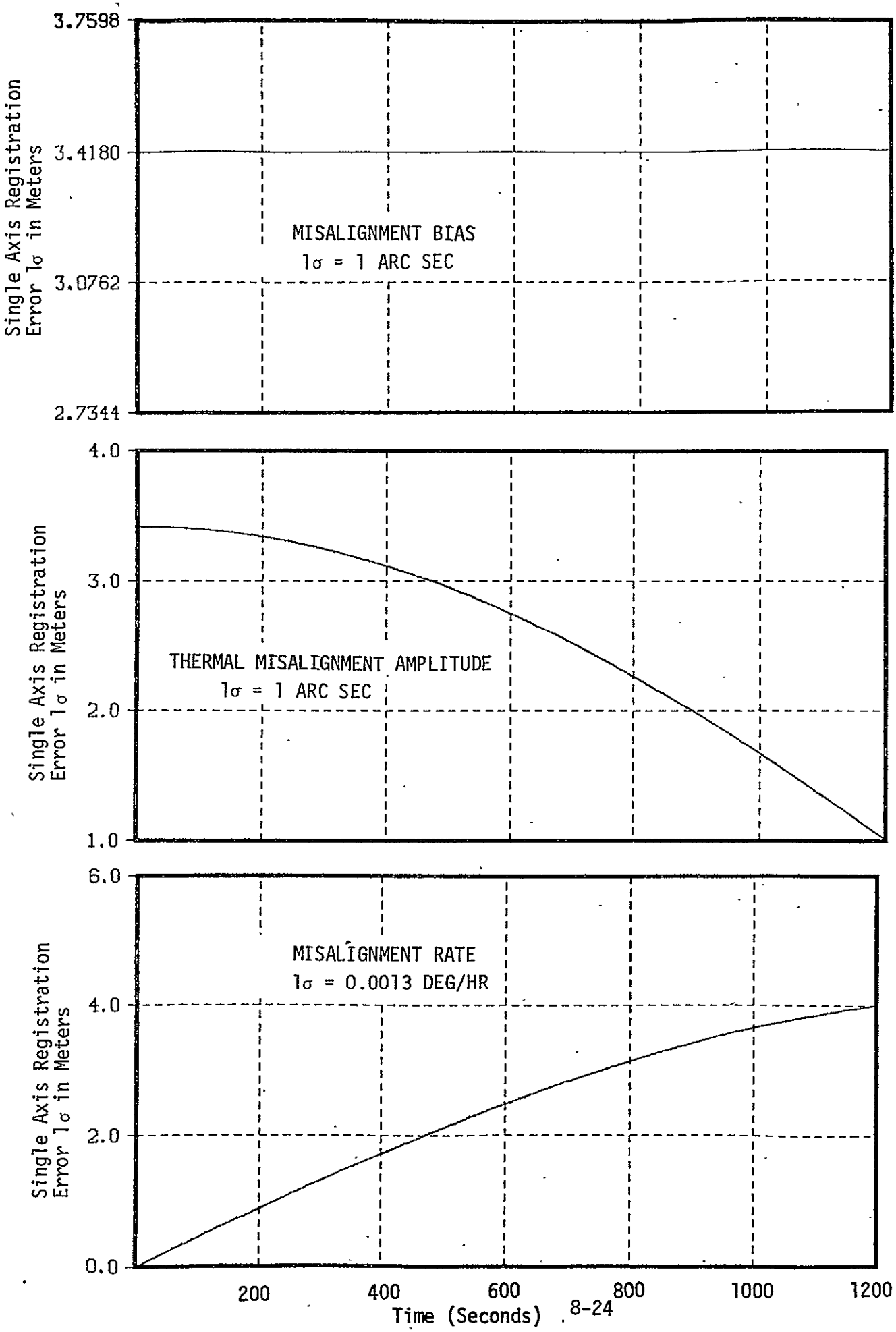

of 1 meter (see References 13 and 14). So we are right on the theoretical limit for GPS position data. Extremely accurate stellar data for updating the ARS (better than 1 arc-second) is required so that the misalignment states can be accurately estimated. Cooperative landmarks are required for estimating the misalignment states. Fractional meter geodetic accuracy is not considered feasible at this date and from an engineering viewpoint the operational requirement of cooperative landmarks is not cost optimal. Geodetic landmark accuracy becomes unimportant, however, if one configures a compensation technique which depends only on landmark registration deviations.

8.3.5 Estimation of Registration Deviations Using Ground Control Points

The simplified Kalman filter uses a model derived by basically setting

$$\cos \gamma = 1$$

$$\sin \gamma = \gamma = \omega_p \Delta t = 0$$

$$\frac{\sin \gamma}{\omega_p} = \Delta t = (4 \sin \gamma - 3 \gamma) \omega_p^{-1}$$

$$\cos \gamma - 1 = (\cos \gamma - 1) \omega_p^{-1} = 0$$

in the state transition matrix for the full 21 states. The simplified ephemeris state transition matrix becomes

$$\begin{bmatrix} r_x(t) \\ r_y(t) \\ r_z(t) \\ v_x(t) \\ v_y(t) \\ v_z(t) \end{bmatrix} = \begin{bmatrix} 1 & 0 & 0 & \Delta t & 0 & 0 \\ 0 & 1 & 0 & 0 & \Delta t & 0 \\ 0 & 0 & 1 & 0 & 0 & \Delta t \\ 0 & 0 & 0 & 1 & 0 & 0 \\ 0 & 0 & 0 & 0 & 1 & 0 \\ 0 & 0 & 0 & 0 & 0 & 1 \end{bmatrix} \begin{bmatrix} r_x(t_o) \\ r_y(t_o) \\ r_z(t_o) \\ v_x(t_o) \\ v_y(t_o) \\ v_z(t_o) \end{bmatrix} \tag{8.3-9}$$

The simplified attitude state transition matrix becomes

$$\begin{bmatrix} \psi_x(t) \\ \psi_y(t) \\ \psi_z(t) \\ \eta_x(t) \\ \eta_y(t) \\ \eta_z(t) \end{bmatrix} = \begin{bmatrix} 1 & 0 & 0 & \Delta t & 0 & 0 \\ 0 & 1 & 0 & 0 & \Delta t & 0 \\ 0 & 0 & 1 & 0 & 0 & \Delta t \\ 0 & 0 & 0 & 1 & 0 & 0 \\ 0 & 0 & 0 & 0 & 1 & 0 \\ 0 & 0 & 0 & 0 & 0 & 1 \end{bmatrix} \begin{bmatrix} \psi_x(t_o) \\ \psi_y(t_o) \\ \psi_z(t_o) \\ \eta_x(t_o) \\ \eta_y(t_o) \\ \eta_z(t_o) \end{bmatrix} \tag{8.3-10}$$

and the simplified transition relation for a typical set of misalignment states becomes

$$\begin{bmatrix} Z_j^1(t) \\ Z_j^2(t) \\ Z_j^3(t) \end{bmatrix} = \begin{bmatrix} 1 & 0 & 0 \\ 0 & 1 & \Delta t \\ 0 & 0 & 1 \end{bmatrix} \begin{bmatrix} Z_j^1(t_o) \\ Z_j^2(t_o) \\ Z_j^3(t_o) \end{bmatrix} \tag{8.3-11}$$

These transition matrices are used to configure the Kalman filter discussed in Reference 15 and are used in the following modelling error study.

Suppose that during the initial pass the 21 states are zero. Let $(r_x, r_y, r_z; v_x, v_y, v_z; \psi_x, \psi_y, \psi_z; \eta_x, \eta_y, \eta_z)^*$ and Z_j^i; $i = 1, 2, 3$; $j = x, y, z$ denote the state at the beginning of the second pass sixteen days later. The downrange registration deviation is

$$R_x(t) = -(2c-1)\, r_x(t_o) - (2s-3\gamma)\, r_z(t_o) - h\, \psi_y(t_o)$$
$$- \frac{(4s-3\gamma)}{\omega_p}\, v_x(t_o) + 2\frac{(c-1)}{\omega_p}\, v_z(t_o) - (\Delta t)\, h\, \eta_y(t_o)$$
$$- h\left\{Z_y^1(t_o) + c\, Z_y^2(t_o) + \frac{s}{\omega_p}\, Z_y^3(t_o)\right\} \qquad (8.3\text{-}12)$$

The deviation at time t_o, using the simplified transition expressions, is

$$R_x(t_o) = -r_x(t_o) - h\, \psi_y(t_o) - h\left\{Z_y^1(t_o) + Z_y^2(t_o)\right\} \qquad (8.3\text{-}13)$$

and the deviation rate at time t_o is

$$\dot{R}_x(t_o) = -v_x(t_o) - h\, \eta_y(t_o) - h\, Z_y^3(t_o) \qquad (8.3\text{-}14)$$

The pitch attitude and rate commands become

$$\psi_{yc}(t_o) = h^{-1} R_x(t_o)$$
$$\dot{\psi}_{yc}(t_o) = h^{-1} \dot{R}_x(t_o) \qquad (8.3\text{-}15)$$

In reality there is a measurement error which corrupts the estimation of $R_x(t_o)$ and $\dot{R}_x(t_o)$. The following paragraphs will treat only the modelling error and neglect the impact of the measurement noise. Suppose that at time t_o + the spacecraft is pitched by $\psi_{yc}(t_o)$ and the gyro data is biased by $\dot{\psi}_{yc}(t_o)$. Then the pitch state becomes

$$\psi_y(t_o+) = \psi_y(t_o) + h^{-1} R_x(t_o)$$
$$= -h^{-1} r_x(t_o) - \left\{ Z_y^1(t_o) + Z_y^2(t_o) \right\} \qquad (8.3\text{-}16)$$

and the pitch gyro bias uncertainty is effectively

$$\eta_y(t_o+) = \eta_y(t_o) + h^{-1} \dot{R}_x(t_o)$$
$$= -h^{-1} v_x(t_o) - Z_y^3(t_o) \qquad (8.3\text{-}17)$$

After subsituting in Equation (8.3-12) $\psi_y(t_o+)$ and $\eta_y(t_o+)$ for $\psi_y(t_o)$ and $\eta_y(t_o)$, the downrange registration deviation evolves as

$$\Delta R_x(t) = -2(c-1)\, r_x(t_o) - (2s-3\gamma)\, r_z(t_o) - 4\,\frac{(s-\gamma)}{\omega_p}\, v_x(t_o)$$
$$+ 2\,\frac{(c-1)}{\omega_p}\, v_z(t_o) - h(c-1)\, Z_y^2(t_o) - h\,\frac{(s-\gamma)}{\omega_p}\, Z_y^3(t_o) \qquad (8.3\text{-}18)$$

The crosstrack registration deviation is

$$R_y(t) = -c\, r_y(t_o) + h\left\{c\, \psi_x(t_o) + s\, \psi_z(t_o)\right\}$$
$$- \frac{s}{\omega_p} v_y(t_o) + h\left\{\frac{s}{\omega_p}\eta_x(t_o) + \frac{(1-c)}{\omega_p}\eta_z(t_o)\right\}$$
$$+ h\left\{Z_x^1(t_o) + c\, Z_x^2(t_o) + \frac{s}{\omega_p}\, Z_x^3(t_o)\right\} \qquad (8.3\text{-}19)$$

The deviation at time t_o, using the simplified transition expressions, is

$$R_y(t_o) = -r_y(t_o) + h\, \psi_x(t_o) + h\left\{Z_x^1(t_o) + {}^{1}Z_x^2(t_o)\right\} \qquad (8.3\text{-}20)$$

and the deviation rate at time t_o is

$$\dot{R}_y(t_o) = -v_y(t_o) + h\, \eta_x(t_o) + h\, Z_x^3(t_o) \qquad (8.3\text{-}21)$$

The roll attitude and rate commands become

$$\psi_{xc}(t_o) = -\, h^{-1}\, R_y(t_o) \qquad (8.3\text{-}22)$$

$$\dot{\psi}_{xc}(t_o) = -\, h^{-1}\, \dot{R}_y(t_o) \qquad (8.3\text{-}23)$$

Suppose that at time t_o+ the spacecraft is pitched by $\psi_{xc}(t_o)$ and the gyro data is biased by $\dot{\psi}_{xc}(t_o)$. Then the pitch state becomes

$$\psi_x(t_o+) = \psi_x(t_o) - h^{-1} R_y(t_o)$$
$$= h^{-1} r_y(t_o) - Z_x^1(t_o) - Z_x^2(t_o) \qquad (8.3\text{-}23)$$

and the roll gyro bias uncertainty is effectively

$$\eta_x(t_o+) = \eta_x(t_o) - h^{-1} \dot{R}_y(t_o)$$
$$= h^{-1} v_y(t_o) - Z_x^3(t_o) \qquad (8.3\text{-}24)$$

After substituting the Equation (8.3-19) $\psi_x(t_o+)$ and $\eta_x(t_o+)$ for $\psi_x(t_o)$ and $\eta_x(t_o)$, the crosstrack registration deviation evolves as

$$\Delta R_y(t) = h\, s\, \psi_z(t_o) + h \frac{(1-c)}{\omega_p} \eta_z(t_o) + h(1-c)\, Z_x^1(t_o) \qquad (8.3\text{-}25)$$

8.3.6 GPS, ARS, and TM to ARS Alignment Requirements

The range modelling error 1σ in meters is shown in Figures 8.3-6 and 8.3-7 for each error source. As an example, a downrange miss on subsequent passes of 10 meters, even when initially corrected by a pseudo attitude pitch and constant pitch rate command, causes a registration deviation in downrange to build to 0.45 meters in 200 seconds. The simplified Kalman filter uses registration deviations to estimate pseudo attitude and attitude rate commands. In this example the spacecraft is 10 meters further downrange than on the previous pass (16 days earlier). Assume that the spacecraft is pitched to eliminate this error at t_o. Then at t_o+ 200 there is a 0.45 meter registration error given by $\Delta R_x = 2(c-1)\, \sigma_x(t_o)$. The state variables which contribute to the downrange modelling error are

- Ephemeris Range
- Ephemeris Altitude
- Ephemeris Range Velocity

Figure 8.3-6. RANGE MODELING ERROR ONE SIGMA IN METERS.

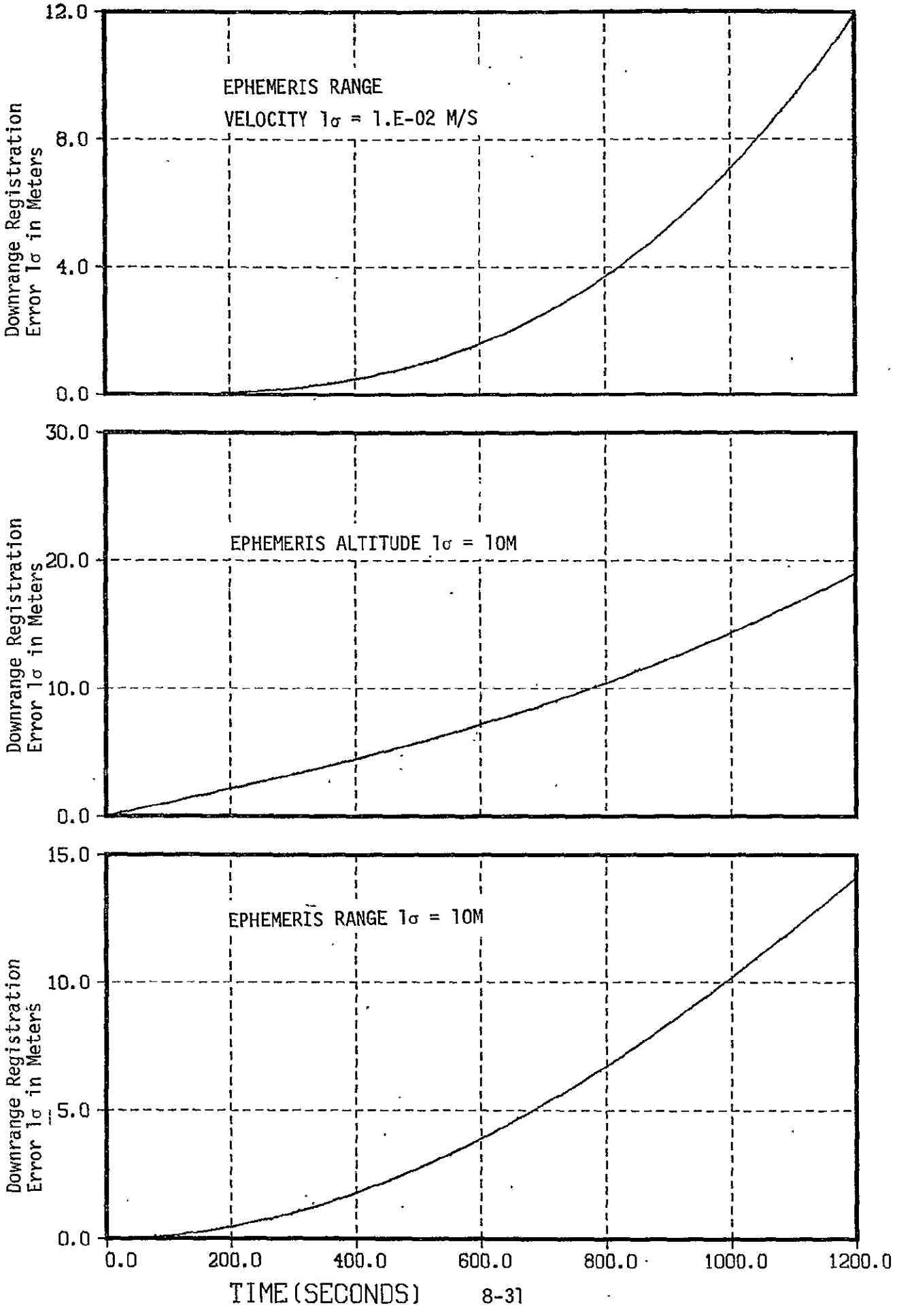

Figure 8.3-7. RANGE MODELING ERROR ONE SIGMA(M).

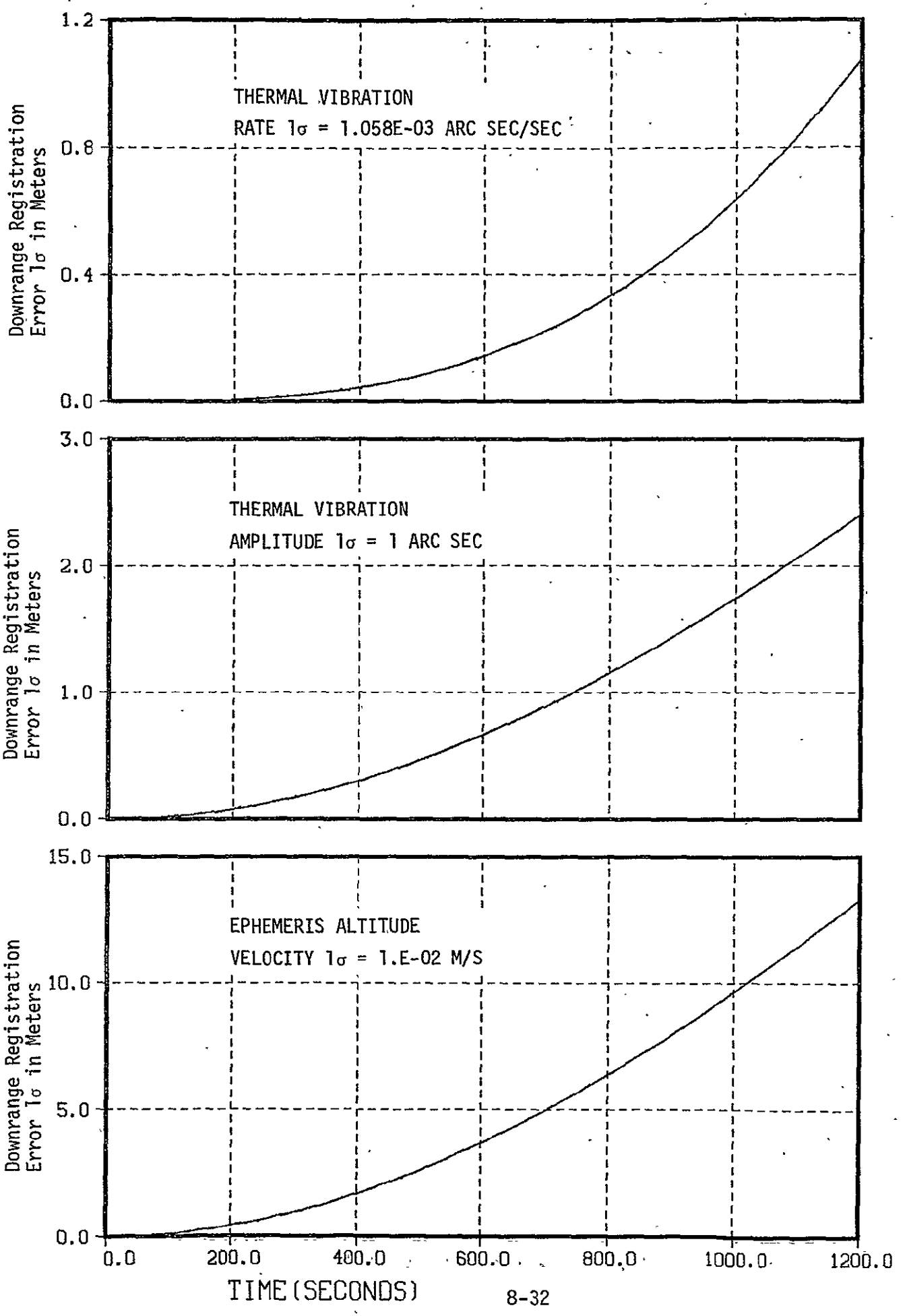

- Ephemeris Altitude Velocity
- Thermal Vibration (Misalignment)
- Thermal Vibration Rate (Misalignment Rate)

A miss in the repeatability of these states on any subsequent pass causes the downrange registration error to diverge between landmark updates. This is the error that occurs in spite of compensating through pitch attitude and attitude rate commands. The attitude and attitude rate commands are assumed estimated without error.

The state variables which contribute to the crosstrack modelling error are

- Yaw
- Yaw Gyro Bias Uncertainty
- Constant Part of TM to ARS Misalignment

and the crosstrack evolution is shown in Figure 3.8-8.

An altitude change of 10 meters between successive 16 day passes causes a 2.15 meter (1σ) downrange deviation in 200 seconds. If one compensates for the altitude change by using accurate GPS data, this modelling error can be greatly reduced and a much larger altitude miss can be tolerated. The downrange registration deviation due to an altitude miss $r_z(t_o)$ is

$$R_x(t) = -(2s-3\gamma)\, r_z(t_o) \qquad (8.3\text{-}26)$$

Suppose GPS allows one to determine the altitude to within some $\delta r_z(t_o)$. Through compensating the pitch gyro with the signal $-\omega_p h^{-1} (r_z(t_o) + \delta r_z(t_o))$, the downrange registration deviation becomes

Figure 8.3-8. CROSS TRACK MODELING ERROR ONE SIGMA IN METERS.

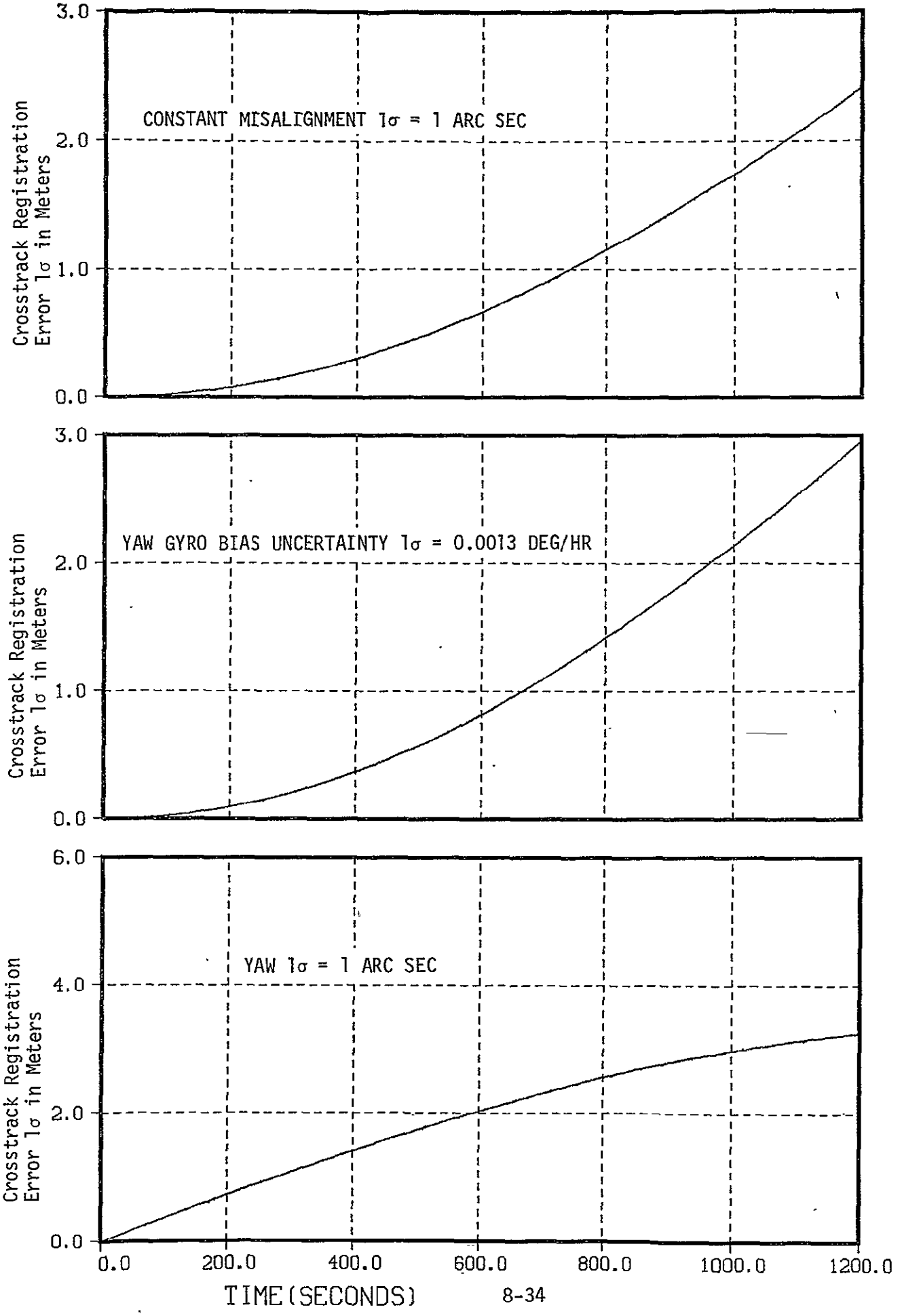

$$\Delta R_x(t) = -2(s-\gamma)\, r_z(t_o) - \omega_p \Delta t\, \delta r_z(t_o) \qquad (8.3\text{-}27)$$

Letting P^m_{33} denote the covariance of the altitude miss and P_{33} the altitude change uncertainty, the ΔP_x 1σ becomes

$$\sqrt{E(\Delta R_x(t))^2} = \left\{4(s-\gamma)^2 P^m_{33} + \gamma^2 P^m_{33}\right\}^{1/2} \qquad (8.3\text{-}28)$$

The results are plotted in Figure 8.3-9. The results show that with altitude compensation through the pitch gyro and landmark updates every 200 seconds that an altitude miss of 100 meters can be tolerated. A 100 meter altitude change without compensation would produce a 21.5 meter range registration error in 200 seconds. Using altitude compensation, a GPS uncertainty (1σ) of 10 meters causes a range registration error of 2.12 meters in 200 seconds. A change in the altitude velocity of 1 cm/second causes a range registration error of 0.42 meters in 200 seconds. A change in the range velocity of 10 cm/second causes a range registration error of 0.6 meters in 200 seconds.

Figures 8.3-6 through 8.3-8 also provides GPS, ARS, and misalignment requirements if it were feasible to control the LANDSAT to the 1σ uncertainty levels indicated in the figures. These uncertainty levels are for the state deviations. Therefore, as an example, altitude must be determined to within $10/\sqrt{2}$ meters (1σ). Suggested GPS requirements are

- Position Uncertainty of $3/\sqrt{2}$ meters (1σ) per axis
- Velocity Uncertainty of 1.0 cm/second (1σ) per axis

An uncertainty in the altitude velocity deviation of 2 cm/second causes a range registration error fo 0.84 meters in 200 seconds. Recall that this is caused by a modelling error. If we are to relax the GPS requirements then autonomous registration using landmark deviations to derived attitude and attitude rate commands having a constant rate profile between landmark updates becomes doubtful with the simplified model.

Figure 8.3-9. Range 1σ Data With and Without Altitude Compensation through Pitch Gyro

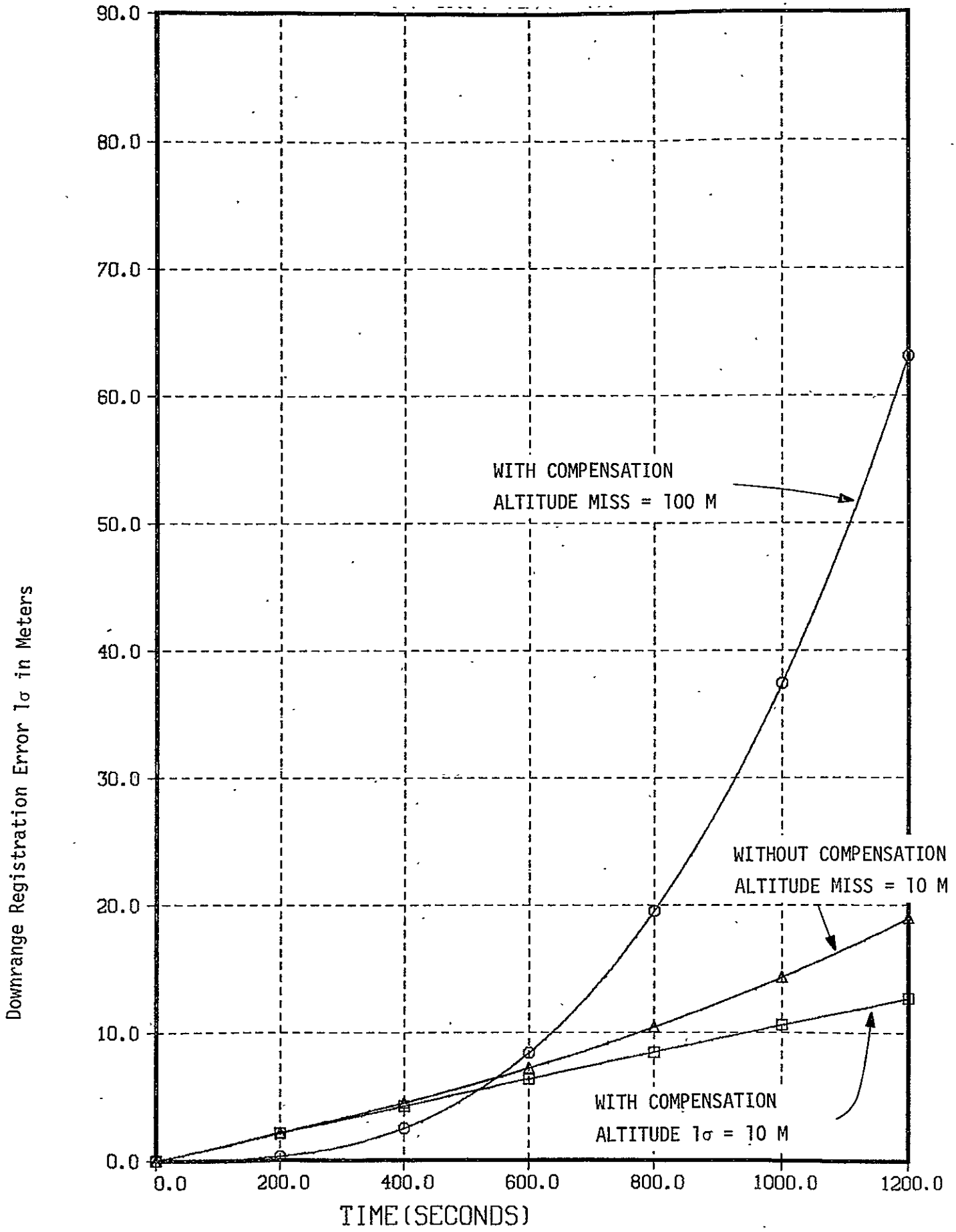

Suggested ARS requirements are

- Attitude Deviation 1σ of 1 arc-second
- Gyro Bias Uncertainty of 0.0013 degree/hour is adequate

and the suggested TM to ARS alignment requirements are

- Bias of 1 arc-second.
- Variable misalignment amplitude of 1 arc-second at orbit frequency.

These requirements are summarized in Table 8.3-2. The GPS 1σ requirements can be doubled if the landmarks are 675 km apart providing an update every 100 seconds.

Table 8.3-2. GPS, ARS, and TM to ARS Alignment Requirements for 200 seconds Landmark Update* to Meet 3 meter Registration Accuracy

GPS

- Position (1σ) = 2.1 meters
- Velocity (1σ) = 1.0 cm/sec

ARS

- Altitude (1σ) = 0.707 arc-sec
- Gyro Bias Uncertainty (1σ) = 0.0013 deg/hr

TM to ARS Alignment

- Bias (1σ) = 1 arc-sec
- Variable Amplitude = 1 arc-sec at orbit rate

*Landmark clusters are separated by 1350 km

8.4 State and Measurement Noise

The acceleration-insensitive drift rate stability of the DRIRU (Reference 16) is 0.003 degree/hour. Assuming that even the 20 minutes between updates, the primary source of the drift rate instability behaves like white torque noise which gives rise to an attitude state noise term $\sigma_v\ t^{1/2}$ that shows up as a 5 meter registration error every 200 seconds between landmark updates. Therefore, the NASA Standard Inertial Reference Unit does not provide the required accuracy. For this reason, state-of-the-art stellar and gyro performance data are reviewed and compared with the performance requirements established in Section 8.3.6.

8.4.1 Star Tracker Performance

The MMS ACS module contains three strapdown star trackers. The Ball Brothers Research Corporation (BBRC) CT-401 strapdown star tracker is used on SAS-C and on HEAO-A and is considered as a candidate tracker. The Center for Space Research at the Massachusetts Institute of Technology (MIT) has synthesized a calibration technique for the CT-401 tracker that assures very accurate star readings over 90% of the FOV. The error analysis in Table 8.4-1 of the calibrated tracker is based on the results obtained by MIT (17), and additionally, the tracker development work going on at TRW. Using the calibration results as published in (17) and also typical data on scale factor changes and null shifts due to aging as observed by TRW, one arrives at the error analysis provided in Table 8.4-1. Note that fixed and very slowly varying tracker biases have no effect on attitude reference stability and that for purposes of assuring the pointing stability one need only be concerned with the random error component of the tracker of 7 arc-seconds (1σ).

The California Institute of Technology Jet Propulsion Laboratory has carried out research on a next generation star tracker utilizing an image sensing Charge-Coupled Device (CCD) operating under microprocessor control (see Reference 18). The magnitude range of stars which may be acquired and tracked extends from -1 to +6. The laboratory model has a 3 degree optical FOV and a 100 x 100 element CCD detector. The microprocessor employs a one part in 16 interpolation routine for determining stellar

Table 8.4-1 BBRC CT-401, 8° x 8° FOV Star Tracker Characteristics

Error Source	Error Without Compensation	1 σ Error With External Compensation (arc-sec)	Comments
Slowly Varying Biases			
Null Offset & Nominal Dynamic Lag	18 arc-sec (1 σ)	---	Calibrated out by bench test
Aging (Null Shifts, Dynamic Lag Shifts, etc.)	4 arc-sec (1 σ)	4.0	No further compensation
Total Biases (RSS)	18.4	4.0	
Errors Appearing Random for Discrete Star Observ.			
Nonlinearity & Nonorthogonality	10 arc-min (peak)	3.0	Bench calibration by polynominal fit: 60 coeffi.
Temperature & Power Sensitivity (± 30°C)	2 arc-sec/°C		
External Magnetic Field (0.4 gauss)	10 arc-sec (peak)	2.5	Correction factors/terms obtained from bench test
Star Intensity (ΔM_V = 3)	30 arc-sec (1 σ)	2.5	
Scale Factor Changes (Aging)	10 arc-sec (1 σ)	1.5	Occasional updates from ground-based Kalman filter
Subtotal (RSS)	203.5	4.9	
Noise			
NEA (Noise Equivalent Angle)	5 arc-sec (1 σ) (τ = 0.5 sec, M_V = 6)	5.0	No compensation
Total Random Errors for Discrete Star Observ.(RSS)	203.6	7.0	
Total 1 σ Accuracy ($\sum$Bias + Random)	222 arc-sec	11 arc-sec	

coordinates to within a resolution of 7 arc-seconds and an accuracy of 10 arc-seconds anywhere within the field of view. CCD arrays having 400 x 400 elements or more are envisioned for the future. The only basic problem with the CCD arrays is local repeatability of the elements. One would prefer to have the optical sensitivity characteristics of adjacent elements very nearly identical. An accuracy improvement can be obtained if more stars are processed. For the LANDSAT application, the yaw deviation between successive passes can be obtained through stellar template matching just prior to going into each subsequent pass.

8.4.2 Gyro Performance

Gyro data is required for propagating the ARS attitude quaternion between stellar updates. The three-axis gyro reference assembly (GRA) can be configured as six skewed strapdown gyros arranged in a dodecahydron for redundancy and reliability considerations. The state noise covariance for the attitude portion of the state vector is derived on the basis of

$$\dot{\bar{\psi}} = \bar{\eta} + \bar{\eta}_v \tag{8.4-1}$$

$$\dot{\bar{\eta}} = \bar{\eta}_u \tag{8.4-2}$$

where $\bar{\psi}$ is the attitude of the ARS reference relative to the target frame, $\bar{\eta}$ is the gyro bias uncertainty, $\bar{\eta}_v$ is the white float torque noise, and $\bar{\eta}_u$ is the white torque derivative noise. The above equations are valid for an inertial hold mode. Since the spacecraft is in the earth pointing mode, the following dynamics are applicable.

$$\dot{\bar{\psi}} = -\bar{\omega}_p \times \bar{\psi} + \bar{\eta} + \bar{\eta}_v \tag{8.4-3}$$

$$\dot{\bar{\eta}} = \bar{\eta}_u \tag{8.4-4}$$

where $\dot{\bar{\psi}}$ and $\dot{\bar{\eta}}$ are derivatives with respect to the moving on-board computational frame. The state transition matrix is defined in Equation (8.3-4). The noise vectors $\bar{\eta}_v$ and $\bar{\eta}_u$ have zero mean white noise components with covariances

$$E\,\bar{\eta}_v\,\bar{\eta}_v^T = \begin{bmatrix} \sigma_{vx}^2 & 0 & 0 \\ 0 & \sigma_{vy}^2 & 0 \\ 0 & 0 & \sigma_{vz}^2 \end{bmatrix} \tag{8.4-5}$$

$$E\,\bar{\eta}_u\,\bar{\eta}_u^T = \begin{bmatrix} \sigma_{ux}^2 & 0 & 0 \\ 0 & \sigma_{uy}^2 & 0 \\ 0 & 0 & \sigma_{uz}^2 \end{bmatrix} \tag{8.4-6}$$

Letting

$$Q_o = \text{diag}\,(\sigma_{vx}^2,\ \sigma_{vy}^2,\ \sigma_{vz}^2,\ \sigma_{ux}^2,\ \sigma_{uy}^2,\ \sigma_{uz}^2) \tag{8.4-7}$$

the state noise covariance becomes

$$Q(t,t_o) = \int_{t_o}^{t} \Phi_{att}\,(t,\tau)\,Q_o\,\Phi_{att}^T\,(t,\tau)\,d\tau \tag{8.4-8}$$

The analytic expressions for the roll, pitch, and yaw axes are given in Table 8.4-2. Factored into the results of Equation (8.4-8) is σ_E which represents the standard deviation of the noise observed in incremental attitude samples for gyros operating in the rate mode.

Table 8.4-2. Gyro Induced Attitude State Noise

$$\text{Roll} : q_{11} = \sigma_v^2 (\Delta t) + \sigma_u^2 \frac{2}{\omega_p^2} \left\{ (\Delta t) - \frac{1}{\omega_p} \sin \omega_p \Delta t \right\} + \sigma_E^2$$

$$\text{Pitch} : q_{22} = \sigma_v^2 (\Delta t) + \sigma_u^2 \frac{(\Delta t)^3}{3} + \sigma_E^2$$

$$\text{Yaw} : q_{33} = q_{11}$$

The Bendix 64-PM-RIG gyro (IUE gyro) is one of the most accurate strapdown gyros currently available. This gyro is believed to provide values of

$$\begin{aligned} \sigma_E &= 0.04 \text{ arc-sec} \\ \sigma_v &= 0.0156 \text{ arc-sec/sec}^{1/2} \\ \sigma_u &= 2.0 \times 10^{-5} \text{ arc-sec/sec}^{3/2} \end{aligned} \qquad (8.4\text{-}9)$$

The gyro bias uncertainty 1σ is taken as

$$\sigma_b = 0.0013 \text{ deg/hr}$$

for attitude and gyro bias updates every 20 minutes from the star tracker and ARS Kalman filter. The effect of σ_b is further compensated for by observing landmarks every 200 seconds and adjusting not only the attitude commands but also the biases on the measured gyro data. Figure 8.3-8 shows that a gyro bias uncertainty 1σ of 0.0013 degree/hour does not preclude the possibility of eliminating registration deviations using ground truth.

Additional ARS errors are

- Computer Roundoff Error
- Commutation Error
- Quantization

Gyro scale factor uncertainty of 50 ppm has a negligible effect on attitude estimation for the earth pointing mode. The gyro input axis alignment uncertainty shows up as part of the gyro bias which is estimated by the ARS Kalman filter. Table 8.4-3 shows the estimated ARS attitude error for 200 seconds.

Table 8.4-3. ARS Attitude Error Accumulated over 200 Seconds

Error Source (1 σ)	1 σ Contribution per Axis (arc-sec)
State Noise • Gyro White Torque Noise, σ_v = 0.0156 arc sec/sec$^{1/2}$ • Gyro White Torque Derivative Noise, $\sigma_u = 2 \times 10^{-5}$ arc sec/sec$^{3/2}$ • Signal Generator Noise	.78
Commutation Error, and Quantization*	10^{-2}
Computer Roundoff Error**	$10^{-3}\sqrt{10}$
* Gyro Scale Factor Equals 0.01 arc sec/pulse ** Gyro Sampling Period T = 200 ms. Assuming a 32 bit Wordlength.	
Total RSS (arc sec)	.79

Simulation results show that over 20 minutes and for the noise characteristics of the Bendix gyro that $\sqrt{q_{11}}$ and $\sqrt{q_{22}}$ vary from one another insignificantly. The evolution of attitude state noise 1σ is shown in Figure 8.4-1.

8.4.3 Variations of the Geopotential

The geodetic ground track on subsequent 16 day passes will be shifted in crosstrack. The spacecraft, therefore, follows a new and different path through the geopotential. The constant shift may give rise to a bias in the geopotential deviation. The change of the satellite geopotential is modelled as an acceleration which is modelled as a bias plus a normal white process.

The results of a 1 μg (9.8×10^{-6} m/second^2) acceleration on the single axis pointing 1σ in meters is shown in Figure 8.4-1. The velocity change due to the normal white acceleration process of autocorrelation

$$R_{nn}(\tau) = A\,\delta(\tau) \tag{8.4-10}$$

is the Wiener-Levy process with autocorrelation

$$R_{vv}(t_1, t_2) = \begin{cases} At_2 & 0 < t_2 < t_1 \\ At_1 & 0 < t_1 < t_2 \end{cases} \tag{8.4-11}$$

v(t) is normal, with zero mean and variance equal to At. The orbital position 1σ is $\sqrt{AT^3/3}$. If we include the unknown bias, the RSS pointing error becomes

$$\text{Pointing } (1\sigma) = \sqrt{a^2\, t^4/4 + At^3/3} \tag{8.4-12}$$

Figure 8.4-1. SINGLE AXIS POINTING ONE SIGMA IN METERS.

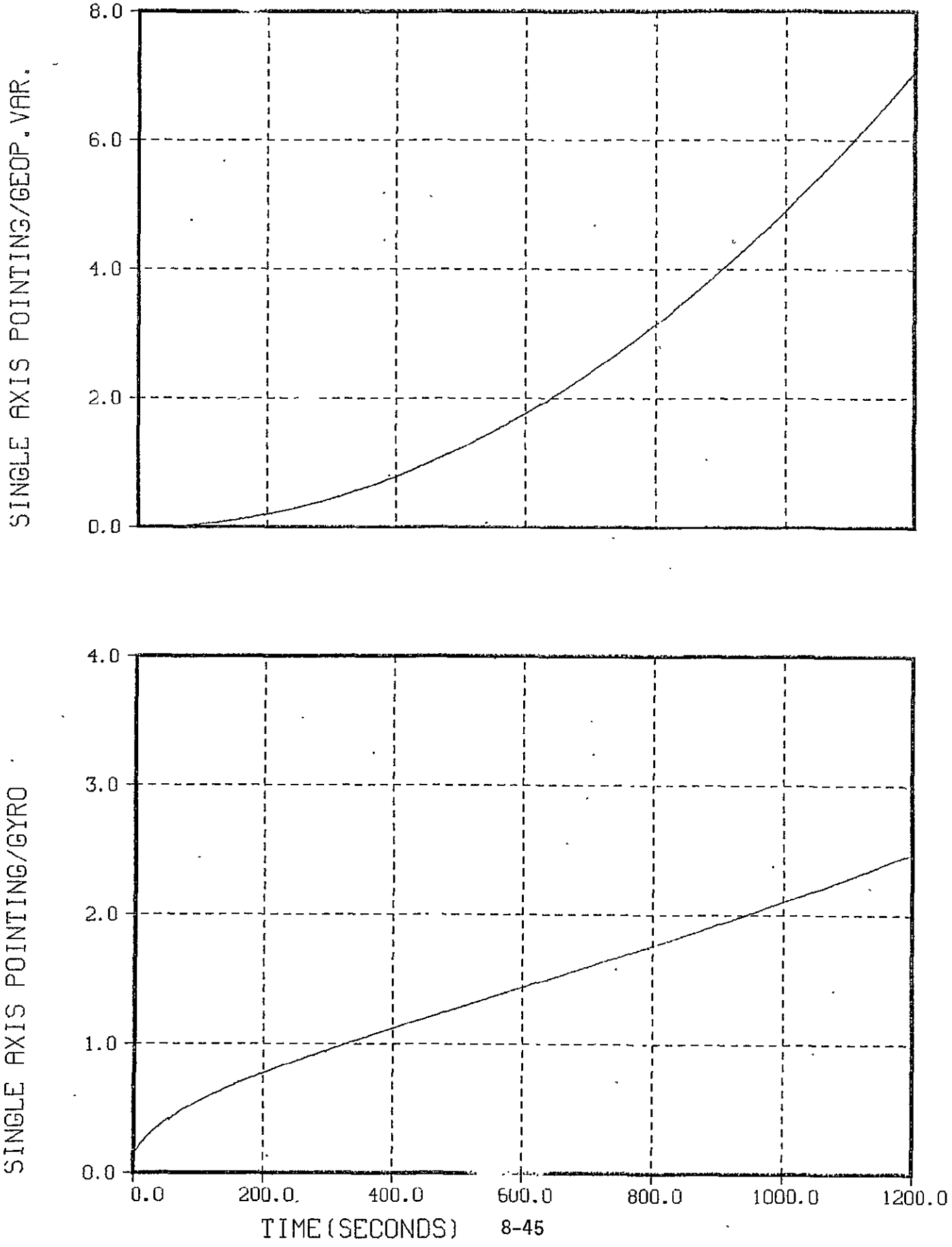

The results for a normal white geopotential noise component with

$$A = 9.8^2 \times 10^{-12} \ m^2/s^3$$

is shown in Figure 8.4-2. At 200 seconds TM boresight pointing uncertainty is 0.016 meters (1σ). For a 1 μg acceleration bias the pointing uncertainty at 200 seconds is 0.2 meters (1σ). The state noise component due to the bias is $0.5\ A(t-t_o)^2$ since compensation for this effect is impossible using state information from the simplified Kalman filter. Note that the satellite geopotential in and of itself is not being addressed here. "A" is not the acceleration bias component over and above the inverse square law, but instead represents the constant part in the change in the satellite geopotential between the initial pass and successive passes separated by roughly 16 days. Repeatability in the satellite geopotential is desired. This analysis suggests that on all subsequent 16 day passes the LANDSAT must orbit through a geopotential cooridor centered on the initial pass satellite geopotential. In term of the bias acceleration shift, a 1 mgal (10^{-5} m/second^2) corridor should be preserved for a 0.204 meter (1σ) geopotential induced registration deviation in 200 seconds.

8.4.4 Scene-to-Scene Variations in Atmospheric Drag

Using a peak orbit velocity change of 0.35 m/s in 16 days, due to atmospheric drag, the peak deceleration is 0.253×10^{-6} m/s^2. The worse case environmental change in 16 days would occur if the atmosphere density were to go to zero. The bias acceleration change in the downrange direction would be 0.253×10^{-6} m/s^2 which produces a registration deviation of 0.0052 meters in 200 seconds. Thus, variations in atmospheric density between 16 day passes at an altitude of 705 km produces an insignificant registration deviation between 200 second (or even 20 minute) landmark updates.

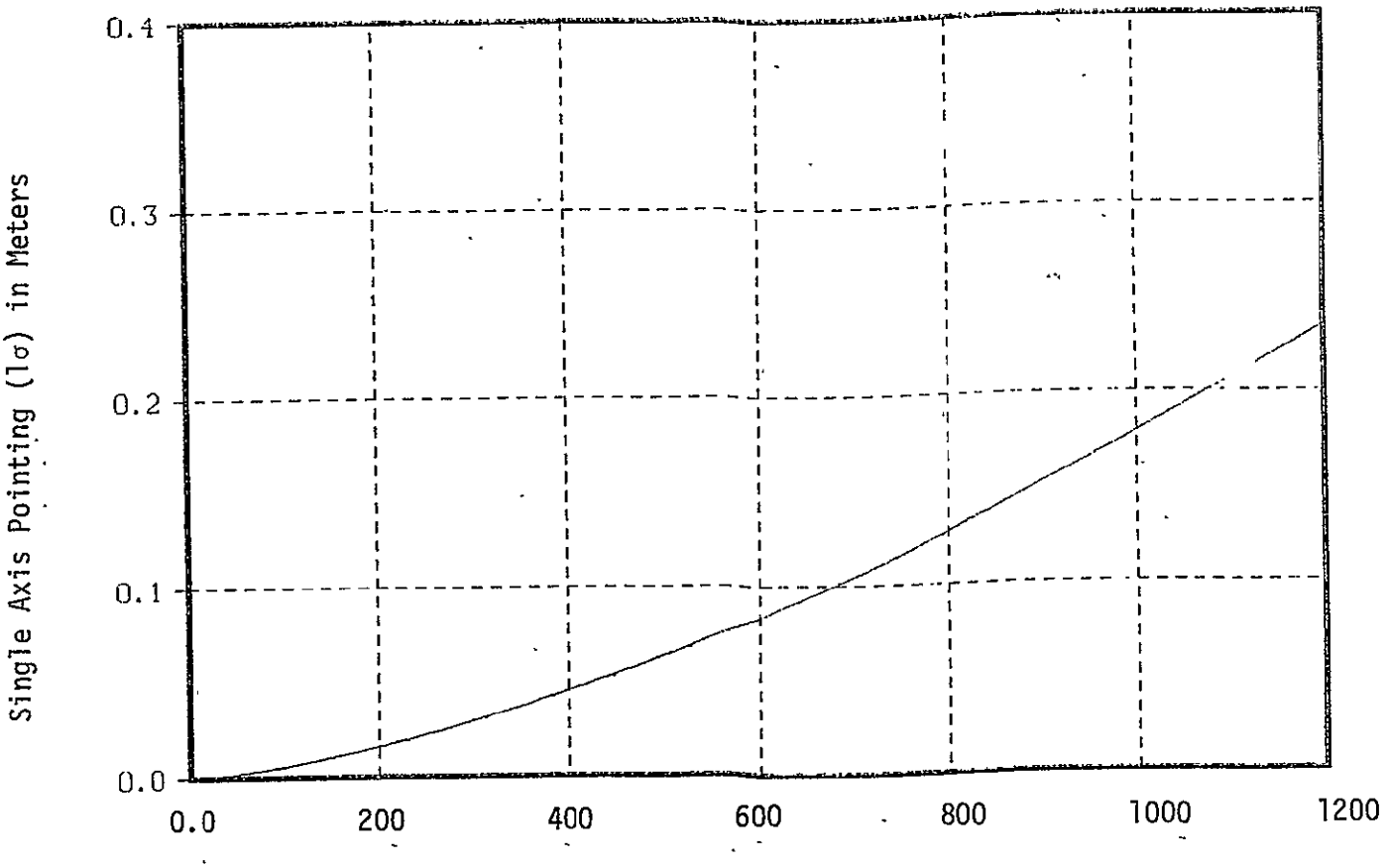

R_{nn}

Acceleration

Normal White Process $\quad R_{nn}(\tau) = A\,\delta(\tau)$

$A = 9.8^2 \times 10^{-12}\ m^2/s^3$

Figure 8.4-2. Single Axis Pointing (1σ) in Meters due to Normal White Noise

8.4.5 Landmark Registration Uncertainty

Landmark registration (processed measurement) to within 1.5 meter (1σ) can be obtained using a cluster of five landmarks whose signature data peaks are separated by 5 to 6 pixels (see Reference 15). The 3σ signature width for a point source such as a beacon is assumed to be 3 pixels. The landmark registration deviation measurements have a 1σ uncertainty of $1.5\sqrt{2}$ meters.

8.5 Conclusions

The feasibility of autonomous elimination of scene-to-scene temporal registration errors for the LANDSAT-D Thematic Mapper (TM) has been addressed. Various approaches and analytical techniques have been traded. The recommended approach uses, in part, landmark registration deviations to estimate pseudo attitude and attitude rate commands for eliminating registration errors caused by changes in spacecraft position, velocity, attitude, gyro bias, and TM to attitude reference system (ARS) misalignment between successive 16 day passes. For short time intervals the spacecraft attitude, ephemeris, and TM misalignment states can be combined to yield a simplified Kalman filter formulation consisting of states which are separable from one another. Separable states in this context means that each filter state impacts the landmark registration deviations in distinctly different ways. The simplified Kalman filter states are TM boresight on ground downrange and downrange rate deviations, and the TM boresight on ground crosstrack and crosstrack rate deviations. The pseudo attitude and attitude rate commands are derived from estimates of the above four filter states using landmark registration deviations and are kept constant between landmark updates.

Because of the modelling error incurred in the simplified Kalman filter formulation the truth diverges from the simplified state estimate following the landmark update. The divergence is functionally dependent on the amplitude of the state deviation between the two successive passes at the time of the landmark update. It also depends on the 1σ accuracy to which the state deviation can be determined if that state is used to compute pseudo attitude and/or attitude rate commands. A simple example will

illustrate these ideas. Consider only an ephemeris downrange deviation $r_x(t_o)$ and downrange velocity deviation $v_x(t_o)$. The downrange registration deviation (see Figure 8.3-1) at time t_o is

$$R_x(t_o) = -r_x(t_o)$$

and the deviation rate at time t_o is

$$\dot{R}_x(t_o) = -v_x(t_o)$$

Assume that $r_x(t_o)$ and $v_x(t_o)$ are both positive for the sake of discussion and let h stand for the orbit altitude. A negative (see Figure 8.3-1) pitch command of $-h^{-1} R_x(t_o)$ removes the downrange registration deviation at time t_o. In addition, suppose that we bias the pitch gyro information by the negative pitch rate $-h^{-1} v_x(t_o)$. One would think that the registration deviation between time t_o and the next landmark update would remain constant. This is, however, not the case. As shown in the text, the downrange registration deviation ΔR_x for t greater than t_o evolves according to

$$\Delta R_x(t) = -2 (\cos\omega_p \Delta t - 1) r_x(t_o) - \frac{4 (\sin\omega_p \Delta t - \omega_p \Delta t) v_x(t_o)}{\omega_p}$$

where

$$\Delta t = t - t_o$$

and ω_p is the orbit rate. The above equation is based on the perturbation expressions for the motion of a satellite in the neighborhood of a circular orbit and for an inverse square law gravitational field. The important thing to note is that the downrange registration deviation diverges between updates and that the magnitude of the divergence depends on the amplitude of the ephemeris downrange deviation $r_x(t_o)$, and the amplitude of the ephemeris downrange velocity $v_x(t_o)$. ΔR_x also depends on Δt which is the

elapsed time following the previous landmark update. ΔR_x is the modelling error and must be included as part of the state noise. Landmark registration deviations permit the estimation of $R_x(t_o)$, and $\dot{R}_x(t_o)$ which are used to compute the pseudo pitch attitude and pitch attitude rate commands. Only the state deviations are important if landmark registration deviations are used in this fashion. Please note that we have a state targetting problem going into the pass. A landmark separation of 1350 km on the ground provides an update every 200 seconds. If during the second pass the ephemeris range deviation continues to grow such that at each successive landmark in the second pass the ephemeris range deviation has increased we are faced with larger and larger state noise between landmark updates until this single component of the ephemeris state exhausts the 0.1 pixel error budget. The state targetting problem and how it is overcome by using more and more frequent ephemeris as the state deviation grows is reserved for future study. The discussion here is restricted to the use of landmark registration deviations and the state noise evolution prior to the second landmark update at 200 seconds. It is shown that the landmark only implementation must be augmented by a constant pitch rate command which is a function of the altitude miss between successive 16 day passes. Using a precomputed pitch attitude command based on accurate GPS supplied ephemeris of LANDSAT-D, an altitude miss of 100 meters contributes only 0.32 meter (1σ) to the registration error after 200 seconds if landmark and ephemeris updates are obtained every 200 seconds (1350 km on the earth's surface).

The DRIRU gyro reference assembly may not provide sufficient accuracy for the attitude reference system and, therefore, a single degree-of-freedom, floated gyro with good drift rate stability, such as the Bendix 64-PM-RIG, is recommended. Also, since an attitude accuracy of better than 10 arc-seconds is required, the NASA standard tracker (BBRC CT-401) cannot be used. Three CCD star trackers each having 3 degree FOV, 400 x 400 element array, and 3σ signature width over 4 pixels might provide the required 0.707 arc-second attitude determination accuracy.

Additional conclusions reached during the study are

- GPS must provide ephemeris to 2.1 meters (1σ) in position, and 0.01 meter/second (1σ) in velocity every 200 seconds in order to achieve the registration accuracy goal of 3 meters with landmark measurements every 200 seconds.

- A velocity state repeatability of 1.4 cm/second has been assumed in the study. This requirement can be relaxed if an active registration error compensation for a larger velocity miss is implemented.

- On subsequent passes the satellite must fly within a geopotential corridor centered on the initial satellite geopotential and within which a bias change not in excess of 10 mgal (10^{-5} meters/second^2) exists.

- Landmark updates are used every 200 seconds. A five cluster beacon landmark is required with the beacons separated from 150 to 180 meters on the ground (for a 705 km altitude). This provides a 1.5 meter (1σ) landmark registration accuracy.

The contribution of the state noise errors by downrange and crosstrack 1σ errors 200 seconds after landmark and ephemeris updates are defined in Tables 8.5-1 and 8.5-2. These error sources are derived on the basis of modelling errors which contribute, in part, to the state noise in the simplified Kalman filter model. There are two important aspects of the modelling error budget. One aspect of the problem is state repeatability and the second is state accuracy. Ephemeris and attitude deviations deal with state repeatability. As an example, in Table 8.5-1 the range is considered repeatable to within 3 meters (1σ) where $3\sqrt{2}$ meters (1σ) represents its ephemeris accuracy. The altitude is considered repeatable to within 100 meters with an uncertainty in the altitude deviation (1σ) of 3 meters due

Table 8.5-1. State Noise Downrange Error 1σ 200 Seconds After Landmark Update

	Downrange (1σ) (meters)
• Ephemeris Deviations	
Range = 3 meters	0.135
Altitude = 100 meters	0.32
Range Velocity = $\sqrt{2}$ cm/sec	0.085
Altitude Velocity = $\sqrt{2}$ cm/sec	0.597
• Ephemeris Accuracy	
Range (1σ) = $3/\sqrt{2}$ meters*	
Altitude (1σ) = $3/\sqrt{2}$ meters	0.63
Range Velocity (1σ) = 1 cm/sec**	
Altitude Velocity (1σ) = 1 cm/sec**	
• Misalignment Errors	
Variable Past (1σ) = 1 arc-sec	0.077
Misalignment Rate (1σ) = 1.058 arc-sec/sec	0.0054
• Gyro Induced Errors	0.79
• Geopotential	
10 mgal (10^{-5} meters/sec^2) Bias Acceleration	0.204
Random Normal White Noise Acceleration	0.016
Total RSS Error (1σ)	1.25

*The ephemeris range deviation accuracy (1σ) is 3 meters and this error has been accounted for in the ephemeris range deviation.

**The range and altitude velocities are taken as repeatable to with the ephemeris velocity accuracy of 1 cm/sec. Their contribution to the error budget is under ephemeris deviations.

Table 8.5-2. State Noise Crosstrack Error 1σ 200 Seconds After Landmark Update

	Crosstrack (1σ) (meters)
• Attitude Deviations	
Yaw = 1 arc-sec	0.72
Gyro Bias Uncertainty = 0.0013 deg/hr	0.094
• Attitude Accuracy	
Yaw (1σ) = $1/\sqrt{2}$ arc-sec*	
Gyro Bias Uncertainty (1σ) = $0.0013/\sqrt{2}$ deg/hr*	
• Misalignment Errors	
Bias (1σ) = 1 arc-sec	0.077
• Gyro Induced Errors	0.79
• Geopotential	
10 mgal (10^{-5} meters/sec^2) Bias Acceleration	0.204
Random Normal White Noise Acceleration	0.016
Total RSS Error (1σ)	1.095

*These errors have been accounted for under attitude deviations

to an ephemeris accuracy (1σ) of $3\sqrt{2}$ meters. Please note that if the ephemeris (position and velocity) were provided every 20 seconds, the constant pseudo attitude and attitude rate commands could be updated every 20 seconds and the ephemeris 1σ requirements could be relaxed. However, the pseudo attitude and attitude rate commands are a function of ephemeris deviations and the more frequent the update, the larger the data storage requirements become. One could conceivably update the ephemeris every second and compute the registration deviations using the ephemeris from the pass 16 days earlier. The simplified Kalman filter (see Reference 15) has a divergent state transition matrix. The performance of this filter is computed as the root-sum-square of the downrange and crosstrack registration deviations which are two of the filter states. The downrange and crosstrack state noise 200 seconds after a landmark update is given in Table 8.5-1 and 8.5-2. By taking the RSS of 1.25 meters and 1.095 meters, the RSS two-axis zero state noise performance requirement on the simplified Kalman filter of 2.50 meters (1σ) can be derived. Velocity repeatability of 1 cm/second is not considered feasible so it appears necessary to update the ephemeris more frequently and adjust the attitude and attitude rate commands. A 1 or 2 cm/second velocity variation has been detected using high precision range-rate data from the synchronous ATS-6 satellite tracking the low earth orbiting Apollo-Soyuz (see Reference 19). Tracking data was collected over 100 revolutions, however. Autonomous registration is feasible using extremely accurate ephemeris and geopotential models to derive precomputed attitude and attitude rate signals for registration error compensation. The next generation satellite laser ranging system will be capable of ranging to low orbit and synchronous orbit satellites with 2 cm accuracy (see Reference 20). Future studies should be directed toward establishing the optimum mix of ephemeris and landmark data assuming an accurate state-of-the-art geopotential model is available. Laser ranging may not be necessary if the lack of ephemeris state repeatability can be tolerated by using an accurate geopotential model.

Filter performance requirements have been established through covariance studies. To assess true filter performance one must have the actual measurement residuals. It is, therefore, recommended that future studies involve a truth model.

9.0 ON-BOARD SOFTWARE REQUIREMENTS

The on-board software capability required to perform the attitude reference algorithm, implement the attitude control laws, and provide Ku-band antenna control during TDRS link acquisition, is provided by the NASA Standard Space Computer, NSSC-1, which is located in the communications and data handling (CDH) module. This section will present preliminary estimates of memory and computation time requirements to perform these functions for LANDSAT-D.

9.1 NASA Standard Space Computer (NSSC-1) Characteristics

The central computer to be used on MMS was designed as a low cost, high speed digital computer and is an outgrowth of the On-Board Processor now flying on OAO-3. This computer, originally known as AOP, has been adopted as the NASA Standard Space Computer, NSSC-1. The computer's design possesses features that readily allow time-shared operation with sufficient inherent reliability to be trusted with mission critical functions. The computer has a modular architecture with dual interconnecting buses between memory and processor modules to avoid the possibility of a catastrophic single point failure. General characteristics of the computer are summarized in Tables 9-1 and 9-2 (Reference 1 , Section 5.0).

9.2 ARS Algorithm Software Requirements

The ARS software is used to process gyro data, to derive rate and attitude, and to process strapdown star tracker measurements in a six-state Kalman filter to develop periodic estimates for updating attitude and gyro drift. Quaternions are used as the kinematic variables to describe spacecraft attitude.

The ARS software organized in terms of individual software modules defined to handle specific functional requirements. The actual linking of these functions is under control of the Executive software. Functional flow of the software execution is shown in Figure 9-1, and the computer software requirements are summarized in Table 9-3. Single precision arithmetic is used throughout, with double precision accumulation of dot

Table 9-1. General Characteristics of NSSC-1

Word Length	18 Bits, 5 Bits Instruction ID, 1 Bit Index, 12 Bits Operand Fetch
Execution Speed	2 μsec Cycle Time, 4 μsec Add, 32 μsec Multiply, and 60 μsec Divide
Memory Capacity	Four 8192 Word Modules for Total of 32,768 Words. (Expandable to 64 K in 8 K Segments.)
Registers	One Double Length Accumulator (36 Bits), Two Registers, One Index Register
Processor Interrupts	16 Levels of Priority Interrupt
Direct Memory Access	16 Cycle Steal Channels
Memory Write Protection	Allowable Storage Areas are Assigned in Segments of 128 Words
Input/Output	I/O is Achieved through Time Multiplexing of Existing Telemetry and Command Hardware
Program Load and Dump	Any 4 K Memory Bank can be Loaded and Dumped via Command and Telemetry_without Software Bootstrap

Table 9-2. Physical Characteristics of NSSC-1

	Size (in^3)	Weight (lbs)	Power (Standby) (watts)	Power (Full Operation) (watts)	Technology
Processor	75	4	6	6	TTL-LSI
Memory 8K x 18 Bits	100	5	0.07	24	Core
Power Converter	100	5	3	8	Discrete
Total (32K) System	275	14	9	38	

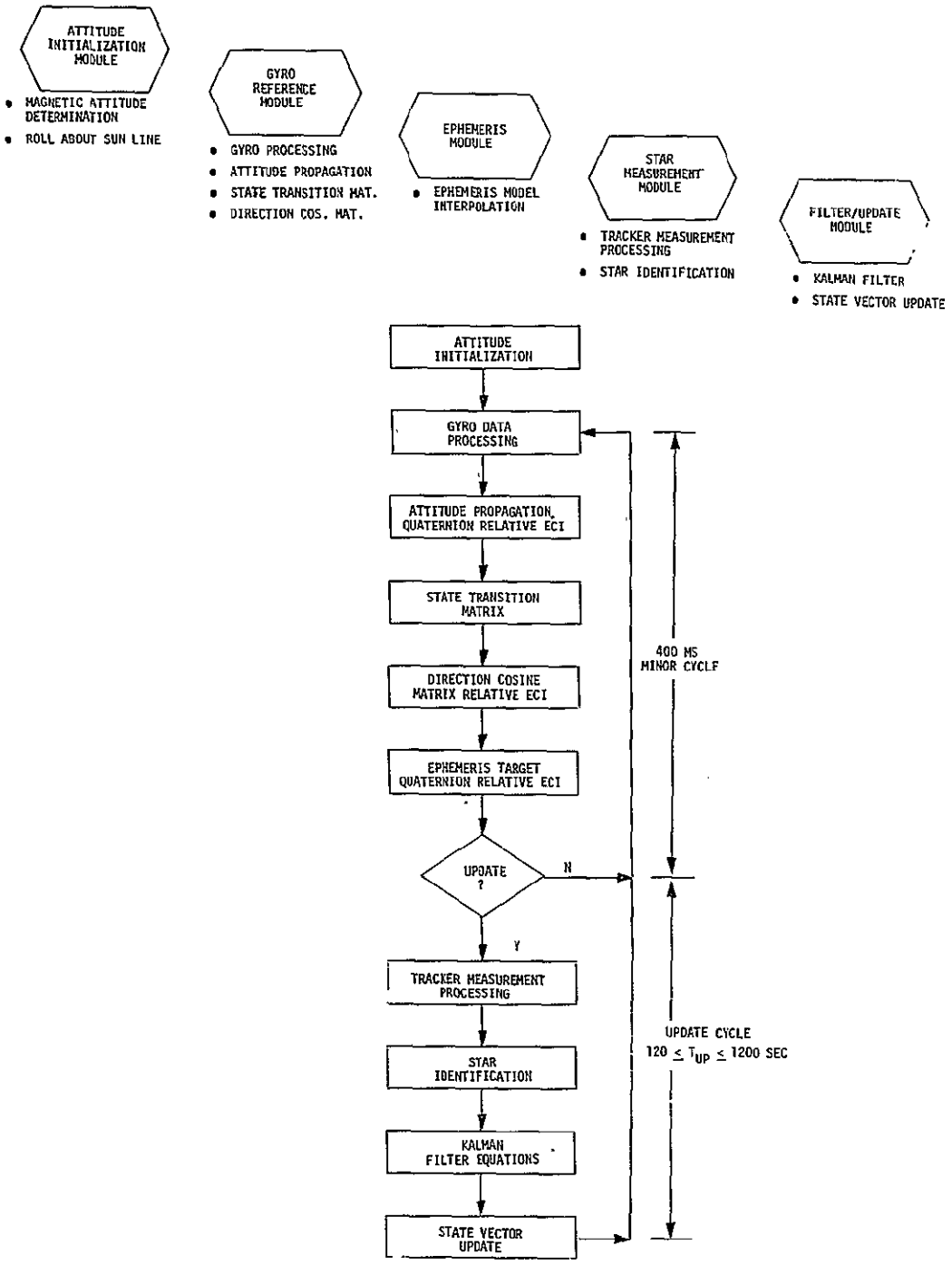

Figure 9-1. ARS Software Functional Flow

Table 9-3. ARS Software Requirements Summary

Functions	Memory (18 bit words)		Computation Time/Cycle (ms)
	Program	Read/Write (Data Base)	
Math Pack	500	50	--
Attitude Initialization Module			
Attitude Determination by Magnetic Field Measurements	100	35†	3.0
Roll about Sun Line	150	35	5.0
Gyro Reference Module			
Gyro Data Processing	140	20	18.0
Attitude Propagation Algorithm	160	20	12.2
State Transition Matrix	70	10	1.8
Direction Cosine Matrix	95	20	9.7
Ephemeris Module			
Fourth Order Hermit Polyn. fit to ten Benchmarks/Orbit	190	1200*	52.0
Ephemeris Computation from Polynomial			1.4
Star Measurement Module (2 Trackers)			
Star Identification	185	253**	25.6
Star Tracker Data Processing	300	50	20.3
Filter/Update Module (1 Star)			
Covariance Propagation	275	42	41.3
Measurement Matrix	240	40	33.0
Kalman Gain Matrix	100	20	27.0
Covariance Matrix Update	60	10	39.0
State Vector Update	95	5	5.3
Total Memory	2660	1810	

*Includes data table of benchmarks for 24 hrs at 6 benchmarks/hr = 864 entries
**Includes star catalog of 75 stars = 225 words (aberration corrected right ascension, declination, and brightness)
†Magnetic Field Model not included

products, utilizing the double length 36 bit accumulator of the NSSC-1. The minor cycle time for the ACS/ARS software is 400 ms. A general purpose math pack of utility subroutines is assumed available. A math pack containing matrix algebra routines (except inverse), sine, cosine, tangent, arc-sine, arctangent, and square root routines would require about 500 words of program storage and 50 words of scratch pad memory. The succeeding paragraphs provide a functional description of the modules and define underlying assumptions.

Attitude Initialization Module

To initialize attitude, the spacecraft first acquires the sun with its negative yaw (-z) axis using the array located coarse sun sensor and the precision digital sun sensor in conjunction with the RCS and reaction wheel attitude control system. Magnetometer earth field measurements are then used to determine orientation about the sun line within about 2 degrees. This is sufficiently accurate to unambiguously identify a reasonably bright and isolated star located in the swath traced out by the tracker when the spacecraft is rotating about the sun line. The residual from this star measurement is then used to initialize the regular Kalman filtering algorithm for computing the first attitude update (the regular filtering and update software is used for this and not included in the initialization module). Storage required for the magnetic field model is also excluded.

Gyro Reference Module

This software module provides the functions associated with maintaining an inertial attitude reference in conjunction with a configuration of strapdown rate integrating gyros. The gyro outputs are processed to compensate for known misalignments, scale factor errors and biases. Rate and attitude of a known reference frame, nominally fixed with respect to the gyro configuration, is derived with respect to a known inertial reference frame, e.g., Earth-Centered-Inertial (ECI). The attitude is described by quaternions and the attitude propagation algorithm uses the closed form solution of the quaternion equations, i.e., $q_k = e^{(1/2)\hat{\Omega}_k T} q_{k-1}$.

Ephemeris Module

The ephemeris algorithm presented in Appendix D of Reference 2 is assumed to be used. The ephemeris is to be provided by a six element vector comprising the radius vector in ECI (three elements) and the velocity vector in the same coordinate system. The module will be provided with a table of benchmark residuals along with an algorithm for computing (approximate) ephemeris at the benchmarks. At a given point in time, the algorithm computes and stores benchmark ephemeris at four points surrounding the current time and from these four benchmarks, ephmeris is computed by means of a fourth order Hermite polynomial interpolation. In addition, the on-board algorithm can be used for extrapolation beyond the limits of the table if necessary. The computational time required for an update not requiring new benchmark information (new benchmarks are provided at least every 10 minutes) requires on the order of 1.5 mseconds. Computation time for cases requiring an update of the benchmarks require over 50 mseconds due to the large number of multipliers involved in generating the benchmarks. Storage of the benchmarks rather than the residuals would reduce the data requirements by 31 words and at the same time reduce the average minor cycle computational requirements.

Star Measurement Module

This software module provides the functions associated with star measurement data processing of two strapdown star trackers, assuming one star in each tracker. The software processes and applies corrections to star tracker data based on stored correction factors generated during an in-orbit star tracker calibration. The software is based on a third order polynomial correction of the type proposed by MIT for the BBRC CT-401 tracker, Reference 17. The measurement software also provides star identification utilizing attitude information and the aberration corrected star catalogue stored in memory.

Filter/Update Module

This software incorporates the Kalman filter associated with providing an optimal estimate of the attitude determination state vector. The

Kalman filter has a six-element state vector consisting of three attitude variables and three gyro bias variables. In using quaternions to represent attitude, it is noted that one of the parameters is redundant, i.e., constrained by a simple algebraic relation. This makes it possible to unambiguously represent variations in the fourth parameter in terms of variations in the first three. It follows that the Kalman filter need estimate only the three variables, and thus its state vector contains only three attitude terms. The linearization of the equations as required by the filter formulations are taken about the past filter estimate.

The equations for the extended Kalman filter are well known.

$$P = \Phi P \Phi^T + Q$$

$$K = PH^T[HPH^T+R]^{-1} \quad .$$

$$P = [I-KH]\,P$$

$$\hat{\delta x} = K\hat{\delta y}$$

The state error covariance matrix, P, is propagated using the state transition matrix, Φ, and the state noise covariance matrix, Q. The state transition matrix is initialized at the time of each update and computed (in the Gyro Reference Module) between updates at each integration step using the gyro derived attitude. The optimal gain matrix, K, is computed from the measurement matrix, H, and the measurement noise covariance matrix, R. The measurement matrix relates variations in the measurement vector to variations in the state vector. The measurement noise covariance matrix, R, is 2 x 2 and the elements are constants whose value is selected based upon the expected (or measured) noise in the star measurement. The gain matrix, K, is used to establish a state correction $\hat{\delta x}$, to the state vector using the measurement residual, $\hat{\delta y}$. The state error covariance matrix is also updated using the gain matrix and measurement matrix, and constrained to remain positive definite.

9.3 Attitude Control Software Requirements

A description of the attitude control system has been provided in subsection 6.4. The ACS software processes estimated attitude, gyro data and sun sensor data to provide control signals to the reaction wheel drives and/or the RCS valve drivers. It also provides the magnetic unloading logic and Ku-band antenna control during TDRS link acquisition.

The ACS software is organized in modules defined to handle specific functional requirements. The linking of these functions is under control of the executive software. Functional flow of the software execution is shown in Figure 9-2, and the computer requirements are summarized in Table 9-4. Single precision arithmetic with double accumulation of dot products is assumed throughout. The computation cycle is 400 ms, synchronized with the ARS minor cycle. An exception is the Ku-band antenna control for TDRS acquisition with a computation cycle of 50 ms. The following paragraphs provide a brief functional description of the software modules.

Sun Sensor Module

This module processes the output signals of the coarse sun sensor located on the solar array (4π steradian coverage), and the fine digital sun sensor located in the ACS module. The processing consists mainly of bias and ADC offset removal, and scale factor corrections. The processed output for each sensor consists of two quantities which define the sun vector in sensor coordinates, yielding essentially x and y errors normal to the sunline which is nominally along the sensor z-axis. For large sun angles, the bilevel signals and sun presence signals must be used.

Attitude Error Module

The spacecraft attitude errors are computed for the different modes of operation. Mode end checks are also included; for instance, when to switch from the coarse to the fine sun acquisition mode. For normal on

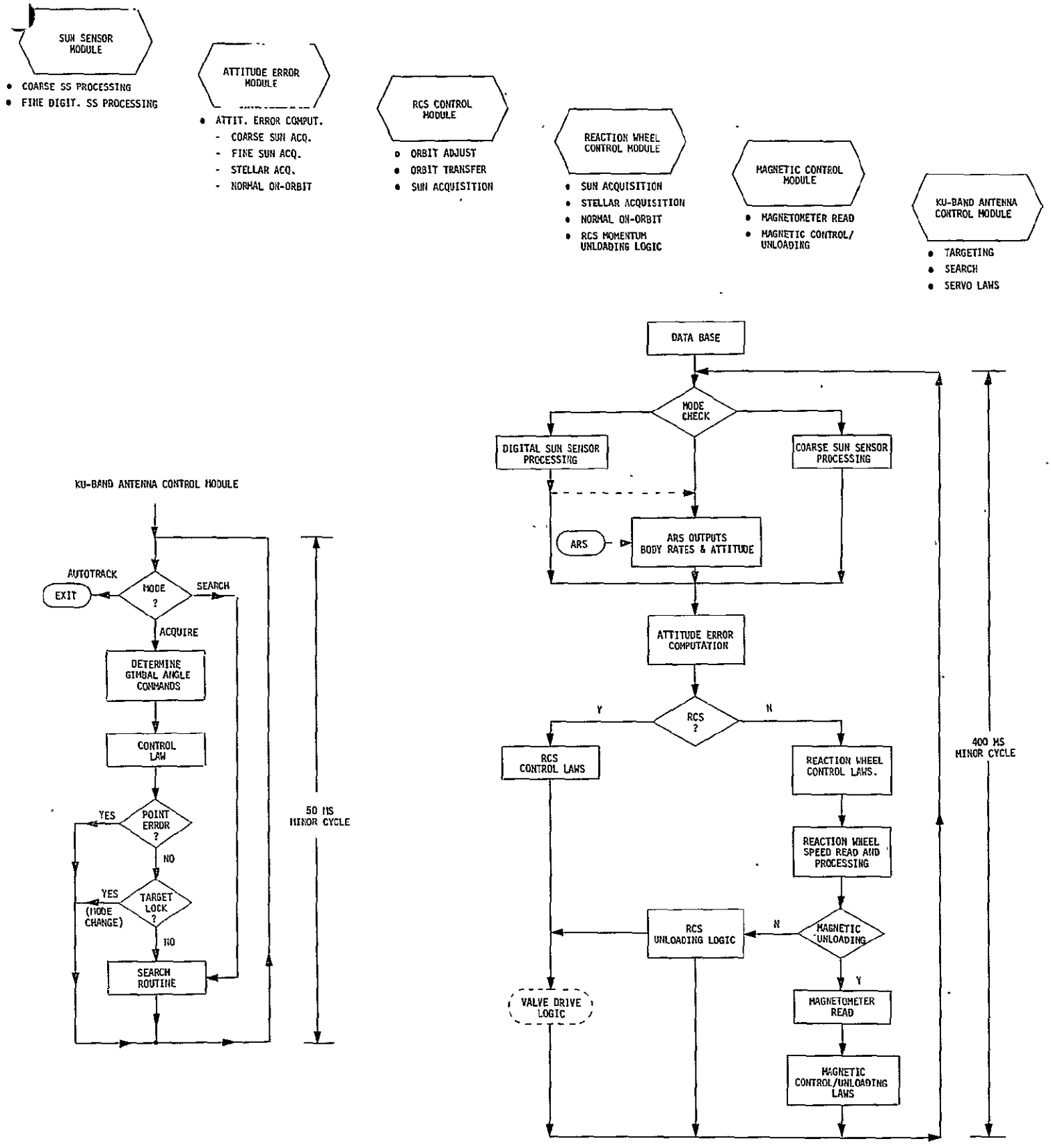

Figure 9-2. ACS Software Functional Flow

Table 9-4. Attitude Control Software Requirements Summary

Functions	Memory (18 bit words)		Computation Time/Cycle (ms)
	Program	Read/Write (Data Base)	
Sensor Module			
Coarse Sun Sensor Processing	60	7	3.6
Digital Sun Sensor Processing	50	7	0.6
Attitude Error Computation Module			
Coarse Sun Acquisition	70	17	0.7
Fine Sun Acquisition/Stellar Acquisition	60	15	0.9
Normal On-Orbit Attitude Error	60	36	3.0
RCS Control Module			
RCS Control Laws (Valve drive logic hard-wired, external)	310	50	5.4
Reaction Wheel Control Module			
Reaction Wheel Control Laws	125	36	2.9
Reaction Wheel Speed Read and Processing	70	10	1.5
Momentum Check/Unloading Logic Using RCS	70	23	0.6
Magnetic Control Module			
Magnetometer Read	70	10	1.5
Magnetic Control Laws	135	40	3.0
Ku-Band Antenna Control Module			
Targeting/Search and Servo Control Law	170	55	2.4*
Total Memory	1250	306	

*Minor computation cycle 50 ms. Only performed during TDRS link acquisition.

orbit operation the small angle attitude errors relative to the local vertical frame are computed from the spacecraft inertial attitude quaternion (obtained from the ARS) and the ephemeris target quaternion, using quaternion algebra.

RCS Control Module

This module contains the software to compute thruster actuation signals from the spacecraft attitude errors and gyro sensed rates. Mode dependent options, control law shaping filters (if required), limiters, and thruster deadzones are programmed in this module. Pulsewidth modulated thruster control is assumed. The outputs of the module are thruster on-time count-down signals in body coordinates. The thruster select logic is assumed to be hardwired, external to the processor.

Reaction Wheel Control Module

This module computes RW torque commands for the various modes of operation of the spacecraft from the attitude errors and the spacecraft rates. Integral compensation, limiters, shaping networks, transformations from body to wheel coordinates, constant speed commands, speed read and momentum computations, etc., are included. The module also contains the momentum unloading logic when using the RCS for unloading, which is not the nominal mode of operation for L-D but must be provided.

Magnetic Control Module

This software processes the magnetometer signals and implements the magnetic control laws for continuously unloading the wheels, interrupted by shutdown signals (all torquer bars off) during star tracker read. The magnetic control law used is

$$\overline{M} = - \frac{K}{B^2} (\overline{B} \times \overline{H}_e)$$

where

$\overline{M}$ = desired magnetic moment of torquer bars

$\overline{B}$ = earth magnetic field

$\overline{H}_e$ = spacecraft momentum error

K = a gain constnat

Ku-Band Antenna Control Module

This module is only exercised when the Ku-band antenna must acquire the TDRS link. Under normal operation, the Ku-band antenna is under autonomous autotrack control and the computer software is not involved. The TDRS link acquisition software solves targeting equations, computes gimbal angle commands that point the antenna to TDRS and synthesizes the control equations required to execute the pointing command, i.e., slewing the antenna and settling into the desired orientation. The software can also command a spiral search about the target area as presented in Section 3.3. When exercised, the minor cycle computation interval for this software module should be on the order of 50 ms since the bandwidth of the antenna servo is expected to be in the 2-3 Hz range.

9.4 Typical Normal On-Orbit Requirements

Tables 9-3 and 9-4 listed ARS and ACS software requirements for various operational modes and conditions of LANDSAT-D. Total memory requirements, are

3910 words of program memory

and

2116 words of read/write memory

Typical software requirements during normal on-orbit operations are summarized in Table 9-5. The top half assumes no ephemeris and attitude updates and arrives at a total execution time of 44.4 ms per 400 ms minor cycle, which is very reasonable. The bottom half of the table adds to this the software requirements for ephemeris and attitude updates,

Table 9-5. Normal On-Orbit ARS/ACS Software Requirements

Functions	Memory (18 bit words)		Computation Time/Cycle (ms)
	Program	Read/Write (Data Base)	
Math Pack	500	50	--
Gyro Data Processing	140	20	18.0
Attitude Propagation Algorithm	160	20	12.2
State Transition Matrix	70	10	1.8
Ephemeris	80	35	1.4
Normal On-Orbit Attitude Error	60	36	3.0
Reaction Wheel Control Laws	125	36	2.9
Reaction Wheel Speed Read and Processing	70	10	1.5
Momentum Check/Magnetic Unloading	170	50	3.6
Subtotals (no update)	1375	267	44.4
Ephemeris Update	110	1165*	52.0
Direction Cosine Matrix	95	20	9.7
Star Measurement Module (2 Trackers)	485	303**	45.9
Filter/Update Module (1 Star)	770	117	145.6
Ku-Band Antenna TDRS Link Acquisition	170	55	19.2†
Total (with update and TDRS Link Acquisition)	3005	1927	316.8

*Contains 864 words of ephemeris benchmarks
**Contains 225 words of star catalog
†8 x (2.4 ms every 50 msec)

processing both trackers, but computing update from only one star. If a second star is present, it is used for updating the state vector in the next minor cycle. Both star trackers are processed at once since it is computationally efficient and it leaves the option open to process the two star measurements simultaneously should this be required at some time. Software requirements for control of the Ku-band antenna during TDRS link acquisition is also included in the bottom half of the table. The required computation time with updates of 316.8 ms still fits nicely into the proposed 400 ms minor cycle. This is not essential, since the attitude update increment, for example, could be computed over several minor cycles and the state transition matrix could be used to finally perform the state update several minor cycles after the star measurements were made. The ephemeris update can also be spread over several minor cycles.

The results above indicate that the software requirement for the ACS/ARS fits nicely into the NSSC-1 computer, leaving ample memory and computation time for the software requirements of the other subsystems.

REFERENCES

(1) "Low Cost Modular Spacecraft Description," NASA/GSFC Report Number X-700-75-140, May 1975.

(2) "Specification for Multi-Mission Modular Spacecraft (MMS) Attitude Control Subsystem," F. J. Kull, NASA Document GSFC-S-700-17, April 1976.

(3) "Telecommunicator Service Via a Tracking and Data Relay Satellite System: Phase II, Implementation and Operations," Proposal to NASA by TRW DSG, Part 2, Volume 4, 15 January 1976.

(4) "Precision Pointing Control System (PPCS) System Design and Analysis," TRW Technical Report Number 13900-6012-R0-01, 1 July 1972.

(5) "Design Study Landsat Follow-On Mission Unique Communications Systems," prepared by TRW DSG for NASA/GSFC, TRW Report Number 14897-6007-RU-00, August 1976.

(6) "ALLMAG, GDALMG, LINTRA: Computer Programs for Geomagnetic Field and Field-Line Calculations," E. G. Stassinopoulos and Gilbert D. Mead, NASA/GSFC Report Number NSSDC-72-12, February 1972.

(7) "The Attitude Determination System for the Orbiting Astronomical Observatory," P. B. Davenport, Proceedings of the Symposium on Spacecraft Attitude Determination, pages 249-256, held at the Aerospace Corporation, El Segundo, California, October 1969.

(8) "Final Report Thematic Mapper Critical Elements Breadboard Program," Hughes Aircraft Company, Report Number HS-236/D2241, 1 April 1976.

(9) G. Wolf and A. Wittman, "The Flight of the FRUSA," AIAA Ninth Electric Propulsion Conference, Bethesda, MD, April 1972.

(10) "Severe Storms Observing Satellite Study: STORMSAT ACS Design Study, Phase II," Interim Technical Report prepared by TRW Systems for NASA/GSFC, TRW Report Number 26818-6002-RU-00, 20 February 1976.

(11) White, Robert L., "Ground Truth Applications to Orbit Refinements," Goddard Space Flight Center Mechanics/Estimation Theory Symposium, August 1975.

(12) White, Robert L., et al., "Interim Technical Report Number 3, Advanced Earth Observation System Instrumentation Study," The Charles Stark Draper Laboratory, Incorporated, December 1975.

(13) Easton, Roger L., et al., "Dissemination of Time and Frequency by Satellite," Proceedings of the IEE, Volume 64, Number 10, October 1976.

(14) Argentiero, P., Garza-Robles, R., and O'Dell, M., "Application of Satellite-to-Satellite Tracking to Orbit Determination and Geopotential Recovery," Goddard Space Flight Center Mechanics/Estimation Theory Symposium, August 1975.

REFERENCES

(continued)

(15) 22296-6001-RU-02, "Earth Observatory Satellite System Definition Study (EOS)," Final Report Number 3, Book 2, 1 October 1974.

(16) GSFC-S-712-10, "Specification for NASA Standard Inertial Reference Unit," Goddard Space Flight Center, Greenbelt, Maryland, May 1976.

(17) Doxsey, Roger, "SAC-C Tracker Analysis," MIT, Center for Space Research, Memo Number 37-595, Cambridge, Massachusetts, May 1974.

(18) Salomon, P. M. and Goss, W. C., "A Microprocessor-Controlled CCD Star Tracker," AIAA Paper Number 76-116, AIAA 14th Aerospace Science Meeting, Washington, D.C., January 1976.

(19) Vonbun, F. O., et al., "Gravity Anomaly Detection from ATS-6/Apollo-Soyuz," Transactions, American Geophysical Union, Volume 56, Number 12, December 1975.

(20) Byrns, D. A., "The Next Generation Satellite Laser Ranging System," Transactions, American Geophysical Union, Volume 56, Number 12, December 1975.

Appendix A

PROGRAM LFQ

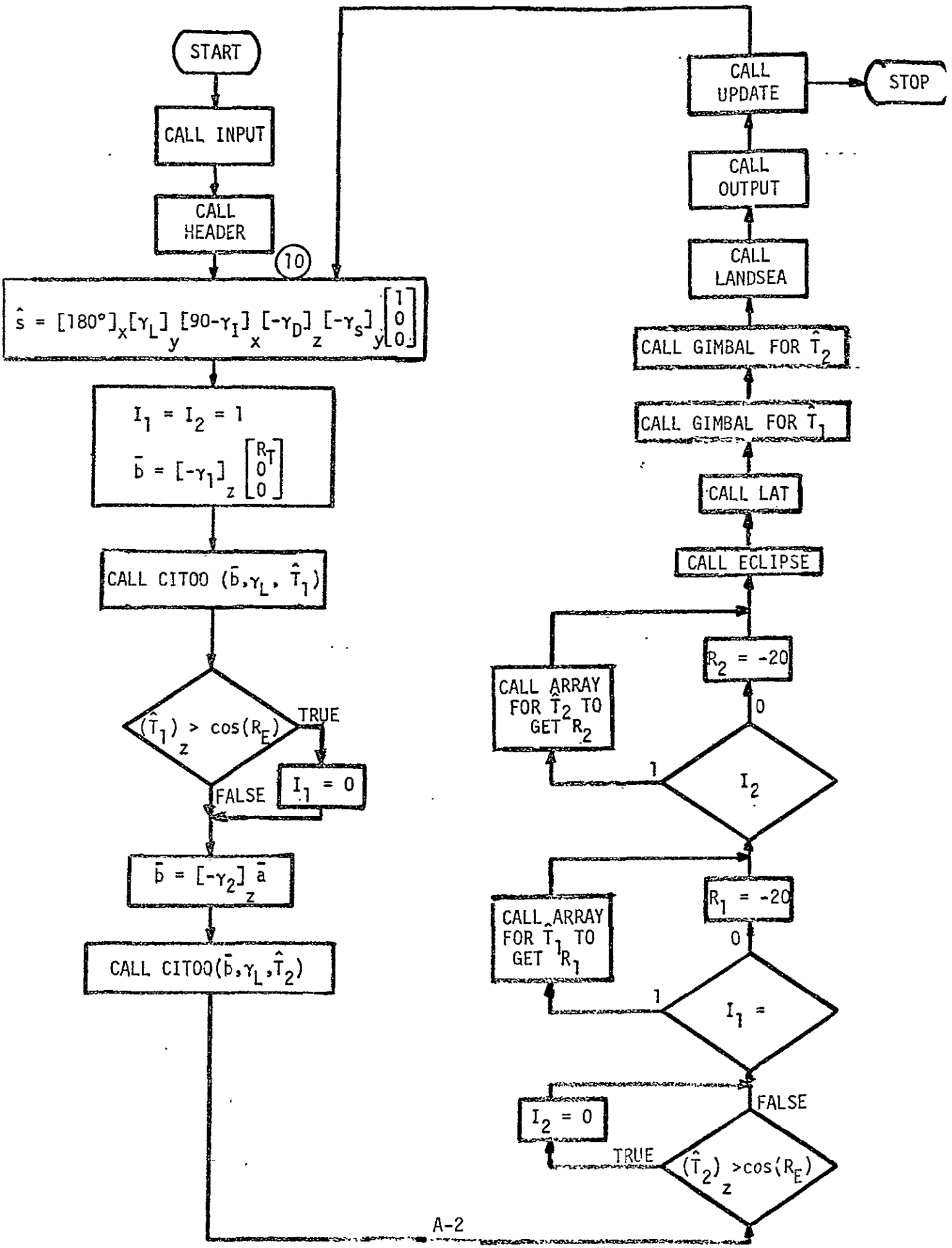
START
CALL INPUT
CALL HEADER
10
$\hat{s} = [180°]_x[\gamma_L]_y[90-\gamma_I]_x[-\gamma_D]_z[-\gamma_s]_y\begin{bmatrix}1\\0\\0\end{bmatrix}$
$I_1 = I_2 = 1$
$\bar{b} = [-\gamma_1]_z \begin{bmatrix}R_T\\0\\0\end{bmatrix}$
CALL CITOO $(\bar{b}, \gamma_L, \hat{T}_1)$
$(\hat{T}_1)_z > \cos(R_E)$
TRUE
FALSE
$I_1 = 0$
$\bar{b} = [-\gamma_2]_z \bar{a}$
CALL CITOO$(\bar{b}, \gamma_L, \hat{T}_2)$
CALL UPDATE
STOP
CALL OUTPUT
CALL LANDSEA
CALL GIMBAL FOR $\hat{T}_2$
CALL GIMBAL FOR $\hat{T}_1$
CALL LAT
CALL ECLIPSE
$R_2 = -20$
CALL ARRAY FOR $\hat{T}_2$ TO GET R_2
0
1
I_2
$R_1 = -20$
CALL ARRAY FOR $\hat{T}_1$ TO GET R_1
0
1
I_1 =
FALSE
$I_2 = 0$
TRUE
$(\hat{T}_2)_z > \cos(R_E)$

SUBROUTINE OUTPUT

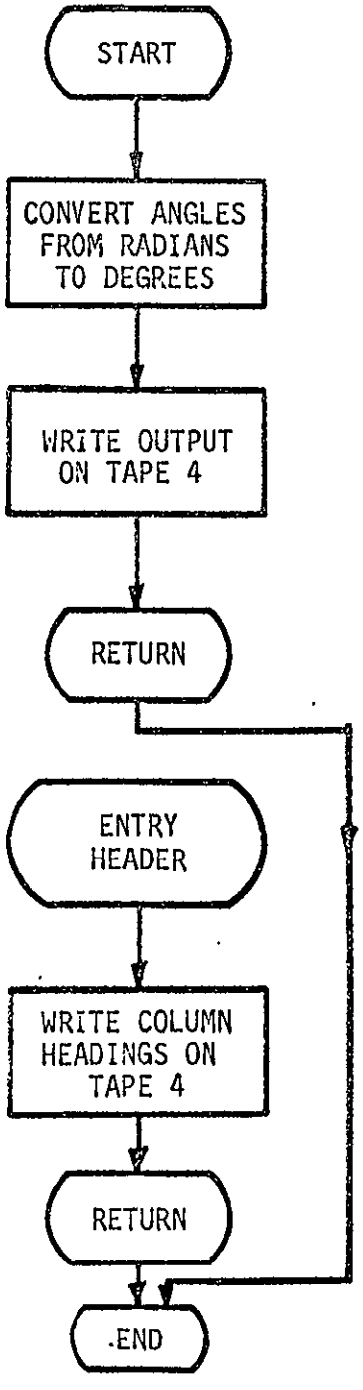

SUBROUTINE UPDATE

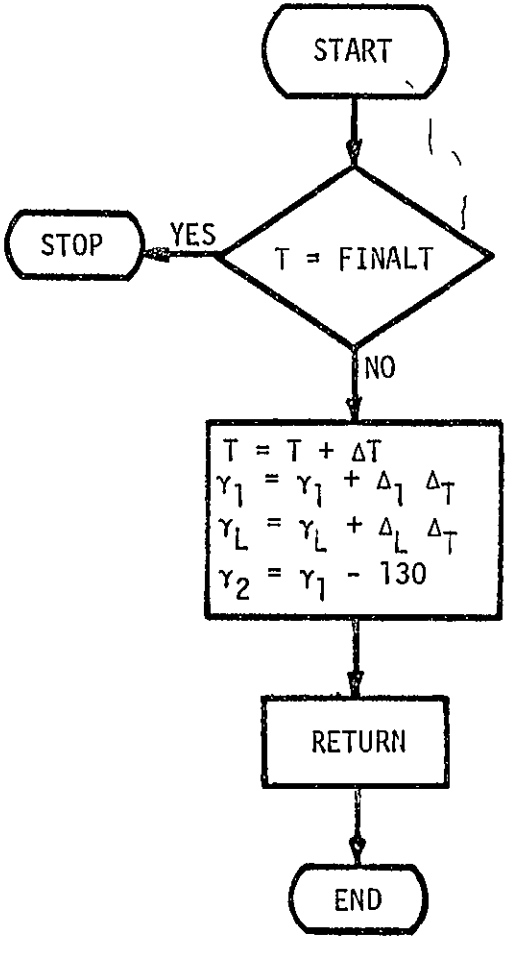

SUNROUTINE INPUT

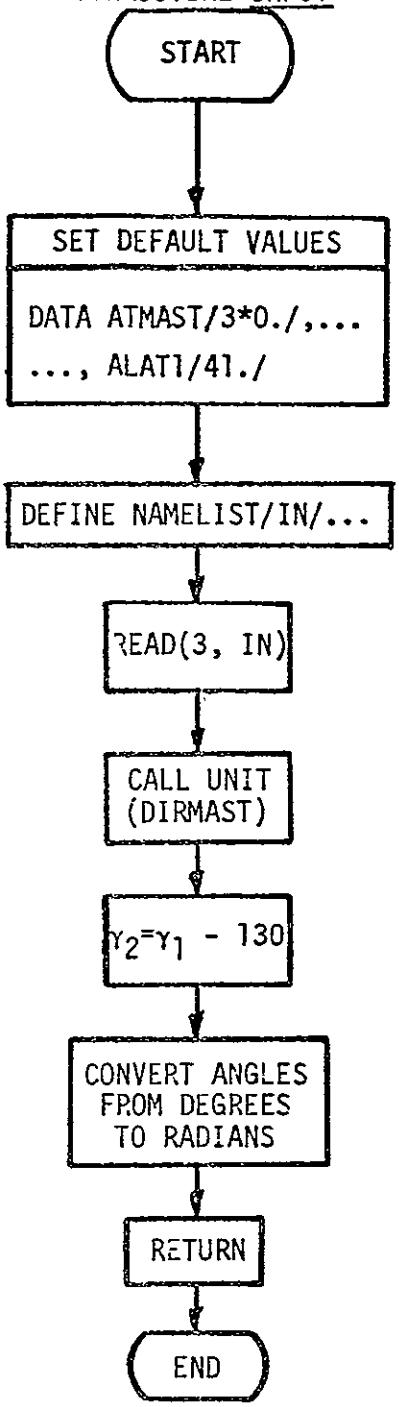

SUBROUTINE BASIS ($\bar{a}$, $\hat{e}$, $\hat{d}$)

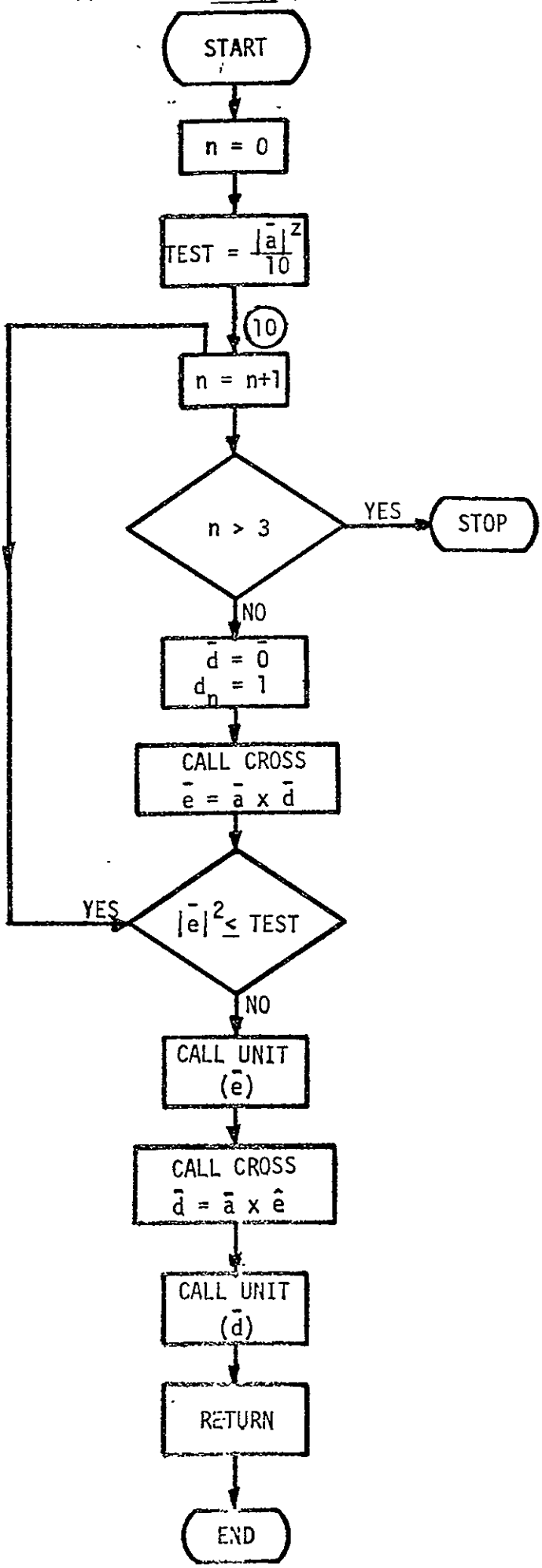

SUBROUTINE ARRAY ($\hat{T}$, $\hat{S}$, R)

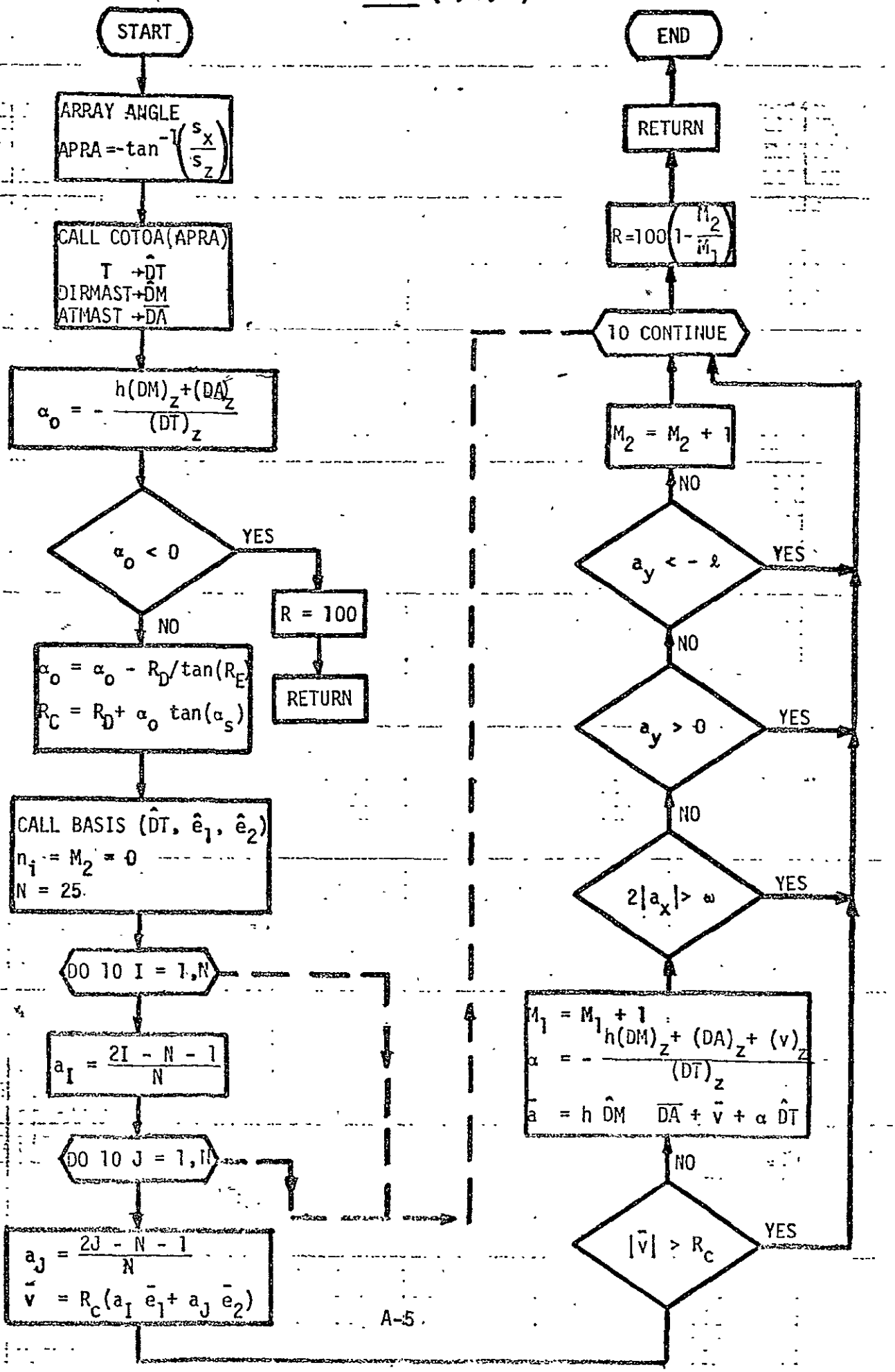

SUBROUTINE LAT

START

$\bar{a} = [\gamma_1 + \gamma_D + \text{ALATI}]_z\ [90.]_y [90 - \gamma_I]_z\ [-\gamma_L]_y \begin{bmatrix}1\\0\\0\end{bmatrix}$

TRUE LATITUDE

$\phi_T = \sin^{-1}(a_z)$

$a_z = 0$

CALL UNIT($\bar{a}$,$\hat{b}$)

CALL DOT

$C = \hat{b} \cdot \begin{bmatrix}1\\0\\0\end{bmatrix}$

LONGITUDE

$$\text{ALONG} = \begin{cases} \cos^{-1}(c), & by \leq 0 \\ -\cos^{-1}(c), & by > 0 \end{cases}$$

GEOGRAPHIC LATITUDE

$\phi_g = \tan^{-1}[p^2 \tan(\phi_T)]$,

$p = 1.00336417$

RETURN

END

SUBROUTINE LANDSEA

START

ENTER LOOKUP TABLE
DATA ARRAY (1)...
ARRAY (688)

LAT = ALAT + 90
R = 20627.53
I_{B1} = R(1+sin(LAT-90))
I_{B2} = R(1+sin(LAT-89))
I_{DB} = IB2 - IB1

$$\text{LON} = \begin{cases} \text{IDB}, & \text{max} \\ \text{IDB}(.5 + \frac{\text{ALONG}}{360}) + 1, & \\ 1, & \text{min} \end{cases}$$

IW = IB1 + LON
L = (IW - 1)/60
M = IW - 60L

LAND = ARRAY(L+1),(M-1)BIT

RETURN

END

SUBROUTINE GIMBAL ($\bar{T}$, G_1, G_2, G_3)

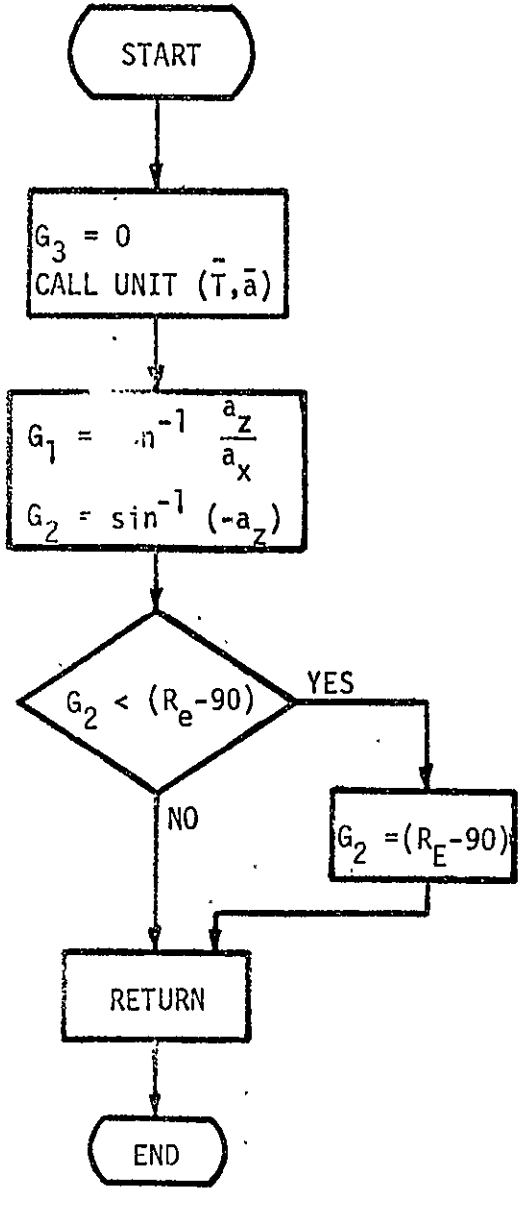

SUBROUTINE ECLIPSE

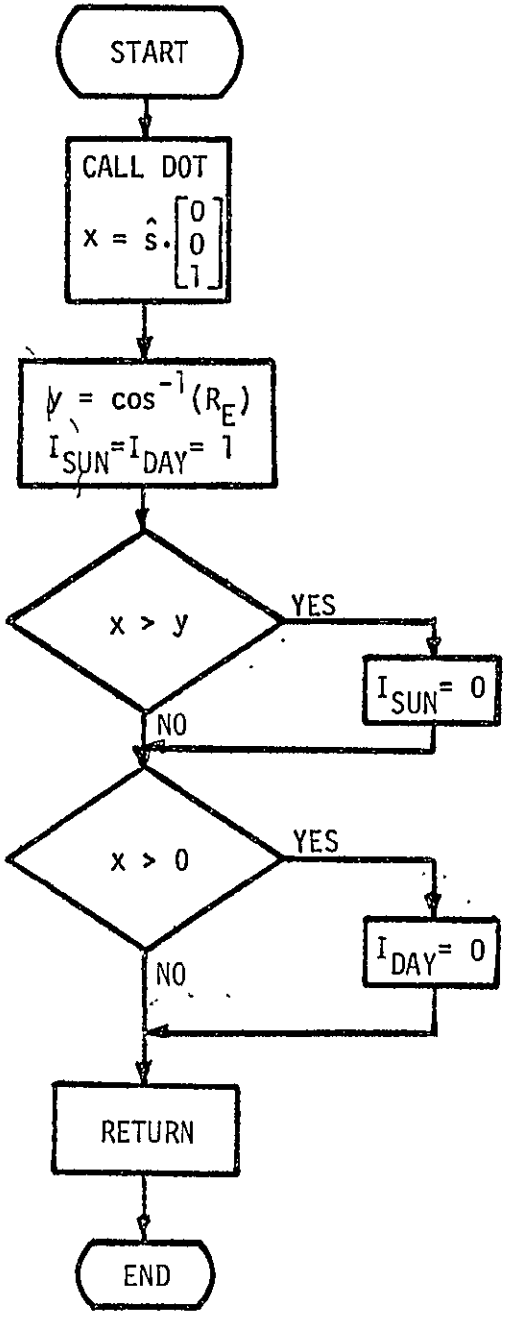

SUBROUTINE CITOO $(\bar{a}, \gamma_L, \hat{b})$

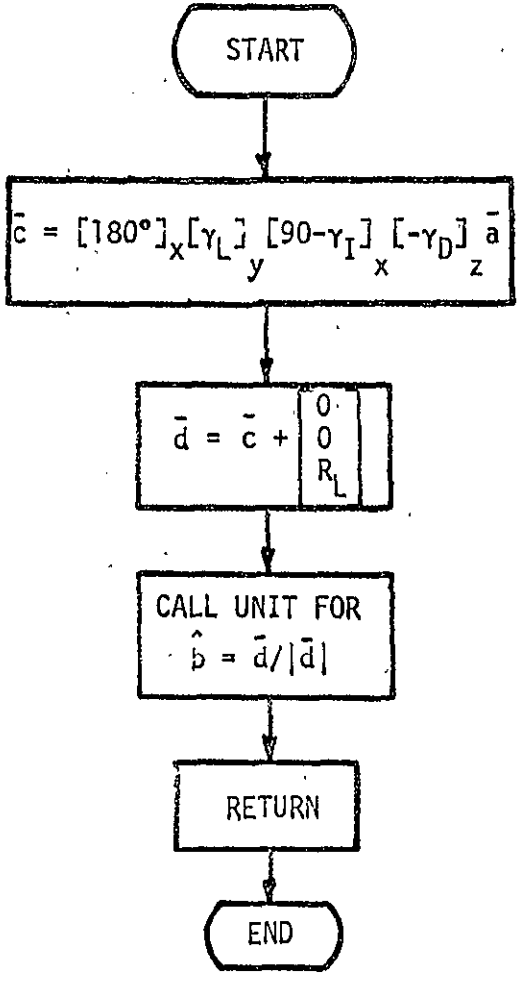

SUBROUTINE COTOA$(\bar{a}, \rho, \bar{b})$

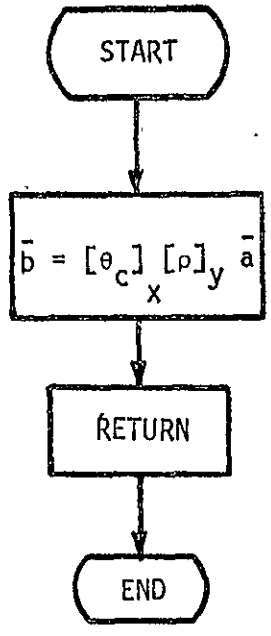

SUBROUTINE ROT($\bar{x}_I$,a,n,$\bar{x}_o$)

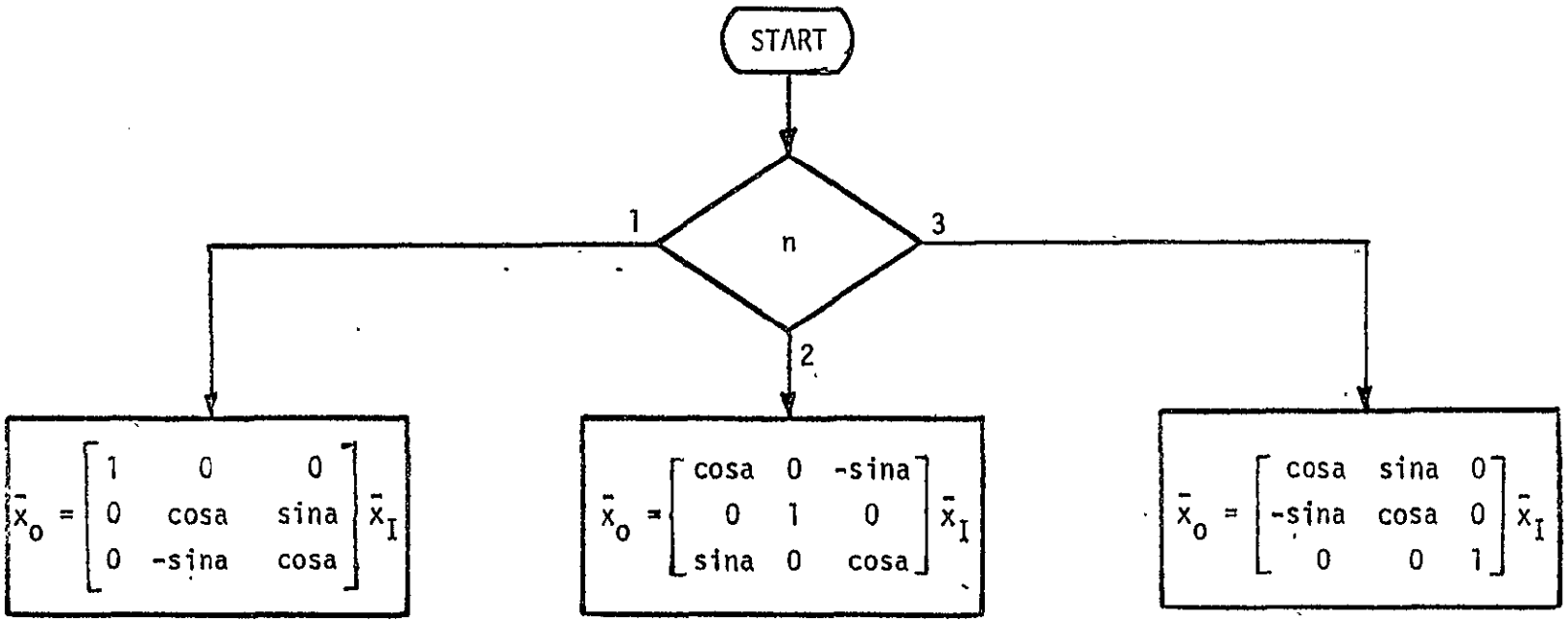

SUBROUTINE UNIT ($\bar{x}$, $\hat{y}$)

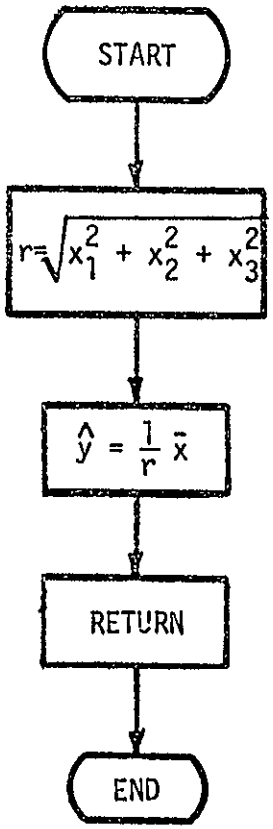

SUBROUTINE DOT ($\bar{x}$,$\bar{y}$,a)

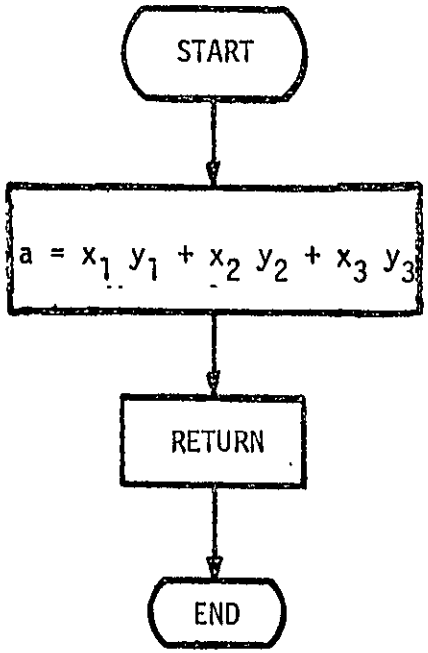

SUBROUTINE

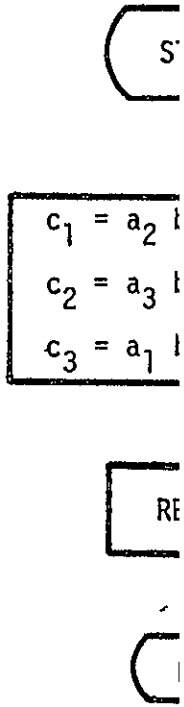

Appendix B

```
00100      PROGRAM LFO(TAPE3,INPUT,OUTPUT,TAPE1=INPUT,TAPE2=OUTPUT,TAPE4)
00110      COMMON/CARR/ATMAST(3),DIRMAST(3),HMAST,RDISH,ALPHAS,
00120     1    ARRW,ARRL,CANT,REARTH
00130      COMMON/CORB/GAMMAI,GAMMAD,RL
00140      COMMON/CML/GAMMAS,GAMMA1,GAMMA2,GAMMAL,RT,ALAT1
00150      COMMON/CUP/DELTA1,DELTAL,DELTAT,FINALT
00160      COMMON/COUT/T1(3),T2(3),S(3)
00170      DIMENSION A(3),B(3),C(3)
00180      F(ARG)=ARG*3.141592654/180.
00190      CALL INPUT
00200      REWIND 4
00210      LAND=2
00220      CALL HEADER(TIME,RL,RT,GAMMA1,GAMMAS,GAMMAL)
00230   10 CONTINUE
00240      A(1)=1.
00250      A(2)=0.
00260      A(3)=0.
00270      CALL ROT(A,-GAMMAS,2,B)
00280      CALL ROT(B,-GAMMAD,3,S)
00290      CALL ROT(S,(F(90.)-GAMMAI),1,B)
00300      CALL ROT(B,GAMMAL,2,C)
00310      CALL ROT(C,F(180.),1,S)
00320      I1=1
00330      I2=1
00340      A(1)=RT
00350      CALL ROT(A,-GAMMA1,3,B)
00360      CALL CITOO(B,GAMMAL,T1)
00370      IF(T1(3).GT.COS(REARTH)) I1=0
00380      CALL ROT(A,-GAMMA2,3,B)
00390      CALL CITOO(B,GAMMAL,T2)
00400      IF(T2(3).GT.COS(REARTH)) I2=0
00410      IF(I1.EQ.1) CALL ARRAY(T1,S,R1)
00420      IF(I2.EQ.1) CALL ARRAY(T2,S,R2)
00430      IF(I1.EQ.0) R1=-20.
00440      IF(I2.EQ.0) R2=-20.
00450      CALL ECLIPSE(S,REARTH,ISUN,IDAY)
00460      CALL LAT(GAMMA1,GAMMAL,GAMMAI,GAMMAD,ALAT1,ALAT,ALONG)
00470      CALL GIMBAL(T1,REARTH,G11,G12,G13)
00480      CALL GIMBAL(T2,REARTH,G21,G22,G23)
00490      CALL LANDSEA(ALAT,-ALONG,LAND)
00500      CALL OUTPUT(TIME,R1,R2,GAMMA1,GAMMA2,GAMMAL,ISUN,IDAY,
00510     1ALAT,ALONG,G11,G12,G21,G22,LAND)
```

```
00520       CALL UPDATE(TIME,GAMMA1,GAMMA2,GAMMAL)
00530       GO TO 10
00540    11 CONTINUE
00550       END
00560       SUBROUTINE INPUT
00570       COMMON/CARR/ATMAST(3),DIRMAST(3),HMAST,RDISH,ALPHAS,
00580      1    ARRW,ARRL,CANT,REARTH
00590       COMMON/CORB/GAMMAI,GAMMAD,RL
00600       COMMON/CML/GAMMAS,GAMMA1,GAMMA2,GAMMAL,RT,ALAT1
00610       COMMON/CUP/DELTA1,DELTAL,DELTAT,FINALT
00620       DIMENSION A(3)
00630       DATA ATMAST/3*0./,DIRMAST/0.,0.,-1./,RDISH/3./,CANT/37.5/,
00640      1ALPHAS/2./,DELTA1/15./,DELTAL/220.31/,RL/7074./,RT/4.224E4/,
00650      2REARTH/64.2/,GAMMA1/0./,GAMMAL/0./,GAMMAS/0./,GAMMAI/98.2/
00660      3,GAMMAD/37.5/,ALAT1/41./
00670       NAMELIST/IN/GAMMA1,GAMMAL,GAMMAS,GAMMAI,REARTH,RL,RT,ATMAST,
00680      1DIRMAST,HMAST,RDISH,ALPHAS,ARRW,ARRL,CANT,DELTAT,FINALT,
00690      2DELTA1,DELTAL,GAMMAD,ALAT1
00700       F(ARG)=ARG*3.141592654/180.
00710       READ(3,IN)
00720       DO 10 I=1,3
00730    10 A(I)=DIRMAST(I)
00740       CALL UNIT(A,DIRMAST)
00750       GAMMA2=GAMMA1-130.
00760       CANT=F(CANT)
00770       REARTH=F(REARTH)
00780       GAMMAS=F(GAMMAS)
00790       GAMMA1=F(GAMMA1)
00800       GAMMA2=F(GAMMA2)
00810       GAMMAL=F(GAMMAL)
00820       GAMMAI=F(GAMMAI)
00830       DELTA1=F(DELTA1)
00840       DELTAL=F(DELTAL)
00850       ALPHAS=F(ALPHAS)
00860       GAMMAD=F(GAMMAD)
00870       ALAT1=F(ALAT1)
00880       RETURN
00890       END
00900       SUBROUTINE UPDATE(TIME,GAMMA1,GAMMA2,GAMMAL)
00910       COMMON/CUP/DELTA1,DELTAL,DELTAT,FINALT
00920       IF(TIME.GE.FINALT) STOP
00930       TIME=TIME+DELTAT
```

```
      GAMMA1=GAMMA1 + DELTAT*DELTA1
      GAMMAL=GAMMAL + DELTAT*DELTAL
      GAMMA2=GAMMA1 - 130.*3.141592654/180.
      RETURN
      END
      SUBROUTINE OUTPUT(TIME,R1,R2,GAMMA1,GAMMA2,GAMMAL,ISUN,
     1IDAY,ALAT,ALONG,G11,G12,G21,G22,LAND)
      COMMON/COUT/T1(3),T2(3),S(3)
   50 FORMAT(1X,1X,F8.3,9(1X,F6.1),4X,I1,3X,I1,2(1X,F6.1),3X,I1)
      F(ARG)=ARG*180./3.141592654
      AL=F(GAMMAL)
      A1=F(GAMMA1)
      A2=F(GAMMA2)
      ALAT=F(ALAT)
      ALONG=F(ALONG)
      G11=F(G11)
      G12=F(G12)
      G21=F(G21)
      G22=F(G22)
      WRITE(4,50)TIME,AL,A1,R1,G11,G12
      1,A2,R2,G21,G22,IDAY,ISUN,ALAT,ALONG,LAND
      RETURN
      ENTRY HEADER
   51 FORMAT(1X,5X,*TIME*,3X,*LF/O*,2X,*TDRS1*,2X,
     1*TRANS*,2X,*GIMBAL ANGLES*,1X,*TDRS2*,2X,*TRANS*,
     22X,*GIMBAL ANGLES*,2X,*DAY*,1X,*SUN*,2X,*LAT*,3X,*LONG*,3X,*LAND*)
      WRITE(4,51)
      RETURN
      END
      SUBROUTINE ARRAY(T,S,RESULT)
      COMMON/CARR/ATMAST(3),DIRMAST(3),HMAST,RDISH,ALPHAS,
     1    ARRW,ARRL,CANT,REARTH
      DIMENSION V(3),E1(3),E2(3),DT(3),DM(3),DA(3),A(3),T(3),S(3)
C     TRANSFORM VECTORS TO ARRAY COORDINATES
      ARRA=-ATAN2(S(1),S(3))
      CALL COTOA(T,ARRA,DT)
      CALL COTOA(DIRMAST,ARRA,DM)
      CALL COTOA(ATMAST,ARRA,DA)
C     FIND ANTENNA PATTERN DIAMETER
      TEMP=-((HMAST*DM(3) + DA(3))/DT(3))
      IF(TEMP.LT.0.) GO TO 300
      ALPHAO=TEMP - RDISH/TAN(REARTH)
```

```
01360       RC=RDISH + ALPHA0*TAN(ALPHAS)
01370 C     DETERMINE EXTENT OF INTERFERENCE
01380       CALL BASIS(DT,E1,E2)
01390       M1=0
01400       M2=0
01410       N=25
01420       DO 10 I=1,N
01430       AI=(2.*I-N-1.)/N
01440       DO 10 J=1,N
01450       AJ=(2.*J-N-1.)/N
01460       DO 11 K=1,3
01470    11 V(K)=RC*(AI*E1(K) + AJ*E2(K))
01480       TEMP=0.
01490       DO 12 K=1,3
01500    12 TEMP=TEMP + V(K)*V(K)
01510       CHECK=SQRT(TEMP)
01520       IF(CHECK.GT.RC) GO TO 10
01530       M1=M1 + 1
01540       ALPHA=-(HMAST*DM(3) + DA(3) + V(3))/DT(3)
01550       DO 13 K=1,2
01560    13 A(K)=HMAST*DM(K) + DA(K) + V(K) + ALPHA*DT(K)
01570       TEMP=2.*ABS(A(1))
01580       IF(TEMP.GT.ARRW) GO TO 10
01590       TEMP=A(2)
01600       IF(TEMP.GT.0.) GO TO 10
01610       IF(TEMP.LT.-ARRL) GO TO 10
01620       M2=M2 + 1
01630    10 CONTINUE
01640       RESULT=100.*(1.-M2/M1)
01650       RETURN
01660   300 RESULT=100.
01670       RETURN
01680       END
01690       SUBROUTINE COTOA(A,PHO,B)
01700       COMMON/CARR/ATMAST(3),DIRMAST(3),HMAST,RDISH,ALPHAS,
01710      1    ARRW,ARRL,CANT,FEARTH
01720       DIMENSION A(3),B(3),C(3)
01730       CALL ROT(A,PHO,2,C)
01740       CALL ROT(C,CANT,1,B)
01750       RETURN
01760       END
01770       SUBROUTINE BASIS(A,B,C)
```

```
01780       DIMENSION A(3),B(3),C(3),D(3),E(3)
01790       N=0
01800       TEMP=0.
01810       DO 9 I=1,3
01820     9 TEMP=TEMP + A(I)*A(I)
01830       TEST=TEMP/10.
01840    10 N=N+1
01850       IF(N.GT.3) GO TO 70
01860       DO 11 I=1,3
01870    11 D(I)=0.
01880       D(N)=1.
01890       CALL CROSS(A,D,E)
01900       TEMP=0.
01910       DO 12 I=1,3
01920    12 TEMP=TEMP + E(I)*E(I)
01930       IF(TEMP.LE.TEST) GO TO 10
01940       CALL UNIT(E,B)
01950       CALL CROSS(A,B,D)
01960       CALL UNIT(D,C)
01970       RETURN
01980    70 DISPLAY*NO BASIS FOUND*
01990       STOP
02000       END
02010       SUBROUTINE ECLIPSE(S,REARTH,ISUN,IDAY)
02020       DIMENSION S(3),A(3)
02030       A(1)=0.
02040       A(2)=0.
02050       A(3)=1.
02060       CALL DOT(S,A,X)
02070       Y=COS(REARTH)
02080       ISUN=1
02090       IDAY=1
02100       IF(X.GT.Y)ISUN=0
02110       IF(X.GT.0.)IDAY=0
02120       RETURN
02130       END
02140       SUBROUTINE LAT(GAMMA1,GAMMAL,GAMMAI,GAMMAD,ALAT1,ALAT,ALONG)
02150       DIMENSION A(3),B(3)
02160       F(ARG)=ARG*3.141592654/180.
02170       G(ARG)=ARG*180./3.141592654
02180       A(1)=1.
02190       A(2)=0.
```

```
      A(3)=0.
      CALL ROT(A,-GAMMAL,2,B)
      CALL ROT(B,(F(90.)-GAMMAI),3,A)
      CALL ROT(A,F(90.),2,B)
      CALL ROT(B,(ALAT1+GAMMAD+GAMMAI),3,A)
      TLAT=ASIN(A(3))
      A(3)=0.
      CALL UNIT(A,B)
      A(1)=1.
      A(2)=0.
      A(3)=0.
      CALL DOT(B,A,C)
      ALONG=ACOS(C)
      IF(B(2).GT.0.) ALONG=-ALONG
      PARAM=(1.00336417)**2
      ALAT=ATAN(PARAM*TAN(TLAT))
      RETURN
      END
      SUBROUTINE GIMBAL(T,REARTH,G1,G2,G3)
      DIMENSION T(3),A(3)
      F(ARG)=ARG*3.141592654/180.
      G3=0.
      CALL UNIT(T,A)
      G1=ATAN2(A(2),A(1))
      G2=ASIN(-A(3))
      TEMP=REARTH - F(90.)
      IF(G2.LT.TEMP) G2=TEMP
      RETURN
      END
      SUBROUTINE CITOG(X,GAMMAL,Y)
      DIMENSION X(3),Y(3),Z(3)
      COMMON/CORB/GAMMAI,GAMMAD,RL
      F(ARG)=ARG*3.141592654/180.
      CALL ROT(X,-GAMMAD,3,Y)
      CALL ROT(Y,(F(90.)-GAMMAI),1,Z)
      CALL ROT(Z,GAMMAL,2,Y)
      CALL ROT(Y,F(180.),1,Z)
      Z(3)=Z(3) + RL
      CALL UNIT(Z,Y)
      RETURN
      END
      SUBROUTINE UNIT(X,Y)
```

```
      DIMENSION X(3),Y(3)
      TEMP=0.
      DO 10 I=1,3
   10 TEMP=TEMP + X(I)*X(I)
      TEMP=SQRT(TEMP)
      DO 20 I=1,3
   20 Y(I)=X(I)/TEMP
      RETURN
      END
      SUBROUTINE DOT(X,Y,A)
      DIMENSION X(3),Y(3)
      A=0.
      DO 10 I=1,3
   10 A=A + X(I)*Y(I)
      RETURN
      END
      SUBROUTINE ROT(XI,A,N,XO)
      DIMENSION XI(3),XO(3)
      IF(N.EQ.2) GO TO 10
      IF(N.EQ.3) GO TO 20
      XO(1)=XI(1)
      XO(2)=XI(2)*COS(A) + XI(3)*SIN(A)
      XO(3)=-XI(2)*SIN(A) + XI(3)*COS(A)
      GO TO 30
   10 XO(1)=XI(1)*COS(A) - XI(3)*SIN(A)
      XO(2)=XI(2)
      XO(3)=XI(1)*SIN(A) + XI(3)*COS(A)
      GO TO 30
   20 XO(1)=XI(1)*COS(A) + XI(2)*SIN(A)
      XO(2)=-XI(1)*SIN(A) + XI(2)*COS(A)
      XO(3)=XI(3)
   30 CONTINUE
      RETURN
      END
      SUBROUTINE CROSS(A,B,C)
      DIMENSION A(3),B(3),C(3)
      C(1)=A(2)*B(3) - A(3)*B(2)
      C(2)=A(3)*B(1) - A(1)*B(3)
      C(3)=A(1)*B(2) - A(2)*B(1)
      RETURN
      END
```

APPENDIX C

DERIVATION OF DYNAMIC EQUATIONS

For simplified dynamic model shown in Figure 3.1, the dynamic equations are derived using the Lagrangian approach. The development here follows closely the one in Appendix A of [4], which starts with a slightly more general model than that shown in Figure 3.1 since it includes a two-degree of freedom spring (flexure) at the hinge point. However, the spring constants K_x and K_y are simply set to infinity for the results here. Variables X_3 and Y_3 are hinge point displacements in a coordinate system fixed to the end of the boom. They will disappear once the flexure is removed.

C.1 Generalized Coordinates and Forces

Choose as generalized coordinates q_k,

$$\bar{q} = (\theta_1, \theta_b, \alpha, y_b, x_1, y_1, x_2, y_2) \tag{C-1}$$

The kinematic relationships with other coordinates are:

$$\theta_2 = \alpha - \theta_1 - \theta_b \tag{C-2}$$

$$x_2 = x_1 + L_1 \cos\theta_1 - y_b \sin\theta_1 + x_3 \cos(\theta_1 + \theta_b) - y_3 \sin(\theta_1 + \theta_b) + L_2 \cos\alpha$$

$$y_2 = y_1 + L_1 \sin\theta_1 + y_b \cos\theta_1 + x_3 \sin(\theta_1 + \theta_b) + y_3 \cos(\theta_1 + \theta_b) + L_2 \sin\alpha$$

Solving the last two equations for x_3 and y_3 yields

$$x_3 = (x_2 - x_1)\cos(\theta_1 + \theta_b) + (y_2 - y_1)\sin(\theta_1 + \theta_b) - L_1 \cos\theta_b - y_b \sin\theta_b - L_2 \cos(\alpha - \theta_1 - \theta_b) \tag{C-3}$$

$$y_3 = (y_2 - y_1)\cos(\theta_1 + \theta_b) - (x_2 - x_1)\sin(\theta_1 + \theta_b) + L_1 \sin\theta_b - y_b \cos\theta_b - L_2 \sin(\alpha - \theta_1 - \theta_b) \quad \text{(C-4)}$$

The generalized external forces Q_k are given by

$$\overline{Q} = (T_1 - T_o, -T_o, T_o, 0, 0, 0, 0, 0)$$

C.2 Spring Matrix for Flexible Boom

Two assumptions are made: (i) Only the first bending mode is significant and higher order modes are neglected. (ii) Only linear bending is considered, i.e., forces acting along the boom do not contribute significantly to the bending since y_b and θ_b are small and since the forces are small.

From Figure A.1,

$$M_1 = F\, l_1 + M_o$$

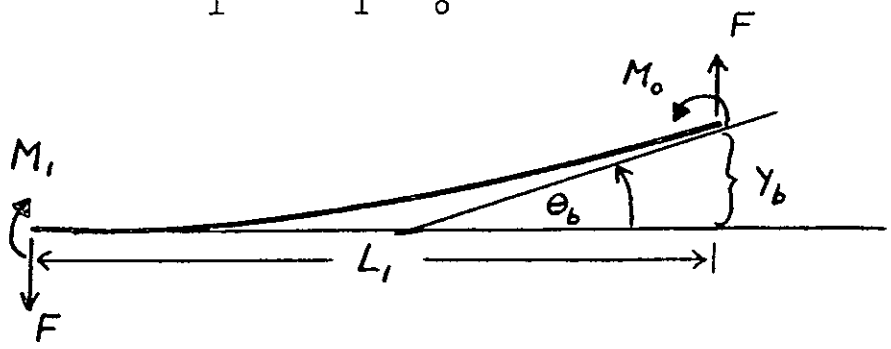

Figure A.1 Flexible Boom

and by the bending moment equation

$$M(x,t) = E\, I \frac{\partial^2 y}{\partial x^2}$$

we obtain

$$y_b = \frac{L_1^3}{3EI} F + \frac{L_1^2}{2EI} M_o \tag{C-5}$$

$$\theta_b = \frac{L_1^2}{2EI} F + \frac{L_1}{EI} M_o \tag{C-6}$$

The spring matrix K_b of the boom satisfies

$$\begin{bmatrix} F \\ M_o \end{bmatrix} = K_b \begin{bmatrix} y_b \\ \theta_b \end{bmatrix} \tag{C-7}$$

so that it is given by

$$K_b = \begin{bmatrix} \frac{12\ EI}{L_1^3} & -\frac{6\ EI}{L_1^2} \\ -\frac{6\ EI}{L_1^2} & \frac{4\ EI}{L_1} \end{bmatrix} \tag{C-8}$$

Thus the potential energy in the boom is

$$V_b = \frac{1}{2} (y_b, \theta_b) K_b \begin{pmatrix} y_b \\ \theta_b \end{pmatrix}$$

or

$$V_b = \frac{2\ EI}{L_1} \left[\theta_b^2 - \frac{3}{L_1} y_b \theta_b + \frac{3}{2} \frac{y_b^2}{L_1} \right] \tag{C-9}$$

C.3 System Energy

The system kinetic energy is given by

$$T = \frac{1}{2} I_1 \dot{\theta}_1^2 + \frac{1}{2} I_2 \dot{\alpha}^2 + \frac{1}{2} m_1 (\dot{x}_1^2 + \dot{y}_1^2) + \frac{1}{2} m_2 (\dot{x}_2^2 + \dot{y}_2^2) \quad \text{(C-10)}$$

and the system potential energy is given by

$$V = \frac{1}{2} k_{\theta 2} (\alpha - \theta_1 - \theta_b)^2 + \frac{1}{2} k_x x_3^2 + \frac{1}{2} k_y y_3^2 + \frac{2EI}{L_1} (\theta_b^2 - \frac{3}{L_1} y_b \theta_b + \frac{3}{L_1^2} y_b^2) \quad \text{(C-11)}$$

C.4 Lagrange Equations of Motion

The equations of motion of the system can then be found by evaluating the Lagrange equations

$$\frac{d}{dt} \left(\frac{\partial L}{\partial \dot{q}_k} \right) - \frac{\partial L}{\partial q_k} = Q_k \, , \; k = 1,2,\ldots,8 \quad \text{(C-12)}$$

where the Lagrangian L is

$$L = T - V \quad \text{(C-13)}$$

The dynamic equations are to be linearized about

$$e : \; x_3 = y_3 = \theta_1 = \theta_b = y_b = 0 \quad \text{(C-14)}$$

but admit a large angle α. The linearized expressions for x_3 and y_3 in terms of the other variables are thus

$$x_3 = x_2 - x_1 - L_1 - L_2 \cos \alpha \quad \text{(C-15)}$$

$$y_3 = y_2 - y_1 - y_b - L_1 \theta_1 - L_2 \sin \alpha \quad \text{(C-16)}$$

The differentiations indicated by (A.12) must however be performed before linearization takes place. Evaluation of (A.12) leads to the following eight equations:

$$I_1 \ddot{\theta}_1 - k_{\theta 2} (\alpha - \theta_1 - \theta_b) - k_y L_1 (y_2 - y_1 - y_b - L_1 \theta_1 - L_2 \sin \alpha) = T_1 - T_o \quad \text{(C-17)}$$

$$-k_{\theta 2} (\alpha - \theta_1 - \theta_b) + \frac{4EI}{L_1} \theta_b - \frac{6EI}{L_1^2} y_b = -T_o \quad \text{(C-18)}$$

$$I_2 \ddot{\alpha} + k_{\theta 2} (\alpha - \theta_1 - \theta_b) + k_x L_2 \sin \alpha (x_2 - x_1 - L_1 - L_2 \cos \alpha) - k_y L_2 \cos \alpha (y_2 - y_1 - y_b - L_1 \theta_1 - L_2 \sin \alpha) = T_o \quad \text{(C-19)}$$

$$-k_y (y_2 - y_1 - y_b - L_1 \theta_1 - L_2 \sin \alpha) - \frac{6EI}{L_1^2} \theta_b + \frac{12EI}{L_1^3} y_b = 0 \quad \text{(C-20)}$$

$$m_1 \ddot{x}_1 - k_x (x_2 - x_1 - L_1 - L_2 \cos \alpha) = 0 \quad \text{(C-21)}$$

$$m_1 \ddot{y}_1 - k_y (y_2 - y_1 - y_b - L_1 \theta_1 - L_2 \sin \alpha) = 0 \quad \text{(C-22)}$$

$$m_2 \ddot{x}_2 + k_x (x_2 - x_1 - L_1 - L_2 \cos \alpha) = 0 \quad \text{(C-23)}$$

$$m_2 \ddot{y}_2 + k_y (y_2 - y_1 - y_b - L_1 \theta_1 - L_2 \sin \alpha) = 0 \quad \text{(C-24)}$$

Equations (A.18) and (A.20) contain no derivatives and thus indicate a dependence among the generalized coordinates. This should cause no concern in this case since the equations merely indicate a static equilibrium condition among some of the coordinates which is a part of the dynamic equilibrium solution of the system. The static equilibrium is caused by the assumption that the boom and the spring are masaless.

To eliminate θ_b and y_b, combine equations (A.17), (A.19) and (A.24) to obtain

$$I_1 \ddot{\theta}_1 + I_2 \ddot{\alpha} + k_x L_2 \sin \alpha (x_2 - x_1 - L_1 - L_2 \cos \alpha) + (L_1 + L_2 \cos \alpha) m_2 \ddot{y}_2 = T_1 \quad \text{(C-25)}$$

From Equations (A.19), (A.20) and (A.24) it follows that

$$L_1 I_2 \ddot{\alpha} + k_{\theta 2} (L_1 \alpha + 2L_2 \sin \alpha + L_1 \theta_1) - m_2 \ddot{y}_2 \left[k_{\theta 2} \left(\frac{L_1 C_1}{3} + \frac{2}{k_y} \right) - L_1 L_2 \cos \alpha \right] - 2k_{\theta 2} (y_2 - y_1) + k_x L_1 L_2 \sin \alpha (x_2 - x_1 - L_1 - L_2 \cos \alpha) = L_1 T_o \quad \text{(C-26)}$$

where

$$C_1 = \frac{L_1^2}{2EI}$$

Furthermore, combining (A.17), (A.18), (A.20) and (A.24) results in

$$C_1 I_1 \ddot{\theta}_1 + L_1 \theta_1 + L_2 \sin \alpha + m_2 \ddot{y}_2 \left(\frac{L_1 C}{3} - \frac{1}{k_y}\right) - (y_2 - y_1) = C_1 T_1 \tag{C-27}$$

Combine also equations (A.22) and (A.24), and (A.21) and (A.23) and obtain

$$m_1 \ddot{y}_1 + m_2 \ddot{y}_2 = o \tag{C-28}$$

and

$$m_1 \ddot{x}_1 + m_2 \ddot{x}_2 = o \tag{C-29}$$

and rewrite (A.23)

$$m_2 x_2 + k_x (x_2 - x_1 - L_1 - L_2 \cos \alpha) = o \tag{C-30}$$

Equations (A.25) - (A.30) are a set of six independent equations in the six unknowns x_1, x_2, y_1, y_2, θ_1 and α.

Let now

$$x = x_2 - x_1 \quad \text{and} \quad y = y_2 - y_1 \tag{C-31}$$

since the quantities of primary interest are the relative positions and velocity of bodies m_1 and m_2 with respect to each other. Using (A.31) together with (A.28) and (A.29), the following equations are obtained by letting k_x and k_y approach infinity.

$$I_1 \ddot{\theta}_1 + I_2 \ddot{\alpha} + a_o (L_1 \ddot{y} + L_2 \ddot{y} \cos \alpha - L_2 \ddot{x} \sin \alpha) = T_1 \quad \text{(C-32)}$$

$$L_1 I_2 \ddot{\alpha} + k_{\theta 2} (L_1 \alpha + 2L_2 \sin \alpha) + k_{\theta 2} L_1 \theta_1 -$$

$$a_1 a_o \ddot{y} + L_1 L_2 a_o \ddot{y} \cos \alpha \quad \text{(C-33)}$$

$$- 2 k_{\theta 2} y - a_o L_1 L_2 \ddot{x} \sin \alpha = L_1 T_o$$

$$C_1 I_1 \ddot{\theta}_1 + L_1 \theta_1 + L_2 \sin \alpha + a_o a_2 \ddot{y} - y = C_1 T_1 \quad \text{(C-34)}$$

$$x - L_1 - L_2 \cos \alpha = o \quad \text{(C-35)}$$

where

$$a_o = \frac{m_1 m_2}{m_1 + m_2} \qquad a_1 = k_{\theta 2} \frac{L_1 C_1}{3}$$

$$a_2 = \frac{L_1 C_1}{3} \qquad C_1 = \frac{L_1^2}{2EI}$$

Equations (C-32) - (C-35) are four equations in four unknowns describing the dynamic behavior of the system. They are identical to Equations (6.2-1) - (6.2-4)

APPENDIX D

DETERMINATION OF TRANSFER FUNCTION COEFFICIENTS AND POLYNOMIAL ROOTS

This Appendix lists the coefficients of the polynomials that comprise the transfer functions of equations (3.15) to (3.18). These are followed by a listing of a FORTRAN program to evaluate the coefficients and extract the roots.

The open loop characteristic polynomial p(s) is given by

$$p(s) = s^2 (a_4 s^4 + a_2 s^2 + a_o) \tag{D-1}$$

where

$$a_4 = -m_2 L_1 I_1 I_2 C_1 \left[\frac{2}{3} L_1 + k_{\theta 2} \frac{C_1}{3}\right] \tag{D-2}$$

$$\begin{aligned} a_2 = {} & m_2 L_1 C_1 k_{\theta 2} \left[\frac{1}{3} L_1 I_1 + L_2 I_1 - \frac{2}{3} L_1 I_2\right] \\ & - k_{\theta 2} m_2 I_1 C_1 \left[2 I_2 \left(\frac{1}{m_2} + \frac{1}{m_1}\right) + (L_1 + L_2)(L_1 + 2 L_2)\right] \\ & - m_2 L_1 \left[L_2^2 I_1 + L_1^2 I_2 + I_1 I_2 \left(\frac{1}{m_2} + \frac{1}{m_1}\right)\right] \end{aligned} \tag{D-3}$$

$$a_o = -\frac{k_{\theta 2} L_1}{m_1} \left[(m_1 + m_2)(I_1 + I_2) + m_1 m_2 (L_1 + L_2)^2\right] \tag{D-4}$$

Next consider the individual transfer functions.

$$G_{11}(s) = \frac{d_4 s^4 + d_2 s^2 + d_o}{p(s)} \tag{D-5}$$

$$d_4 = - m_2 L_1 C_1 I_2 \left[\frac{2}{3} L_1 + k_{\theta 2} \frac{C_1}{3}\right] \tag{D-6}$$

$$d_2 = - m_2 L_1 I_2 \left[\frac{1}{m_2} + \frac{1}{m_1} + \frac{2 k_{\theta 2} C_1}{L_1} \left(\frac{1}{m_2} + \frac{1}{m_1}\right)\right]$$

$$- m_2 L_1 C_1 k_{\theta 2} \left[2 L_2 + \frac{2}{3} L_1 + \frac{2 L_2^2}{L_1}\right] - m_2 L_1 L_2^2 \tag{D-7}$$

$$d_o = - k_{\theta 2} L_1 \left(1 + \frac{m_2}{m_1}\right) \tag{D-8}$$

$$\frac{d_4}{a_4} = \frac{1}{I_1} \tag{D-9}$$

$$G_{21}(s) = \frac{C_2 s^2 + C_o}{p(s)} \tag{D-10}$$

$$C_2 = m_2 L_1 k_{\theta 2} \left[L_2 C_1 + \frac{L_1 C_1}{3}\right] + m_2 L_1^2 L_2 \tag{D-11}$$

$$C_o = - k_{\theta 2} L_1 \left(1 + \frac{m_2}{m_1}\right) \tag{D-12}$$

$$K_{12} = \frac{C_2}{a_4} \tag{D-13}$$

$$G_{10}(s) = \frac{s^2 (f_2 s^2 + f_o)}{p(s)} = \frac{f_2 s^2 + f_o}{a_4 s^4 + a_2 s^2 + a_o} \quad \text{(D-14)}$$

$$f_2 = - L_1 I_2 m_2 \frac{L_1 C_1}{3} \quad \text{(D-15)}$$

$$f_o = L_1 I_2 \left(1 + \frac{m_2}{m_1}\right) + L_1 L_2 m_2 (L_1 + L_2) \quad \text{(D-16)}$$

$$K_{10} = \frac{f_2}{a_4} \quad \text{(D-17)}$$

$$G_{20}(s) = \frac{s^2 (g_2 s^2 + g_o)}{p(s)} = \frac{g_2 s^2 + g_o}{s_4 s^4 + a_2 s^2 + a_o} \quad \text{(D-18)}$$

$$g_2 = L_1 I_1 m_2 \frac{L_1 C_1}{3} - L_1 C_1 I_1 m_2 (L_1 + L_2) \quad \text{(D-19)}$$

$$g_o = - L_1 I_1 \left(1 + \frac{m_2}{m_1}\right) - L_1^2 m_2 (L_1 + L_2) \quad \text{(D-20)}$$

$$K_{20} = \frac{g_2}{a_4} \quad \text{(D-21)}$$

```
      PROGRAM KOEFFS (INPUT,OUTPUT,TAPE7)
      COMPLEX Z, ZZ
      DIMENSION A(5), Z(4)
      DIMENSION AA(7), ZZ(6)
C
      DATA RM1,RM2,RI1,RI2 /1497., 29.84, 2671., 4.4 /
      DATA RL1,RL2,EI     /3.84, 0.3, 49623. /
      DATA RKTHET2 /0.0135562   /
      DATA RK11, F11 / 2003.25,  0.7 /
      NDEG = 4
C
      RM = (1./RM1 + 1./RM2)
C
      C1 = 0.5*RL1**2/EI
      D0 = -RKTHET2*RL1*(1.+RM2/RM1)
      D2 = -RM2*RL1*RI2*(RM + 2.*RKTHET2*C1*RM/RL1) - RM2*RL1*
     1     C1*RKTHET2*(2.*RL2 + .6666667*RL1 + 2.*RL2**2/RL1)
     2     -RM2*RL1*RL2*RL2
      D4 = -RM2*RL1*C1*RI2*(.66667*RL1 + RKTHET2*C1/3.)
C
      A0 = -(RKTHET2*RL1/RM1)*((RM1+RM2)*(RI1+RI2)
     1     + RM1*RM2*(RL1+RL2)*(RL1+RL2))
      A2 = RM2*RL1*C1*RKTHET2*(RL1*RI1/3. + RL2*RI1
     1     - .666667*RL1*RI2)
     2     -RKTHET2*RM2*RI1*C1*(2.*RI2*RM
     3     +(RL1+RL2)*(RL1 + 2.*RL2))
     4     -RM2*RL1*(RL2*RL2*RI1 + RL1*RL1*RI2 + RI1*RI2*RM)
      A4 = -RM2*RL1*RI1*RI2*C1*(.66667*RL1 + RKTHET2*C1/3.)
C
      WRITE(7,100) D0, D2, D4
  100 FORMAT( * D0, D2, D4, * 3E16.6 )
      WRITE(7,101) A0, A2, A4
  101 FORMAT(/* A0, A2, A4, * 3E16.6 )
C
      A(1) = 1.
      A(2) = 0.
      A(3) = A2/A4
      A(4) = 0.
      A(5) = A0/A4
C
      CALL ZPOLR( A, NDEG, Z, IER)
C
```

```
      WRITE(7,105)
      WRITE(7,102) Z(1)
      WRITE(7,102) Z(2)
      WRITE(7,102) Z(3)
      WRITE(7,102) Z(4)
  102 FORMAT(/6X, E16.6, 3X, E16.6)
C
      A(1) = 1.
      A(2) = 0.
      A(3) = D2/D4
      A(4) = 0.
      A(5) = D0/D4
      WRITE(7,105)
C
      CALL ZPOLR( A, NDEG, Z, IER)
C
      WRITE(7,102) Z(1)
      WRITE(7,102) Z(2)
      WRITE(7,102) Z(3)
      WRITE(7,102) Z(4)
      WRITE(7,105)
C
C     CLOSED LOOP FUNCTION COEFFICIENTS
C
C
      RK22 = 1.0
      F22 = 14.14
      A0=RK11*F11
      A1=RKTHET2*RL1
      A3=C1*R11
      A4=C1*RK11
      A5=C1*A0+RL1
C
      B0=RK22*F22
      B1=RL1*RI2
      B2=RL1*RK22
      B3=RL1*B0 + RKTHET2*(RL1+2.*RL2)
C
      D0=RM2*(RL1+RL2)
      D1=-RM2*(RKTHET2*(C1*RL1/3.) -RL1*RL2)
      D2=-2.*RKTHET2*(1.+RM2/RM1)
      D3=RM2*(RL1*C1/3.)
```

```
      D4=-(1.+RM2/RM1)
C
      C6=RI1*B1*D3+D1*RI2*A3-D0*A3*B1
      C5=D3*(RI1*B2+RK11*B1)+D1*(RI2*A4+RK22*A3)-D0*(A3*B2+A4*B1)
      C4=D3*(RI1*B3+RK11*B2+A0*B1)
      C4=C4+D4*RI1*B1+D1*(RI2*A5+RK22*A4+B0*A3)+D2*RI2*A3
      C4=C4-D0*(A3*B3+A4*B2+A5*B1)-RL2*D1*RI1-A1*D3*RI2
      C3=D3*(RK11*B3+A0*B2)+D4*(RI1*B2+RK11*B1)+D1*(RK22*A5+B0*A4)
      C3=C3+D2*(RI2*A4+RK22*A3)-D0*(A4*B3+A5*B2)-RL2*D1*RK11
      C3=C3-A1*D3*RK22
      C2=A0*B3*D3+D4*(RI1*B3+RK11*B2+A0*B1)+D1*B0*A5+A1*RL2*D0
      C2=C2+D2*(RI2*A5+RK22*A4-B0*A3)-D0*A5*B3-RL2*(A0*D1+D2*RI1)
      C2=C2-A1*(D3*B0+D4*RI2)
      CX=D4*(RK11*B3+A0*B2)+D2*(RK22*A5+B0*A4)-RL2*D2*RK11
      CX=CX-A1*D4*RK22
      C0=D4*A0*B3+D2*B0*A5-RL2*A0*D2-A1*D4*B0
C
      U4=RL1*(RI1*D3-D0*A3)
      U3=RL1*(RK11*D3-D0*A4)
      U2=RL1*(A0*D3+RI1*D4-D0*A5)
      U1=RL1*RK11*D4
      U0=RL1*A0*D4
C
      WRITE(7,103)
  103 FORMAT(* A4..A0, B3..B0, C6..C0, D4..D0, U4..U0 *)
      WRITE(7,105)
      WRITE(7,104)A4,A3,A2,A1,A0
      WRITE(7,105)
  105 FORMAT( / )
      WRITE(7,104) B3,B2,B1,B0
      WRITE(7,105)
      WRITE(7,104) C6,C5,C4,C3,C2,CX,C0
      WRITE(7,105)
      WRITE(7,104)D4,D3,D2,D1,D0
      WRITE(7,105)
      WRITE(7,104)U4,U3,U2,U1,U0
  104 FORMAT(*   *E14.4/)
C
      A(1) = 1.0
      A(2) = U3/U4
      A(3) = U2/U4
      A(4) = U1/U4
```

```
      A(5) = U0/U4
C
      CALL ZPOLR( A, NDEG, Z, IER)
C
      WRITE(7,102) Z(1)
      WRITE(7,102) Z(2)
      WRITE(7,102) Z(3)
      WRITE(7,102) Z(4)
      WRITE(7,105)
C
      AA(1) = 1.0
      AA(2) = C5/C6
      AA(3) = C4/C6
      AA(4) = C3/C6
      AA(5) = C2/C6
      AA(6) = CX/C6
      AA(7) = C0/C6
C
      NDEG = 6
C
      CALL ZPOLR( AA, NDEG, ZZ, IER )
C
      WRITE(7,102) ZZ(1)
      WRITE(7,102) ZZ(2)
      WRITE(7,102) ZZ(3)
      WRITE(7,102) ZZ(4)
      WRITE(7,102) ZZ(5)
      WRITE(7,102) ZZ(6)
C
      RKRTLOC = U4/C6
C
      WRITE(7,105)
      WRITE(7,106) RKRTLOC
  106 FORMAT(*ROOT LOCUS GAIN U4/C6 =* E16.6)
C
      WRITE(7,105)
      WRITE(7,107) RK11, F11, RK22, F22
      WRITE(7,105)
  107 FORMAT(* RK11, F11, RK22, F22, *  7X,3E10.2,/30X,3E10.2)
      WRITE(7,105)
      WRITE (7,108) RM1,RM2,RL1,RL2,RI1,RI2
  108 FORMAT(* RM1, RM2, RL1, RL2, RI1, RI2 * 3E10.2,/30X,3E10.2)
```

```
      WRITE(7,105)
      WRITE (7,109) EI,  RKTHET2
  109 FORMAT(* EI, RKTHET2,                    *2E12.2)
C
      STOP
      END
```

APPENDIX E

BENDING MODE EQUATIONS OF MOTION

The derivation of the bending mode equations of motion for the model in Figure 6-33 is lengthy and entirely similar to the derivation of the LANDSAT antenna mast bending equations. Since this derivation is performed in Appendix C and Reference [4], it is not duplicated here. Only the necessary refinements to obtain the final form of the equations are given. The notation of Appendix C and Reference [4] agrees with that here except that $T_a(t)$ here represents the vehicle torque while $T_1(t)$ is the corresponding torque in Appendix C and/or Reference [4].

From Appendix B of Reference [4], the transfer function relating $\theta_1(s)$ to $T_1(s)$ is

$$\frac{\theta_1(s)}{T_a(s)} = \frac{\alpha_4 S^4 + \alpha_2 S^2 + \alpha_0}{S^2 (\beta_4 S^4 + \beta_2 S^2 + \beta_0}$$

where the α_i and β_i are given by

$$\alpha_4 = - m_2 L_1 C_1 I_2 \left[\frac{2}{3} L_1 + k_{\theta 2} \frac{C_1}{3}\right]$$

$$\alpha_2 = - m_2 L_1 I_2 \left[\frac{1}{m_2} + \frac{1}{m_1} + \frac{2 k_{\theta 2} C_1}{L_1} \left(\frac{1}{m_2} + \frac{1}{m_1}\right)\right]$$

$$- m_2 L_1 C_1 k_{\theta 2} \left[2 L_2 + \frac{2}{3} L_1 + \frac{2 L_2^2}{L_1}\right] - m_2 L_1 L_2^2$$

$$\alpha_0 = - k_{\theta 2} L_1 \left(1 + \frac{m_2}{m_1}\right)$$

and

$$\beta_4 = -m_2 L_1 I_1 I_2 C_1 \left[\frac{2}{3} L_1 + k_{\theta 2} \frac{C_1}{3}\right]$$

$$\beta_2 = m_2 L_1 C_1 k_{\theta 2} \left[\frac{1}{3} L_1 I_1 + L_2 I_1 - \frac{2}{3} L_1 I_2\right]$$

$$- k_{\theta 2} m_2 I_1 C_1 \left[2 I_2 \left(\frac{1}{m_2} + \frac{1}{m_1}\right) + (L_1 + L_2)(L_1 + 2 L_2)\right]$$

$$- m_2 L_1 \left[L_2^2 I_1 + L_1^2 I_2 + I_1 I_2 \left(\frac{1}{m_2} + \frac{1}{m_1}\right)\right]$$

$$\beta_0 = - \frac{k_{\theta 2} L_1}{m_1} \left[(m_1 + m_2)(I_1 + I_2) + m_1 m_2 (L_1 + L_2)^2\right]$$

Setting L_2 equal to zero, and $K_{\theta 2}$ equal to a very large spring constant yields the new set of coefficients α_2' and β_2' for the present system. It was found that, for the present array inertia, values of $K_{\theta 2} \approx 10^5$ N-m/rad or above gave essentially no change in the roots of the numerator and denominator polynomials and thus 10^5 N-m/rad is considered an infinite spring constant here. Using the computed α_2' and β_2', the transfer functions in (3-1) and (3-2) were evaluated and solved for the closed-loop poles and zeros.

APPENDIX F

DETERMINATION OF K_1 FOR ARRAY MODEL

Before computing the array K_1, some definitions are necessary. Starred quantities represent normalized quantities required in computing K_1.

$$\omega_1^* = \omega_1 \sqrt{\frac{\sigma w}{P}}\, \ell$$

σ = Mass/area

ℓ = Array Length

w = Array width

P = Tension on array

M = Array tip mass

$$M^* = \frac{m}{\sigma w \ell}$$

I_{2b} = Vehicle Inertia

$$I_{2b}^* = \frac{I_{2b}}{\sigma w^3 \ell}$$

$$I_2^* = I_{2b}^* + \frac{1}{6}(1 + m^*)$$

The following mode function is also required,

$$f_n(\lambda) = \cos \omega_n^* \lambda - 1 - 6\, I_{2b}^*\, \omega_n^* \sin \omega_n^* \lambda$$

and is used to compute θ_n^2 by the relation

$$\theta_n^2 = \frac{6}{\int_0^1 f_n^2(\lambda)\, d\lambda + m^* f_n^2(1)}$$

With the above quantities computed, K_1 may be computed by the relation

$$k_n = \frac{I_2^* \theta_n^2}{1 - I_2^* \theta_n^2}$$

After the integration is performed, a computer program can be written to rapidly evaluate the various coefficients for different system parameters. This facilitates repeated evaluation of K_1 for sensitivity studies. Further details on the calculation of K_1 may be found in "Recent Advances in the Attitude Dynamics of Spacecraft with Flexible Solar Arrays" by R. C. Hughes in the April 1973 issue of Canadian Aeronautics and Space Journal.